MCEER
EARTHQUAKE ENGINEERING TO EXTREME EVENTS

ISSN 1520-295X

Seismic Isolation of Nuclear Power Plants using Sliding Bearings

by
Manish Kumar, Andrew S. Whittaker
and Michael C. Constantinou

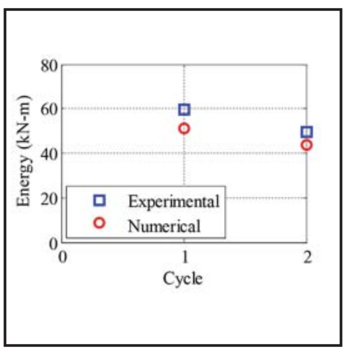

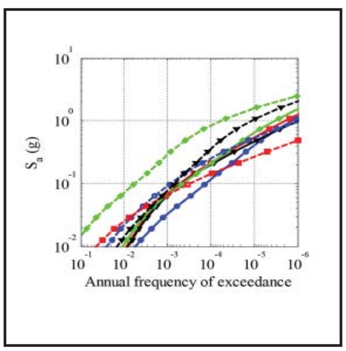

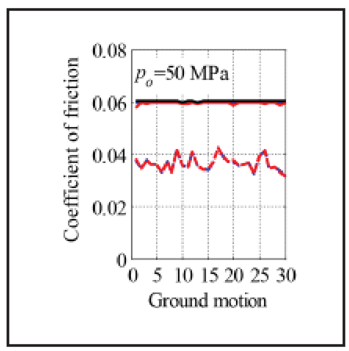

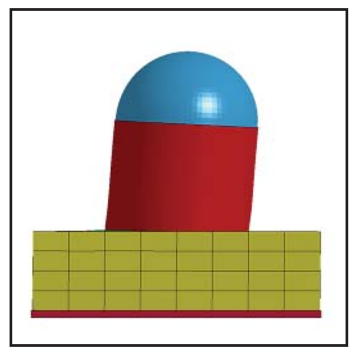

Technical Report MCEER-15-0006

December 27, 2015

This research was conducted at the University at Buffalo, State University of New York, and was supported by MCEER and The Regents of the University of California-Lawrence Berkeley National Laboratory Subcontract No. 6978802, issued under U.S. Deparment of Energy Prime Contract DE-AC02-05CH11231.

Seismic Isolation of Nuclear Power Plants using Sliding Bearings

by

Manish Kumar,[1] Andrew S. Whittaker[2] and Michael C. Constantinou[3]

Publication Date: May 8, 2015
Submittal Date: December 27, 2015

Technical Report MCEER-15-0006

MCEER Thrust Area 3: Innovative Technologies and
Subcontract No. 6978802 from The Regents of the University of California-
Lawrence Berkeley National Laboratory issued under
U.S. Dept. of Energy Prime Contract DE-AC02-05CH11231

1 Assistant Professor, Discipline of Engineering, Indian Institute of Technology Gandhinagar; former graduate student, Department of Civil, Structural and Environmental Engineering, University at Buffalo, State University of New York
2 Professor, Chair, and MCEER Director, Department of Civil, Structural and Environmental Engineering, University at Buffalo, State University of New York
3 SUNY Distinguished Professor, Department of Civil, Structural and Environmental Engineering, University at Buffalo, State University of New York

MCEER
University at Buffalo, State University of New York
212 Ketter Hall, Buffalo, NY 14260
E-mail: *mceer@buffalo.edu*; Website: *http://mceer.buffalo.edu*

PREFACE

MCEER is a national center of excellence dedicated to the discovery and development of new knowledge, tools and technologies that equip communities to become more disaster resilient in the face of earthquakes and other extreme events. MCEER accomplishes this through a system of multidisciplinary, multi-hazard research, in tandem with complimentary education and outreach initiatives.

Headquartered at the University at Buffalo, The State University of New York, MCEER was originally established by the National Science Foundation in 1986, as the first National Center for Earthquake Engineering Research (NCEER). In 1998, it became known as the Multidisciplinary Center for Earthquake Engineering Research (MCEER), from which the current name, MCEER, evolved.

Comprising a consortium of researchers and industry partners from numerous disciplines and institutions throughout the United States, MCEER's mission has expanded from its original focus on earthquake engineering to one which addresses the technical and socio-economic impacts of a variety of hazards, both natural and man-made, on critical infrastructure, facilities, and society.

The Center derives support from several Federal agencies, including the National Science Foundation, Federal Highway Administration, National Institute of Standards and Technology, Department of Homeland Security/Federal Emergency Management Agency, and the State of New York, other state governments, academic institutions, foreign governments and private industry.

This report presents a study on the seismic isolation of nuclear power plants (NPPs), with a focus on single concave sliding bearings. The key goals of the study were to 1) characterize the coefficient of friction at the sliding surface, 2) determine the influence of the definition of the coefficient of friction and alternate representations of seismic hazard on the response of isolated NPPs, and 3) quantify the seismic vulnerability of isolated NPPs. Consideration of heating effects may substantially influence the response of an isolated NPP. The uniform hazard response spectrum should be used to define seismic hazard for analysis of isolated NPPs with explicit consideration of the difference in amplitude of the orthogonal horizontal components of ground shaking. A hard stop must be provided to ensure that failure of the isolation system is not a key contributor to the seismic core damage frequency. Seismic risk can be reduced by designing and testing isolators for displacements greater than those expected in beyond design basis shaking.

ABSTRACT

Nuclear power plants (NPP) are designed for earthquake shaking with very long return periods. Seismic isolation is a viable strategy to protect NPPs from extreme earthquake shaking because it filters a significant fraction of earthquake input energy. This study addresses the seismic isolation of NPPs using sliding bearings, with a focus on the single concave Friction Pendulum™ (FP) bearing.

Friction at the sliding surface of an FP bearing changes continuously during an earthquake as a function of sliding velocity, axial pressure and temperature at the sliding surface. The temperature at the sliding surface, in turn, is a function of the histories of coefficient of friction, sliding velocity and axial pressure, and the travel path of the slider. A simple model to describe the complex interdependence of the coefficient of friction, axial pressure, sliding velocity and temperature at the sliding surface is proposed, and then *verified* and *validated*.

Seismic hazard for a seismically isolated nuclear power plant is defined in the United States using a uniform hazard response spectrum (UHRS) at mean annual frequencies of exceedance (MAFE) of 10^{-4} and 10^{-5}. A key design parameter is the clearance to the hard stop (CHS), which is influenced substantially by the definition of the seismic hazard. Four alternate representations of seismic hazard are studied, which incorporate different variabilities and uncertainties. Response-history analyses performed on single FP-bearing isolation systems using ground motions consistent with the four representations at the two shaking levels indicate that the CHS is influenced primarily by whether the observed difference between the two horizontal components of ground motions in a given set is accounted for in the analyses.

The UHRS at the MAFE of 10^{-4} is increased by a design factor ($\geq$ 1) for a conventional (fixed-base) nuclear structure to achieve a target annual frequency of unacceptable performance. Risk-oriented calculations are performed for eight sites across the United States to show that the factor is equal to 1.0 for seismically isolated NPPs, if the risk is dominated by horizontal earthquake shaking.

Response-history analyses using different models of seismically isolated NPPs are performed to understand the importance of the choice of friction model, model complexity and vertical ground motion for calculating horizontal displacement response across a wide range of sites and shaking intensities. A friction model for the single concave FP bearing should address heating. The pressure- and velocity-dependencies were not important for the models and sites studied. Isolation-system displacements can be computed using a macro model comprising a single FP bearing.

ACKNOWLEDGEMENTS

This research project is supported by a grant to MCEER from the United States Nuclear Regulatory Commission (USNRC) and the Lawrence Berkeley National Laboratory (LBNL). This financial support is gratefully acknowledged.

A review panel was formed by LBNL to help guide our work and to provide timely feedback on interim deliverables. We sincerely thank members of the panel for their intellectual contributions to the project: Dr. Robert Budnitz (Chair), Dr. Nilesh Chokshi, Dr. Antonio Godoy, Dr. James Johnson, Dr. Annie Kammerer, Dr. Robert Kennedy, Mr. Don Moore, and Professor Jonathan Stewart.

Robert Roche provided the DYNA model of the sample nuclear power plant studied in this report. Yin-Nan Huang of the National Taiwan University supplied the ground motions for response-history analysis. We thank Drs. Roche and Huang for their assistance.

Any opinions, finding and conclusions or recommendations expressed in this publication are those of the authors and do not necessarily reflect the views of MCEER, the University at Buffalo, LBNL or the USNRC.

TABLE OF CONTENTS

TABLE OF CONTENTS (CONT'D)

TABLE OF CONTENTS (CONT'D)

TABLE OF CONTENTS (CONT'D)

TABLE OF CONTENTS (CONT'D)

TABLE OF CONTENTS (CONT'D)

TABLE OF CONTENTS (CONT'D)

TABLE OF CONTENTS (CONT'D)

LIST OF FIGURES

LIST OF FIGURES (CONT'D)

LIST OF FIGURES (CONT'D)

LIST OF FIGURES (CONT'D)

LIST OF FIGURES (CONT'D)

LIST OF FIGURES (CONT'D)

Figure **Title** **Page**

LIST OF FIGURES (CONT'D)

Figure **Title** **Page**

LIST OF FIGURES (CONT'D)

Figure **Title** **Page**

LIST OF FIGURES (CONT'D)

LIST OF FIGURES (CONT'D)

LIST OF FIGURES (CONT'D)

Figure **Title** **Page**

LIST OF FIGURES (CONT'D)

Figure **Title** **Page**

LIST OF FIGURES (CONT'D)

Figure **Title** **Page**

LIST OF FIGURES (CONT'D)

Figure **Title** **Page**

LIST OF FIGURES (CONT'D)

Figure **Title** **Page**

LIST OF FIGURES (CONT'D)

LIST OF FIGURES (CONT'D)

Figure **Title** **Page**

LIST OF FIGURES (CONT'D)

Figure **Title** **Page**

LIST OF FIGURES (CONT'D)

LIST OF FIGURES (CONT'D)

LIST OF FIGURES (CONT'D)

LIST OF TABLES

LIST OF TABLES (CONT'D)

LIST OF TABLES (CONT'D)

LIST OF TABLES (CONT'D)

CHAPTER 1

INTRODUCTION

1.1 Nuclear Power Plants and Seismic Isolation

In the United States, nuclear power plants (NPPs) are designed for severe internal and external hazards, including earthquakes. Severe earthquakes can challenge new and existing NPPs, with large forces expected in their internal structures, systems and components (SSCs) in design basis shaking. Base isolation is a viable strategy to seismically protect SSCs in NPPs, since it effectively filters a significant fraction of the high frequency horizontal earthquake shaking, and it facilitates standardization of plant designs.

Two impediments to the deployment of base isolation in nuclear power plant structures have been a) a small number of new build NPPs in the United States, and b) a lack of regulatory guidance. The forthcoming NUREG (Kammerer *et al.*, forthcoming) will address the second impediment by providing guidance on analysis and design of seismically isolated NPPs and on testing of prototype and production isolators. This NUREG will identify three types of bearings that could be used to seismically isolate an NPP in the United States: Low damping rubber (LDR), Lead rubber (LR) and Friction Pendulum™ (FP) bearings. This study focuses on the seismic isolation of NPPs using single FP bearings, with emphases on isolator behavior, system response and risk calculations.

1.2 Objectives of the Report

The key objectives of this report are:

i. Develop and code a model to characterize the coefficient of friction at the sliding surface accounting for changes in the coefficient of friction with sliding velocity, temperature at the sliding surface and axial pressure during the course of earthquake-induced shaking,
ii. Verify and validate the code, following ASME best practice in computational mechanics,
iii. Examine the influence of alternate seismic hazard definitions on the distribution of isolation-system displacements,
iv. Perform risk-based calculations to compute design factors for seismically isolated nuclear power plants, and
v. Understand the influence of modeling choices (e.g., friction model) and loading condition (e.g., static axial pressure, inclusion of vertical ground motion) on the response quantities.

1.3 Organization of the Report

This report is organized into ten chapters and nine appendices. A brief introduction to the seismic isolation of structures is presented in Chapter 2. A model to account for the interdependence of coefficient of friction, sliding velocity, axial pressure and temperature is developed in Chapter 3. The proposed friction model is coded in a new OpenSees (PEER, 2014) element *FPBearingPTV*, which simulates the behavior of a single FP bearing. The assumptions involved in modeling the single FP bearing are discussed, and results on verification and validation of the code are presented in Chapter 4.

Four alternate representations of seismic hazard are discussed in Chapter 5 and ground motions consistent with these representations are developed for different shaking levels. The development of response spectra and the ground motions, and the results of response-history analyses performed on single FP bearing subjected to these ground motions are presented. Risk calculations are performed to determine the design factors for seismically isolated nuclear power plants in Chapter 6.

Chapter 7 presents results of response-history analyses performed with a macro isolator with a range of bearing properties and loading conditions to study the influence of choice of friction model on the horizontal response of a simplified FP isolation system as a function of shaking intensity and bearing parameters (e.g., reference axial pressure, reference coefficient of friction). Chapter 8 presents results of response-history analyses performed with two models of an NPP that answer three practical questions, namely, 1) How significantly does the choice of friction model affect horizontal displacement response?, 2) How does the vertical component of ground motion affect horizontal displacement response?, and 3) Can key response quantities be estimated with a macro model of the isolation system?.

The research project is summarized and its important conclusions are presented in Chapter 9. References are listed in Chapter 10.

Appendix A presents the ground motions used for the verification and validation studies. The effect of decoupling the pressure and velocity dependencies of the coefficient of sliding friction is examined in Appendix B.

The vertical accelerations of the slider relative to the sliding surface are estimated in Appendix C for single FP bearing with a range of geometric properties subjected to ground motions scaled to different intensities. Appendix D describes the relative vertical displacement of the sliders in an isolation system composed of single FP bearings subjected to combinations of translational and rotational displacements.

Appendix E presents the seed ground motions that are matched to a number of response spectra in Chapter 5.

Risk calculations for isolation systems designed in accordance with the forthcoming edition of ASCE Standard 4 are presented in Appendix F.

Issues related to amplitude scaling ground motions to represent seismic hazard are discussed in Appendix G. The assumption of lognormality in a number of response quantities of a seismically isolated nuclear structure is confirmed in Appendix H. Details on the OpenSees model of the auxiliary and shield building used in Chapter 8 are presented in Appendix I.

CHAPTER 2

SEISMIC ISOLATION OF STRCTURES: AN OVERVIEW

2.1 General

Numerous efforts have been made in the past century to control the response of structures during earthquakes. Recent approaches include the use of 1) mechanisms to change the dynamic properties of a structure to limit the input energy (Robinson, 1982; Zayas *et al.*, 1987), and 2) energy dissipating devices (Aiken *et al.*, 1993; Constantinou and Symans, 1992; Kelly *et al.*, 1972; Pall and Marsh, 1982). Seismic isolation both increases the natural period of a structure to reduce its seismic response and dissipates some of the input energy.

Buildings, bridges and viaducts (e.g., Christopoulos and Filiatrault (2006)), oil platforms (e.g., Fenz *et al.* (2011), Clarke *et al.* (2005)), and nuclear reactors (e.g., Grandis *et al.* (2011)) have been seismically isolated. Records of performance are available for some of the isolated buildings that have experienced significant earthquake shaking.

This chapter presents a brief history of the seismic isolation of buildings. The seismic performance of some isolated buildings is discussed. An overview of the seismic isolation of nuclear structures is presented. The three types of seismic isolation bearings (low damping rubber, lead-rubber and FP bearings) likely to be used in the United States for seismic isolation of nuclear structures are introduced.

2.2 A Review of Seismic Isolation of Building Structures

2.2.1 Early proposals

Constantinou *et al.* (2007) note that the first seismic isolation system for building structures was proposed by Joules Touaillon in 1870 (US Patent No. 99973). It consisted of two “strong plates” with uniformly located spherical “depressions”. Rigid rollers were placed between the two plates at the locations of these depressions. The isolation system is similar to the double concave Friction Pendulum (DCFP) bearing (e.g., Fenz and Constantinou (2006)) with the articulated sliders replaced by rigid rollers. An isolation system with units of two cast-iron plates separated by rigid balls was proposed and implemented by John Milne in 1880s. A handful of ¼ in diameter cast-iron shot was placed between the two cast-iron plates in each unit of the isolation system (Naeim and Kelly, 1999). In 1891, Kawai proposed to put a building on layers of cylindrical logs, which would roll during earthquakes. The layers were to be placed in orthogonal directions on top of each other (Izumi, 1988). More proposals to construct a building on rollers were made by Jacob Bechtold in 1907 (US Patent No. 845046) and by Italian and Portuguese engineers in 1909 (Tassios, 2009).

The first isolation system based on sliding was proposed in 1909 by a British medical doctor, A. Calantarients. He proposed to construct building structures on a “free joint” made up of a layer of sand or talc, which would allow the building to slide in the event of an earthquake (Naeim and Kelly, 1999).

2.2.2 Early applications

To the knowledge of the author, a seven-story reinforced concrete building in the Crimea is the second building in the world (first was the one designed by John Milne, as discussed in Section 2.2.1) to be isolated using rollers. The isolation system comprised of egg-shaped bearings, which would force the building to rise when subjected to lateral deformation, generating a restoring force (Nazin, 1978).

A building constructed in Tokyo in 1921 responded during 1923 Kanto earthquake as if it was supported on a sliding system. The building foundation rested on a thick layer of good quality soil, below which was there a layer of mud. The building survived the devastating earthquake without much damage, as the layer of mud functioned as a “cushion” to protect the building from seismic waves (Wright, 1977). There have been cases of accidental sliding isolation of buildings, due to poor connection between the superstructure and the foundation. The 1930 Dhubri and 1934 Bihar earthquakes in India (Arya, 1984) and the 1966 Xintai, 1969 Bohai and 1976 Tangshan earthquakes in China (Buckle and Mayes, 1990) provide examples.

A three-story brick and reinforced concrete building constructed in Ashkhabad, Russia in 1959 was likely the first pendulum-suspended building in the world. Columns of this building rested on cradles hanging from the foundation through 1 m long cables (Buckle and Mayes, 1990).

The first building to be isolated using bearings made of natural rubber was a three-story concrete building in Yugoslavia. Completed in 1969, the building rested on large blocks of solid rubber (not reinforced with steel shims like modern elastomeric bearings). The isolation system had comparable values of stiffness in the vertical and horizontal directions (Kelly, 1986).

2.2.3 Modern applications

Seismic isolation became an attractive alternative for protecting new and existing buildings with the development of technology to perform experiments and numerical simulations. In Japan, the number of seismically isolated buildings was about 75 before 1994. The good performance of isolated buildings in the 1995 Kobe earthquake led to a rapid increase in the use of seismic isolation, with more than 700 buildings isolated in Japan by 2003 (Clark *et al.*, 1999; Kelly, 2004). A similar uptick is taking place in Italy following the 2009 Abruzzo earthquake, which caused significant damage to many conventional buildings and heritage structures (Martelli *et al.*, 2011). Figure 2-1 shows the history of the number of seismically isolated buildings in Japan and Italy.

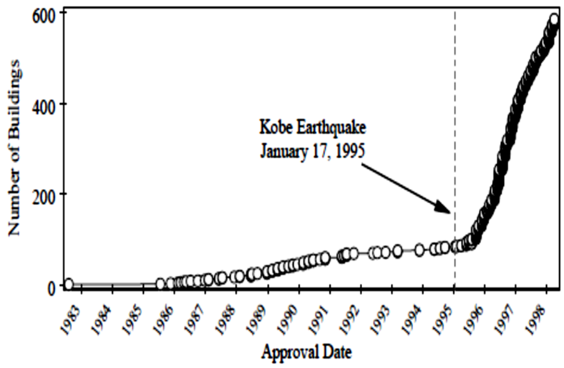

(a) Japan (Clark *et al.*, 1999)

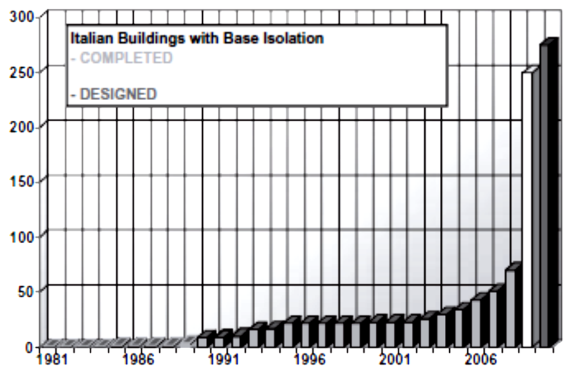

(b) Italy (Martelli *et al.*, 2011)

Figure 2-1: Number of seismically isolated buildings

The modern era in seismic isolation began in 1978 with the isolation of the Clayton Building in New Zealand using lead rubber (LR) bearings (Buckle, 1985; Skinner *et al.*, 1991). Since then, the technology has been used for many new and existing structures, at times to retain the architectural features of a building. Seismic isolation has been preferred over other methods of rehabilitation to preserve historical buildings, with applications including the Oakland, San

Francisco and Los Angeles City Halls, the US Court of Appeals building in San Francisco, and the New Zealand Parliament building in Wellington, New Zealand.

The first isolated building in the United States was the Foothill Communities Law and Justice Center, which was isolated in 1985 using LR bearings. Although the building received significant attention in the engineering community (Kelly, 2004), only seven buildings were isolated in the United States before 1990 and less than 40 were isolated prior to 2000.

2.3 Performance of Seismically Isolated Buildings

Observations of performance of seismically isolated buildings after earthquakes, including the 1994 Northridge earthquake (Clark *et al.*, 1996), 1995 Kobe earthquake (Kelly, 2004) and 2005 Fukuoka earthquake (Morita and Takayama, 2008), have indicated that damage to structural framing systems is minimal. For non-structural components, performance depends on the absolute acceleration or velocity history of the floor on which the component rests (Badillo-Almaraz *et al.*, 2007; Burningham *et al.*, 2007; Filiatrault *et al.*, 2004). Records of acceleration response at different floor levels are available for some isolated buildings that experienced earthquakes. The following sections present discussion on the response of selected isolated buildings in terms of recorded accelerations at different floor levels.

2.3.1 Earthquakes in the USA and Japan during the late 1980s

Buckle and Mayes (1990) report measured peak accelerations in isolated buildings in the US and Japan during earthquakes in the 1980s, as reproduced in Figure 2-2. The peak roof acceleration recorded in all of the isolated buildings was less than the corresponding peak ground acceleration and was significantly less than the peak roof acceleration recorded in near-by fixed base buildings.

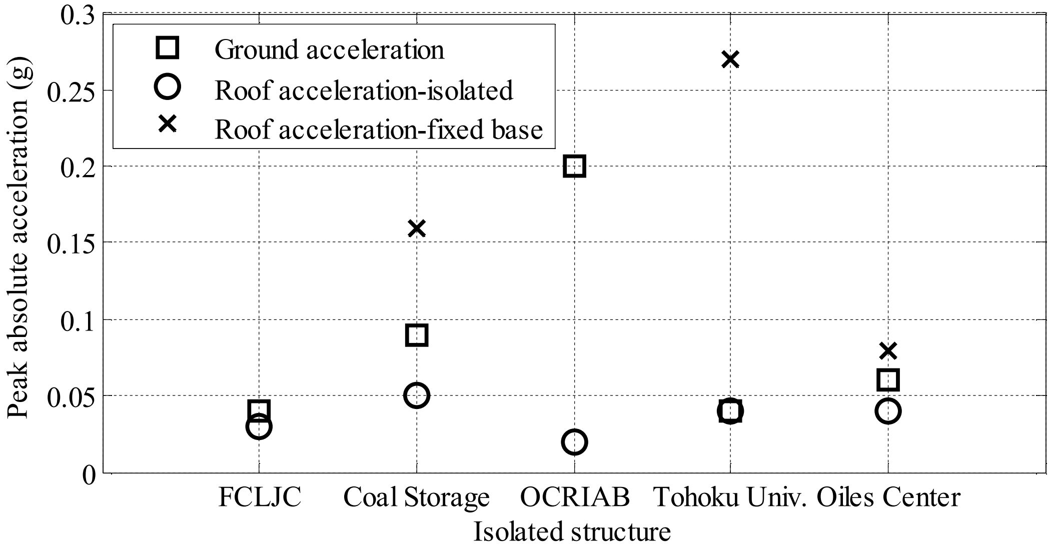

Figure 2-2: Recorded values of maximum absolute acceleration for buildings in USA and Japan during different earthquakes during the period 1985-89 (reproduced from Buckle and Mayes (1990))

2.3.2 1994 Northridge earthquake

Clark *et al.* (1996) reported peak floor accelerations in isolated buildings recorded during 1994 Northridge earthquake. The buildings identified in Figure 2-3, namely, private residence, University of Southern California (USC) Teaching Hospital, Los Angeles Fire Command and Control Facility (LAFCCF), Rockwell Computer Center Seal Beach, and Foothill Communities Law and Justice Center (FCLJC) were located 21 km, 36 km, 38 km, 66 km and 90 km from the epicenter of the earthquake, respectively. The peak roof acceleration is smaller than the peak ground acceleration (PGA) for the USC Teaching Hospital building only. For the other four structures, the peak roof acceleration was greater than the corresponding PGA due to either

1) impact of the isolated structure on non-structural components placed within the moat, or 2) the small intensity of shaking not triggering the isolation system.

Makris and Deoskar (1996) simulated the response of the private residence, which was close to the epicenter. They concluded that the maximum roof acceleration would have been approximately 1.0 g if the structure was not isolated, significantly greater than the observed acceleration of 0.6 g.

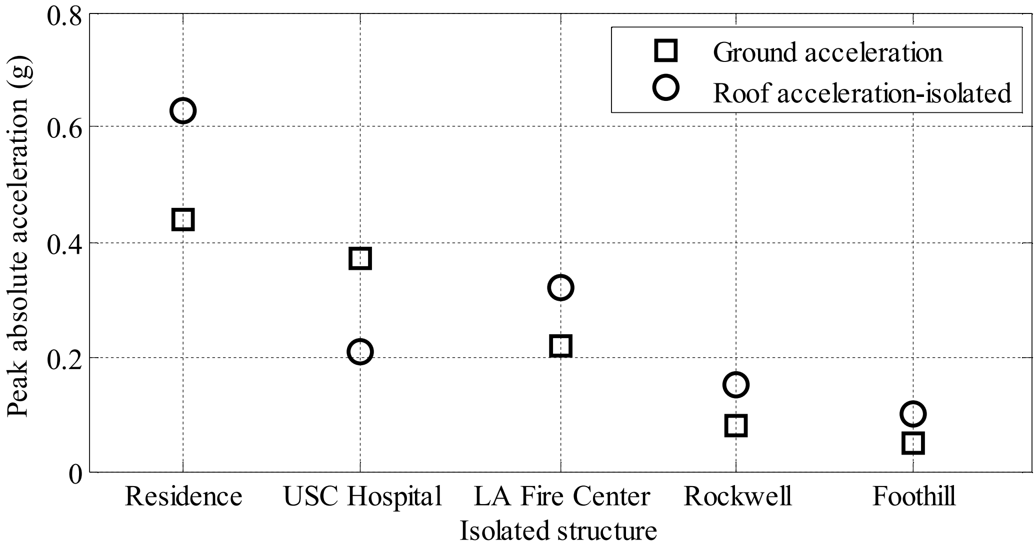

Figure 2-3: Recorded values of peak ground acceleration and maximum roof acceleration of isolated buildings during 1994 Northridge earthquake (reproduced from Clark *et al.* (1996))

Clark *et al.* (1996) assign the impact at the level of isolation system in the LAFCCF building to the presence of an architectural feature in the seismic gap (moat). A detailed study on the impact was performed by Nagarajaiah and Sun (2001). The acceleration in one horizontal direction was amplified along the height of the structure due to the impact (shown in Figure 2-3). However, in the orthogonal direction, the isolation system was effective because the maximum acceleration at the foundation and roof were 0.18 g and 0.09 g, respectively.

The isolation system of the USC Hospital building performed well as the peak roof acceleration was 0.21 g, about 40% smaller than the peak ground acceleration. The peak acceleration in the lower floors was smaller than 0.13 g (Clark *et al.*, 1996). The amplification of acceleration observed in the FCLJC building was attributed to a small PGA of 0.05 g, which did not trigger the isolation system (Kelly, 2004).

2.3.3 1995 Kobe earthquake

The rapid increase in the number of seismically isolated buildings in Japan after the 1995 Kobe earthquake (see Section 2.2.3) was attributed in part to the excellent performance of two seismically isolated buildings, Matasumura-Gumi Technical Research Institute and West Japan Postal Saving Computer Center (Kelly, 2004; Nakashima and Chulisp, 2003), during that earthquake. Figure 2-4 presents recorded peak accelerations in these two buildings during the Kobe earthquake, as reported by Kelly (2004). For both buildings, the maximum acceleration recorded at the roof was similar to or less than the PGA in both horizontal directions. The peak vertical acceleration was amplified in both buildings, with the peak roof acceleration being more than 1.6 times the peak vertical ground acceleration. For the Postal Center building, the maximum vertical acceleration at the foundation, first floor and roof were 0.22 g, 0.20 g and 0.38 g, respectively. These values indicate that amplification in vertical acceleration was negligible across the isolation system. The peak roof acceleration could have been high due to the vertical flexibility of the roof framing (e.g., Almazán *et al.* (1998)).

2.3.4 2005 Fukuoka earthquake

The March 20, 2005 M 7.0 Fukuoka earthquake shook thirteen isolated buildings in the city. Morita and Takayama (2008) reported values of maximum acceleration in two of those buildings (see Figure 2-5). Significant de-amplification of acceleration due to seismic isolation is seen for both buildings in the two horizontal directions.

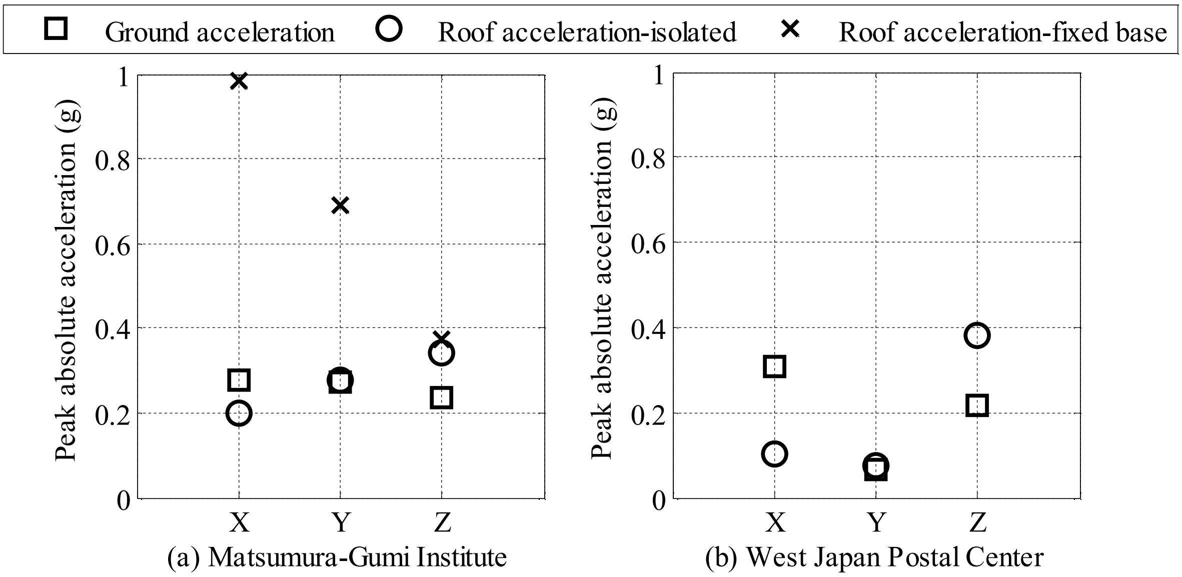

Figure 2-4: Recorded values of maximum acceleration at ground and roof of isolated and near-by buildings in Japan during the 1995 Kobe earthquake (reproduced from Kelly (2004))

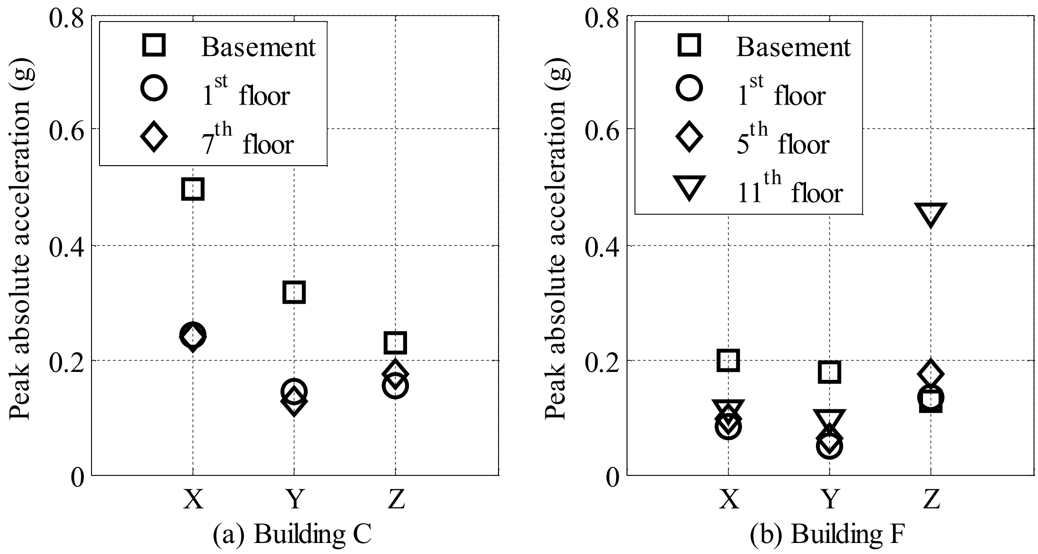

Figure 2-5: Maximum recorded acceleration of two buildings during the 1995 Fukuoka earthquake in Japan (reproduced from Morita and Takayama (2008))

Like the Postal Center building (Section 2.3.3), amplification of the vertical motion was very small across the isolation system for the two buildings. For the seven story Building C, the peak roof acceleration (0.18 g) was smaller than the PGA (0.23 g) in the vertical direction. However, for the eleven story Building F, the peak vertical acceleration at the roof was 3.5 times the vertical PGA.

2.4 Seismic Isolation of Safety-related Nuclear Power Plant Structures

Although there have been more than 10,000 applications of seismic isolation in the world to different types of structures, such as buildings, bridges and offshore oil platforms, only two nuclear power plants had utilized seismically isolated reactors until recently, one in Cruas, France with four Pressurized Water Reactors (PWR) and one in Koeberg, South Africa with two PWRs. Both plants started operating in the early 1980s. The construction of the seismically isolated Jules Horowitz Reactor and International Thermonuclear Experimental Reactor (ITER) in Cadarache, France is in progress (Grandis *et al.*, 2011; Syed *et al.*, 2014).

There are no seismically isolated nuclear structures in the US at present although studies were performed in the late 1980s (e.g., Kelly (1993), Tajirian *et al.* (1990)). Most of the nuclear power plants in the US were licensed in 1970s and 80s, as shown in Figure 2-6. Only four licenses were granted in the 1990s. No license was granted in the 2000s. Two new licenses have been granted recently for nuclear power generation at Vogtle in Georgia and at Summer in South Carolina (USNRC, 2013). More recent studies on the seismic isolation of nuclear structures (Huang *et al.*, 2007; Huang, 2008) have focused on reduction in seismic risk. The first seismic isolation NUREG will be published in 2015 (Kammerer *et al.*, forthcoming).

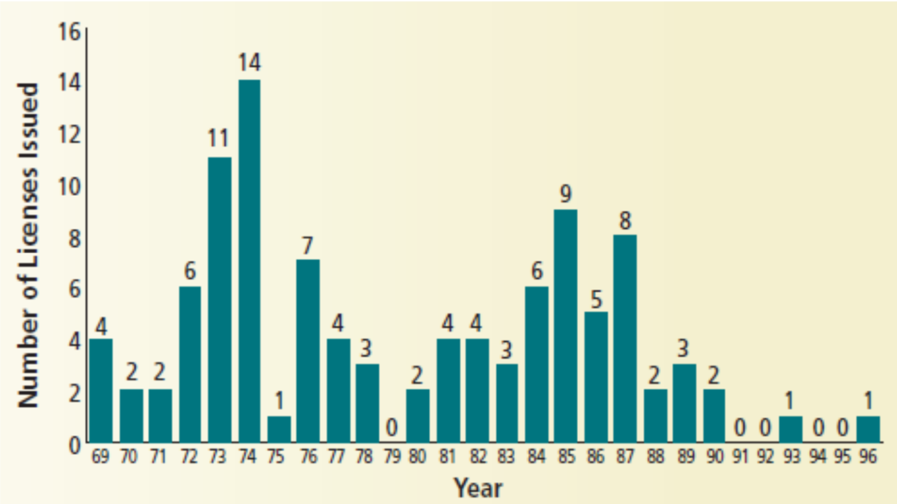

Figure 2-6: Number of licenses issued by the United States Nuclear Regulatory Commission to generate nuclear power at commercial scale (USNRC, 2012)

2.5 Seismic Isolation Bearings

Three types of seismic isolation bearings are likely to be considered in the US for the seismic isolation of nuclear structures: Low damping rubber (LDR), Lead rubber (LR) and Friction Pendulum™ (FP) bearings (Kammerer *et al.*, forthcoming). A brief discussion of each of these bearings is presented next.

2.5.1 Low damping rubber (LDR) bearing

Elastomeric bearings are fabricated using alternating layers of rubber and steel shims. Figure 2-7 shows a section through an older elastomeric bearing. Elastomeric bearings can be of three types: low damping rubber (LDR), high damping rubber (HDR) and synthetic rubber. Different elastomers are used in each. The lateral stiffness of a LDR bearing is a function of the shear modulus of rubber, the bonded area, the total thickness of rubber, the axial pressure, the lateral displacement and the ambient temperature (Kumar *et al.*, 2014).

LDR bearings are used often in combination with LR bearings that increase the energy dissipation capacity of an isolation system. Applications of LDR bearings include Salt Lake City and County building, USC University Hospital, Oakland City Hall and the Long Beach Hospital, and the Parliament buildings and National Museum in New Zealand.

Figure 2-7: Internal construction of an elastomeric bearing (Naeim and Kelly, 1999)

2.5.2 Lead rubber (LR) bearing

Lead-rubber (LR) bearings are elastomeric bearings with added lead plug (or plugs) to increase energy dissipation capacity (e.g., Robinson (1982)). Figure 2-8 shows the interior construction of a typical LR bearing. The post-yield stiffness of an LR bearing is essentially that of the LDR bearing discussed above. The elastomer is natural rubber. The lead core significantly increases the yield strength and pre-yield stiffness of an LR bearing, which reduces the movement of the superstructure during small earthquakes and under wind loading. The yield strength of the lead core depends on its area, its confinement and on its temperature, which is a function of the loading history. LR bearings were also used in the applications identified in the Section 2.5.1, together with LDR bearings.

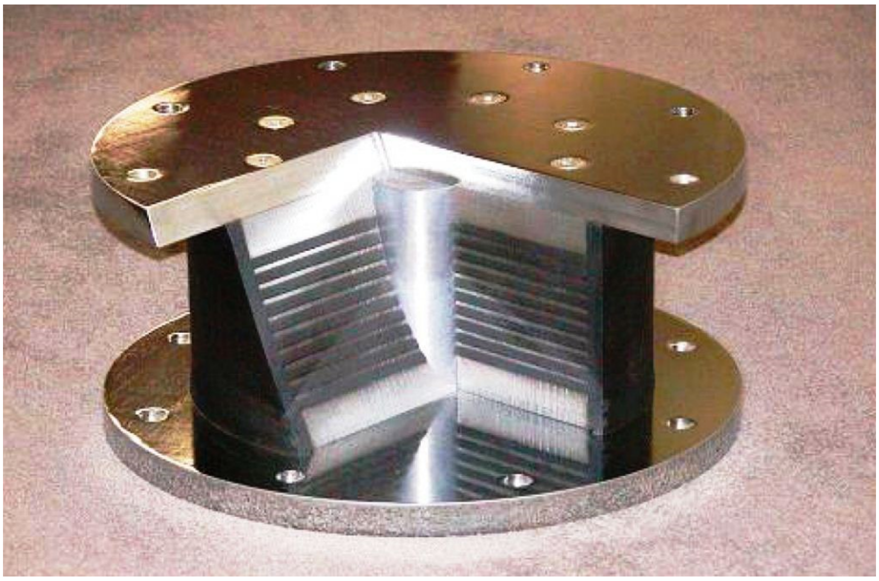

Figure 2-8: Internal construction of a lead-rubber bearing (Constantinou *et al.*, 2007)

2.5.3 Friction Pendulum™ (FP) bearing

Figure 2-9 shows a single concave Friction Pendulum™ (FP) bearing comprising a spherical sliding surface of stainless steel, a slider coated with a PTFE-type composite material and a housing plate. The lateral force-displacement relationship of an FP bearing is a function of the coefficient of friction between slider and the sliding surface, the radius of curvature of the sliding surface, the velocity of sliding, the axial load and the temperature at the sliding surface. Chapter 3 presents a model to characterize the lateral force-displacement relationship of FP bearings accounting for those factors that affect the coefficient of friction. Applications of FP bearings include the US Court of Appeals, Hayward City Hall, San Francisco International

Airport Terminal, Pasadena City Hall and Benicia-Martinez Bridge, Liquefied Natural Gas Tanks in Greece, and Ataturk International Airport in Turkey.

Figure 2-9: Sliding plate, slider and housing plate for a single Friction Pendulum bearing (EPS, 2011)

CHAPTER 3

FRICTION IN SLIDING ISOLATION BEARINGS

3.1 Introduction

The lateral force-displacement behavior of the Friction Pendulum™ (FP) bearing is a function of the coefficient of sliding friction, axial load on the bearing and effective radius of curvature of the sliding surface. The characteristic strength (force at which sliding begins) of the bearing is the product of the coefficient of friction and instantaneous axial load. The coefficient of friction varies during the course of the earthquake with sliding velocity, axial pressure and temperature at the sliding surface. The sliding velocity and axial pressure on the bearing depend on the superstructure response to the earthquake shaking. The temperature on the sliding surface, at a given instant in time, is a function of the histories of the coefficient of friction, sliding velocity and axial pressure, and the travel path of slider on the sliding surface, together with parameters characterizing heat transfer of the materials that form the interface.

A model to simulate the lateral force-displacement behavior of an FP bearing should be able to account for interdependence of the coefficient of sliding friction, the sliding velocity, the temperature at the sliding surface and the instantaneous axial pressure. For nonlinear response-history analysis, the coefficient of sliding friction may have to be updated at every time step depending on the instantaneous values of sliding velocity, temperature at sliding surface and axial pressure. This chapter presents an approach to account for the dependence of the coefficient of friction on these three quantities. Expressions to define the relationship between the coefficient of friction and sliding velocity, axial pressure, and temperature are proposed, based on available experimental data. A suitable assumption is made to decouple the influence of axial pressure and sliding velocity on the coefficient of friction. A method to compute temperature at a point on the sliding surface is described. The temperatures at different points on the sliding surface vary depending on the loading history. A representative value of temperature on the sliding surface is needed to update the coefficient of friction. Two approaches to compute the representative temperature are compared.

3.2 Force-displacement Behavior

Friction Pendulum™ (FP) bearings are widely used in the United States for seismic isolation of structures. In its single concave configuration, the FP bearing includes a sliding surface of polished stainless steel and an articulated slider coated with PTFE-type composite material. Figure 3-1 is a section through an FP bearing.

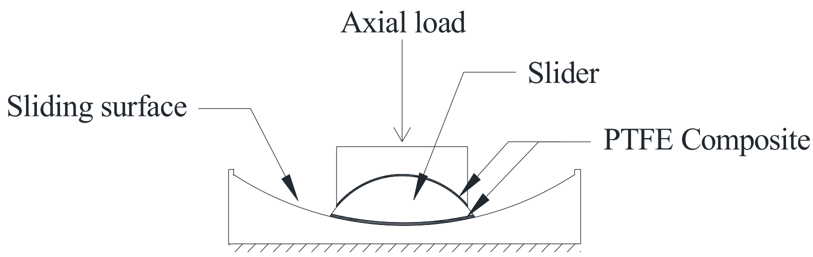

Figure 3-1: Section through a single concave Friction Pendulum™ (FP) bearing

For fixed values of axial load on the bearing and the coefficient of sliding friction between the sliding surface and the slider, the force-displacement behavior of an FP bearing in a horizontal direction can be represented by a bilinear curve of Figure 3-2. The curve is characterized by characteristic strength Q, the product of the coefficient of friction and the axial load, and post-yield stiffness K, the ratio of supported axial load to the effective radius of curvature of the bearing. The axial load on a bearing changes continuously during earthquake shaking because of the superstructure response to the vertical and horizontal shaking, leading to continuous changes in Q and K. In addition, the coefficient of sliding friction is a function of the instantaneous values of sliding velocity, axial pressure on the bearing and temperature at the sliding surface, which also change Q. The temperature at the sliding surface at a given instant depends on the histories of sliding velocity, axial pressure and coefficient of friction, and the path traveled by the slider (see Figure 3-3).

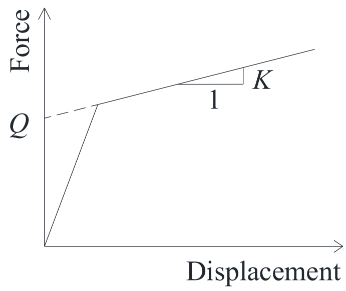

Figure 3-2: Lateral force-displacement relationship of a single concave Friction Pendulum™ (FP) bearing (Zayas *et al.*, 1987)

3.2.1 Dependence of the coefficient of friction on the velocity of sliding

The relationship between the coefficient of friction and the velocity of sliding at the interface can be described by an exponential function given by Mokha *et al.* (1988):

$$\mu(v) = \mu_{\max} - (\mu_{\max} - \mu_{\min})e^{-av} \tag{3-1}$$

where $\mu_{\min}$ and $\mu_{\max}$ are the values of the coefficient of friction at very small and very high velocities of sliding, respectively, a is a parameter describing the shape of the curve, and v is the sliding velocity. The rate parameter a depends on the properties of the PTFE-type composite coating on the slider. For the composite material used in an FP bearing, a is approximately 100 s/m, as noted by Constantinou *et al.* (2007) based on the experimental studies performed by Constantinou *et al.* (1993) and Tsopelas *et al.* (1994a). For this study, a is set equal to 100 s/m, which is the value adopted in past studies (e.g., Fenz and Constantinou (2006), Fenz and Constantinou (2008a)).

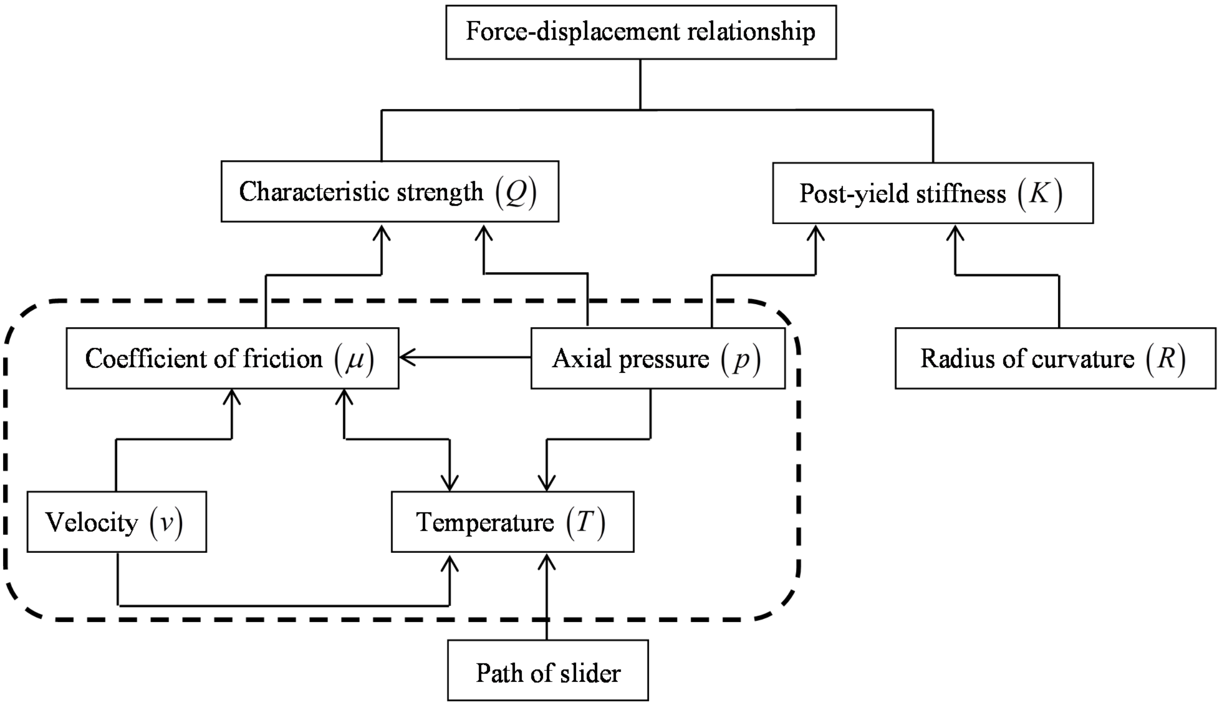

Figure 3-3: Interdependence of quantities defining the force-displacement relationship in an FP bearing

It is useful to present the relationship between $\mu_{\min}$ and $\mu_{\max}$ as a ratio, since it allows $\mu(v)$ in Equation (3-1) to be expressed as a product of $\mu_{\max}$ and a factor accounting for the effect of velocity on friction:

$$\mu(v) = \mu_{\max} \times \left(1 - \left(1 - \frac{\mu_{\min}}{\mu_{\max}}\right) e^{-av}\right) \tag{3-2}$$

where all the parameters are defined previously. To simplify the modeling of the velocity dependence of friction for response-history analysis, a fixed value of the ratio of $\mu_{\min}$ to $\mu_{\max}$ can be based on experimental observations. Table 3-1 presents the recorded values of $\mu_{\min}$ and

$\mu_{\max}$ for different PTFE-type composite materials and different values of axial pressure. Material No. 1 was identical to the material used in the FP bearings installed in the retrofit of U.S. Court of Appeals building in San Francisco, California (Constantinou *et al.*, 1993). The ratio of $\mu_{\min}$ to $\mu_{\max}$ varies between 0.4 and 1.0. Four of the seven observations reported in Table 3-1 did not exhibit velocity-dependent friction. The ratio of $\mu_{\min}$ to $\mu_{\max}$ was 0.39, 0.67 and 0.64 for the remaining three cases. Although the three observations correspond to different materials and different values of axial pressure, it is reasonable to fix the ratio of $\mu_{\min}$ to $\mu_{\max}$ at 0.50 and assume it to be applicable for a range of values of axial pressure and for different materials. This value of the ratio was used for each sliding interface in the modeling of Triple Friction Pendulum (TFP) bearings by Fenz and Constantinou (2008a). The expression to define the velocity dependence of the coefficient of friction then simplifies to:

$$\mu(v) = \mu_{\max} \times \left(1 - 0.5e^{-av}\right) \tag{3-3}$$

Table 3-1: Observed values of low and high velocity coefficient of friction (adapted from Constantinou *et al.* (1993))

Pressure (MPa)	Material	$\mu_{\min}$	$\mu_{\max}$	$\mu_{\min}/\mu_{\max}$	Comments
17.2	No. 1	0.040	0.104	0.385	
	No. 2	0.115	0.122	0.943	Essentially Coulomb friction
	No. 3	0.090	0.120	0.667	
	No. 4	0.114	0.114	1.000	Essentially Coulomb friction
275.6	No. 1	0.034	0.053	0.642	
	No. 2	0.058	0.058	1.000	Essentially Coulomb friction
	No. 3	0.062	0.062	1.000	Essentially Coulomb friction

3.2.2 Dependence of the coefficient of friction on axial pressure

Constantinou *et al.* (2007) present a theory for the relationship between the coefficient of friction and axial pressure. The shear strength, s_{μ}, of the interface of an FP bearing can be considered to vary linearly with axial pressure, p_r, given by the following equation.

$$s_{\mu} = s_{o_{\mu}} + \alpha p_r \tag{3-4}$$

where $s_{o_{\mu}}$ is shear strength at zero axial pressure, α is a constant and other parameters were defined earlier. The friction force F_{μ} is the product of s_{μ} and the area of contact A_r. The coefficient of friction μ can be obtained as the ratio of the friction force to the normal force N, as given by the following equation:

$$\mu = \frac{F_{\mu}}{N} = \frac{s_{\mu} A_r}{p_r A_r} = \frac{\left(s_{o_{\mu}} + \alpha p_r\right) A_r}{p_r A_r} = \frac{s_{o_{\mu}}}{p_r} + \alpha \tag{3-5}$$

where all the terms were defined earlier. The coefficient of friction decreases asymptotically with increase in axial pressure. This trend is also supported by experimental data, as seen in Figure 3-4, which is adapted from Mokha *et al.* (1996). The figure plots observed values of the coefficient of friction measured at a high velocity against applied axial pressure. The information presented in the figure is based on the experiments performed by Zayas *et al.* (1987), Constantinou *et al.* (1993) and Al-Hussaini *et al.* (1994). Constantinou *et al.* (1993) note that the coefficient of friction at a very small velocity of sliding is not affected by the variation in axial pressure.

The following sections present models proposed in the past to describe pressure dependence of coefficient of friction.

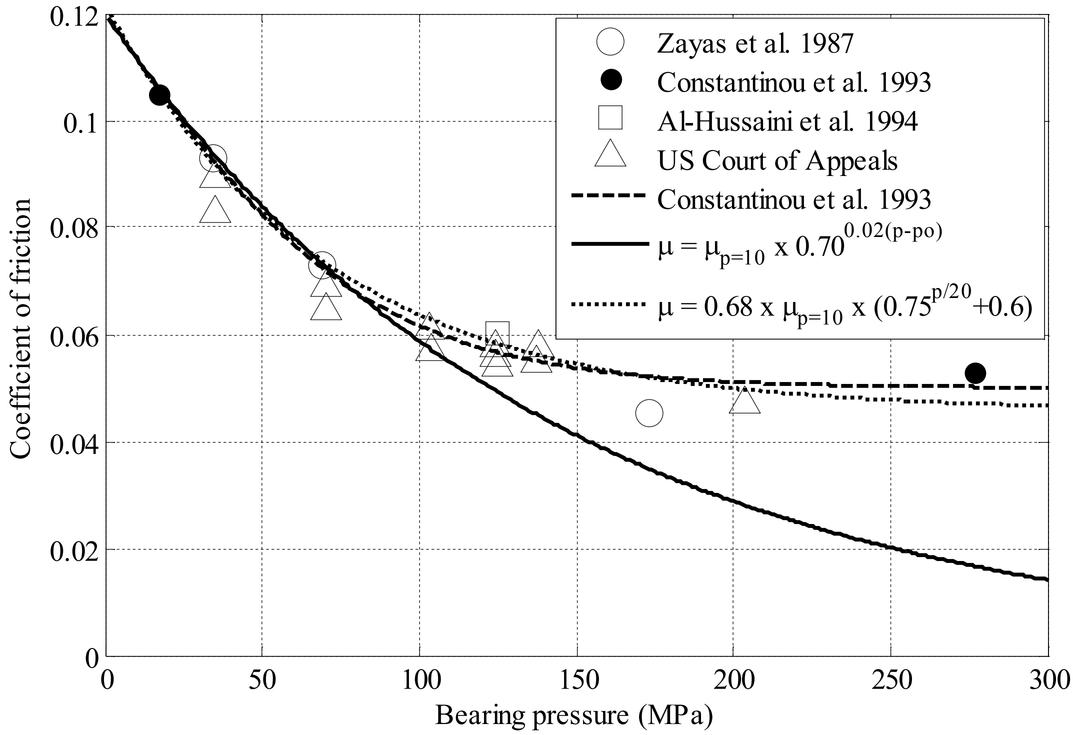

Figure 3-4: Coefficient of friction measured at a high velocity of sliding plotted against bearing pressure (adapted from Mokha *et al.* (1996))

3.2.2.1 Past studies

3.2.2.1.1 Chang et al. (1990)

The variation in the small velocity coefficient of friction with axial pressure is described by Chang *et al.* (1990) using the following expression:

$$\mu_{\min} = \frac{1}{\lambda_1 + \lambda_2 p} \tag{3-6}$$

where λ_1 and λ_2 are determined using experimental data, and p is axial pressure. The coefficient of friction, $\mu(p,v)$, accounting for the coupled effect of sliding velocity and axial pressure is given by

$$\mu(p,v) = \mu_{\min}\left(1+\beta_1\left(\ln\left(1+\beta_2 v\right)\right)\right) \tag{3-7}$$

where $\mu_{\min}$ is defined by Equation (3-6), β_1 and β_2 are obtained from experiments, and v is sliding velocity.

3.2.2.1.2 Tsopelas et al. (1994b)

The relationship between the coefficient of friction at a high velocity of sliding and axial pressure is described using a tangent hyperbolic function as

$$\mu(p) = \mu_{p=0} - \left(\mu_{p=0} - \mu_{\max p}\right)\tanh\left(\varepsilon p\right) \tag{3-8}$$

where $\mu_{p=0}$ is the coefficient of friction at zero axial pressure measured at a high velocity of sliding, $\mu_{\max p}$ is the coefficient of friction at very high axial pressure measured at a high velocity of sliding, ε is a parameter governing the shape of the curve, and p is the axial pressure on the bearing in MPa. Figure 3-4 plots the relationship given by Equation (3-8) with the values of parameters $\mu_{p=0}$, $\mu_{\max p}$ and ε fixed at 0.12, 0.05 and 0.012, respectively. This curve fits quite well to the experimental data presented in Constantinou *et al.* (1993) (see Figure 3-4). This relationship has been incorporated in the computer program 3D-BASIS-ME (Tsopelas *et al.*, 1994b).

Equation (3-8) can be rewritten to allow $\mu(p)$ to be expressed as a product of $\mu_{\max p}$ and a factor accounting for the effect of pressure on the coefficient of friction, as given by the following expression.

$$\mu(p) = \mu_{\max p} \times \left(\frac{\mu_{p=0}}{\mu_{\max p}} - \left(\frac{\mu_{p=0}}{\mu_{\max p}} - 1 \right) \tanh(\varepsilon p) \right) \tag{3-9}$$

where all the terms were defined previously. Values for $\mu_{p=0}$ and $\mu_{\max p}$ for a particular PTFE-type composite material can be determined by experiments.

3.2.2.1.3 Tsai (1997)

An approach similar to Chang *et al.* (1990) has been used by Tsai (1997) to define the pressure and velocity dependence of coefficient of friction:

$$\mu(p,v) = \mu_{\min}\left(1 + \chi_1\left(1 - e^{-\chi_2 v}\right)\right) \tag{3-10}$$

where χ_1 and χ_2 are obtained from experiments and all other parameters were defined previously.

3.2.2.1.4 Dao et al. (2013)

Dao *et al.* (2013) used Equation (3-1) to describe the velocity dependence of the coefficient of friction. The exponent a in the equation is modeled as a function of the instantaneous axial load W:

$$a = \alpha_0 + \alpha_1 W + \alpha_2 W^2 \tag{3-11}$$

where α_0, α_1 and α_2 are constants estimated using experimental data (see panel (a) of Figure 3-5). The variables $\mu_{\max}$ and $\mu_{\min}$ are expressed as

$$\mu_{\max} = A_{\max} W^{n_{\max}-1} \tag{3-12}$$

$$\mu_{\min} = A_{\min} W^{n_{\min}-1} \tag{3-13}$$

where $A_{\max}$, $A_{\min}$, $n_{\max}$ and $n_{\min}$ are estimated using experimental data (see panel (b) of Figure 3-5); $n_{\max}$ and $n_{\min}$ are positive numbers smaller than 1. This empirical model lacks a physical basis because μ is function of contact pressure and not axial load.

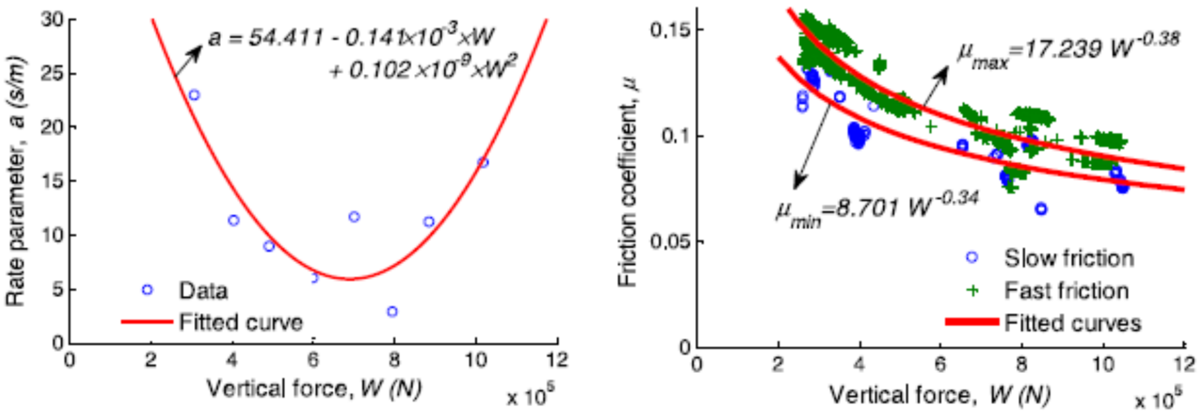

(a) Rate parameter vs. vertical force (b) Coefficient of friction vs. vertical force

Figure 3-5: Modeling velocity and pressure dependence of coefficient of friction (Dao *et al.*, 2013)

3.2.2.2 Proposed model

This study assumes that the coefficient of friction at a very small velocity is half that at a very high velocity of sliding (see Section 3.2.1) for all values of axial pressure. This assumption leads to the velocity dependence of coefficient of friction being defined as the product of the high velocity coefficient of friction and a factor that depends only on the sliding velocity, and not on axial pressure (Equation (3-3)). The assumption does not materially affect the maximum displacement and absolute acceleration responses of an isolated structure, as demonstrated in Appendix B.

The proposed relationship between axial pressure, p, and the coefficient of friction at a high velocity of sliding, $\mu(p)$, is given by

$$\mu(p) = \mu_{p=p_o} \times \alpha^{\beta(p-p_o)} \tag{3-14}$$

where $\mu_{p=p_o}$ is the coefficient of friction at a reference axial pressure p_o measured at a high velocity of sliding, and α and β are constants to be determined from experiments. The constants α and β determine the shape of the curve. The relationship for the pressure dependence of the coefficient of friction can be readily obtained once α, β and $\mu_{p=p_o}$ are established. Figure 3-4 presents Equation (3-14) with values of p_o, $\mu_{p=p_o}$, α and β set equal to 10, 0.11, 0.70 and 0.02, respectively.

Equation (3-14) is applicable only for a range of axial pressure, which is smaller than the range covered by Equation (3-9). For example, $\mu(p) = 0.11 \times 0.7^{0.02(p-10)}$ represents the relationship between the coefficient of friction and axial pressure best if the axial pressure is less than 100 MPa (see Figure 3-4). The parameters of the equation may need to be modified to better fit the experimental data in the desired range of axial pressure.

The target static axial pressure varied between 40 MPa and 110 MPa in the 256 FP bearings used to isolate the U.S. Court of Appeals building (Mokha *et al.*, 1996). The target axial pressure for the 22 FP bearings used in the Benicia-Martinez Bridge was 20 MPa (Zayas *et al.*, 2001). For the 252 Triple Friction Pendulum™ bearings used to isolate the Istanbul Sabiha Gokcen International Airport Terminal Building, the average target axial pressure was 20 MPa on the outer sliding surfaces and 30 MPa on the inner sliding surfaces (Zekioglu *et al.*, 2009). The four FP bearings used in the Arkutun-Dagi oil platform support a total axial load of about 50,000 tons and the average target static axial pressure on the bearings is 50 MPa (Fenz *et al.*, 2011). A total of 69 TFP bearings are planned for New San Bernardino Courthouse. Thirty-two of those bearings have an average target static axial pressure of 10 MPa on the outer sliding surface and 40 MPa on the inner sliding surface. For the remaining 37 bearings, the average axial pressure on the outer and inner sliding surfaces are 20 MPa and 50 MPa, respectively (Sarkisian *et al.*, 2012). This information suggests that FP bearings used in recent applications are subjected to a static axial pressure well below 100 MPa.

Equation (3-14) with appropriate values of the constants satisfactorily fits the experimental data for axial pressure smaller than 100 MPa: $\mu(p) = 0.11 \times 0.7^{0.02(p-10)}$. The assumption that the small velocity coefficient of friction is one half the high velocity coefficient of friction at all levels of axial pressure allows the relationship between the coefficient of friction and the axial pressure to be expressed directly in terms of the coefficient of friction measured at a reference axial pressure multiplied by a factor depending only on axial pressure. The inclusion of additional parameters in Equation (3-14) allows the relationship between the coefficient of friction and axial pressure to be applied for the wide range of values of axial pressure covered in Figure 3-4. A modified expression is:

$$\mu(p) = \delta_1 \times \mu_{p=p_o} \times \left(\delta_2^{\delta_3 p} + \delta_4\right) \tag{3-15}$$

where δ_1, δ_2, δ_3 and δ_4 are constants (different from Equation (3-14)) determined using experimental data, and the remaining parameters were defined previously. With the values of p_o, $\mu_{p=p_o}$, δ_1, δ_2, δ_3 and δ_4 set equal to 10, 0.11, 0.68, 0.75, 20 and 0.6, respectively, the curve of Equation (3-15) fits well the entire range of experimental observations seen in Figure 3-4.

3.2.3 Dependence of the coefficient of friction on temperature

3.2.3.1 Studies in the past

Past studies have shown that the coefficient of friction decreases with an increasing number of cycles even if axial pressure and sliding velocity are kept constant, due to the partial melting of the PTFE-type composite coating caused by the increase in temperature at the sliding surface (see Figure 3-6). The decrease in the coefficient of friction has been modeled as a function of the history of the work done on the sliding surface (e.g., Chang *et al.* (1990)) as given by the following expression:

$$\mu(T) = \mu(p,v) \times \left((1-\gamma_1) + \gamma_1 e^{-\gamma_2 \int_0^t \frac{\mu(T,t)-\mu_{\min}(t)}{\mu_{\min}(t)} du} \right) \tag{3-16}$$

where $\mu(p,v)$ is given by Equation (3-7), γ_1 and γ_2 are determined from experiments, $\mu(T,t)$ is the temperature dependent coefficient of friction at time t and $\mu_{\min}(t)$ is the small velocity coefficient of friction at time t. A similar approach to account for the temperature dependence of friction was adopted by Tsai (1997).

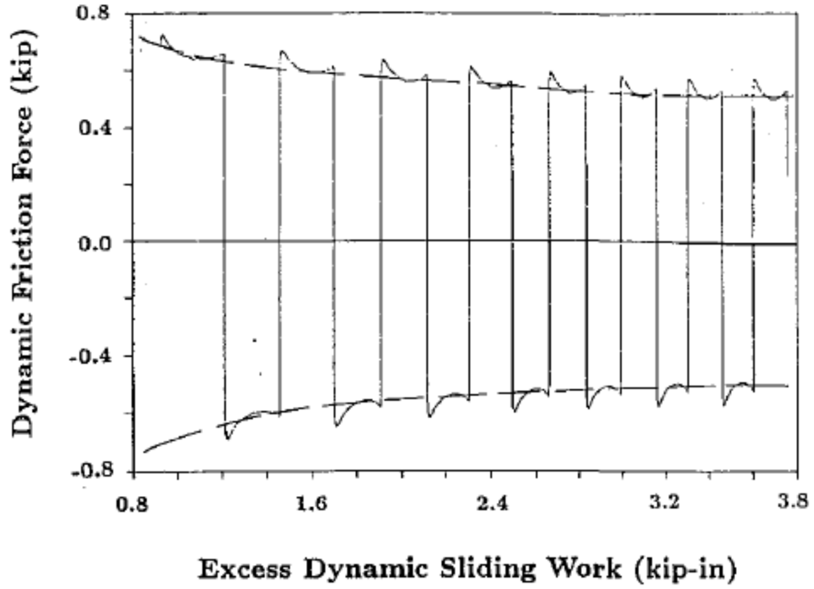

Figure 3-6: Reduction in friction force with number of cycles (Chang *et al.*, 1990)

The change in the coefficient of sliding friction with an increasing number of cycles (or work done on sliding surface) is reflected in the lateral force-displacement relationship of an FP bearing. Figure 3-7 presents the force-displacement response of an FP bearing when the cyclic displacement was applied at different rates. The coefficient of friction (the ratio of lateral force to normal force at zero displacement) decreases with increases in the number of cycles of loading and the peak velocity.

The sliding at the PTFE-type composite material and steel interface leads to increase in temperature. The change in the coefficient of friction can be expressed as a function of the temperature at the sliding surface. However, the measurement of temperature[1] at the sliding surface is difficult when sliding is taking place (e.g., Wolff (1999), Constantinou *et al.* (1999)).

---

[1] A measurement of temperature at the sliding surface is needed to 1) determine the relationship between the coefficient of friction and temperature (e.g., present study), 2) quantify wear in the liner material (e.g., Drozdov *et al.* (2007), Drozdov *et al.* (2010)), and 3) design experiments for seismic qualification of bearings (e.g., Fenz *et al.* (2011)).

The temperature at a depth below the sliding surface can be measured using a thermocouple, but depending on the properties (e.g., diameter) of the thermocouple, there can be a time lag associated with the measurement of temperature.

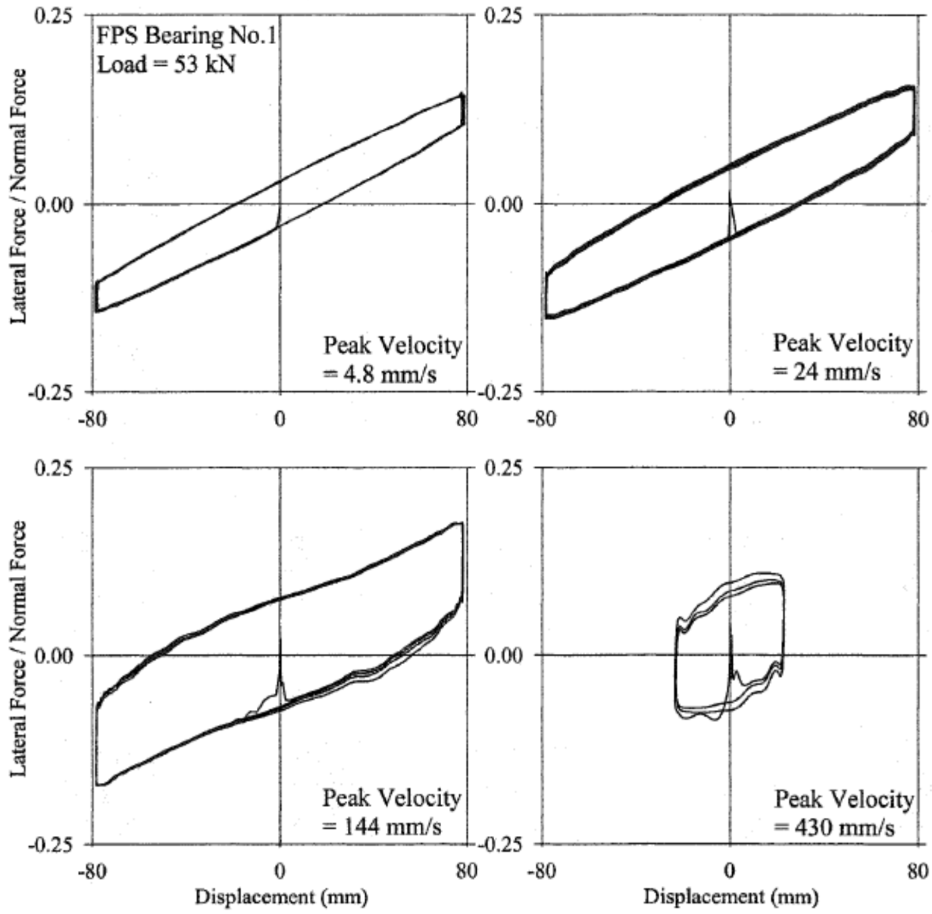

Figure 3-7: Force-displacement histories for FP bearings with different magnitudes of maximum velocity of sliding (Wolff, 2003)

An expression to define the temperature dependence of the coefficient of friction has been suggested by Sarlis and Constantinou (2013).

$$\mu(T) = \mu_{\max T} + (\mu_{\min T} - \mu_{\max T}) e^{-a_h T} \tag{3-17}$$

where $\mu_{\min T}$ is the coefficient of friction at the beginning of the motion at the sliding surface, when the temperature is a minimum, $\mu_{\max T}$ is the coefficient of friction at a high temperature $\left(\approx 1/a_h\right)$, and a_h is the heating rate parameter.

3.2.3.2 Proposed relationship

Equation (3-17) describes the decrease in the coefficient of friction from $\mu_{\min T}$ to $\mu_{\max T}$ with increase in temperature from zero to $1/a_h$. If $\mu_{\min T}$ is known at a temperature T_o instead of at zero temperature, then T in the exponent of the equation can be replaced with $\left(T-T_o\right)$ to describe the temperature dependence of the coefficient of friction. The shape of the curve described by Equation (3-17) depends on the base e. As will be shown in later chapters, the temperature at the sliding surface affects the response quantities (e.g., peak displacement, peak acceleration) most significantly. It may therefore be necessary to have better control on the rate of decrease in the coefficient of friction with an increase in temperature to best fit available experimental data, which can be achieved by replacing the base e with another number a_e (to be determined from experiments). The resulting equation is

$$\mu\left(T\right)=\mu_{\max T}+\left(\mu_{\min T}-\mu_{\max T}\right)a_e^{-a_h\left(T-T_o\right)} \qquad \text{(3-18)}$$

where all terms were defined previously. It is desirable to define the coefficient of friction as a product of a reference coefficient of friction and a factor depending only on the temperature at the sliding surface:

$$\mu\left(T\right)=\mu_{T=T_o}\times\phi\left(b^{T/c}+d\right) \qquad \text{(3-19)}$$

where $\mu_{T=T_o}$ is the high velocity coefficient of friction at a reference temperature T_o, and b, c and d are determined from experiments, and ϕ is related to b, c and d as follows

$$\phi = \left(b^{T_o/c} + d \right)^{-1} \tag{3-20}$$

Constantinou *et al.* (2007) provide information about the change in the coefficient of friction with temperature (see Figure 3-8). A very sharp drop in the coefficient of friction takes place as the temperature at the sliding interface increases from -40˚C to 20˚C. The coefficient decreases further, although not as sharply, as the temperature increases to 50˚C. It is expected that the decrease in the coefficient of sliding friction is smoother at higher temperature and that the coefficient tends to converge to a fixed value at a very high temperature (>250˚C). For the purpose of this study, it was assumed that the ratios of the coefficients of sliding friction with T set equal to -40˚C, 20˚C and 250˚C are 3:2:1 for all values of sliding velocity and axial pressure. The following expression is proposed to define the temperature dependence of friction:

$$\mu(T) = \mu_{T=T_o} \times 0.79 \times \left(0.70^{T/50} + 0.40 \right) \tag{3-21}$$

where $\mu_{T=T_o}$ is the coefficient of friction measured at a reference temperature T_o and $\mu(T)$ is the coefficient of friction at a temperature T measured in °C. T_o is set equal to 20°C. The ratios of the coefficient of friction per Equation (3-21) are 3.0:2.2:1.0, and very close to the target of 3:2:1. The effect of the choice of ratio on maximum displacement response is studied later in the chapter.

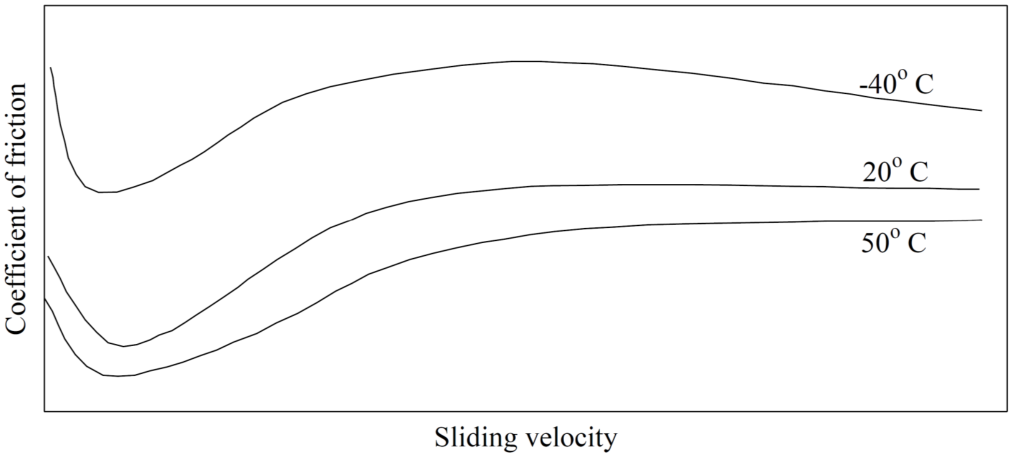

Figure 3-8: Schematic of the variation in the coefficient of friction with sliding velocity and temperature (adapted from Constantinou *et al.* (2007))

3.2.3.3 Method to compute temperature

The temperature at a point on the sliding interface depends on the loading path (prior heating of the sliding surface and its decay with time) and the instantaneous heat flux, which in turn is a function of the temperature at the sliding interface. At a given point on the sliding surface, the temperature rise ΔT during the beginning of motion to the time t is calculated using Equation (3-22), which assumes a half space below the contact surface (Constantinou *et al.*, 2007).

$$\Delta T(x,t) = \frac{\sqrt{D}}{k\sqrt{\pi}} \int_0^t q(t-\tau)\, e^{\left(\frac{-x^2}{4D\tau}\right)} \frac{d\tau}{\sqrt{\tau}} \tag{3-22}$$

where x is the depth measured from the sliding surface, D is the thermal diffusivity of steel, k is thermal conductivity of steel and q is heat flux. Based on the information presented in Constantinou *et al.* (2007), D and k are set equal to 4.44x10^{-6} m^2/s and 18 W/(m$^{\circ}$C), respectively. The instantaneous heat flux at a monitoring location is the product of the instantaneous values of coefficient of friction, axial pressure and the velocity of sliding, if the monitoring location falls below the slider, and zero otherwise. For the ease of computation, the circular slider is approximated by a square of same area. The temperature at a monitoring location is then calculated as the sum of temperature at the sliding interface at the beginning of the motion and the temperature rise ΔT.

The temperature at a monitoring point increases as the slider passes over it and decreases slowly towards ambient temperature otherwise. Panel (a) of Figure 3-9 shows a schematic of the path of the center of slider as it starts from point 1, travels through points 2, 3 and 4, comes back to point 2 again before heading to point 5. Panel (b) of the figure presents a schematic of the temperature at point 2 as a function of location of the center of slider. There is no change in the temperature as the slider travels from point 1 to point 2. The temperature rises sharply as the slider passes over point 2. The temperature at the point 2 decreases as the slider travels over points 3 and 4, and rises again as the slider passes over it again. The temperature then decreases as the slider moves away towards point 5.

There are two key assumptions involved in the method to compute the temperature at a point on the sliding surface, namely, 1) there is half space below the sliding surface, and 2) radiation losses are insignificant. The significance of the two assumptions in the estimation of the response of sliding isolation systems is examined in the next chapter.

3.2.3.4 Representative temperature monitoring location at the sliding surface

The modifications in the properties of the PTFE-type composite coating of the slider due to heating effects, and consequent changes in the coefficient of friction, are a function of the path of the slider on the sliding surface and the temperature at the points on the sliding surface directly below the slider. This section compares the maximum displacement responses of an FP bearing obtained using two approaches to incorporate the temperature dependence of the coefficient of friction defined by Equation (3-21) in a response-history analysis.

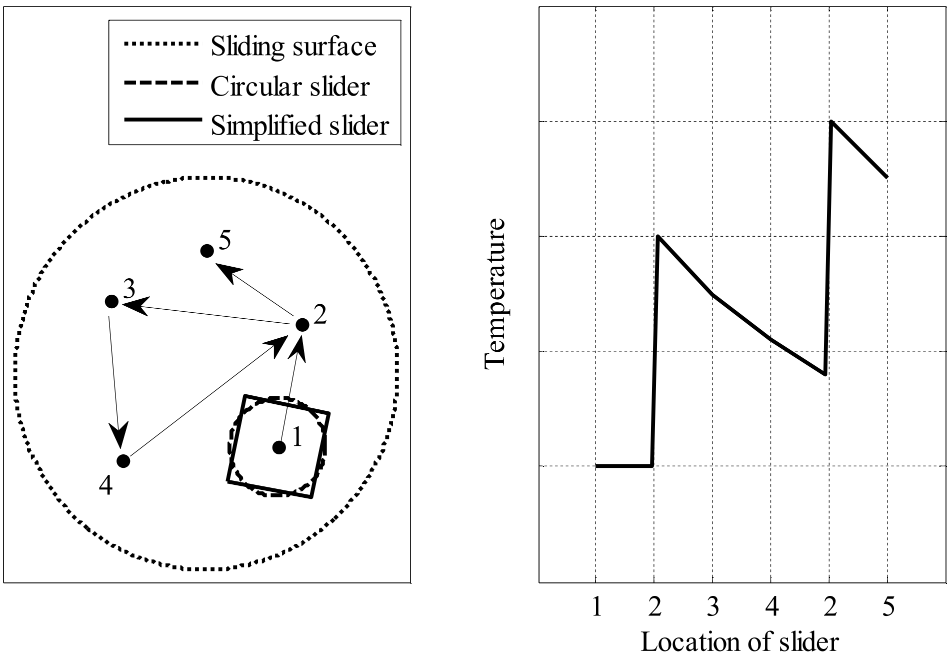

(a) Path of slider

(b) Temperature at monitoring location 2

Figure 3-9: Schematic of rise and decay in temperature at a monitoring location at the sliding surface as the slider is passes through the location

In the first approach, temperature is tracked at uniformly distributed monitoring locations (points) on the sliding surface and the average value of the temperature at points directly below the slider is used for T in Equation (3-21). Panel (a) of Figure 3-10 shows the plan view of an FP bearing with the points distributed in a square pattern. It also shows the path of the center of the slider, when the bearing is subjected to a ground motion. The sides of the equivalent square slider are oriented parallel to the two horizontal axes. For the configuration shown in the panel, the average of the temperature at the two points directly below the slider is used in Equation (3-21) to compute the coefficient of friction, adjusted for heating effects.

Panels (a) and (b) of Figure 3-11 show the path of the center of the slider of an FP bearing with the sliding period of 3 s, the Coulomb-type coefficient of friction 0.06 and static axial pressure of 50 MPa, subjected to ground motions 1 and 30, respectively (details of these ground motions are presented in Appendix A). The radius of the circular slider is 0.2 m. The equivalent square slider is over the center of the sliding surface if the center of the slider is within the dashed circle. It is clear from the two panels that the center of the sliding surface is the most traversed point on the sliding surface. For the second approach to incorporate the temperature dependence of friction in a response-history analysis, the temperature at the center of the sliding surface is used in Equation (3-21), which increases when slider is directly above the center of the bearing and decreases otherwise. The sides of the equivalent square slider are oriented either parallel or perpendicular to the line joining the centers of the slider and the sliding surface, as shown in panel (b) of Figure 3-10. This approach has also been suggested by Constantinou *et al.* (2007).

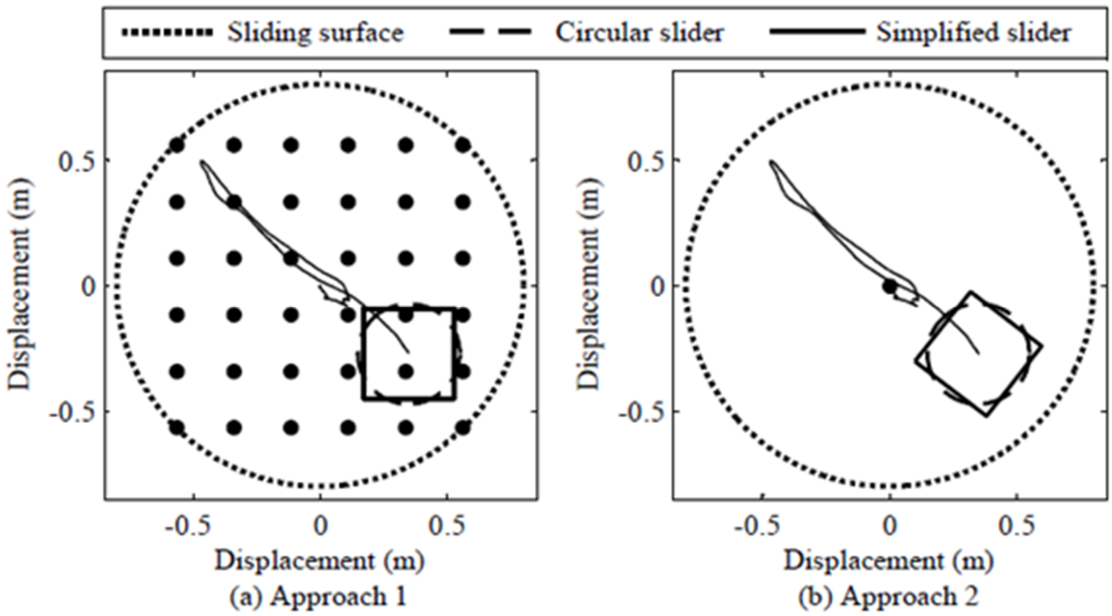

Figure 3-10: Approaches to incorporate temperature dependence of coefficient of friction in response-history analysis

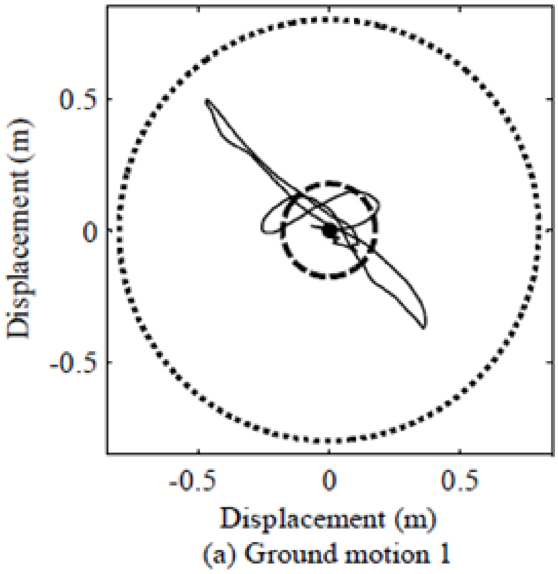

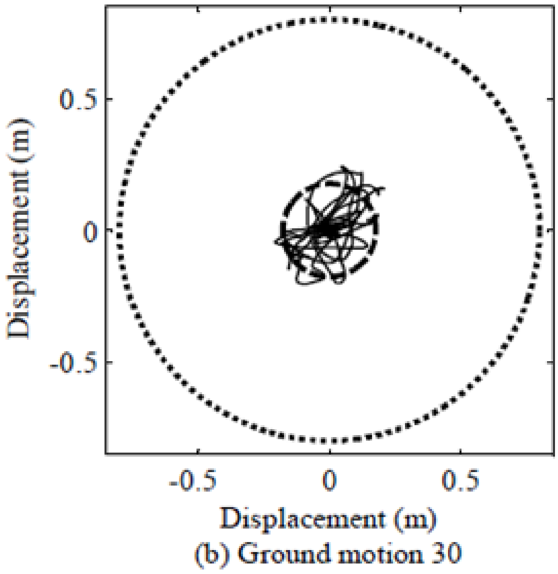

Figure 3-11: Path of the center of slider of an FP bearing subjected to the ground motions

An FP bearing with sliding period of 3 s, static axial pressure of 50 MPa and the temperature dependence of coefficient of friction defined using the two approaches (Figure 3-10) was subjected to the thirty ground motions (see Appendix A). Two values of spacing between the adjacent points are considered for the first approach: 250 mm and 150 mm. The coefficient of friction at the reference temperature of 20°C is 0.06. Mass proportional damping of 2% of critical was assigned to the system with the proportionality constant updated at every step of the analysis based on the instantaneous eigenvalue of the system.

Figure 3-12 presents the distribution of maximum displacement responses (assuming lognormal distribution) for bearings with the temperature dependent coefficient of friction at the sliding surface defined using the two approaches. The median estimates of maximum displacement obtained using the first approach with spacing of 250 mm and 150 mm differ by less than 2 mm, indicating that the response is not sensitive to the spacing of the points where temperature is computed. The difference in the median responses estimated using the two approaches is 5 mm, whereas 99th percentile response obtained using the first approach is greater by 30 mm compared to that obtained using second approach. Across the thirty ground motions, the minimum, mean and maximum differences in the maximum displacement responses obtained using the two approaches are 0 mm, 20 mm and 80 mm, respectively. It is, therefore, clear that the two approaches approximately yield the same results. Considering its simplicity, the second approach (defining temperature dependence of coefficient of friction based on the temperature at the center of the sliding surface) is adopted in this study.

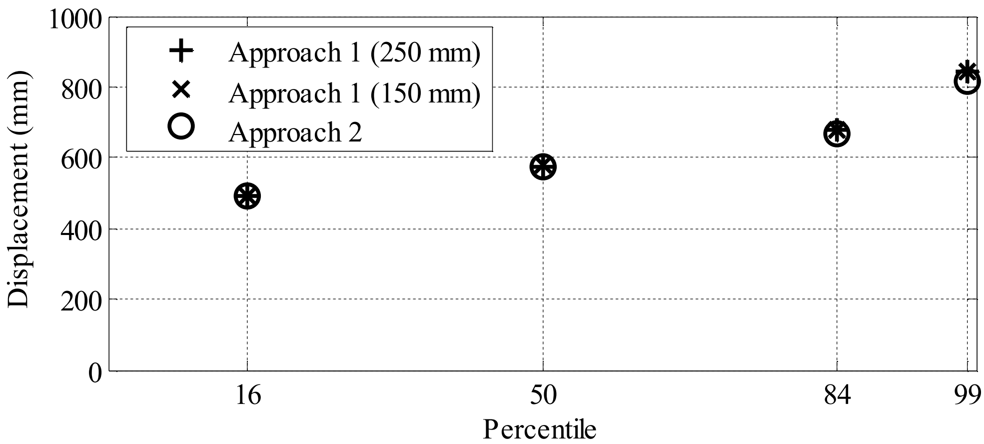

Figure 3-12: Distribution of maximum displacement of FP bearing with the temperature dependent coefficient of friction defined using different approaches

3.2.4 Combined effect of velocity, pressure and temperature on friction

This section presents the approach to consider the effect of one or more quantities (e.g., pressure and temperature) on the coefficient of friction. The right side of equations (3-3), (3-14) and (3-19) are the product of a reference coefficient of friction multiplied by a factor accounting for velocity, pressure and temperature, respectively. In Equation (3-3), $\mu_{\max}$ is the reference coefficient of friction at a very high velocity of sliding. Similarly, in equations (3-14) and (3-19),

$\mu_{p=p_o}$ and $\mu_{T=T_o}$ are the coefficient of friction at a reference axial pressure p_o and a reference temperature T_o, respectively. Based on assumptions and experimental observations mentioned above, the factors accounting for the effect of velocity (k_v), axial pressure (k_p) and temperature (k_T) are given by the following equations.

$$k_v = 1 - 0.5e^{-100v} \tag{3-23}$$

$$k_p = 0.70^{(p-p_o)/50} \tag{3-24}$$

$$k_T = 0.79 \times \left(0.70^{T/50} + 0.40\right) \tag{3-25}$$

where all the terms are defined previously. Unless stated otherwise, the equations are assumed to be applicable for all PTFE-type composite materials, and the entire range of temperature, axial pressure and velocity of sliding, although the parameters for the equations are obtained based on the experiments performed on bearings with different materials under different loading conditions.

A reference coefficient of friction μ_{ref} is considered, which is defined as the coefficient of friction at a bearing pressure p_o, measured at a high velocity of sliding with the temperature at the sliding surface being T_o (fixed at 20˚C). To consider more than one effect at a time μ_{ref} is multiplied by appropriate factors. For example, the coefficient of friction accounting for the effect of velocity and temperature is obtained by multiplying μ_{ref} by k_v and k_T.

Based on the equations (3-23), (3-24) and (3-25), panels (a) to (c) of Figure 3-13 show the variation in coefficient of friction with increase in the temperature at the sliding interface for three values of velocity of sliding, 1000 mm/s, 10 mm/s and 0.001 mm/s, with μ_{ref} fixed at 0.09, 0.06 and 0.03, respectively. Panels (d) to (f) of the figure plot the coefficient of friction against axial pressure.

For the temperature at the sliding interface fixed at 200˚C, 50˚C and 20˚C, panels (a) to (c) of Figure 3-14 plot coefficient of friction versus axial pressure, and panels (d) to (f) of the figure show the variation in the coefficient of friction with velocity of sliding at the interface with μ_{ref} set equal to 0.09, 0.06 and 0.03, respectively.

Figure 3-15 shows the plots of coefficient of friction versus temperature at the sliding interface in panels (a) to (c), and the plots of coefficient of friction versus velocity of sliding in panels (d) to (f) for of μ_{ref} set equal to 0.09, 0.06 and 0.03, respectively, for two values of axial pressure: 10 MPa and 50 MPa. The reference coefficients of friction μ_{ref} in Figure 3-13, Figure 3-14 and Figure 3-15 are assumed to be measured at a high velocity of sliding (≈200 mm/s), at a reference axial pressure p_o equal to 10 MPa and at a reference temperature at the sliding interface T_o equal to 20˚C.

3.3 Summary

This chapter focuses on characterization of coefficient of friction at the sliding surface of a Friction Pendulum™ (FP) bearing. The coefficient of friction updates during the course of an earthquake depending on sliding velocity, axial pressure and temperature at the sliding surface. Expressions to define the dependence of coefficient of friction on the three quantities are proposed based on available experimental data. Suitable assumptions are made in order to decouple the expressions. Two methods of tracking temperature at the sliding surface are compared in terms of the impact on the maximum displacement response of a bearing.

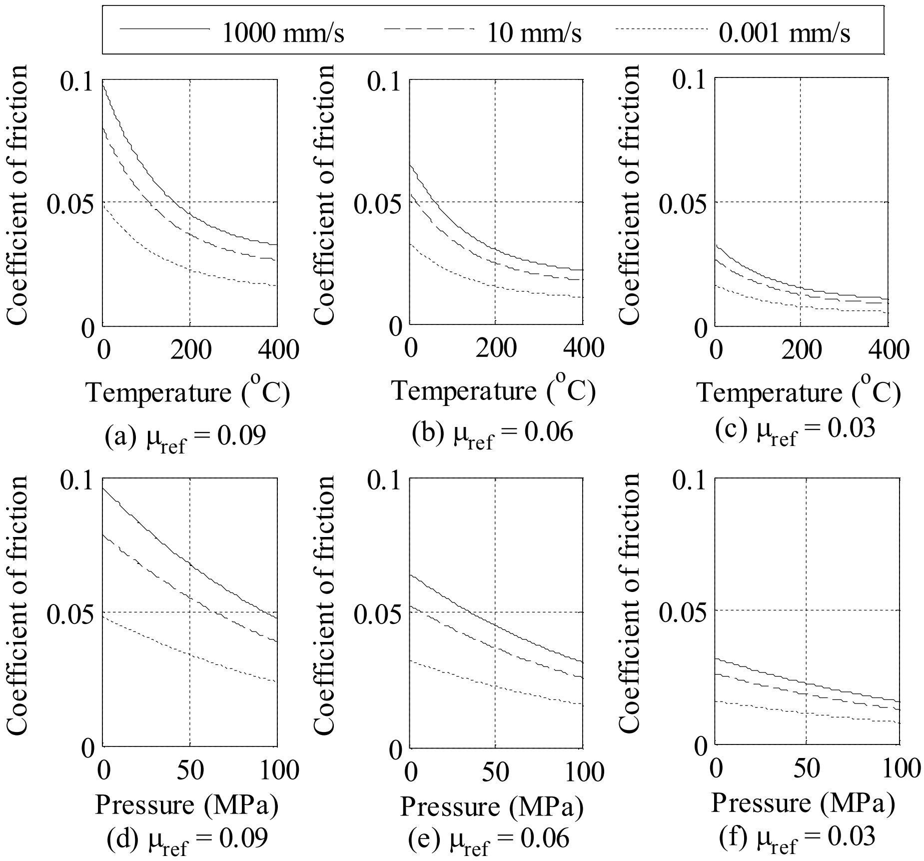

Figure 3-13: Coefficient of friction plotted against temperature (panels (a)–(c)) and pressure (panels (d)–(f)) for three values of reference coefficient of friction (0.09, 0.06, 0.03) and three values of sliding velocity (1000 mm/s, 10 mm/s, 0.001 mm/s)

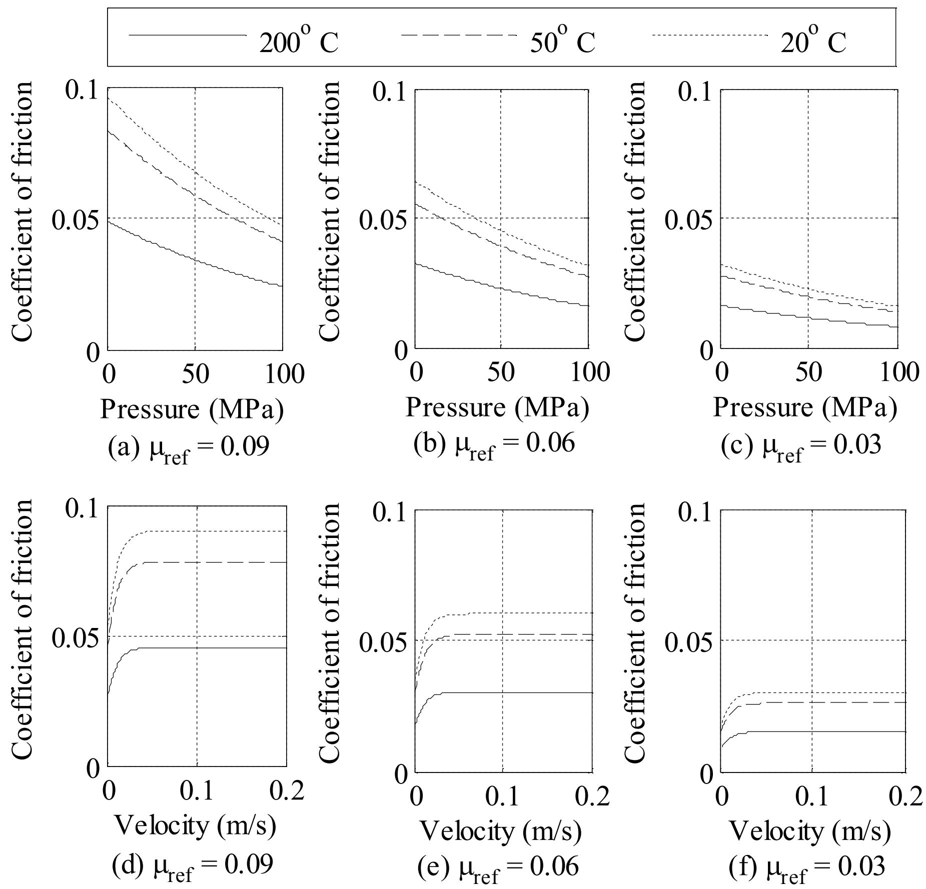

Figure 3-14: Coefficient of friction plotted against axial pressure (panels (a)–(c)) and sliding velocity (panels (d)–(f)) for three values of reference coefficient of friction (0.09, 0.06, 0.03) and three values of temperature at the sliding surface (200°C, 50°C, 20°C)

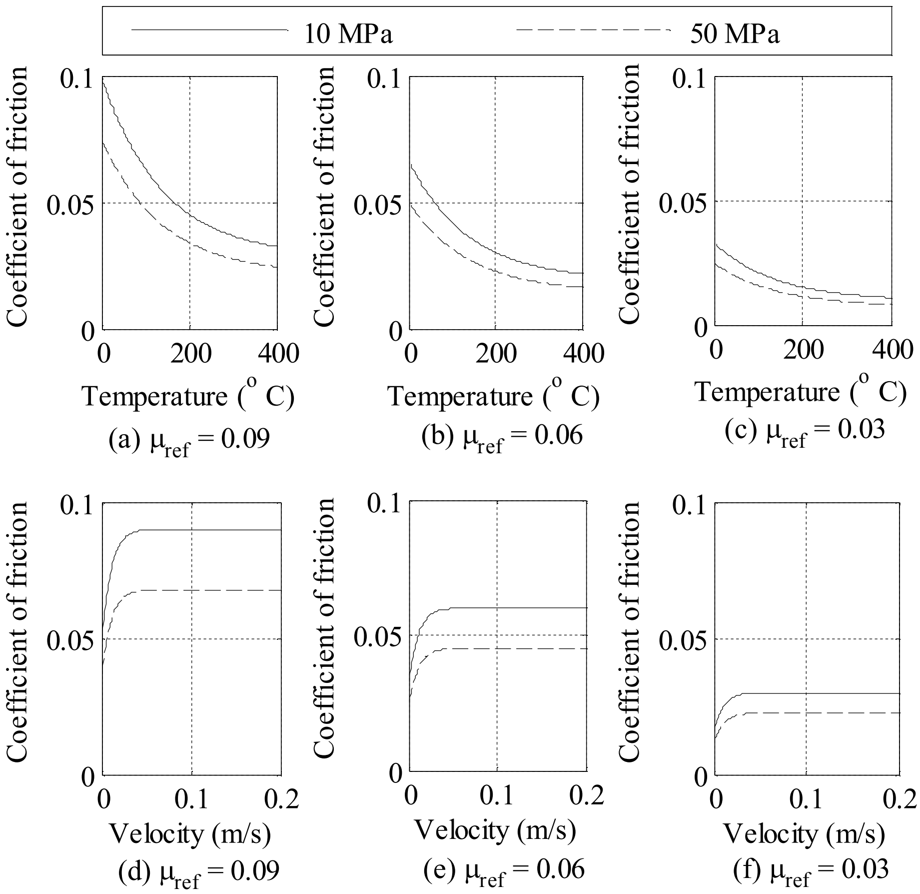

Figure 3-15: Coefficient of friction plotted against temperature (panels (a)–(c)) and sliding velocity (panels (d)–(f)) for three values of reference coefficient of friction (0.09, 0.06, 0.03) and two values of axial pressure (10 MPa, 50 MPa)

CHAPTER 4

OPENSEES SLIDING BEARING ELEMENT: VERIFICATION AND VALIDATION

4.1 Introduction

A model to describe friction as a function of axial pressure, temperature at the sliding surface and velocity of sliding was proposed in Chapter 3. This chapter presents the features of the new OpenSees element *FPBearingPTV* that incorporates the friction model. The assumptions in the modeling of the Friction Pendulum™ (FP) bearing are discussed. The element is verified and validated.

4.2 Mathematical Modeling

The FP bearing can displace in six directions, namely, rotate about two horizontal axes, twist about a vertical axis, translate in the vertical direction, and translate in the two horizontal directions. The boundary conditions imposed on the bearing by a foundation and the supported superstructure generally do not allow the bearing to rotate about the two horizontal axes. For torsional motion about the vertical axis to take place, the moment capacity due to friction at the sliding surface or that due to friction between the slider and the housing plate has to be overcome. The slider is considered to be rigid in the vertical direction, but vertical rigid-body motion of the slider accompanies displacement in the horizontal direction.

The translational motion of an FP bearing in the two horizontal directions is a function of the geometrical and material properties (e.g., coefficient of friction at the sliding surface, radius of curvature) and axial load on the bearing. A model to characterize the coefficient of friction at the sliding surface was presented in Chapter 3. For given values of coefficient of friction, axial load and radius of curvature of the sliding surface, the lateral force-displacement of the FP bearing under cyclic loading is described by the curve shown in Figure 4-1(a).

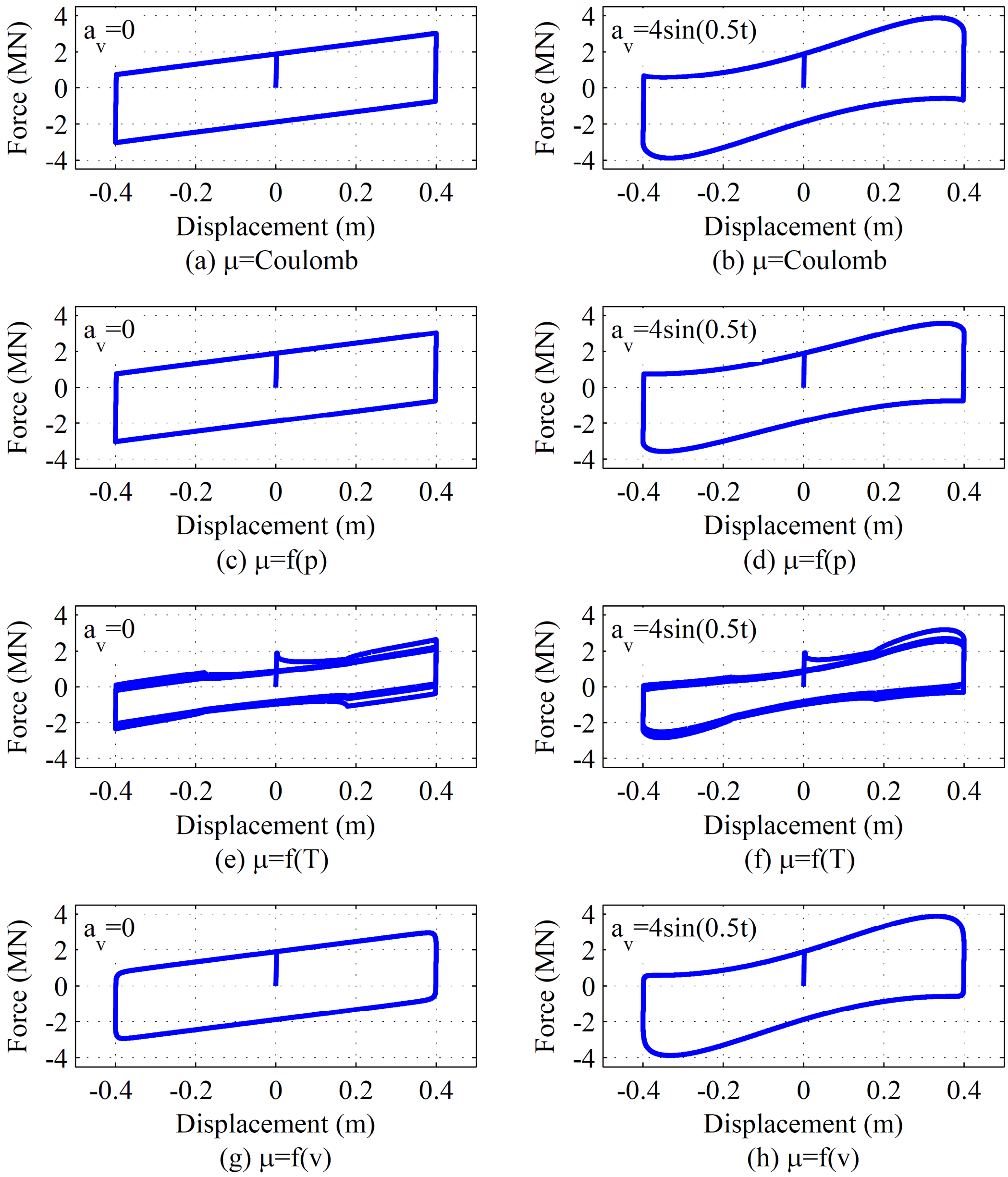

Figure 4-1: Force-displacement response of an FP bearing subjected to cyclic horizontal and vertical loading with different choices of friction model (Coulomb, pressure-dependent, temperature-dependent and velocity-dependent)

The lateral force-displacement relationship can be mathematically modeled using the theory of plasticity. The motion at the sliding surface is elastic when the resultant external force on the bearing is smaller than that required to overcome friction. Sliding takes place thereafter. The motion on the sliding surface in the elastic and sliding regimes is modeled using the theory of plasticity, which is discussed in detail by Simo and Hughes (1998), Sivaselvan and Reinhorn (2004) and Ray (2013), among others. For a given horizontal displacement increment, the force increment is given by the following expression (Mosqueda *et al.*, 2004):

$$\begin{bmatrix} \Delta F_x \\ \Delta F_y \end{bmatrix} = \frac{W}{R}\begin{bmatrix} \Delta u_x \\ \Delta u_y \end{bmatrix} + \mu W \frac{1}{\|\dot{u}\|}\begin{bmatrix} \dot{u}_x \\ \dot{u}_y \end{bmatrix} \tag{4-1}$$

where Δu_x and Δu_y are the displacement increments in the two horizontal directions X and Y, W is the instantaneous axial load on the bearing, R is the radius of curvature of the sliding surface, μ is the coefficient of friction, $\|\dot{u}\|$ is the magnitude of velocity of sliding, $\dot{u}_x$ and $\dot{u}_y$ are the sliding velocities, and ΔF_x and ΔF_y are the incremental forces in the X and Y directions, respectively.

4.3 Features of OpenSees Element *FPBearingPTV*

The element *singleFPBearing* is available in the software program OpenSees (PEER, 2014) to model a single Friction Pendulum™ (FP) bearing. It permits the user to choose a friction model with the coefficient of friction defined as a function of sliding velocity, axial pressure or both. There is no friction model available in OpenSees that considers the dependence of the coefficient of friction on temperature at the sliding surface. Suitable modifications were made in the source code of the *singleFPBearing* element to incorporate the dependence of coefficient of friction on sliding velocity, axial pressure and temperature at the sliding surface, as defined in Chapter 3. The new element is named *FPBearingPTV*. The key features of the new element are discussed below.

Figure 4-1(a) presents the force-displacement response of a bearing with the coefficient of friction defined using a Coulomb model, a sliding period of 3 s, a static axial pressure of 50 MPa, a slider radius of 0.2 m, and a reference coefficient of friction, μ_{ref} of 0.3, subjected to cyclic loading with horizontal displacement described by $u = 0.4\sin(0.25t)$ meters[1].

Figure 4-1(b) presents the force-displacement response of the bearing subjected to a vertical acceleration of $a_v = 4\sin(0.5t)$ m/s^2 in addition to the horizontal cyclic loading of Figure 4-1(a). Figures 4-1(c), 4-1(e) and 4-1(g) present the force-displacement response of the bearing subjected to the horizontal cyclic loading of panel (a), but with the coefficient of friction considered to vary with axial pressure, temperature at the sliding surface and sliding velocity, respectively. Figures 4-1(d), 4-1(f) and 4-1(h) plot the force-displacement response when the bearing is subjected to the horizontal and vertical cyclic loading of panel (b) and the coefficient of friction is pressure-, temperature- and velocity-dependent, respectively.

It is clear from Figure 4-1 that the temperature at the sliding surface affects the coefficient of friction (and the force-displacement history) most significantly (see panels (e) and (f)) during the cyclic loading, for the loadings considered and assumptions made. The coefficient of friction decreases with an increasing number of cycles when the temperature-dependent friction model is considered (compare panel (e) with panels (a), (c) and (g)). It can also be observed from

[1] This combination is selected to demonstrate clearly the influence of sliding velocity and temperature on μ. The chosen values are impractical for a seismic isolation system in a nuclear structure.

panel (e) that the change in the coefficient of friction is greater (the force-displacement loop is "thinner") when the imposed displacement is smaller than the radius of slider (= 0.2 m), compared to the case for which the displacement is greater than the radius. This is because the temperature at the center of the sliding surface is used to update the coefficient of friction (see Chapter 3). The temperature increases (and the coefficient of friction decreases) when the slider is directly above the center of the bearing and decreases otherwise.

The effect of the velocity dependence of friction can be observed by comparing Figures 4-1(a) and 4-1(g) at the peak displacements (= ±0.4 m). A change in direction of motion takes places at this displacement and the velocity decreases from a positive value to zero to a negative value (or vice-versa). The reduction in the velocity-dependent coefficient of friction associated with the decrease in velocity (as the slider approaches the peak displacement) results in a smoother change in force compared with the Coulomb model.

Figures 4-1(a) and 4-1(c) present the force-displacement histories of the bearing for the Coulomb and pressure-dependent friction models, respectively. The axial pressure is constant for the bearing in the two panels and there is no variation in the coefficient of friction due to change in axial pressure. The force-displacement histories in the two panels are identical. Figures 4-1(b) and 4-1(d) present the force-displacement responses for the Coulomb and the pressure-dependent friction model, respectively, when the time-varying axial load (associated with the vertical acceleration) is imposed on the bearing. The influence of changes in axial pressure on the coefficient of sliding friction is seen by comparing the two force-displacement histories (see Figure 4-2).

4.4 Assumptions in Modeling FP Bearings

The assumptions involved in the modeling of FP bearings using the OpenSees element *FPBearingPTV* are discussed in this section.

4.4.1 Normal force on the sliding surface

Figure 4-3(a) shows the forces acting on an FP bearing as the slider rotates through angle θ. Panel (b) of the figure shows the normal force, N, and shear force, S, on the sliding surface. The equilibrium equations in the horizontal and vertical directions on the slider are (e.g., Fenz and Constantinou (2008b)):

$$F - N\sin\theta - S\cos\theta = 0 \tag{4-2}$$

$$W + S\sin\theta - N\cos\theta = 0 \tag{4-3}$$

where F is the horizontal force, W is the vertical force, and other parameters were defined previously. Solving the two equations yields the following expression for the horizontal force F.

$$F = \frac{W}{R\cos\theta}u + \frac{S}{\cos\theta} \tag{4-4}$$

where u is the horizontal displacement, R is the radius of curvature of the sliding surface, and other parameters were defined previously. Variables u, R and θ are related by the following expression.

$$u = R\sin\theta \tag{4-5}$$

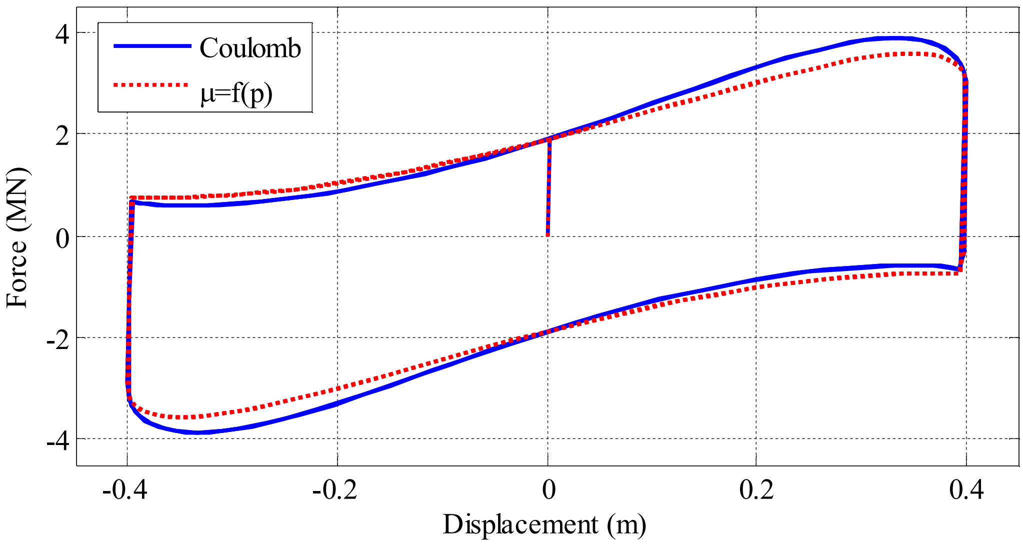

Figure 4-2: Force-displacement response of an FP bearing subjected to cyclic horizontal and vertical loading with friction described using Coulomb model and a pressure dependent friction model

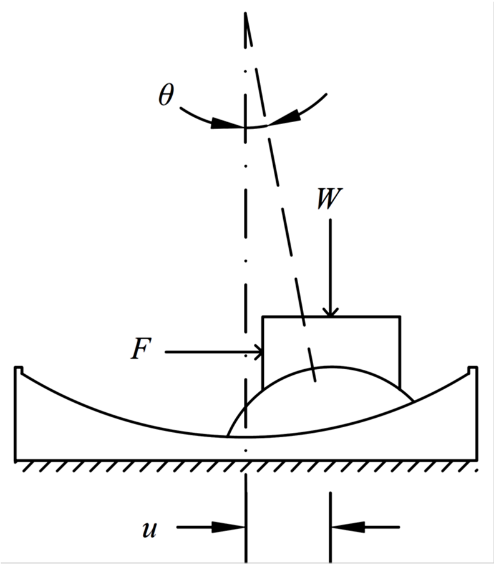

(a) Forces on an FP bearing

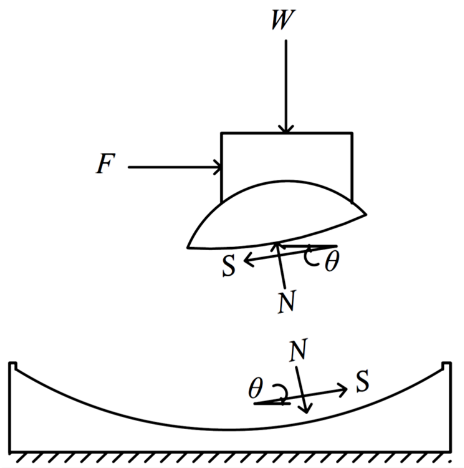

(b) Forces on the sliding surface

Figure 4-3: Friction Pendulum bearing in a deformed configuration

The shearing force, S, is the product of the coefficient of sliding friction, μ, and the normal force N.

$$S = \mu N \tag{4-6}$$

The normal force, N, is related to the horizontal force, F, and the vertical force, W, as follows:

$$N = F\sin\theta + W\cos\theta \tag{4-7}$$

where all terms were defined previously. Combining (4-4), (4-5), (4-6) and (4-7) yields the following relationship between the normal force, N, and the vertical force, W.

$$N = \frac{W}{\sqrt{1-\left(\frac{u}{R}\right)^2} - \mu\frac{u}{R}} = \frac{W}{\cos\theta - \mu\sin\theta} \tag{4-8}$$

This expression assumes that the normal pressure on the sliding surface is uniform and the resultant normal force N acts through the center of the contact area at the sliding surface. This, however, is not the case as N shifts from the center of the contact area to balance the horizontal force F, as seen in Figure 4-4, which is adapted from Sarlis and Constantinou (2013). The magnitude of N is a function of forces F and W, and the geometry of the slider. Equation (4-8) does not include the influence of the geometry of the slider.

The ratio of N to W is 1.00, 1.01, 1.03 and 1.07, when u/R is equal to 5%, 10%, 20% and 30%, respectively, per Equation (4-8), with a coefficient of friction at the sliding surface of 0.06. Because $N \approx W$, N is set equal to W for this study, as assumed by Sarlis and Constantinou (2013).

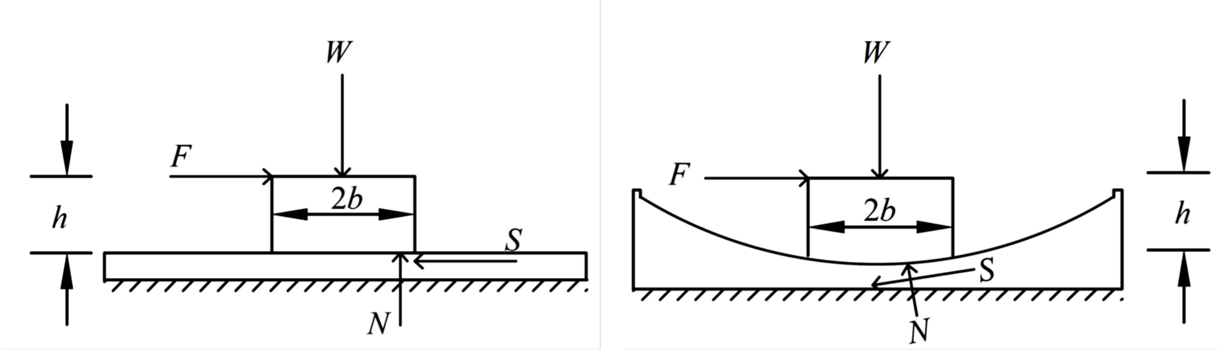

(a) Flat slider (b) FP bearing

Figure 4-4: Resultant normal force on sliding surfaces (adapted from Sarlis and Constantinou (2013))

4.4.2 Vertical acceleration due to curvature

The motion of a slider in the horizontal and vertical directions is coupled due to the curvature of the sliding surface. The acceleration of the slider relative to the sliding surface adds to the ground acceleration in the vertical direction, affecting the inertial force and the axial pressure on the bearing, which in turn influences the force-displacement response. Figure 4-5 shows the vertical motion of the slider relative to the sliding surface and that of the ground. In this study, the component of vertical acceleration due to relative motion of the slider on the sliding surface is assumed to be small compared to the vertical component of ground acceleration. See Appendix C for details.

4.4.3 Relative vertical displacement in adjacent bearings

The slider of an FP bearing rises as it displaces laterally. The increase in height depends on the geometrical properties of the bearing, translation and rotation in the isolation system and location of the bearing in the isolation system. An isolation system comprising 289 FP bearings spread uniformly over plan dimensions of 96 m × 96 m (centerline spacing of 6 m) is subjected to combined translations and rotations such that the resultant peak displacement of at least one FP bearing in the system is greater than $0.2R$ (a traditional limit on the maximum displacement in an FP bearing; see Constantinou *et al.* (2011)). A translation of 0.200 m (0.600 m) and/or a rotation of 0.12° (0.36°) is imposed on the isolation system comprising 2 s (4 s) bearings; the rotation corresponds to a displacement of 0.100 m (0.300 m) for the bearing in the outermost row and closest to the center of the isolation system. The maximum increase in height of an FP bearing across all the loading combinations is 0.116 m, and the maximum relative vertical displacement between adjacent bearings is 0.009 m over a distance of 6 m (a gradient of 1/667). This relative displacement is too small to produce significant stresses in an isolated superstructure. See Appendix D for details.

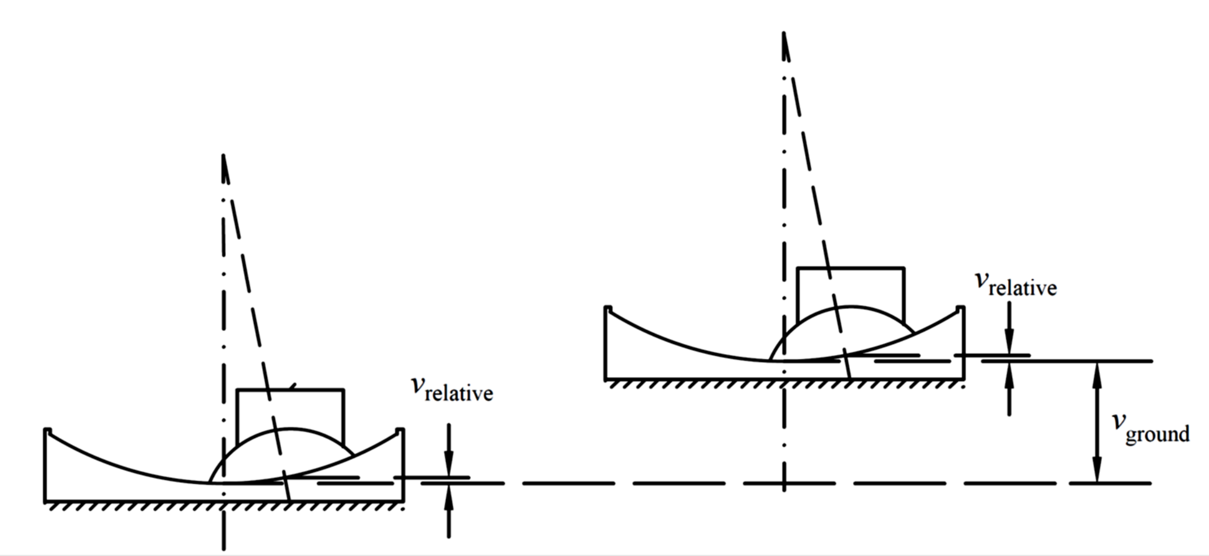

(a) Translation of slider relative to sliding surface, v_{relative}

(b) Ground translation, v_{ground}, and v_{relative}

Figure 4-5: Vertical translation of the slider of an FP bearing

4.4.4 Moment due to horizontal force associated with relative vertical displacement

A moment, M_W, due to the vertical force, W, is transferred to the foundation, depending on the horizontal distance, $u_{\text{horizontal}}$, between the center of the sliding surface and the line of action of the force (see Figure 4-6):

$$M_W = Wu_{\text{horizontal}} \tag{4-9}$$

For simplicity, $u_{\text{horizontal}}$ is assumed equal to the horizontal displacement of the slider relative to the sliding surface. A moment is transferred to the top of the foundation due to the horizontal force on the slider, F, depending on the vertical distance between the top of the foundation and the line of action of the horizontal force. The component of the moment, M_F, due to the horizontal force associated with the increase in height of the FP bearing, v_{relative}, is given by (see Figure 4-6):

$$M_F = Fv_{\text{relative}} = \left(\mu W + \frac{W}{R} u_{\text{horizontal}} \right) v_{\text{relative}} \tag{4-10}$$

where R is the radius of curvature, μ is the coefficient of friction at the sliding surface and the other parameters were defined previously. Figure 4-6 shows the forces and distances in the horizontal and vertical directions. The distances v_{relative} and $u_{\text{horizontal}}$ are related as follows:

$$v_{\text{relative}} = R - \sqrt{R^2 - u_{\text{horizontal}}^2} \tag{4-11}$$

where all terms were defined previously. For an FP bearing with the radius of curvature of the sliding surface of R, vertical load of W, coefficient of friction (Coulomb-type) of 0.06

subjected to the horizontal displacement, $u_{\text{horizontal}}$, equal to 10%, 20% and 30% of R, the ratios of moments M_F to M_W are 0.01, 0.03 and 0.06, respectively. Therefore, M_F is considered small and is not included in the moment transferred to the sliding surface.

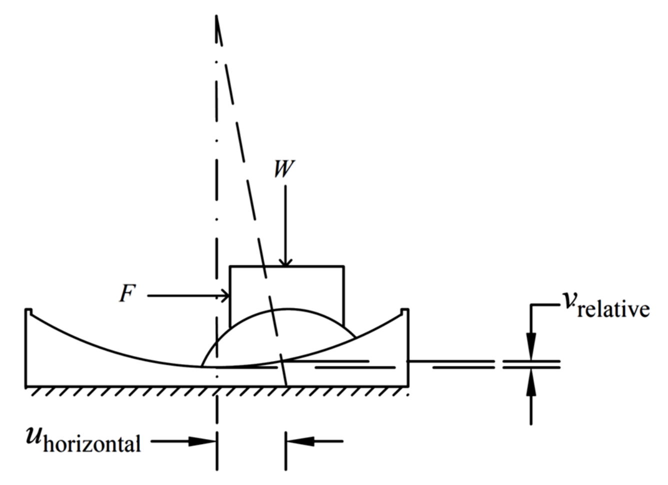

Figure 4-6: Forces and displacements in an FP bearing in the horizontal and vertical directions

4.4.5 Impact following uplift

During very severe earthquake-induced shaking, there is a possibility of loss of contact between slider, sliding surface and/or housing plate of an FP bearing. The re-engagement of slider with the sliding surface and/or the housing plate following uplift will involve impact, which may produce high axial forces in the bearing. The OpenSees element *FPBearingPTV* does not address this behavior and the axial load is set equal to zero in the event of uplift.

4.4.6 Assumption of half-space in temperature calculations

The heat generated at the sliding surface has been assumed to be transferred to the sliding surface as if it is a semi-infinite space: 1) the heat generated at the sliding surface is transferred into the stainless steel, and 2) the transfer of heat is perpendicular to the sliding surface. These two assumptions are discussed below.

The slider of an FP bearing is coated with a PTFE-type composite material and the sliding surface is polished stainless steel. The heat generated at the sliding surface is distributed to the composite coating on the slider and the polished stainless steel in a ratio depending on the thermal conductivity and thermal diffusivity of the two materials. At 20°C, stainless steel has a thermal conductivity (= 16.3 W/(m.°C)) of about 70 times that of a PTFE-type composite, and the thermal diffusivity of stainless steel (= 4.44×10^{-6} m^2/s) is about 50 times that of the PTFE-type composite (e.g., Constantinou *et al.* (2007)). The fraction of the heat transferred to the PTFE-type composite material is very small and ignored hereafter.

The assumption that heat is transferred in the direction perpendicular to the sliding surface allows for computation of temperature at a point on the sliding surface using a closed form integral. Constantinou *et al.* (2007) estimated (assuming the half-space) that for an FP bearing with the axial pressure of 30.8 MPa, coefficient of friction of 0.05, and a slider radius of 0.250 m, subjected to 10 cycles of displacement-controlled loading with an amplitude of 0.260 m and frequency of 0.6 Hz, the penetration of heat into the sliding surface is 0.030 m (temperature rise at this depth was negligible). This depth is small compared with the size of the heat source (= 0.500 m, the diameter of the slider) and also with the thickness of the sliding surface (> 0.086 m), implying that the assumption of a half-space is valid at the sliding surface.

4.4.7 Radiation losses

Heat is emitted from a point on the sliding surface through radiation, when the point is exposed to the environment and temperature at the point is greater than the ambient temperature. The heat flux at a point due to radiation, q_r, is given by the Stefan-Boltzmann law (e.g., Incropera and Dewitt (1985)):

$$q_r = \sigma_r \left(T^4 - T_o^4 \right) \tag{4-12}$$

where σ_r is the Stefan-Boltzmann constant (= 5.67 x 10^{-8} W/(m^2K^4)), and T and T_o are temperature at the exposed surface and the ambient temperature, respectively, measured in Kelvin.

Figure 4-7(a) presents the heat flux generated due to friction at the center of the sliding surface of a 3 s FP bearing with a static axial pressure of 50 MPa and a reference coefficient of friction of 0.06, subjected to ground motion 10 (GM10: see Appendix A). Coulomb-type friction is assumed. Mass proportional damping of 2% of critical is assigned to the system with the proportionality constant updated at every time step of the analysis based on the instantaneous fundamental frequency of the system. Figure 4-7(d) plots the heat lost per unit area per unit time (or heat flux) at the center of the sliding surface due to radiation for the bearing, assuming T_o = 20˚C. Figures 4-7(b) and 4-7(c) present the heat flux generated due to friction, and Figures 4-7(e) and 4-7(f) plot the radiation losses at the center of the bearing, when it is subjected to GM20 and GM30, respectively. The range of the heat flux in panels (a) through (c) is 100 times that of panels (d) through (f). It is clear that the radiation losses are very small compared with the heat generated during sliding.

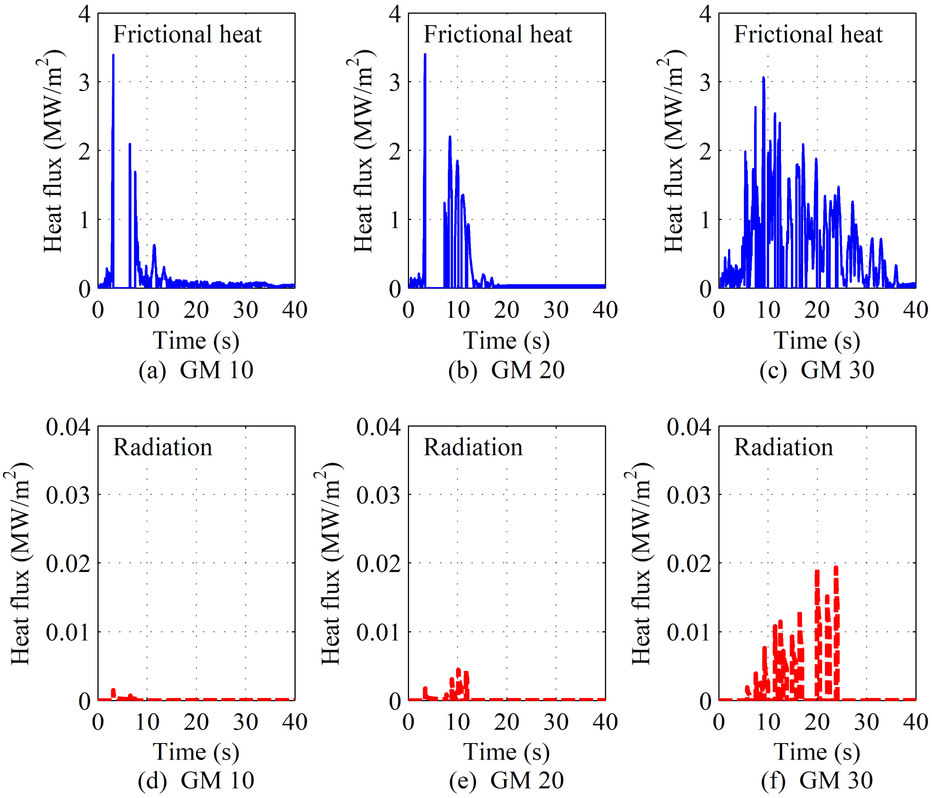

Figure 4-7: Heat flux histories due to conduction and radiation at the center of the sliding surface of an FP bearing

4.5 Verification of OpenSees Element *FPBearingPTV*

The new OpenSees element, *FPBearingPTV*, is verified in this section. Various agencies and professional organizations, such as the US Department of Defense, American Institute of Aeronautics and Astronautics, and American Society of Mechanical Engineers have adopted definitions of verification and validation; see Oberkampf and Roy (2010). Software is verified to ensure that it provides accurate numerical solutions to a mathematical model, which is often an approximate representation of the conceptual model. Validation ensures that the numerical models and algorithms reasonably recover experimental results. Verification of software often involves comparisons of results obtained using other verified and validated software for select problems. Figure 4-8 shows the process of verification and validation described by the American Society of Mechanical Engineers (ASME, 2006).

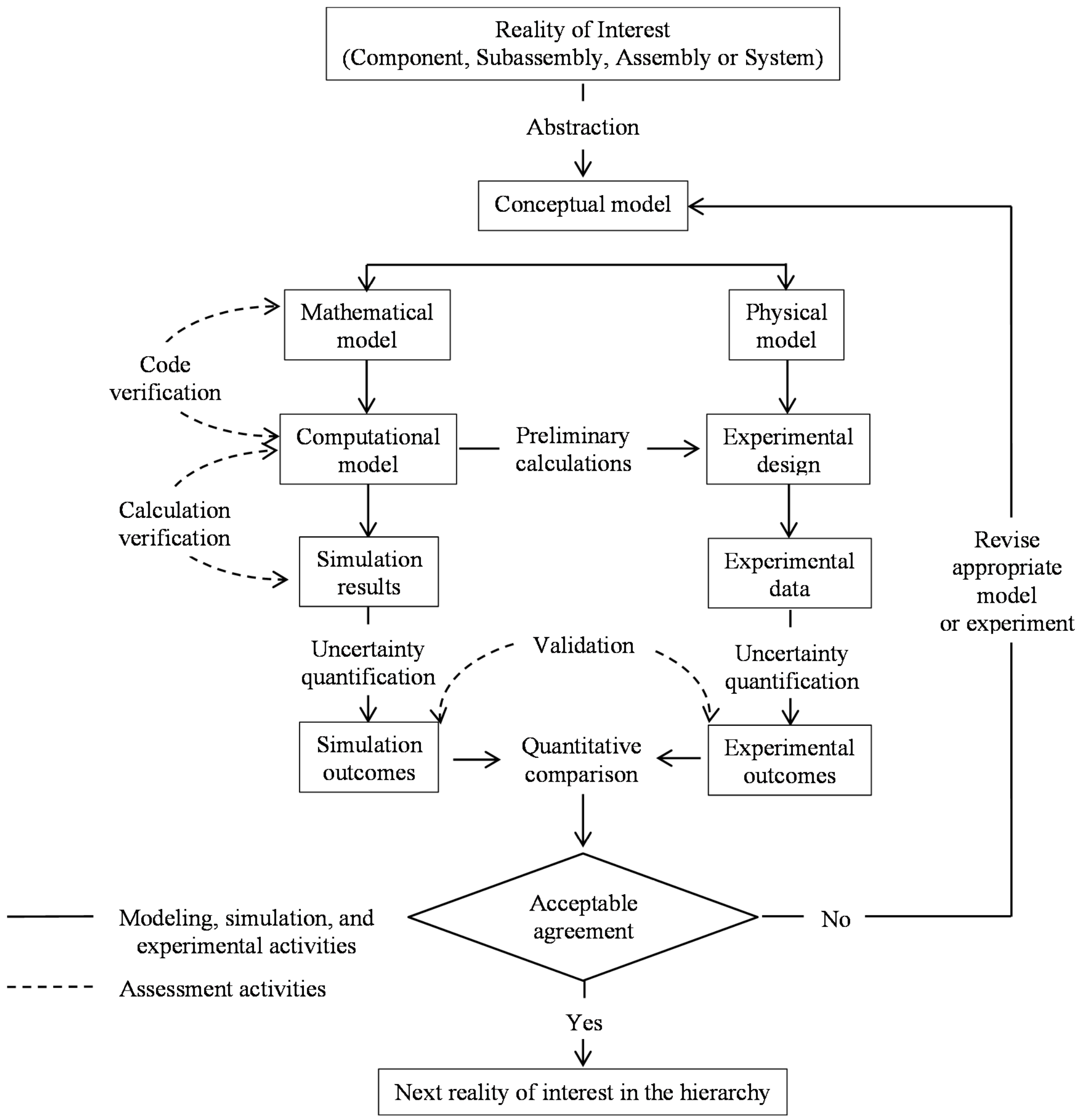

Figure 4-8: Verification and validation process (reproduced from ASME (2006))

The procedure suggested by Oberkampf and Roy (2010) is generally followed for the verification of the new OpenSees element. A similar approach has been used for the verification of new OpenSees elements for elastomeric and lead-rubber bearings (Kumar *et al.*, 2014). Validation of *FPBearingPTV* element is based on available experimental data.

Suitable metrics are needed to quantify the differences between the response histories obtained using two software programs (verification) or from software and an experiment (validation). The norms L_1 and L_2 are commonly used to quantify the differences (e.g., Sarin *et al.* (2010), Oberkampf and Roy (2010)). The two norms can characterize the magnitude of the differences between the two response histories.

$$L_1 = \frac{1}{N}\sum_{i=1}^{N}\left|r_{i,1} - r_{i,2}\right| \tag{4-13}$$

$$L_2 = \left(\frac{1}{N}\sum_{i=1}^{N}\left(\left|r_{i,1} - r_{i,2}\right|\right)^2\right)^{1/2} \tag{4-14}$$

where N is the number of data points, and r_{i1} and r_{i2} are the values of response quantities at the i^{th} step obtained from either the software programs, or from the software and the experimental studies. The metrics are normalized (e.g., Oberkampf and Barone (2006)) to quantify the differences between a response quantity (e.g., force history, displacement history) obtained from two processes, independent of the magnitude of the response quantity.

$$L_{1,\mathrm{n}} = \frac{1}{N}\sum_{i=1}^{N}\left|\frac{r_{i,1} - r_{i,2}}{r_{i,1}}\right| \times 100 \tag{4-15}$$

$$L_{2,n} = \left(\frac{1}{N}\sum_{i=1}^{N}\left(\left|\frac{r_{i,1} - r_{i,2}}{r_{i,1}}\right|\right)^2\right)^{1/2} \tag{4-16}$$

where $L_{1,\mathrm{n}}$ and $L_{2,\mathrm{n}}$ are the normalized estimates of the differences in the two response histories, and other parameters were defined previously.

The normalized metrics (e.g., (4-15)) can be high due to small *base* values, as noted by Schwer (2007) and Kat and Els (2012). For example, suppose at the 10th step of an analysis that the lateral force responses, $r_{10,1}$ and $r_{10,2}$, obtained from two programs are 2000 kN and 2100 kN, respectively, and at the 20th step of analysis the responses, $r_{20,1}$ and $r_{20,2}$, are 10 kN and 110 kN, respectively. The difference in force at the 10th and 20th steps are both 100 kN, whereas the percentage differences at the two steps are 5% and 1000%, respectively. The normalized percentage difference for the response histories incorporates the percentage differences of 5% and 1000% with equal weight (= $1/N$), if computed using (4-15). A better representation of accuracy can be achieved by assigning a weight, w_i, based on the amplitude of the response at an analysis step, which reduces the contribution of small to inconsequential values to the percentage difference:

$$w_i = \frac{|r_{i1}|}{\sum_{i=1}^{N} |r_{i1}|} \tag{4-17}$$

The resulting metric, weighted average absolute percentage difference, λ, is expressed as:

$$\lambda = \sum_{i=1}^{N} w_i \left| \frac{r_{i1} - r_{i2}}{r_{i1}} \right| \times 100 \tag{4-18}$$

Another expression for λ is obtained by substituting (4-17) into (4-18):

$$\lambda = \sum_{i=1}^{N} \left| \frac{r_{i1} - r_{i2}}{\sum_{i=1}^{N} |r_{i1}|} \right| \times 100 = \frac{\sum_{i=1}^{N} |r_{i1} - r_{i2}|}{\sum_{i=1}^{N} |r_{i1}|} \times 100 \tag{4-19}$$

The differences between two response histories may be great if there is a phase difference between the two histories, even when the amplitudes of the peaks compare well. Metrics have been proposed to quantify the differences due to magnitude and phase differences separately (e.g., Schwer (2007), Kat and Els (2012)). However, the relatively simple metrics given by (4-13), (4-15) and (4-19) are used here. The metric given by (4-19) is less sensitive to the phase difference between the response histories than (4-15); the former metric assigns a smaller weight for smaller base values[1], whereas the later metric adds the differences with equal weight. In addition to these three metrics, relative differences between peaks of the histories are compared. The differences between the peaks of two histories do not depend on the phase difference between the histories.

4.5.1 Code verification

Code verification is performed to ensure that the software produces correct results by examining for algorithmic and coding mistakes. In the following sections, three tests, namely, symmetry test, code-to-code comparison and order-of-accuracy test, are performed on an FP bearing modeled using the OpenSees element *FPBearingPTV*.

4.5.1.1 Symmetry test

A schematic of the symmetry test is presented in Figure 4-9. Panel (a) shows the global coordinate system. Panel (b) of the figure presents the undeformed configuration of the element between two nodes. Node 1 is assigned fixed boundary conditions. Figure 4-9(c) shows a horizontal load applied to Node 2, which results in a deformation Δ. The element along with the

[1] A phase difference may lead to a great estimate of percentage difference between two histories with maximum contributions from differences at small base values.

boundary conditions is then inverted in Figure 4-9(d). The horizontal force of Figure 4-9(c) on the element in Figure 4-9(d) should produce a displacement equal to that in Figure 4-9(c).

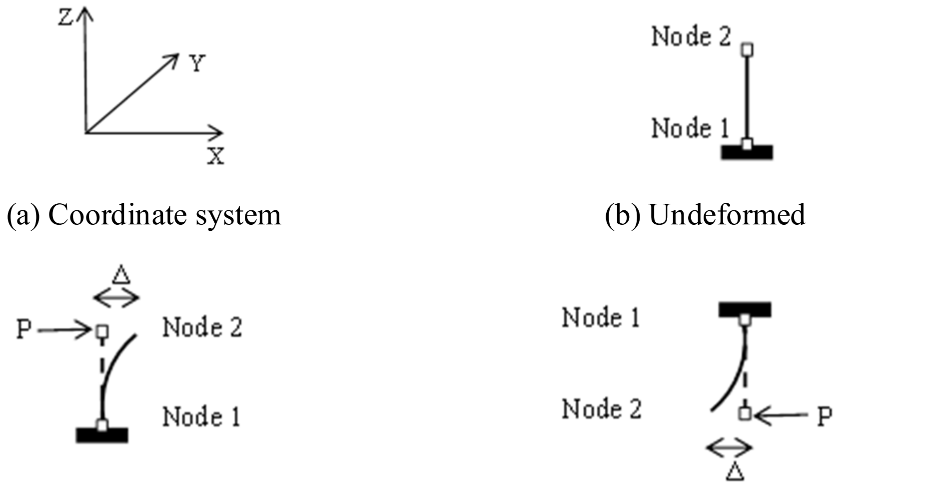

(a) Coordinate system

(b) Undeformed

(c) Deformed (Case 1)

(d) Inverted and deformed (Case 2)

Figure 4-9: The symmetry test (e.g., Oberkampf and Roy (2010))

To perform the symmetry test on the *FPBearingPTV* element, two cases are considered. For Case 1, the slider is atop the sliding surface, the sliding surface is fixed to the ground, and a cyclic displacement history is applied to the slider (Figure 4-9(c)). The bearing is inverted for Case 2; the sliding surface is atop the slider. The sliding surface is assigned fixed boundary conditions and the cyclic displacement history of Case 1 is applied to the slider (Figure 4-9(d)) but in the opposite direction. The resulting force and moment histories on the slider and sliding surface are then compared.

An FP bearing with the sliding period of 3 s, static axial pressure of 50 MPa and the reference coefficient of friction of 0.3 is subjected to a cyclic displacement history $u = 0.4\sin\left(0.25t\right)$, in units of meters and seconds. The friction at the sliding surface is Coulomb-type. The radius of the slider is 0.2 m. The displacement history is applied at Node 2 in the positive and negative X directions for Case 1 and Case 2, respectively (see Figure 4-9). The maximum expected lateral force (moment) is 3009 kN (2513 kN-m); the computed value is 3029 kN (2514 kN-m). Figure 4-10(a) shows the external force histories at Node 1 (sliding surface) in the positive X direction for Case 1 and Case 2. The force histories are equal in magnitude, but opposite in sign. Figure 4-10(b) presents the force histories at Node 2 (slider). Figures 4-10(c) and 4-10(d) present the forces in the positive Z direction at Node 1 and Node 2, respectively, for the two cases. The forces are equal in magnitude but opposite in sign. Figure 4-10(e) plots the moment history at Node 1 (sliding surface) for the two cases and Figure 4-10(f) plots the history at Node 2 (slider), which is zero as the slider is considered articulated and does not allow moment transfer.

4.5.1.2 Code-to-code comparison

This exercise compares response quantities obtained from the analysis of an identical model using different software. The verification of the new OpenSees element *FPBearingPTV* is performed in two steps. In the first step, a single FP bearing with friction at the sliding surface described by the Coulomb model is subjected to a set of horizontal and vertical ground motions and the force-displacement responses are compared with those obtained from the analyses performed using ABAQUS (Dassault, 2013) and SAP2000 (CSI, 2013).

In the second step, an FP bearing with a flat sliding surface is subjected to displacement histories with different amplitudes and frequencies, and implementation of the pressure-, temperature- and velocity-dependent friction models are verified. The history of total force at the sliding surface in the horizontal direction and of temperature at selected points on the sliding surface obtained using the ABAQUS and OpenSees models are compared.

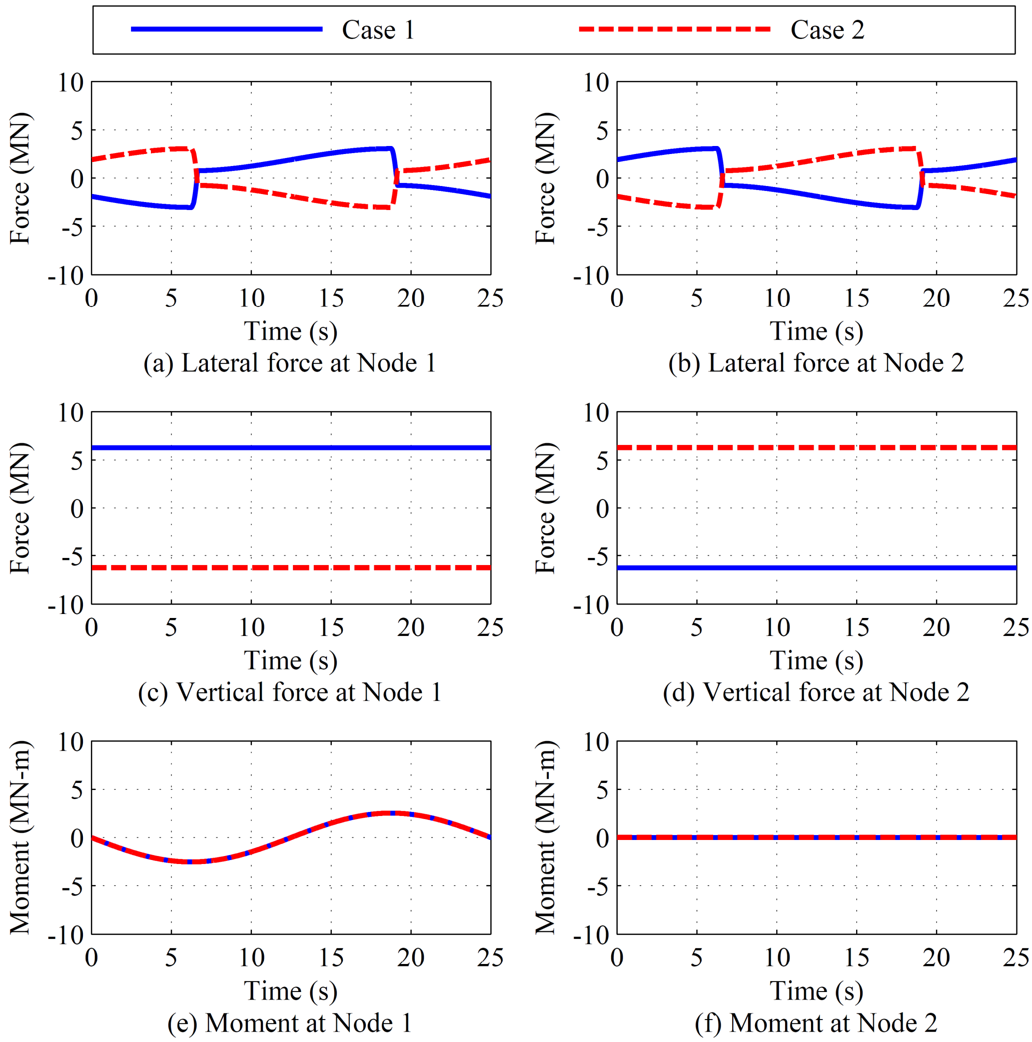

Figure 4-10: History of forces and moments at sliding surface (Node 1) and slider (Node 2) for Case 1 and Case 2 of Figure 4-9

4.5.1.2.1 Code verification

The base codes used to verify the new OpenSees element are SAP (CSI, 2013) and ABAQUS (Dassault, 2013). The program SAP is widely used to perform analysis of fixed-base and seismically isolated buildings, bridges and other structures, including seismically isolated nuclear structures (e.g., Huang *et al.* 2007, 2013). To the knowledge of the author, SAP has not been formally verified. ABAQUS is a finite element program that provides numerical solutions to a wide range of problems, including structural and thermo-mechanical. The components of the software (e.g., elements, materials) have been verified against analytical solutions. Details on verification are provided on the webpage: http://xn--90ajn.xn--p1ai:2080/v6.12/books/ver/default.htm. ABAQUS has been used for many studies related to the nuclear industry (e.g., Kadak (2000), Inagaki *et al.* (2004), Cizelj and Simonovski (2011)).

4.5.1.2.2 Comparison of response-history analysis results

A single FP bearing with a static axial pressure of 50 MPa, a coefficient of friction of 0.06, and friction at the sliding surface described using the Coulomb model is subjected to GM1 of Appendix A. No damping is assigned to the system. The yield displacement is 0.001 m. The analysis is performed using the *FPBearingPTV* element in OpenSees and the *Friction Isolator* link element in SAP2000. The link element in SAP2000 has been used to simulate the results from a shake table test performed on a seven story steel building isolated using FP bearings, as reported in the documentation of the software. Figure 4-11 shows the displacement (panels (a) and (b)) and force (panels (c) and (d)) histories of the slider in the two horizontal directions obtained using SAP2000 and OpenSees.

The maximum difference in the peak displacements at a given time instant are 0.003 m and 0.002 m in the two horizontal directions, which are tiny compared with the corresponding maximum displacements of 0.480 m and 0.510 m. The value of λ (Equation (4-19)) for the displacement response histories obtained using SAP and OpenSees are 0.6% and 0.3% in the X and Y directions, respectively. The peak difference in force at a given time instant is 110 kN in both horizontal directions, compared with the maximum forces of 2300 kN and 2400 kN, respectively. The value of λ for the lateral force histories obtained using SAP and OpenSees are 0.7% and 0.8% in the X and Y directions, respectively.

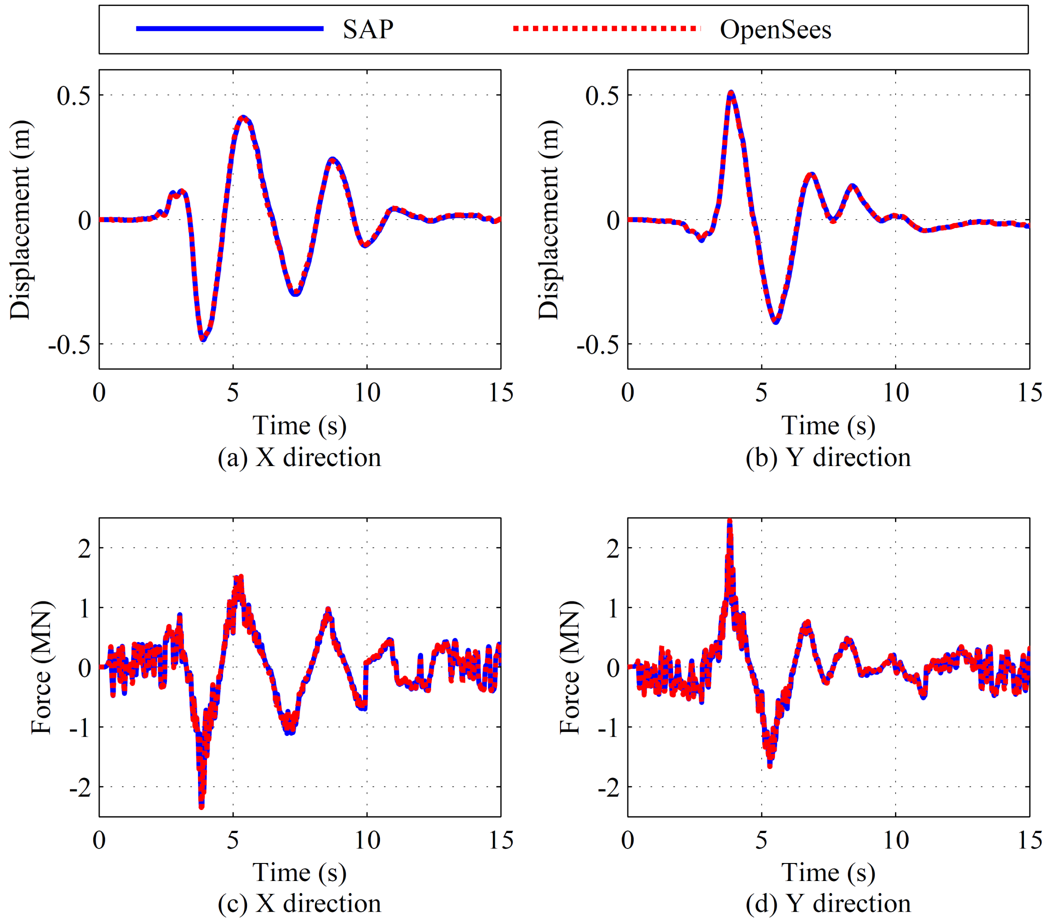

Figure 4-11: Force-displacement histories of an FP bearing subjected to GM1 obtained using SAP2000 and OpenSees

4.5.1.2.3 Verification of the implementation of the friction model

The second step of code verification verifies the implementation of the axial pressure, temperature and sliding velocity dependent friction models in the OpenSees element *FPBearingPTV*. A flat slider is used for this purpose. The flat surface is realized in OpenSees by assigning a very high value of radius of curvature for a single FP bearing. The slider is square with side dimensions of 0.060 m. The eight analysis cases of Table 4-1 are considered. In addition to a static pressure of 50 MPa, a sinusoidal pressure history with the amplitude of 50 MPa and the loading frequency of 1 Hz is applied to the slider in the vertical direction. Figure 4-12(a) presents the axial pressure history on the slider. The slider is subjected to two displacement histories, one with small amplitude and high frequency (cases 1–4 in Table 4-1) and the other with high amplitude and low frequency (cases 5–8 in Table 4-1). The peak velocities associated with the two displacement histories are 0.075 m/s and 0.190 m/s, respectively. Figure 4-12(b) presents the horizontal displacement histories imposed on the slider. The assumption of an infinite half space made for the temperature calculation at the center of the sliding surface (see Chapter 3) is realized when the amplitude of motion is small (cases 1–4 in Table 4-1).

It was established in Chapter 3 that the temperature at the center of the sliding surface is representative of the temperature at the sliding surface when the bearing is subjected to earthquake ground motion, and can be used to update the temperature-dependent coefficient of sliding friction during a response-history analysis. For this set of analyses, the reference coefficient of friction at the sliding surface, measured at a high velocity of sliding, at the temperature of 20^{o}C and at a static axial pressure of 50 MPa, is set equal to 0.3[1]. Four friction models, namely, Coulomb (cases 1 and 5), velocity dependent (cases 2 and 6), axial pressure dependent (cases 3 and 7) and temperature dependent (cases 4 and 8) are considered.

[1] The dimensions of the slider and the sliding plate, and peak displacement were selected so that the 1) computational time for analyses was not great, and 2) temperature rise at the external surfaces of the sliding plate (except the sliding surface) was zero at the end of analysis. The size of the slider selected for this study (0.060 m square) is small compared with that commonly used in practice.

The results obtained from the displacement-controlled analyses performed using OpenSees are compared with those obtained using ABAQUS. Figure 4-13 shows the meshed model of the flat slider in ABAQUS. The eight-node C3D8T coupled temperature-displacement brick elements are assigned to the mesh. The sliding plate is 0.240 m long, 0.120 m wide and 0.030 m thick. The slider's dimensions are $0.060 \times 0.060 \times 0.010$ m. Master and slave surfaces are selected by the user for a surface-to-surface contact problem in ABAQUS. Finer meshes are recommended for the slave surface than the master surface. For the present study, the mesh sizes for the sliding plate (slave) and slider (master) are 0.005 m and 0.006 m, respectively. The slider and the sliding plate are assumed to be steel with thermal conductivity and specific heat of 18 W/(m^{o}C) and 516.44 J/(kg^{o}C), respectively. Mass density, Young's modulus and Poisson's ratio considered for steel are 7,850 kg/m^3, 210 GPa and 0.3, respectively. The heat generated during sliding is assigned to the sliding plate. The initial temperature of the slider and the sliding surface is 20^{o}C. The sliding plate is assigned fixed boundaries and the slider is free to translate.

Table 4-1: Analysis cases to verify the implementation of friction model in the OpenSees element *FPBearingPTV*

Case	p_o (MPa)[1]	u_o (mm)[2]	f_h (Hz)[2]	f_v (Hz)[1]	Friction model	Notation
1	50	6	2	1	Coulomb	$\mu =$ Coulomb
2	50	6	2	1	Velocity dependent	$\mu = f(v)$[3]
3	50	6	2	1	Pressure dependent	$\mu = f(p)$[1]
4	50	6	2	1	Temperature dependent	$\mu = f(T)$[4]
5	50	60	0.5	1	Coulomb	$\mu =$ Coulomb
6	50	60	0.5	1	Velocity dependent	$\mu = f(v)$
7	50	60	0.5	1	Pressure dependent	$\mu = f(p)$
8	50	60	0.5	1	Temperature dependent	$\mu = f(T)$

[1]Vertical loading history: $p = p_o\left(1+\sin\left(2\pi f_v t\right)\right)$; t: time; p: axial pressure; f_v: vertical loading frequency

[2]Horizontal displacement history: $u = u_o \sin\left(2\pi f_h t\right)$; u: displacement; f_h: horizontal displacement frequency

[3] v: sliding velocity

[4] T: temperature at the sliding surface

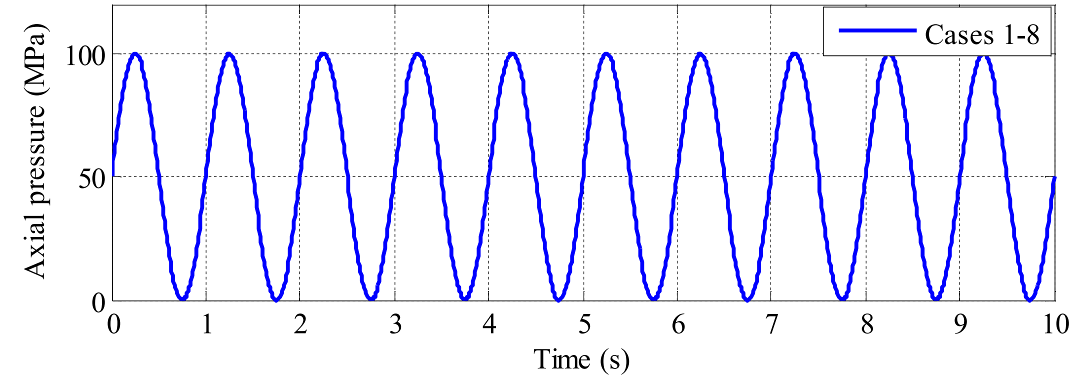

(a) Axial pressure history

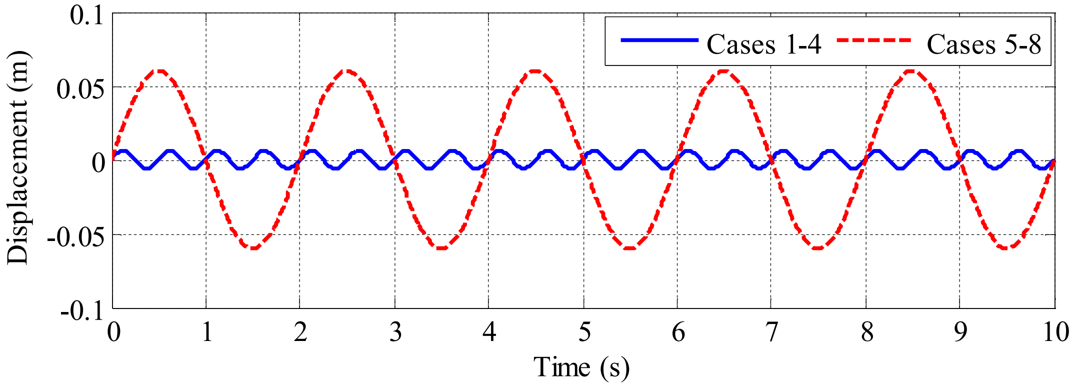

(b) Displacement history

Figure 4-12: Axial pressure and displacement histories applied on the slider of the flat slider

Figure 4-14 shows the temperature at the surface of the flat slider at the end of 10 seconds of motion $u = 0.006\sin(4\pi t)$ (Case 1 of Table 4-1). The maximum temperature at the surface is 300°C. The corresponding temperature profile at a section perpendicular to the sliding surface is shown in Figure 4-15. The maximum depth of heat penetration into the plate below at 10 s is less than 0.015 m (half its total thickness). Figure 4-16 presents the temperature profile at the sliding surface when a displacement history $u = 0.06\sin(\pi t)$ is imposed on the slider (Case 5 of Table 4-1). The maximum temperature at the sliding surface is about 400°C. The maximum depth of heat penetration into the plate below is less than 0.015 m, as seen in Figure 4-17.

Figure 4-18(a) plots the lateral force at the surface of the flat slider obtained using ABAQUS and OpenSees, when the coefficient of friction at the sliding surface is defined using Coulomb model and the slider is subjected to a displacement history $u = 0.006\sin(4\pi t)$ (Case 1 of Table 4-1). The lateral force histories compare well; the difference in the amplitudes of the peaks is 1% and λ for the ABAQUS and OpenSees force histories for the 10 s of motion is 7% (see Table 4-2). The maximum percentage difference between the force histories occurs when the direction of motion changes, as seen in Figure 4-19: time interval between 2 s and 2.5 s from Figure 4-18. The differences for all eight cases are listed in Table 4-2.

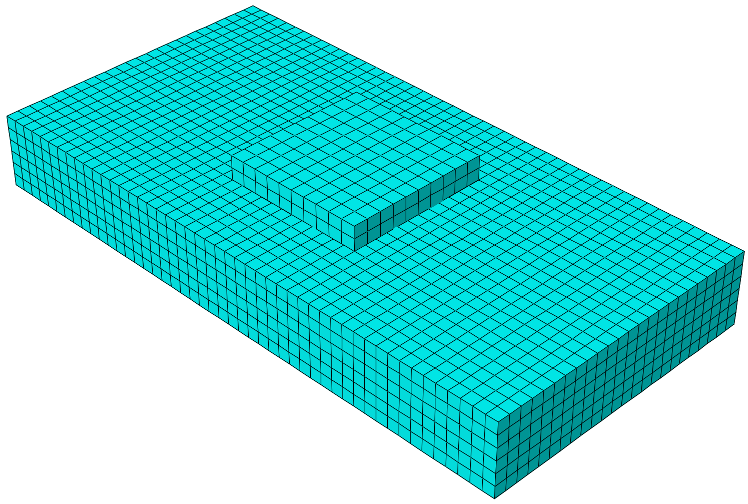

Figure 4-13: The model of flat slider bearing in ABAQUS

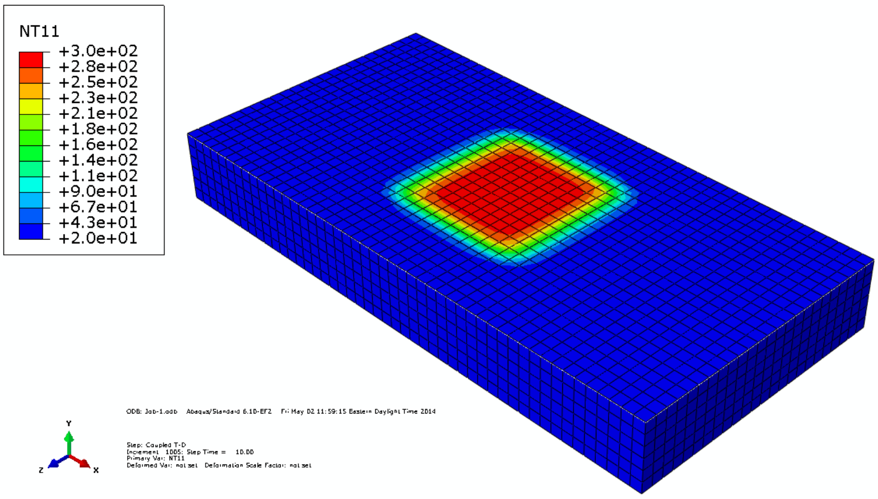

Figure 4-14: Temperature (^{o}C) distribution at the sliding surface with friction defined using Coulomb model, horizontal displacement history of $u = 0.006\sin(4\pi t)$, Case 1 of Table 4-1

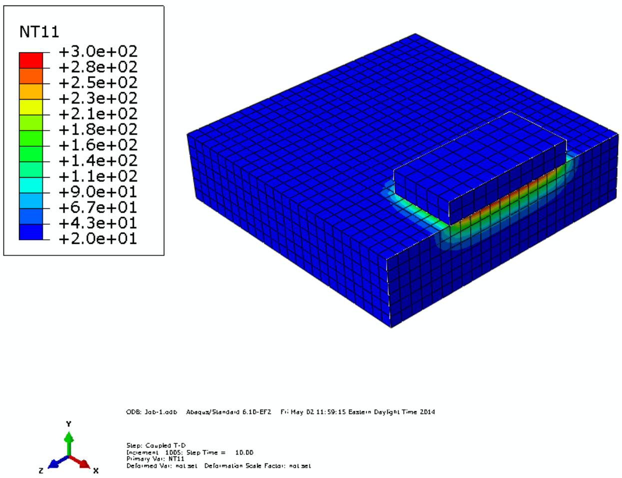

Figure 4-15: Temperature (^{o}C) distribution at a section perpendicular to the sliding surface with friction defined using Coulomb model, horizontal displacement history of $u = 0.006\sin(4\pi t)$, Case 1 of Table 4-1

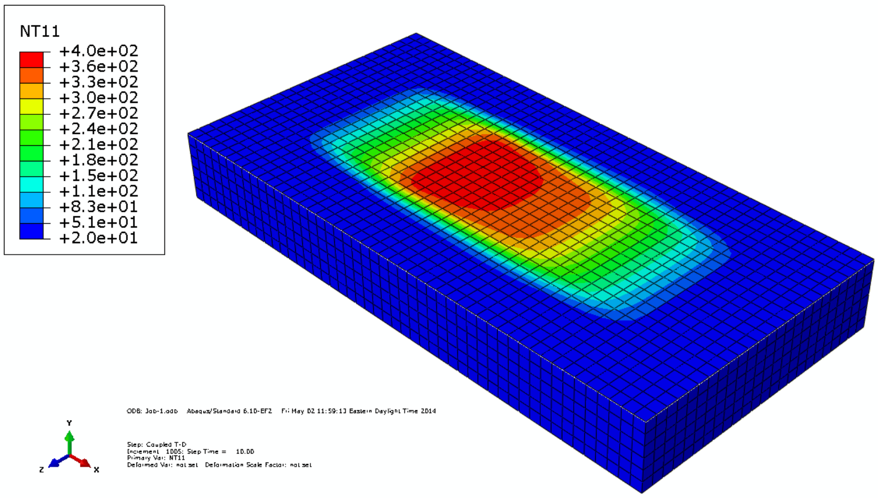

Figure 4-16: Temperature (^{o}C) distribution at the sliding surface with friction defined using Coulomb model, horizontal displacement history of $u = 0.06\sin(\pi t)$, Case 5 of Table 4-1

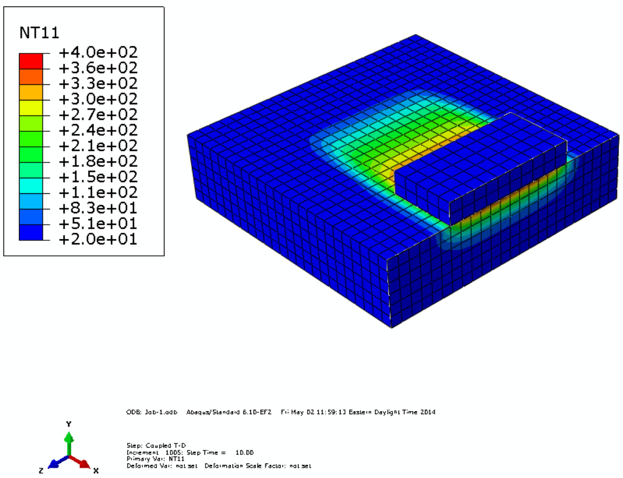

Figure 4-17: Temperature (^{o}C) distribution at a section perpendicular to the sliding surface with friction defined using Coulomb model, horizontal displacement history of $u = 0.06\sin(\pi t)$, Case 5 of Table 4-1

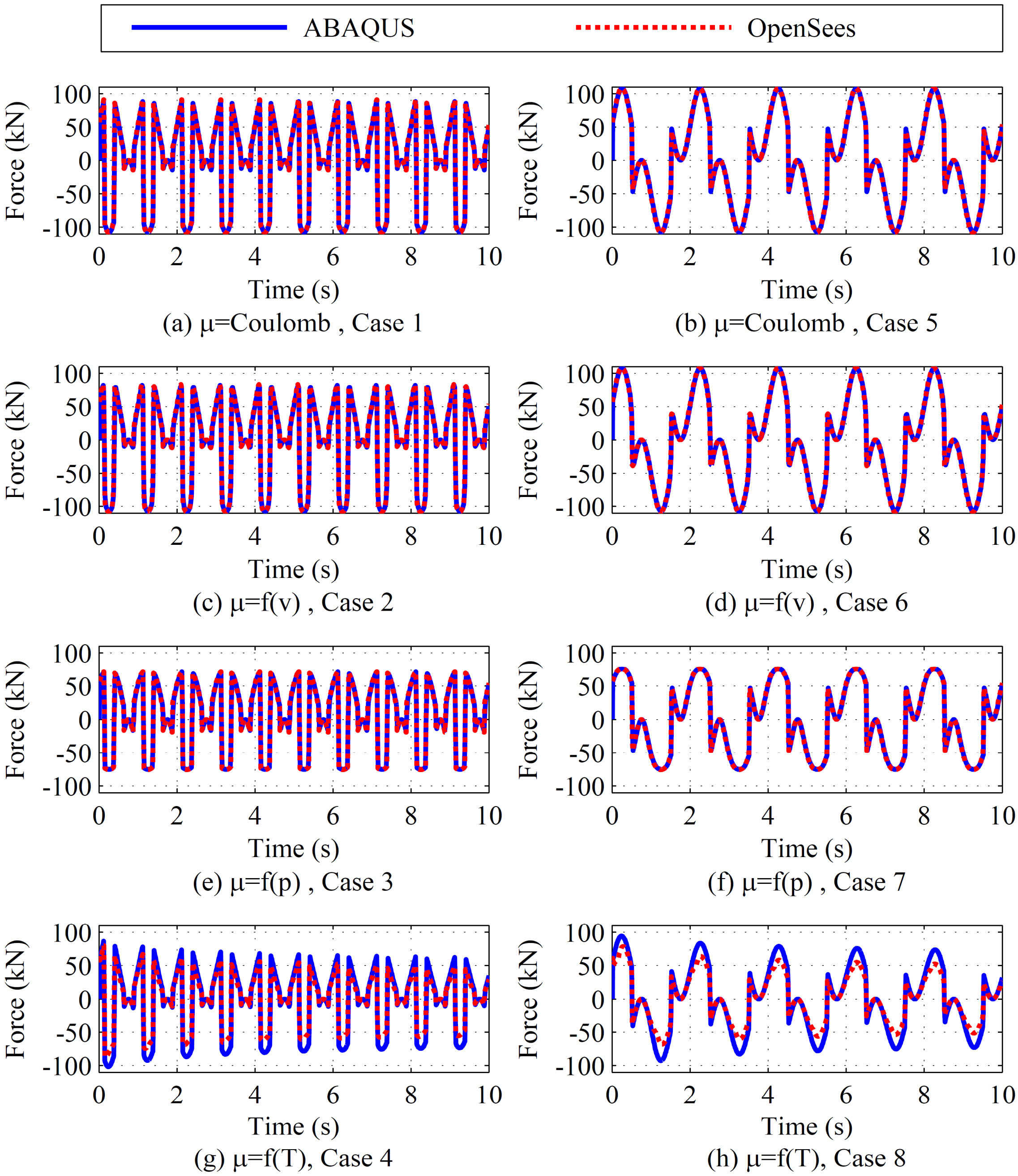

Figure 4-18: Lateral force histories for the eight cases listed in Table 4-1

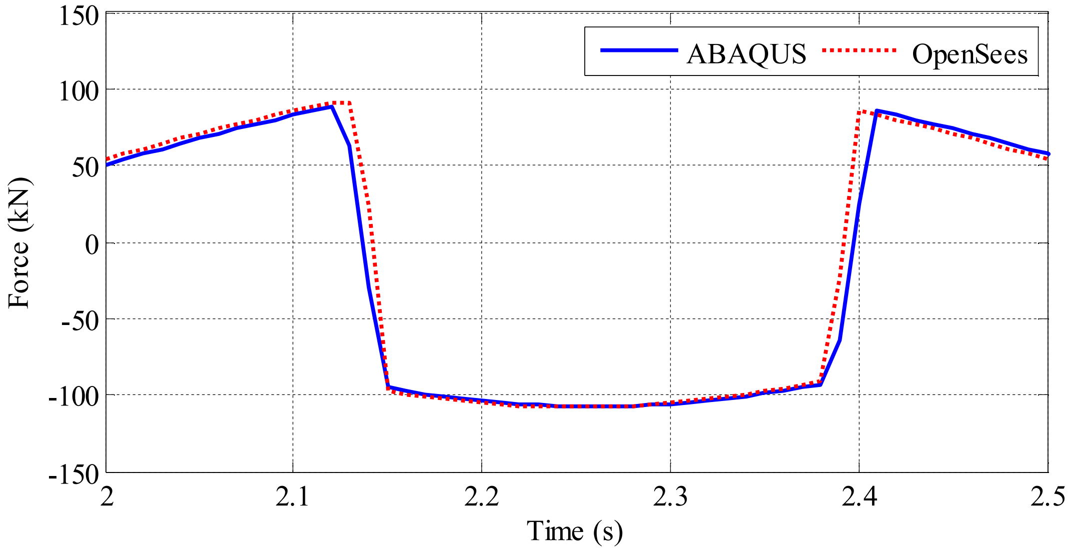

Figure 4-19: Lateral force histories for Case 1 of Table 4-1

Table 4-2: Differences between force and temperature histories obtained using ABAQUS and OpenSees

Case	Friction model	Force		Temperature	
		% difference between peaks	% difference, λ	% difference between peaks	% difference, λ
1	$\mu =$ Coulomb	1	7	10	9
2	$\mu = f(v)$	1	7	10	9
3	$\mu = f(p)$	0	8	7	9
4	$\mu = f(T)$	14	24	11	14
5	$\mu =$ Coulomb	0	5	25	12
6	$\mu = f(v)$	0	5	25	12
7	$\mu = f(p)$	0	4	25	12
8	$\mu = f(T)$	17	26	4	20

The peak forces computed using ABAQUS and OpenSees differ by less than 1% when the friction model does not include heating effects and λ for these six cases ranges between 4% and 8% (panels (a) through (f) of Figure 4-18; also see Table 4-2). The differences are greater for panels (g) and (h), which present force histories for the cases when the coefficient of friction varies with temperature at the sliding surface. The difference in the peak values and the value of λ for these two panels are 15% and 25%, respectively (see Table 4-2). The differences in these force histories are great because the temperature at the sliding surface is calculated differently in the two software, which in turn affects the coefficient of friction and the lateral force. In the OpenSees element *FPBearingPTV*, the temperature at the center of the 0.240×0.120 m plate below the slider is considered to be representative of the temperature at the interface. In ABAQUS, the coefficient of friction at a point of contact on the sliding surface is computed using the temperature at the contact point. Further, the OpenSees element assumes an infinite half space below (heat flows vertically downward) to compute temperature, whereas the ABAQUS solution considers that the heat imparted into the sliding plate flows in all directions.

Figure 4-20(a) plots the temperature histories at the center of the sliding surface for Case 1 of Table 4-1 obtained using ABAQUS and OpenSees. The difference between the peaks of the two histories is 10% (see Table 4-2). The difference for Figure 4-20(b) is 25%, which presents results for Case 5 of Table 4-1. The peaks computed using OpenSees are greater than those computed using ABAQUS for both the panels because of the infinite half space conditions assumed in the OpenSees temperature calculations. The percentage difference is greater in Figure 4-20(b) as the conditions at the center of the sliding surface are substantially different from an infinite half space during the relatively large amplitude motion (see Figure 4-21 for the schematic). Figure 4-21(a) shows the entire sliding surface receiving heat from an external source (e.g., frictional heating); panel (b) shows the heat source (slider) symmetrically located with respect to the center of sliding surface, and panels (c) and (d) show the configuration of the slider in which the center of the slider is away from the center of sliding surface. The configuration of Figure 4-21(a) most closely produces the conditions of an infinite half space. The assumption of a half space leads to a small overestimation in the temperature at the center of the sliding surface for the configuration of panel (b), but substantial overestimations for the configurations of panels (c) and (d).

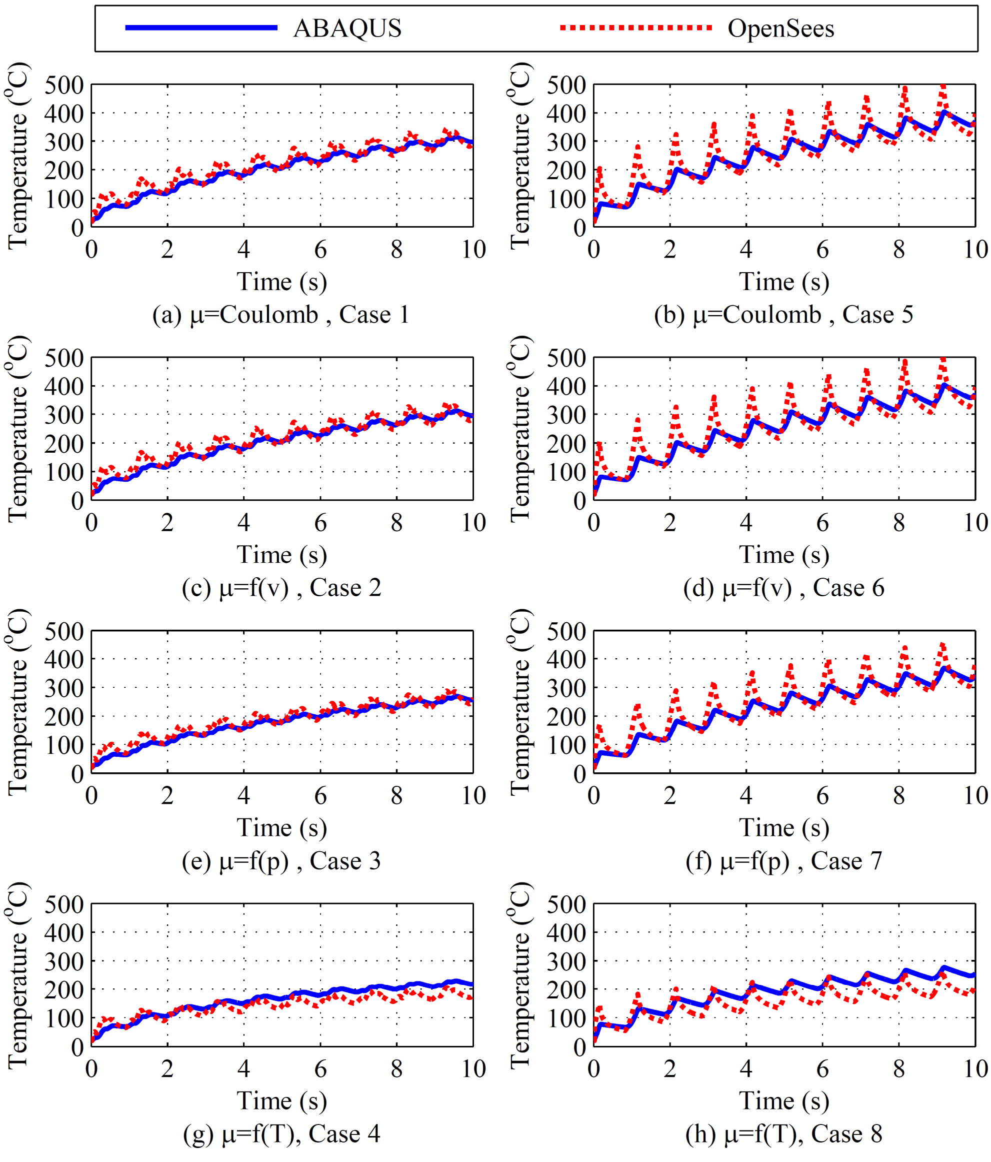

Figure 4-20: Temperature histories at the sliding surface of the flat slider for the eight cases listed in Table 4-1

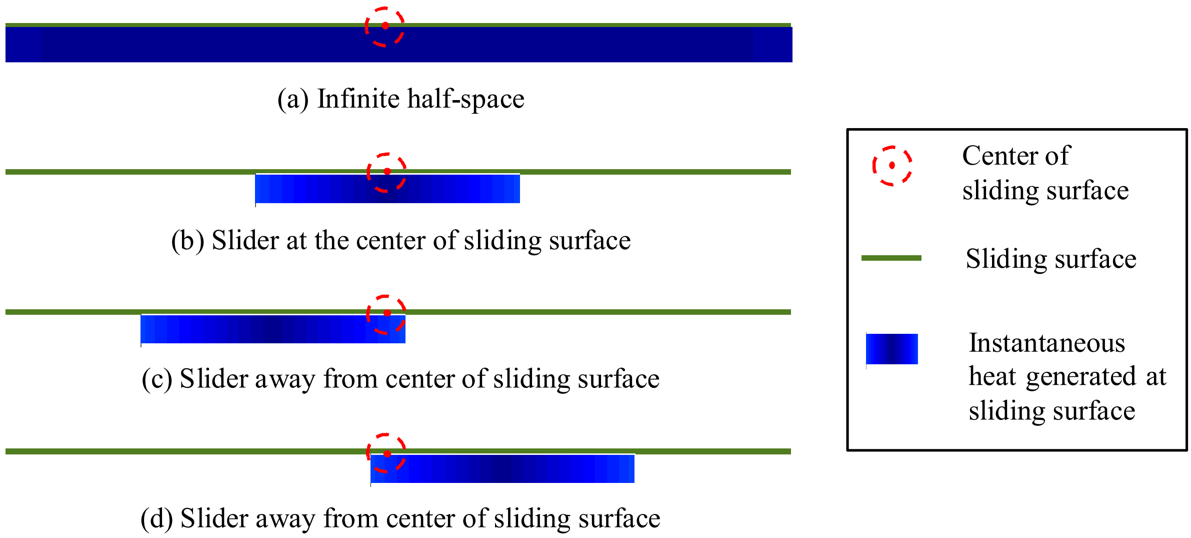

Figure 4-21: Location of heat source (slider) relative to the center of the sliding surface at different time instants

Friction at the sliding surface was described using the Coulomb model for Figures 4-20(a) and 4-20(b). Figures 4-20(c) and 4-20(d) plot the temperature histories for the velocity-dependent friction model, and Figures 4-20(e) and 4-20(f) plot the histories for the pressure-dependent friction model. The temperature histories in panels Figures 4-20(c) and 4-20(e) are similar to that in Figure 4-20(a). The differences in the peak amplitudes obtained using ABAQUS and OpenSees are between 7% and 10% for the three panels. The parameter λ for each of the three panels is 9%. The difference between the peak amplitudes and λ are 25% and 12%, respectively, for each of Figures 4-20(b), 4-20(d) and 4-20(f) (see Table 4-2).

Figures 4-20(g) and 4-20(h) present results for the case where friction is temperature-dependent. The peak amplitudes obtained using the two programs differ by 11% and 4%, and λ is 14% and 20%, for the two panels, respectively. The values of λ for these two panels are greater than for the other six panels. Moreover, the ABAQUS-predicted temperature is greater than that obtained using OpenSees for most of the history for these two panels, unlike the other six panels. This is expected since the temperature histories computed using OpenSees are greater compared to

ABAQUS when the friction models do not include heating effects (Figures 4-20(a) through 4-20(f)) and a temperature-dependent friction model would result in smaller values of the coefficient of friction, heat generated at the sliding surface and temperature rise.

The results presented in this section are summarized as follows. The OpenSees element *FPBearingPTV* produces accurate estimates of lateral force histories (peaks computed within 1% error) when the friction model does not include heating effects. The error can be as great as 15% when heating effects are considered in the friction model. The element computes the peak temperature at the center of sliding surface with an error of about 10% (25%) when amplitude of displacement loading is small (large).

4.5.1.3 Order-of-accuracy test

A discretized solution to a differential equation converges to the exact solution (or becomes accurate) as the discretization step in time and/or space is reduced. The order of accuracy refers to the rate at which the numerical solution converges to the exact solution. The rate can be estimated using theoretical and empirical methods and are called *formal order of accuracy* and *observed order of accuracy*, respectively. Oberkampf and Roy (2010) discuss formal and observed orders of accuracy. The approaches to compute the formal and observed orders of accuracy of the numerical solution to the mathematical model of the FP bearing (Equation (4-1)) are presented in this section.

The lateral force-displacement relationship of an FP bearing can be described using a bilinear relationship, if it is subjected to a monotonic loading. Figure 4-22(a) presents the lateral force-displacement relationship of an FP bearing. Before sliding, the lateral stiffness, k_1, is:

$$k_1 = \frac{\mu W}{u_y} \tag{4-20}$$

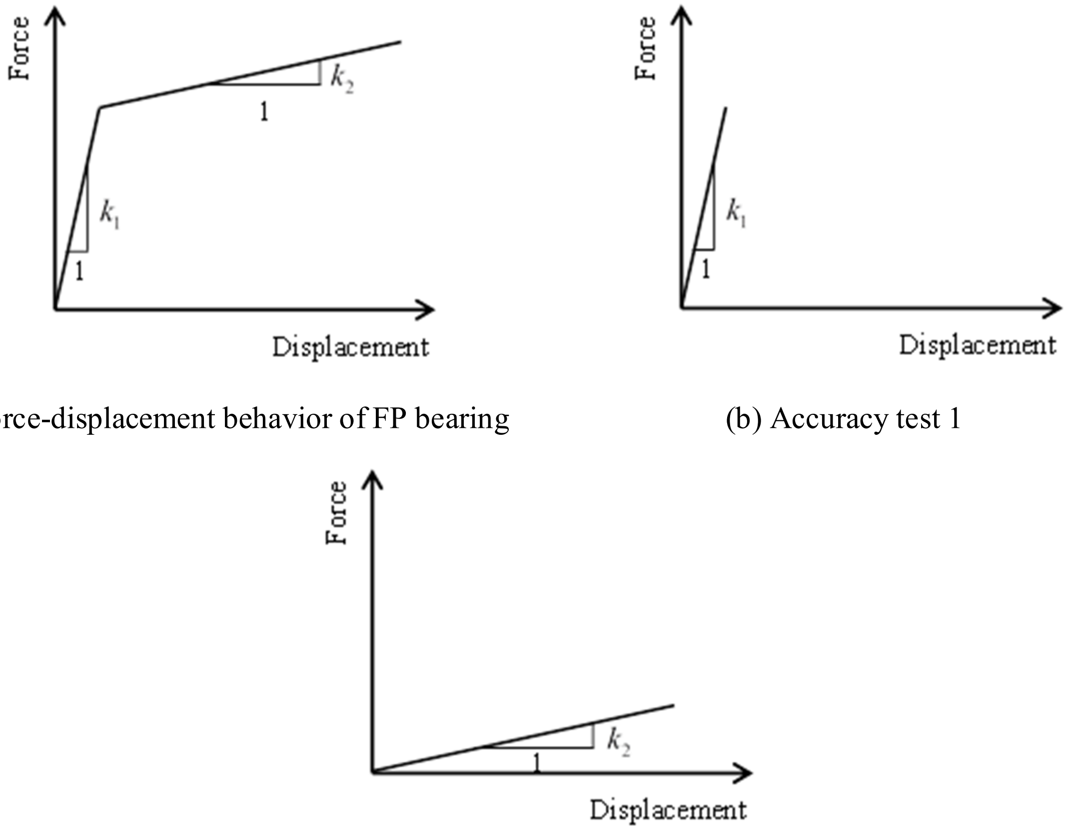

(a) Force-displacement behavior of FP bearing

(b) Accuracy test 1

(c) Accuracy test 2

Figure 4-22: Schematic of order of accuracy tests

where μ the coefficient of friction defined using the Coulomb model, W is the axial load on the bearing, and u_y is the displacement at which the slope of the curve changes. The stiffness of the second segment of the force-displacement relationship, k_2, is given by the ratio of axial load, W, to the radius of curvature of the sliding surface, R:

$$k_2 = \frac{W}{R} \tag{4-21}$$

where all terms were defined previously.

The undamped equation of motion of the slider of the FP bearing is given by the following equation.

$$m\ddot{u}+k\left(u\right)u=f_o \tag{4-22}$$

where m is the mass associated with the slider, u is the lateral displacement, $\ddot{u}$ is the acceleration, $k\left(u\right)$ is the instantaneous stiffness, which can be either k_1 or k_2, and f_o is the external force. For convenience, the order of accuracy test is performed in two steps. In the first step, a sinusoidal acceleration history with high frequency but small amplitude is applied to the slider so that the maximum displacement of the slider is less than u_y (Figure 4-22(b)). In the second step, the FP bearing is subjected to another sinusoidal history with small frequency and high amplitude (Figure 4-22(c)). The coefficient of friction is set equal to an extremely small value in this case to realize the linear system with an stiffness of k_2. The discretized form of (4-22) is

$$m\frac{u_{i+1}-2u_i+u_{i-1}}{\left(\Delta t\right)^2}+k\left(u\right)u_i-f_{oi}=0 \tag{4-23}$$

where u_i is the displacement of slider relative to the sliding surface and f_{oi} is the external force acting on the slider in the i^{th} time step, Δt is the length of time step, and other variables were defined previously. The Taylor series expansion of u_{i+1} and u_{i-1} relative to u_i are given below.

$$u_{i+1}=u_i+\left.\frac{\partial u}{\partial t}\right|_i\Delta t+\left.\frac{\partial^2 u}{\partial t^2}\right|_i\frac{\left(\Delta t\right)^2}{2!}+\left.\frac{\partial^3 u}{\partial t^3}\right|_i\frac{\left(\Delta t\right)^3}{3!}+\left.\frac{\partial^4 u}{\partial t^4}\right|_i\frac{\left(\Delta t\right)^4}{4!}+O\left(\Delta t^5\right) \tag{4-24}$$

$$u_{i-1} = u_i - \left.\frac{\partial u}{\partial t}\right|_i \Delta t + \left.\frac{\partial^2 u}{\partial t^2}\right|_i \frac{(\Delta t)^2}{2!} - \left.\frac{\partial^3 u}{\partial t^3}\right|_i \frac{(\Delta t)^3}{3!} + \left.\frac{\partial^4 u}{\partial t^4}\right|_i \frac{(\Delta t)^4}{4!} + O(\Delta t^5) \tag{4-25}$$

where $\left.\frac{\partial^n u}{\partial t^n}\right|_i$ is n^{th} derivative of u with respect to t at i^{th} time step, and all other terms were defined previously. Combining equations (4-23), (4-24) and (4-25) yields

$$m\frac{u_{i+1} - 2u_i + u_{i-1}}{(\Delta t)^2} + ku_i - f_{oi} = m\frac{\partial^2 u}{\partial t^2} + ku - f_o\Big|_i + \underbrace{m\frac{\partial^4 u}{\partial t^4}.\frac{(\Delta t)^2}{12}\Big|_i}_{\text{Truncation error}} + \ldots \tag{4-26}$$

where all the terms were defined previously. The formal order of accuracy of the numerical scheme is 2, the highest power of Δt in the truncation error.

The *observed order of accuracy* is the actual order of accuracy computed for a series of finite elements meshes and is defined as (Oberkampf and Roy, 2010):

$$\hat{p} = \frac{\ln\left(\frac{\varepsilon_{2h}}{\varepsilon_h}\right)}{\ln(2)} \tag{4-27}$$

where $\hat{p}$ is the observed order of accuracy and ε_h is the discretization error when the mesh size is h; ε_h is computed as

$$\varepsilon_h = \frac{1}{N_{data}} \sum_{i=1}^{N_{data}} \left| u_{exact,i} - u_{h,i} \right| \tag{4-28}$$

where N_{data} is the number of data points, $u_{exact,i}$ is the exact solution at the i^{th} step, $u_{h,i}$ is the numerical solution when mesh size is h at the i^{th} step and $|\,.\,|$ denotes an absolute value.

The sliding surface of an FP bearing with a sliding period of 3 s, static axial pressure of 50 MPa, and a Coulomb-type coefficient of friction of 0.3 is subjected to an acceleration history $\ddot{u}_g = \sin(8\pi t)$ m/s^2 and *observed order of accuracy* is computed for the elastic range (see Figure 4-22b). The radius of the slider is 0.200 m. The yield displacement (the displacement at the transition between the two slopes in Figure 4-22(a)) is set equal to 0.001 m. The acceleration history is chosen such that the maximum relative displacement response of the bearing (= 0.0006 m) is smaller than the yield displacement (= 0.001 m). The 0.5 s long input acceleration history is defined at 0.01 s intervals. Numerical solutions are computed (in double precision; 16 significant digits) using OpenSees with analysis steps set equal to 0.01 s, 0.005 s, 0.0025 s, 0.00125 s, 0.000625 s and 0.0003125 s. The numerical solutions obtained using the Generalized Richardson Extrapolation method are considered as the exact solutions (e.g., Roy *et al.* (2003)):

$$\bar{u} = u_h + \frac{u_h - u_{2h}}{3} \tag{4-29}$$

where $\bar{u}$ is the "exact" solution, h is the analysis time step (= 0.00005 s), and u_h is the numerical solution corresponding to an analysis step h. Table 4-3 presents the *observed order of accuracy* (given by (4-27)) for different analysis step sizes, which approaches 2 as the step size is reduced, which is also the formal order of accuracy for the numerical scheme. Figure 4-23 plots the numerically obtained displacement histories for the different analysis steps. Figure 4-24 presents the corresponding force-displacement histories.

Table 4-3: Order of accuracy for the analysis scheme used in the OpenSees element *FPBearingPTV*

Regime	Analysis step size (s)		Observed order of accuracy (Equation (4-27))	Formal order of accuracy
	Δt_2	Δt_1		
Elastic	0.01	0.005	1.976	2
	0.005	0.0025	1.999	
	0.0025	0.00125	1.999	
	0.00125	0.000625	2.000	
	0.000625	0.0003125	2.000	
Plastic	0.01	0.005	2.000	
	0.005	0.0025	2.000	
	0.0025	0.00125	2.000	
	0.00125	0.000625	2.000	
	0.000625	0.0003125	2.000	

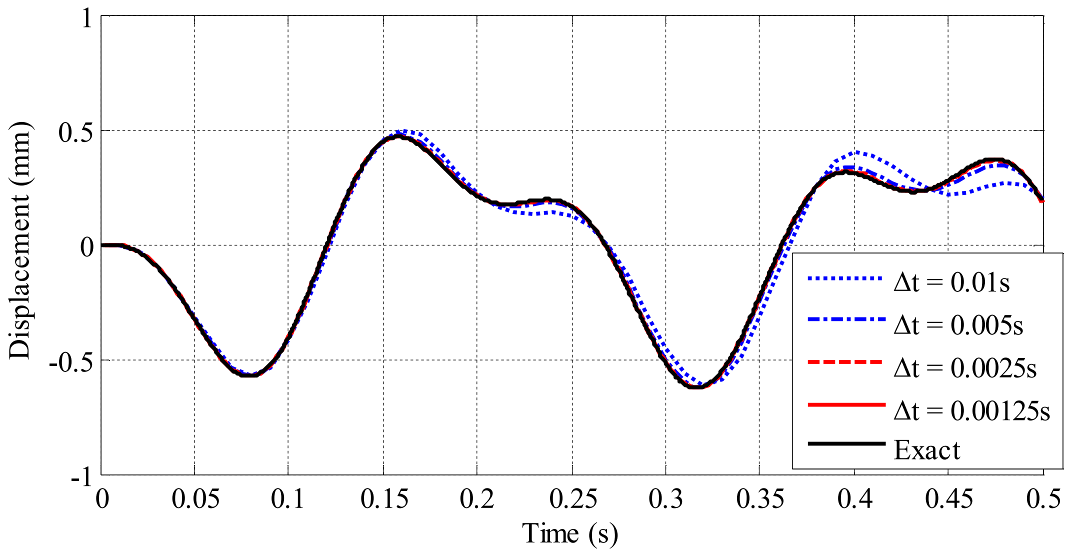

Figure 4-23: Relative displacement histories in the elastic range (Figure 4-22(b))

The same 3 s FP bearing with 50 MPa static axial pressure but now with a Coulomb-type coefficient of friction of 0.00000001 is subjected to an acceleration history $\ddot{u}_g = \sin(\pi t)$ m/s^2 and *observed order of accuracy* is computed (in double precision; 16 significant digits) for the plastic range (Figure 4-22(c)). The yield displacement of the bearing is set equal to 0.0000000001 m. No external damping is provided. The exact solution is obtained using the method used for elastic range. Figure 4-25 presents the displacement histories for different analysis steps. Figure 4-26 plots the force-displacement histories. The *observed order of accuracy* is equal to the formal order of accuracy (= 2) for all time steps (see Table 4-3).

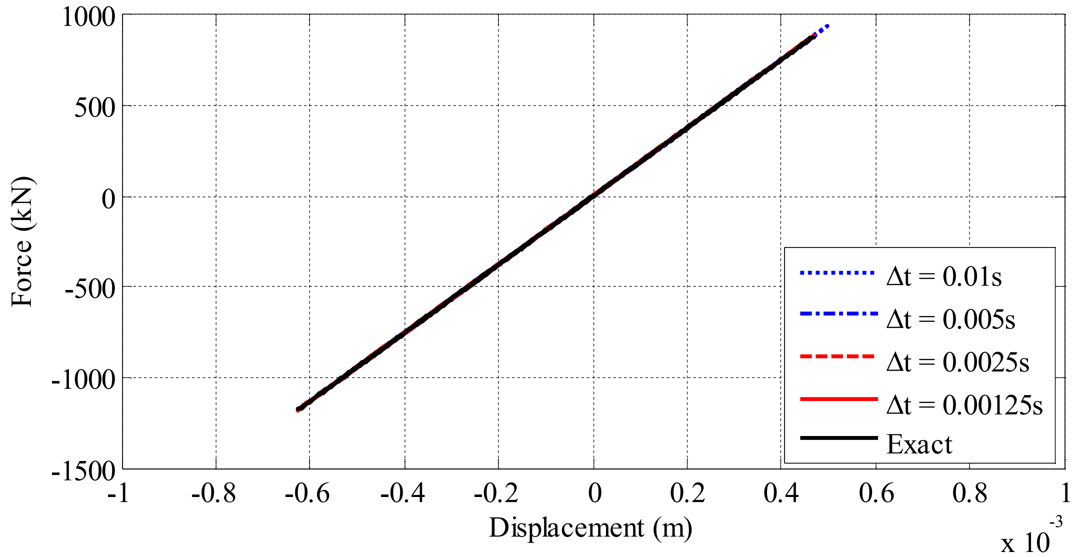

Figure 4-24: Force-displacement histories in the elastic range (Figure 4-22(b))

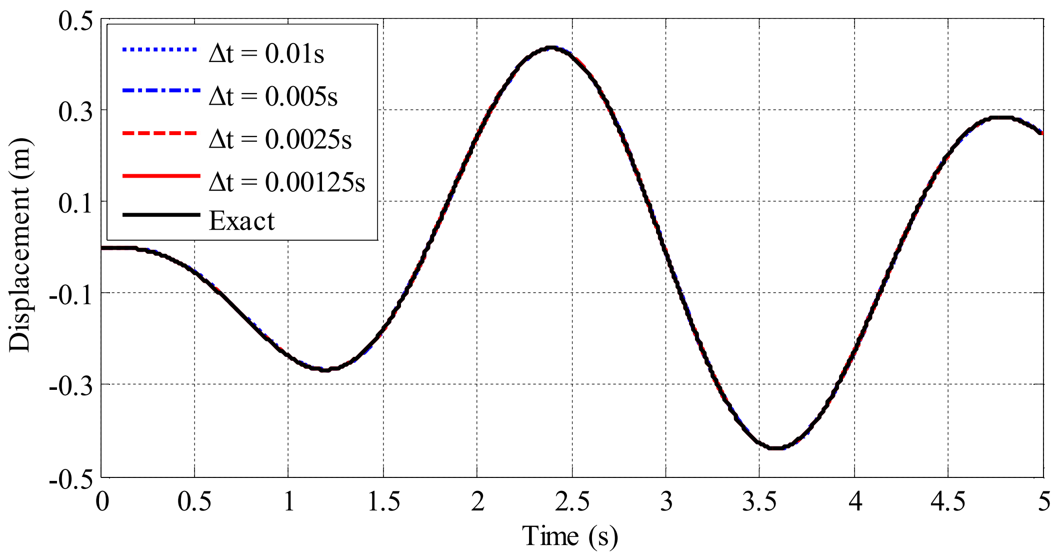

Figure 4-25: Relative displacement histories in the inelastic range (Figure 4-22(c))

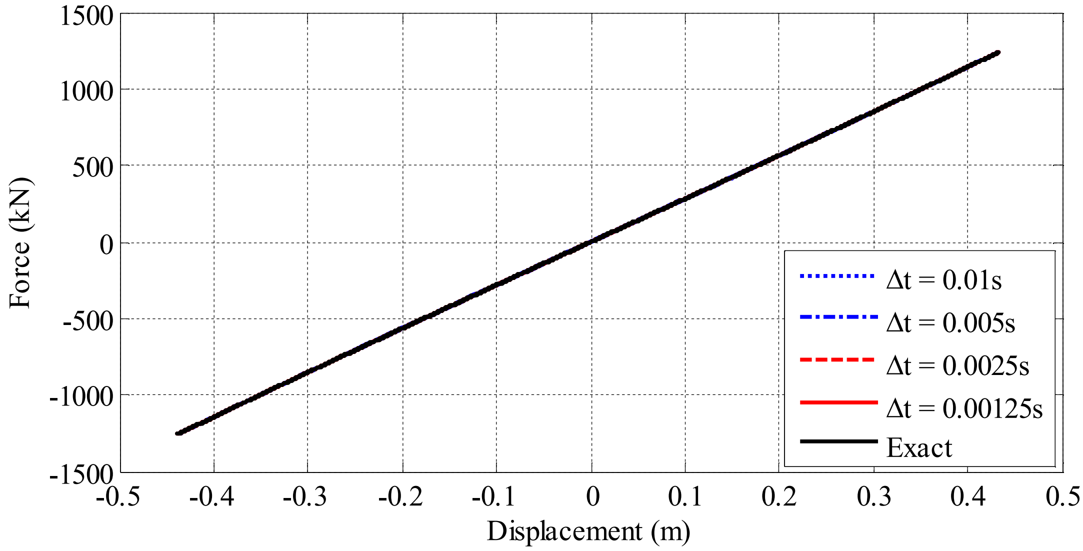

Figure 4-26: Force-displacement histories in the inelastic range (Figure 4-22(c))

4.5.2 Solution verification

A numerical solution can have four sources of error, namely, 1) round-off error, 2) statistical sampling error, 3) iterative error, and 4) discretization error. Round-off errors arise due to low precision (small number of significant digits) in computations. Such errors may be significant for an ill-conditioned system. Round-off errors are small compared to the discretization errors. This is demonstrated by comparing the errors in numerical solutions (Equation (4-28)) reported in Figure 4-25, when computations are performed with single and double precision (Table 4-4). For a given analysis time step, the choice of precision has negligible influence on the error. The error, however, decreases by 75% with a reduction in analysis time step by 50%. Statistical sampling errors are not relevant for this study since deterministic equations are solved. Iterative error is the difference in the numerical and exact solutions due to the tolerance set for an acceptable numerical solution. This error can be controlled by setting a sufficiently small tolerance. Discretization is usually the largest source of error in a numerical solution and is the focus of this study.

Table 4-4: Discretization errors for computations performed in single and double precisions

	Precision	Analysis time step		
		0.01 s	0.005 s	0.0025 s
Error (m) (Equation (4-28))	Single	0.00005269	0.00001316	0.00000328
	Double	0.00005268	0.00001317	0.00000329

4.5.2.1 Discretization error

The discretization error is defined as the difference between the exact solution and the numerical solution computed using a mesh size h:

$$\varepsilon_h = u_h - \tilde{u} \tag{4-30}$$

where u_h is the numerical solution computed using a mesh size h, $\tilde{u}$ is the exact solution and other parameters were defined previously. The new OpenSees element *FPBearingPTV* does not involve discretization in space, so h in the above equation refers to the analysis time step. Discretization error is computed in this section for an FP bearing with the force-displacement behavior shown in Figure 4-22(a). The exact solution is estimated using the Generalized Richardson Extrapolation method (e.g., Oberkampf and Roy (2010)) discussed below.

The expression for discretization error in a p^{th}-order accurate numerical scheme is

$$\varepsilon_h = u_h - \tilde{u} = g_p h^p + g_{p+1} h^{p+1} + g_{p+2} h^{p+2} + \ldots \tag{4-31}$$

where g_i are constants and other parameters were defined previously. For two grid spacings h and rh $(r > 1)$, the numerical solutions can be written as

$$
\begin{aligned}
u_h &= \tilde{u} + g_p h^p + g_{p+1} h^{p+1} + O\left(h^{p+2}\right) \\
u_{rh} &= \tilde{u} + g_p \left(rh\right)^p + g_{p+1} \left(rh\right)^{p+1} + O\left(h^{p+2}\right)
\end{aligned}
\tag{4-32}
$$

where all terms were defined previously. Equation (4-32) is simplified to

$$
\tilde{u} = u_h + \frac{u_h - u_{rh}}{r^p - 1} + g_{p+1} h^{p+1} \frac{r^p \left(r-1\right)}{r^p - 1} + O\left(h^{p+2}\right) = \bar{u} + O\left(h^{p+1}\right) \tag{4-33}
$$

where $\bar{u}$ is the Generalized Richardson Extrapolation estimate of the exact solution given by

$$
\bar{u} = u_h + \frac{u_h - u_{rh}}{r^p - 1} \tag{4-34}
$$

where all the terms were defined previously. The order of accuracy, p, is not known for the differential equation representing the force-displacement relationship of an FP bearing (Figure 4-22(a)). However, p is 2 when the two segments of the force-displacement curve are considered separately (see Section 4.5.1.3). For r equal to 2 (e.g., Roy *et al.* (2003)) and p equal to 2, (4-34) reduces to

$$
\bar{u} = u_h + \frac{u_h - u_{2h}}{3} \tag{4-35}
$$

and is used to estimate the exact solution and the discretization error. Equation (4-35) is identical to (4-29).

An FP bearing with a sliding period of 3 s, static axial pressure of 50 MPa and a Coulomb-type coefficient of sliding friction of 0.06 is subjected to a sinusoidal ground acceleration history $\ddot{u}_g = \sin\left(\pi t\right)$ m/s^2. The acceleration history is specified at intervals of 0.01 s. The response-history analyses are performed at the time-steps of 0.01 s, 0.005 s, 0.0025 s and 0.00125 s. The input ground acceleration at an analysis step (e.g., 0.005 s) is obtained from the ground acceleration history (specified at 0.01 s) using linear interpolation. The yield displacement of the bearing is 0.001 m. No damping is assigned to the system. Figure 4-27 presents the displacement histories of the slider for different time steps. Figure 4-28 plots the computed force histories. Figure 4-29 presents the force-displacement loops. The differences between the histories and loops computed using different time steps are negligible. The average absolute errors (given by (4-28)) in displacement are 0.000014 m, 0.000007 m and 0.000001 m for time steps of 0.01 s, 0.005 s and 0.0025 s, respectively; the maximum displacement is 0.130 m. The average absolute errors in the computed lateral force histories are 80 N, 30 N and 5 N, respectively, for the three time steps; the maximum force is 740,000 N.

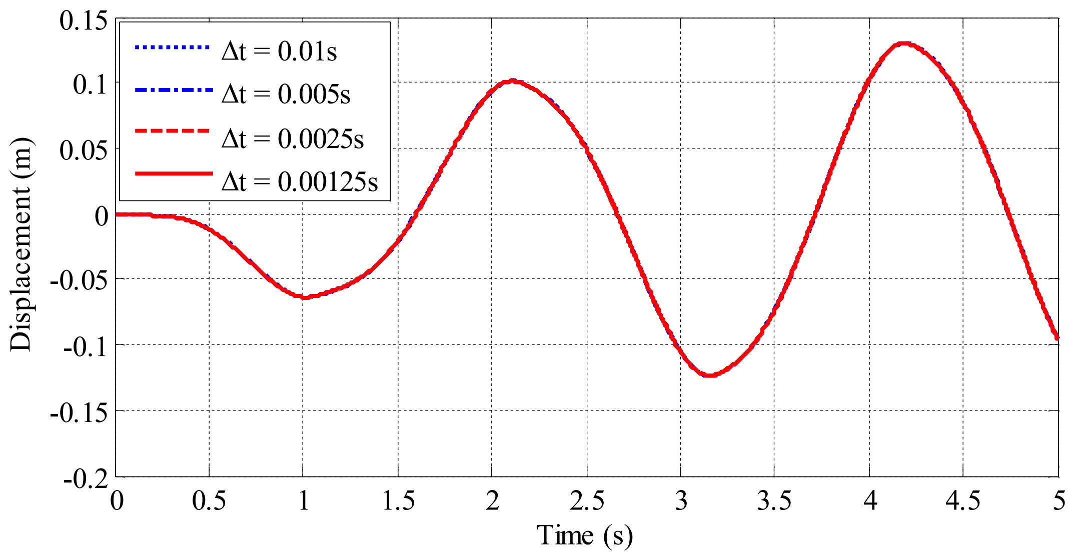

Figure 4-27: Displacement histories calculated using different time steps

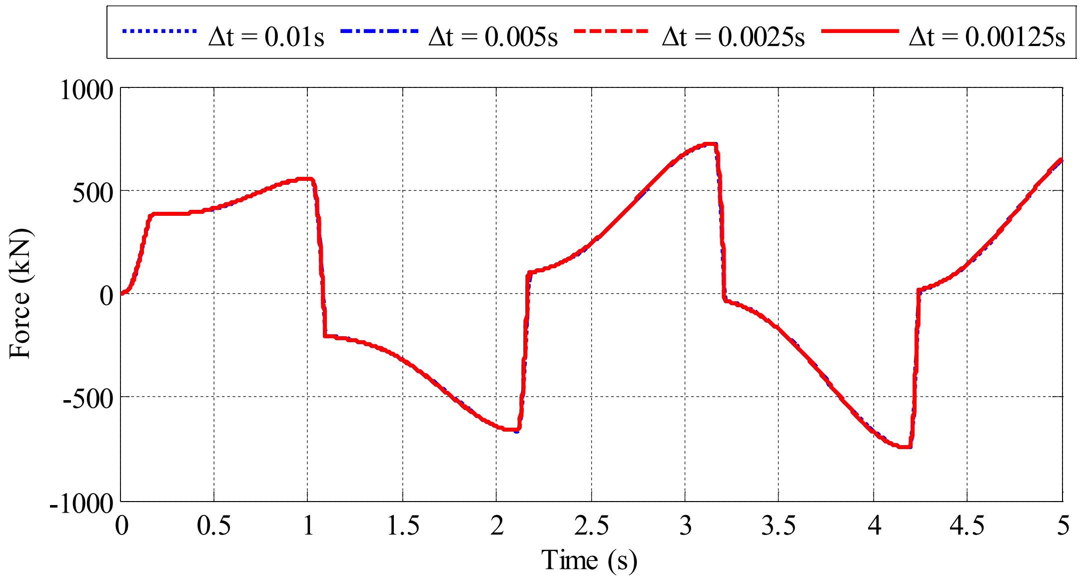

Figure 4-28: Lateral force histories calculated using different time steps

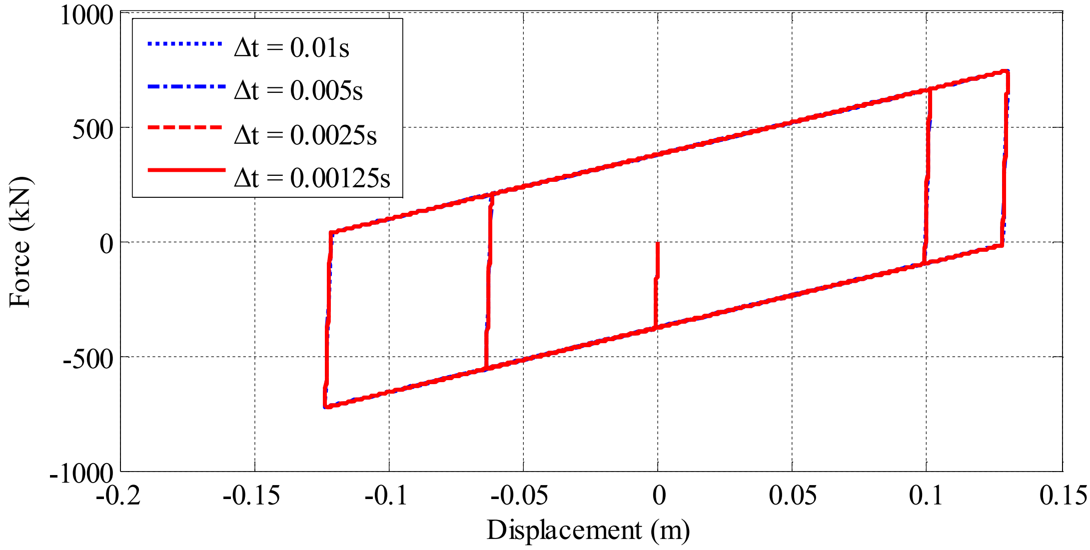

Figure 4-29: Force-displacement relationships calculated using different time steps

4.5.2.2 Influence of integration scheme

The numerical solution approaches the exact solution as the analysis time step is reduced (see Section 4.5.2.1). These numerical integrations were performed using the Constant Average Acceleration method (Bathe, 1996). Responses calculated using different numerical integration schemes, namely, Linear Acceleration, Hilber-Hughes-Taylor (HHT) and Generalized-α, are compared below.

The following equations represent a family of numerical integration methods known as Newmark's method (e.g., Chopra (2007)):

$$\begin{aligned} \dot{u}_{i+1} &= \dot{u}_i + \left((1-\gamma)\Delta t\right)\ddot{u}_i + (\gamma\Delta t)\ddot{u}_{i+1} \\ u_{i+1} &= u_i + (\Delta t)\dot{u}_i + \left((0.5-\beta)(\Delta t)^2\right)\ddot{u}_i + \left(\beta(\Delta t)^2\right)\ddot{u}_{i+1} \end{aligned} \tag{4-36}$$

where u_i is the displacement response at the i^{th} time-step, an overdot represents the derivative with respect to time, γ and β are parameters that define the variation of acceleration over a time step, and other parameters were defined previously. Newmark's method is known as the Constant Average Acceleration method for γ of 1/2 and β of 1/4, and the Linear Acceleration method for γ of 1/2 and β of 1/6. Equations (4-36) and (4-37) are used to compute the response quantities u_{i+1}, $\dot{u}_{i+1}$ and $\ddot{u}_{i+1}$.

$$m\ddot{u}_{i+1} + ku_{i+1} = f_{o,i+1} \tag{4-37}$$

where all parameters were defined previously.

The HHT method (Hilber *et al.*, 1977) uses Newmark's scheme (Equation (4-36)) with a change in the equilibrium equation (Equation (4-37)) as follows.

$$m\ddot{u}_{i+1} + (1+\alpha_H)ku_{i+1} - \alpha_H ku_i = f_{o,i+1} \tag{4-38}$$

where α_H is a new parameter introduced in the HHT method. For Newmark's methods, α_H is 0.

Like the HHT method, the Generalized-α method (Chung and Hulbert, 1993) uses Newmark's scheme to compute the displacement and velocity (Equation (4-36)) but introduces a new parameter, α_M, in the equilibrium equation.

$$\left[(1+\alpha_M)m\ddot{u}_{i+1} - \alpha_M m\ddot{u}_i\right] + (1+\alpha_H)ku_{i+1} - \alpha_H ku_i = f_{o,i+1} \tag{4-39}$$

An FP bearing with a sliding period of 3 s, static axial pressure of 50 MPa and a Coulomb-type coefficient of friction of 0.06 is subjected to a ground acceleration history $\ddot{u}_g = \sin(\pi t)$ m/s^2. No additional damping is assigned to the system. The acceleration history is specified at 0.01 s intervals and the response-history analyses are performed at time steps of 0.005 s. The analyses are performed for the five sets of the parameters α_H, α_M, γ and β listed in Table 4-5. Figure 4-30 plots the lateral displacement histories for the five sets. The differences are negligible with peak displacements ranging between 0.130 m and 0.133 m.

Table 4-5: Parameters for numerical schemes used in analyses

Numerical scheme	Analysis case	γ	β	α_H	α_M
Newmark's Method	Case 1	0.5	0.25	0	0
Newmark's Method	Case 2	0.5	0.166	0	0
HHT Method	Case 3	0.8	0.4225	0.3	0
HHT Method	Case 4	0.6	0.3025	0.1	0
Generalized-α Method	Case 5	0.5	0.25	0.2	0.2

4.5.3 Concluding remarks on verification studies

The new OpenSees element *FPBearingPTV* is verified because 1) the element produces correct results when used in an inverted configuration, 2) pressure, velocity and temperature dependencies of the coefficient of friction are coded correctly, 3) the rates of convergence of the numerical solutions for the elastic and inelastic regimes (separately examined) are equal to the respective theoretical rates, and 4) the errors in the numerical solutions are negligible compared to the magnitudes of the quantities of interest.

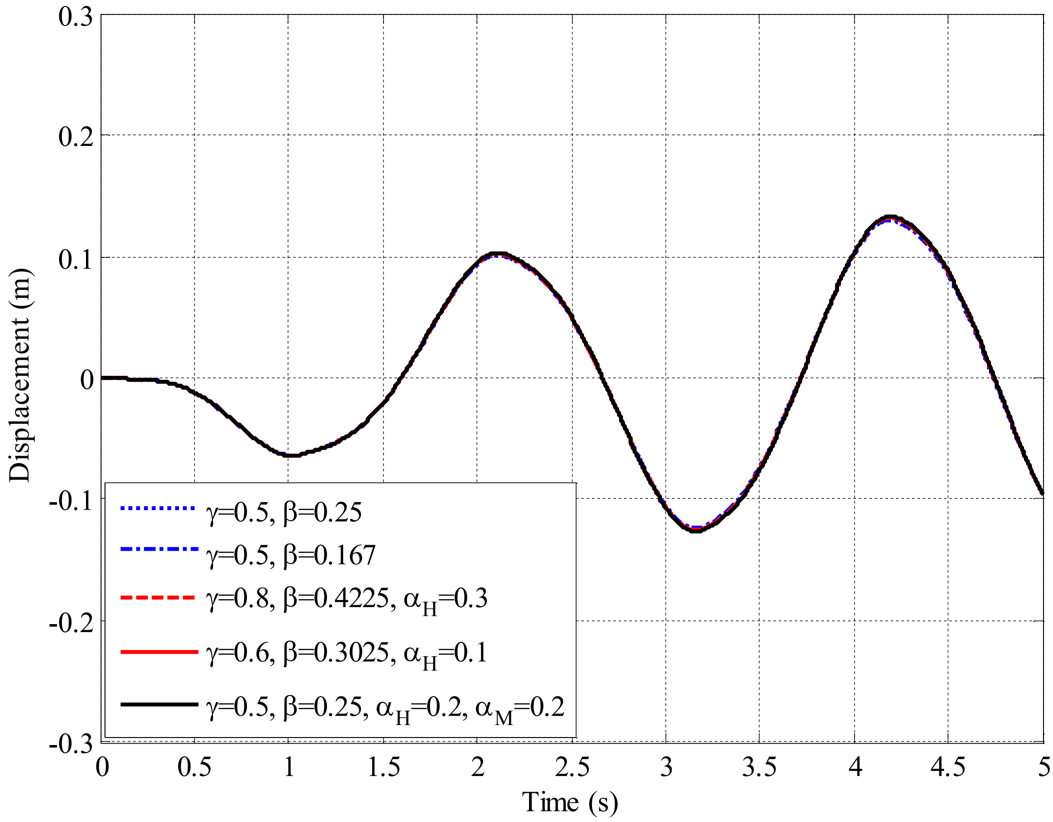

Figure 4-30: Lateral displacement histories for the five sets of analysis parameters listed in Table 4-5

4.6 Validation of OpenSees Element *FPBearingPTV*

Validation of a software program is performed to determine if it is capable of simulating experimental observations (Oberkampf and Roy, 2010). The OpenSees element *FPBearingPTV* incorporates the model presented in Chapter 3 to account for the dependencies of the coefficient of sliding friction on axial pressure, sliding velocity and temperature at the sliding interface. Validation of the element requires that the experimentally recorded responses of FP bearings with known geometrical and material properties (e.g., reference coefficient of friction measured at a given static pressure, temperature of $20^{o}C$ and a high sliding velocity) are captured by the *FPBearingPTV* element.

Experimental data are used to validate the element (see Table 4-6), which investigate force-displacement response and/or temperature below the sliding surfaces of FP bearings with different geometrical and material properties, and different levels of axial pressure, subjected to cycles of displacement-controlled loading. Many of the figures that follow present data reported by others; these data were digitized from the original documents.

The axial pressure was reportedly held constant for each experiment considered in this study (but there is no way to confirm this). Validation of the model for the pressure dependence of friction under cyclic loading is therefore not possible using available data. However, and as shown in later chapters of this report, consideration of the pressure dependence of friction is not important for the accurate estimation of key response quantities in isolated structures, including peak isolator displacements and floor spectral ordinates.

The velocity dependence of the coefficient of friction is not validated herein because it matters only when the sliding velocity is small (during low intensity ground motions), which is of no practical importance. The small-velocity experiments are simulated[1] using μ_{ref} equal to the maximum coefficient of friction during the experiment[2] rather than using the definition adopted in Chapter 3.

[1] Experimentally recorded temperature below the sliding surface has been used to validate the theory to compute temperature at the sliding surface. Some of these experiments were performed at small velocities.

[2] The relationship between velocity and coefficient of friction for liner materials may be different from that assumed in this study. Numerical simulations with reference coefficient of friction corresponding to a high velocity of sliding will not capture recorded responses during small-velocity tests. These experimental responses are captured best using a reference coefficient of friction equal to the maximum coefficient of friction recorded during the experiment.

Table 4-6: List of experiments used to validate the OpenSees element *FPBearingPTV*

Experiment Number	Paper/report	Bearing properties			Loading		
		R[1] (m)	μ[2]	$r_{contact}$[3] (m)	Axial Pressure (MPa)	u[4] (m)	n_{cycle}[5]
1	CERF (1998)	2.2	0.12	0.14	10.9	$0.15\sin(\pi t)$	3
2			0.09	0.14	10.9	$0.076\sin(4\pi t)$	2.5
3			0.09	0.14	36.3	$0.11\sin(4\pi t)$	2.5
4			0.13	0.20	25.7	$0.31\sin(\pi t)$	2
5	Wolff (1999), Constantinou *et al.* (1999)	∞[7]	0.10	0.0475	13.8	$0.025\cos(0.5\pi t)$	1
6			0.12	0.0475	13.8	$0.025\cos(\pi t)$	2
7			0.13	0.0475	13.8	$0.025\cos(2\pi t)$	2
8			0.13	0.0475	13.8	$0.025\cos(4\pi t)$	3
9			0.13	0.0475	12	$0.096\cos(0.26\pi t)$	2
10			0.15	0.0475	12	$0.096\cos(0.52\pi t)$	2
11			0.14	0.0475	12	$0.096\cos(1.06\pi t)$	3
12	Constantinou *et al.* (2007)	3.96	0.05	0.26	30.8	0.25 m amplitude, 0.6 Hz frequency	10[6]
13	Lomiento *et al.* (2013)	2.5	0.08	0.26	15	$0.2\sin(0.002\pi t)$	1
14			0.06	0.26	30	$0.2\sin(0.002\pi t)$	1
15			0.11	0.26	15	$0.2\sin(0.16\pi t)$	2
16			0.075	0.26	30	$0.2\sin(0.16\pi t)$	2

[1]Radius of curvature of sliding surface
[2]Back calculated reference coefficient of friction
[3]Radius of contact area
[4]Lateral displacement history of the slider
[5]Number of simulated force-displacement cycles
[6]First three and last cycle simulated
[7]Flat slider

Temperature is expected to be the most important factor that influences the coefficient of friction at the sliding surface during an earthquake. There are two ways to validate *FPBearingPTV* for temperature dependence of friction: 1) compare the computed temperature at the sliding surface with experimentally recorded temperature (e.g., experiment 5 in Table 4-6), and 2) indirectly by comparison of computed and experimentally recorded lateral force and/or force-displacement histories (e.g., experiment 12 in Table 4-6).

It is extremely difficult to measure a temperature history at a sliding surface, while sliding is taking place, for the reasons described in Wolff (1999). However, most experiments on FP bearings report lateral force-displacement histories.

The reference coefficients of friction (along with the values of axial pressure, temperature and sliding velocity, at which the coefficient of friction was measured) were not reported for any of the experiments considered in this study. Rather, these have been estimated from available information (e.g., recorded force-displacement response) for the simulations discussed below. In addition to the estimated value of the reference coefficient of friction, the reported values for axial pressure, loading history, radius of curvature of bearings, and the radius of slider are used to develop the model. The coefficient of friction is considered to vary with axial pressure, temperature on the sliding surface, and sliding velocity, as described in Chapter 3, for the simulations of the following sections unless noted otherwise. The force-displacement histories[1] and/or temperature histories below the center of sliding surface simulated using the *FPBearingPTV* element are compared with the experimentally recorded responses for the 16 experiments of Table 4-6.

4.6.1 CERF (1998)

FP bearings with a sliding period of 3 s (radius of curvature of 2.23 m) were subjected to different levels of axial load and horizontal displacement histories. The radius of the contact area at the sliding surface for the first three experiments was 0.140 m, and was 0.200 m for the fourth experiment. The static axial pressure on the bearing ranged between 11 MPa (experiments 1

[1] The force-displacement histories are compared in terms of 1) energy dissipated during different cycles, and 2) coefficients of friction at zero horizontal displacement.

and 2) and 36 MPa (experiment 3). The peak velocities for the experiments were between 0.470 m/s (experiment 1) and 1.380 m/s (experiment 3).

Figure 4-31(a) plots the experimentally recorded and simulated (using the *FPBearingPTV* element in OpenSees) force-displacement histories for experiment number 1 of Table 4-6. The properties of the bearing, and the imposed static and displacement-controlled loading history used in the numerical simulation are listed in the table: μ_{ref} = 0.12, p_o = 10.9 MPa, R = 2.23 m, slider radius = 0.14 m, $u = 0.15\sin(\pi t)$ in meters. The sudden drop in the force at the beginning of experiment is attributed to the chosen cyclic loading history. Subjecting a bearing to a sinusoidal displacement history with an initial displacement of zero (a sine function) requires the initial velocity (a cosine function) to increase quickly, generating inertial effects at the beginning of the experiment that distorts the force-displacement relationship. The reduction in the coefficient of friction is evident from the change in the level of shearing force at a given displacement with an increasing number of cycles.

The experimentally recorded and numerically simulated force-displacement histories are compared using a) energy dissipated in each cycle, and b) the coefficient of friction at zero lateral displacement. Figure 4-31(b) plots the first experimentally recorded and numerically simulated cycles considered for the energy calculation, which begin and end at +0.135 m, namely, a displacement cycle +0.135 m → +0.150 m → -0.150 m → +0.135 m[1]. The beginning and end of the cycle are identified in the figure. The energy dissipated during this cycle is 40 kN-m. Figure 4-31(c) presents the energy dissipated in the first three cycles computed from the digitized force-displacement curve from the experiment and from the numerical simulation.

[1] The cycle is considered to begin at displacement equal to +0.135 m instead of the beginning of the experiment (0.000 m) so that the aforementioned inertial effects are not included in the energy calculations.

The *experimental*[1] and *numerical*[1] values differ by between 1% and 8% for the three cycles. The difference in the total energy dissipated in the three cycles is 3%.

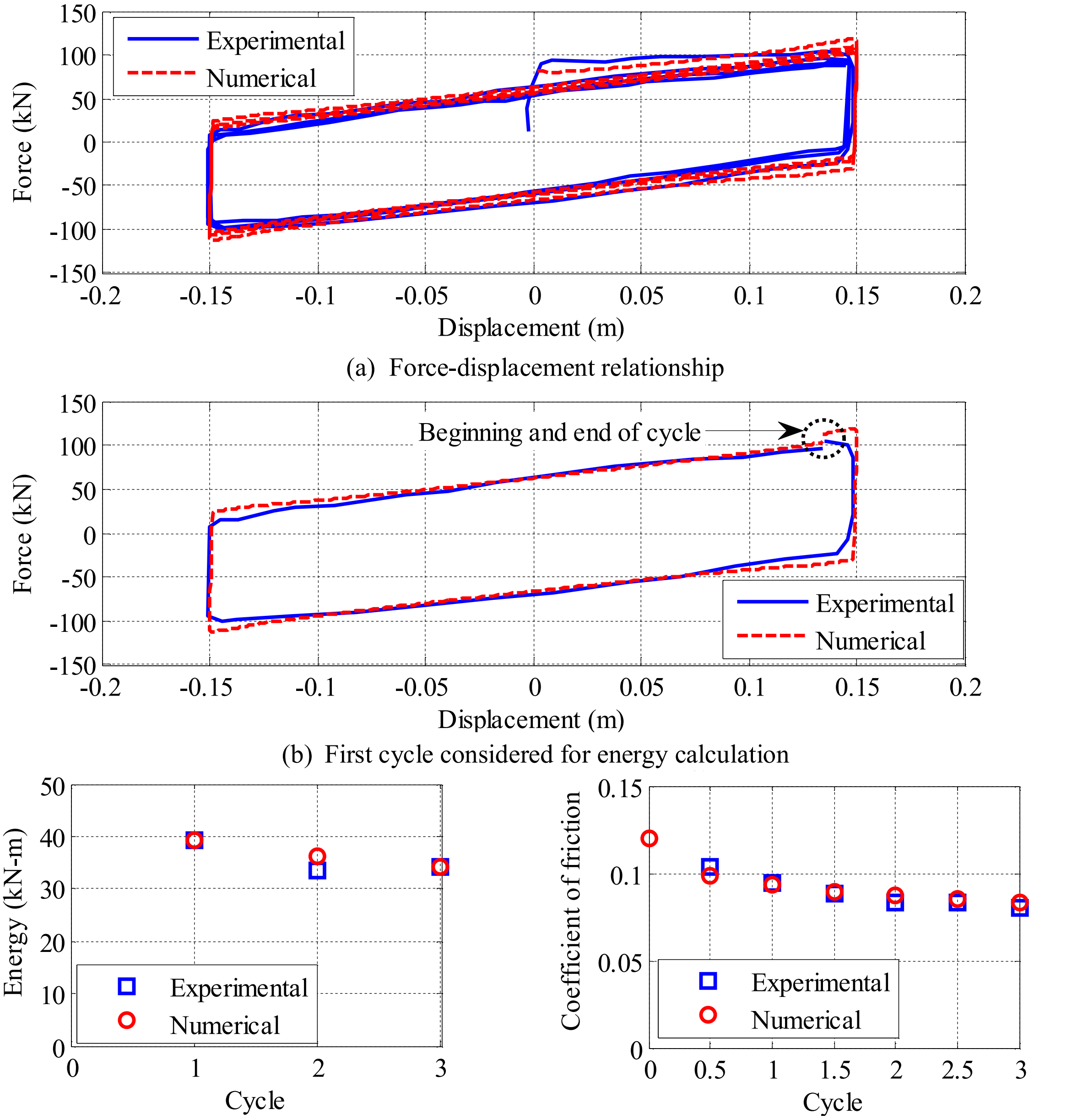

(a) Force-displacement relationship

(b) First cycle considered for energy calculation

(c) Energy dissipated

(d) Coefficient of friction

Figure 4-31: Experimentally recorded and numerically simulated force-displacement relationships for experiment number 1 of Table 4-6

[1] Herein, an *experimental* value is that calculated using data from the experiment and a *numerical* value is that calculated from the simulations using *FPBearingPTV*.

Figure 4-31(d) plots the coefficient of friction at zero displacement for experiment 1. The coefficient decreased from 0.1 to 0.08 between the end of the first half cycle and the end of the third cycle. The maximum difference between the *experimental* and *numerical* values is 5%.

The maximum and minimum values of energy dissipated in a cycle during the experiment, and the coefficients of friction at zero displacement obtained from the experimental data are listed in Table 4-7. The table also presents the percentage difference between the total energy dissipated and the coefficient of friction at zero displacement in the experiments and in the numerical simulations.

The force-displacement histories, energy dissipated per cycle and coefficient of friction at zero displacement for experiments 2, 3 and 4 of Table 4-6 are presented in Figures 4-32, 4-33 and 4-34, respectively, together with *numerical* responses. Table 4-6 lists the parameters used to perfom these numerical simulations. The energy dissipated in a cycle for these experiments is computed as described previously in the section (e.g., Figure 4-31(b)). Results are summarized in Table 4-7. The difference in the total energy dissipated in the experiments and the numerical simulations ranges between 2% and 14% for the four tests. The maximum differences in the coefficients of friction at zero displacement range between 5% and 17%.

4.6.2 Wolff (1999), Constantinou *et al.* (1999)

Experiments 5 to 11 in Table 4-6 are reported in Wolff (1999) and Constantinou *et al.* (1999). Two sets of experimental data are available: 1) normalized force-displacement histories, and 2) temperature histories at a point 0.0015 m below the center of the sliding surface. The radius of the contact area for the bearings in the experiments was 0.0475 m. The static axial pressure (displacement amplitude) was 13.8 MPa (0.025 m) for experiments 5 through 8, and 12 MPa

(0.096 m) for experiments 9, 10 and 11. The properties of the bearings and the loading parameters used in the numerical simulations of the experiments are listed in Table 4-6.

Table 4-7: Energy dissipated and coefficient of friction at zero displacement in different cycles of loading for the experiments of Table 4-6

Exp. No	Figure	Number of cycles	Energy dissipated per cycle (kN-m)			Coefficient of friction		
			Max[1]	Min[1]	% difference between total energies[2]	Max[1]	Min[1]	Maximum % difference
1	Figure 4-31	3	40	34	3	0.10	0.08	5
2	Figure 4-32	2.5	22	18	2	0.08	0.06	10
3	Figure 4-33	2.5	60	50	14	0.06	0.04	14
4	Figure 4-34	2	310	220	7	0.09	0.06	17
5	Figure 4-35	1	1	1	1	0.10	0.10	4
6	Figure 4-36	2	1	1	3	0.12	0.10	4
7	Figure 4-37	2	1	1	3	0.13	0.11	6
8	Figure 4-38	3	1	1	5	0.13	0.10	9
9	Figure 4-39	2	4	4	9	0.13	0.12	5
10	Figure 4-40	2	4	4	11	0.14	0.13	3
11	Figure 4-41	3	4	3	6	0.14	0.11	8
12	Figure 4-45	3	280	210	14	0.04	0.02	19
13	Figure 4-47	1	210	210	5	0.08	0.08	4
14	Figure 4-48	1	320	320	4	0.06	0.06	6
15	Figure 4-49	2	260	210	1	0.11	0.07	19
16	Figure 4-50	2	330	250	3	0.08	0.04	23

[1]Obtained from experiment
[2]Total energy dissipated in completed cycles (e.g., 2 cycles if 2.5 cycles are simulated)

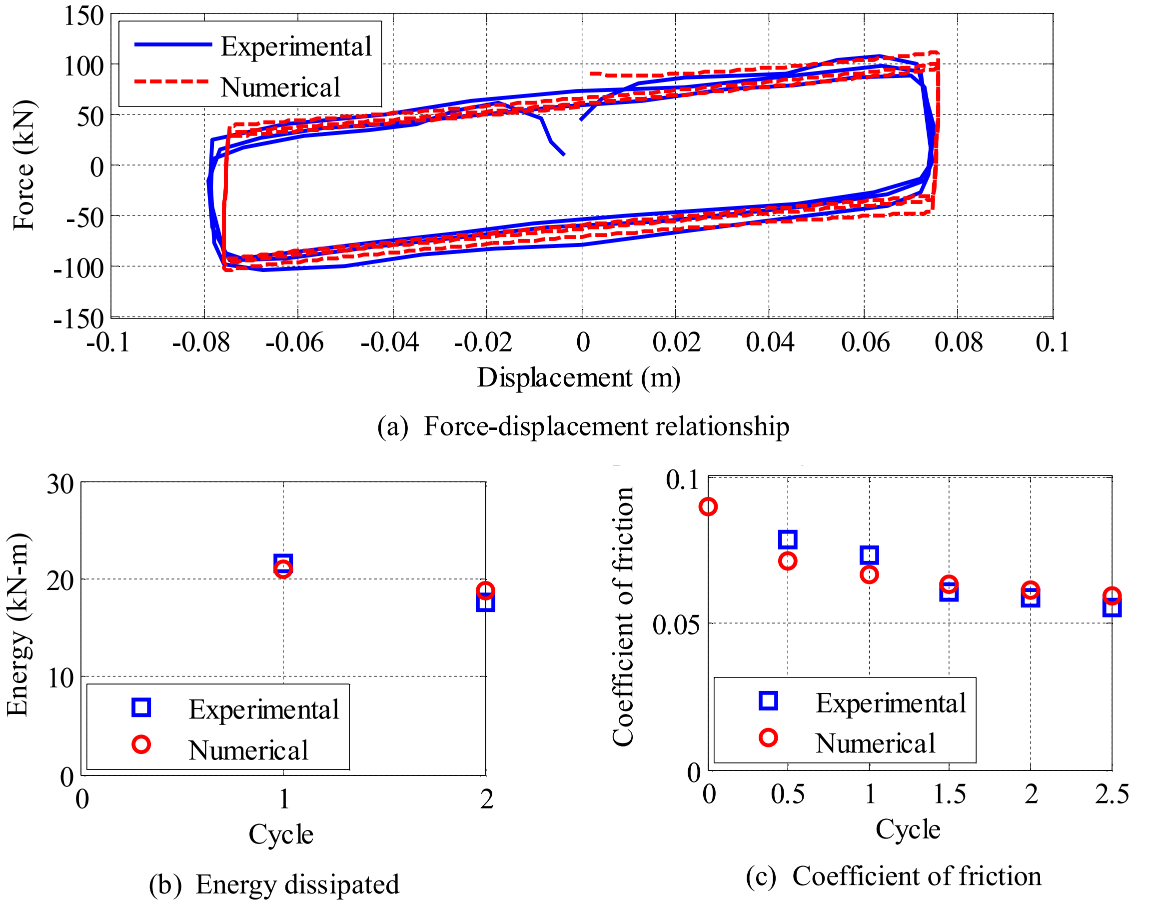

Figure 4-32: Experimentally recorded and numerically simulated force-displacement relationships for experiment number 2 of Table 4-6

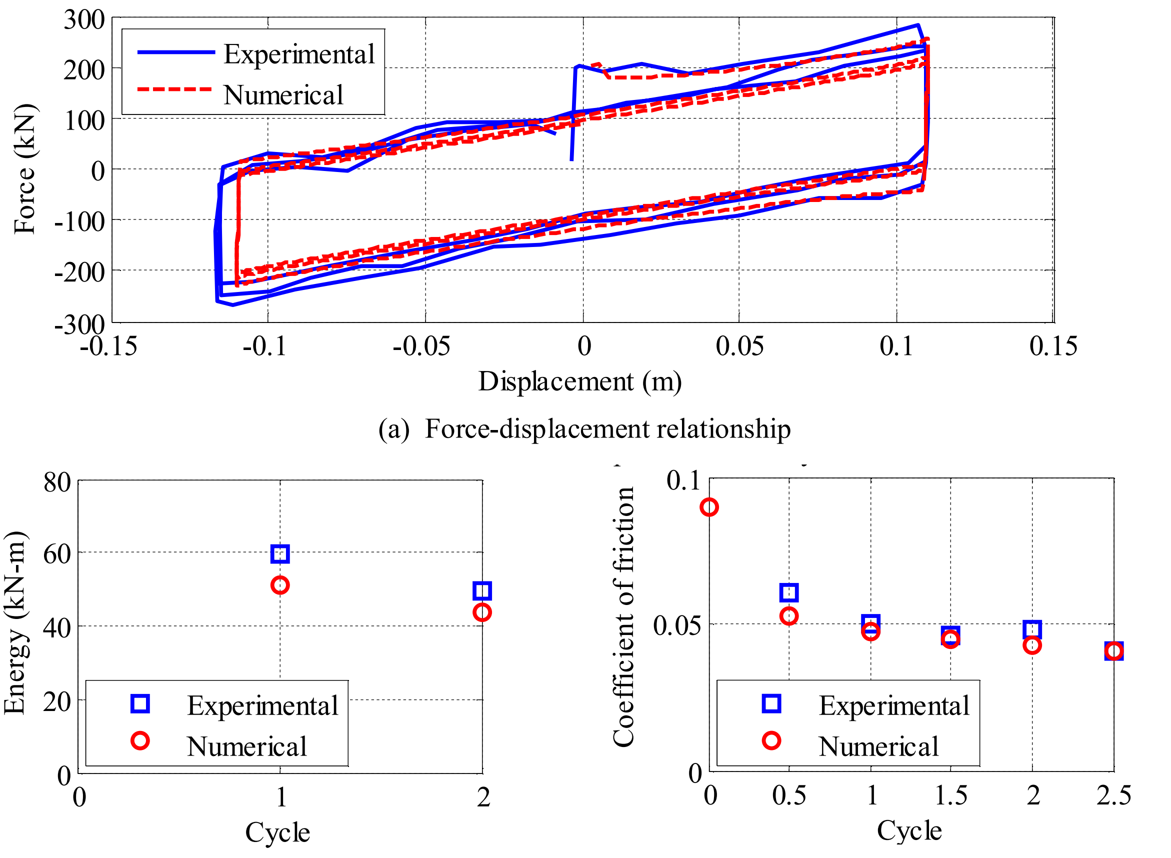

(a) Force-displacement relationship

(b) Energy dissipated

(c) Coefficient of friction

Figure 4-33: Experimentally recorded and numerically simulated force-displacement relationships for experiment number 3 of Table 4-6

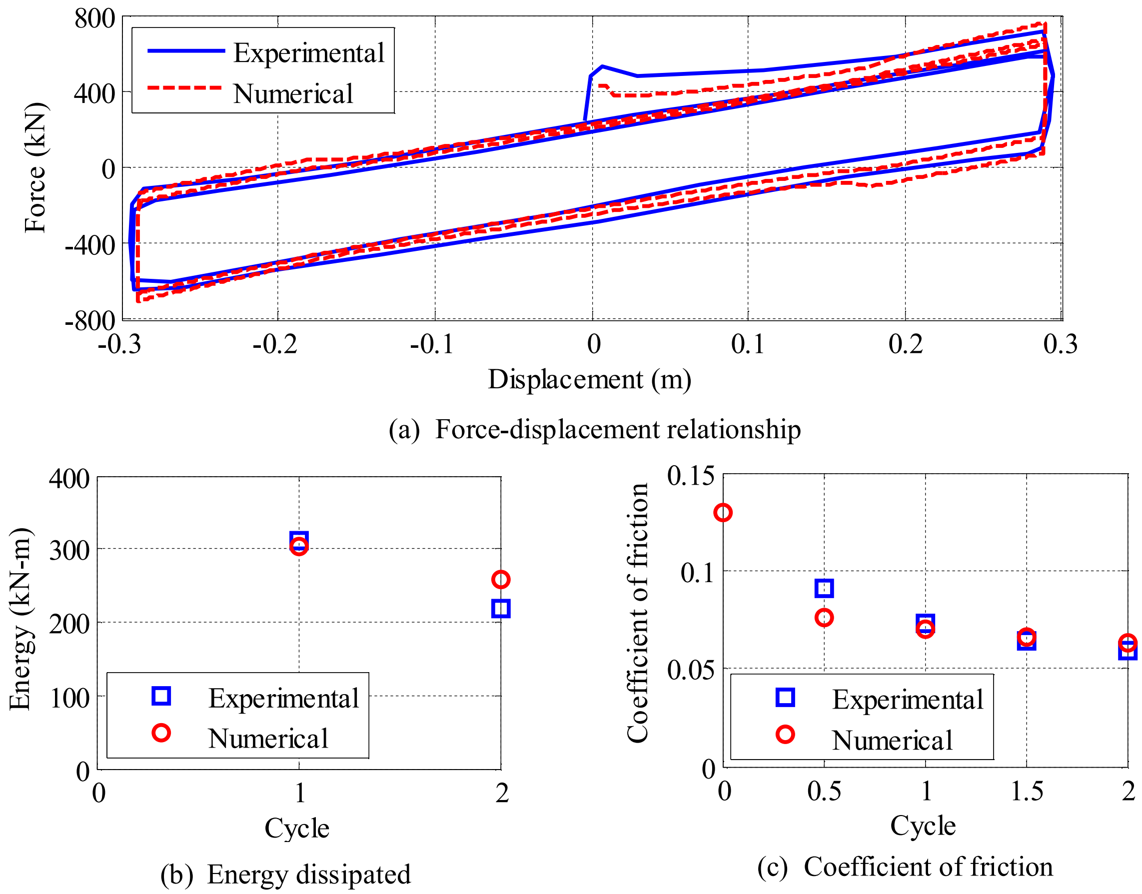

(a) Force-displacement relationship

(b) Energy dissipated

(c) Coefficient of friction

Figure 4-34: Experimentally recorded and numerically simulated force-displacement relationships for experiment number 4 of Table 4-6

4.6.2.1 Force-displacement response

Figure 4-35(a) presents the recorded and numerically simulated force-displacement relationships for experiment 5 of Table 4-6: p_o = 13.8 MPa, radius of curvature = ∞ (flat slider), slider radius = 0.0475 m, $u = 0.025\sin(0.5\pi t)$ in meters. The peak velocity for this experiment was 0.00625 m/s (small-velocity test; see Chapter 3 and Section 4.6). The value of μ_{ref} is set equal to 0.10 for the simulation, which is the maximum coefficient of friction recorded during the experiment. Figures 4-35(b) and 4-35(c) present the energy dissipated per cycle and the coefficient of friction at zero displacement, respectively. The energy dissipated in the cycle obtained from the experiment and the numerical simulation differs by 1%. The coefficients of friction at zero displacement differ by less than 4%.

Figures 4-36, 4-37 and 4-38 present the force-displacement responses for experiments 6, 7 and 8 of Table 4-6, respectively. The geometry of the FP bearing, axial pressure and amplitude of motion in the three experiments are the same as those for experiment 5, but the loading frequencies are 0.5 Hz, 1 Hz and 2 Hz, respectively. The other parameters used for the simulations are listed in Table 4-6. Results for the four experiments are summarized in Table 4-7. The total energy dissipated in the experiments and the numerical simulations differ by less than 5%, and the maximum differences between the *experimental* and *numerical* values of the coefficient of friction at zero displacement range between 4% and 9%.

Experiments 9, 10 and 11 were performed by subjecting sliders to a static pressure of 12 MPa, and displacement history with an amplitude of 0.096 m and frequencies of 0.13 Hz, 0.26 Hz and 0.53 Hz, respectively. Table 4-6 lists the values of the parameters used for the simulations. Figures 4-39, 4-40 and 4-41 present the experimental and numerical force-displacement relationships for the three experiments, respectively. Results are summarized in Table 4-7. The total energy dissipated during the experiments differ from the numerically simulated values by between 6% to 11%, and the *experimental* and *numerical* values of the coefficient of friction at zero displacement differ by less than 8% for the three tests.

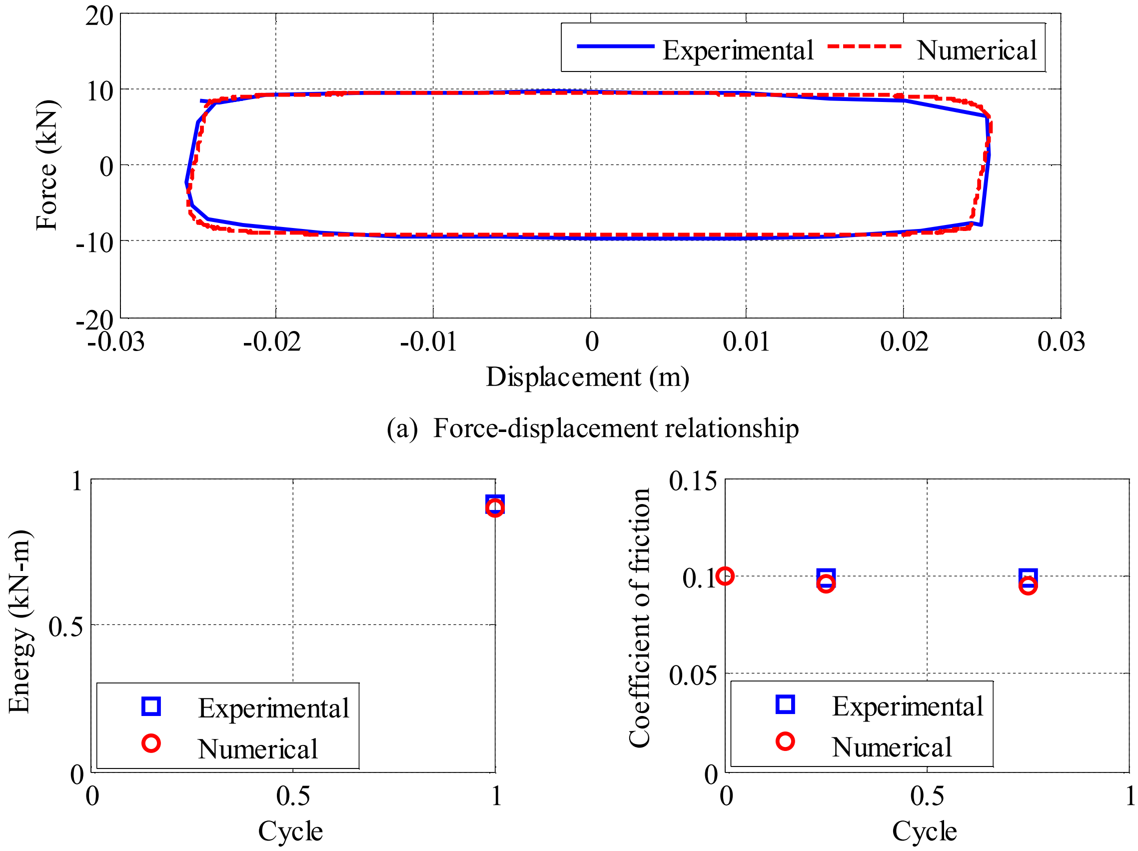

(a) Force-displacement relationship

(b) Energy dissipated

(c) Coefficient of friction

Figure 4-35: Experimentally recorded and numerically simulated force-displacement relationships for experiment number 5 of Table 4-6

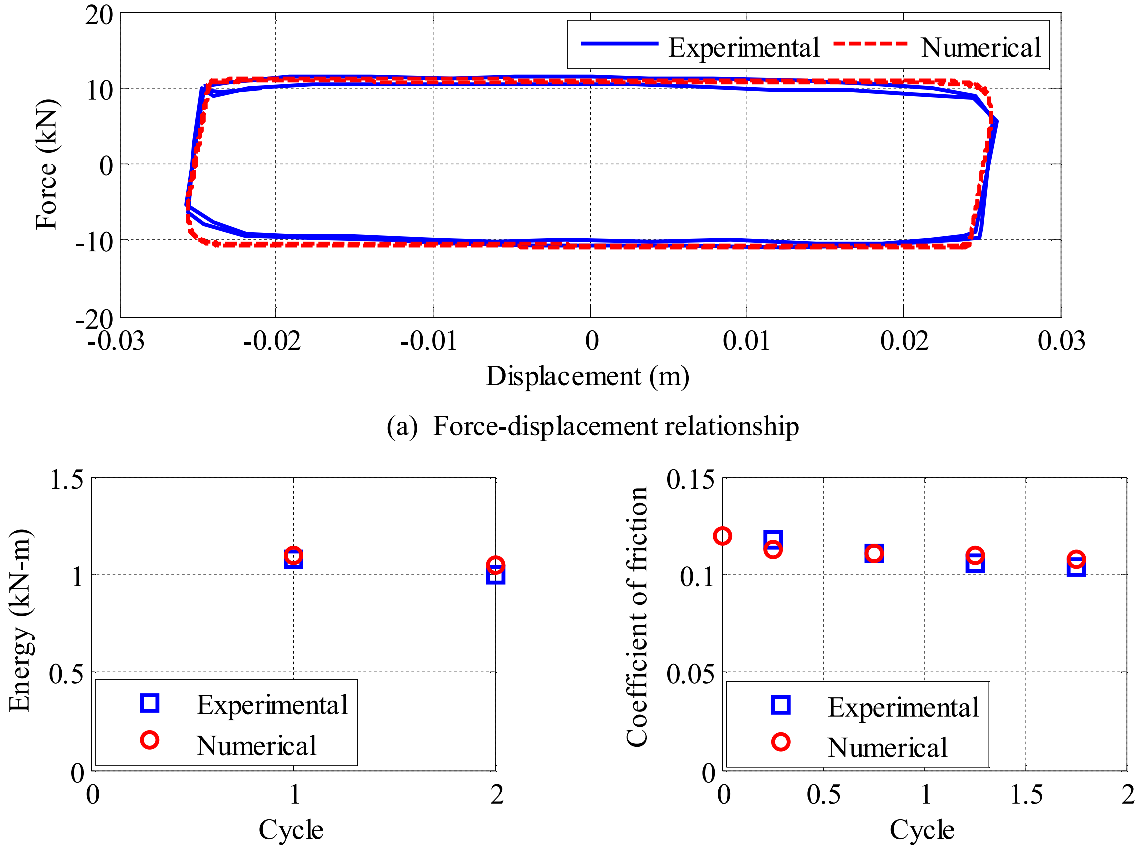

(a) Force-displacement relationship

(b) Energy dissipated

(c) Coefficient of friction

Figure 4-36: Experimentally recorded and numerically simulated force-displacement relationships for experiment number 6 of Table 4-6

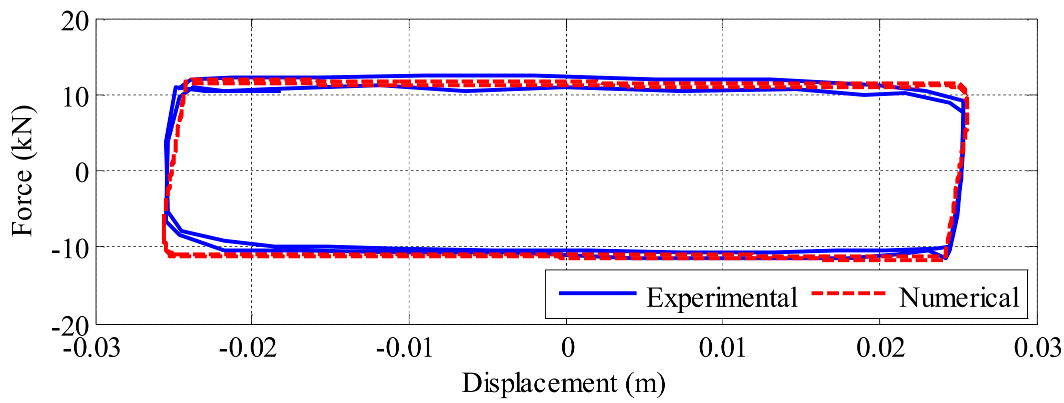

(a) Force-displacement relationship

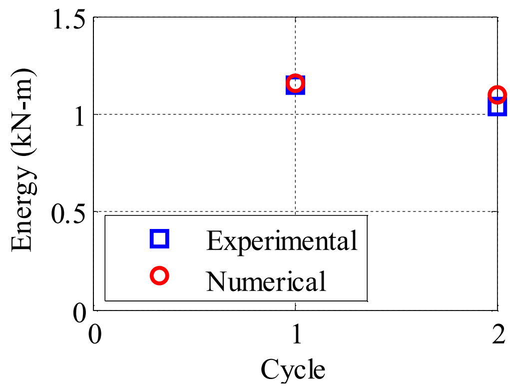

(b) Energy dissipated

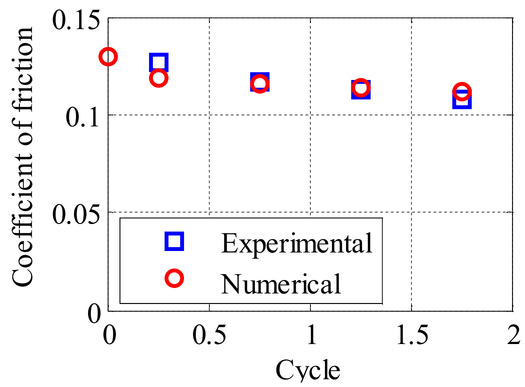

(c) Coefficient of friction

Figure 4-37: Experimentally recorded and numerically simulated force-displacement relationships for experiment number 7 of Table 4-6

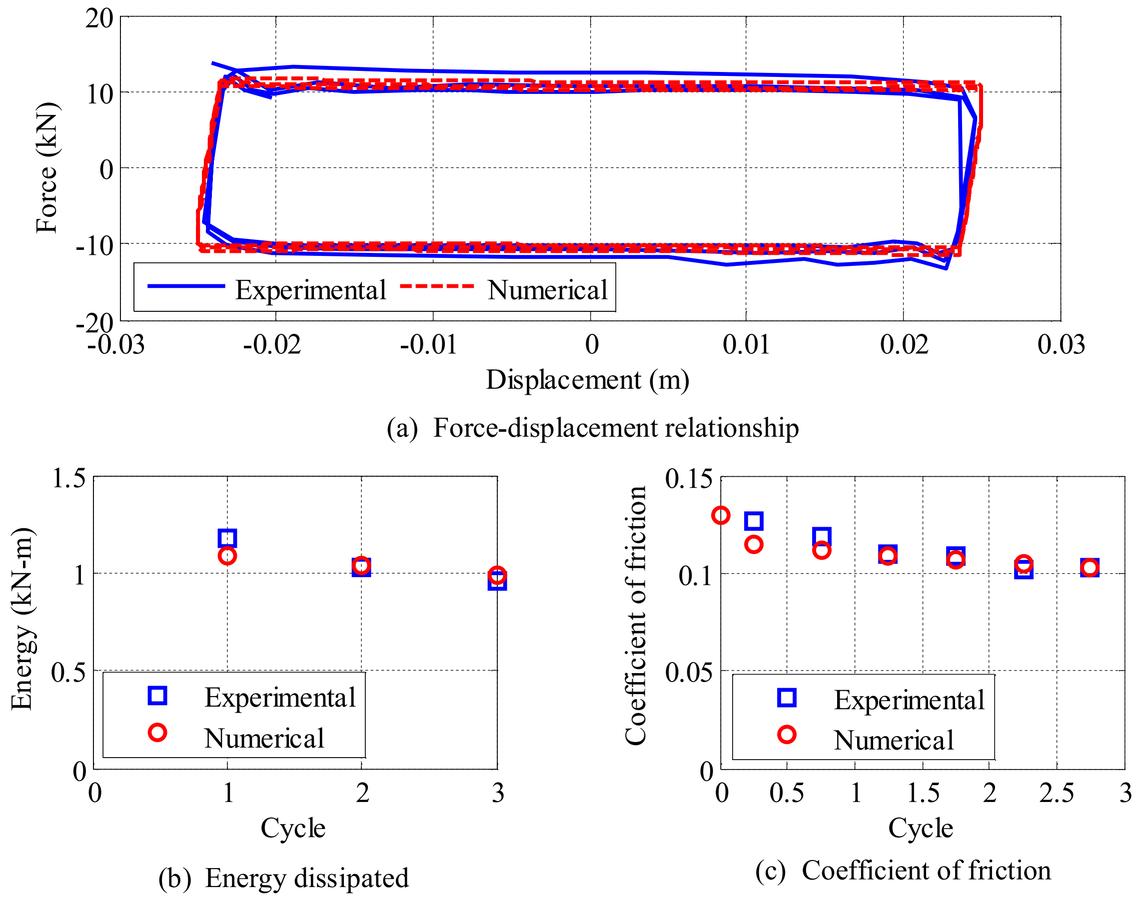

Figure 4-38: Experimentally recorded and numerically simulated force-displacement relationships for experiment number 8 of Table 4-6

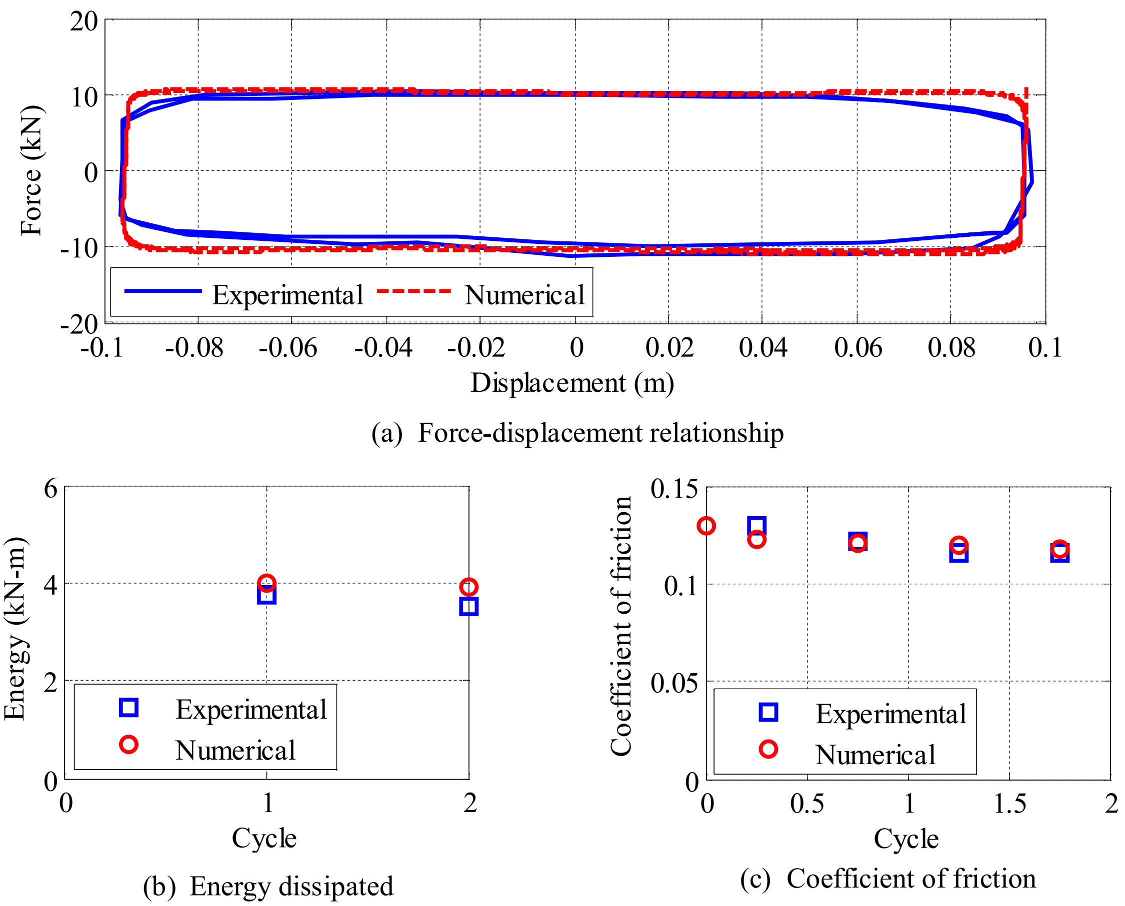

Figure 4-39: Experimentally recorded and numerically simulated force-displacement relationships for experiment number 9 of Table 4-6

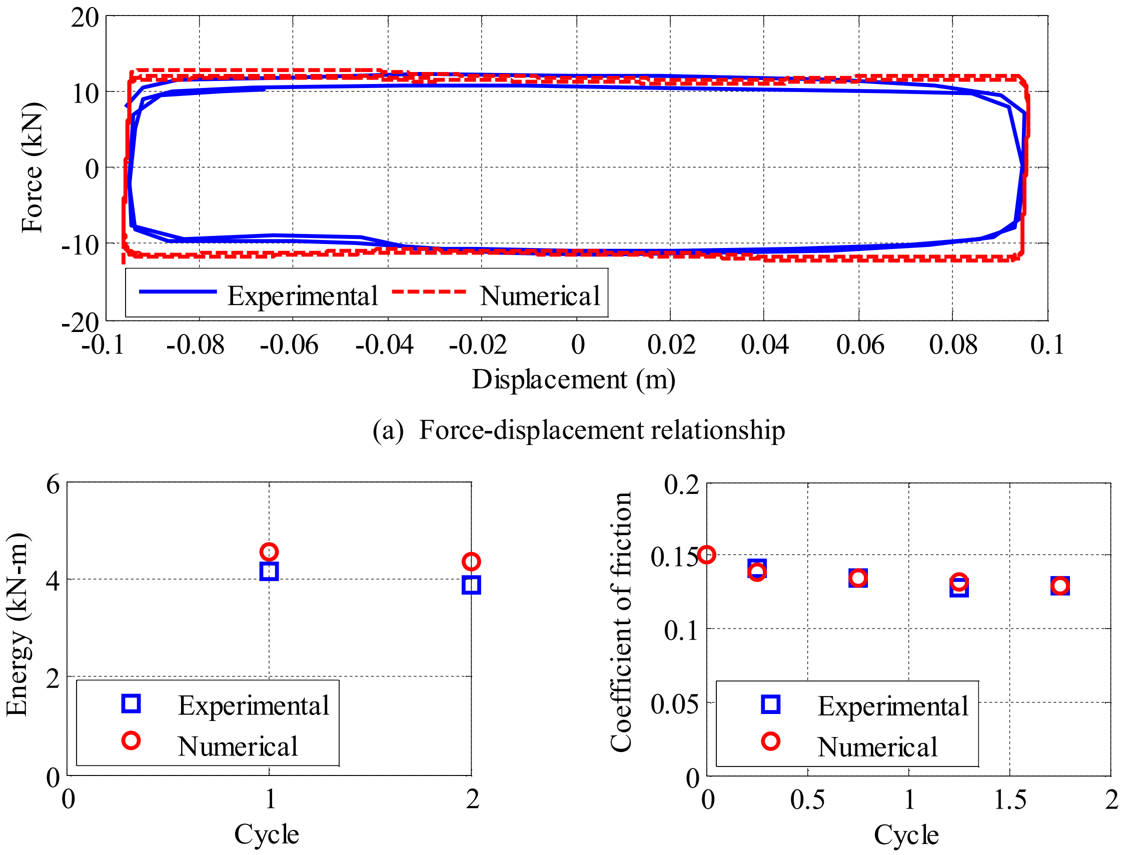

(a) Force-displacement relationship

(b) Energy dissipated

(c) Coefficient of friction

Figure 4-40: Experimentally recorded and numerically simulated force-displacement relationships for experiment number 10 of Table 4-6

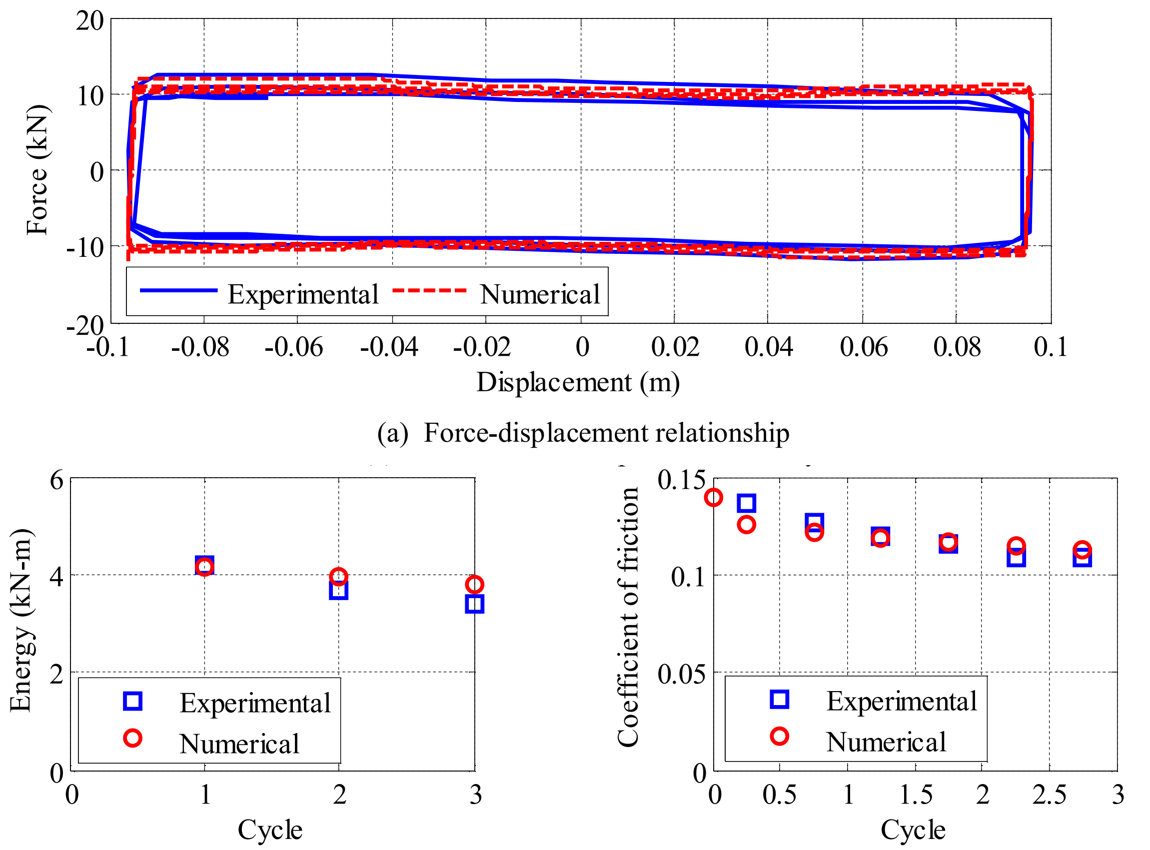

(a) Force-displacement relationship

(b) Energy dissipated

(c) Coefficient of friction

Figure 4-41: Experimentally recorded and numerically simulated force-displacement relationships for experiment number 11 of Table 4-6

4.6.2.2 Temperature at the sliding surface

The temperature histories at a point below the center of the sliding surface for experiments 5 through 11 of Table 4-6 are compared with numerical predictions in support of the validation exercise. Details on the bearings and loading parameters used in the simulations are provided in Table 4-6. The OpenSees element *FPBearingPTV* computes temperature at the center of the sliding surface using (3-22) with depth below sliding surface set equal to zero. The temperature histories below the sliding surface are computed using (3-22) and compared with the experimental results.

Figure 4-42(a) presents the experimentally recorded and computed histories of temperature at a point 0.0015 m below the center of the sliding surface of the flat slider subjected to a static axial pressure of 13.8 MPa, and a lateral displacement history with an amplitude of 0.025 m and a frequency of 0.25 Hz (experiment 5 of Table 4-6). The radius of the contact area is 0.0475 m. Panels (b), (c) and (d) of the figure present histories for loading frequencies of 0.5 Hz, 1 Hz and 2 Hz, respectively (experiments 6, 7 and 8). The computed history matches the recorded history well when the frequency of loading is small. The differences between the two histories increase with loading frequency, which is attributed to the time lag with which the thermocouple records temperature (see Chapter 3).

Figure 4-43(a) presents temperature histories at a point 0.0015 m below the center of the sliding surface. The axial pressure on the bearing was 12 MPa. A sinusoidal displacement history with amplitude of 0.096 m and a frequency of 0.13 Hz was imposed on the slider (experiment 9 of Table 4-6). Figures 4-43(b) and 4-43(c) present results for a loading frequency of 0.26 Hz and 0.53 Hz, respectively (experiments 10 and 11). The temperature rises as the slider passes over the center of the sliding surface and decreases otherwise. The computed histories match the experimentally recorded histories well, especially for the lower loading frequencies: 0.13 Hz and 0.26 Hz.

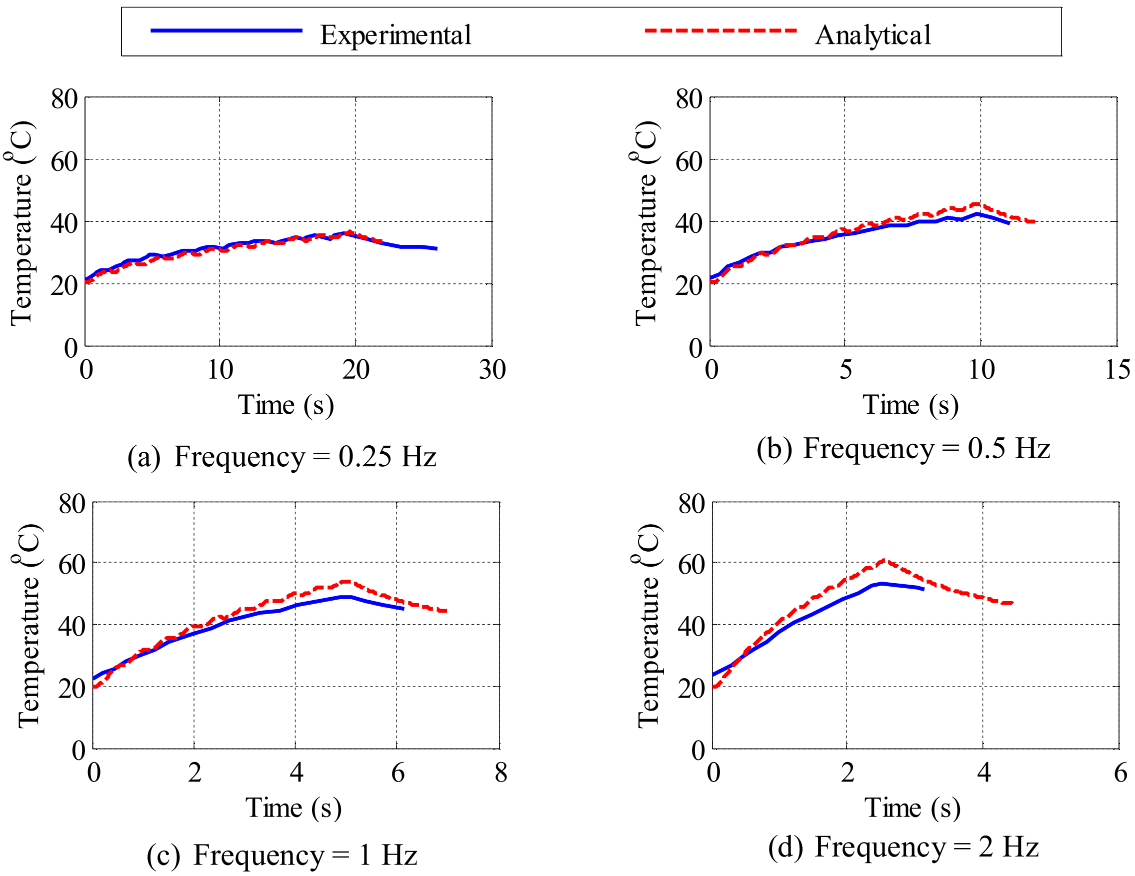

Figure 4-42: Histories of temperature at a point 1.5 mm below the center of a flat slider with static axial pressure of 13.8 MPa subjected to a lateral displacement loading with an amplitude of 25 mm (experiments 5, 6, 7 and 8 of Table 4-6)

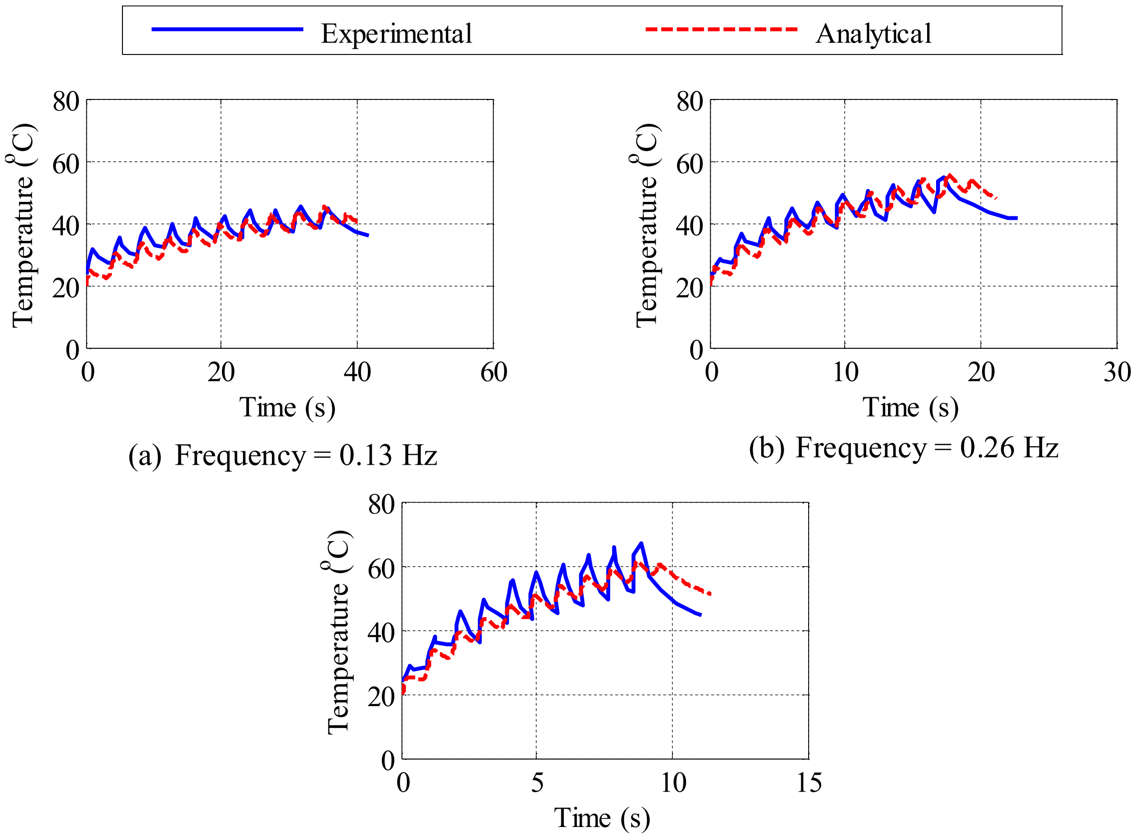

(a) Frequency = 0.13 Hz

(b) Frequency = 0.26 Hz

(c) Frequency = 0.53 Hz

Figure 4-43: Histories of temperature at a point 1.5 mm below the center of a flat slider with static axial pressure of 12 MPa subjected to a lateral displacement loading with amplitude of 96 mm (experiments 9, 10 and 11 of Table 4-6)

4.6.3 Constantinou *et al.* (2007)

Constantinou *et al.* (2007) report the results of tests performed on an FP bearing with a radius of curvature of 3.96 m, a static axial pressure of 30.8 MPa and the displacement history plotted in Figure 4-44 (experiment 12 of Table 4-6). Figure 4-45(a) presents the first three force-displacement cycles obtained from the experiment and the numerical simulation. The parameters used in the numerical simulation are listed in Table 4-6. Panels (b) and (c) of the figure present the energy dissipated in the first three cycles and the coefficients of friction at zero displacement. The total energy dissipated in the experiment and in the numerical simulation differs by 14%. The differences between the coefficients of friction at zero displacement are 4%, 19%, 4%, 15%, 11% and 4% (see Table 4-7). There appears to be a bias in the experimentally recorded force-displacement loops (the coefficient of friction increased instead of decreasing from the end of 0.25 (1.25, 2.25) cycle to the end of 0.75 (1.75, 2.75) cycle; see Figure 4-45(c)), which led to significant differences between the experimental and numerical values of the coefficients of friction.

The FP bearing was subjected to 10 loading cycles of which three are reproduced in Figure 4-45. It was not possible to digitize the experimentally recorded force-displacement histories between the fourth and ninth cycles. The experimentally recorded and numerically simulated force-displacement histories for the 10^{th} cycle are presented in Figure 4-46. The energy dissipated in the experiment in the 10^{th} cycle is 142 kN-m; the numerically simulated value is 147 kN-m. The experimentally recorded and numerically simulated values of the coefficient of friction are both approximately 0.02 in the 10^{th} cycle. The temperature at the center of sliding surface at the end of 10 cycles of loading is estimated to be 262°C and the coefficient of friction decreased by about 50% during the experiment[1].

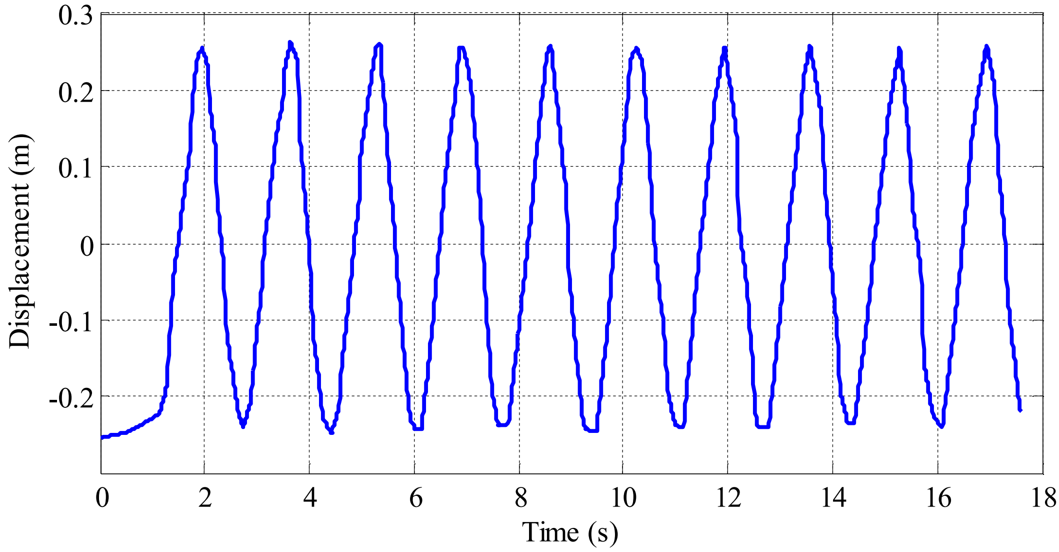

Figure 4-44: FP bearing displacement history from experiment 12 of Table 4-6 (adapted from Constantinou *et al.* (2007))

[1] The temperature-dependent friction model proposed in Chapter 3 assumes the ratio of $\mu(T)$ at T = 20°C and 250°C is 2:1

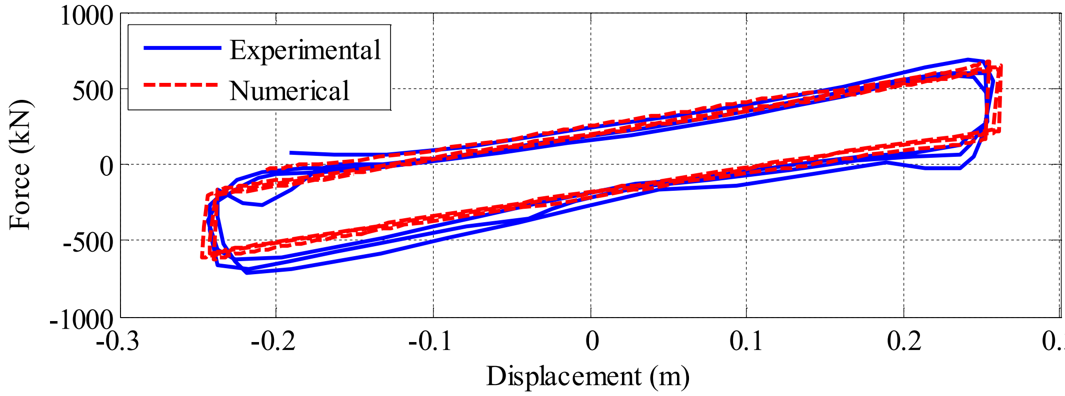

(a) Force-displacement relationship

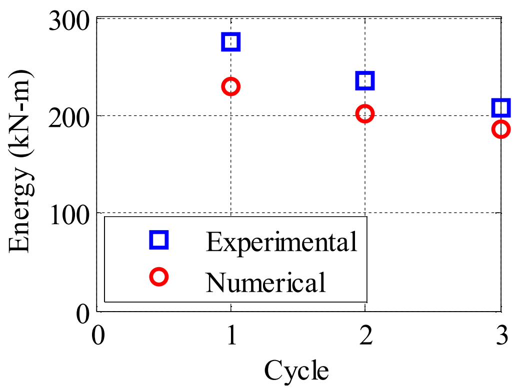

(b) Energy dissipated

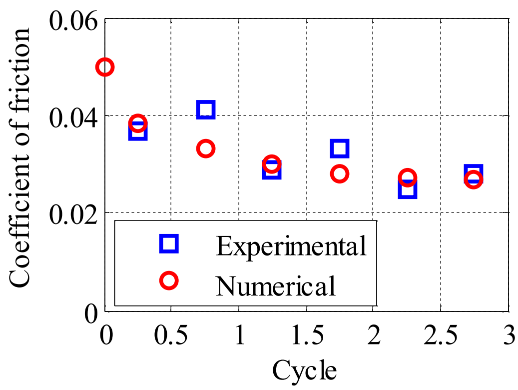

(c) Coefficient of friction

Figure 4-45: First three cycles of experimentally recorded and numerically simulated force-displacement relationships for experiment number 12 of Table 4-6

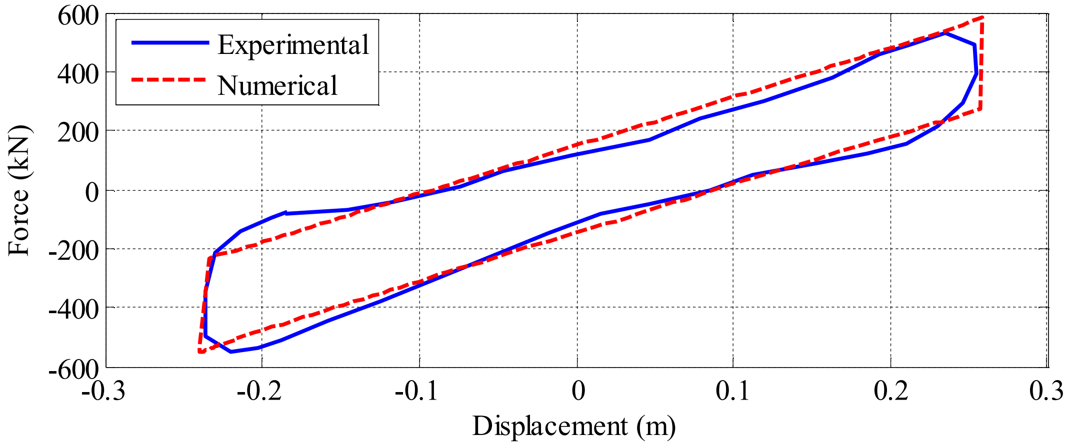

Figure 4-46: Tenth cycle of experimentally recorded and numerically simulated force-displacement relationships for experiment number 12 of Table 4-6

4.6.4 Lomiento *et al.* (2013)

Lomiento *et al.* (2013) performed experiments on an FP bearing with a radius of curvature of 2.5 m at two loading frequencies (0.001 and 0.08 Hz) and two axial pressures (15 and 30 MPa). The parameters used for the numerical simulations are listed in Table 4-6. Figure 4-47(a) presents the force-displacement relationships of the FP bearing with 15 MPa static axial pressure subjected to a displacement history with amplitude of 0.200 m and frequency of 0.001 Hz (experiment 13 of Table 4-6). Figures 4-47(b) and 4-47(c) present the energy dissipated and coefficients of friction at zero displacement. Figures 4-48, 4-49 and 4-50 present results for experiments 14, 15 and 16, respectively. Experiments 13 and 14 are small-velocity tests; experiments 15 and 16 are high-velocity tests. The energy dissipated in the experiments and calculated from the numerical simulations differs by less than 5%. The difference between the *experimental* and *numerical* values of the coefficient of friction at zero displacement ranges between 4% and 23% (see Table 4-7).

4.6.5 Concluding remarks on validation

Experimental data are used to validate the new OpenSees element *FPBearingPTV*. Two responses are considered: force-displacement relationships, and recorded temperature below the sliding surface. Challenges with these validation studies include: 1) key parameters including the coefficient of friction (along with reference pressure and reference temperature) and material properties of the liner were not reported for any experiment, and 2) the axial pressure was kept (approximately) constant during the experiments, which did not allow the model to be validated for the pressure dependence of the coefficient of friction under cyclic loading.

The new OpenSees element reasonably simulates 1) the experimentally recorded force-displacement relationships when the coefficient of sliding friction does not change considerably during the experiment (e.g., in small-velocity tests), 2) the reduction in the coefficient of friction associated with the increase in temperature at the sliding surface due to frictional heating for a range of loading conditions and mechanical properties, and 3) the recorded temperature history below the sliding surface[1], especially when the amplitude and frequency of the displacement-controlled loading are small.

[1] The model for the temperature dependence of friction coded in the *FPBearingPTV* element is used to compute the temperature below the sliding surface.

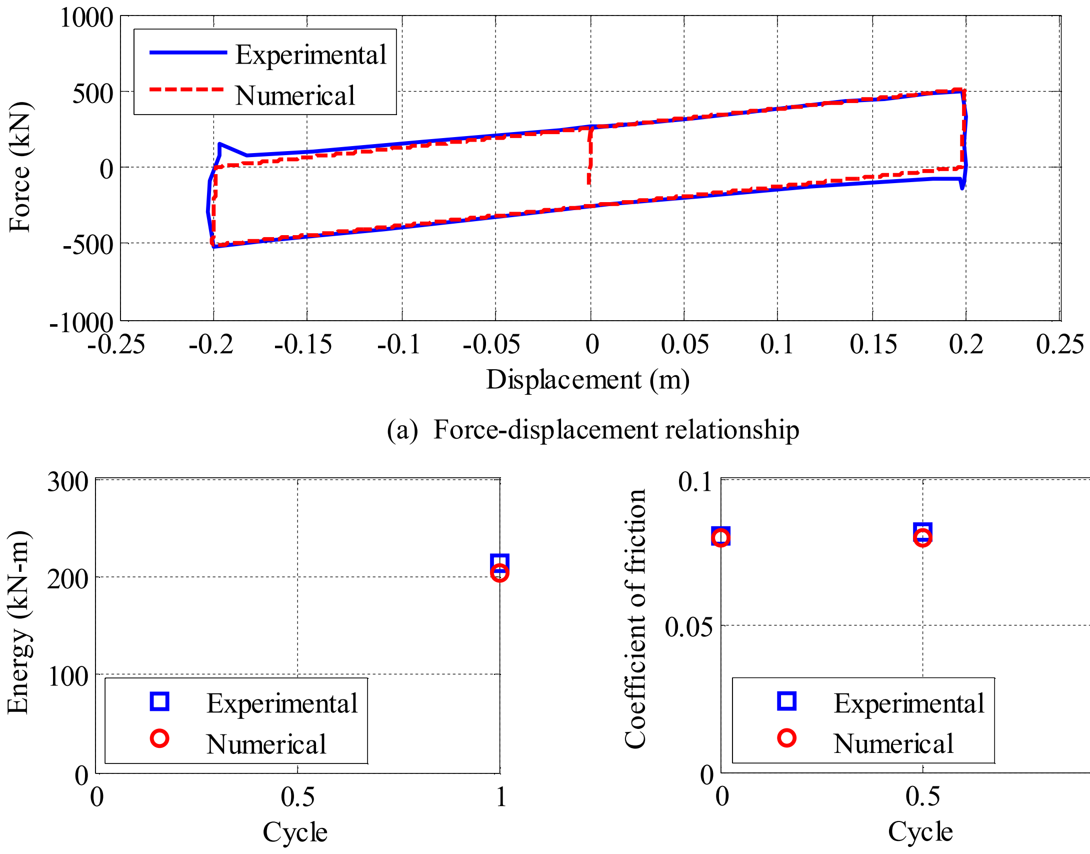

(a) Force-displacement relationship

(b) Energy dissipated

(c) Coefficient of friction

Figure 4-47: Experimentally recorded and numerically simulated force-displacement relationships for experiment number 13 of Table 4-6

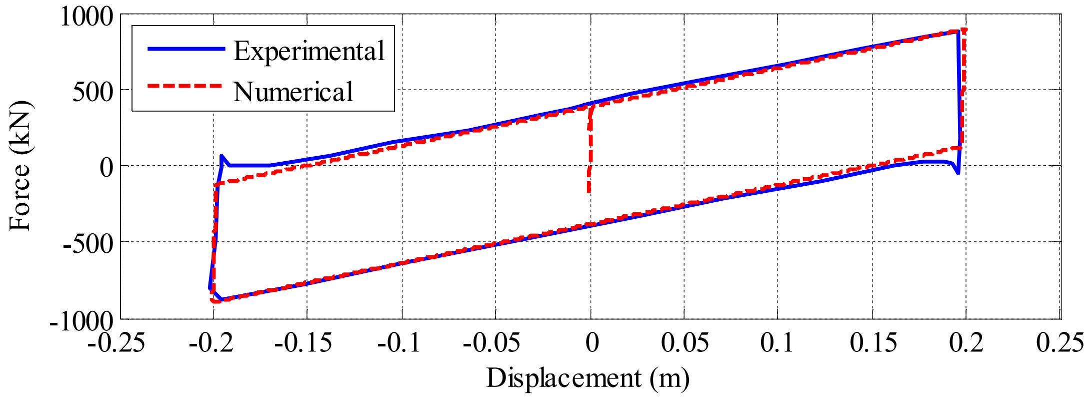

(a) Force-displacement relationship

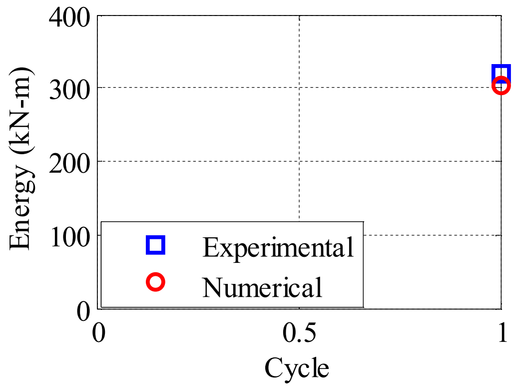

(b) Energy dissipated

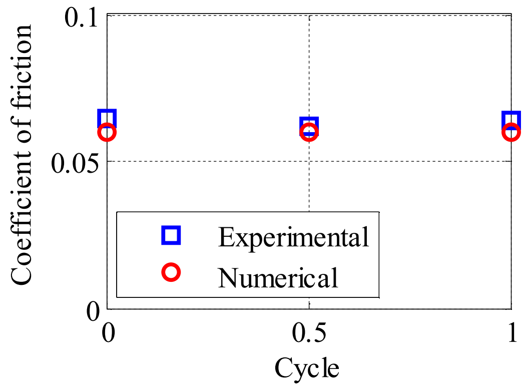

(c) Coefficient of friction

Figure 4-48: Experimentally recorded and numerically simulated force-displacement relationships for experiment number 14 of Table 4-6

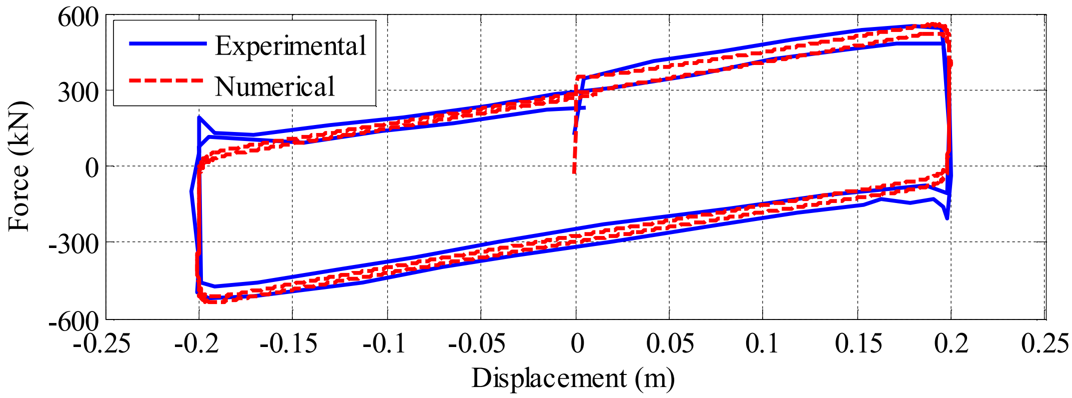

(a) Force-displacement relationship

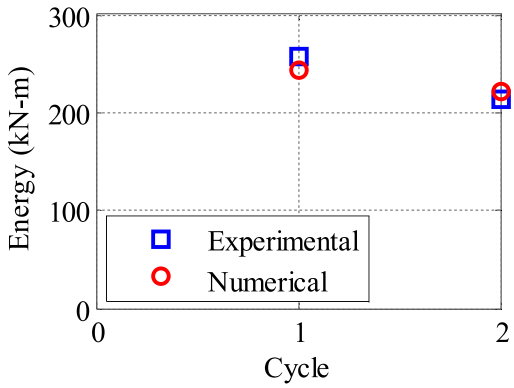

(b) Energy dissipated

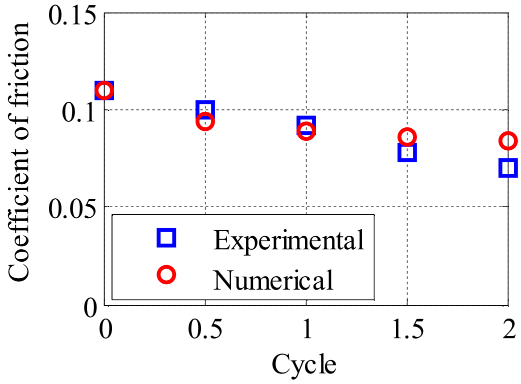

(c) Coefficient of friction

Figure 4-49: Experimentally recorded and numerically simulated force-displacement relationships for experiment number 15 of Table 4-6

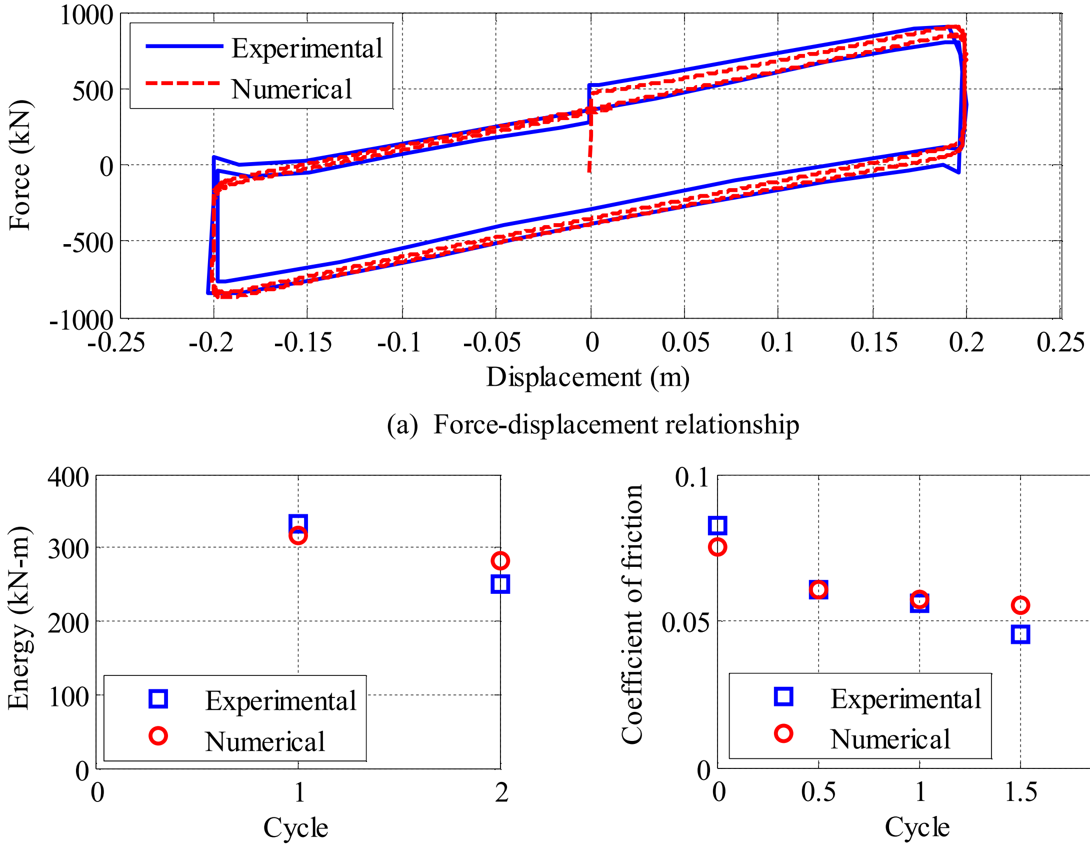

(a) Force-displacement relationship

(b) Energy dissipated

(c) Coefficient of friction

Figure 4-50: Experimentally recorded and numerically simulated force-displacement relationships for experiment number 16 of Table 4-6

CHAPTER 5

ALTERNATE REPRESENTATIONS OF SEISMIC HAZARD FOR SEISMICALLY ISOLATED NUCLEAR STRUCTURES

5.1 Introduction

Two levels of seismic hazard will be considered for the design of seismically isolated nuclear structures: ground motion response spectrum+ (GMRS+) and extended design basis (EDB) GMRS, at the mean annual frequencies of exceedance (MAFE) of 10^{-4} and 10^{-5}, respectively (see Kammerer *et al.* (forthcoming)). Distributions of responses of the seismically isolated nuclear structure are computed for each hazard level, which are then used to determine values of design parameters (e.g., clear distance between the isolated superstructure and the hard stop). These distributions are significantly influenced by the definition of the seismic hazard.

Three basic representations of seismic hazard are investigated in this chapter: uniform hazard response spectrum (UHRS), conditional mean spectrum (CMS), and conditional spectra (CS). The UHRS is the traditional measure of seismic hazard in the nuclear industry. The CMS, which was proposed relatively recently, is based on the UHRS, but has a spectral shape consistent with that of recorded ground motions. The CS account for the variability in the ordinates of CMS at periods other than the conditioning period. Given a representation of the hazard (UHRS, CMS or CS), the spectra in the two orthogonal horizontal directions are the same. A fourth characterization of seismic hazard is also considered, constructed using the UHRS, but recognizing that the amplitude of one horizontal component is different from its perpendicular component: UHRS-MaxMin (e.g., Huang *et al.* (2009)). The uncertainties included in these four hazard descriptions are discussed in Section 5.2.

The four representations of seismic hazard are compared in terms of distributions of spectral displacement and the peak displacement response of single FP bearings, as introduced in Section 5.3. Sets of ground motions consistent with the UHRS, UHRS-MaxMin, CMS and CS, with MAFEs of 10^{-4} and 10^{-5}, for the site of the Diablo Canyon Nuclear Generating Station in California are developed in Sections 5.4 and 5.5, respectively. The distributions of displacement demand on Friction Pendulum™ (FP) bearings with different geometrical and material properties, subjected to the ground motions consistent with the four representations of ground motion, are computed and analyzed in Section 5.6. Recommendations for design practice are proposed in Section 5.7

5.2 Uncertainty and Variability in Alternate Representations of Seismic Hazard

5.2.1 Introduction

The uncertainties and variabilities in UHRS, UHRS-MaxMin, CMS and CS are discussed in the following sections.

5.2.2 Uniform hazard response spectrum (UHRS)

The seismic hazard at a site is typically described using a UHRS (see McGuire (2004) for details). The spectral ordinate at each period in the UHRS has the same probability of exceedance (e.g., 2%) in a specified time interval (e.g., 50 years). The probability of exceedance is also described in terms of an annual frequency of exceedance. For example, a probability of exceedance of 2% in 50 years is equivalent to an annual frequency of exceedance of approximately 4×10^{-4}. The UHRS accounts for the aleatory[1] uncertainties in magnitude and

[1] Uncertainties associated with a random process that cannot be reduced by collection of additional data.

location (source characteristics) of a possible earthquake, and in the intensity measure (IM[1]) given the magnitude, location and other source properties. Different models (e.g., ground motion prediction equations[2, 3]) are used to quantify the source characteristics and IMs, because of uncertainties in the understanding of earthquake processes (e.g., type of faults, wave propagation characteristics). Such uncertainties are epistemic, which may be reduced as more data becomes available. These model uncertainties are generally accounted for using logic trees, each branch of which represents a model (e.g., a ground motion prediction equation) that is assigned a weight, based typically on engineering judgment. Finally, and period-by-period, the weighted spectral ordinates are added to construct the UHRS at a user-specified mean annual frequency of exceedance (MAFE).

Uniform hazard response spectra with MAFEs of 10^{-4} and 10^{-5} are considered here for the design of seismically isolated nuclear power plants (see Kammerer *et al.* (forthcoming)). Figure 5-1 shows the UHRS[4] (solid line) for the site of the Diablo Canyon Nuclear Generating Station in Southern California corresponding to the hazard with 2% probability of exceedance in 200 years (an MAFE of 1.01×10^{-4} or a return period of 9,900 years), obtained from http://geohazards.usgs.gov/deaggint/2008/ on June 15, 2014, for the shear wave velocity in the upper 30 m of the soil column of 760 m/s: the boundary between Site Classes B and C per ASCE

[1] Typically spectral acceleration.

[2] The ground motion prediction equation for a spectral acceleration in a horizontal direction (e.g., Campbell and Bozorgnia (2008)) is obtained from regression analysis performed on the geometric mean of the spectral accelerations in two orthogonal horizontal directions. The prediction equation for vertical spectral acceleration is obtained either by regression analysis on measured vertical spectral acceleration or by using ratios of vertical to horizontal spectral acceleration (e.g., Gülerce and Abrahamson (2011)).

[3] The geometric mean of the spectral accelerations in two horizontal directions depends on the orientation of the recording device. The recorded motions in the two directions can be rotated through all possible angles and a median value can be used in the derivation of a ground motion prediction equation (e.g., Boore et al. (2006), Beyer and Bommer (2006)).

[4] The USGS website provides CMS for a user-specified conditioning period. The UHRS ordinate at the conditioning period T^* is equal to the CMS ordinate.

7-10 (ASCE, 2010). Data for an MAFE of 1.00×10^{-4} is not available at the USGS website. Other data from this website are used to develop consistent UHRS and CMS.

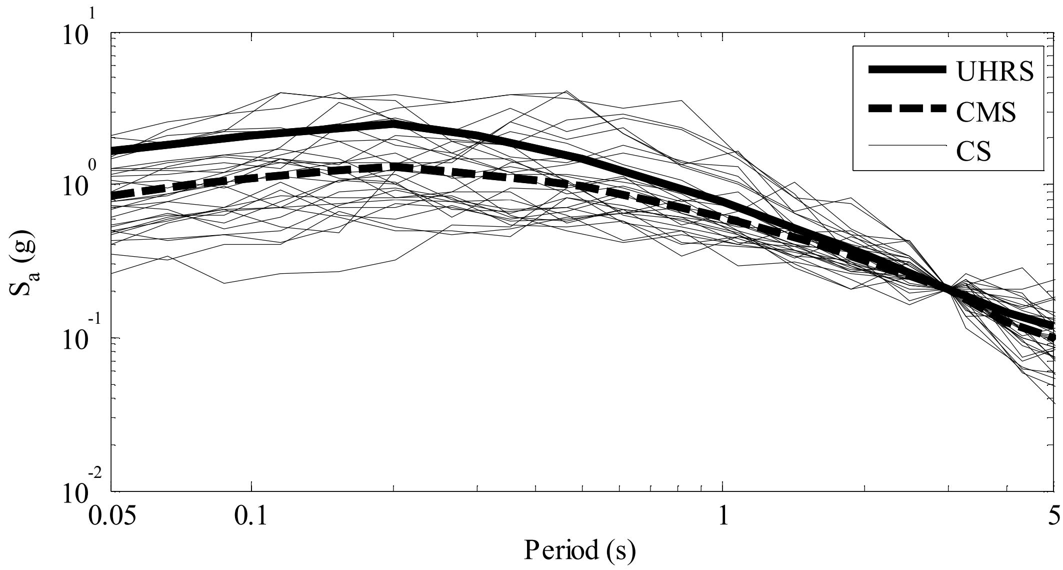

Figure 5-1: Examples of a uniform hazard response spectrum (UHRS), and a conditional mean spectrum (CMS) and conditional spectra (CS) with a conditioning period of 3 s

The hazard corresponding to MAFEs of 1.00×10^{-4} and 1.01×10^{-4} are not significantly different as evident by comparing the spectral acceleration ordinates at Diablo Canyon and seven other sites[1] of nuclear facilities across the United States and four periods (see Table 5-1). The ordinates were obtained using a different USGS application available at http://geohazards.usgs.gov/hazardtool/application.php, accessed on December 30, 2014. The spectral accelerations at these two hazard levels are computed assuming a linear variation in spectral acceleration with MAFE in the logarithmic space. There is a less than 1% difference between the spectral accelerations at these two hazard levels for the eight sites and four periods. Therefore, for the purpose of the discussion that follows, the seismic hazard at a 2% probability

[1] The seismic hazard at these sites is studied in Chapter 6.

of exceedance in 200 years (MAFE of 1.01×10^{-4}, return period of 9,900 years) is considered identical to the seismic hazard at an MAFE of 10^{-4}.

Table 5-1: Ratios of spectral ordinates corresponding to MAFE of 1.00×10^{-4} and 1.01×10^{-4}

Period (s)	Site							
	Diablo Canyon	North Anna	Summer	Vogtle	Oak Ridge	Hanford	Idaho	Los Alamos
0.1	1.003	1.006	1.005	1.005	1.005	1.004	1.004	1.005
0.2	1.003	1.006	1.005	1.004	1.006	1.004	1.003	1.006
1	1.003	1.006	1.004	1.004	1.005	1.004	1.003	1.006
2	1.004	1.005	1.004	1.004	1.005	1.004	1.004	1.006

A UHRS can be disaggregated by magnitude, site-to-source distance, and epsilon, where the latter is the number, positive or negative, of log standard deviations the UHRS ordinate exceeds the median spectral ordinate calculated using a given ground motion prediction equation. Figures 5-2 and 5-3 present the hazard disaggregation of the UHRS of Figure 5-1 at periods of 0.5 s and 3 s, respectively. The (M, r, ε) combinations (modal) at these two periods are (7.0, 6.8 km, 1.2) and (7.4, 5.7 km, 1.0), respectively.

5.2.3 Uniform hazard response spectrum with maximum and minimum components (UHRS-MaxMin)

The response spectra corresponding to the two orthogonal horizontal components of recorded ground motion are consistently different from each other (e.g., Boore *et al.* (2006), Beyer and Bommer (2006)). Ground motions spectrally matched to the UHRS cannot address the difference between orthogonal components. A uniform hazard response spectrum with *maximum* and *minimum* components (UHRS-MaxMin) accounts for the variability in the ratio of spectral accelerations in the two orthogonal horizontal directions, in addition to the uncertainties considered in the development of UHRS. The UHRS-MaxMin response spectra can be derived by amplitude scaling the UHRS, up and down, by a set of factors (e.g., Huang *et al.* (2009)).

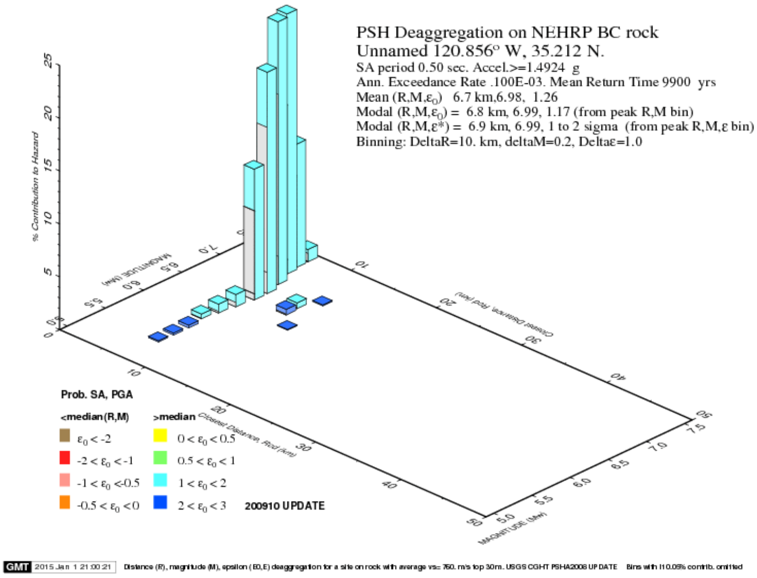

Figure 5-2: Disaggregation of 10,000-year seismic hazard at 0.5 s period for the Diablo Canyon site

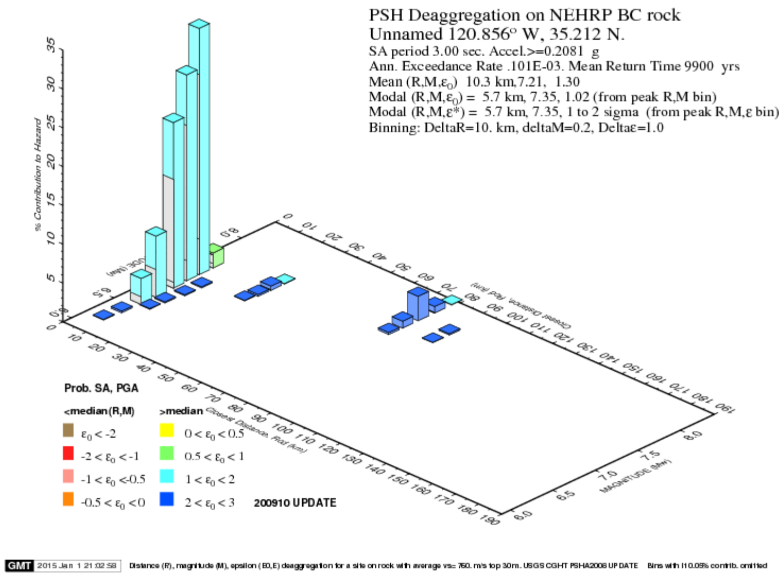

Figure 5-3: Disaggregation of 10,000-year seismic hazard at 3 s period for the Diablo Canyon site

5.2.4 Conditional mean spectrum (CMS)

Baker and Cornell (2006) developed the conditional mean spectrum, also described by some as a scenario spectrum, to better describe the ground motion spectrum associated with a combination of magnitude, distance, and epsilon. The CMS is derived from a UHRS using a conditioning period and correlations between spectral accelerations at different periods, where the correlation coefficients are based on equations derived from recorded ground motion data. The conditioning period is commonly set equal to the first mode translational period (e.g., see NIST (2011)). At this period, the ordinate of the CMS is set equal to that of the UHRS. The choice of conditioning period may not be clear if the structure is irregular or has different first mode translational periods in the two orthogonal horizontal directions (e.g., FEMA (2012)), but that is not an issue with seismically isolated structures. The ordinates of the CMS of Figure 5-1 (dashed line) are similar to those of the UHRS in the vicinity of the conditioning period (3 s), which is an expected outcome for large epsilon motions.

5.2.5 Conditional spectra (CS)

Conditional spectra (CS) address the randomness in the CMS ordinates given the spectral ordinate at the conditioning period (e.g., Jayaram *et al.* (2011), NIST (2011)). Figure 5-1 presents 30 CS with conditioning period of 3 s, representing the seismic hazard at the Diablo Canyon site with an MAFE of 10^{-4}. The spectral ordinates of the UHRS, CMS and CS are equal at 3 s. The mean of the conditional spectral ordinates at a given period is equal to the CMS ordinate at that period.

5.3 Seismic Hazards, Spectral Displacements and Isolator Displacements

The draft NUREG "Technical considerations for seismic isolation of nuclear facilities" (Kammerer *et al.*, forthcoming) requires that the probability of unacceptable performance of a seismically isolated nuclear structure be less than 1% and 10% under seismic hazard represented by GMRS+ and EDB GMRS, respectively. Impact of the isolated structure on the surrounding stop is considered unacceptable performance. Estimates of the 99th and 90th percentile peak isolation-system displacements for the two levels of earthquake shaking, respectively, are needed to determine the minimum clear distance between the isolated structure and the stop. The distributions of the peak displacements are a function of the chosen representation of the GMRS and EDB GMRS. Alternate representations are presented and investigated in the following sections.

Four representations of the seismic hazard are considered. The first three are 1) uniform hazard response spectrum (UHRS), 2) conditional mean spectrum (CMS), and 3) conditional spectra (CS). Traditional practice in the nuclear industry (ASCE, 2005) defines seismic input using a UHRS. Each of the three spectra is a geometric mean spectrum: a composite of the ordinates along two orthogonal horizontal axes, which are assumed to be identical. A fourth representation of ground shaking is considered, also based on the UHRS, for which the ordinates of the spectra along one horizontal axis are consistently different from those on the perpendicular axis: the Max-Min spectra developed by Huang et al. (2009) that were used to underpin the isolation provisions in Section 7.7 of the forthcoming edition of ASCE Standard 4.

The following sections investigate the 10,000-year and 100,000-year UHRS, UHRS-MaxMin, CMS and CS for the site of the Diablo Canyon Nuclear Generating Station. Distributions of spectral displacements for the four representations are compared for the two return periods. Ground motions consistent with these response spectra are developed. Distributions of peak displacement response of single FP bearings with a range of geometrical and material properties subjected to the ground motions consistent with different representations of seismic hazard are studied.

5.4 10,000-year Spectra, Ground Motions, Spectral Displacements and Isolator Displacements

5.4.1 UHRS, UHRS-MaxMin, CMS and CS

Figure 5-1 presents the 5% damped UHRS, and CMS and CS with a conditioning period of 3 s for the site of the Diablo Canyon Nuclear Generating Station (latitude = 35.21162 N, longitude = 120.85562 W) at a 2% probability of exceedance in 200 years (return period = 9900 years, MAFE = 1.01×10^{-4})[1] assuming an average shear wave velocity in the upper 30 m of the soil column of 760 m/s. Conditional mean spectra are obtained from the USGS website http://geohazards.usgs.gov/deaggint/2008/, accessed on June 15, 2014, using the GMPE of Campbell and Bozorgnia (2008). A consistent UHRS is obtained from CMS with different conditioning periods, noting that the UHRS ordinate at a period T^* is equal to the CMS ordinate at T^*, where T^* is the conditioning period. Conditional spectra are calculated using software available at http://web.stanford.edu/~bakerjw/gm_selection.html, accessed on June 15, 2014. This software uses the Campbell and Bozorgnia (2008) GMPE[2] to generate a set of CS. The (M, r, ε) triple at a period of 3 seconds is (6.71, 5.5 km, 1.92), using the Campbell and Bozorgnia

[1] The spectral accelerations with 2% exceedance probability in 200 years (MAFE of 1.01×10^{-4}) are assumed to be identical to those corresponding to an MAFE of 1.00×10^{-4} (see Section 5.2.2).
[2] The only GMPE coded into the software.

(2008) GMPE. The CMS from the USGS website and the covariance matrix obtained using the software of the Baker Research Group are used to generate the 30 conditional spectra of Figure 5-1.

A set of 30 ground motions is spectrally matched to the UHRS using RSPMatch (Hancock *et al.*, 2006). The horizontal components of the UHRS-scaled ground motions are then amplitude scaled by a set of factors (e.g., f_1 for the GM1 component in the X direction and $1/f_1$ for the GM1 component in the Y direction) to recognize that the response spectrum of one horizontal component of the recorded ground motion is different from that in the orthogonal horizontal direction. The derivation of the factors are described in Huang *et al.* (2009) and the factors are listed in Table 5-2. These ground motions are designated as either "UHRS-MaxMin-scaled" or "MaxMin-scaled", and the corresponding response spectra are designated as either "UHRS-MaxMin" or "MaxMin".

Ten thousand year return period UHRS, and CMS and 30 CS corresponding to conditioning periods of 2, 3 and 4 seconds are generated for the Diablo Canyon site. Figure 5-4(a) presents 5% damped UHRS, and CMS and CS in the horizontal direction corresponding to a conditioning period, T^*, of 2 s for the Diablo Canyon site and an MAFE of 10^{-4} (or return period of 10,000 years). Figures 5-4(b) and 5-4(c) present similar information for T^* of 3 s and 4 s, respectively. Response spectra in the vertical direction are generated using vertical-to-horizontal (V-H) ratios (Gülerce and Abrahamson, 2011) and a (magnitude, distance) pair of (7, 5 km). Figure 5-5 presents the V-H ratios for a rock site and the source-to-site distance of 5 km. Figure 5-5(a) presents the ratios from Gülerce and Abrahamson (2011) for a range of magnitudes. Figure 5-5(b) presents the ratios used in this study to obtain vertical UHRS, CMS and CS.

Table 5-2: List of factors used to amplitude scale the ground motions spectrally matched to the UHRS

GM	Direction		GM	Direction	
	X	Y		X	Y
1	1.21	0.83	16	1.49	0.67
2	1.26	0.79	17	1.24	0.81
3	1.09	0.92	18	1.40	0.71
4	1.17	0.85	19	1.56	0.64
5	1.71	0.58	20	1.61	0.62
6	1.32	0.76	21	1.44	0.69
7	1.42	0.70	22	1.28	0.78
8	1.25	0.80	23	1.38	0.72
9	1.22	0.82	24	1.31	0.76
10	1.52	0.66	25	1.46	0.68
11	0.99	1.01	26	1.05	0.95
12	1.11	0.90	27	1.37	0.73
13	1.34	0.75	28	1.35	0.74
14	1.14	0.88	29	1.29	0.78
15	1.19	0.84	30	1.16	0.86

5.4.2 Ground motions spectrally matched to UHRS

The set of 30 ground motions listed in Table E-1 are scaled to match the UHRS of Figure 5-4 in the period range of 0.5 s to 4 s, where the choice of period range is based on the following analysis.

The lateral force-displacement relationship for an FP bearing with a Coulomb-type coefficient of friction under constant axial load can be described by a bilinear relationship. The natural period before sliding, T_1, is given by:

$$T_1 = 2\pi\sqrt{\frac{u_y}{\mu g}} \tag{5-1}$$

where u_y is the lateral displacement at which sliding begins and μ is the coefficient of friction.

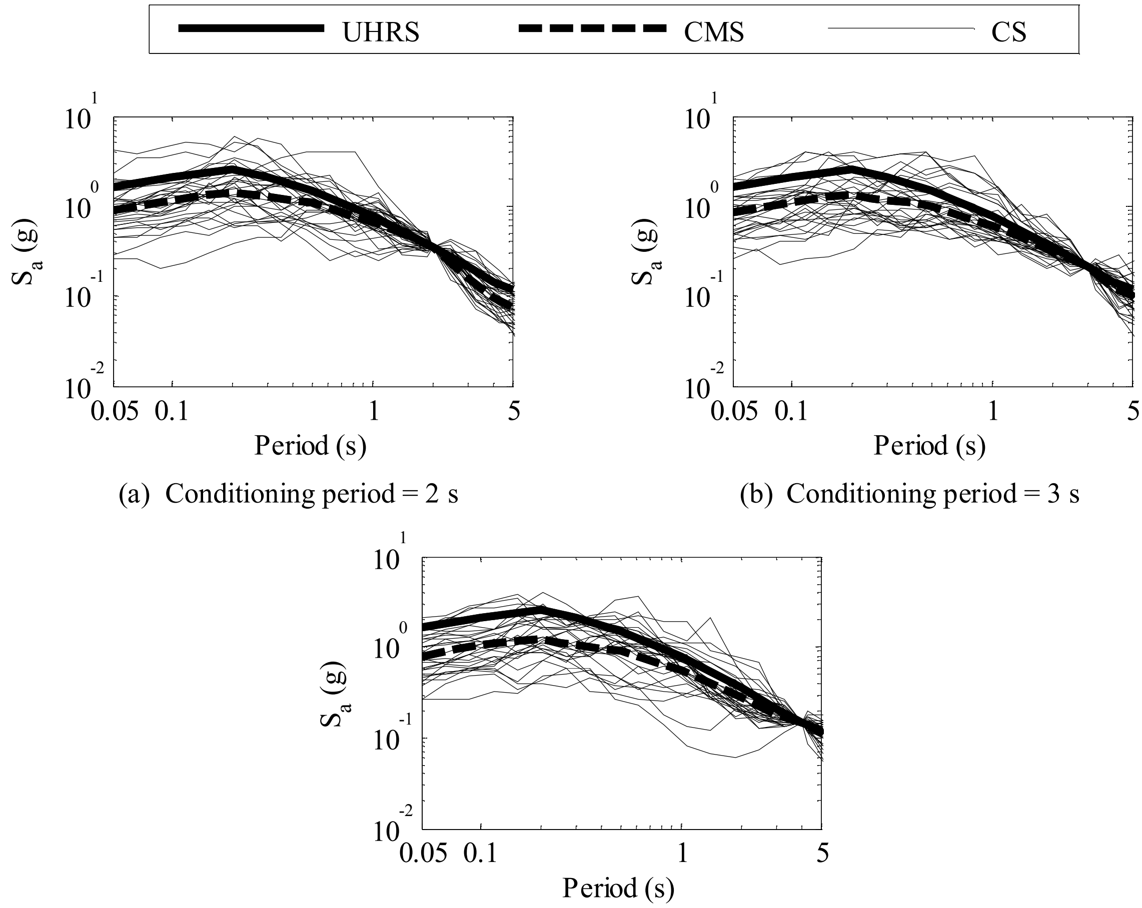

(a) Conditioning period = 2 s

(b) Conditioning period = 3 s

(c) Conditioning period = 4 s

Figure 5-4: Target uniform hazard spectrum (UHRS), and conditional mean spectrum (CMS) and conditional spectra (CS) with conditioning periods of 2 s, 3 s and 4 s for the Diablo Canyon site corresponding to a return period of 10,000 years

The yield displacement u_y can be taken as 0.001 m and a representative coefficient of friction is 0.06 (0.1). The corresponding T_1 is 0.25 s (0.2 s), suggesting initially that the lower bound on the range should be 0.25 s. The sliding periods of the FP bearings considered in this study are no greater than 4 s, with effective periods, based on secant stiffness, of much less than 4 s if the displacement is small. The period range[1] for spectral matching of 0.5 s to 4 s (and not 0.2 s to

[1] Spectrally matching a ground motion component to a randomly generated conditional spectrum (discussed later) can be computationally expensive if the period range is broad. Accordingly, the seed ground motions are spectrally matched over a period range that will significantly influence peak isolation-system displacement, namely, 0.5 s to 4 s.

4 s) is a compromise associated with the significant computational expense of decreasing the lower bound on the range from 0.5 s to 0.2 s. The influence of the value of yield displacement on peak displacement is examined later in this chapter.

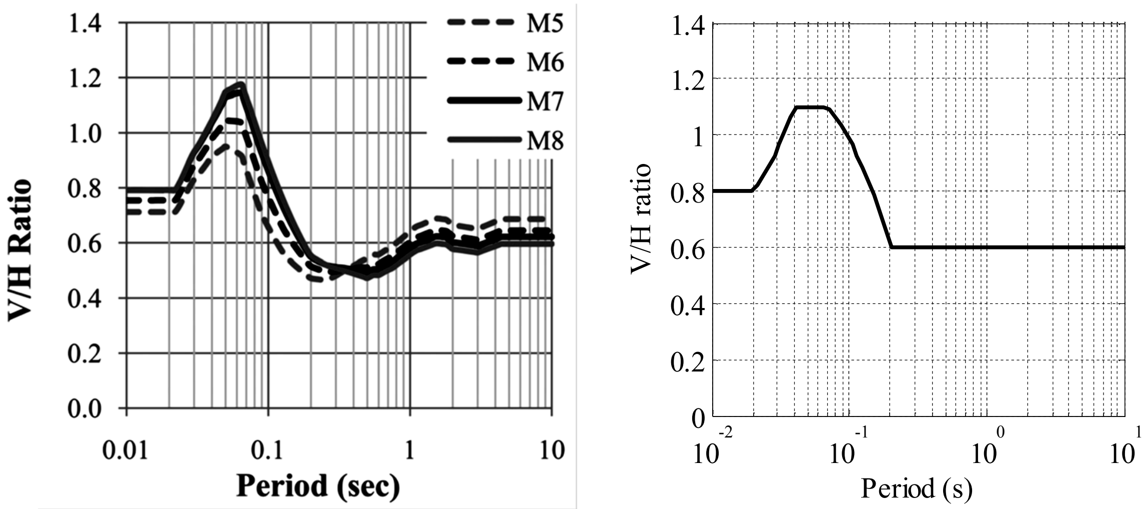

(a) Gülerce and Abrahamson (2011) (b) Assumed V/H ratio

Figure 5-5: Median ratio of vertical to horizontal spectral response on a rock site with a source-to-site distance of 5 km

For the UHRS, the target spectra in the two orthogonal horizontal directions are identical. The (horizontal) UHRS of Figure 5-4 is multiplied by the V-H ratios of Figure 5-5(b) to obtain the target spectrum in the vertical direction. Figure 5-6(a) presents the response spectra of the 30 seed ground motions of Table E-1 spectrally matched to the UHRS in X direction. The UHRS is plotted in the panel. Figures 5-6(b) and 5-6(c) present identical information in the Y and Z directions, respectively. The spectra of the matched motions are virtually identical to the target spectra.

5.4.3 Ground motions consistent with UHRS-MaxMin

The response spectra of the scaled ground motions of Section 5.4.2 are identical in the two horizontal directions. The ground motions consistent with UHRS-MaxMin spectra are developed by amplitude scaling, up or down, the two horizontal components of the spectrally matched ground motions of Section 5.4.2. The scaling factors are listed in Table 5-2. The vertical component of UHRS-MaxMin-scaled motions is identical to that for the UHRS-scaled motions. Figure 5-7 presents the response spectra of the ground motions consistent with UHRS-MaxMin.

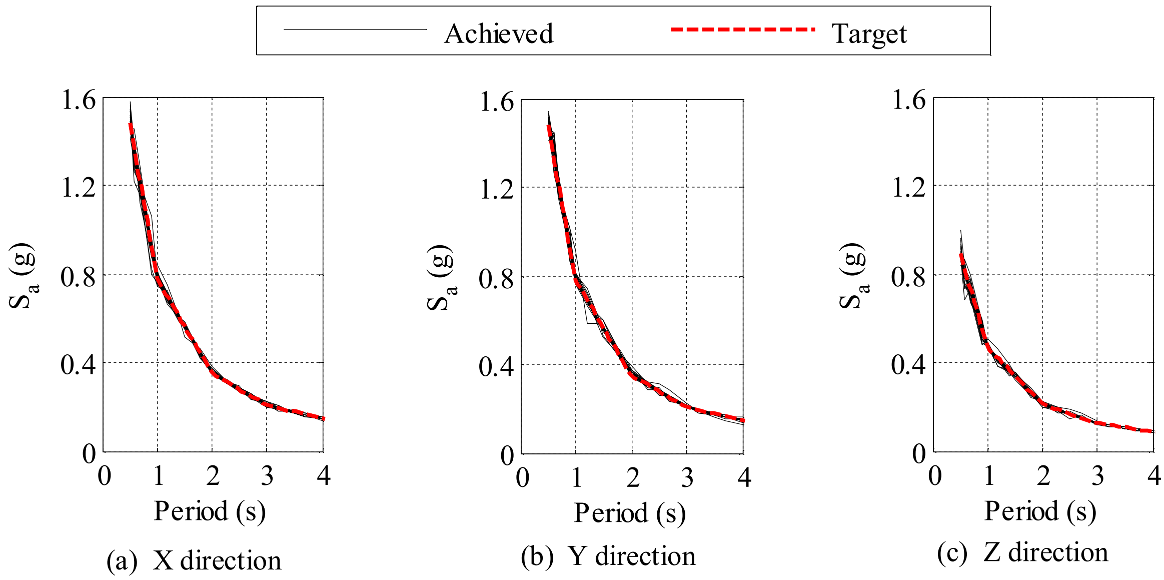

Figure 5-6: Response spectra of 30 seed ground motions spectrally matched to the 10,000 year uniform hazard spectra for the Diablo Canyon site

5.4.4 Ground motions spectrally matched to CMS

Conditional mean spectra with conditioning periods of 2 s, 3 s and 4 s are used to represent 10,000-year seismic hazard at the Diablo Canyon site. The three CMS are plotted in Figure 5-4. The 30 seed motions of Table E-2 are spectrally matched to the three CMS, in the vertical and two horizontal directions, in the period range of 0.5 s to 4 s. The CMS in the vertical direction are obtained by multiplying the (horizontal) CMS of Figure 5-4 by the V/H of Figure 5-5(b). Figures 5-8(a), 5-8(b) and 5-8(c) present the target conditional mean spectrum with a conditioning period of 2 s and the response spectra of the 30 spectrally matched motions in the X, Y and Z directions, respectively. The other panels in the figure present identical information for conditioning periods of 3 s and 4 s. The spectra of the matched motions are virtually identical to the target spectra.

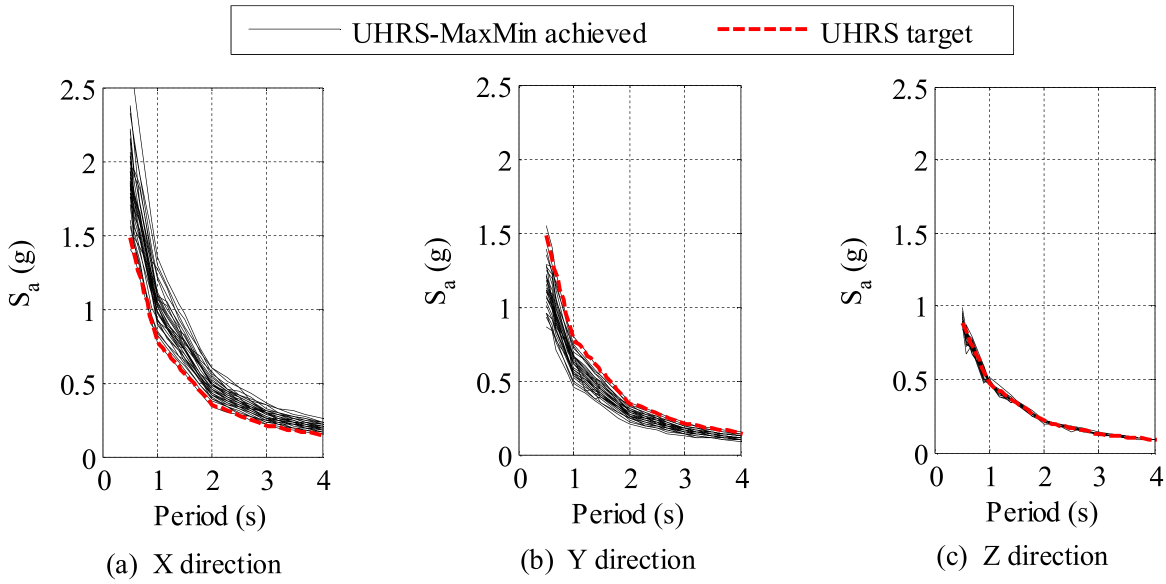

Figure 5-7: Response spectra of 30 ground motions consistent with the 10,000-year UHRS-MaxMin for the Diablo Canyon site

5.4.5 Ground motions spectrally matched to CS

A set of 30 conditional spectra is generated for each of the three conditioning periods: 2 s, 3 s and 4 s (see Figure 5-4): CS Set 1, CS Set 2 and CS Set 3. Three sets of 30 seed ground motions are used: GM Set 1, GM Set 2 and GM Set 3. Details on the seed motions are presented in Appendix E. The 30 ground motion records of GM Set 1 are matched to the 30 conditional spectra of CS Set 1 (each record scaled to one conditional spectrum). Similarly, the ground motions of GM Set 2 and GM Set 3 are matched to the spectra of CS Set 1. The three sets of seed ground motions are also matched to the other two sets of conditional spectra, CS Set 2 and CS Set 3. The end product of this exercise is three sets of ground motions matched to each of the three sets of conditional spectra.

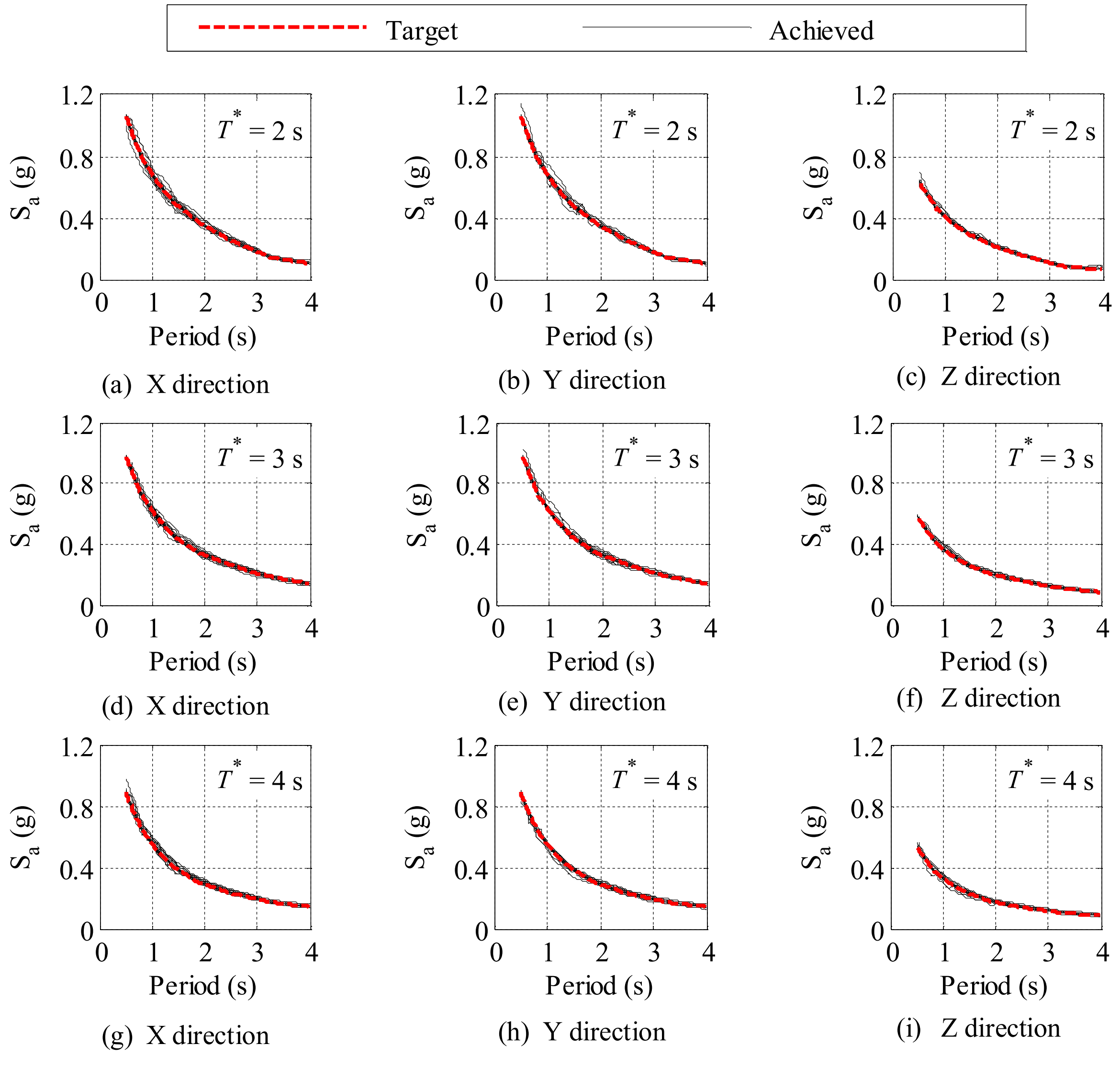

Figure 5-8: Response spectra of 30 seed ground motions spectrally matched to the 10,000-year conditional mean spectra for the Diablo Canyon site

Figure 5-9(a) presents the 12^{th} of the 30 conditional spectra in the horizontal direction corresponding to $T^* = 2$ s (Figure 5-4(a)) and a return period of 10,000 years. The 5% damped response spectra of a horizontal component (say X) of the 12^{th} ground motion record from

GM Set 1 (NGA number 3269), GM Set 2 (NGA Number 1488) and GM Set 3 (NGA Number 2897) spectrally matched to the 12th conditional spectrum are also plotted in the figure. The ground motions are listed in Tables E-3, E-4 and E-5, respectively. Figures 5-9(b) and 5-9(c) present identical information in the Y (horizontal) and Z (vertical) directions, respectively. Figures 5-9(d), 5-9(e) and 5-9(f) present information for T^* = 3 s (Figure 5-4(b)), in the X, Y and Z directions, respectively. Figures 5-9(g), 5-9(h) and 5-9(i) present data for a conditioning period of 4 s. The target and computed spectra compare well in each of the nine panels.

Figure 5-10(a) presents the percentage difference between the 30 target spectra of Figure 5-4(a) and the 30 spectrally matched ground motions using GM Set 1 (Table E-3). Results are presented for the two horizontal and vertical directions, and five natural periods: 0.5 s, 1 s, 2 s, 3 s and 4 s. Figure 5-10(d) and 5-10(g) present information for conditioning periods of 3 s and 4s. The remaining panels in Figure 5-10 present identical information for the other GM sets and all three conditioning periods.

There are 15 curves plotted in Figure 5-10(a) (3 directions × 5 natural periods). The percentage difference averaged across all the 30 ground motions is less than 0.6% for periods less than 3 s in the two horizontal and vertical directions. The maximum absolute difference ranges between 2% and 9% for periods less than 3 s. The averaged percentage error is less than 4.5% for a period of 4 s; the maximum absolute difference is 30%. The spectral ordinates are often very small (e.g., 0.03 g) at 4 s (see Figure 5-4) and a difference of even 0.01 g between the target and computed spectra results in a high percentage difference. Figure 5-10 presents the percentage differences for all the 810 combinations (3 conditioning periods × 3 GM Sets × 30 ground motions × 3 directions). Across all combinations, the maximum absolute difference between the target and computed spectra is less than 15% for periods less than 3 s and less than 35% for the 4 s period.

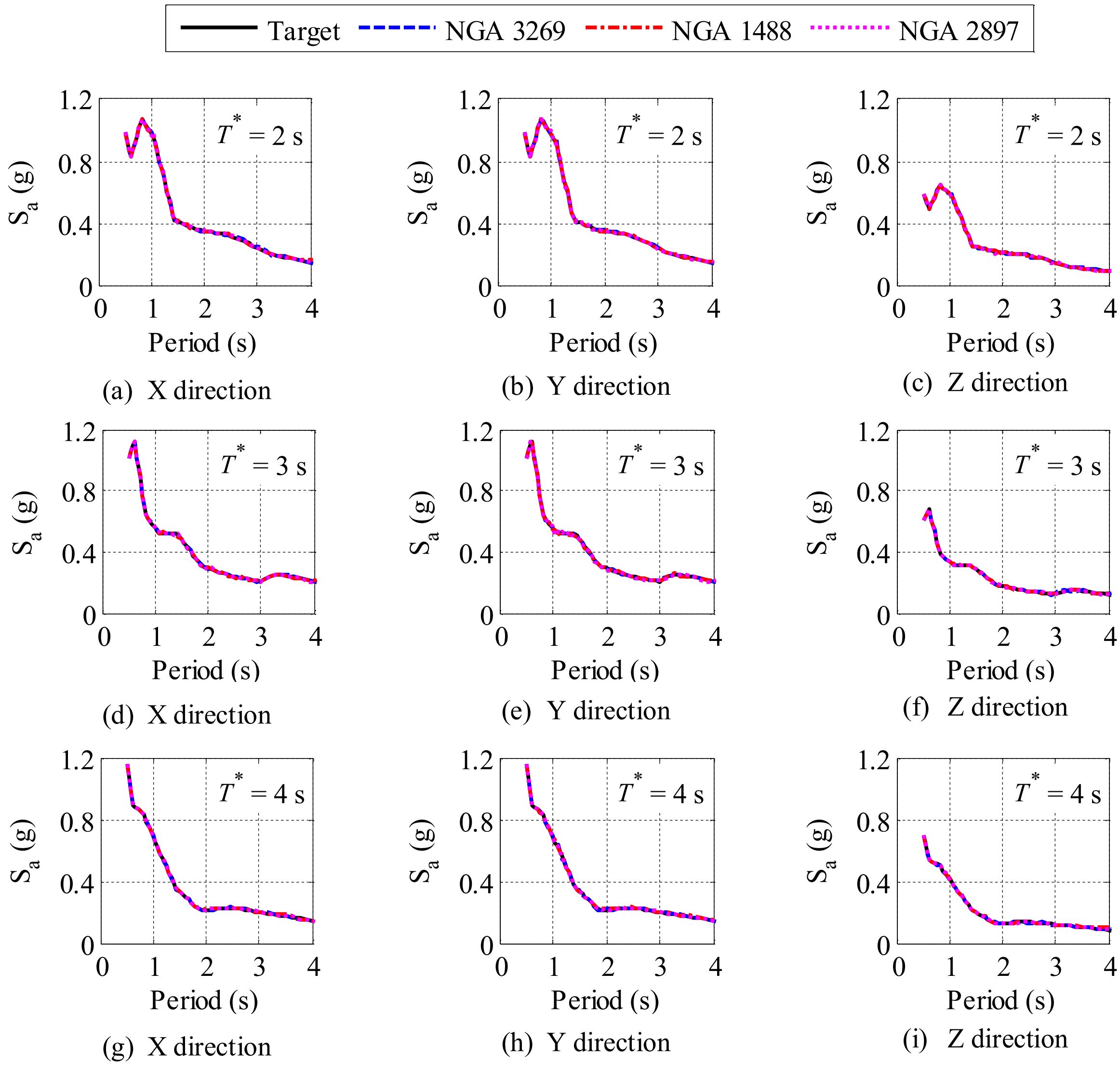

Figure 5-9: Target conditional spectrum number 12 and response spectra of ground motion record number 12 from the three sets (NGA numbers 3269, 1488 and 2897 from GM Sets 1, 2 and 3, respectively, of Appendix E) spectrally matched to the corresponding target conditional spectrum

Figure 5-11(a) presents the mean of the 30 target conditional spectra for the conditioning period of 2 s (Figure 5-4(a)) and the mean of the computed spectra of the X component of the 30 ground motions for each of the three spectrally matched GM Sets (Tables E-3, E-4 and E-5). Figure 5-11(b) presents the standard deviation in the target and computed spectra, noting that the value is zero at the conditioning period of 2 s. The remaining panels in the figure present the corresponding information for conditioning periods of 3 s and 4 s. The mean and standard deviation of the spectral ordinates of the scaled motions compare very well with the target values.

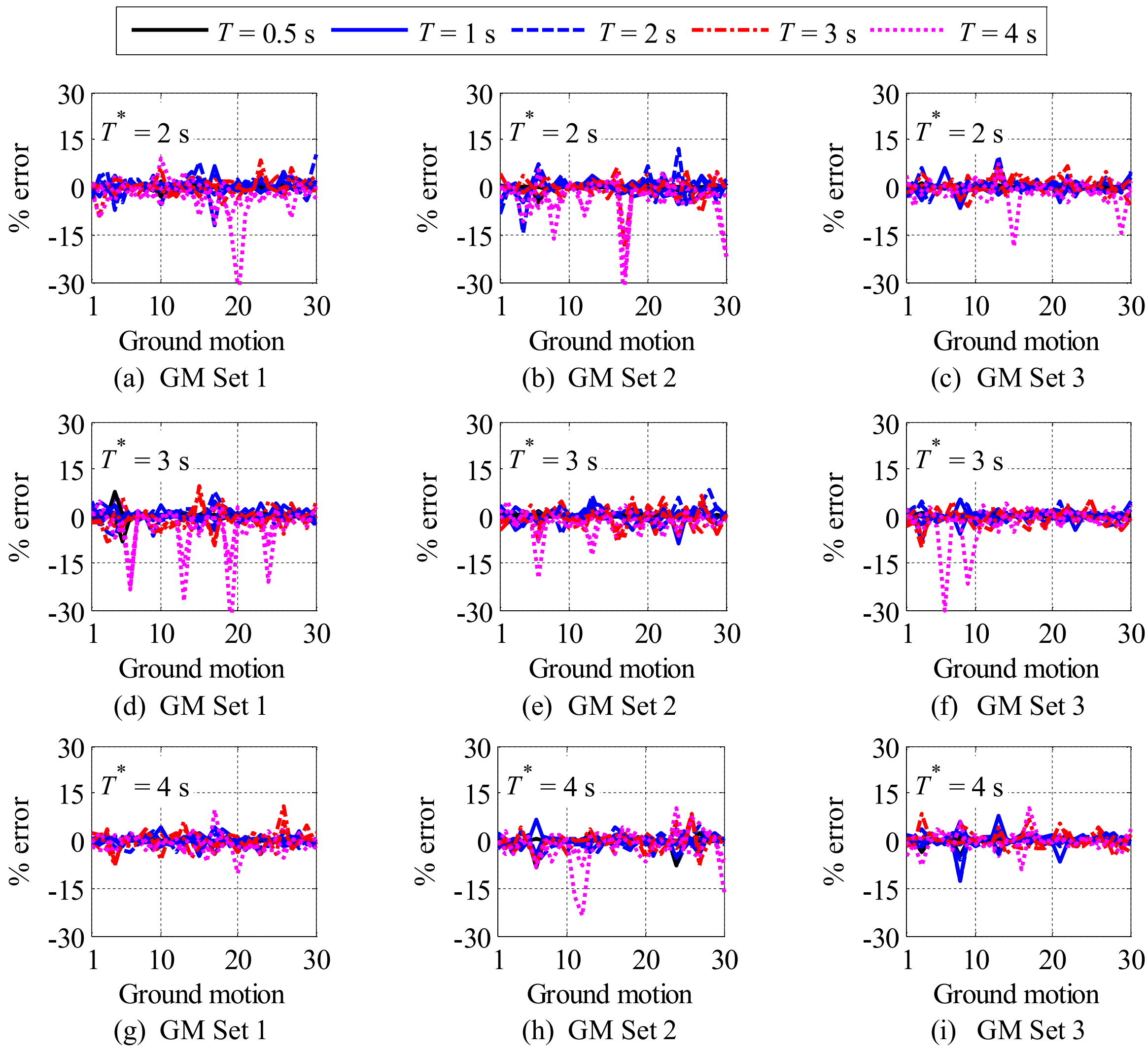

Figure 5-10: Percentage difference between the target and computed 5%-damped acceleration response spectra for three conditioning periods, three sets of 30 ground motions, two horizontal and one vertical directions, and five values of natural period

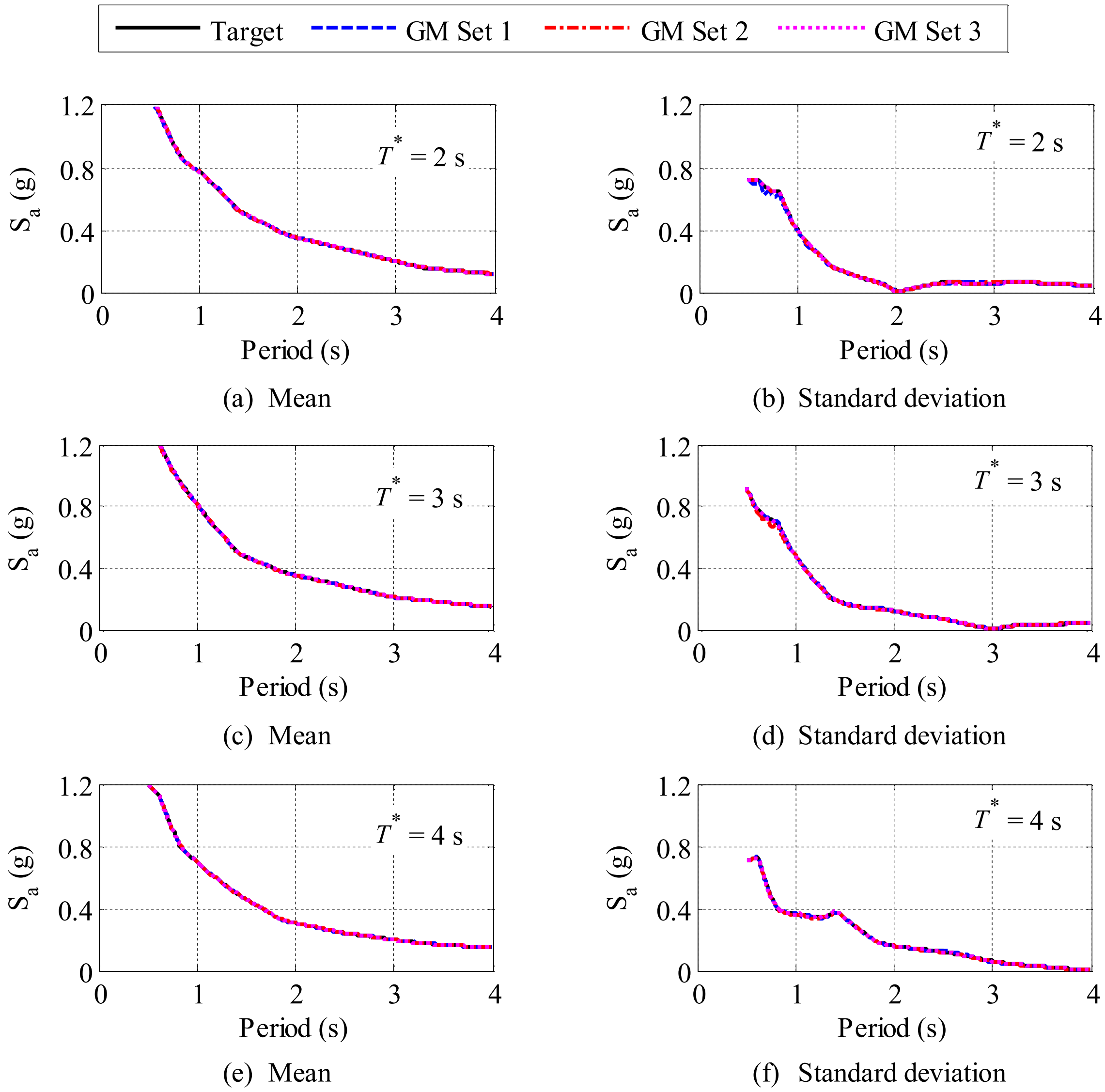

Figure 5-11: Mean and standard deviation of target conditional spectra and spectra of spectrally matched motions in the X direction

5.4.6 Spectral displacements

The four preceding subsections present sets of 10,000-year ground motions spectrally matched to the UHRS (1), UHRS-MaxMin (1), CMS with three conditioning periods (3), and CS with three conditioning periods (9). All 14 sets of 30 spectrally matched ground motions could represent the 10,000-year return period seismic hazard at Diablo Canyon.

Figure 5-12 (Figure 5-13) presents the distributions of spectral displacement of the 14 sets of 30 ground motions at different periods in the X (Y) direction. The Max (Min) component of the MaxMin set is aligned in the horizontal X (Y) direction (see Table 5-2). The spectral displacements for a set of scaled ground motions are assumed to distribute lognormally at a given period.

Figure 5-12(a) presents the distributions of spectral displacement in the X direction at a period of 1.5 s for the ground motions spectrally matched to the 1) UHRS, 2) UHRS-MaxMin, 3) CMS with T^* = 2 s, and 4) CS with T^* = 2 s. The UHRS- (CMS-) scaled ground motions produce a median spectral displacement of 0.31 m (0.27 m) and differ from the corresponding 99th percentile spectral displacement by only 0.02 m (0.02 m). The UHRS-MaxMin-scaled ground motions produce a median (99th percentile) spectral displacement of 0.41 m (0.55 m). The spectral displacements of the three sets of 30 CS-scaled ground motions distribute in similar manner to one another since the ground motions are scaled to the same set of CS. The median (99th percentile) spectral displacements for each of the three sets of CS scaled ground motions is 0.26 m (0.49 m).

Figure 5-12(b) presents the distributions of spectral displacement at a period of 2 s with T^* = 2 s. There is little difference in the distribution of the spectral displacements for the UHRS-, CMS- and CS-scaled ground motions, which is an expected result given the scaling procedures employed. A similar observation is made for Figures 5-12(g) and 5-12(l), distributions of spectral displacement at periods of 3 s and 4 s, respectively, and T is equal to T^*. The distributions of spectral displacements corresponding to the UHRS-MaxMin scaled motions in these three panels are similar to that in Figure 5-12(a).

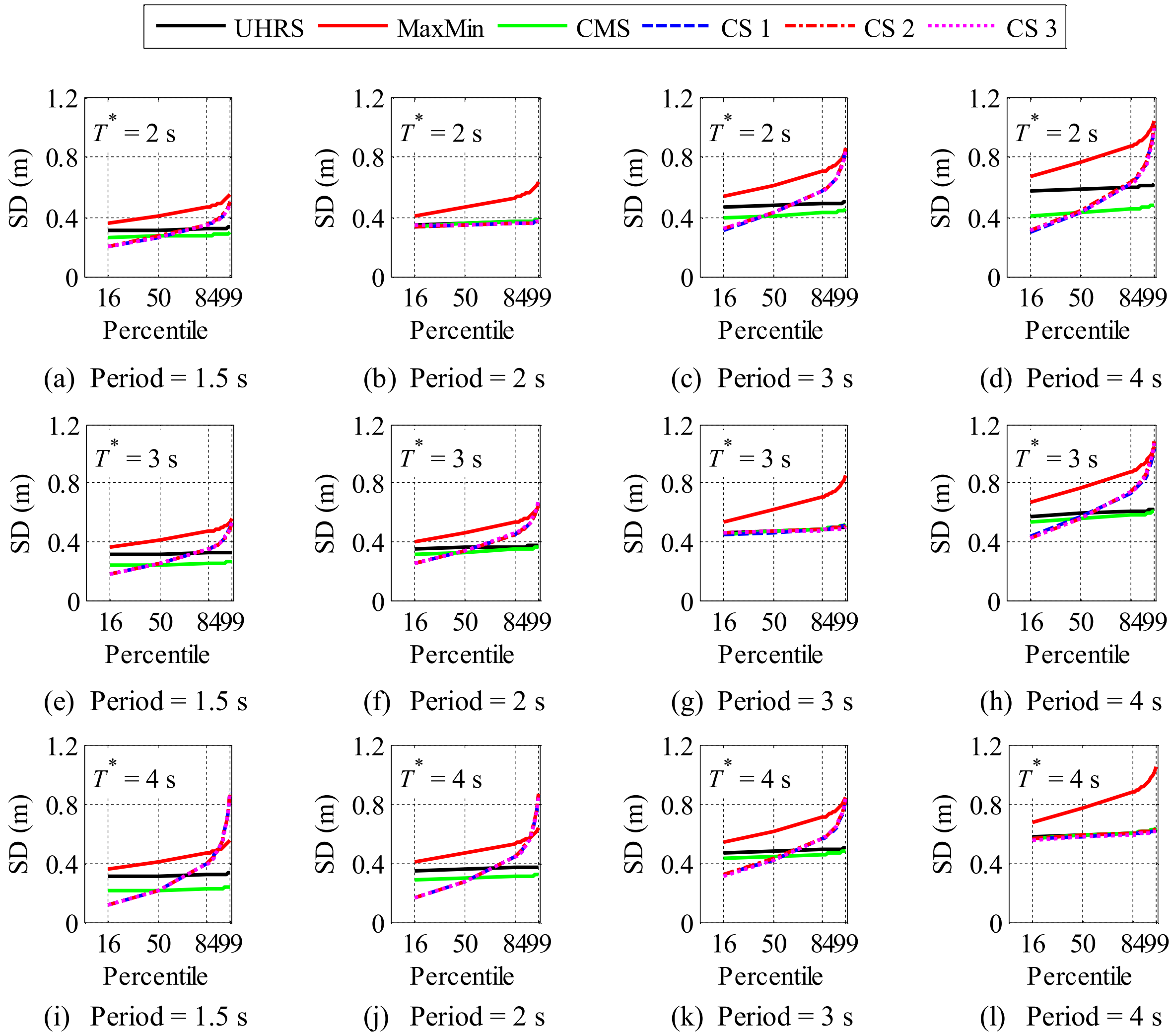

Figure 5-12: Distributions of spectral displacement (SD) for the UHRS-, UHRS-MaxMin-, CMS-, and CS-scaled ground motions in the X direction at periods of 1.5 s, 2 s, 3 s and 4 s, and conditioning periods, T^*, of 2 s, 3 s, and 4 s for the CMS and CS

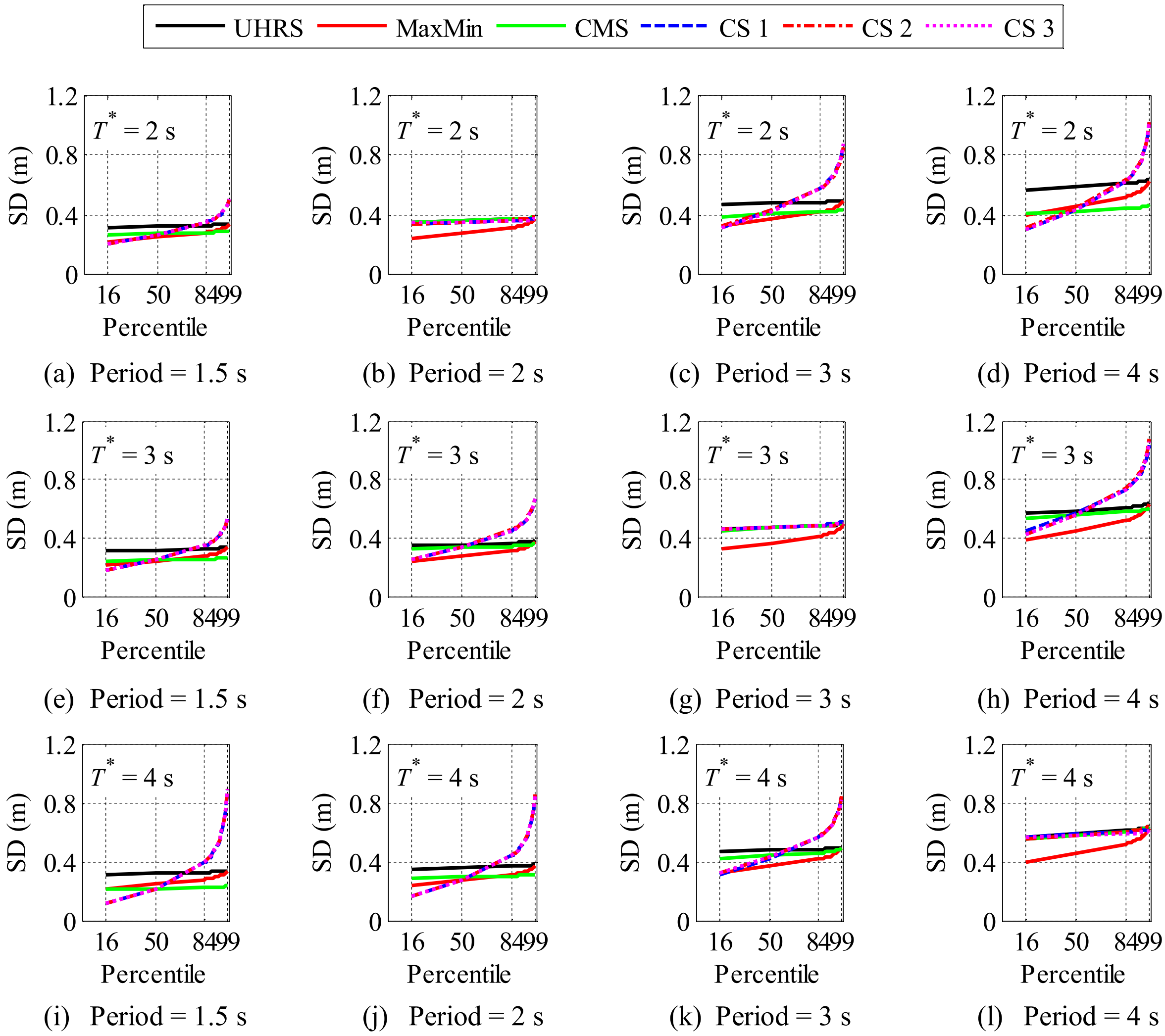

Figure 5-13: Distributions of spectral displacement (SD) for the UHRS-, UHRS-MaxMin-, CMS-, and CS-scaled ground motions in the Y direction at periods of 1.5 s, 2 s, 3 s and 4 s, and conditioning periods, T^*, of 2 s, 3 s, and 4 s for the CMS and CS

For those cases where $T \neq T^*$ (panels other than (b), (g) and (l)), the trends are similar to Figure 5-12(a), namely, 1) the spectral displacements of the UHRS-scaled motions are greater than those of the CMS-scaled motions, 2) the distributions of spectral displacement of the three sets of CS-scaled motions are similar, 3) the spectral displacements of the UHRS-scaled ground motions exceed those of the CS-scaled ground motions until approximately the 65th percentile, 4) the 84+th spectral displacements of the CS-scaled motions are significantly greater than those of the

UHRS- and CMS-scaled motions, and 5) the spectral displacements for the ground motions consistent with UHRS-MaxMin exceed those for the other three spectra at percentiles below 90 and ordinates for the CS-scaled motions exceed those for UHRS-MaxMin-scaled motions at percentiles greater than 90 in some cases.

The distributions of spectral displacement reported in Figure 5-13 (Y direction) are identical to those in Figure 5-12 (X direction), except for the UHRS-MaxMin-scaled ground motions because they were amplitude scaled with reciprocal (and smaller in almost all cases) factors (see Table 5-2).

All 14 sets of ground motions (consistent with UHRS, UHRS-MaxMin, CMS or CS) considered in this section reasonably represent the 10,000-year earthquake hazard at the Diablo Canyon site. There are significant differences in the spectral displacements at a given period for the 14 sets of ground motions. The subsequent section examines the influence of hazard representation on the displacement response of simple isolation systems with FP bearings.

5.4.7 Response of FP bearings

The distributions of peak displacement of FP bearings with a range of geometrical properties, subjected to the sets of 10,000-year return period ground motions introduced previously, are presented and compared in this section.

The seed ground motions of Appendix E are scaled over a period range of 0.5 s to 4 s (see Sections 5.4.2 through 5.4.5). Consequently, there is limited *control* on the peak ground acceleration (PGA) of the scaled ground motions in the three orthogonal directions. If the ground motions had been scaled in the period range that included much short periods (e.g., 0.01 s), the vertical PGA of the UHRS-scaled motions would have been the product of the horizontal PGA (= 0.95 g) and V-H ratio at a short period (= 0.8, Figure 5-5(b)), namely, about 0.8 g. However, the PGA of the UHRS-scaled motions in the vertical direction ranged between 0.3 g to 2.9 g. Loss of contact between the slider and the sliding surface (uplift) takes place when the vertical ground acceleration exceeds 1 g because the superstructure is assumed rigid in the vertical direction. The lateral stiffness of the FP bearings is zero when the supported weight is zero (i.e., uplift). The calculation of the peak displacement of an FP bearing may be incorrect if two conditions are met, namely, 1) the vertical ground motions are not scaled appropriately in the short period range, and 2) the vertical PGA of the ground motion is much larger than the greater of the target vertical PGA and 1.0 g.

To understand the importance of the vertical component of the ground motion on peak horizontal displacement response, an FP bearing with a sliding period of 3 s, a Coulomb-type coefficient of friction of 0.1 and a static axial pressure of 50 MPa is analyzed[1]. The vertical PGA for 23 of the 30 ground motions spectrally matched to the UHRS is less than 1.0 g. Two sets of response-history analyses are performed for these 23 motions: 1) considering the vertical component, and 2) ignoring the vertical component. Mass proportional damping of 2% is assigned to the system with the proportionality coefficient computed using the sliding period of the bearing. The distributions of peak horizontal displacement for the two cases are presented in Figure 5-14. The displacement responses are assumed to distribute lognormally. The distributions match closely. The peak horizontal displacement is not considerably affected by the vertical component of ground motion, provided there is no loss of contact at the sliding surface, as observed in

[1] Single FP bearings with these properties are also studied in the latter sections of the chapter. The choice of properties is considerably limited by the excessive displacement demand on the bearings subjected to the ground motions representing 100,000-year seismic hazard.

experiments by Mosqueda *et al.* (2004). The vertical component of ground motion is thus ignored for the response-history analyses performed in the remainder of this chapter.

The spectral matching exercise was performed over a period range of 0.5 s to 4 s, because increasing the lower bound from 0.2 s to 0.5 s (corresponding to u_y equal to 0.006 m and a coefficient of friction of 0.1) would not significantly affect peak displacement responses in the isolation systems. Figure 5-15 presents the distribution of peak horizontal displacement responses of the FP bearing of Figure 5-14 subjected to the 23 ground motions, including vertical components, with u_y set equal to 0.001 m and 0.006 m. The differences in the peak displacements are tiny and support the decision to set the lower bound on the period for spectral matching to 0.5 s.

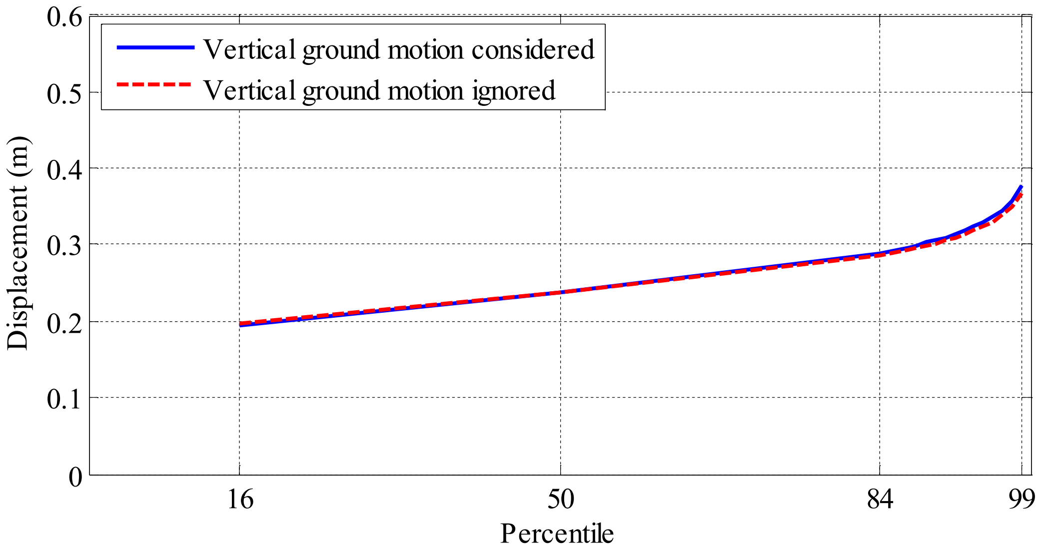

Figure 5-14: Distributions of peak horizontal displacement of an FP bearing subjected to 23 ground motions

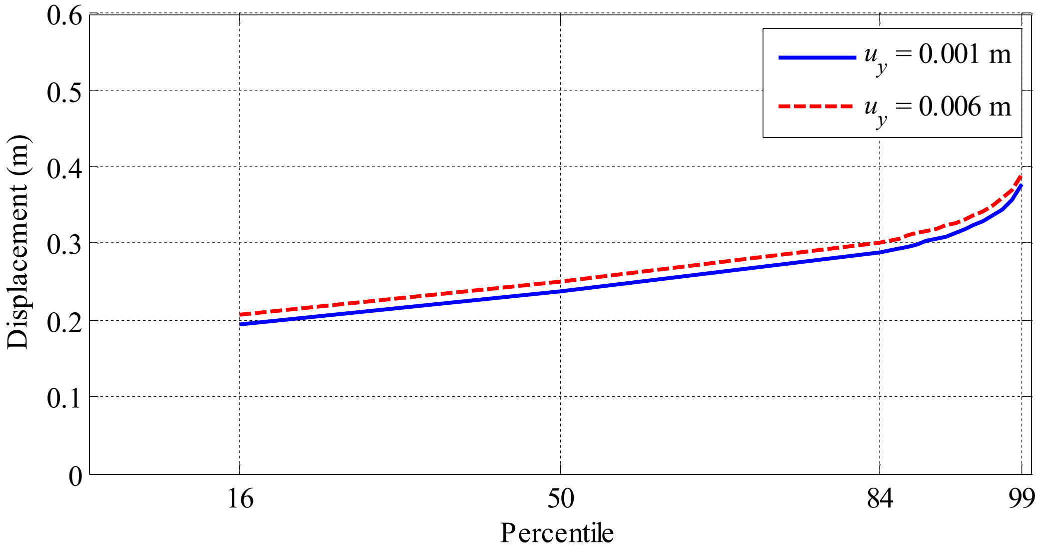

Figure 5-15: Distribution of displacement demand for 23 ground motions with yield displacement set equal to 0.001 m and 0.006 m

A series of analyses are performed to study the response of isolated structures subjected to the ground motions consistent with the four alternate representations of seismic hazard (see Sections 5.4.2 through 5.4.5). Friction Pendulum bearings with sliding periods, T_{sliding}, of 3 s and 4 s, with a Coulomb-type coefficient of friction of 0.1[1, 2], and static axial pressure of 50 MPa are subjected to 1) a set of 30 ground motions spectrally matched to the UHRS, 2) the 30 UHRS-scaled motions amplitude scaled to be consistent with UHRS-MaxMin, 3) a set of 30 seed ground motions spectrally matched to the CMS of Figure 5-4 with the conditioning periods, T^*, of 2 s, 3 s and 4 s, and 4) three sets of 30 ground motions spectrally matched to the three sets of CS of Figure 5-4. Mass proportional damping of 2% is assigned to the system, with the proportionality coefficient based on the sliding period of the bearing. The peak horizontal displacements are

[1] The ground motions considered in this section and in the following section impose significant displacement demand on the FP bearings, which dictates the choice of properties of FP bearings: sliding period of 3 s and 4 s, and coefficient of friction of 0.1.

[2] The 3 s (4 s) FP isolator has a radius of curvature, R, of 2.3 m (4 m). For the coefficient of friction of 0.1, the effective period of the isolator is 1.7 s (2.3 s), 2.1 s (2.8 s) and 2.5 s (3.3 s), respectively, at the displacement of 0.05R, 0.1R and 0.2R.

assumed to distribute lognormally. Figure 5-16 presents the distributions of peak horizontal displacements of the FP bearings subjected to the seven sets of 30 ground motions.

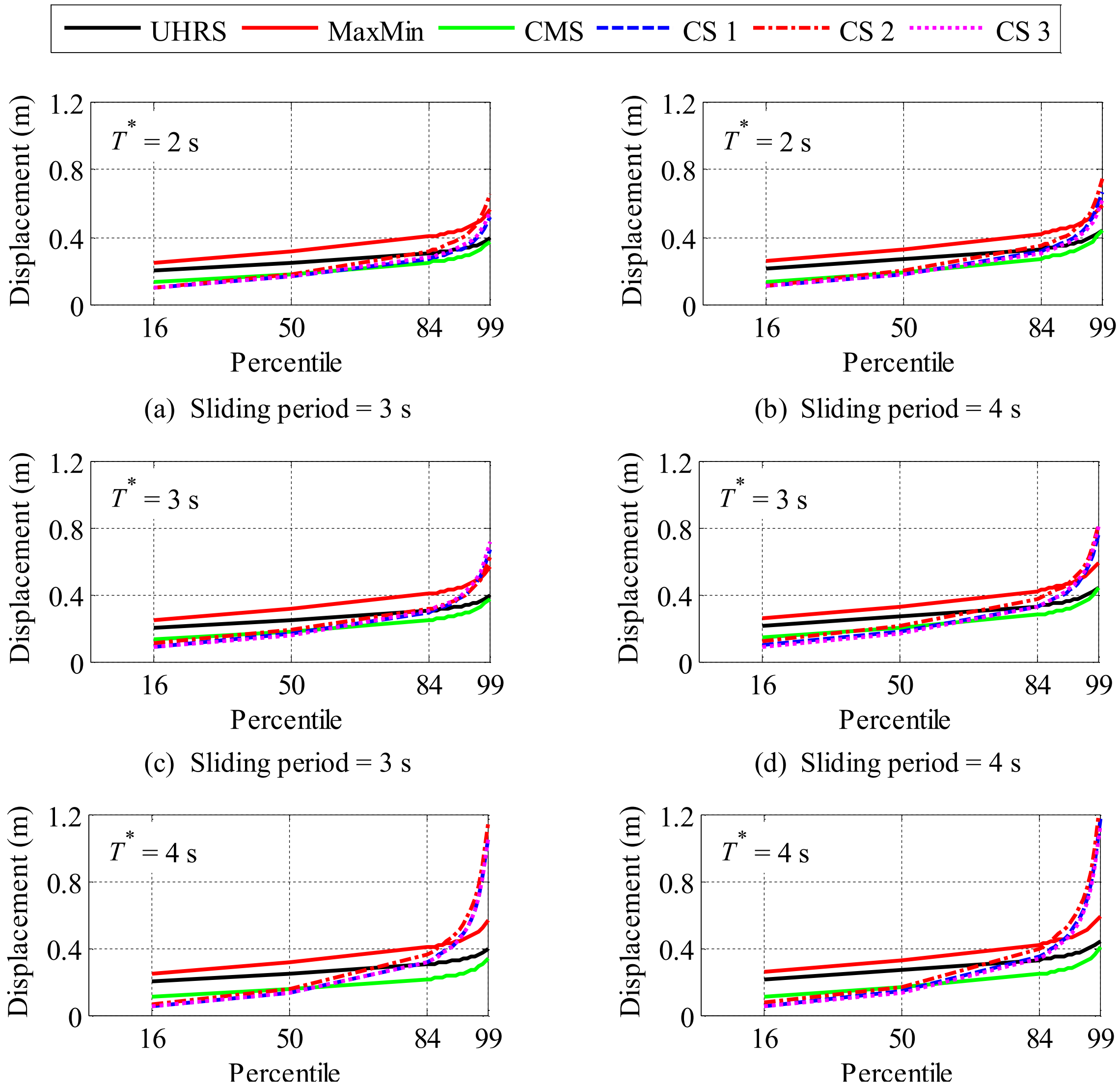

(a) Sliding period = 3 s
(b) Sliding period = 4 s
(c) Sliding period = 3 s
(d) Sliding period = 4 s
(e) Sliding period = 3 s
(f) Sliding period = 4 s

Figure 5-16: Distributions of maximum displacement of FP bearings with a Coulomb-type coefficient of friction of 0.1 and a static axial pressure of 50 MPa subjected to ground motions consistent with different representations of 10,000-year shaking at the Diablo Canyon site

Figure 5-16(a) presents the distributions of peak displacement of the 3 s FP bearing subjected to the ground motions consistent with UHRS, UHRS-MaxMin, and CS and CMS with T^* of 2 s

(Figure 5-4(a)). The peak displacements for the UHRS-scaled motions are greater than the CMS- and CS- scaled motions at percentiles smaller than 80; the displacements for the CMS- and CS-scaled motions are comparable up to 80th percentile. The displacements for the UHRS-MaxMin-scaled motions are greater than those for the other three representations of seismic hazard, at percentiles less than 95. The CS-displacements are greatest at 95+ percentiles. The ratios of displacements for UHRS-MaxMin- (CMS-, CS[1]-) to UHRS-scaled motions are 1.26 (0.73, 0.72), 1.34 (0.85, 1.15) and 1.42 (0.95, 1.67) at 50th, 90th and 99th percentiles, respectively. The observations for the 4 s bearing (Figure 5-16(b)) are similar to those for the 3 s bearing.

Data for conditioning periods of 3 s and 4 s are presented in Figures 5-16(c) through 5-16(f). The general trends are the same as those noted above for a conditioning period of 2 s. The 95+th percentile peak displacements are greatest for the CS-scaled motions. The ratios[2] of peak displacements for the UHRS-MaxMin- (CMS-, CS-) to UHRS-scaled motions are 1.26 (0.75, 0.79), 1.34 (0.87, 1.25) and 1.42 (0.98[3], 1.83) at the 50th, 90th and 99th percentiles, respectively, for a conditioning period of 3 s, and 1.26 (0.63, 0.62), 1.34 (0.77, 1.44) and 1.42 (0.91, 2.89), respectively, for a conditioning period of 4 s.

Different representations of the 10,000-year seismic hazard at the site of the Diablo Canyon Nuclear Generating Station have been investigated: the traditional UHRS; a variant of the UHRS

[1] The greatest of the three values (one for each of the three sets of CS-scaled motions) is used.
[2] Greater among those for bearings with sliding periods of 3 s and 4 s.
[3] The 99th percentile displacements for the CMS-scaled motions differ by less than 2% from those for the UHRS-scaled motions, even though the CMS ordinates are considerably smaller than the UHRS ordinates at periods other than the conditioning period (see Figures 5-12 and 5-13). This is explained by the higher dispersion in the CMS-displacements. For example, the peak displacements of an FP bearing with a sliding period of 3 s and coefficient of friction of 0.1 subjected to the 30 UHRS-scaled motions range between 0.16 m and 0.36 m, with a median of 0.25 m. The displacements range between 0.087 m and 0.32 m, with a median of 0.18 m, for the bearing subjected to the 30 CMS-scaled motions with conditioning period of 3 s. Although the median CMS displacement is smaller than the median UHRS displacement, the greater dispersion (standard deviation of 0.059 m vs. 0.050 m) increases the 99th percentile displacement, computed assuming a lognormal distribution, to within 2% of the UHRS value.

to account for differences in the two horizontal components of ground motions: UHRS-MaxMin; and the CMS and CS. Isolation-system displacements for the UHRS-MaxMin-scaled ground motions are greater than those for the other three representations at percentiles less than about 90. The displacements for the CMS- and CS- scaled motions are comparable at percentiles smaller than 80, especially for conditioning periods of 2 s and 3 s. The UHRS isolation-system displacements are greater than the CMS- and CS-displacements at percentiles smaller than 70, which is an expected result for nonlinear isolators such as the FP (and lead-rubber) bearings. The ratio of the displacements for CMS- or CS-scaled motions to the UHRS-scaled motions at a given percentile is a function of the conditioning period and the isolator sliding period.

5.5 100,000-year Spectra, Ground Motions, Spectral Displacements and Isolator Displacements

5.5.1 UHRS, UHRS-MaxMin, CMS and CS

Figure 5-17 presents the UHRS for the Diablo Canyon site for return periods of 10,000 and 100,000 years and Site Class B per ASCE 7-10. The ratios of the spectral ordinates at the two return periods are plotted in Figure 5-18. The ratios are between 2.0 to 2.2 over a period range of 0.5 s to 4 s. The 100,000-year UHRS is reasonably well calculated by multiplying the 10,000-year UHRS by 2.1. The UHRS-MaxMin spectra consistent with the 100,000-year hazard are also obtained by amplitude scaling the 10,000-year UHRS-MaxMin spectra[1] by a factor of 2.1.

Figures 5-19(a), 5-19(b) and 5-19(c) present the magnitude, source-to-site distance and ε, respectively, for a range of return periods and natural structural periods, corresponding to the

[1] The distributions of amplitude scaling factors in the two directions are assumed identical for the two return periods.

Campbell and Bozorgnia (2008) GMPE (data obtained from http://geohazards.usgs.gov/deaggint/2008/, June 15, 2014). The magnitude, distance and ε each trend to constant values at longer return periods. For a period of 2 s, the magnitude corresponding to 75-year return period is 6.19, which increases to 6.66 for a 10,000-year return period and to 6.72 for 20,000-year return period. The corresponding values for source-to-site distance are 34.7 km, 5.7 km and 4.8 km, respectively, and for ε are 0.63, 1.88 and 2.02. Only ε changes appreciably at the longer return periods. Assuming that the magnitude and distance for a 100,000-year return period are equal to those for a 20,000-year return period (the greatest return period for which USGS data are available), the values of ε for 100,000-year hazard at periods of 2 s, 3 s and 4 s are 2.85, 2.91 and 2.84, respectively, which are considerably greater than the values of 2.02, 2.08 and 2.08, respectively, for a return period of 10,000 years.

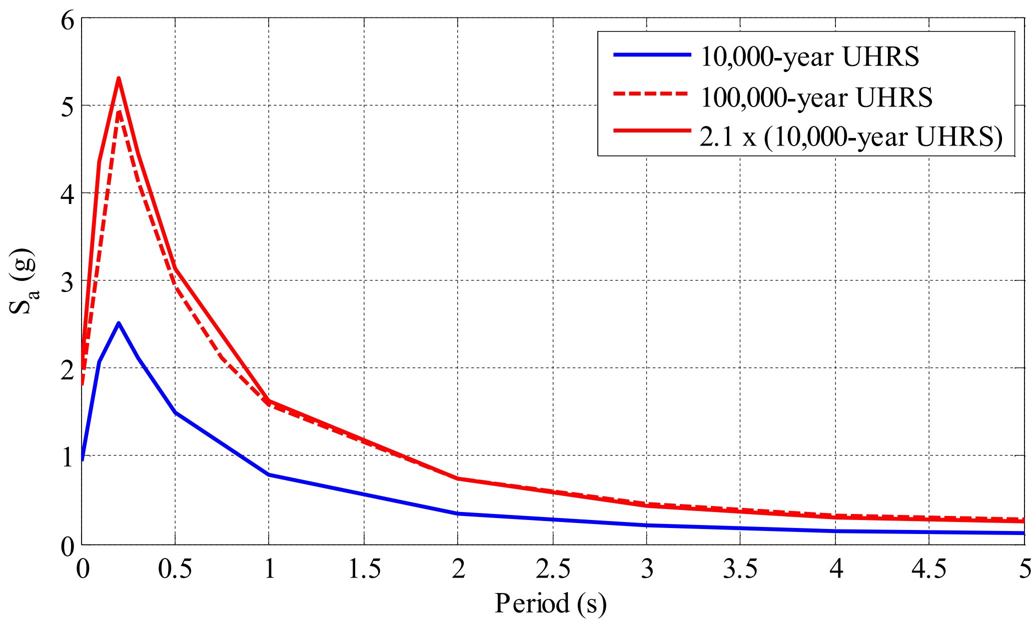

Figure 5-17: 10,000- and 100,000-year return period UHRS for Diablo Canyon site

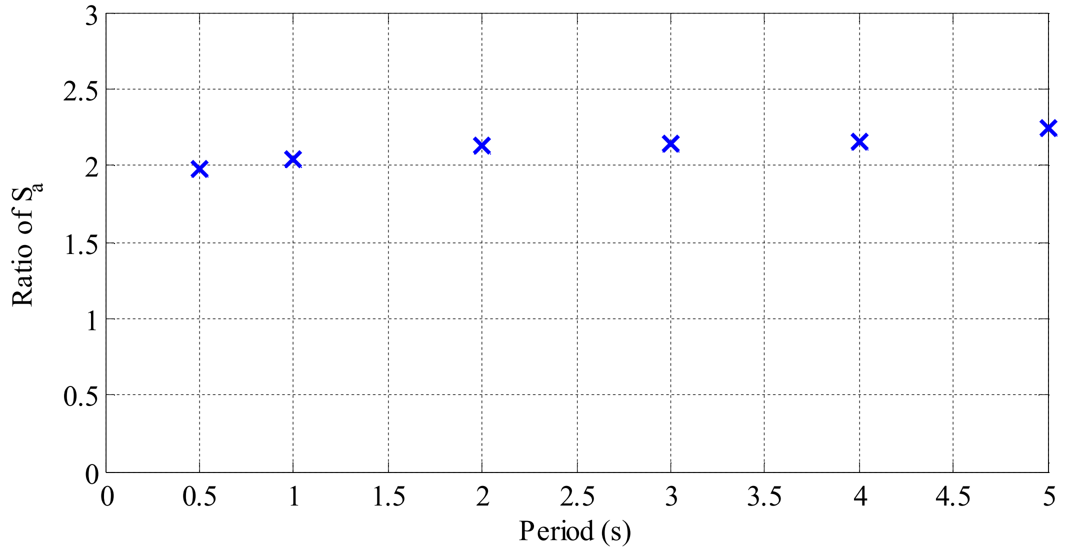

Figure 5-18: Ratio of spectral ordinates of the UHRS at 100,000 years to 10,000 years at the Diablo Canyon site

Conditional mean spectra with a conditioning period of 3 s are plotted in Figure 5-20 for return periods of 10,000 and 20,000 years for Diablo Canyon. Also plotted in the figure is the 10,000-year CMS increased by a factor of 1.26. The spectral ordinate of the scaled 10,000-year CMS is equal to that for the 20,000-year CMS at the conditioning period, and is greater than that for the 20,000-year CMS at other periods. The shape of the CMS at a given conditioning period is a function of the hazard level and the shape of a CMS can be expected to be sharper at the conditioning period at greater hazard levels: an attribute of positive epsilon motions identified by Baker and Cornell (2006).

The USGS website does not provide CMS for a return period of 100,000 years. In this study, 100,000-year CMS are obtained by amplitude scaling the corresponding 10,000-year CMS by 2.1 (see Section 5.5.1), which is a conservative representation of the seismic hazard (see for example Figure 5-20) for periods other than the conditioning period.

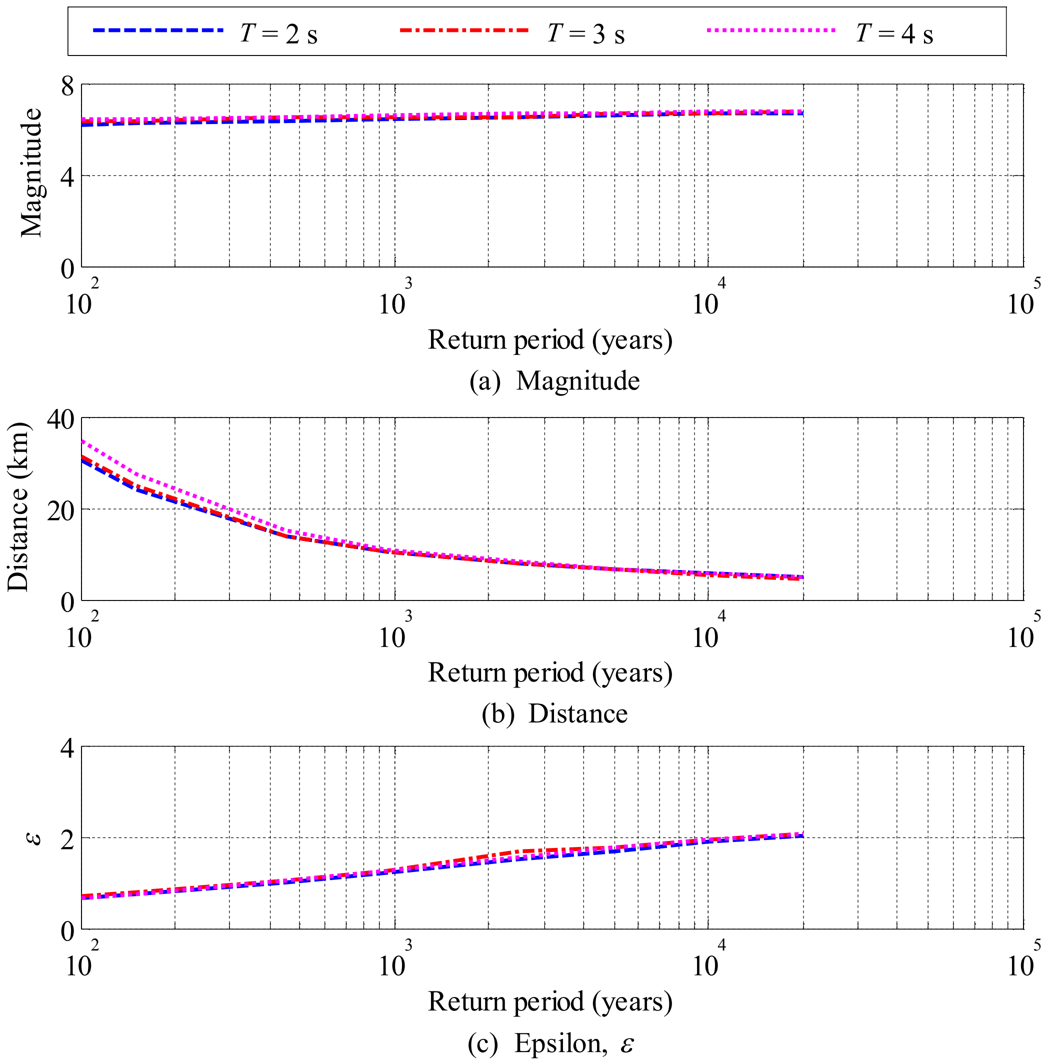

Figure 5-19: Combinations of magnitude, source-to-site distance, and ε for the Diablo Canyon site

As noted previously, the CS account for the variability in the CMS ordinates at periods other than the conditioning period. The variability is a function of the parameters of the earthquake (M and R) and the correlations between ε at different periods (see for example Jayaram *et al.* (2011), Baker and Jayaram (2008)). The correlation coefficient between ε at two periods is a function only of the two periods and not of the values of ε at the two periods. Therefore, the distributions of the CS ordinates at periods other than the conditioning period are controlled by M and R but not ε. Since the disaggregated M and R are not considerably different for the

10,000-year and 100,000-year return periods (see Figure 5-19), the distributions of the CS ordinates at different periods are expected to be comparable at the two hazard levels.

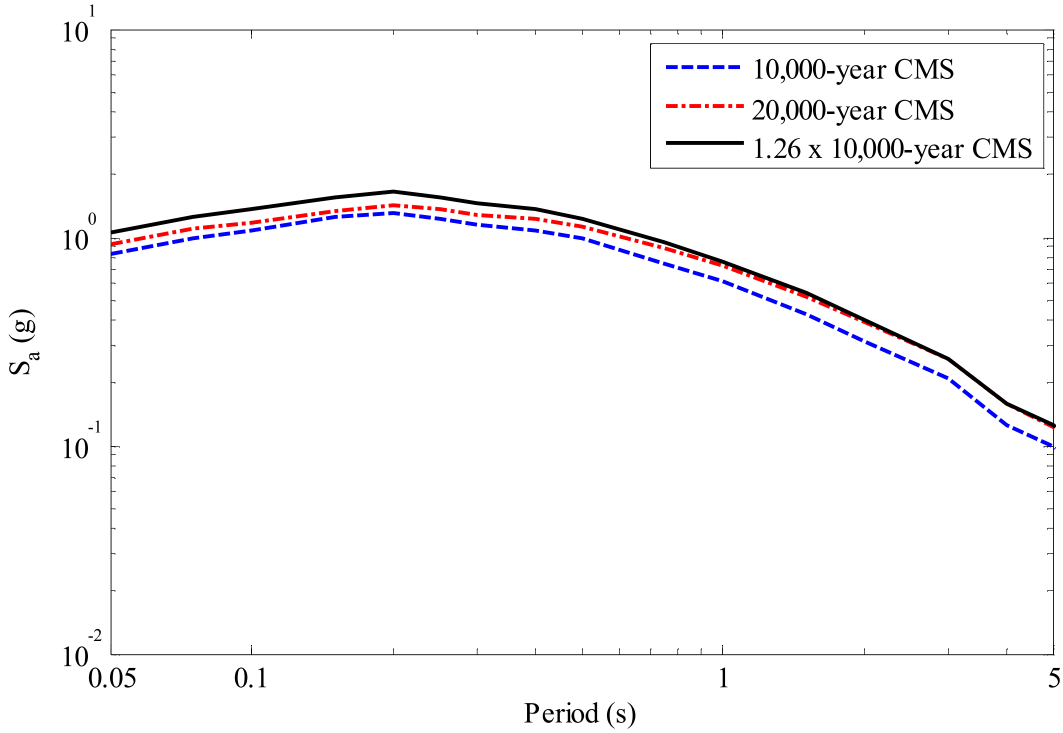

Figure 5-20: Conditional mean spectra a conditioning period of 3 s for seismic hazards with the return periods of 10,000 and 20,000 years

The information necessary to generate 100,000-year CS are not available on the USGS website and they are obtained instead by amplitude scaling the corresponding 10,000-year CS. Noting that the shape of the CMS becomes sharper at the conditioning period as the return period is increased, and thus an increased ε given constant values of M and R, the CS obtained by amplitude scaling are likely conservative for the 100,000-year return period. Accordingly, the 100,000-year CS are obtained by amplitude scaling the corresponding 10,000-year CS by a factor of 2.1.

5.5.2 Ground motions

The 100,000-year UHRS (UHRS-MaxMin) ground motions are obtained by amplitude scaling the 10,000-year UHRS (UHRS-MaxMin) ground motions by a factor of 2.1. The ground motions consistent with the 100,000-year CMS (CS) for the conditioning periods of 2 s, 3 s and 4 s are obtained by amplitude scaling the corresponding 10,000-year CMS (CS) ground motions by a factor of 2.1.

5.5.3 Spectral displacements

Since the 100,000-year UHRS, UHRS-MaxMin, CMS and CS are developed by amplitude scaling the corresponding 10,000-year response spectra, the spectral displacements for the 100,000-year ground motions are obtained by amplitude scaling the spectral displacements for the 10,000-year ground motions (Figures 5-12 and 5-13) by 2.1.

5.5.4 Response of FP bearings

Figure 5-16 presented the distributions of peak horizontal displacement of FP bearings with sliding periods of 3 s and 4 s, a Coulomb-type coefficient of friction of 0.1, and a static axial pressure of 50 MPa, subjected to ground motions representing a return period of 10,000 years. Figure 5-21 presents the corresponding distributions for a return period of 100,000 years. The general trends in the distributions of the peak displacements are similar. These distributions are studied further in the following section.

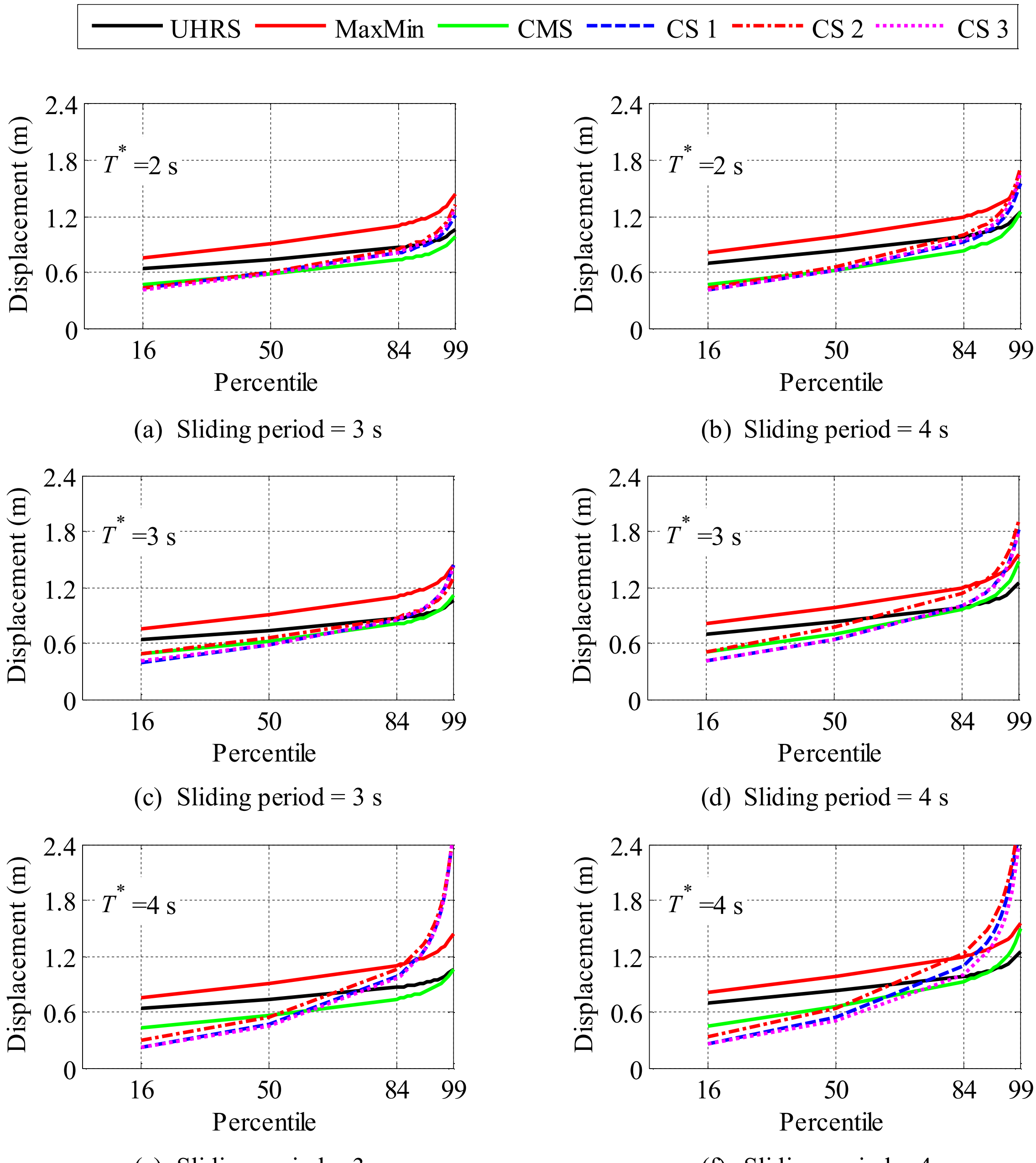

(a) Sliding period = 3 s

(b) Sliding period = 4 s

(c) Sliding period = 3 s

(d) Sliding period = 4 s

(e) Sliding period = 3 s

(f) Sliding period = 4 s

Figure 5-21: Distributions of maximum displacement of FP bearings with a Coulomb-type coefficient of friction of 0.1 and a static axial pressure of 50 MPa subjected to ground motions consistent with different representations of 100,000-year shaking at the Diablo Canyon site

5.6 Response of FP Bearings to 10,000- and 100,000-year Ground Motions

The 50^{th}, 90^{th} and 99^{th} percentile displacements from Figure 5-16 (10,000-year hazard) and Figure 5-21 (100,000-year hazard) are compared in Figures 5-22 and 5-23 for the 3 s and 4 s FP bearings, respectively.

Figure 5-22(a) presents the median responses of an FP bearing with a sliding period of 3 s subjected to ground motions consistent with 10,000-year UHRS, UHRS-MaxMin, CMS and CS. The median responses are greatest for the UHRS-MaxMin-scaled motions followed by the UHRS-scaled motions. The responses for CMS- and CS-scaled motions are comparable. The median responses for the 100,000-year ground motions presented in Figure 5-22(b) follow a similar trend to the responses for the 10,000-year ground motions. Figures 5-22(c) and 5-22(d) present the 90^{th} percentile responses for 10,000-year and 100,000-year ground motions, respectively. The UHRS-MaxMin responses exceed those for the UHRS-scaled, and CMS- and CS-scaled motions with conditioning periods of 2 s and 3 s. The responses for the CS-scaled motions with a conditioning period of 4 s are either similar or greater than those for the UHRS-MaxMin motions. Figure 5-22(e) presents the 99^{th} percentile responses for the 10,000-year ground motions. The responses for CS-scaled motions are considerably greater than those for the UHRS-MaxMin-scaled motions, especially for the conditioning period of 4 s[1]. The responses for UHRS-scaled motions are virtually identical to those for the CMS-scaled motions. Figure 5-23 presents the companion results for the 4 s FP bearing. The general trends in the two figures are similar.

[1] The choice of conditioning period of 4 s for the sliding period of 3 s would be poor because the effective period of the isolation system will always be less than 3 s.

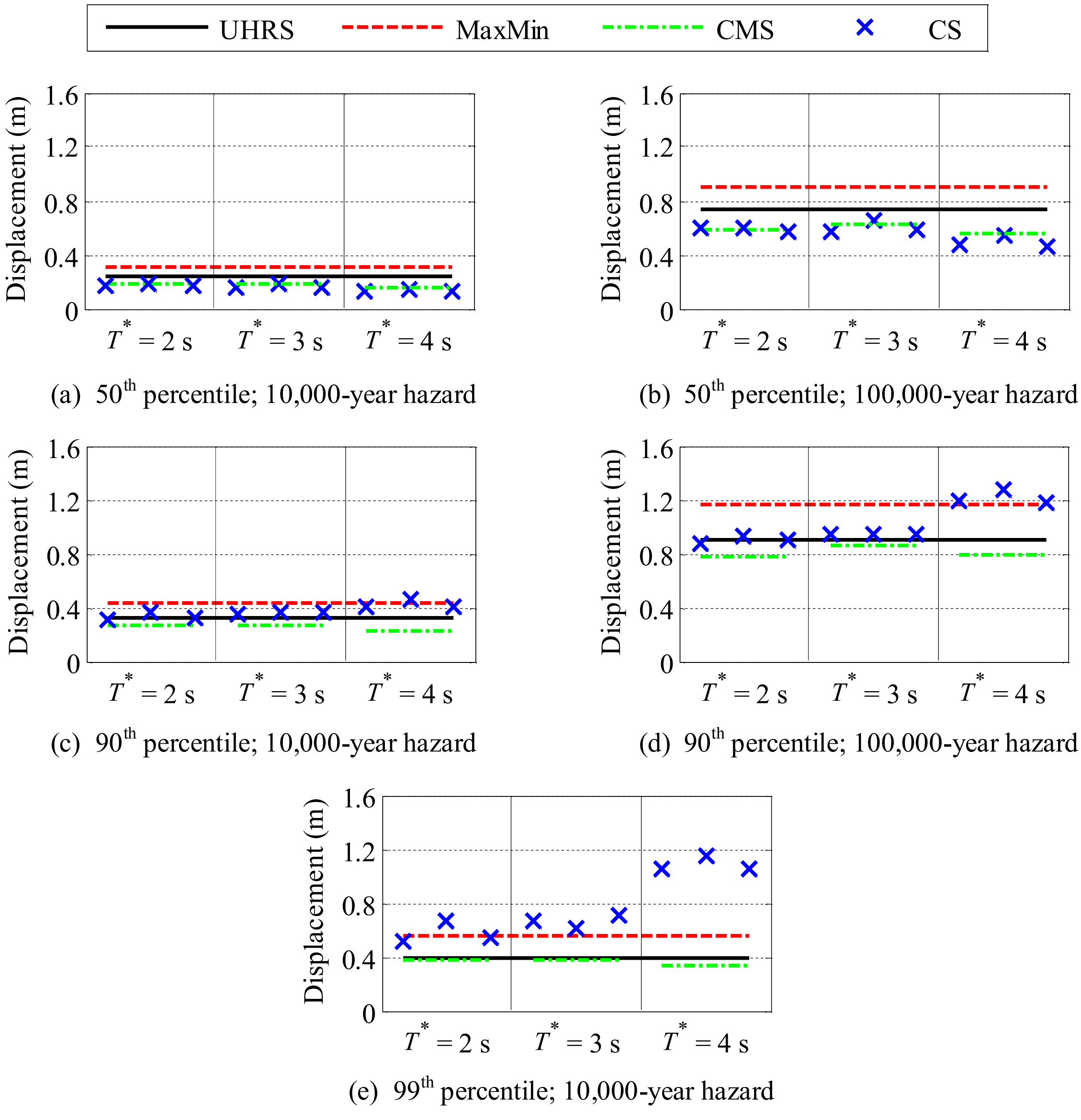

Figure 5-22: Median, 90th and 99th percentile peak displacement responses of an FP bearing with a sliding period of 3 s subjected to 10,000-year and 100,000-year UHRS-, UHRS-MaxMin-, CMS- and CS-scaled ground motions

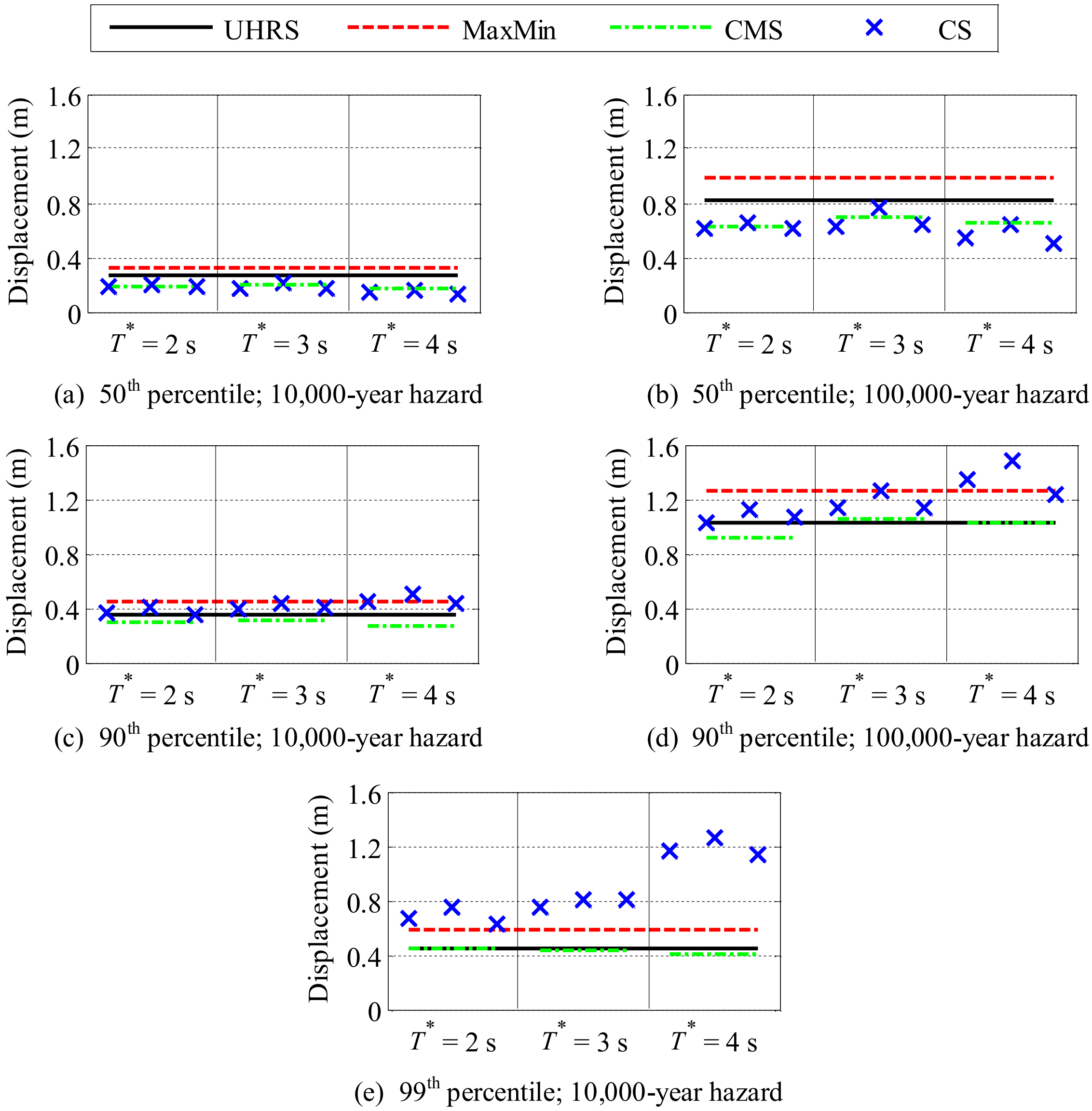

Figure 5-23: Median, 90th and 99th percentile peak displacement responses of an FP bearing with a sliding period of 4 s subjected to 10,000-year and 100,000-year UHRS-, UHRS-MaxMin-, CMS- and CS-scaled ground motions

The 90th percentile peak displacements corresponding to a return period of 100,000 years are greater than the 99th percentile peak displacements corresponding to a return period of 10,000 years, regardless of the choice of target spectra (UHRS, UHRS-MaxMin, CMS or CS). Therefore, the 90th percentile displacement for the 100,000-year earthquake shaking will determine the clear distance between the isolated superstructure and surrounding hard stop. At percentiles less than 90, the responses for UHRS-MaxMin motions are greater than those for the other three representations of seismic hazard. The 90th percentile peak displacements for the 100,000-year (and 10,000-year) earthquake shaking calculated using UHRS-MaxMin-scaled ground motions exceed those for the UHRS-scaled motions by a factor of between 1.2 and 1.4. The 90th percentile responses for the CMS-scaled (CS-scaled) motions, with conditioning periods of 2 s and 3 s, differ from those for the UHRS-scaled motions by between 2% and 16% (0% and 26%), at the two hazard levels.

Figures 5-22 and 5-23 present the response of FP bearings with sliding periods of 3 s and 4 s, static axial pressure of 50 MPa, and a Coulomb-type coefficient of friction of 0.1, subjected to the sets of ground motions consistent with the four representations of 10,000-year and 100,000-year earthquake shaking. To determine if the conclusions drawn from these results are broadly applicable, single FP bearings with a sliding period of 3 s, reference coefficients of friction of 0.06 and 0.1, static axial pressures of 10 MPa and 50 MPa, and friction at the sliding surface described using both the Coulomb model and the *p-T-v* model, are subjected to all of the ground motions of Sections 5.4 and 5.5, except for the CS-scaled motions with a conditioning period of 4 s (the displacements of the FP bearings subjected to the 100,000-year CS-scaled motions with a conditioning period of 4 s exceed, for some ground motions, the radius of curvature of the bearing, leading to numerical problems). The 50th, 90th and 99th percentiles peak displacements are presented in Figures 5-24 through 5-31. The observations made on the results presented in Figures 5-22 and 5-23 for the 3 s and 4 s FP bearings are also applicable to the 3 s FP bearings, irrespective of the axial pressure on the bearing, the choice of friction model, and/or to hazard level. These observations are summarized below:

i. The peak horizontal displacement responses of FP bearings are most significantly influenced by the choice of target spectra: UHRS, UHRS-MaxMin, CMS or CS.

ii. Three sets of 30 ground motions were matched to each CS set. The choice of seed ground motions was found to have an insignificant effect on the response, compared with the choice of the target spectra.

iii. The median peak horizontal displacements are greatest for the UHRS-MaxMin-scaled ground motions followed by UHRS-scaled motions. The median responses to the CMS- and CS-scaled motions are similar.

iv. At the 90th percentile, the peak horizontal displacements for

    a. the CMS-scaled motions with conditioning periods of 2 s and 3 s differ by between 2% and 16% from those for the UHRS-scaled motions, and

    b. the UHRS-MaxMin-scaled motions are greater than those for other three representations of seismic hazard.

v. At the 99th percentile, the peak horizontal displacement for 10,000-year shaking for

    a. the CMS-displacements differ from those for the UHRS-displacements by up to 9%.

    b. the UHRS-MaxMin motions are substantially greater than those for the UHRS- or CMS-scaled motions.

vi. The 90th percentile peak horizontal displacement for 100,000-year shaking is greater than the 99th percentile peak horizontal displacement for 10,000-year shaking, for a given choice of target spectrum.

vii. The 90th percentile peak horizontal displacements for the UHRS-MaxMin-scaled motions are approximately 1.3 times those for the UHRS-scaled motions for both 10,000- and 100,000-year shaking.

viii. The 90^{th} percentile peak displacement of an FP bearing with friction defined using the *p*-*T*-*v* model subjected to the UHRS-MaxMin-motions is greater than that of an FP bearing with friction defined using the Coulomb model subjected to the UHRS-motions by a factor of between 1.4 and 1.7 (1.3 and 1.5) for 10,000-year (100,000-year) shaking, for all combinations of static axial pressure and reference coefficient of friction. The factor increases with increases in static axial pressure from 10 MPa to 50 MPa and reference coefficient of friction from 0.06 to 0.1.

5.7 Conclusions

The following conclusions are drawn from the results of the response-history analyses performed on single FP bearings with a range of properties subjected to ground motions consistent with return periods of 10,000 years and 100,000 years at the site of Diablo Canyon Nuclear Generating Station:

i. The UHRS should be used as the target spectrum with explicit consideration of the differences between the orthogonal horizontal components of the ground motions: UHRS-MaxMin ground motions.

ii. An important design parameter for a seismic isolation system is the clearance to the hard stop, which is required to be greater than the 99^{th} (90^{th}) percentile peak displacement for 10,000-year (100,000-year) shaking. The 90^{th} percentile peak displacement for the 100,000-year shaking is consistently greater than the 99^{th} percentile peak displacement for the 10,000-year shaking. A smaller set of ground motions (e.g., 30) can be used to compute a 90th percentile displacement than would be needed to compute a 99th percentile displacement.

iii. The 90th percentile peak displacement of an FP bearing with friction described using *p*-*T*-*v* model subjected to 100,000-year UHRS-MaxMin motions can be estimated by multiplying the median displacement of an FP bearing with friction described by the Coulomb model, subjected to the 10,000-year UHRS motions, by a factor of between 3.4 and 4.3, that depends on the static axial pressure and the reference coefficient of friction.

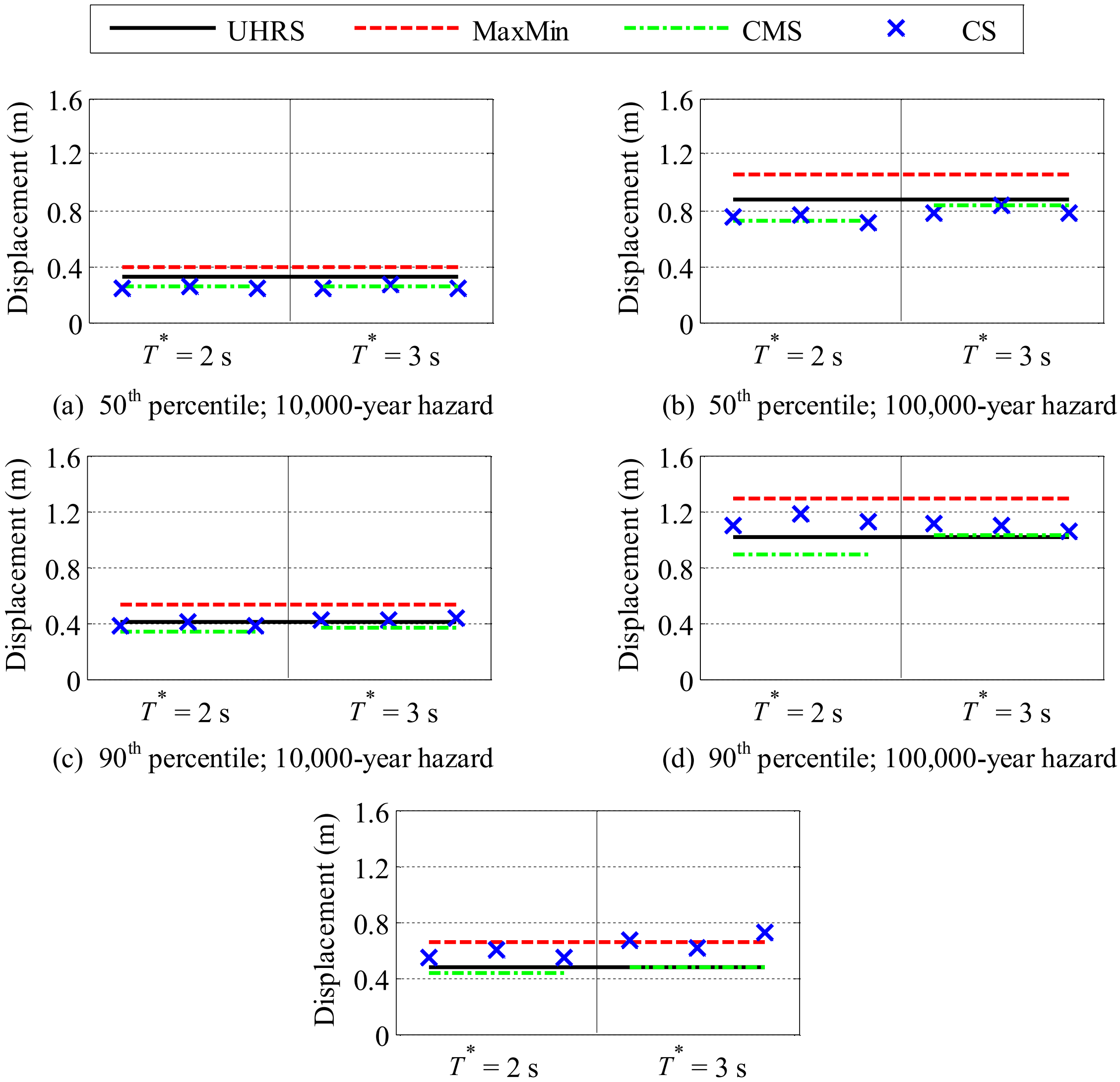

(a) 50th percentile; 10,000-year hazard

(b) 50th percentile; 100,000-year hazard

(c) 90th percentile; 10,000-year hazard

(d) 90th percentile; 100,000-year hazard

(e) 99th percentile; 10,000-year hazard

Figure 5-24: Median, 90th and 99th percentile peak displacement responses of an FP bearing with a sliding period of 3 s, static axial pressure of 10 MPa, reference coefficient of friction of 0.06, and Coulomb friction model, subjected to 10,000-year and 100,000-year UHRS-, UHRS-MaxMin-, CMS- and CS-scaled ground motions

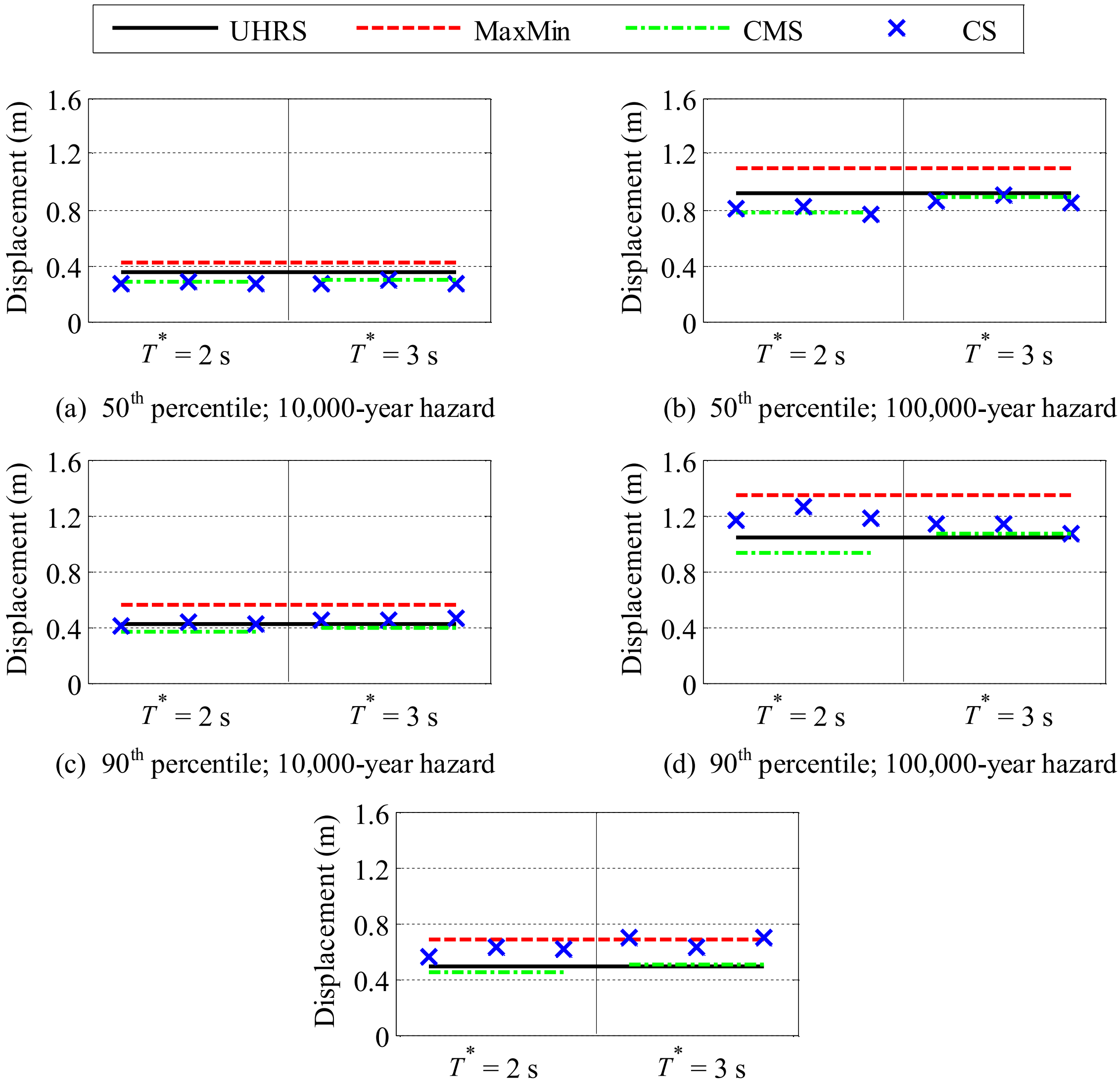

(a) 50th percentile; 10,000-year hazard

(b) 50th percentile; 100,000-year hazard

(c) 90th percentile; 10,000-year hazard

(d) 90th percentile; 100,000-year hazard

(e) 99th percentile; 10,000-year hazard

Figure 5-25: Median, 90th and 99th percentile peak displacement responses of an FP bearing with a sliding period of 3 s, static axial pressure of 10 MPa, reference coefficient of friction of 0.06, and *p-T-v* friction model, subjected to 10,000-year and 100,000-year UHRS-, UHRS-MaxMin-, CMS- and CS-scaled ground motions

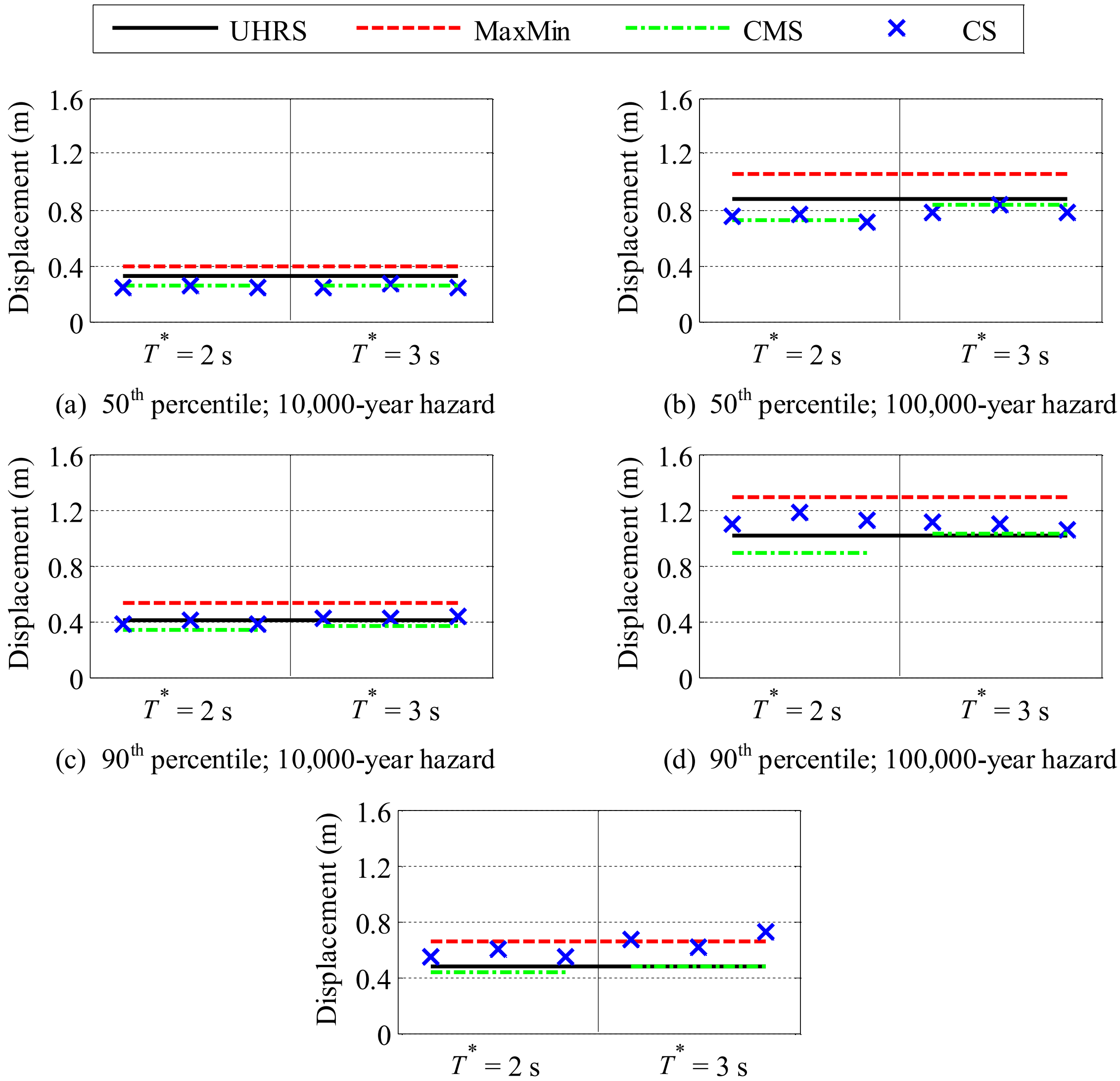

(a) 50th percentile; 10,000-year hazard

(b) 50th percentile; 100,000-year hazard

(c) 90th percentile; 10,000-year hazard

(d) 90th percentile; 100,000-year hazard

(e) 99th percentile; 10,000-year hazard

Figure 5-26: Median, 90th and 99th percentile peak displacement responses of an FP bearing with a sliding period of 3 s, static axial pressure of 50 MPa, reference coefficient of friction of 0.06, and Coulomb friction model, subjected to 10,000-year and 100,000-year UHRS-, UHRS-MaxMin-, CMS- and CS-scaled ground motions

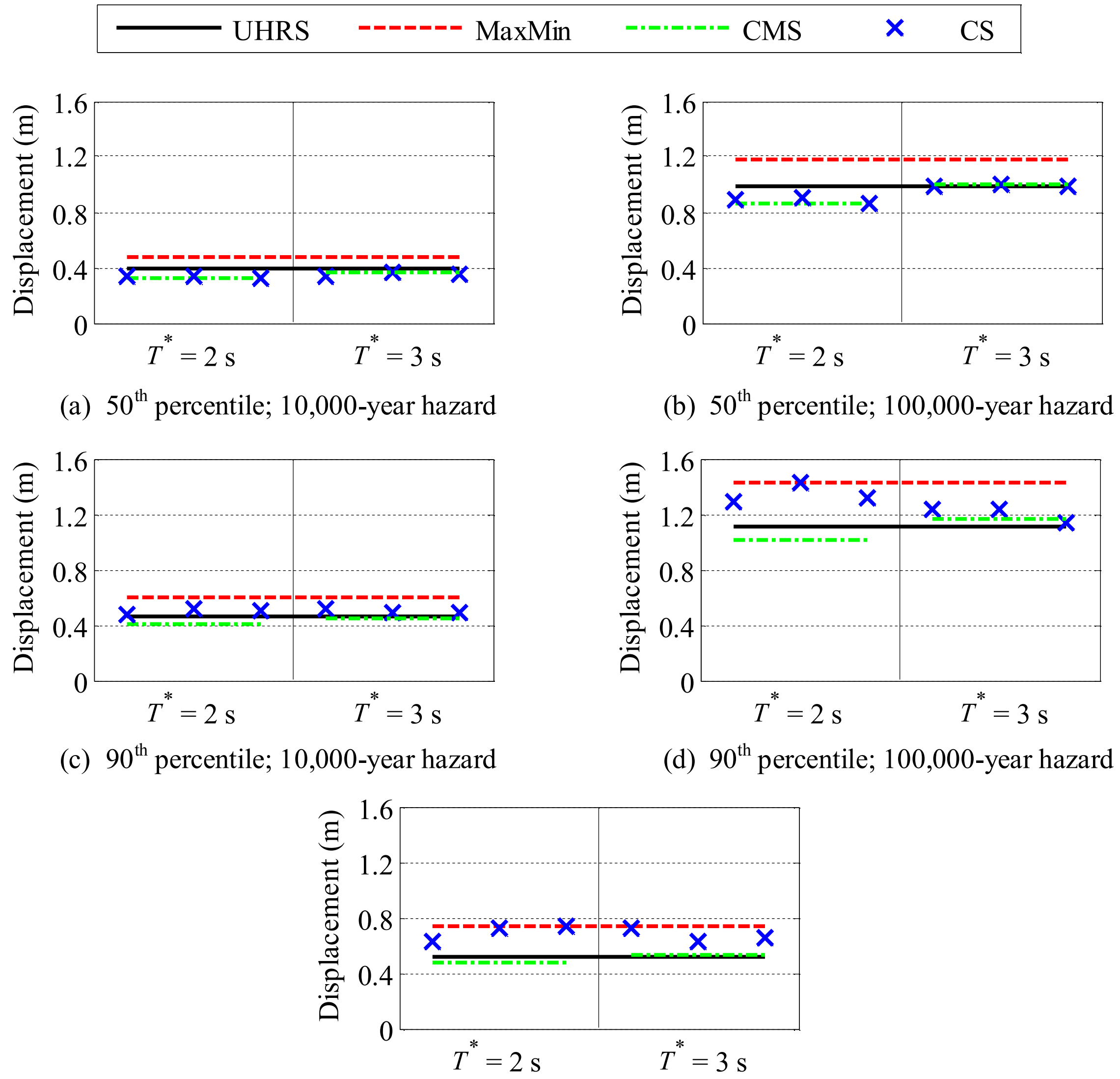

(a) 50th percentile; 10,000-year hazard

(b) 50th percentile; 100,000-year hazard

(c) 90th percentile; 10,000-year hazard

(d) 90th percentile; 100,000-year hazard

(e) 99th percentile; 10,000-year hazard

Figure 5-27: Median, 90th and 99th percentile peak displacement responses of an FP bearing with a sliding period of 3 s, static axial pressure of 50 MPa, reference coefficient of friction of 0.06, and *p-T-v* friction model, subjected to 10,000-year and 100,000-year UHRS-, UHRS-MaxMin-, CMS- and CS-scaled ground motions

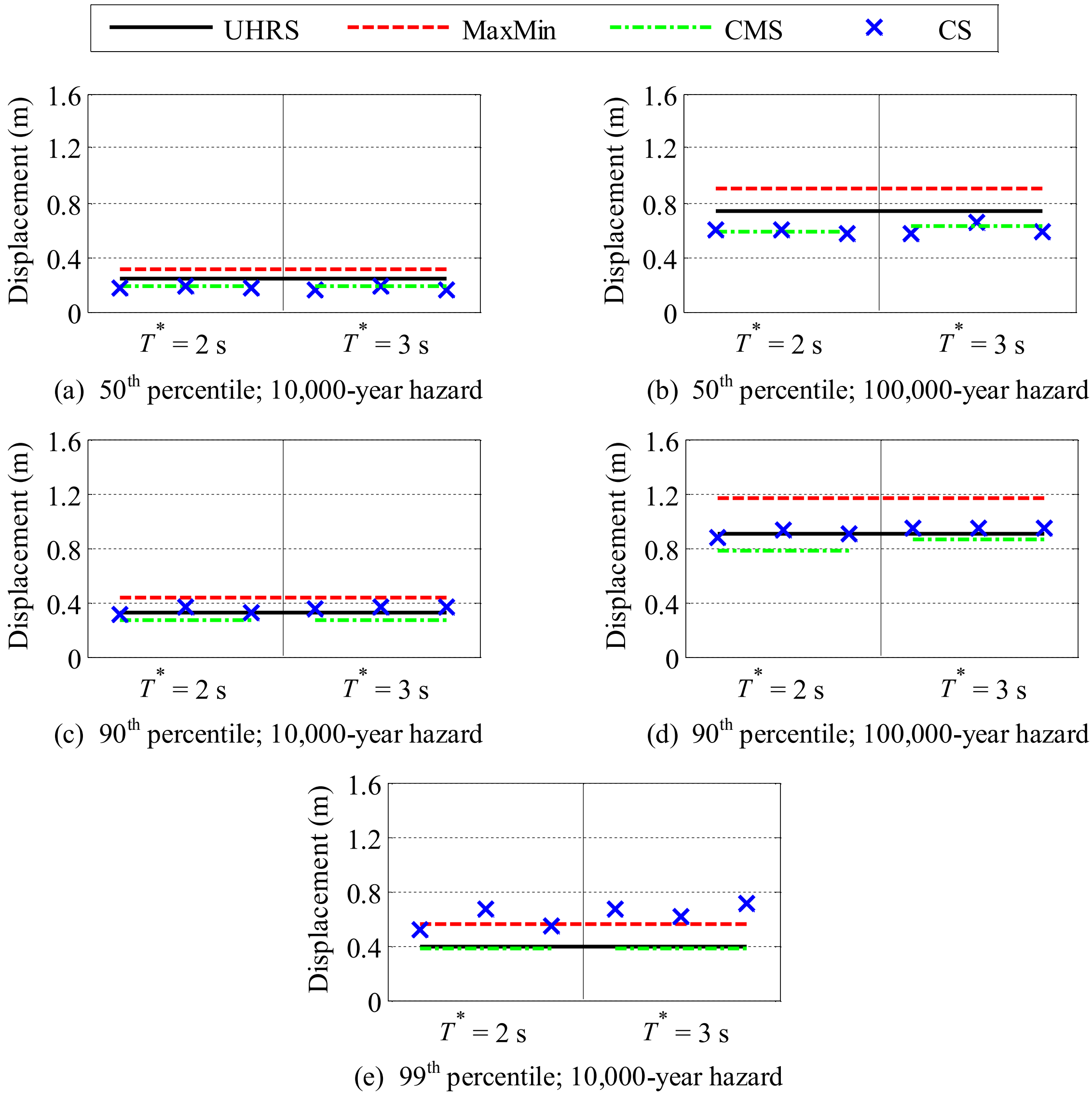

Figure 5-28: Median, 90th and 99th percentile peak displacement responses of an FP bearing with a sliding period of 3 s, static axial pressure of 10 MPa, reference coefficient of friction of 0.1, and Coulomb friction model, subjected to 10,000-year and 100,000-year UHRS-, UHRS-MaxMin-, CMS- and CS-scaled ground motions

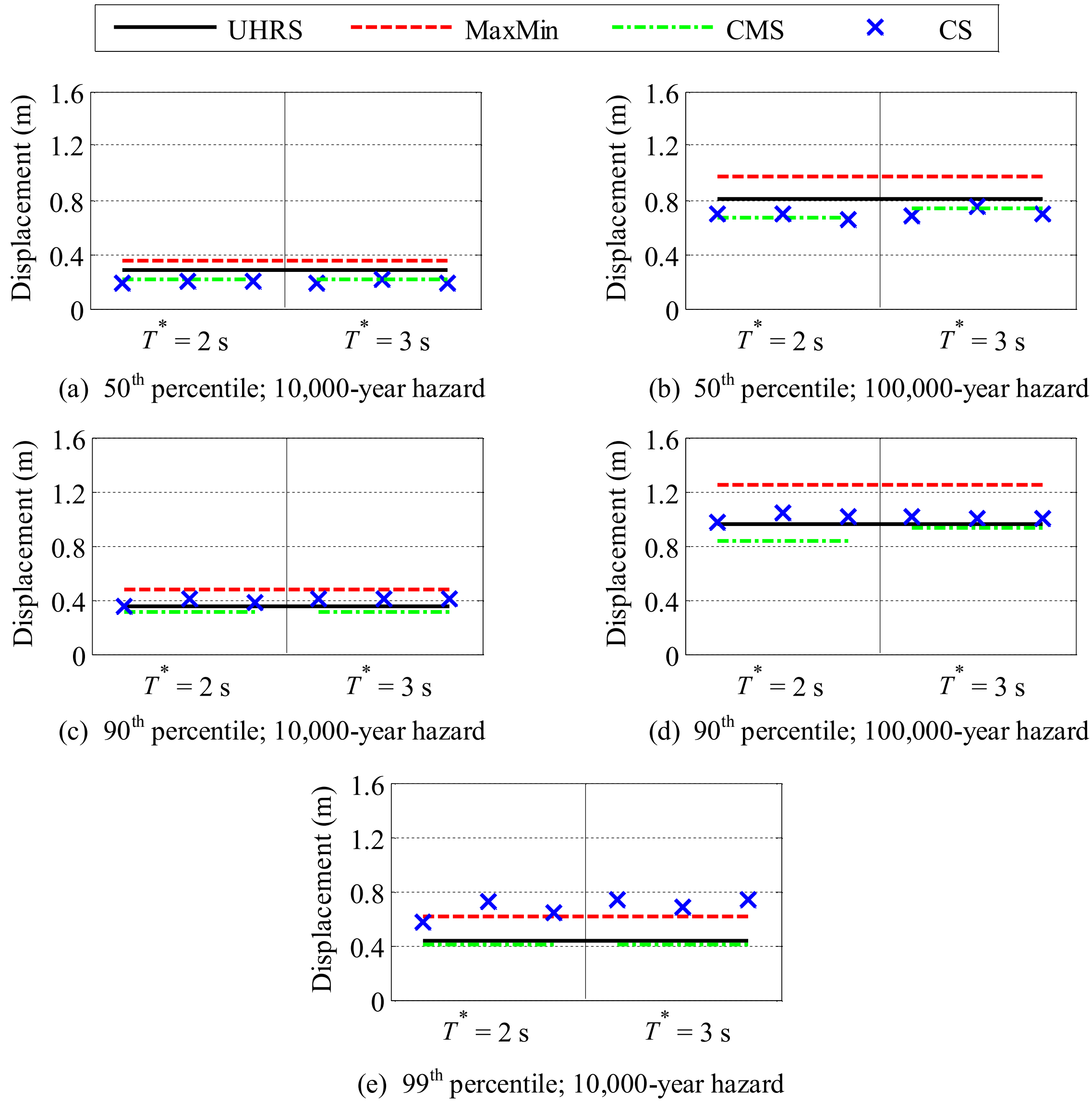

Figure 5-29: Median, 90th and 99th percentile peak displacement responses of an FP bearing with a sliding period of 3 s, static axial pressure of 10 MPa, reference coefficient of friction of 0.1, and *p-T-v* friction model, subjected to 10,000-year and 100,000-year UHRS-, UHRS-MaxMin-, CMS- and CS-scaled ground motions

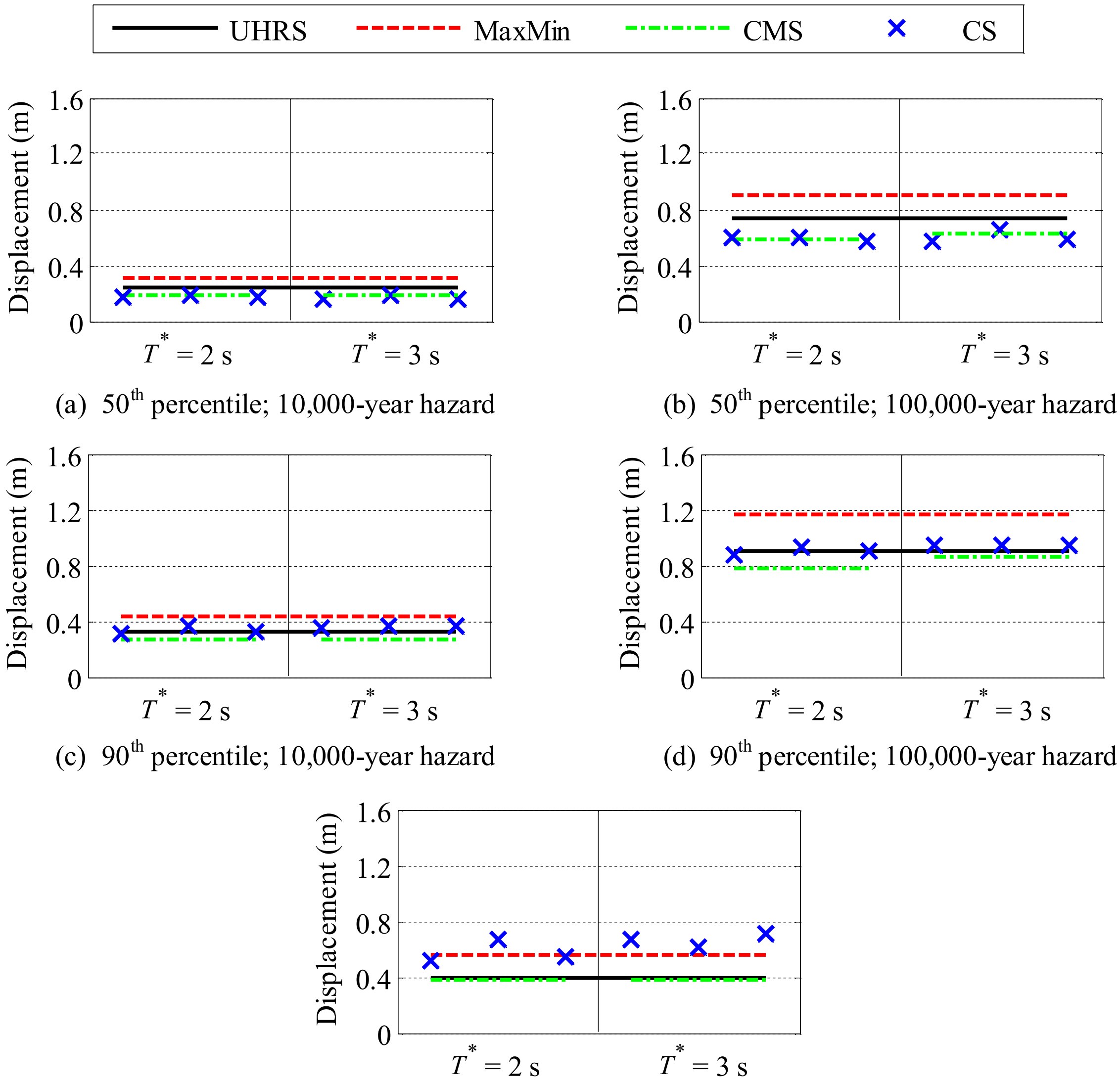

(a) 50th percentile; 10,000-year hazard

(b) 50th percentile; 100,000-year hazard

(c) 90th percentile; 10,000-year hazard

(d) 90th percentile; 100,000-year hazard

(e) 99th percentile; 10,000-year hazard

Figure 5-30: Median, 90th and 99th percentile peak displacement responses of an FP bearing with a sliding period of 3 s, static axial pressure of 50 MPa, reference coefficient of friction of 0.1, and Coulomb friction model, subjected to 10,000-year and 100,000-year UHRS-, UHRS-MaxMin-, CMS- and CS-scaled ground motions

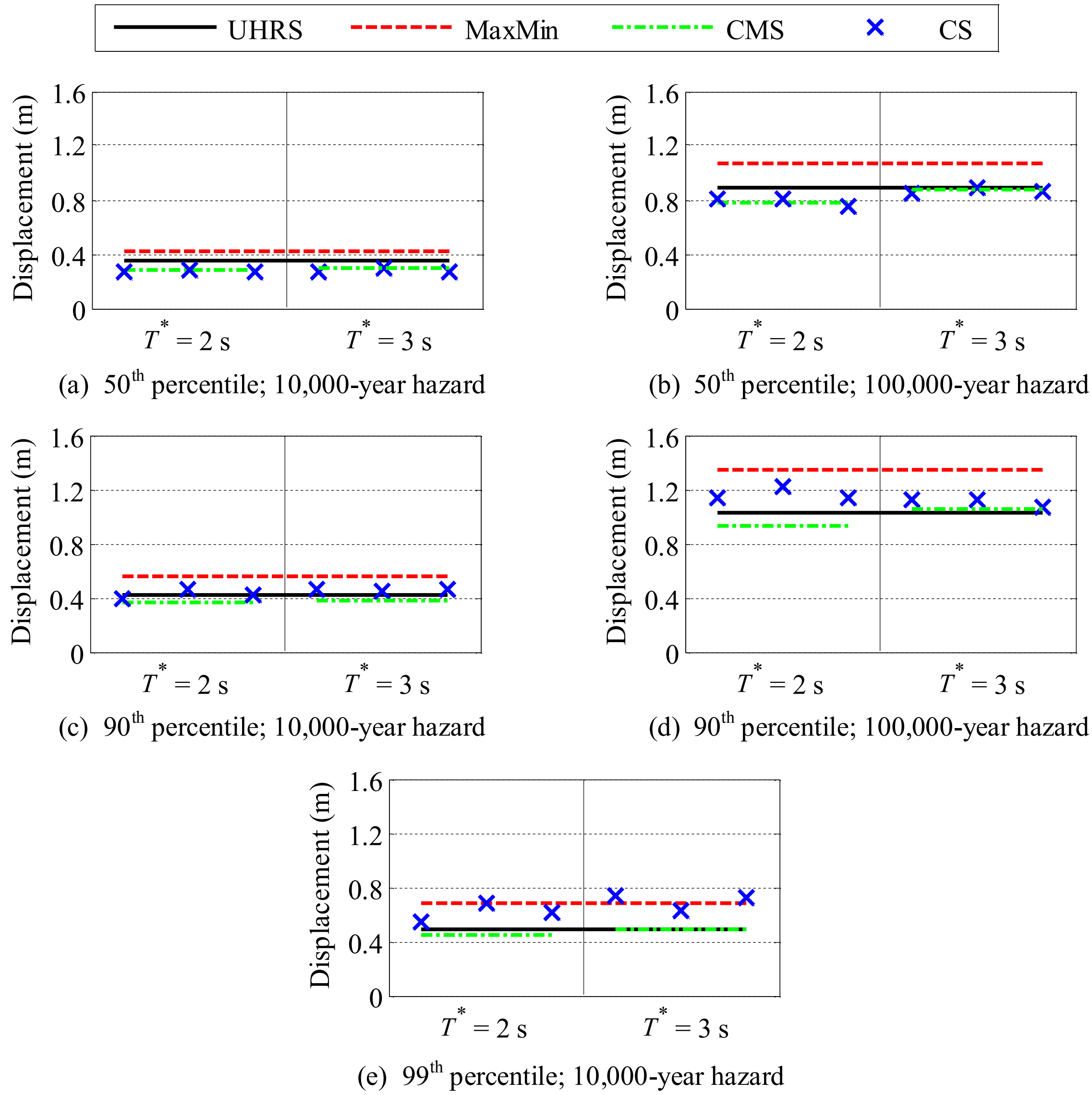

Figure 5-31: Median, 90th and 99th percentile peak displacement responses of an FP bearing with a sliding period of 3 s, static axial pressure of 50 MPa, reference coefficient of friction of 0.1, and *p-T-v* friction model, subjected to 10,000-year and 100,000-year UHRS-, UHRS-MaxMin-, CMS- and CS-scaled ground motions

CHAPTER 6

SEISMIC HAZARD DEFINITIONS FOR NUCLEAR POWER PLANTS

6.1 Introduction

The seismic design of a conventional (or fixed-base) nuclear structure is performed using a graded approach outlined in ASCE 43-05 (ASCE, 2005) entitled "Seismic design criteria for structures, systems, and components and nuclear facilities". Five seismic design categories (SDCs) and four limit states are identified. The target annual frequencies of unacceptable performance are smaller for higher SDCs. The four limit states, A through D, refer to large, moderate and limited permanent deformations, and essentially elastic behavior, respectively. Seismic design categories 3, 4 and 5 are addressed in ASCE 43-05. A nuclear structure, system or component is assigned an SDC according to ANSI/ANS 2.26 (ANS, 2010). Nuclear power plants are assigned to SDC 5.

The seismic hazard for the analysis and design of *conventional* (or fixed-base) nuclear structures is defined as the product of a uniform hazard response spectrum (UHRS) at a SDC-based mean annual frequency of exceedance (MAFE) and a design factor (e.g., RG 1.208 (USNRC, 2007a), ASCE (2005) and ASCE (forthcoming)). Two levels of seismic hazard will be considered for the analysis and design of seismically *isolated* nuclear structures: 1) a design basis earthquake per ASCE 43 and ASCE 4 (ASCE, forthcoming) and a ground motion response spectrum (GMRS) per RG 1.208, and 2) a beyond design basis earthquake per ASCE 4 and an extended design basis GMRS per Kammerer *et al.* (forthcoming). The hazard definitions and performance goals for conventional and isolated nuclear power plants are studied in this chapter, with the objective of determining design factors for seismically isolated nuclear power plants. Design factors for other isolated safety-related nuclear structures are not calculated.

Seismic hazard curves for eight sites of nuclear facilities in the United States are presented in Section 6.2. The definitions of seismic hazard and performance goals for conventional and seismically isolated nuclear power plants are discussed in Sections 6.3 and 6.4, respectively. Seismic hazard definitions for conventional and seismically isolated nuclear power plants are compared in Section 6.5. The total annual frequencies of unacceptable performance for the isolated superstructure, individual isolators and umbilical lines are estimated in Section 6.6 for a seismically isolated nuclear power plant at each of the eight sites. Companion risk calculations for Department of Energy-regulated isolated nuclear structures are presented in Appendix F. Design factors are determined in Section 6.7.

6.2 Seismic Hazard at the Site of Nuclear Facilities in the United States

Figure 6-1 presents seismic hazard curves (spectral acceleration versus MAFE) at eight sites of nuclear facilities across the United States (see Figure 6-2) for four periods: 0.1 s, 0.2 s, 1 s and 2 s and 5% damping. The data are downloaded from the USGS website: http://geohazards.usgs.gov/hazardtool/application.php (accessed on December 30, 2014) and are associated with a shear wave velocity in the upper 30 m of the soil column of 760 m/s. For each of the eight sites and four periods of Figure 6-1, the spectral accelerations at MAFE of 10^{-3}, 4×10^{-4} and 10^{-4} are computed assuming a linear variation of spectral acceleration with MAFE in logarithmic space between adjacent data points. A similar assumption of linearity in the logarithmic space for a 10-fold change in MAFE is made in ASCE (2005). For the remainder of this chapter, spectral acceleration at a given MAFE (or MAFE for a given spectral acceleration) is computed assuming linearity between two adjacent data points of the seismic hazard curve in the logarithmic space, unless noted otherwise.

The spectral accelerations at MAFE of 10^{-3}, 4×10^{-4} and 10^{-4} are used to normalize the data of Figure 6-1 to a spectral acceleration of 1.0 g at the three MAFE, and the normalized curves are plotted in Figures 6-3, 6-4[1] and 6-5[2], respectively.

6.3 Conventional Nuclear Power Plants

6.3.1 Seismic hazard definition

The seismic hazard for the analysis and design of conventional (or fixed-base) nuclear structures is defined in ASCE 43-05 (ASCE, 2005). This risk-oriented definition of hazard was first implemented in the United States Department of Energy guideline "Natural phenomena hazards design and evaluation criteria for Department of Energy facilities" (USDOE, 1994). The design response spectrum, DRS, is obtained by multiplying the ordinates of the UHRS by a design factor, DF:

$$DRS = DF \times \text{UHRS} \tag{6-1}$$

and it represents design basis earthquake shaking.

For a non-isolated nuclear structure, the UHRS is increased by DF to achieve the target R_P (e.g., 10) for a given H_D (e.g., 10^{-4}). ASCE 43-05 provides an expression to compute DF, namely,

[1] The figure is similar to Figure C1-1 of ASCE 43-05.
[2] The figure is similar to Figure C2-1 of ASCE 43-05, with horizontal and vertical axes switched.

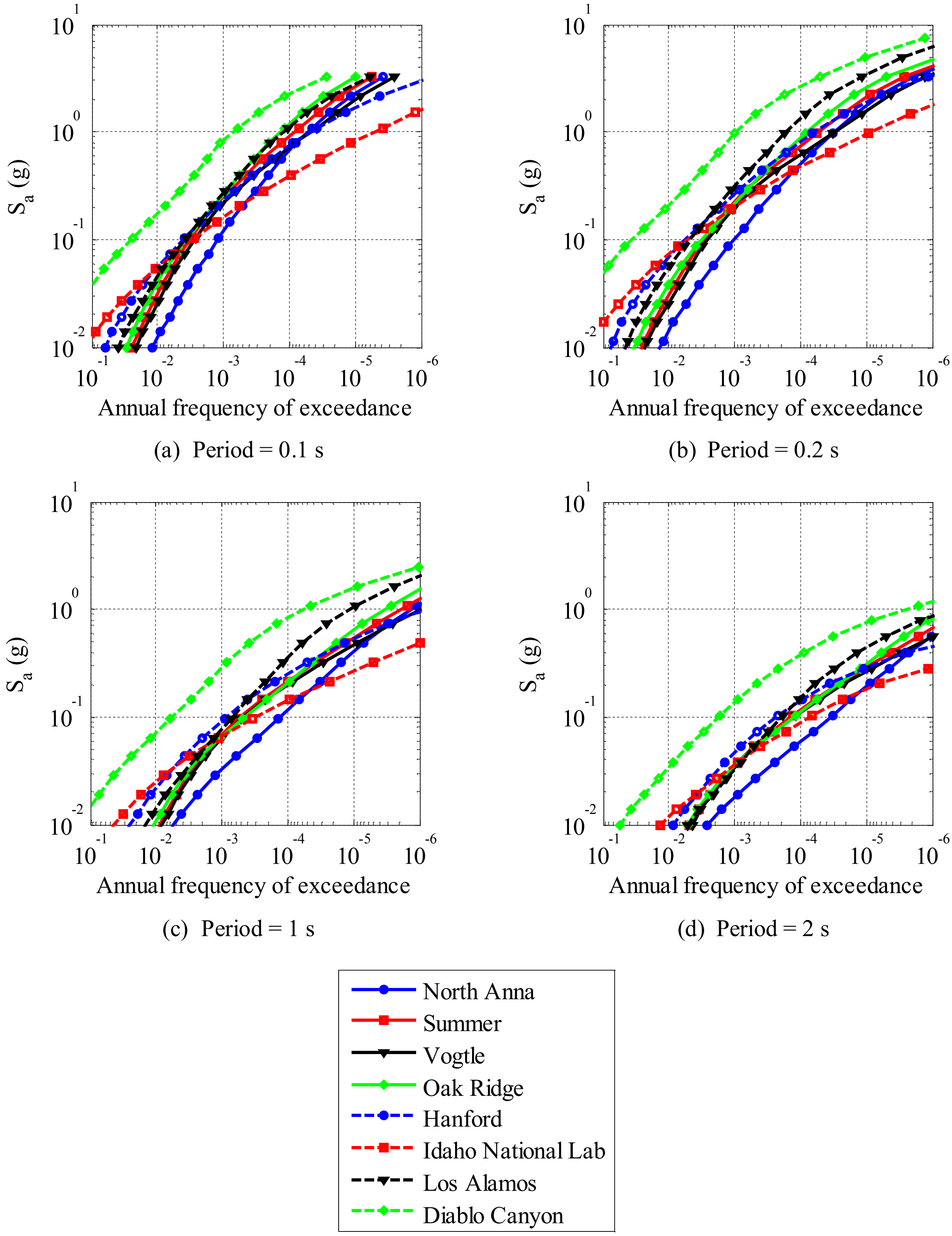

Figure 6-1: Seismic hazard curves for eight sites of nuclear facilities in the United States and 5% damping

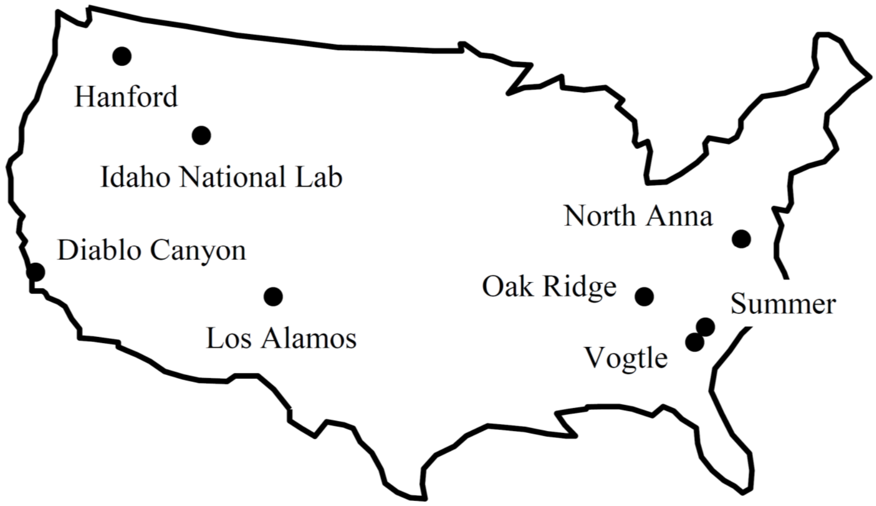

Figure 6-2: Locations of eight nuclear facilities in the United States

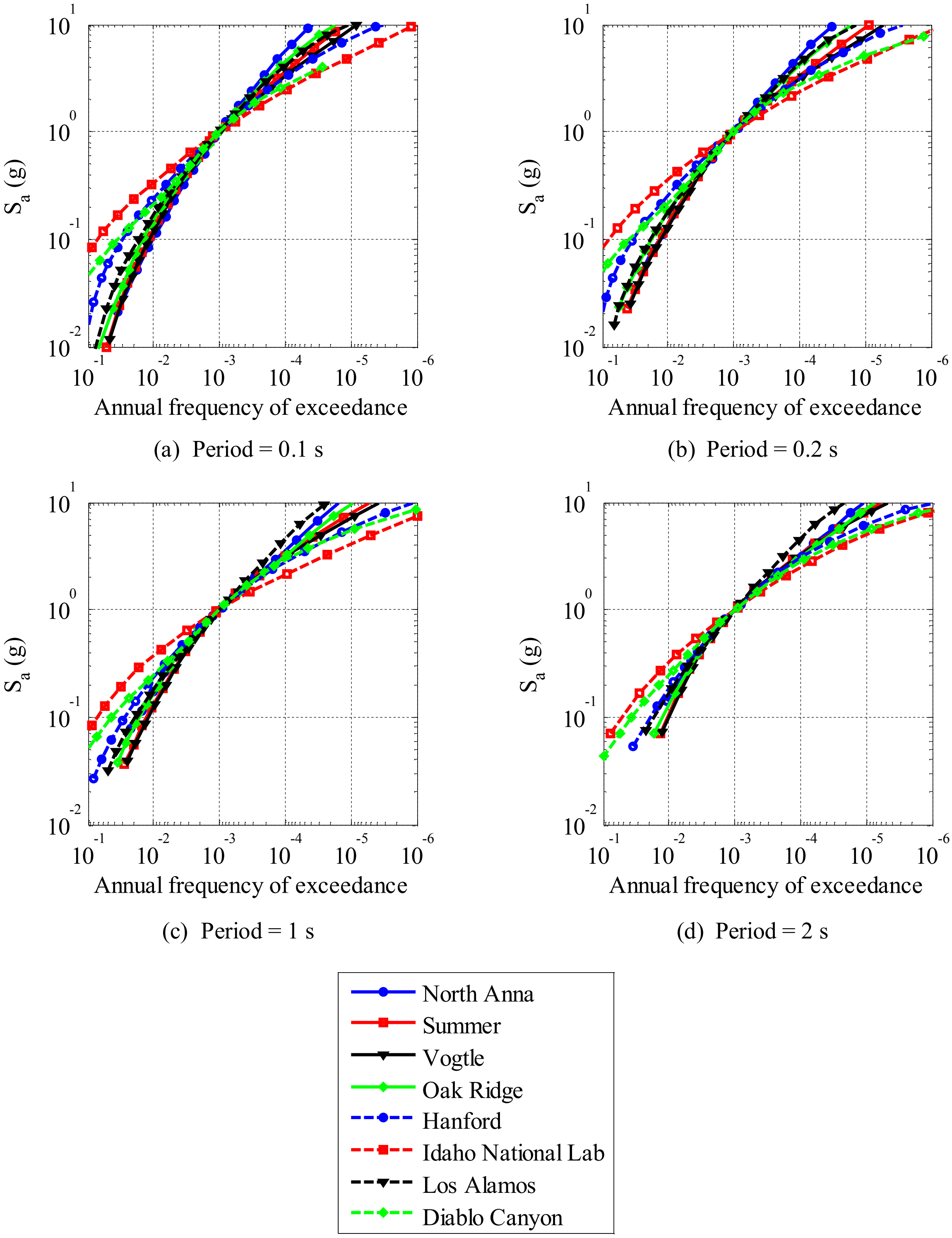

Figure 6-3: Seismic hazard curves normalized by the spectral ordinate at an annual frequency of exceedance of 10^{-3}

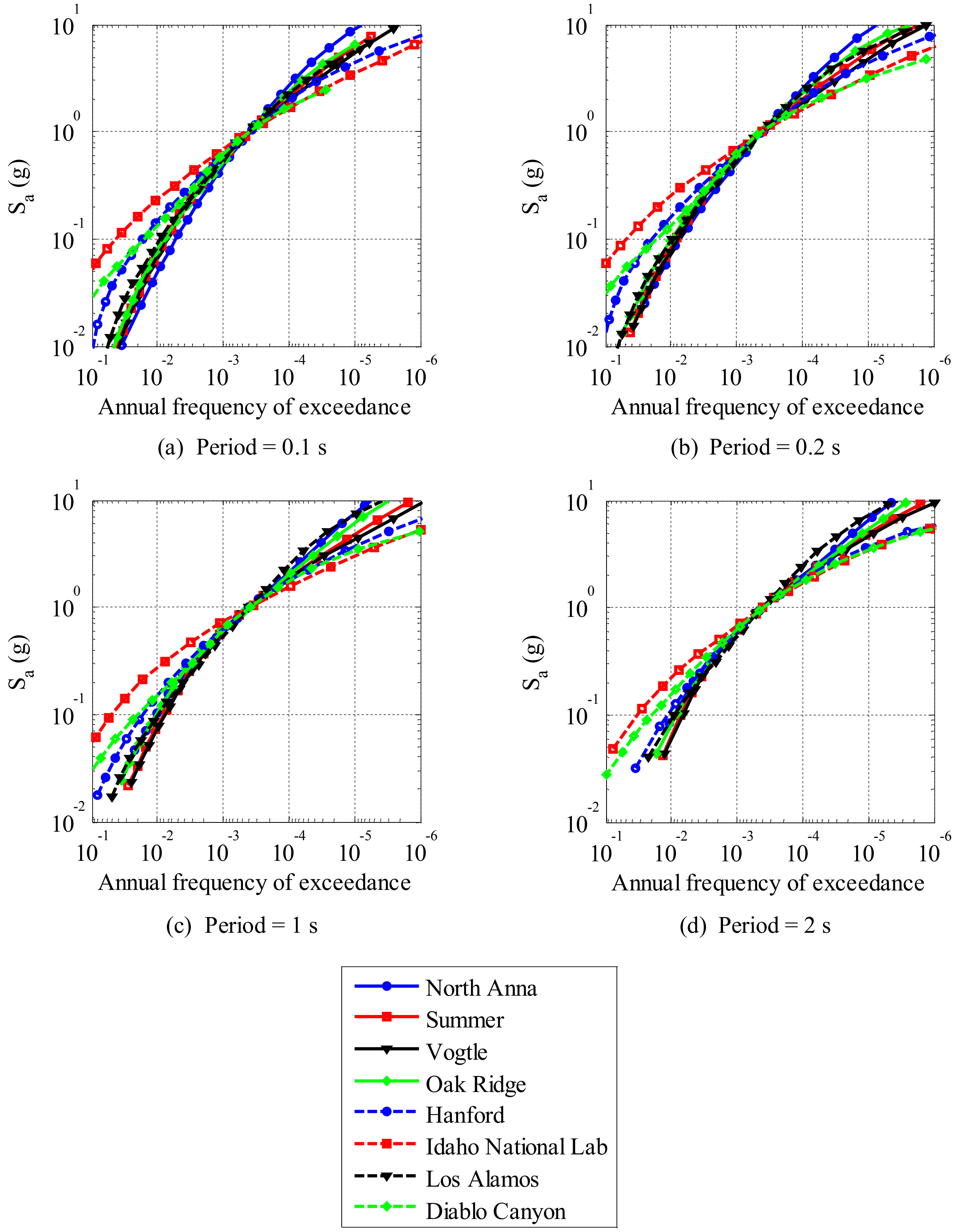

Figure 6-4: Seismic hazard curves normalized by the spectral ordinate at an annual frequency of exceedance of 4×10^{-4}

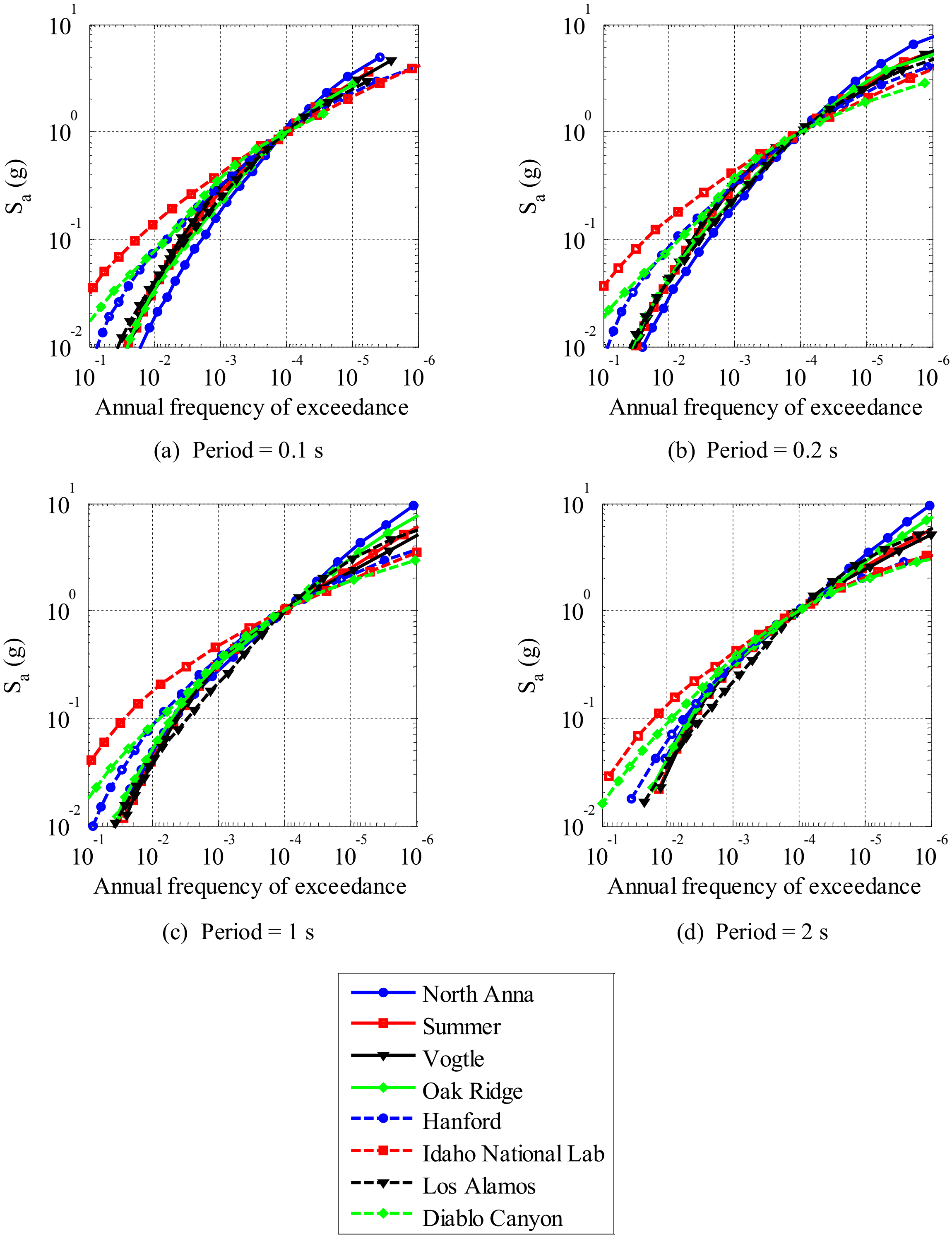

Figure 6-5: Seismic hazard curves normalized by the spectral ordinate at an annual frequency of exceedance of 10^{-4}

Table 6-1: Values of A_R for sites of nuclear facilities in the United States

Period (s)	H_D	Site							
		North Anna	Summer	Vogtle	Oak Ridge	Hanford	Idaho	Los Alamos	Diablo Canyon
0.1	10^{-2}	9.8	8.2	8.3	6.7	4.2	2.9	6.0	4.7
	10^{-3}	5.6	3.6	3.3	4.5	3.2	2.4	4.2	2.7
	10^{-4}	3.4	2.9	2.8	2.8	2.3	2.1	2.5	-[1]
0.2	10^{-2}	7.2	7.3	7.6	5.5	3.9	2.8	5.7	4.7
	10^{-3}	5.0	3.3	3.1	4.1	3.1	2.3	4.3	2.7
	10^{-4}	3.4	2.8	2.5	2.9	2.3	2.0	2.6	1.9
1	10^{-2}	5.5	7.7	8.1	5.9	4.2	2.7	5.5	4.0
	10^{-3}	3.6	3.2	3.1	3.2	2.7	2.1	4.6	2.9
	10^{-4}	3.5	2.5	2.3	3.1	2.1	1.9	2.9	1.9
2	10^{-2}	6.5	9.3	9.8	7.6	5.5	3.1	5.8	4.0
	10^{-3}	3.3	3.3	3.2	3.1	3.0	2.5	4.6	2.8
	10^{-4}	3.2	2.5	2.4	2.8	2.0	2.0	2.9	2.0

[1] Information not available at the USGS website.

$$DF = \max\left(1.0,\ 0.6\left(A_R\right)^{\alpha}\right) \tag{6-2}$$

where α is 0.4 (0.8, 0.8) for SDC 3 (4, 5), and A_R is

$$A_R = \frac{SA_{0.1H_D}}{SA_{H_D}} \tag{6-3}$$

where $SA_{0.1H_D}$ and SA_{H_D} are 5% damped spectral accelerations corresponding to annual frequencies of exceedance of 0.1 H_D and H_D, respectively.

Figures 6-3, 6-4 and 6-5 show that the values of A_R depend strongly on the site and the value of MAFE considered. North Anna is an Eastern US site; Hanford is a Western US site. For a period of 0.1 s and MAFE of 10^{-2} (10^{-3}, 10^{-4}), A_R for these two sites are 9.8 (5.6, 3.4) and 4.2 (3.2, 2.3), respectively. The values of A_R for all eight sites are listed in Table 6-1. Focusing on an MAFE of 10^{-4}, which is the basis for the design of nuclear power plants (NPPs) in the United

States, it is clear that A_R is greater in the Eastern and Central United States than in the Western United States, irrespective of period. For conventional (fixed-base) nuclear facilities, the data at periods of 0.1 s and 0.2 s are relevant for calculating the design factor. For isolated nuclear facilities, the data at periods of 1 s and 2 s must also be considered.

6.3.2 Performance objectives

The design of non-isolated, safety-related nuclear structures follows a graded approach. Five seismic design categories (SDCs 1 through 5) and four limit states (A, B, C and D) are considered, as introduced previously.

The target frequencies of unacceptable performance, P_F, for the three SDCs (3, 4 and 5) are 10^{-4}, 4×10^{-5} and 10^{-5} for shaking with mean annual exceedance frequencies, H_D, of 4×10^{-4}, 4×10^{-4} and 10^{-4}, respectively. A probability ratio, R_P, is defined as the ratio of the H_D and P_F:

$$R_P = \frac{H_D}{P_F} \tag{6-4}$$

For SDC 5, which is appropriate for nuclear power plants, H_D, P_F and R_P are 10^{-4}, 10^{-5} and 10, respectively.

The design factor is derived considering uncertainties in seismic demand and deterministic component capacity, and expected component inelastic energy dissipation to achieve a target R_P. It is given by (e.g., USDOE (1994), ASCE (2005)):

$$DF = \frac{1}{F_{Np}} \left(R_P e^{-\left(X_P K_H \beta - \frac{1}{2}(K_H \beta)^2 \right)} \right)^{1/K_H} \tag{6-5}$$

where F_{Np} is the nominal frequency of unacceptable performance, K_H is a parameter to characterize the slope of the seismic hazard curve between two MAFEs[1] (wherein the slope is linear in the log-log space), β is a composite standard deviation associated with the mean seismic fragility curve, X_p is the standard normal variable corresponding to a failure probability, and other parameters were defined previously. The value of β typically ranges between 0.3 and 0.6 for nuclear structures and components (see Section 2.2.1.2 of the commentary to ASCE 43-05). The parameter K_H in (6-5) and A_R in (6-2) are related by (ASCE, 2005)

$$K_H = \frac{1}{\log(A_R)} \tag{6-6}$$

where all parameters were defined previously. The DF given by (6-5) is approximated using (6-2), which is derived from a regression analysis between DF and A_R for different values of R_P and β (e.g., USDOE (1994)).

The target performance goals specified in ASCE 43-05 can also be achieved if it is demonstrated that 1) the probability of unacceptable performance under the seismic hazard DRS is less than 1%, and 2) the probability of unacceptable performance under 1.5 times DRS is less than 10%. It is shown in the commentary to the ASCE 43-05 that the target performance goals for the three SDCs (3, 4 and 5) are reasonably achieved if the above two criteria are satisfied and DF is given by (6-2).

[1] A ten-fold ratio is considered (e.g., between MAFEs of 10^{-4} and 10^{-5}).

6.4 Seismically Isolated Nuclear Power Plants

6.4.1 Seismic hazard definition

The draft United States Nuclear Regulatory Commission guideline (NUREG) entitled "Technical considerations for seismic isolation of nuclear facilities" (Kammerer *et al.*, forthcoming) identifies two levels of seismic hazard for design, namely, a ground motion response spectrum+ (GMRS+) and an extended design basis (EDB) GMRS. The GMRS is calculated per Regulatory Guide RG 1.208 (USNRC, 2007a), "A performance-based approach to define the site-specific earthquake ground motion". This Regulatory Guide is based on ASCE 43-05 (ASCE, 2005), which was drafted for conventional (fixed-base) nuclear structures. The GMRS is the product of the UHRS with an MAFE of 10^{-4} (SDC 5) and DF, and is similar to the DRS for conventional nuclear structures. The GMRS+ is the envelope of the GMRS and a regulator-specific minimum response spectrum (e.g., an appropriate spectral shape anchored to a peak ground acceleration of 0.1 g). The EDB GMRS envelopes a uniform hazard response spectrum with an MAFE of 10^{-5} and a spectrum with ordinates 167% of the GMRS+.

6.4.2 Performance objectives

The following performance goals are outlined in Kammerer *et al.* (forthcoming) for the isolated superstructure, individual isolators and umbilical lines: 1) the probability of the isolated superstructure striking the surrounding hard stop should be less than 1% for GMRS+ shaking, 2) the probability of the isolated superstructure striking the hard stop should be less than 10% for EDB GMRS shaking, 3) the probability of loss of axial load capacity of the isolators at a displacement equal to the clearance to the hard stop (CHS) should be less than 10%, and 4) there should be a less than 10% probability of loss for function for safety-related umbilical lines at a displacement equal to the CHS. These performance objectives are satisfied by providing the CHS equal to or greater than the 90th percentile displacement under EDB GMRS shaking[1], and designing/testing the bearings and umbilical lines to perform with 90% confidence at a displacement equal to the CHS. The performance objectives are summarized in Table 6-2. The annual frequencies of unacceptable performance for the isolated superstructure, individual isolators and the umbilical lines are estimated in the following section, assuming the objectives of Table 6-2 are achieved.

Table 6-2: Performance and design expectations for seismically isolated nuclear power plant structures[1] (adapted from Kammerer *et al.* (forthcoming))

Ground motion levels	Isolation system: Isolation unit and system design and performance criteria	Isolation system: Approach to demonstrating acceptable performance of isolator unit	Superstructure design and performance	Umbilical line design and performance	Moat or hard stop design and performance
GMRS+[2] The envelope of the RG1.208 GMRS and the minimum foundation input motion[3] for each spectral frequency	No long-term change in mechanical properties. Extremely high confidence of the isolation system surviving without damage when subjected to the mean displacement of the isolator system under the GMRS+ loading.	Production testing must be performed on each isolator for the mean system displacement under the GMRS+ loading level and corresponding axial force.	The superstructure design and performance must conform to NUREG-0800 under GMRS+ loading.	Umbilical line design and performance must conform to NUREG-0800 under GMRS+ loading.	The moat is sized such that there is less than 1% probability of the superstructure contacting the moat or hard stop under GMRS+ loading.
EDB[4] GMRS The envelope of the ground motion amplitude with a mean annual frequency of exceedance of $1x10^{-5}$ and 167% of the GMRS+ spectral amplitude	90% probability of each isolator and the isolation system surviving without loss of gravity-load capacity at the mean displacement under EDB GMRS loading.	Prototype testing must be performed on a sufficient number of isolators at the CHS[5] displacement and the corresponding axial force to demonstrate acceptable performance with 90% probability. Limited isolator unit damage is acceptable but load-carrying capacity must be maintained.	There should be less than a 10% probability of the superstructure contacting the moat or hard stop under EDB GMRS loading.	Greater than 90% probability that each type of safety-related umbilical line, together with its connections, remains functional for the CHS displacement. Performance can be demonstrated by testing, analysis or a combination of both.[6]	CHS displacement must be equal to or greater than the 90th percentile isolation system displacement under EDB GMRS loading. Moat or hard stop designed to survive impact forces associated with 95th percentile EDB GMRS isolation system displacement.[7] Limited damage to the moat or hard stop is acceptable but the moat or hard stop must perform its intended function.

1. Analysis and design of safety-related components and systems should conform to NUREG-0800, as in a conventional (non-isolated) nuclear structure.
2. 10CFR50 Appendix S requires the use of an appropriate free-field spectrum with a peak ground acceleration of no less than 0.10g at the foundation level. RG1.60 spectral shape anchored at 0.10g is often used for this purpose.
3. The analysis can be performed using a single composite spectrum or separately for the GMRS and the minimum spectrum.
4. The analysis can be performed using a single composite spectrum or separately for the 10^{-5} MAFE response spectrum and 167% GMRS.
5. CHS=Clearance to the Hard Stop
6. Seismic Category 2 SSCs whose failure could impact the functionality of umbilical lines should also remain functional for the CHS displacement.
7. Impact velocity calculated at the displacement equal to the CHS assuming cyclic response of the isolation system for motions associated with the 95th percentile (or greater) EDB displacement.

[1] It was shown in Chapter 5 that the clearance to the hard stop is controlled by the 90th percentile EDB GMRS displacement.

6.5 Spectral Demands for Conventional and Isolated Nuclear Power Plants

This section compares the definitions of seismic hazard for conventional and seismically isolated nuclear power plant structures, namely, 1) UHRS[1] at MAFE of 10^{-4}, 2) $1.67\times$UHRS at MAFE of 10^{-4}, 3) UHRS at MAFE of 10^{-5}, and 4) $DF\times$UHRS at MAFE of 10^{-4}, for the eight sites of Figure 6-2 and 5% damping. Spectral acceleration at an MAFE is computed assuming a linear variation of spectral acceleration with MAFE between two adjacent data points on the seismic hazard curve in the logarithmic space (see Section 6.2). The first three hazard definitions are relevant for seismically isolated nuclear power plants and the fourth, given by (6-1), forms the design basis for conventional (non-isolated) nuclear power plants. The design factor, DF, is computed for SDC 5, which is appropriate for nuclear power plant structures, per (6-2) and is used to calculate the DRS for a conventional (non-isolated) nuclear power plant. Figure 6-6(a) presents the 5%-damped spectral acceleration ordinates for the four hazard levels, for the North Anna site, at periods of 1 s and 2 s: periods relevant for isolated nuclear structures. The ordinates at 1 s (2 s) are 0.12 g (0.06 g), 0.19 g (0.09 g), 0.19 g (0.09 g) and 0.41 g (0.19 g) for the UHRS at MAFE of 10^{-4}, $DF\times$UHRS at MAFE of 10^{-4}, $1.67\times$UHRS at MAFE of 10^{-4}, and UHRS at MAFE of 10^{-5}, respectively. Figures 6-6(b) through 6-6(h) present the ordinates for the other seven sites. The ordinates for $1.67\times$UHRS at MAFE of 10^{-4} are a) greater than those of the DRS for conventional nuclear structures, namely, $DF\times$UHRS at MAFE of 10^{-4}, and b) always smaller than those of the UHRS at MAFE of 10^{-5}. The spectral accelerations presented in Figure 6-6 are tabulated in Table 6-3 and the return periods corresponding to the spectral accelerations are listed in Table 6-4.

[1] It is demonstrated later in the chapter that the design factors can be set equal to 1.0 for seismically isolated nuclear power plants.

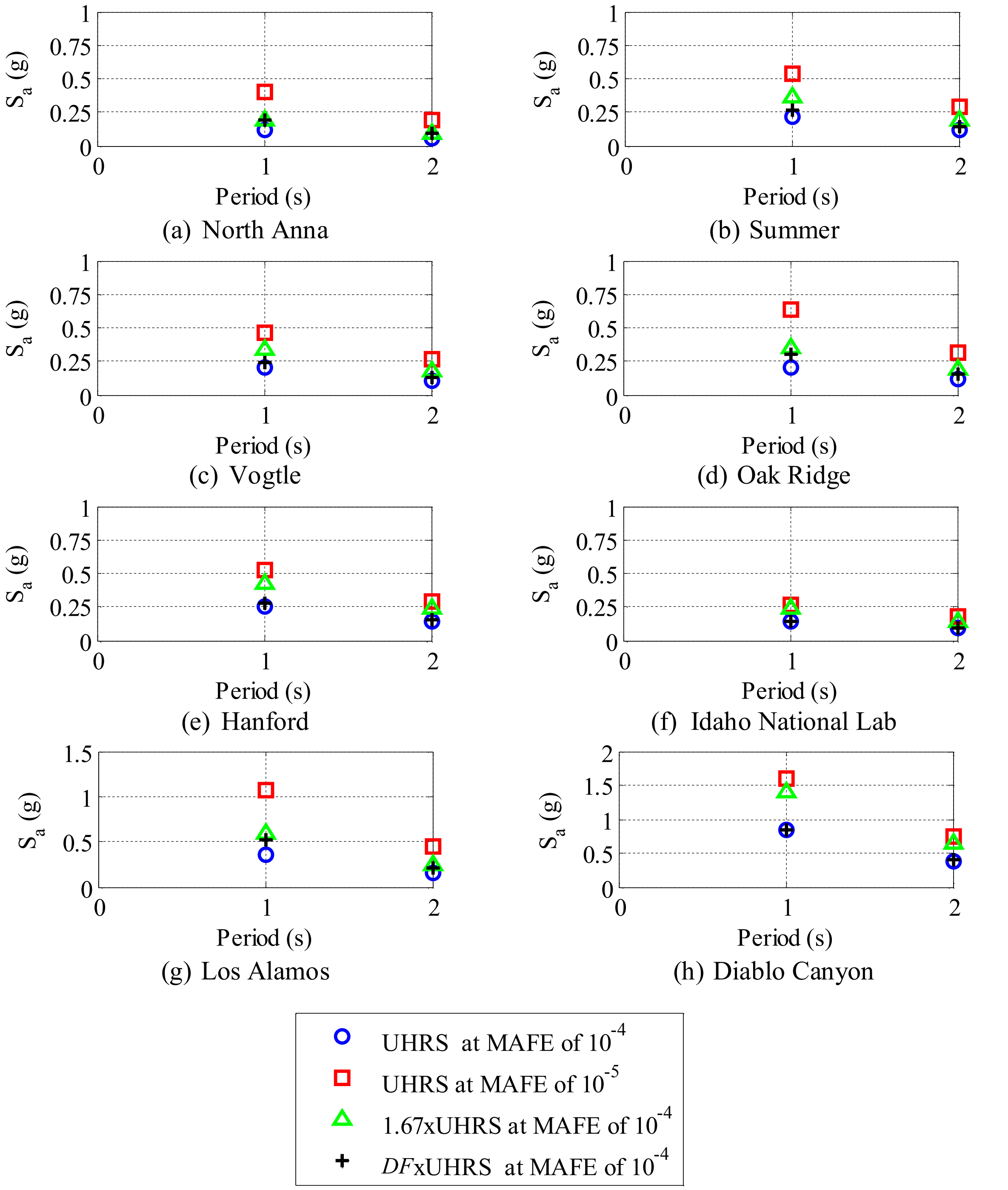

Figure 6-6: Spectral ordinates corresponding to different definitions of seismic hazard at eight sites of nuclear facilities; 5% damping

Table 6-3: Five percent damped spectral ordinates (in g) at 1 s and 2 s for seismic hazards defined for conventional and seismically isolated nuclear power plants at eight sites of nuclear facilities (also see Figure 6-6)

Period (s)	Hazard definition	Site							
		North Anna	Summer	Vogtle	Oak Ridge	Hanford	Idaho	Los Alamos	Diablo Canyon
1	UHRS1[1]	0.12	0.22	0.20	0.21	0.25	0.14	0.36	0.83
	UHRS2[2]	0.41	0.54	0.47	0.64	0.53	0.27	1.06	1.59
	1.67×UHRS1	0.19	0.36	0.34	0.35	0.42	0.23	0.60	1.39
	DF×UHRS1	0.19	0.27	0.24	0.31	0.27	0.14	0.51	0.84
2	UHRS1	0.06	0.12	0.11	0.11	0.14	0.09	0.15	0.38
	UHRS2	0.19	0.29	0.26	0.31	0.29	0.18	0.44	0.75
	1.67×UHRS1	0.10	0.19	0.18	0.19	0.24	0.15	0.25	0.64
	DF×UHRS1	0.09	0.15	0.13	0.15	0.15	0.09	0.21	0.39

[1]UHRS with an MAFE of 10^{-4}
[2]UHRS with an MAFE of 10^{-5}

Table 6-4: Return periods corresponding to the 5% damped spectral accelerations at 1 s and 2 s reported in Table 6-3 (in 1000s of years)

Period (s)	Hazard definition	Site							
		North Anna	Summer	Vogtle	Oak Ridge	Hanford	Idaho	Los Alamos	Diablo Canyon
1	UHRS1[1]	10	10	10	10	10	10	10	10
	UHRS2[2]	100	100	100	100	100	100	100	100
	1.67×UHRS1	25	35	39	28	46	61	26	59
	DF×UHRS1	24	17	15	21	13	10	19	10
2	UHRS1	10	10	10	10	10	10	10	10
	UHRS2	100	100	100	100	100	100	100	100
	1.67×UHRS1	28	34	36	31	48	48	26	54
	DF×UHRS1	24	17	16	20	12	12	19	11

[1]UHRS with an MAFE of 10^{-4}
[2]UHRS with an MAFE of 10^{-5}

6.6 Annual Frequency of Unacceptable Performance of Isolated Nuclear Power Plants

6.6.1 Hazard definition

The seismic hazard is defined, for the purpose of estimating the annual frequency of unacceptable performance, as multiples, m, of the UHRS at MAFE of 10^{-4}, taken as the average of the spectral acceleration ordinates at 1 s and 2 s[1, 2] reported in Figure 6-1. This definition does not include the design factor recommended by RG 1.208 and ASCE 43-05 at the MAFE of 10^{-4} (see Section 6.3.1) for the reason shown later. The seismic hazard curves considered for the nuclear facilities at the eight sites of Figure 6-2 are plotted in Figure 6-7.

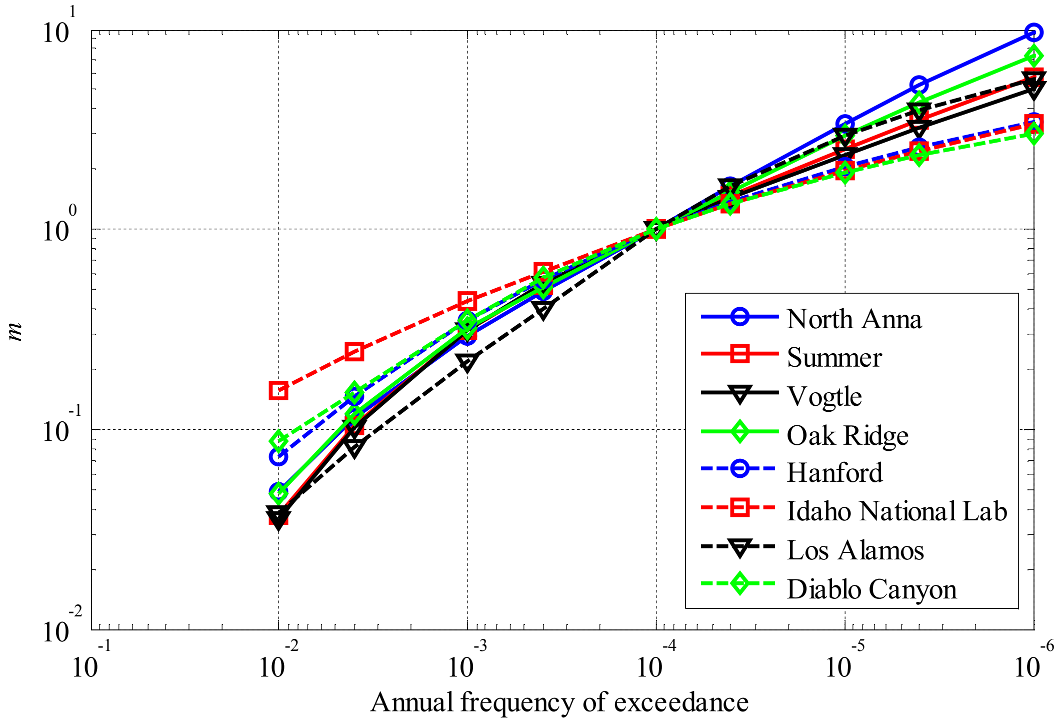

Figure 6-7: Annual frequency of exceedance of multiples, *m*, of UHRS with MAFE of 10^{-4}

6.6.2 Annual frequency of unacceptable performance of the isolated superstructure

The superstructure of a seismically isolated nuclear power plant will include structural components that will be designed in accordance with materials standards such as ACI 349 (ACI, 2013a), ACI 359 (ACI, 2013b) and AISC N690 (AISC, 2012) and safety-critical mechanical and electrical systems and components designed in accordance with standards prepared by the

[1] The periods of 1 s and 2 s are relevant for seismically isolated structures, as noted previously.
[2] The amplification ratios for 1 s and 2 s and at MAFE of 10^{-4} differ by less than 10% for the eight sites of Table 6-1.

American Society of Mechanical Engineers (ASME) and the Institute of Electrical and Electronics Engineers (IEEE). These structural, mechanical and electrical components must be designed, per materials standards, for the forces, displacements and accelerations associated with GMRS+ shaking per Table 6-2, as a minimum.

Seismic isolation of certified plant designs has been proposed as a viable strategy to expand the use of nuclear power plants, where some of these certified designs have been seismically qualified for horizontal design basis shaking that is represented by a USNRC RG 1.60 (USAEC (1973), USNRC (2014)) spectrum anchored to peak ground acceleration of 0.3 g. For this spectrum and peak acceleration, and assuming that the period of the fixed-base superstructure is in the range of 0.1 to 0.3 seconds, the horizontal spectral response at 5% damping will be no less than 0.75 g, which would form the design basis for the structural components. The mechanical and electrical safety-related systems and components would be typically designed, per ASME and IEEE standards, for floor spectral demands much in excess of 1.0 g. If the annual frequency of unacceptable performance of structures, systems and components in a (fixed-base) certified plant design meets the requirements of USNRC, there will exist a considerable margin if the certified plant is seismically isolated. Noting that the focus to date has been on response to horizontal shaking, the response to vertical shaking will be no better and no worse if the superstructure is isolated using either sliding or elastomeric bearings. In summary, the isolation of a certified plant design will reduce the annual frequency of unacceptable performance of the superstructure below the value permitted by the USNRC.

Huang *et al.* (2010) showed that the seismic robustness of structures, systems and components (SSCs) in nuclear power plants could be substantially reduced if the plant was seismically isolated. The associated reduction in cost of the structures, systems and components could substantially offset (or eliminate) the costs associated with the seismic isolators, pedestals, foundation and associated excavation (if the plant is embedded). If this reduction in demand is incorporated in design, the nuclear steam supply system vendor would have to demonstrate, through plant-level systems analysis, that the resultant SSC designs met USNRC-required performance goals.

Herein, it is assumed that the annual frequency of unacceptable performance of the isolated superstructure, system and components is less than that of the corresponding fixed-base nuclear power plant.

One requirement of the forthcoming seismic isolation NUREG is that there be a less than 10% probability of the superstructure impacting the moat or hard stop under EDB GMRS shaking. This deterministic objective is met by setting the clearance to the stop, along each horizontal axis of the plant, to be no less than the 90th percentile displacement calculated for EDB GMRS shaking along that axis. Analysis of the isolated superstructure for impact loadings associated with collision with the hard stop is not required if this clearance to the hard stop is provided.

6.6.3 Annual frequency of unacceptable performance of the isolation system

In the seismic domain, the isolation system represents a singleton: failure of the isolation system could correspond to unacceptable performance of the nuclear plant in terms of core damage or large release of radiation. It is not possible to generically relate the failure of individual isolators to the failure of an isolation system. The failure of one isolator in a system of four could trigger system failure. The failure of one isolator in a system of 250 would be inconsequential. Herein, and very conservatively, the failure of one isolator is assumed to represent the failure of the isolation system.

To compute the annual frequency of unacceptable performance of an isolator unit, an isolator-unit fragility function must be convolved over an appropriate seismic hazard curve. The hazard curves assumed here for the eight sites of Figure 6-2 are based on the averaged values, site by site, for periods of 1.0 and 2.0 seconds. The fragility function for an isolator unit is defined by a median, θ, and log standard deviation, β, as follows

$$\theta - X_p\beta = \log(m) \tag{6-7}$$

where X_p corresponds to a probability of exceedance of p for a normally distributed data set, and other parameters were defined previously. If tight quality control on isolator production is maintained, the variability in the properties of isolator units of a given size will be small. Three values of β are considered here, namely, 0.01, 0.02 and 0.05. If a hard stop is constructed, the probability of isolator failure at calculated displacements equal to or greater than the clearance to the hard stop (CHS) is equal to that at the hard stop. Two calculations of the annual frequency of isolator failure are performed below, one assuming that no hard stop is present and one assuming the hard stop is installed at the 90th percentile EDB GMRS displacement.

As noted in Section 6.4.2, isolators are *prototype* tested to ensure that they can sustain the 90th percentile EDB GMRS displacement and the co-existing axial force with 90+% confidence. Practically, this requires all of the prototype isolators to resist this combination of displacement and axial force unless very large numbers of prototypes are to be tested (to achieve the 90+% confidence). Likely a small number of *prototype* isolators will be tested to greater displacements and forces to demonstrate compliance. Assume that the displacement capacity of the isolation system is equal to the 90th percentile displacement for EDB GMRS shaking, which is approximately equal to the median displacement for 110% EDB GMRS[1] shaking, as shown in Chapter 7. Based on this assumption, and values of 90% (1 isolator in 10 fails), 95% (1 isolator in 20 fails) and 99% (1 isolator in 100 fails) confidence, (6-7) is rewritten as:

$$\theta - \alpha\beta = \log\left(f_{AR} \times \overline{A}_R\right) \tag{6-8}$$

where α is 1.28, 1.64, and 2.33, respectively, and f_{AR} is 1.1. The fragility curves for isolators tested with 90% confidence at median displacement for 110% EDB GMRS shaking (or 90th percentile displacement for EDB GMRS shaking) are shown in Figure 6-8. The fragility curves for 95% and 99% confidence at median displacement for 110% EDB GMRS shaking are shown in Figures 6-10 and 6-11, respectively. Figure 6-12 presents fragility curves for 90% confidence at median displacement for 125% EDB GMRS shaking $\left(f_{AR} = 1.25\right)$.

The total annual frequency of unacceptable performance of the isolation system, $P_{F,\text{isolation}}$, is given by (e.g., ASCE (2005)):

$$P_{F,\text{isolation}} = -\int_0^{\infty} \frac{d}{dm} H_D \times \left(P_f \mid GM = m\right) dm \tag{6-9}$$

where $\left(P_f \mid GM = m\right)$ is the annual frequency of unacceptable performance conditioned on m times UHRS shaking at an MAFE of 10^{-4}, and other parameters were defined previously. Table 6-5 presents a sample calculation of $P_{F,\text{isolation}}$ for the site of Diablo Canyon, and β, α and f_{AR} set equal to 0.01, 1.28 and 1.1, respectively (i.e., 90% confidence on bearings tested at median

[1] These calculations are performed in Chapter 7 for three sites, namely, Diablo Canyon, Vogtle and North Anna, to cover the range of A_R at H_D of 10^{-4} for 1 s and 2 s and the eight sites of Figure 6-2 (see Table 6-1). One hundred and ten percent is appropriate for Diablo Canyon and conservative (low) for the other eight sites.

displacement for 110% EDB GMRS shaking). The hazard and fragility curves for Diablo Canyon, plotted in Figures 6-7 and 6-8(a), respectively, are used to generate Table 6-5. This data can be used to disaggregate the risk, as presented in Figure 6-9(a). Table 6-6 presents the same calculation as Table 6-5, but for the site of North Anna; corresponding disaggregation of risk is presented in Figure 6-9(b). The disaggregated risk peaks at m of 2.2 and 3.9 for the two sites, respectively, which correspond to 1.14 and 1.16 times the EDB GMRS shaking at Diablo Canyon and North Anna, respectively. Shifting the peaks to greater values of m would reduce total risk, because the disaggregated risk for a given range of m would correspond to a smaller H_D. This shift can be achieved by either testing the bearings with a greater confidence or testing them for greater displacements and axial forces (i.e., greater shaking intensity).

The annual frequencies of exceedance for the eight sites of Figure 6-2 are presented in Tables 6-7, 6-8, 6-9 and 6-10 corresponding to the fragility curves of Figures 6-8, 6-10, 6-11 and 6-12, respectively. The frequencies are less than 10^{-5} for all combinations of site and β. Expectedly, the annual frequency of unacceptable performance of the isolation system decreases if the bearings are tested with a greater confidence at a given displacement.

Importantly, the annual frequency of unacceptable performance for the isolation system will be much smaller than the values presented in Tables 6-7, 6-8, 6-9 and 6-10, because 1) failure of a small fraction of the isolators in an isolation system will not compromise the performance of the isolation system, and 2) the displacement and force demands on the isolators will not be fully correlated. (The prototype isolators will be tested by type, for maximum and not average axial forces and displacements.)

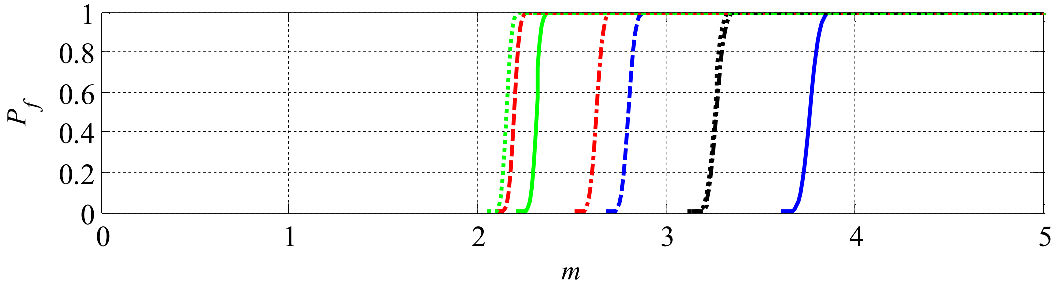

(a) β = 0.01

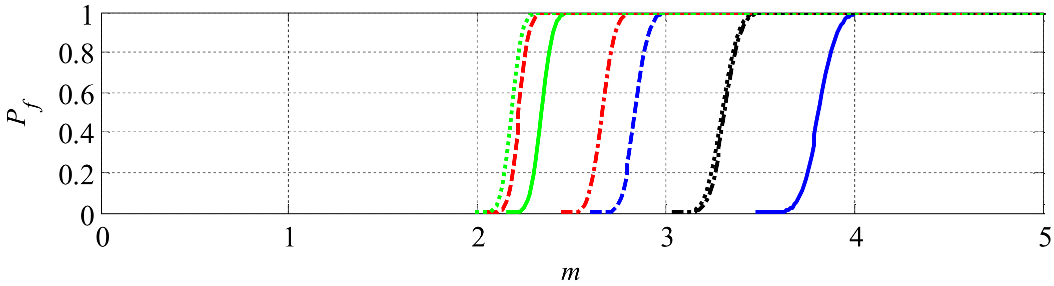

(b) β = 0.02

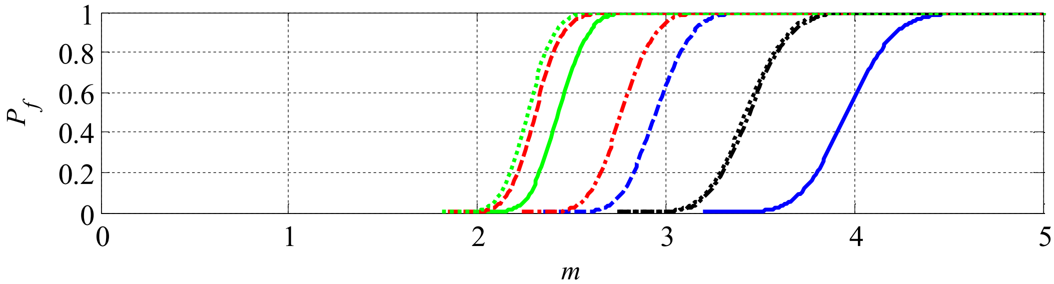

(c) β = 0.05

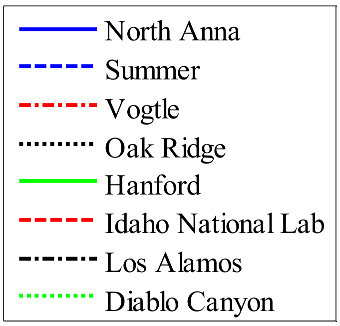

Figure 6-8: Probability of unacceptable performance, P_f, of individual isolator units for 90% confidence at median displacement for 110% EDB GMRS shaking plotted against multiples, *m*, of UHRS shaking with MAFE of 10^{-4}, without a hard stop

Table 6-5: Example calculation of total annual frequency of unacceptable performance of individual isolator units at Diablo Canyon for β = 0.01, f_{AR} = 1.1 and α = 1.28 (90% confidence)

1	2	3	4	5	6	7	8
m_1	m_2	$m_3 = (m_1 + m_2)/2$	$P_f(m_3)$ [1]	$H_D(m_1)$	$H_D(m_2)$	ΔH_D (Col 5 – 6)	$P_f(m_3) \times \Delta H_D$
0.500	1.000	0.750	0	5.2×10^{-4}	1.0×10^{-4}	4.2×10^{-4}	0
1.000	1.500	1.250	0	1.0×10^{-4}	2.7×10^{-5}	7.3×10^{-5}	0
1.500	2.067	3.567	0	7.3×10^{-5}	7.2×10^{-5}	1.0×10^{-6}	0
2.067	2.087	2.077	1.4×10^{-4}	7.2×10^{-6}	6.8×10^{-6}	3.3×10^{-7}	4.7×10^{-11}
2.087	2.107	2.097	3.7×10^{-3}	6.8×10^{-6}	6.5×10^{-6}	3.1×10^{-7}	1.2×10^{-9}
2.107	2.147	2.127	0.1	6.5×10^{-6}	6.0×10^{-6}	5.8×10^{-7}	6.1×10^{-8}
2.147	2.187	2.167	0.73	6.0×10^{-6}	5.4×10^{-6}	5.2×10^{-7}	3.8×10^{-7}
2.187	2.207	2.197	0.98	5.4×10^{-6}	5.2×10^{-6}	2.4×10^{-7}	2.3×10^{-7}
2.207	2.227	2.217	1.0	5.2×10^{-6}	5.0×10^{-6}	2.3×10^{-7}	2.3×10^{-7}
2.227	2.247	2.237	1.0	5.0×10^{-6}	4.8×10^{-6}	2.2×10^{-7}	2.2×10^{-7}
2.247	2.500	3.768	1.0	4.8×10^{-6}	2.7×10^{-6}	2.1×10^{-6}	2.1×10^{-6}
2.500	3.000	2.750	1.0	2.7×10^{-6}	1.0×10^{-6}	1.7×10^{-6}	1.7×10^{-6}
3.000	4.000	3.500	1.0	1.0×10^{-6}	1.3×10^{-7}	8.7×10^{-6}	8.7×10^{-7}
4.000	5.000	4.500	1.0	1.3×10^{-7}	1.8×10^{-8}	1.1×10^{-7}	1.1×10^{-7}
5.000	5.288	5.144	1.0	1.8×10^{-8}	1.0×10^{-8}	8×10^{-9}	8×10^{-9}
					$P_{F,\text{isolation}} = \sum P_f(m_3) \times \Delta H_D = 5.9\times10^{-6}$		

[1] $P_f(m_3) = (P_f \mid GM = m_3)$

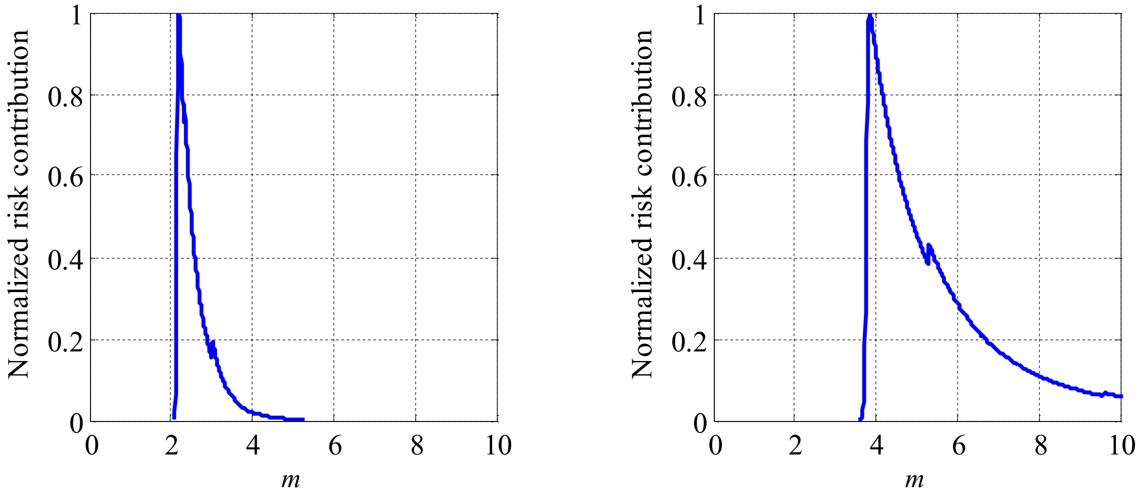

(a) Diablo Canyon (b) North Anna

Figure 6-9: Disaggregation of risk for individual isolators

Consider Tables 6-7 and 6-10 and the sites of Los Alamos and Diablo Canyon. Increasing the displacement for prototype isolator testing from median displacement for 110% EDB GMRS shaking to median displacement for 125% EDB GMRS shaking reduces the annual frequency of unacceptable performance by 30% to 50%. The percentage reduction is smaller for North Anna because a significant fraction of the risk accrues at large values of m (see Figure 6-9). The disaggregated risk for m between 4 and 5 is 2.6×10^{-6} for North Anna (see Table 6-6) and 1.1×10^{-7} for Diablo Canyon (see Table 6-5): a difference by a factor of more than 20.

Table 6-6: Example calculation of total annual frequency of unacceptable performance of individual isolator units at North Anna for β = 0.01, f_{AR} = 1.1 and α = 1.28 (90% confidence)

1	2	3	4	5	6	7	8
m_1	m_2	$m_3 = (m_1+m_2)/2$	$P_f(m_3)$ [1]	$H_D(m_1)$	$H_D(m_2)$	ΔH_D (Col 5 – 6)	$P_f(m_3)\times\Delta H_D$
0.500	1.000	0.750	0	3.8×10^{-4}	9.9×10^{-5}	2.8×10^{-4}	0
1.000	2.000	1.500	0	9.9×10^{-5}	2.7×10^{-5}	7.2×10^{-5}	0
2.000	3.000	2.500	0	2.7×10^{-5}	1.3×10^{-5}	1.4×10^{-5}	0
3.000	3.601	3.301	0	1.3×10^{-5}	8.8×10^{-6}	4.2×10^{-6}	0
3.601	3.641	3.621	5.4×10^{-5}	8.8×10^{-6}	8.6×10^{-6}	2.0×10^{-7}	1.1×10^{-11}
3.641	3.681	3.661	2.8×10^{-3}	8.6×10^{-6}	8.4×10^{-6}	1.9×10^{-7}	5.2×10^{-10}
3.681	3.721	3.701	4.6×10^{-2}	8.4×10^{-6}	8.2×10^{-6}	1.8×10^{-7}	8.4×10^{-9}
3.721	3.761	3.741	2.7×10^{-1}	8.2×10^{-6}	8.0×10^{-6}	1.8×10^{-7}	4.8×10^{-8}
3.761	3.801	3.781	6.7×10^{-1}	8.0×10^{-6}	7.9×10^{-6}	1.7×10^{-7}	1.2×10^{-7}
3.801	3.841	3.821	9.3×10^{-1}	7.9×10^{-6}	7.7×10^{-6}	1.7×10^{-7}	1.6×10^{-7}
3.841	3.881	3.861	9.9×10^{-1}	7.7×10^{-6}	7.5×10^{-6}	1.6×10^{-7}	1.6×10^{-7}
3.881	3.921	3.901	1	7.5×10^{-6}	7.4×10^{-6}	1.6×10^{-7}	1.6×10^{-7}
3.921	3.961	3.941	1	7.4×10^{-6}	7.2×10^{-6}	1.5×10^{-7}	1.5×10^{-7}
3.961	4.001	3.981	1	7.2×10^{-6}	7.1×10^{-6}	1.5×10^{-7}	1.5×10^{-7}
4.001	5	4.5005	1	7.1×10^{-6}	4.5×10^{-6}	2.6×10^{-6}	2.6×10^{-6}
5	10	7.5	1	4.5×10^{-6}	9.0×10^{-7}	3.6×10^{-6}	3.6×10^{-6}
10	20	15	1	9.0×10^{-7}	1.3×10^{-7}	7.7×10^{-7}	7.7×10^{-7}
20	40	30	1	1.3×10^{-7}	1.2×10^{-7}	1.2×10^{-7}	1.2×10^{-7}
					$P_{F,\text{isolation}} = \sum P_f(m_3)\times\Delta H_D = 8.0\times10^{-6}$		

[1] $P_f(m_3) = (P_f \mid GM = m_3)$

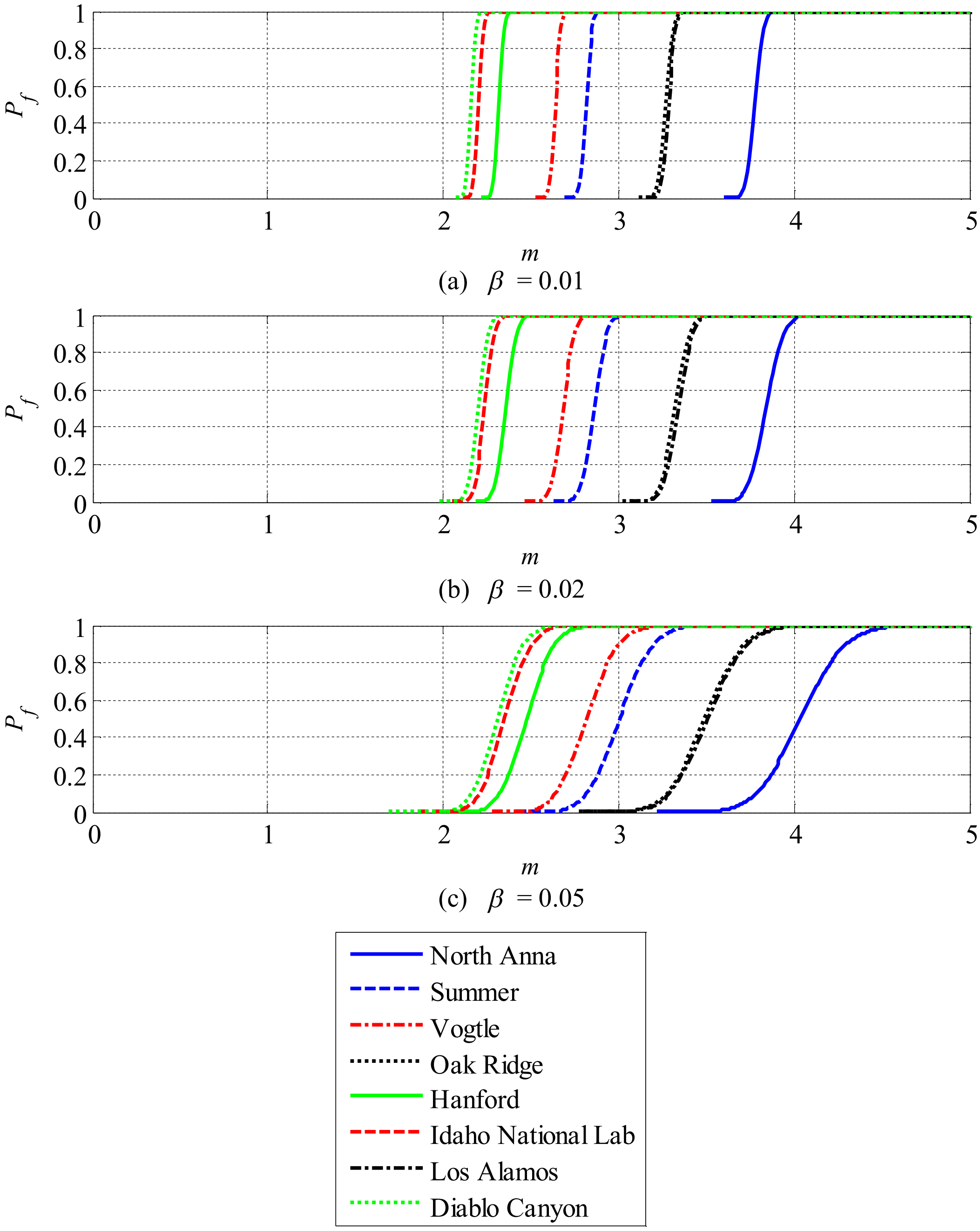

Figure 6-10: Probability of unacceptable performance, P_f, of individual isolator units for 95% confidence at median displacement for 110% EDB GMRS shaking plotted against multiples, m, of UHRS shaking with MAFE of 10^{-4}, without a hard stop

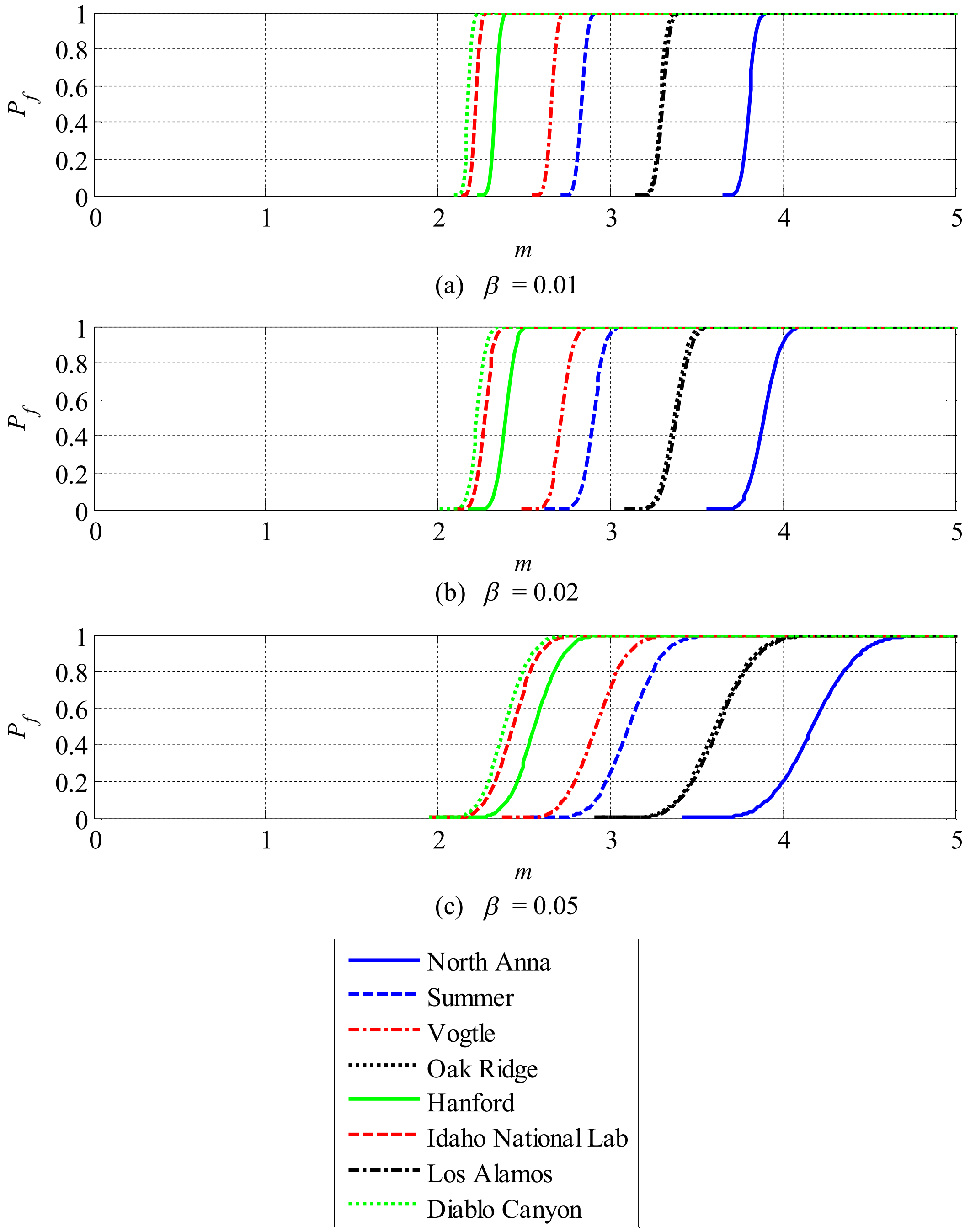

Figure 6-11: Probability of unacceptable performance, P_f, of individual isolator units for 99% confidence at median displacement for 110% EDB GMRS shaking plotted against multiples, m, of UHRS shaking with MAFE of 10^{-4}, without a hard stop

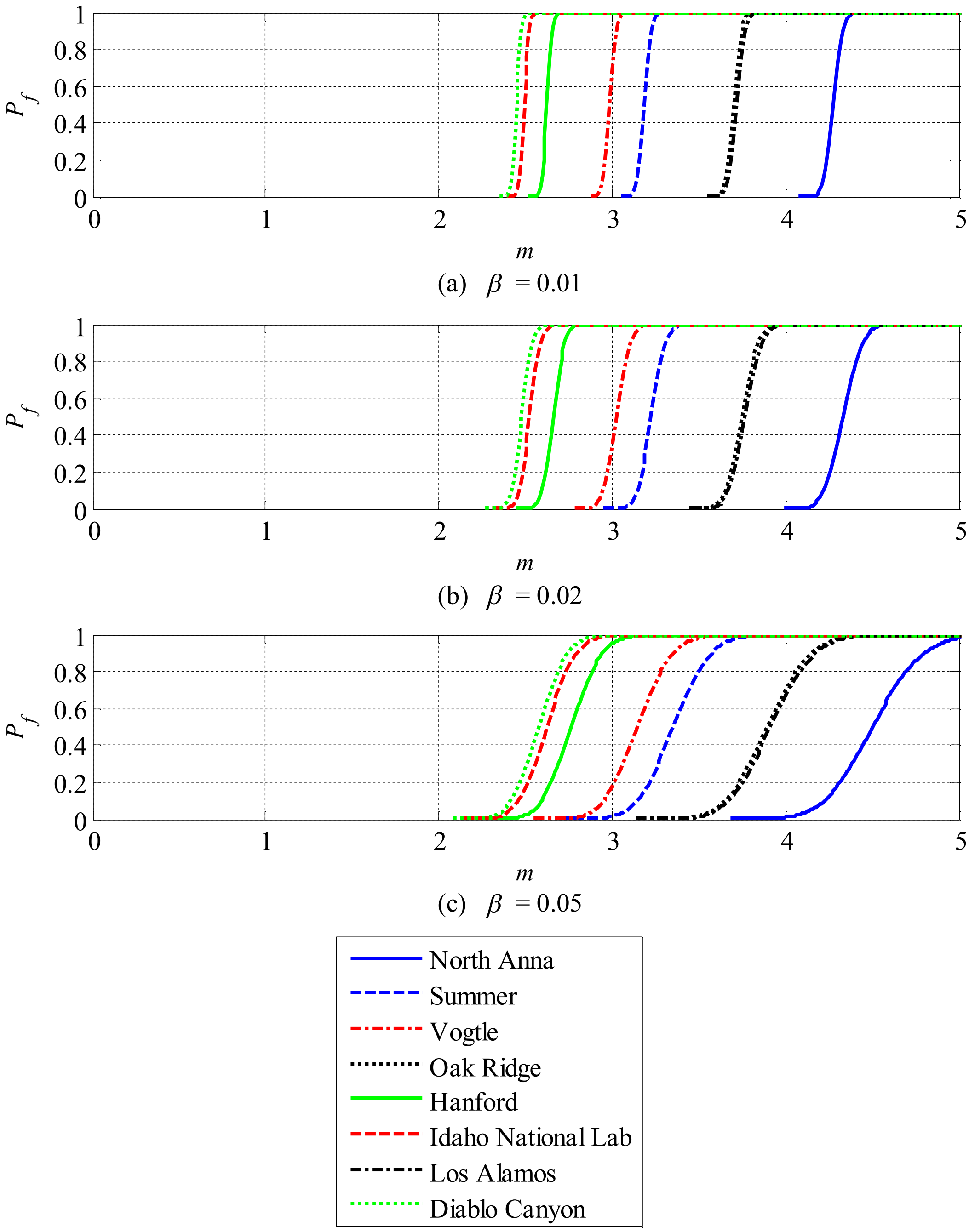

Figure 6-12: Probability of unacceptable performance, P_f, of individual isolator units for 90% confidence at median displacement for 125% EDB GMRS shaking plotted against multiples, m, of UHRS shaking with MAFE of 10^{-4}, without a hard stop

Table 6-7: Annual frequency of unacceptable performance ($\times 10^{-6}$) of individual isolator units tested with 90% confidence at median displacement for 110% EDB GMRS shaking, without a hard stop

	Site							
	North Anna	Summer	Vogtle	Oak Ridge	Hanford	Idaho	Los Alamos	Diablo Canyon
$\beta = 0.01$	8.0	7.5	7.2	7.8	6.5	6.5	7.1	5.9
$\beta = 0.02$	7.8	7.2	7.0	7.5	6.2	6.2	6.9	5.5
$\beta = 0.05$	7.3	6.6	6.3	6.9	5.3	5.4	6.2	4.7

Table 6-8: Annual frequency of unacceptable performance ($\times 10^{-6}$) of individual isolator units tested with 95% confidence at median displacement for 110% EDB GMRS shaking, without a hard stop

	Site							
	North Anna	Summer	Vogtle	Oak Ridge	Hanford	Idaho	Los Alamos	Diablo Canyon
$\beta = 0.01$	8.0	7.4	7.2	7.7	6.4	6.4	7.1	5.8
$\beta = 0.02$	7.7	7.1	6.8	7.4	6.0	6.0	6.7	5.4
$\beta = 0.05$	7.0	6.3	5.9	6.6	5.0	5.0	5.8	4.3

Table 6-9: Annual frequency of unacceptable performance ($\times 10^{-6}$) of individual isolator units tested with 99% confidence at median displacement for 110% EDB GMRS shaking, without a hard stop

	Site							
	North Anna	Summer	Vogtle	Oak Ridge	Hanford	Idaho	Los Alamos	Diablo Canyon
$\beta = 0.01$	7.9	7.3	7.0	7.6	6.2	6.2	6.9	5.6
$\beta = 0.02$	7.5	6.8	6.6	7.2	5.6	5.7	6.4	5.0
$\beta = 0.05$	6.5	5.7	5.3	6.1	4.3	4.3	5.2	3.6

Table 6-10: Annual frequency of unacceptable performance ($\times 10^{-6}$) of individual isolator units tested with 90% confidence at median displacement for 125% EDB GMRS shaking, without a hard stop

	Site							
	North Anna	Summer	Vogtle	Oak Ridge	Hanford	Idaho	Los Alamos	Diablo Canyon
$\beta = 0.01$	6.2	5.3	4.9	5.7	3.8	3.8	4.8	3.1
$\beta = 0.02$	6.0	5.1	4.7	5.6	3.6	3.6	4.6	2.9
$\beta = 0.05$	5.6	4.7	4.3	5.1	3.1	3.1	4.1	2.4

The peak isolator displacement will vary as a function of isolation system (period, coefficient of friction) and site. To enable a comparison of horizontal displacement demands at the eight sites, consider that 100,000-year spectral demands at a period of 2 s and 5% damping presented in Table 6-3. The spectral displacement at six of the eight sites of Figure 6-2, namely, North Anna, Summer, Vogtle, Oak Ridge, Hanford and Idaho are less than one half that at Diablo Canyon. Increasing the displacement capacity of the isolation system and testing the isolator units at one half of the 90th percentile displacement for EDB GMRS shaking at Diablo Canyon will reduce the risk of unacceptable performance but may not increase the cost of the isolation system. The corresponding isolator fragility curve can be derived approximately by increasing the factor f_{AR} in (6-8) by the ratio, κ, of one half the 100,000-year 2 s spectral acceleration for Diablo Canyon to the 100,000-year 2 s spectral acceleration at the site. The ratio κ ranges between 1.2 and 2.1 for the six sites. The fragility functions are shown in Figure 6-13 for β = 0.01, 0.02, and 0.05. The annual frequencies of unacceptable performance for the isolator units tested at a displacement (and corresponding axial force) equal to half the 90th percentile displacement for EDB GMRS shaking at Diablo Canyon are listed in Table 6-11. These frequencies are smaller than those reported in Table 6-7 by a factor of between 2 and 35.

The above calculations were performed assuming no hard stop was present. If a hard stop is constructed at the 90th percentile EDB GMRS displacement, the fragility curves presented in the Figures 6-8, 6-10, 6-11 and 6-12 will be truncated as shown in Figures 6-14, 6-15, 6-16 and 6-17, respectively. The corresponding annual frequencies of unacceptable performance of individual isolator units are listed in Tables 6-12, 6-13, 6-14 and 6-15, respectively. These frequencies are smaller than 10^{-6} for all combinations of site and β, and decrease substantially with greater confidence in an isolator's performance.

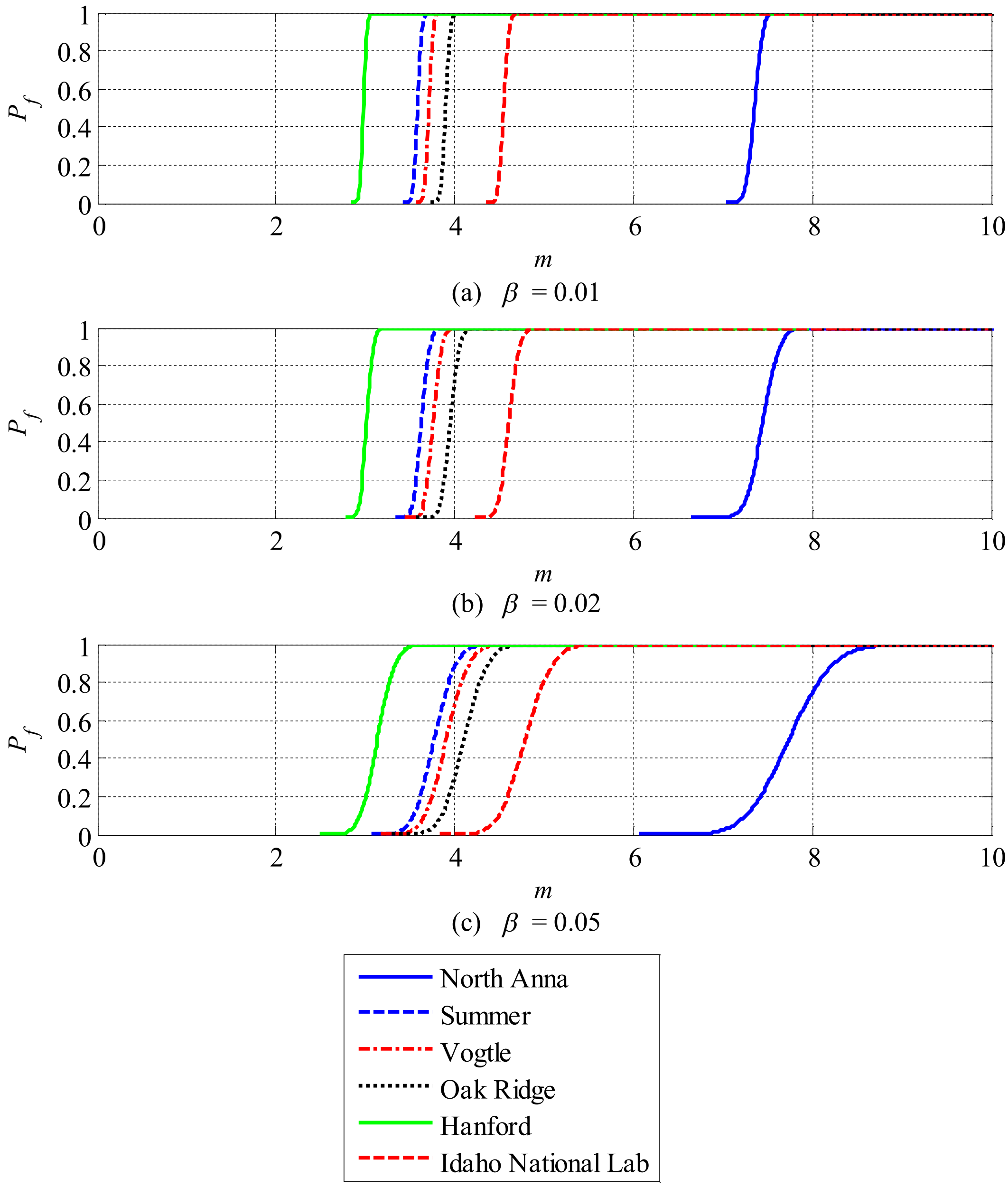

Figure 6-13: Probability of unacceptable performance, P_f, of the individual isolator units tested with 90% confidence at one half of the 90th percentile displacement for EDB GMRS shaking for Diablo Canyon ($f_{AR} = 1.1\kappa$) plotted against multiples, m, of UHRS shaking with MAFE of 10^{-4}, without a hard stop

Table 6-11: Annual frequency of unacceptable performance ($\times 10^{-6}$) of individual isolator units tested with 90% confidence at one half of the 90th percentile displacement for EDB GMRS shaking for Diablo Canyon, without a hard stop

	Site					
	North Anna	Summer	Vogtle	Oak Ridge	Hanford	Idaho
$\beta = 0.01$	1.9	3.8	2.5	5.1	2.1	0.2
$\beta = 0.02$	1.8	3.7	2.4	4.9	2.0	0.2
$\beta = 0.05$	1.7	3.4	2.2	4.5	1.7	0.2

Providing a hard stop (and thus the displacement capacity of FP bearing) at the six sites of Figure 6-13 equal to one half that required at Diablo Canyon would reduce the annual frequency of unacceptable performance. The fragility curves corresponding to $f_{AR} = 1.1\kappa$ are plotted in Figure 6-18 and the annual frequencies of unacceptable performance are listed in Table 6-16. These frequencies are smaller than those of Table 6-12 by a factor of between 2 and 40.

6.6.4 Annual frequency of unacceptable performance of the safety-related umbilical lines

The safety-related umbilical lines are designed per NUREG-0800 (USNRC, 2007b) at GMRS+ shaking and the *prototypes* are tested for a 90+% confidence at a displacement equal to the CHS (or 90th percentile displacement for EDB GMRS shaking), as noted in Section 6.4.2. The forthcoming NUREG requires that all prototype safety-related umbilical lines be tested to demonstrate a 90+% confidence. Testing a smaller number of *prototype* umbilical lines may be sufficient if the variability in the behavior of umbilical lines is small and a confidence of greater than 90% is established at a displacement equal to the CHS.

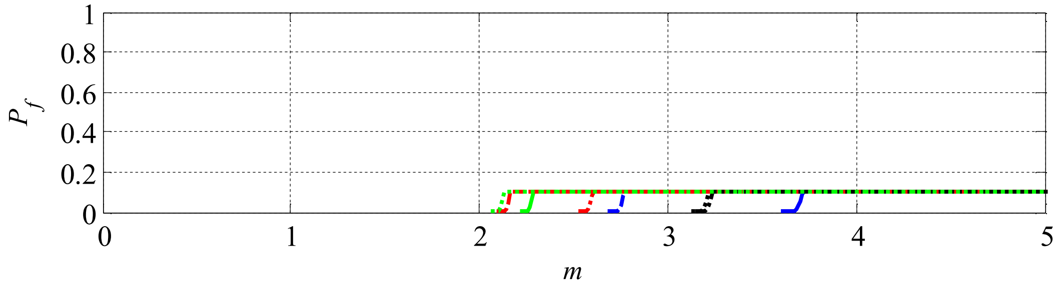

(a) β = 0.01

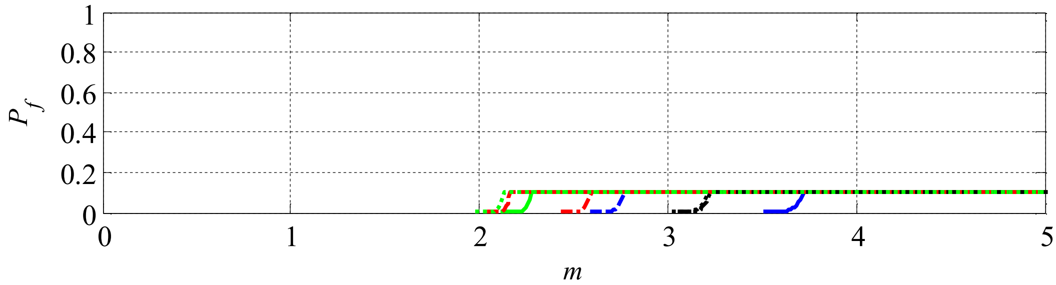

(b) β = 0.02

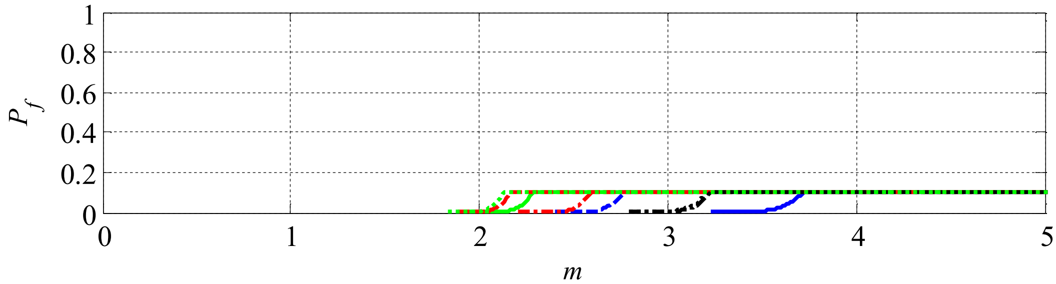

(c) β = 0.05

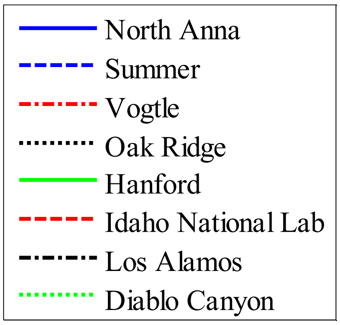

Figure 6-14: Probability of unacceptable performance, P_f, of individual isolator units for 90% confidence at median displacement for 110% EDB GMRS shaking plotted against multiples, m, of UHRS shaking with MAFE of 10^{-4}, with a hard stop at the 90th percentile displacement for EDB GMRS shaking

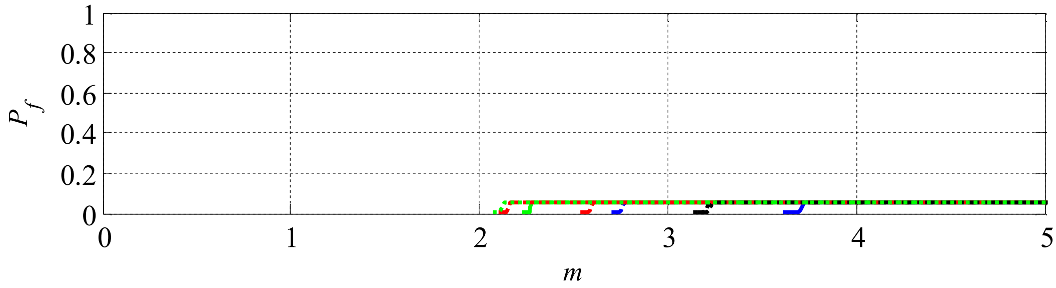

(a) β = 0.01

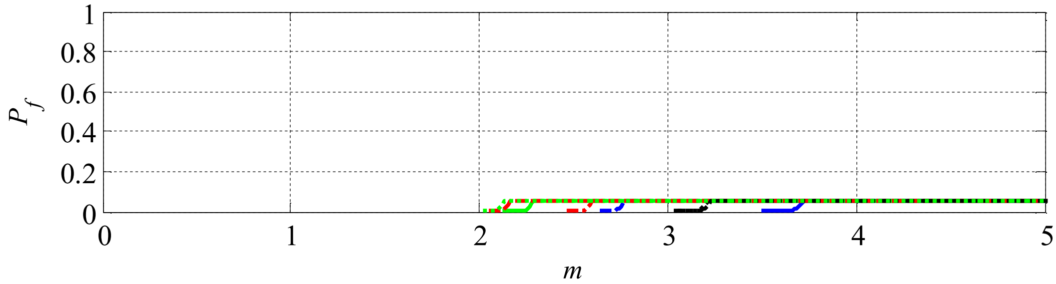

(b) β = 0.02

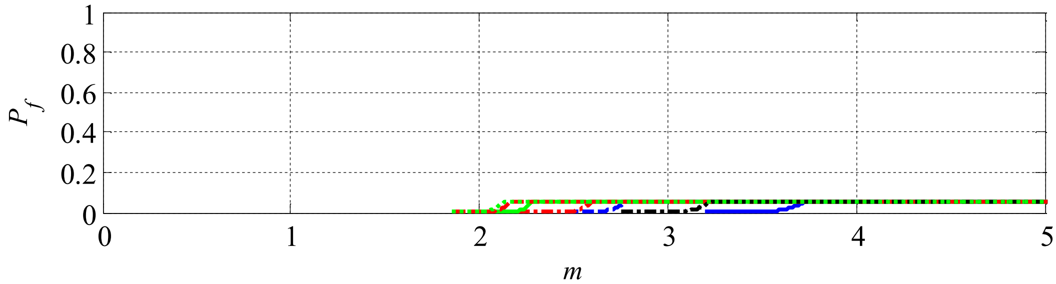

(c) β = 0.05

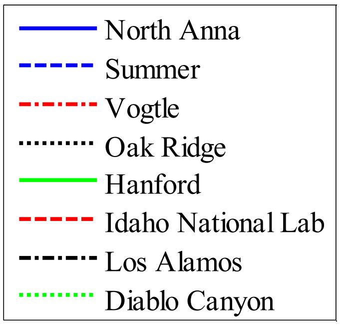

Figure 6-15: Probability of unacceptable performance, P_f, of individual isolator units for 95% confidence at median displacement for 110% EDB GMRS shaking plotted against multiples, *m*, of UHRS shaking with MAFE of 10^{-4}, with a hard stop at the 90th percentile displacement for EDB GMRS shaking

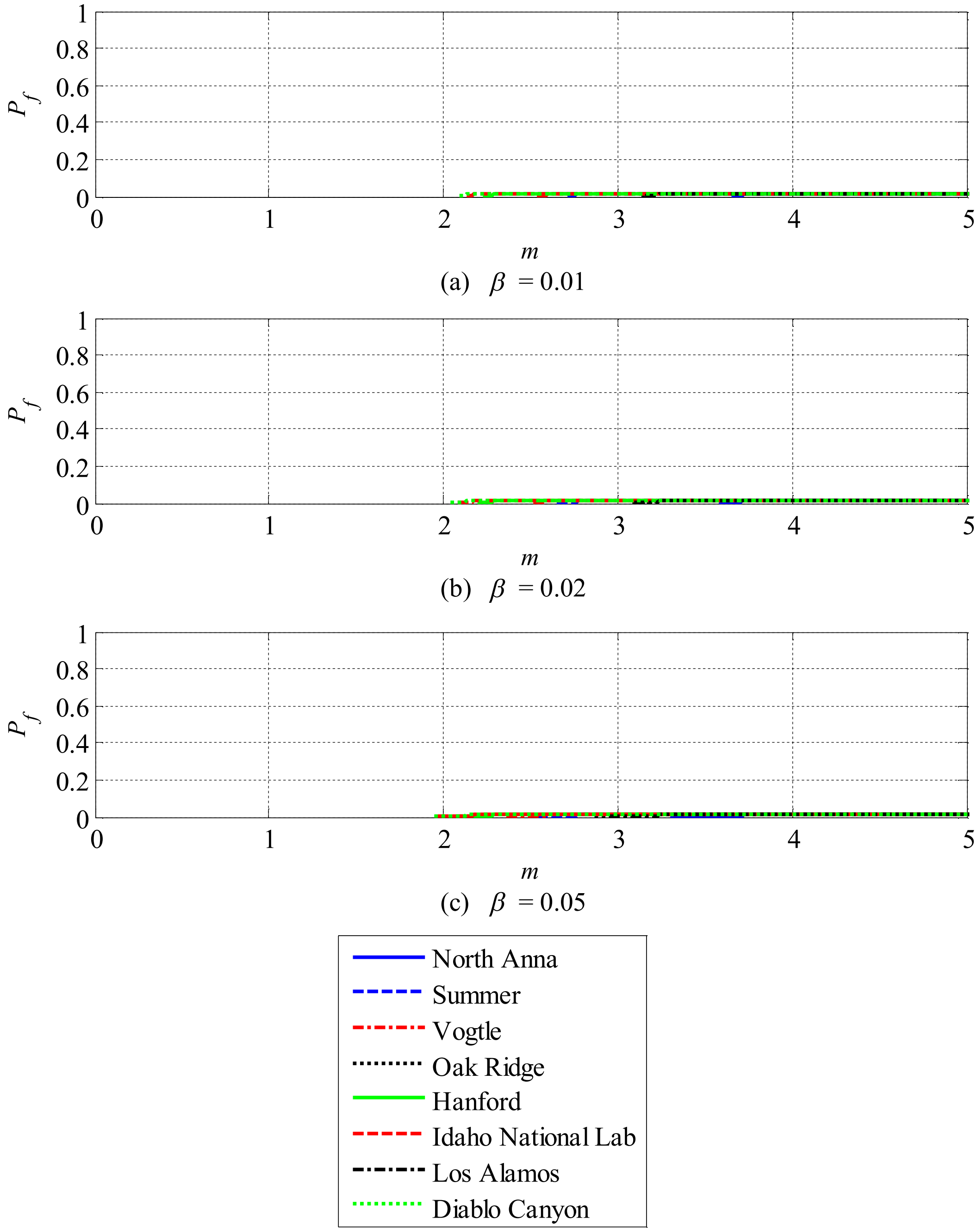

Figure 6-16: Probability of unacceptable performance, P_f, of individual isolator units for 99% confidence at median displacement for 110% EDB GMRS shaking plotted against multiples, *m*, of UHRS shaking with MAFE of 10^{-4}, with a hard stop at the 90th percentile displacement for EDB GMRS shaking

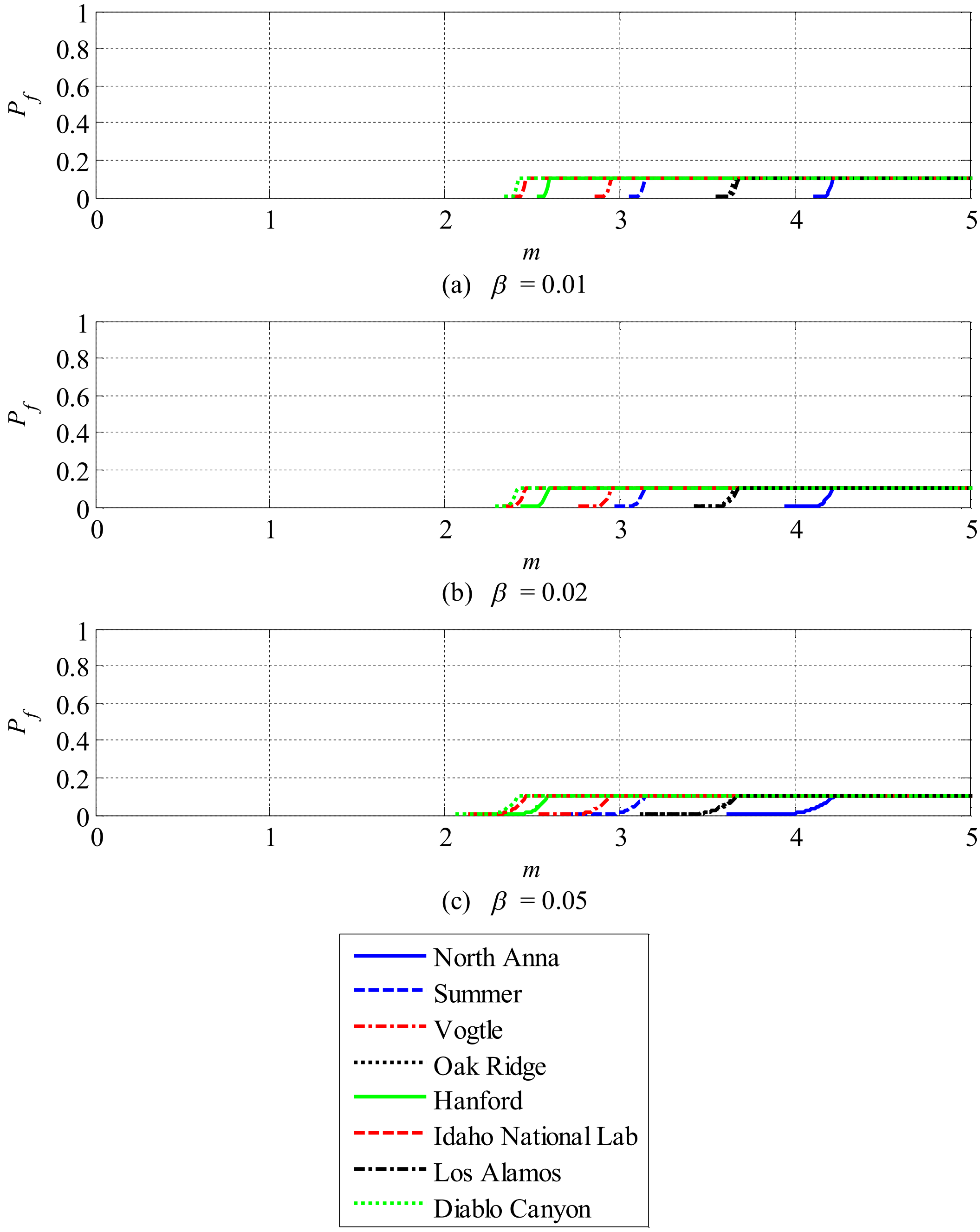

Figure 6-17: Probability of unacceptable performance, P_f, of individual isolator units for 90% confidence at median displacement for 125% EDB GMRS shaking plotted against multiples, m, of UHRS shaking with MAFE of 10^{-4}, with a hard stop at the 90th percentile displacement for EDB GMRS shaking

Table 6-12: Annual frequency of unacceptable performance ($\times 10^{-6}$) of individual isolator units tested with 90% confidence at median displacement for 110% EDB GMRS shaking, with a hard stop at the 90th percentile displacement for EDB GMRS shaking

	Site							
	North Anna	Summer	Vogtle	Oak Ridge	Hanford	Idaho	Los Alamos	Diablo Canyon
$\beta = 0.01$	0.8	0.8	0.8	0.8	0.7	0.7	0.8	0.6
$\beta = 0.02$	0.8	0.8	0.8	0.8	0.7	0.7	0.8	0.7
$\beta = 0.05$	0.9	0.8	0.8	0.8	0.8	0.8	0.8	0.7

Table 6-13: Annual frequency of unacceptable performance ($\times 10^{-6}$) of individual isolator units tested with 95% confidence at median displacement for 110% EDB GMRS shaking, with a hard stop at the 90th percentile displacement for EDB GMRS shaking

	Site							
	North Anna	Summer	Vogtle	Oak Ridge	Hanford	Idaho	Los Alamos	Diablo Canyon
$\beta = 0.01$	0.4	0.4	0.4	0.4	0.3	0.3	0.4	0.3
$\beta = 0.02$	0.4	0.4	0.4	0.4	0.4	0.4	0.4	0.3
$\beta = 0.05$	0.4	0.4	0.4	0.4	0.4	0.4	0.4	0.3

Table 6-14: Annual frequency of unacceptable performance ($\times 10^{-6}$) of individual isolator units tested with 99% confidence at median displacement for 110% EDB GMRS shaking, with a hard stop at the 90th percentile displacement for EDB GMRS shaking

	Site							
	North Anna	Summer	Vogtle	Oak Ridge	Hanford	Idaho	Los Alamos	Diablo Canyon
$\beta = 0.01$	0.08	0.08	0.08	0.08	0.07	0.07	0.08	0.06
$\beta = 0.02$	0.08	0.08	0.08	0.08	0.07	0.07	0.08	0.07
$\beta = 0.05$	0.09	0.08	0.08	0.08	0.07	0.07	0.08	0.07

Table 6-15: Annual frequency of unacceptable performance ($\times 10^{-6}$) of individual isolator units tested with 90% confidence at median displacement for 125% EDB GMRS shaking, with a hard stop at the 90th percentile displacement for EDB GMRS shaking

	Site							
	North Anna	Summer	Vogtle	Oak Ridge	Hanford	Idaho	Los Alamos	Diablo Canyon
$\beta = 0.01$	0.6	0.6	0.5	0.6	0.4	0.4	0.5	0.3
$\beta = 0.02$	0.6	0.6	0.5	0.6	0.4	0.4	0.5	0.3
$\beta = 0.05$	0.7	0.6	0.5	0.6	0.4	0.4	0.5	0.4

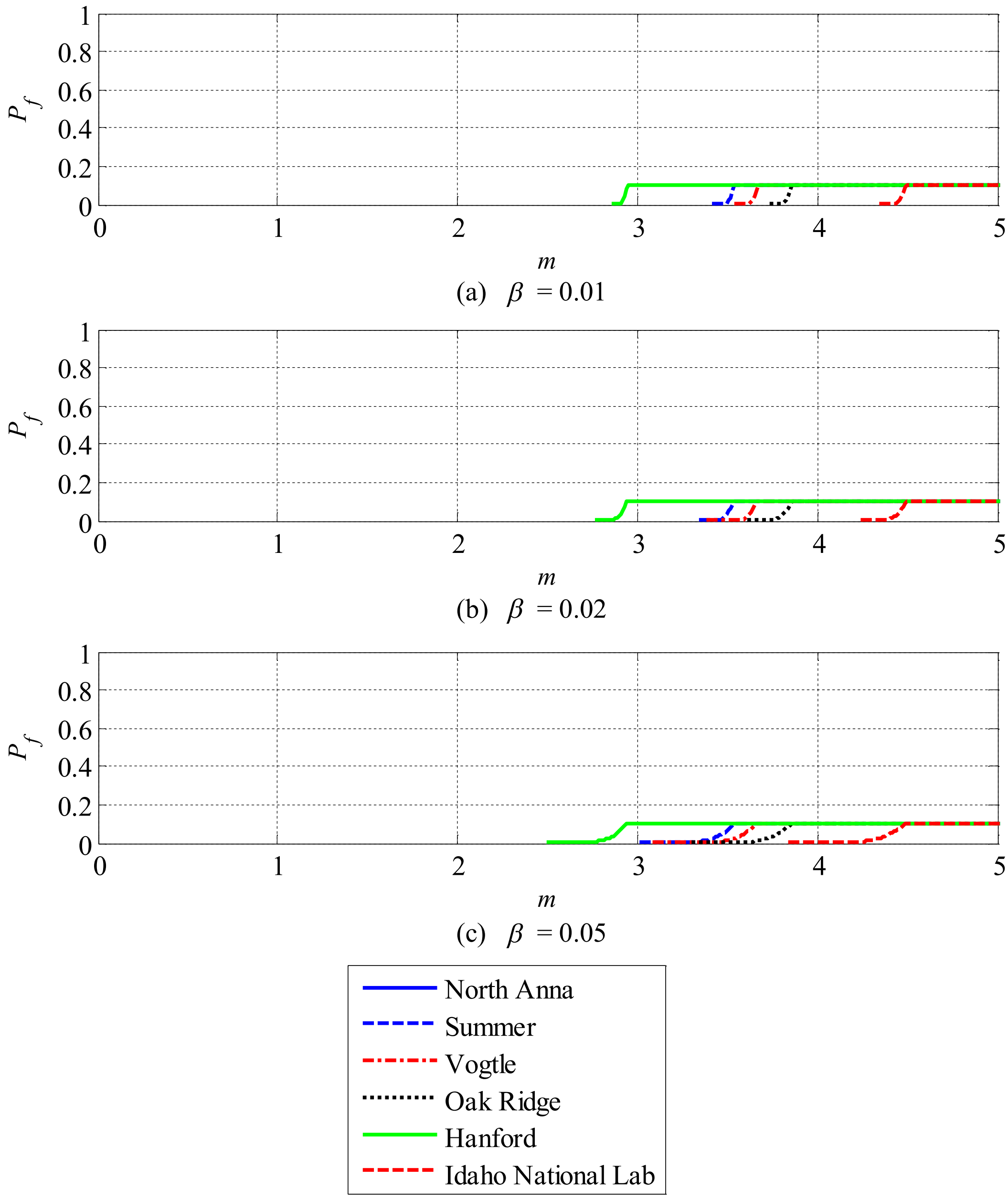

Figure 6-18: Probability of unacceptable performance, P_f, of individual isolator units tested with 90% confidence for median displacement for 110% κ EDB GMRS shaking plotted against multiples, m, of UHRS shaking with MAFE of 10^{-4}, with a hard stop at median displacement for 110% κ EDB GMRS shaking

Table 6-16: Annual frequency of unacceptable performance ($\times 10^{-6}$) of individual isolator units tested with 90% confidence at median displacement for 110%κ EDB GMRS shaking, with a hard stop at median displacement for 110%κ EDB GMRS shaking

	Site					
	North Anna	Summer	Vogtle	Oak Ridge	Hanford	Idaho
$\beta = 0.01$	0.19	0.40	0.27	0.53	0.23	0.02
$\beta = 0.02$	0.20	0.41	0.27	0.54	0.23	0.02
$\beta = 0.05$	0.20	0.43	0.28	0.55	0.25	0.02

The annual frequency of unacceptable performance of safety-related umbilical lines is calculated using an approach similar to that for the isolation system presented in Section 6.6.3. Failure of each safety-related umbilical line is very conservatively assumed to result in core melt and release of radiation, because mitigating measures are ignored, noting they will vary as a function of plant design. The fragility curves of the umbilical lines tested with different confidence and shaking level combinations are considered identical to those plotted in Figures 6-8 through 6-12 for individual isolator units, if a hard stop is not present, and Figures 6-14 through 6-17, if a hard stop is present. The resulting annual frequencies of unacceptable performance are less than 10^{-5} and 10^{-6} if a hard stop is absent and present, respectively (see Tables 6-7 through 6-15).

6.7 Design Factor for Seismically Isolated Nuclear Power Plants

The target annual frequency of unacceptable performance for a structure, system or component in a conventional (fixed base) nuclear power plant (SDC 5 per ASCE 43-05) is 10^{-5}. This goal is achieved by using materials standards such as ACI 349 and seismic demands consistent with a ground motion response spectrum calculated as the product of a UHRS at an annual frequency of exceedance of 10^{-4} and a design factor, DF, which is 1.0 or greater.

The calculations presented in Section 6.6 were based on a GMRS calculated using a UHRS at an annual frequency of exceedance of 10^{-4} and DF equal to 1.0, and an EDB GMRS that is defined, for the sites considered here, by a UHRS at an annual frequency of exceedance of 10^{-5}. These calculations show that the annual frequency of unacceptable performance is less than 10^{-5} if no hard stop is provided and less than 10^{-6} if a hard stop is installed at the 90th percentile EDB GMRS displacement, confirming that DF can be set equal to 1.0 for seismically isolated nuclear power plants.

The derivation of the design factor in ASCE 43-05 focuses on the effects of horizontal earthquake shaking. The vertical elements in the gravity and lateral load resisting systems in a nuclear power plant such as AP1000 (Schulz, 2006) are walls and not columns, for which failure due to excessive vertical loading is extremely unlikely because design axial stresses are very low. A much greater seismic margin is expected in the vertical direction than the horizontal direction. Since the vertical seismic demands in an isolated nuclear power plant should be no greater than those in a conventional (fixed base) nuclear power plant, there is no need to increase the vertical UHRS by a design factor to compute the GMRS. Seismically isolated nuclear structures with columns providing much of the vertical load resistance (regardless of cause) should be evaluated for shaking in excess of design basis to ensure their annual frequency of unacceptable performance is less than 10^{-5}.

CHAPTER 7

SEISMIC ISOLATION OF NUCLEAR STRUCTURES USING FRICTION PENDULUM™ BEARINGS

7.1 Introduction

This chapter presents the results of response-history analyses of rigid nuclear structures seismically isolated using Friction Pendulum™ (FP) bearings. A single FP bearing is considered appropriate to represent the isolated superstructure, with the mass of the superstructure attached to the slider of the bearing and the sliding surface fixed to the ground. Bearings are subjected to ground motions consistent with 10,000-year and 100,000-year seismic hazard at two sites: 1) Diablo Canyon, CA, a site of high seismicity, and 2) Vogtle, GA, a site of moderate seismicity. A set of 30 ground motions are spectrally matched to the 10,000-year uniform hazard response spectrum (UHRS) for the Diablo Canyon site. Sets of ground motions consistent with 100,000-year hazard for Diablo Canyon, and 10,000-year and 100,000-year hazards for Vogtle are obtained by amplitude scaling the spectrally matched motions. The 10,000-year ground motions for Diablo Canyon are also amplitude scaled by 1.5 and 1.67 to represent the minimum hazard level for the site of Diablo Canyon for which the probability of unacceptable performance of isolated nuclear structures, systems and components must be less than 10% per the provisions of ASCE 43-05 (2005) and Kammerer *et al.* (forthcoming), respectively.

Single FP bearings with a range of geometrical and material properties are subjected to the ground motions at the two hazard levels for the two sites with a goal of answering the following questions:

i. What is the influence of the choice for model for the variation in the coefficient of friction at the sliding surface (e.g., Coulomb model, pressure-dependent) on key response quantities (e.g., isolation system displacement, floor spectra)?

ii. Is the influence of the choice of friction model, if any, a function of shaking intensity and/or bearing parameters (e.g., static axial pressure, reference coefficient of friction)?

iii. How does the response of a single FP bearing change with shaking intensity and/or change in bearing parameters?

iv. Is the clearance to the hard stop determined by the 90th percentile peak displacement for 100,000-year shaking or the 99th percentile peak displacement for the 10,000-year shaking?

v. Is the median displacement for 1.1 times 100,000-year shaking less than or equal to the 90th percentile displacement for 100,000-year shaking?

Ground motions consistent with 10,000-year and 100,000-year earthquake shaking are developed in Sections 7.2 and 7.3 for the sites of Diablo Canyon and Vogtle, respectively. Modeling of isolators and analysis are discussed in Section 7.4. Key results are presented in Section 7.5.

7.2 Diablo Canyon: 10,000-year and 100,000-year Earthquake Shaking

Figure 7-1 presents the UHRS for the Diablo Canyon site and a return period of 10,000 years, obtained from the USGS website http://geohazards.usgs.gov/hazardtool/application.php (accessed on July 15, 2014). The set of 30 seeds motions listed in Table 7-1 are spectrally matched to the UHRS in the two horizontal directions. The target spectrum in the vertical direction is obtained by multiplying the UHRS of Figure 7-1 with the ratio of vertical to horizontal spectra of Figure 5-5. The period range considered for spectral matching is 0.01 s to 5 s. The response spectra of the scaled motions are plotted with the target spectra in Figure 7-2.

The 100,000-year UHRS for horizontal shaking is also obtained from the USGS website. The ratios of the 100,000-year to 10,000-year spectral ordinates at selected natural periods are plotted in Figure 7-3. The ratios range between 1.8 and 1.9 for period less than 1 s and between 1.9 and 2.1 at longer periods. The 10,000-year ground motions for Diablo Canyon (see Figure 7-2) amplitude scaled by a factor of 2.0[1] are considered to represent 100,000-year shaking at the site. A discussion on appropriateness of amplitude scaling the ground motions consistent with a shaking level at a site to represent the seismic hazard at a different shaking level is presented in Appendix G.

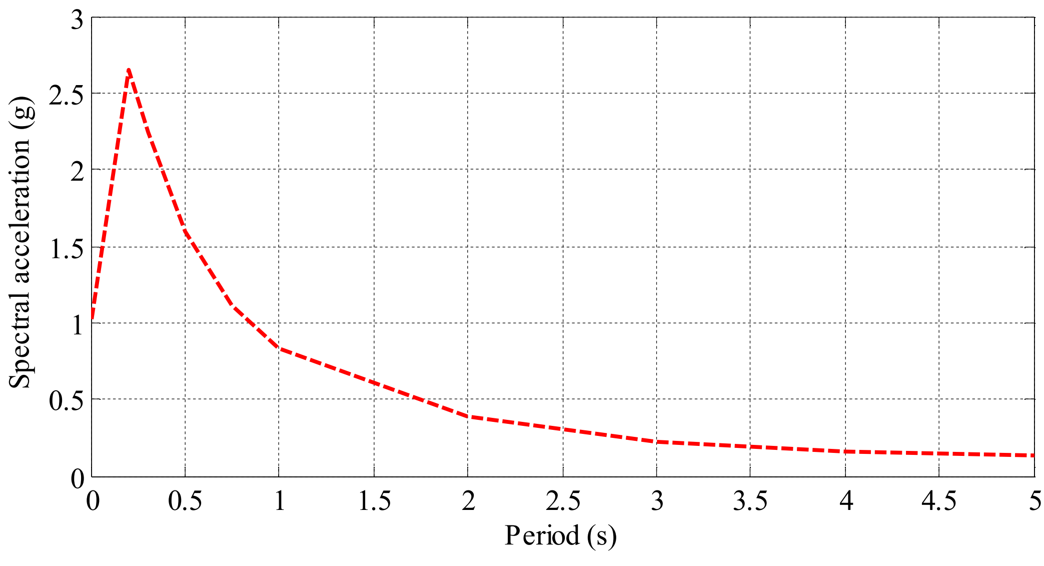

Figure 7-1: 10,000 year return period UHRS for the Diablo Canyon site

[1] The 10,000-year CMS, UHRS and CS are consistent with each other in Chapter 5. These ordinates are obtained from CMS data available at the USGS website. Conditional mean spectrum data are not available for 100,000-year shaking, which is obtained directly from the hazard curves from the USGS assuming a linear relationship between frequency and an intensity measure (e.g., PGA) in the log space. Uniform hazard response spectrum data are available at both return periods from the USGS website.

Table 7-1: Seed motions

Sl No	NGA Number	Event	Year	Magnitude	Epicentral Distance (km)
1	72	San Fernando	1971	6.6	24
2	77	San Fernando	1971	6.6	12
3	80	San Fernando	1971	6.6	39
4	180	Imperial Valley	1979	6.5	28
5	284	Irpinia	1980	6.9	33
6	285	Irpinia	1980	6.9	23
7	68	San Fernando	1971	6.6	40
8	292	Irpinia	1980	6.9	30
9	763	Loma Prieta	1989	6.9	29
10	179	Imperial Valley	1979	6.5	27
11	161	Imperial Valley	1979	6.5	43
12	810	Loma Prieta	1989	6.9	16
13	184	Imperial Valley	1979	6.5	27
14	957	Northridge	1994	6.7	64
15	1107	Kobe	1995	6.9	24
16	994	Northridge	1994	6.7	25
17	1011	Northridge	1994	6.7	19
18	1012	Northridge	1994	6.7	14
19	1021	Northridge	1994	6.7	50
20	1050	Northridge	1994	6.7	20
21	1051	Northridge	1994	6.7	20
22	1078	Northridge	1994	6.7	15
23	1091	Northridge	1994	6.7	38
24	1528	Chi-Chi	1999	7.6	45
25	159	Imperial Valley	1979	6.5	3
26	879	Landers	1992	7.3	44
27	754	Loma Prieta	1989	6.9	31
28	802	Loma Prieta	1989	6.9	27
29	1633	Manjil	1990	7.4	40
30	1144	Gulf of Aqaba	1995	7.2	93

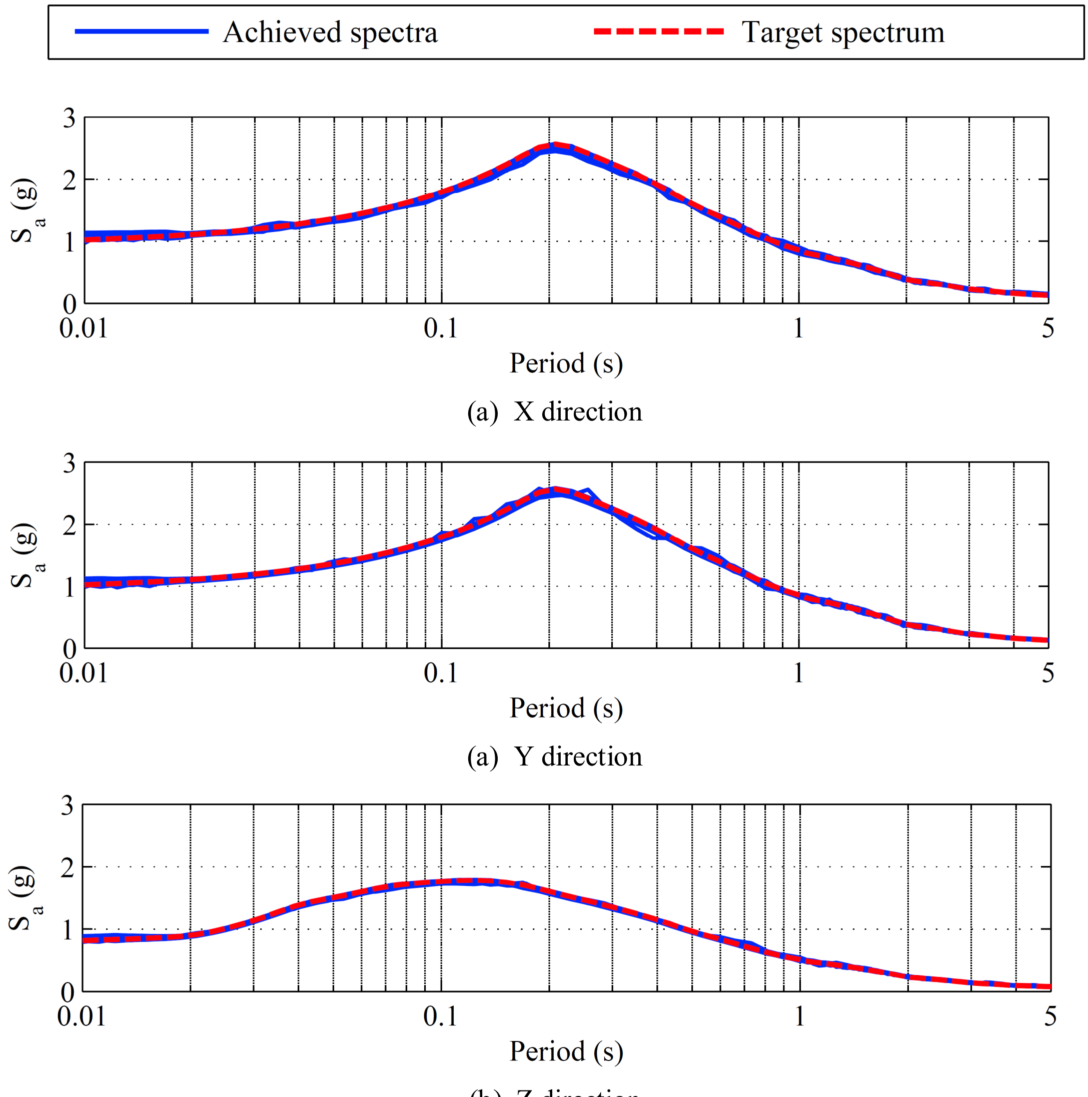

Figure 7-2: Response spectra of the ground motions spectrally matched to the 10,000 year return period UHRS for the Diablo Canyon site

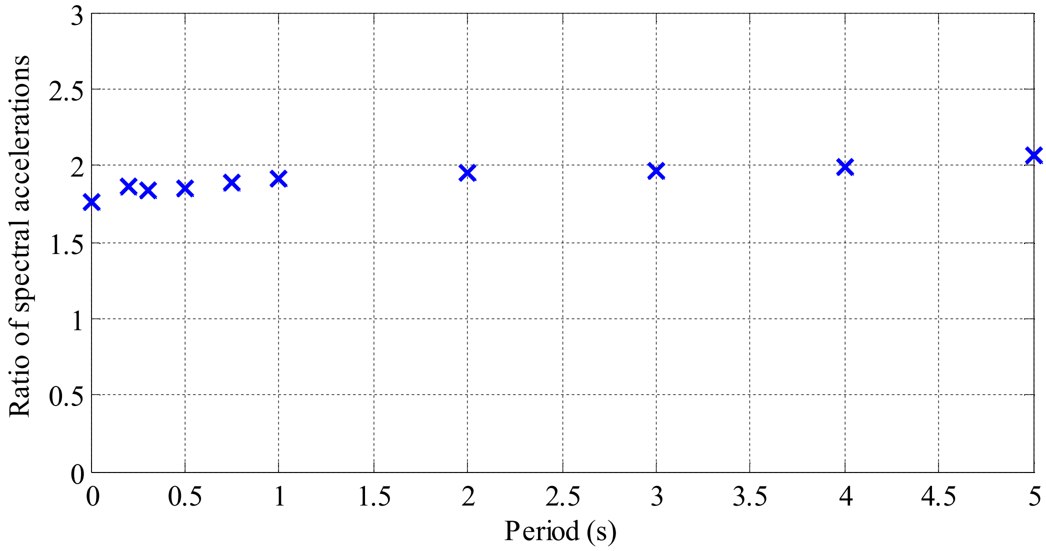

Figure 7-3: Ratio of UHRS spectral ordinates for 100,000 years to 10,000 years at the Diablo Canyon site

7.3 Vogtle: 10,000-year and 100,000-year Earthquake Shaking

The 10,000-year and 100,000-year UHRS for the site of the Vogtle nuclear power plant (latitude: 33.1433 N, longitude: 81.7606 W) are obtained from the USGS website identified previously. The two spectra are plotted in Figure 7-4 for Site Class B per ASCE 7-10 (ASCE (2010)), namely, V_{s30} equal to 760 m/s.

The ground motions of Figure 7-2 are amplitude scaled to represent 10,000-year and 100,000-year shaking at the Vogtle site. The ratio of 10,000-year UHRS ordinates for Vogtle to Diablo Canyon ranges between 0.2 and 0.3 for periods between 0.01 s and 2 s (see Figure 7-5). Similarly, the ratio of the spectral ordinates of the Vogtle 100,000-year UHRS to the Diablo Canyon 10,000-year UHRS ranges between 0.5 and 0.9 at periods less than 1 s, and between 0.5 and 0.7 at longer periods. The ground motions of Figure 7-2, amplitude scaled by the factors of

0.25 and 0.6, are assumed to approximately represent 10,000-year and 100,000-year earthquake shaking, respectively, at the site of the Vogtle nuclear power plant (see also Appendix G).

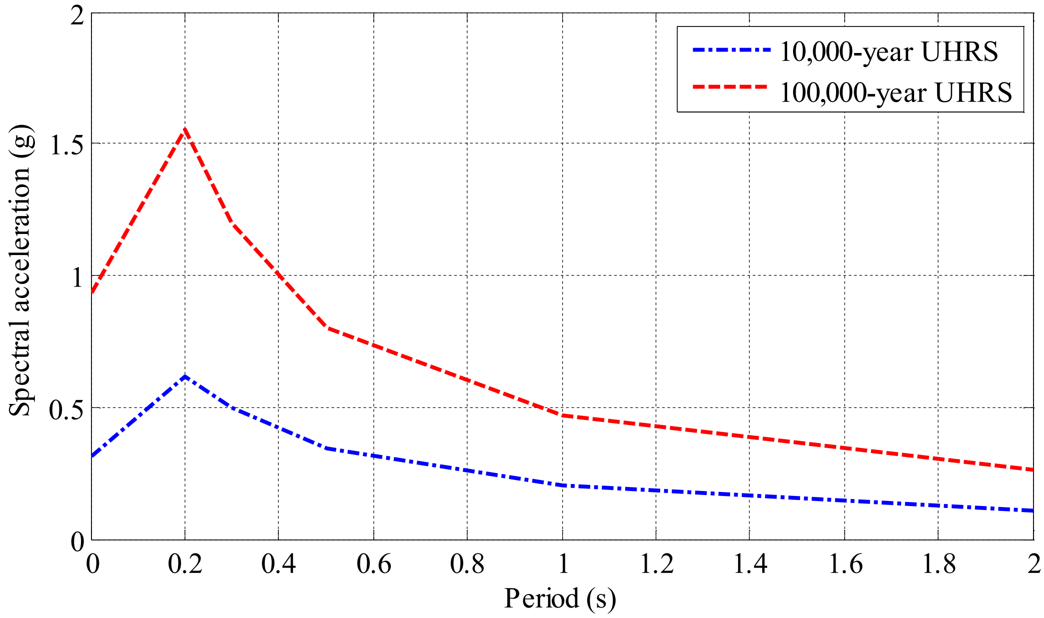

Figure 7-4: 10,000-year and 100,000-year return period uniform hazard spectra for the site of the Vogtle nuclear power plant (V_{s30} = 760 m/s)

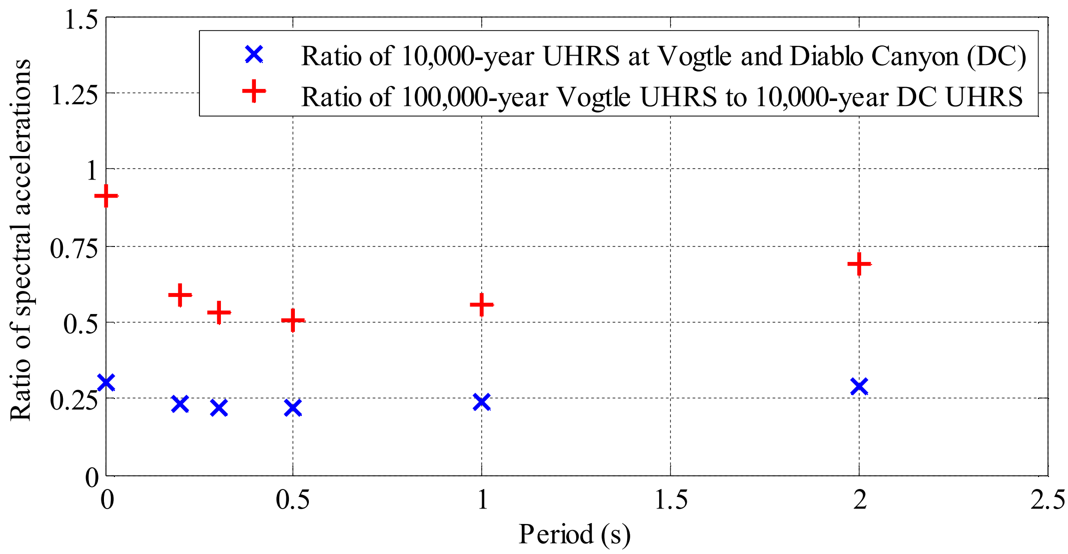

Figure 7-5: Ratios of spectral accelerations of 10,000-year and 100,000-year UHRS for the Vogtle site to spectral accelerations of 10,000-year UHRS for the Diablo Canyon site

7.4 Isolator Modeling and Analysis

7.4.1 Properties of Friction Pendulum™ bearings

Four values of sliding period (1.5 s, 2 s, 3 s and 4 s) are considered herein. The coefficient of friction, $\mu(p,T,v)$, adjusted for the effects of instantaneous values of axial pressure on the bearing, p, temperature at the sliding surface, T, and sliding velocity, v, is given by

$$\mu(p,T,v) = \mu_{ref} \times (k_p k_T k_v) \tag{7-1}$$

where μ_{ref} is the reference coefficient of friction, and k_p, k_T and k_v are factors (see Chapter 3) to account for the effects of pressure, temperature and velocity, respectively, and all other parameters were defined previously. Three values of μ_{ref} are considered: 0.03, 0.06 and 0.09. The factor k_p is defined for a reference axial pressure, p_o. Two values of p_o are considered: 10 MPa and 50 MPa. Five models to characterize coefficient of friction at the sliding surface that consider the influences of pressure, temperature and velocity are listed in Table 7-2.

Table 7-2: Friction models that consider pressure, temperature and velocity effects

	Friction model	Notation
Model 1	Coulomb	μ = Coulomb
Model 2	Pressure dependent	$\mu = f(p)$
Model 3	Temperature dependent	$\mu = f(T)$
Model 4	Velocity dependent	$\mu = f(v)$
Model 5	Pressure, temperature and velocity dependent	$\mu = f(p,T,v)$

7.4.2 Input ground motions

Thirty sets of ground motions spectrally matched to the 10,000-year UHRS for Diablo Canyon, with six amplitude scaling factors, namely, 0.25, 0.6, 1.0, 1.5, 1.67 and 2.0, are used for analysis. The purpose of each scale factor is described in Table 7-3.

Table 7-3: Amplitude scaling factors to represent seismic hazard at different sites

Amplitude scaling factor	Shaking intensity	Remarks
0.25	25%	10,000-year hazard at Vogtle
0.6	60%	100,000-year hazard at Vogtle
1.0	100%	10,000-year hazard at Diablo Canyon
1.5	150%	Minimum hazard level for Diablo Canyon at which target probability of unacceptable performance is less than 10% per ASCE (2005)
1.67	167%	Minimum hazard level for Diablo Canyon at which target probability of unacceptable performance is less than 10% per Kammerer *et al.* (forthcoming)
2.0	200%	100,000-year hazard at Diablo Canyon

7.4.3 Modeling

A single FP bearing is modeled in OpenSees using the verified and validated OpenSees element *FPBearingPTV* (see Chapter 4). The mass corresponding to the static axial pressure on the bearing is assigned to the slider of the bearing in the two horizontal and vertical directions. The sliding surface is a fixed boundary. The rotational degrees of freedom about the two horizontal axes of the slider are restrained, and the slider is free to translate in the two horizontal directions. Assumptions on the modeling of FP bearings are discussed in Chapter 4. Mass proportional damping of 2% of critical, with the proportionality constant based on the sliding period of the FP bearing, is assigned to the system.

7.4.4 Vertical component of ground motions

The instantaneous axial load on an FP bearing subjected to a set of three-component ground motion is a function of the static weight and the vertical component of ground motion. The instantaneous axial load is zero and loss of contact at the sliding surface takes place when the vertical ground acceleration exceeds the acceleration due to gravity. The lateral strength and stiffness of the single FP bearing are zero following the loss of contact. The vertical components of the ground motions are ignored in this chapter for amplitude scaling factors (see Table 7-3) greater than or equal to 1.5 because contact for the single isolator "system" is lost. The effects of ignoring the vertical component of ground motion on response are examined in Chapter 8.

7.4.5 Analysis cases

FP bearings with four values of sliding period, three values of μ_{ref}, two values of reference axial pressure and friction at the sliding surface defined by five friction models are subjected to thirty sets of ground motions scaled to six intensities: a total of 21,600 (= $4 \times 3 \times 2 \times 5 \times 30 \times 6$) response-history analyses. The bearings experienced displacement demand greater than the corresponding radius of curvature for some combinations of geometrical, material properties, and intensity levels, leading to numerical problems. These combinations are ignored and are listed in Table 7-4 (a total of 4,200 response-history analyses). Select results from the remaining 17,400 response-history analyses are presented in the following sections.

Table 7-4: Combinations of amplitude scaling factor, sliding period and reference coefficient of friction not considered

Amplitude scaling factor	Sliding period	μ_{ref}
1.0	1.5 s	0.03
1.5	1.5 s	0.03, 0.06, 0.09
1.67	1.5 s	0.03, 0.06, 0.09
1.67	2 s	0.03
2.0	1.5 s, 2 s	0.03, 0.06, 0.09

7.5 Results

7.5.1 Coefficient of friction

The change in the coefficient of friction over the duration of strong shaking is studied in this section. The duration of strong shaking for a component of the ground motion record is estimated using the approach suggested by Trifunac and Brady (1975). The history of cumulative sum of square of acceleration ordinates is computed

$$\zeta(t) = \int_{t=0}^{t} a(t)^2 \, dt \tag{7-2}$$

where $\zeta(t)$ is the sum of square of the acceleration ordinates between time 0 and t, and $a(t)$ is the acceleration ordinate at time t. The duration of strong shaking for an acceleration history is defined by the difference in time between $\zeta(t)$ equal to 5% and 95% of its maximum value, and for a three-component ground motion is taken as the greater of the values computed for the two horizontal directions. Figure 7-6 presents the beginning and end of strong shaking for the 30 ground motions. The duration of strong shaking ranges between 6.6 s for ground motion (GM) number 18 to 30.9 s for GM29.

Figure 7-7(a) presents the histories of the coefficient of friction at the sliding surface of the FP bearing with a sliding period of 3 s, μ_{ref} of 0.06 and a static axial pressure of 50 MPa subjected to GM29 with amplitude scaling factor of 1.0. The histories are presented for two friction models: $\mu = f(p,T,v)$ and $\mu = \text{Coulomb}$. Also shown in the panel are the beginning and end of strong shaking for the ground motion. The duration of strong shaking is denoted by T_{ss} in the figure. The value of μ at the start of shaking is 0.03 $(= \mu_{\min} = \mu_{\max}/2)$ because the velocity is small. The coefficient of friction ranges between 0.02 and 0.05 over the duration of strong shaking, with an average of 0.03 for the $\mu = f(p,T,v)$ model. The coefficient is 0.06 for the Coulomb model.

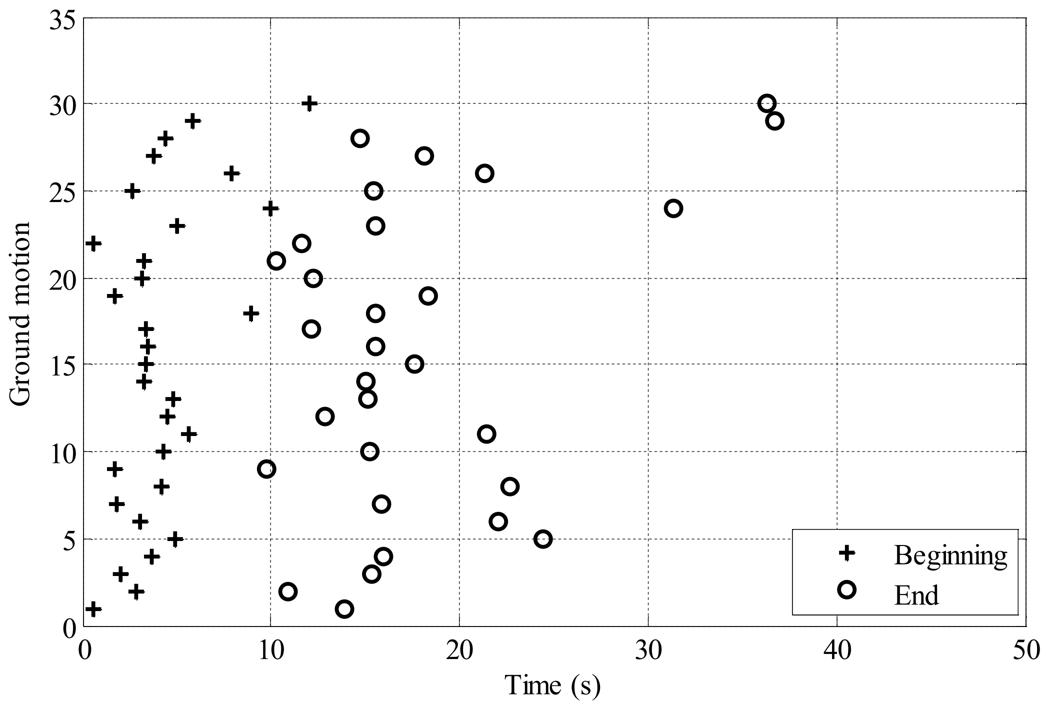

Figure 7-6: Duration of strong shaking for the ground motions

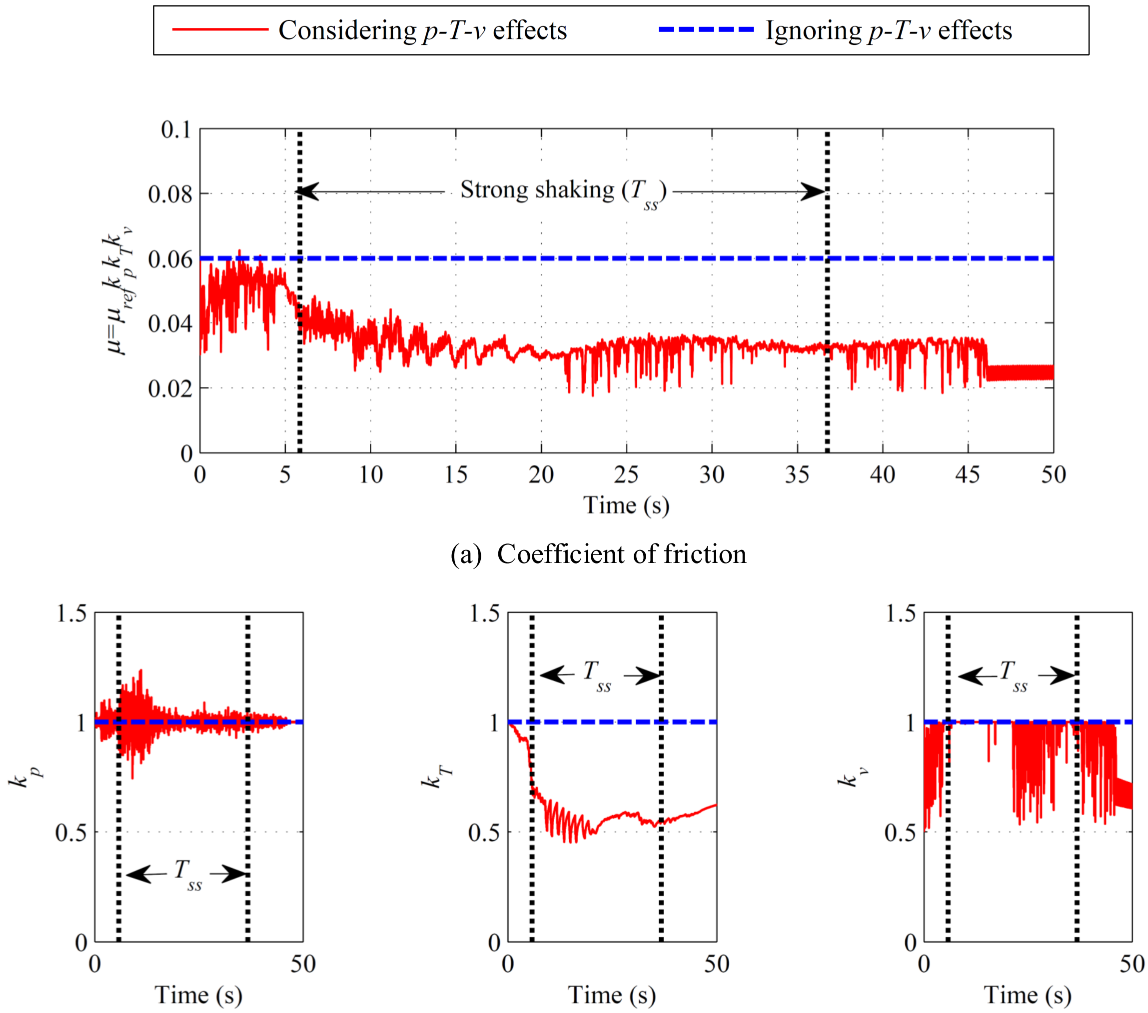

(b) Pressure factor (c) Temperature factor (d) Velocity factor

Figure 7-7: Histories of coefficient of friction, and factors accounting for the influences of axial pressure, temperature and velocity for the 3 s FP bearing with a reference coefficient of friction of 0.06 subjected to GM29

High frequency changes in the pressure factor, k_p, observed in Figure 7-7(b) are due to the vertical component of ground motion. The factor k_p varies between 0.7 and 1.2, with an average of 1.0. Figure 7-7(c) presents the history of the temperature factor, k_T, which varies between 0.5 and 0.7, with an average of 0.6 over the duration of strong shaking. The velocity factor, k_v, varies between 0.5 and 1.0, with an average of about 1.0 during the strong shaking (Figure 7-7(d)).

Figure 7-8(a) presents the coefficient of friction at the sliding surface averaged over the duration of strong shaking for the FP bearing with a sliding period of 2 s, p_o of 10 MPa and μ_{ref} of 0.06, for each of the 30 ground motions with an amplitude scaling factor of 1.0. The averaged coefficients are reported for each of the five friction models of Table 7-2.

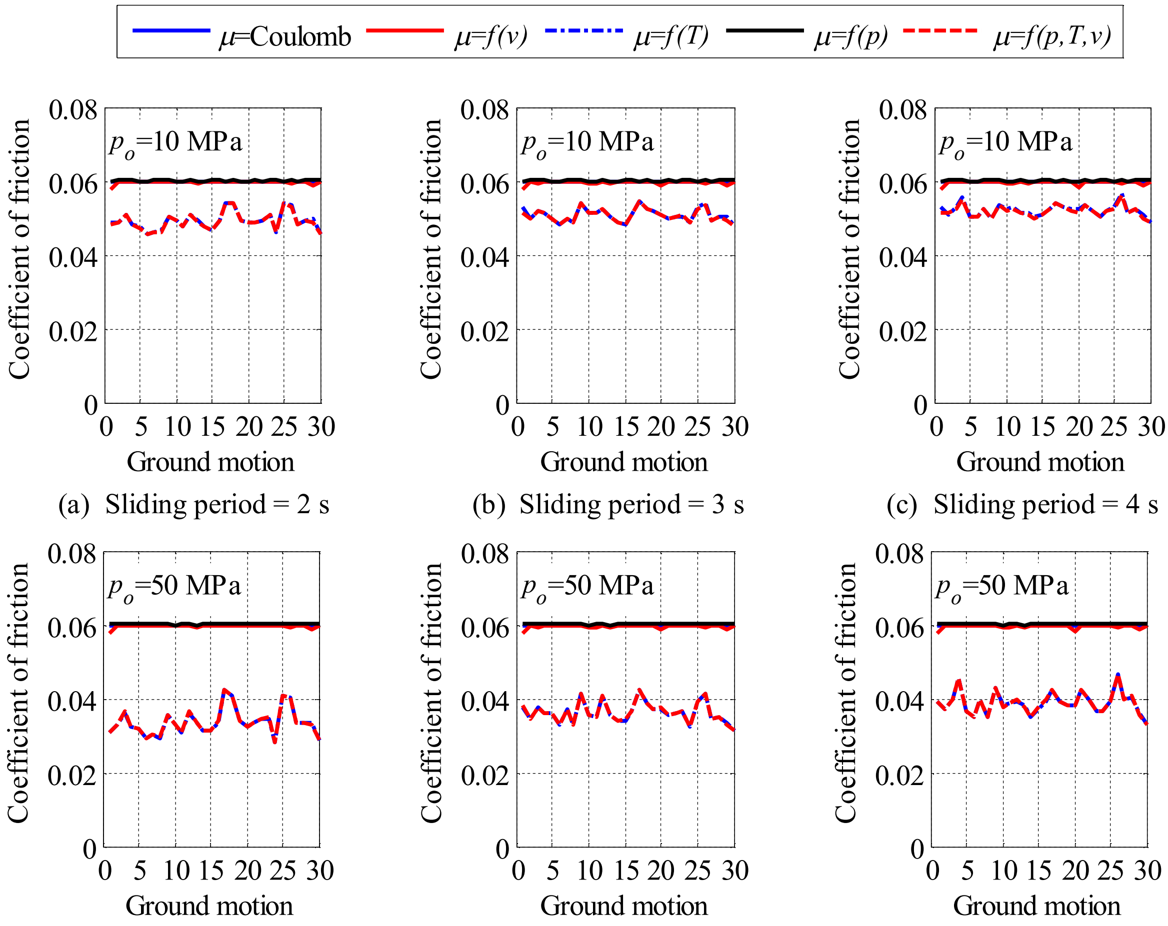

(a) Sliding period = 2 s (b) Sliding period = 3 s (c) Sliding period = 4 s

(d) Sliding period = 2 s (e) Sliding period = 3 s (f) Sliding period = 4 s

Figure 7-8: Coefficient of friction averaged over the duration of strong shaking for bearings with different geometrical properties and static axial load; μ_{ref} = 0.06, amplitude scale factor = 1.0

The results of Figure 7-8(a) can be grouped into two bins, depending on whether the friction model includes heating effects. The average coefficients of friction are 0.06 when friction is defined using the Coulomb model, pressure-dependent model or velocity-dependent model, and range between 0.046 and 0.054 when the friction is defined using the temperature-dependent model or the model that considers all the three dependencies. Across the 30 ground motions, the average coefficient of friction over the duration of shaking is 0.049 (0.06) when heating effects are considered (ignored). In the remainder of this chapter, "average-30 coefficient of friction" is the average value of the coeffcient of friction over the duration of strong shaking for the 30 ground motions, unless noted otherwise.

Figures 7-8(b) and 7-8(c) present the average coefficient of friction over the duration of strong shaking for the bearings with sliding periods of 3 s and 4 s, respectively, for each ground motion set. The average coefficients of friction are 0.06 when heating effects are ignored, and 0.051 and 0.052 for the two panels, respectively, when the effects are considered. Figures 7-8(d), 7-8(e) and 7-8(f) present results for the 2 s, 3 s and 4 s FP bearings, respectively, with p_o of 50 MPa. Heating effects are more prominent for these three panels as the higher static axial pressure leads to greater heat generation at the sliding surface, greater increase in temperature, and a larger reduction in the coefficient of friction. The average-30 coefficient of friction is 0.034, 0.036 and 0.039, respectively, for the three panels when the heating effects are included in the friction model.

The results presented in Figure 7-8 suggest that the average coefficient of friction for a given ground motion is most heavily influenced by 1) whether the friction model includes heating effects, and 2) the static axial pressure on the bearing. The coefficient is 15% (35-40%) smaller when the friction model includes heating effects and p_o is 10 MPa (50 MPa). The change in the average-30 coefficient of friction due to heating with sliding period is small, with the least effect at a sliding period of 4 s.

Figure 7-9 presents the average-30 coefficients of friction for the FP bearing with a sliding period of 3 s, μ_{ref} of 0.03, 0.06 and 0.09, and p_o of 10 MPa and 50 MPa subjected to the ground motions scaled by the six factors of Table 7-3. The velocity and temperature dependencies of friction influence the average-30 coefficient of friction for an amplitude scale factor of 0.25: the minimum average-30 coefficient of friction computed using all five friction models is 9% (12%, 13%) smaller than μ_{ref} for p_o of 10 MPa and μ_{ref} of 0.03 (0.06, 0.09), as seen in Figure 7-9(a) (7-9(c), 7-9(e)). The difference is 17% (22%, 26%) for p_o of 50 MPa (see Figure 7-9(b) (7-9(d), 7-9(f))). The average-30 coefficient of friction is influenced primarily by whether heating effects are included in the friction model for amplitude scale factors of 0.6 or greater; velocity effects are negligible for these scale factors (≥0.6). Average-30 coefficient of friction are smaller for a higher μ_{ref} and/or p_o. The average-30 coefficient of friction increases at greater shaking intensities, which appears to be counter intuitive. However, at the greater intensities of shaking, the slider traverses a much greater distance, spending less time over the center of the bearing, where the temperature is computed. Although more energy is dissipated at the higher intensities of shaking, it is distributed over a much greater area of the sliding surface.

Figure 7-10 presents the average-30 coefficient of friction as a function of shaking intensity up to 60% for FP bearings with a sliding period of 1.5 s, where an intensity of 100% corresponds to design basis shaking at Diablo Canyon. Figure 7-11 presents the results for a 2 s bearing for factors up to 1.0[1]. Figure 7-12 presents results for a 4 s FP bearing subjected to the ground motions with scaling factors of 0.25, 0.60, 1.00, 1.50, 1.67 and 2.00. From Figures 7-9 through 7-12, it can be observed that

i. The influence of the choice of friction model is small when the shaking intensity and p_o are small: 25% and 10 MPa, respectively. In this case, the effect of heating on the average-30 coefficient of friction is less than 10% (on average), regardless of the sliding period and μ_{ref}.

ii. The average-30 coefficient of friction computed using a temperature-dependent friction model is smaller than the corresponding μ_{ref} by approximately 10% (15%, 20%) for μ_{ref} of 0.03 (0.06, 0.09), p_o of 10 MPa and shaking intensity of 60% and greater.

iii. At p_o of 50 MPa and a shaking intensity of 25% ($\geq$60%), the average-30 coefficient of friction, adjusted for heating effects, is smaller than μ_{ref} by approximately 15% (30%), 20% (40%) and 25% (45%) for μ_{ref} of 0.03, 0.06 and 0.09, respectively.

iv. The difference between the average-30 coefficient of friction computed using a temperature-dependent friction model and μ_{ref} increases as shaking intensity increases from 25% to 60% or 100% due to greater sliding velocities resulting in more heat generation and a higher reduction in the coefficient of friction. At even greater intensities (>100%), the difference between the average-30 coefficient of friction and μ_{ref} tends to decrease, which is attributed to the distribution of the heat generated on the sliding surface in a relatively large area.

[1] Higher intensities for the 1.5 s and 2.0 s bearings give rise to displacements greater than 0.5*R*, which are impractical for FP isolators.

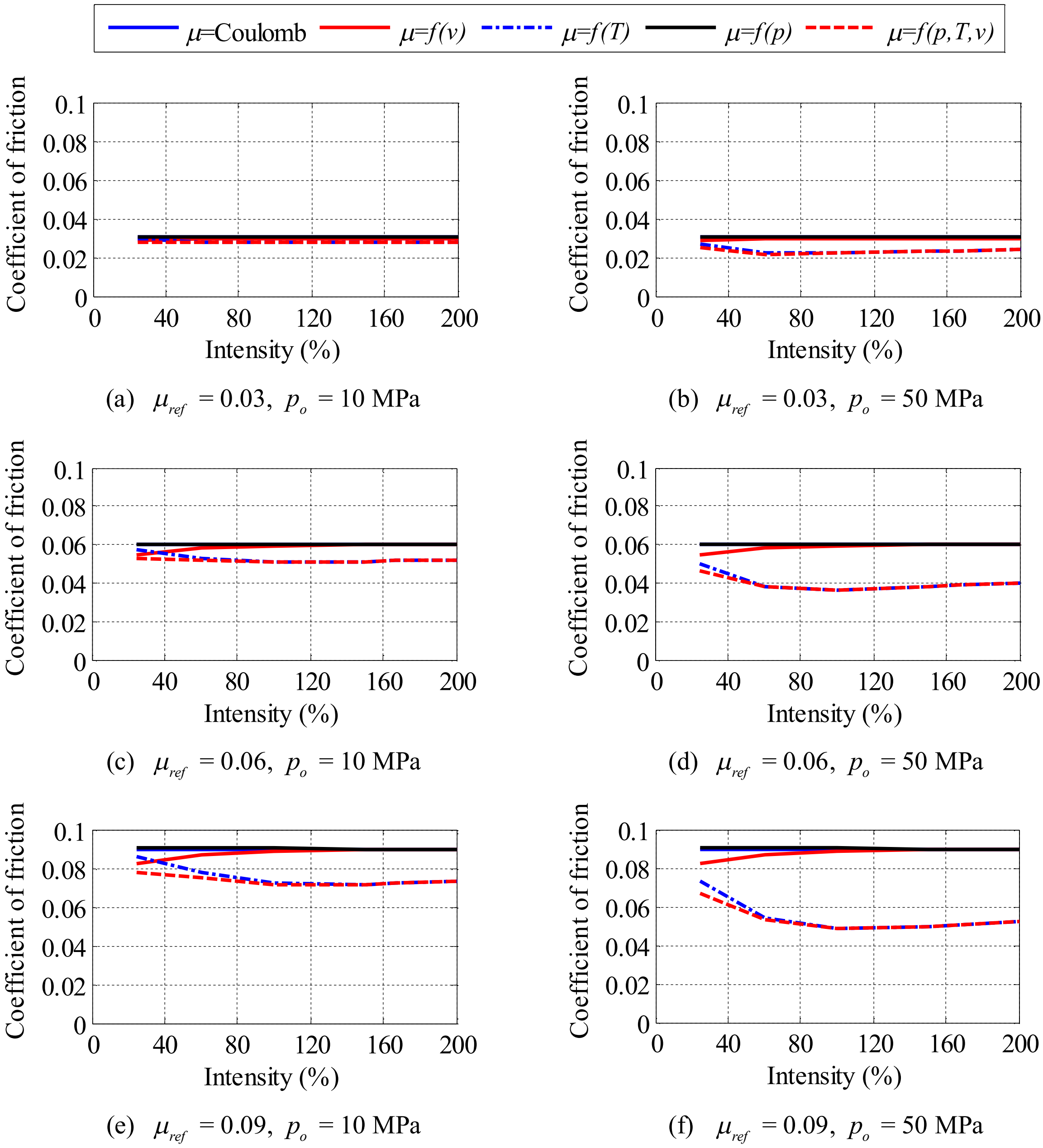

Figure 7-9: Coefficient of friction in the duration of strong shaking averaged over 30 ground motions as a function of shaking intensity for an FP bearing with a sliding period of 3 s

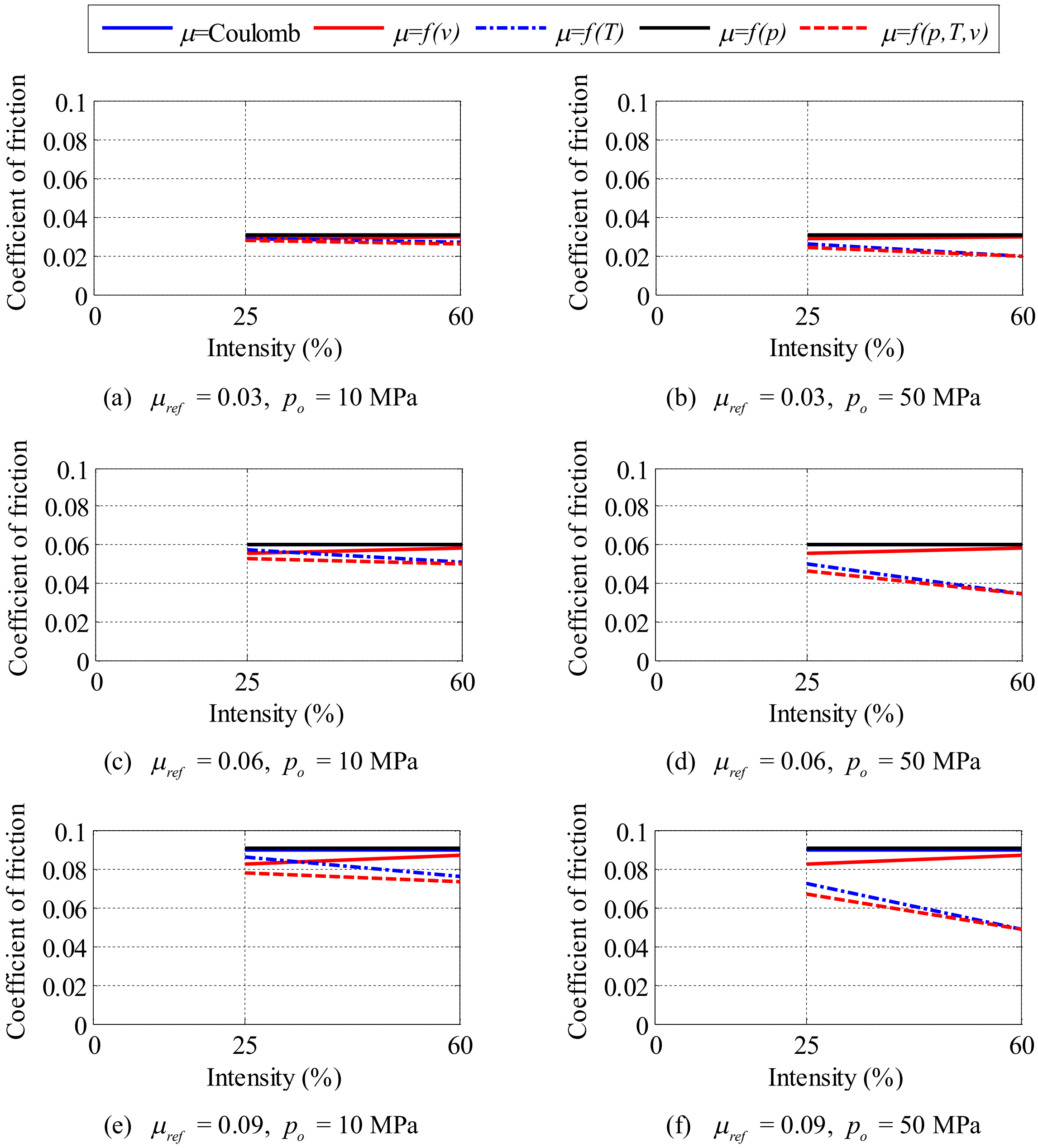

Figure 7-10: Coefficient of friction in the duration of strong shaking averaged over 30 ground motions as a function of shaking intensity for an FP bearing with a sliding period of 1.5 s

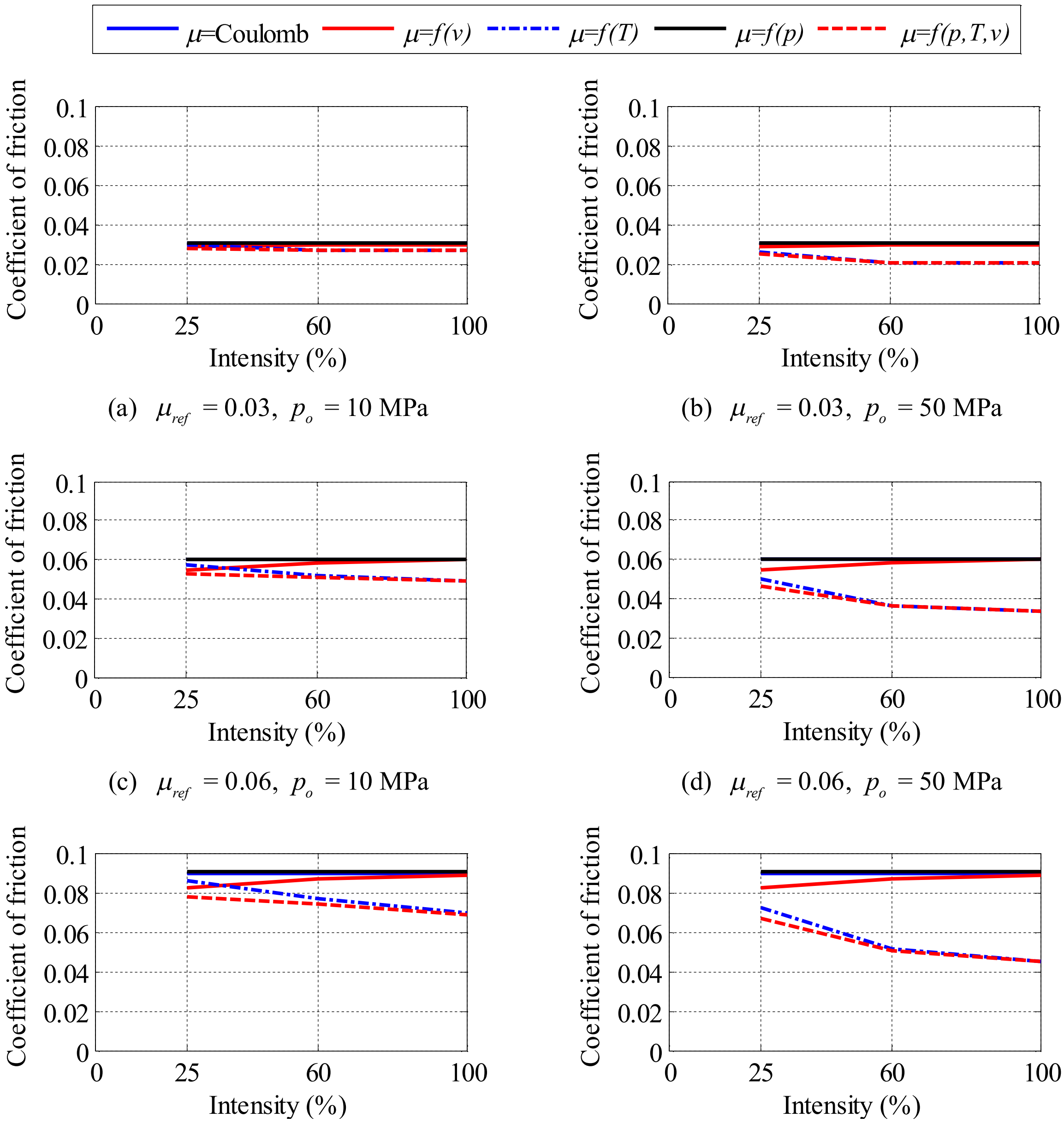

(a) $\mu_{ref} = 0.03,\ p_o = 10$ MPa

(b) $\mu_{ref} = 0.03,\ p_o = 50$ MPa

(c) $\mu_{ref} = 0.06,\ p_o = 10$ MPa

(d) $\mu_{ref} = 0.06,\ p_o = 50$ MPa

(e) $\mu_{ref} = 0.09,\ p_o = 10$ MPa

(f) $\mu_{ref} = 0.09,\ p_o = 50$ MPa

Figure 7-11: Coefficient of friction in the duration of strong shaking averaged over 30 ground motions as a function of shaking intensity for an FP bearing with a sliding period of 2 s

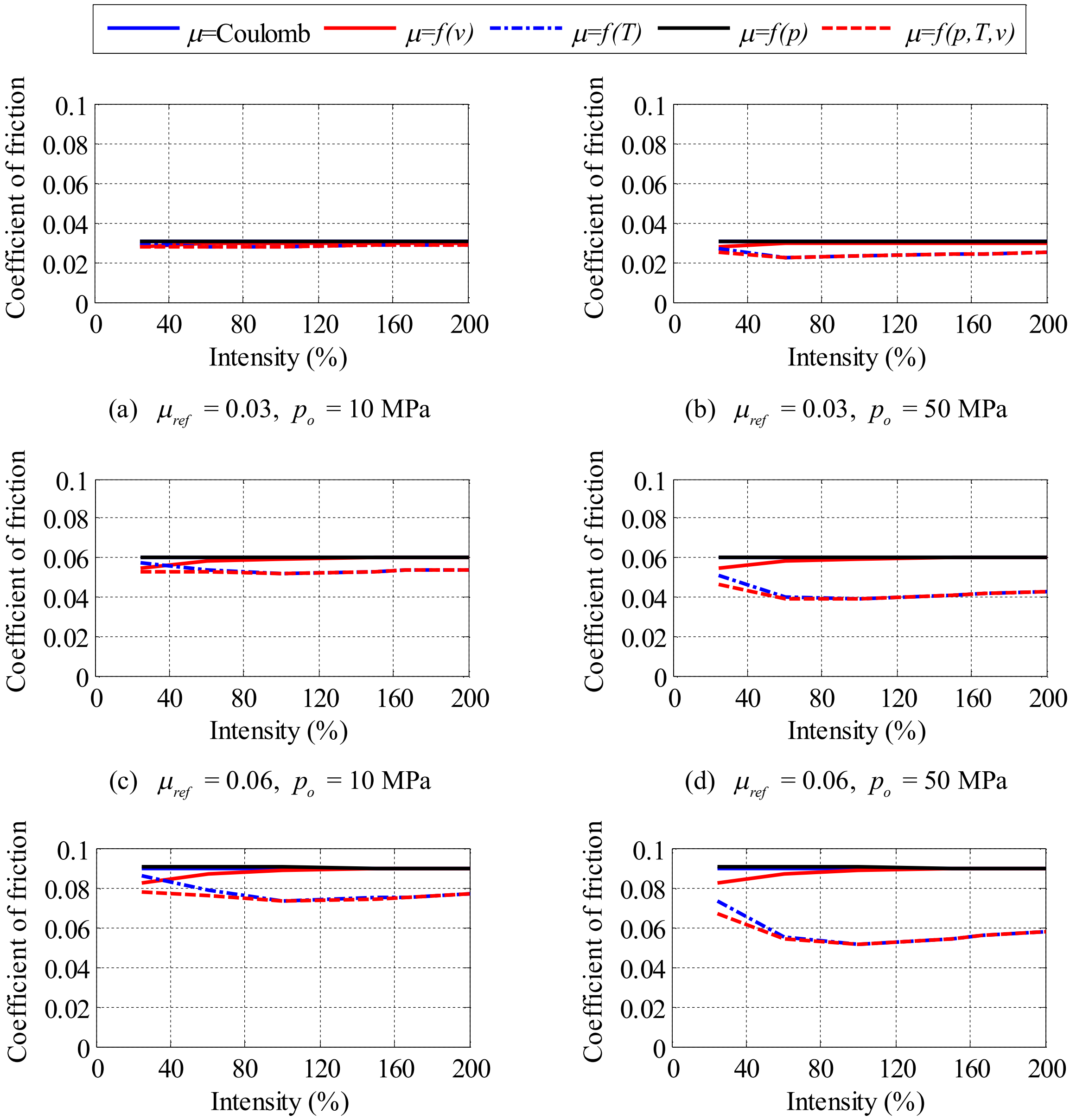

(a) $\mu_{ref} = 0.03$, $p_o = 10$ MPa (b) $\mu_{ref} = 0.03$, $p_o = 50$ MPa

(c) $\mu_{ref} = 0.06$, $p_o = 10$ MPa (d) $\mu_{ref} = 0.06$, $p_o = 50$ MPa

(e) $\mu_{ref} = 0.09$, $p_o = 10$ MPa (f) $\mu_{ref} = 0.09$, $p_o = 50$ MPa

Figure 7-12: Coefficient of friction in the duration of strong shaking averaged over 30 ground motions as a function of shaking intensity for an FP bearing with a sliding period of 4 s

7.5.2 Force-displacement response

Figure 7-13(a) presents the force-displacement response in a horizontal direction (say X) of the single FP bearing with a sliding period of 3 s, μ_{ref} of 0.06, friction at the sliding surface defined using the Coulomb model, and p_o of 10 MPa, subjected to GM30 with the amplitude scaling factor of 1.0. Figure 7-13(c) presents the response when friction is described using $\mu = f\left(p,T,v\right)$ model. The reduction in the coefficient of friction is evident by comparing the shearing forces in panels (a) and (c). The maximum displacements in the two panels are 0.27 m and 0.30 m, respectively. Panels (b) and (d) present the force-displacement response for p_o of 50 MPa, and friction at the sliding surface described by the Coulomb model and $\mu = f\left(p,T,v\right)$ model, respectively. The peak displacements in these two panels are 0.27 m and 0.39 m, respectively. There is a greater reduction in the coefficient of friction at the higher static axial pressure.

7.5.3 Displacement demand

Figure 7-14(a) presents the 16th, 50th, 84th and 99th percentiles of peak displacements of the FP bearing with a sliding period of 3 s, a μ_{ref} of 0.03 with the coefficient of friction defined using the five models of Table 7-2, and a p_o of 10 MPa subjected to the 30 ground motions amplitude scaled by 1.0. The 30 values of peak displacements are assumed to distribute lognormally; the assumption is verified in Appendix H. The distribution is virtually unaffected by the choice of friction model. Figures 7-14(b) and 7-14(c) present the distributions of peak displacements for μ_{ref} of 0.06 and 0.09, respectively. The median (99th percentile) peak displacements for the five friction models differ from each other by approximately 10% (5%).

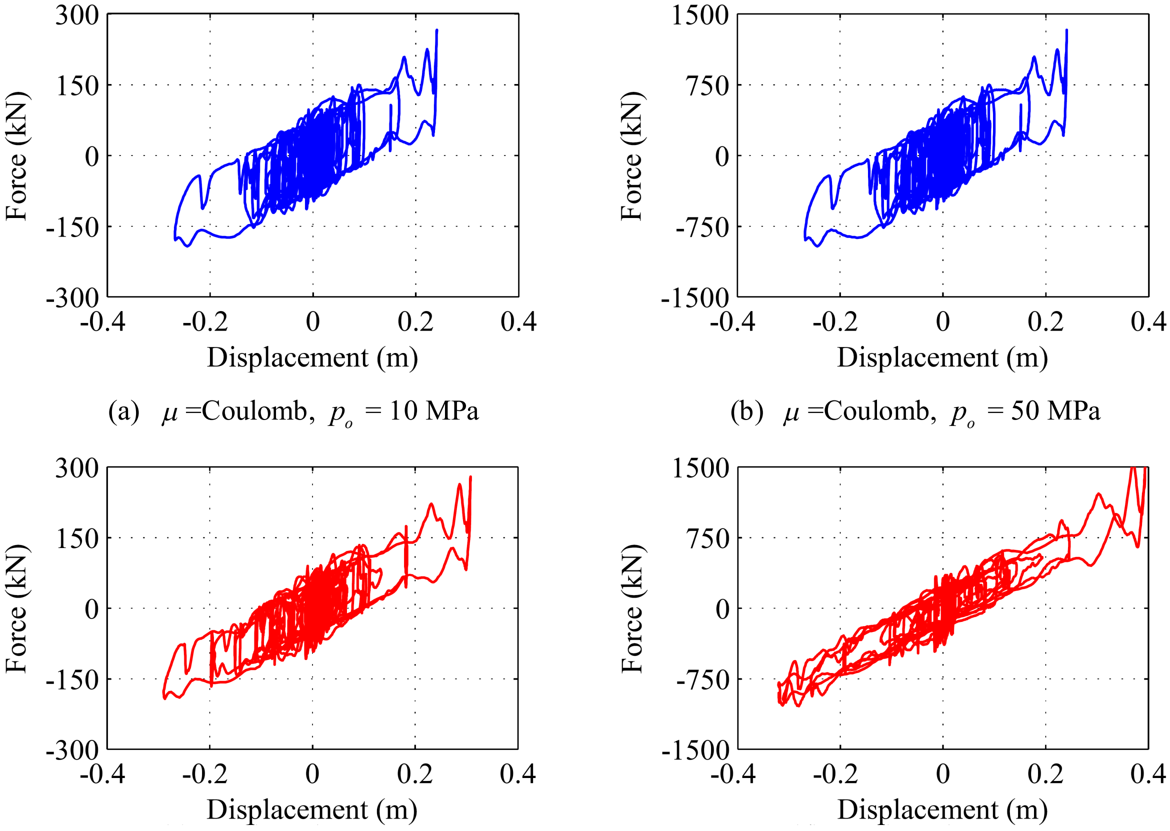

(a) μ =Coulomb, p_o = 10 MPa   (b) μ =Coulomb, p_o = 50 MPa

(c) $\mu = f(p,T,v)$, p_o = 10 MPa   (d) $\mu = f(p,T,v)$, p_o = 50 MPa

Figure 7-13: Force-displacement histories of an FP bearing in X direction with a sliding period of 3 s and μ_{ref} of 0.06, subjected to GM30 at 100% shaking intensity

Figures 7-14(d), 7-14(e) and 7-14(f) present the distributions for p_o of 50 MPa and μ_{ref} of 0.03, 0.06 and 0.09, respectively. The distributions are significantly influenced by heating effects. The median (99th percentile) displacement estimates are greater by about 10% (10%), 25% (15%) and 40% (15%), respectively, for the three panels if the effects of heating are included in the friction model.

Figure 7-15 presents the 50th percentile (or median) peak displacements of the 3 s FP bearing subjected to ground motions scaled using the six factors of Table 7-3. Median displacements for p_o of 10 MPa and μ_{ref} of 0.03 are plotted against shaking intensity in Figure 7-15(a). The displacements are not influenced by the choice of friction model. Figures 7-15(c) and 7-15(e) present results for μ_{ref} of 0.06 and 0.09, respectively. The median displacements are greater by less than 10% (15%) when the friction model addresses heating, for μ_{ref} of 0.06 (0.09). The percentage difference is greatest for shaking intensities of 60% or 100% for the reason given previously.

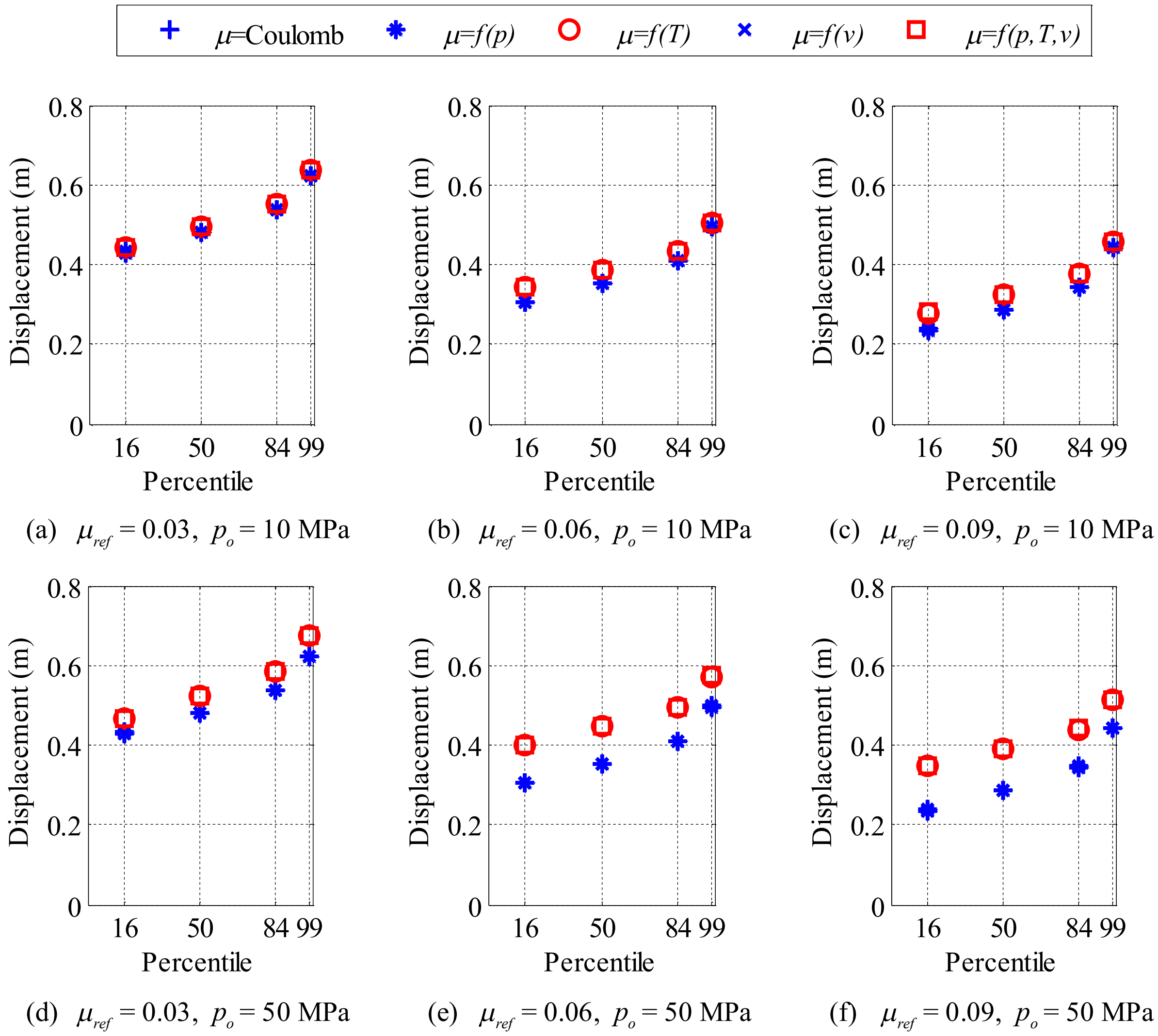

Figure 7-14: Distribution of peak displacements of FP bearing with a sliding period of 3 s, subjected to the 30 ground motions amplitude scaled by 1.0

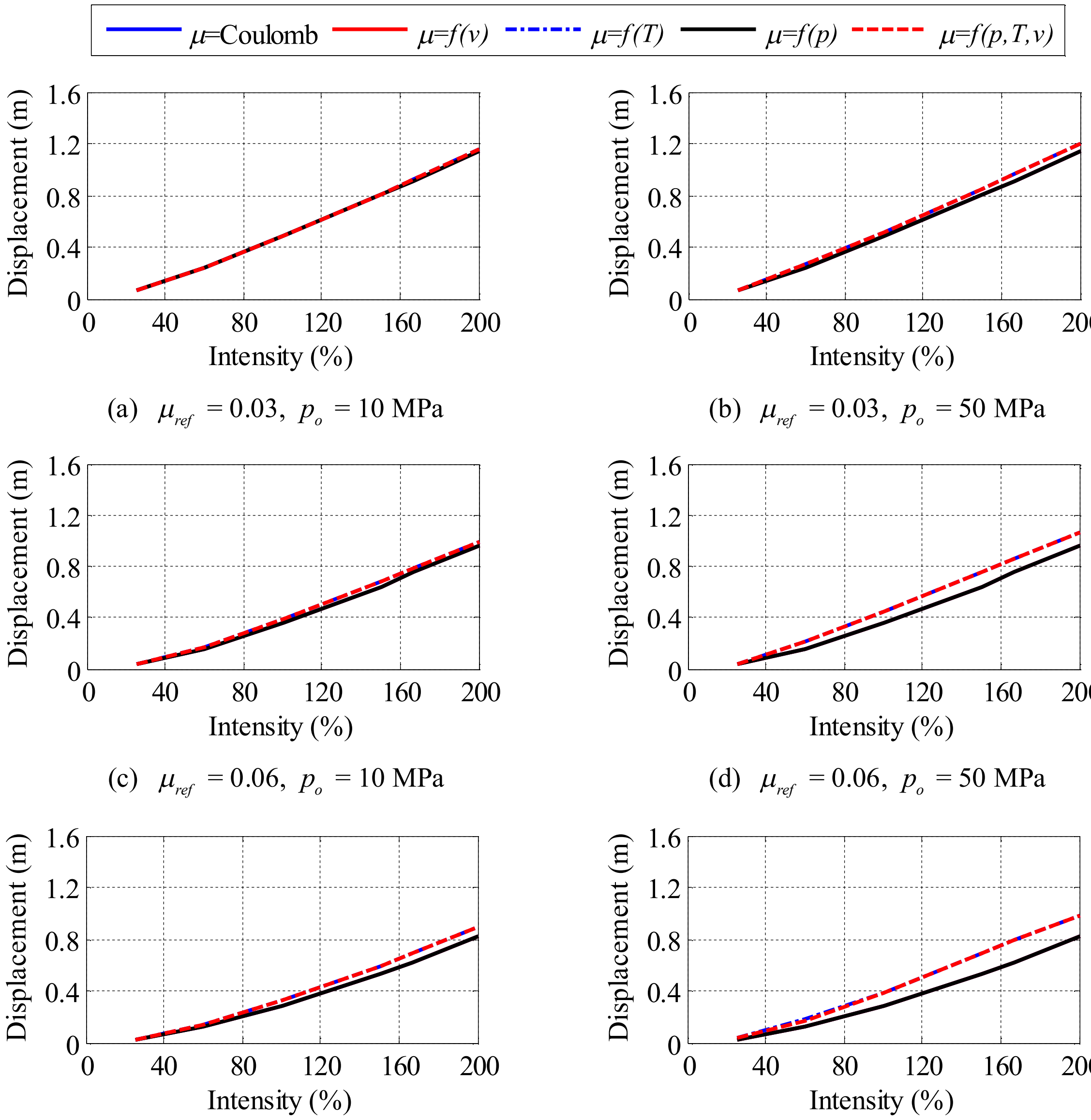

(a) $\mu_{ref} = 0.03$, $p_o = 10$ MPa

(b) $\mu_{ref} = 0.03$, $p_o = 50$ MPa

(c) $\mu_{ref} = 0.06$, $p_o = 10$ MPa

(d) $\mu_{ref} = 0.06$, $p_o = 50$ MPa

(e) $\mu_{ref} = 0.09$, $p_o = 10$ MPa

(f) $\mu_{ref} = 0.09$, $p_o = 50$ MPa

Figure 7-15: Median displacement demand on an FP bearing with a sliding period of 3 s subjected to the 30 ground motions amplitude scaled to different intensities

Figure 7-15(b) presents results for the bearing and ground motions of Figure 7-15(a) but for p_o of 50 MPa. The median peak displacements obtained using the temperature-dependent friction models are greater than those obtained using the Coulomb model by between 5% to 15%. Figure 7-15(d) presents results for μ_{ref} of 0.06. The maximum percentage difference is approximately

30%, at the shaking intensity of 60%, which decreases to 15% (10%) at the shaking intensity of 25% (200%). Figure 7-15(f) presents results for μ_{ref} of 0.09. The peak percentage difference is 40% at a shaking intensity of 60%. The difference decreases to 10% (20%) at a shaking intensity of 25% (200%). Figure 7-16 presents the 90th percentile peak displacements of the FP bearing with a sliding period of 3 s. At p_o of 10 MPa (50 MPa), the displacements obtained using a friction model that accounts for heating effects are greater by less than 2% (10%), 5% (20%) and 10% (25%) for μ_{ref} of 0.03, 0.06 and 0.09, respectively, for different intensities.

Figure 7-17 (Figure 7-18) presents the median (90th percentile) peak displacement demand on an FP bearing with sliding period of 1.5 s subjected to ground motions with shaking intensities of 25% and 60%. Figure 7-19 (Figure 7-20) presents the median (90th percentile) peak displacements of the 2 s FP bearing subjected to the 30 ground motions with shaking intensities of 25%, 60% and 100%. Figure 7-21 (Figure 7-22) presents the median (90th percentile) peak displacements of the 4 s FP bearings subjected to ground motions scaled to intensities of 25%, 60%, 100%, 150%, 167% and 200%. From Figures 7-14 through 7-22, it can be observed that

i. The influence of the choice of friction model on peak displacement is negligible at a shaking intensity of 25%, irrespective of sliding period, p_o and μ_{ref}.

ii. At shaking intensities of 60% or greater, the choice of friction model does not affect the peak displacements materially at p_o = 10 MPa. The influence of the choice of friction model increases slightly with an increase in μ_{ref}.

iii. Heating effects significantly influence the peak displacement at p_o = 50 MPa. Peak displacements are very sensitive to the choice of μ_{ref}. At shaking intensities of 60+%, the median peak displacement estimated using a temperature-dependent friction model can be 15%, 30% and 45% greater than that estimated using a Coulomb model for μ_{ref} of 0.03, 0.06 and 0.09, respectively. The percentage differences are comparatively insensitive to the sliding period.

iv. The 90th percentile displacements are less influenced by the choice of friction model than the median estimates, in a relative sense.

v. Peak displacements are most influenced by the choice of friction model at a shaking intensity of 60% and/or 100%, because the travel path increases significantly at intensities greater than 100%.

7.5.3.1 Clear distance between an isolated nuclear structure and its hard stop

The forthcoming Nuclear Regulatory guideline for seismically isolated nuclear power plants requires the clear distance between the isolated superstructure and the hard stop to no less than the 99th (90th) percentile peak displacement for 10,000 (100,000)-year earthquake shaking, calculated along each axis of the structure. Two sites are considered herein, Vogtle and Diablo Canyon, to establish which hazard level controls the required clearance. The set of 30 ground motions for 10,000-year shaking at Diablo Canyon are amplitude scaled by 0.25 (0.60) to characterize 10,000 (100,000)-year shaking at Vogtle (see Section 7.3 and Appendix G). Similarly, the ground motions are scaled by 1.0 (2.0) to represent 10,000 (100,000)-year shaking at Diablo Canyon (see Section 7.2 and Appendix G).

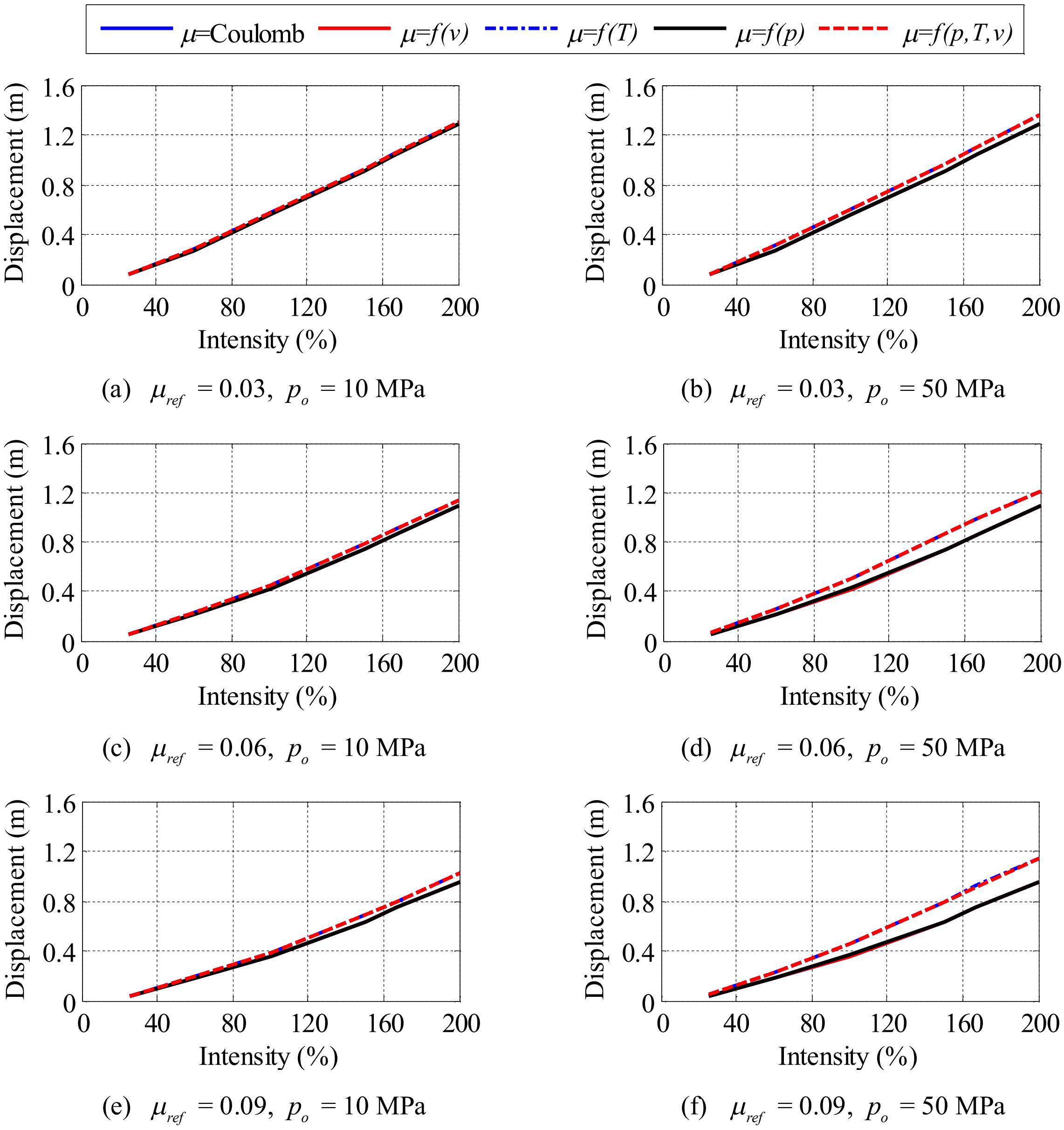

Figure 7-16: 90th percentile displacement demand on an FP bearing with a sliding period of 3 s subjected to the 30 ground motions amplitude scaled to different intensities

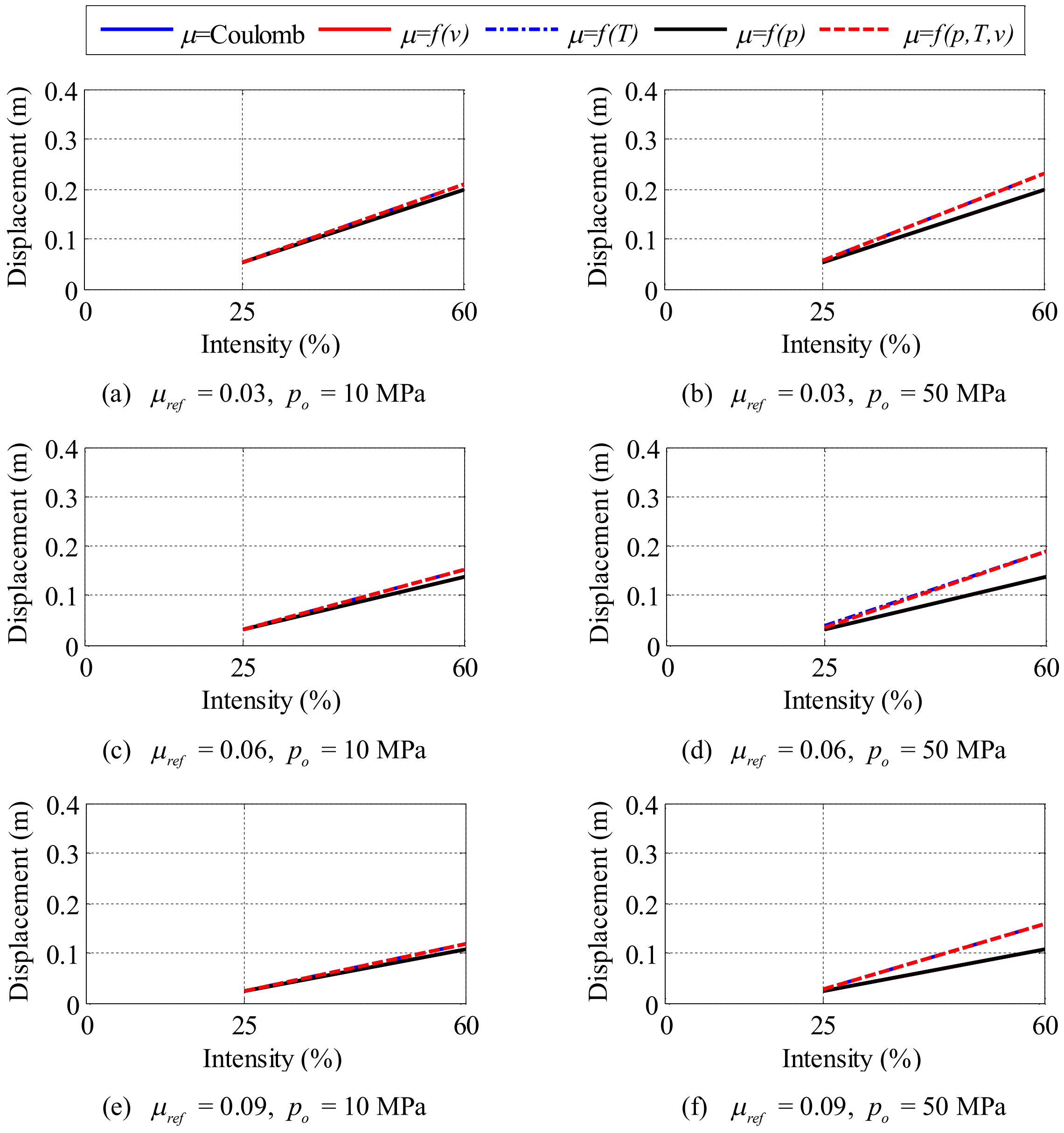

Figure 7-17: Median displacement demand on an FP bearing with a sliding period of 1.5 s subjected to the 30 ground motions amplitude scaled to different intensities

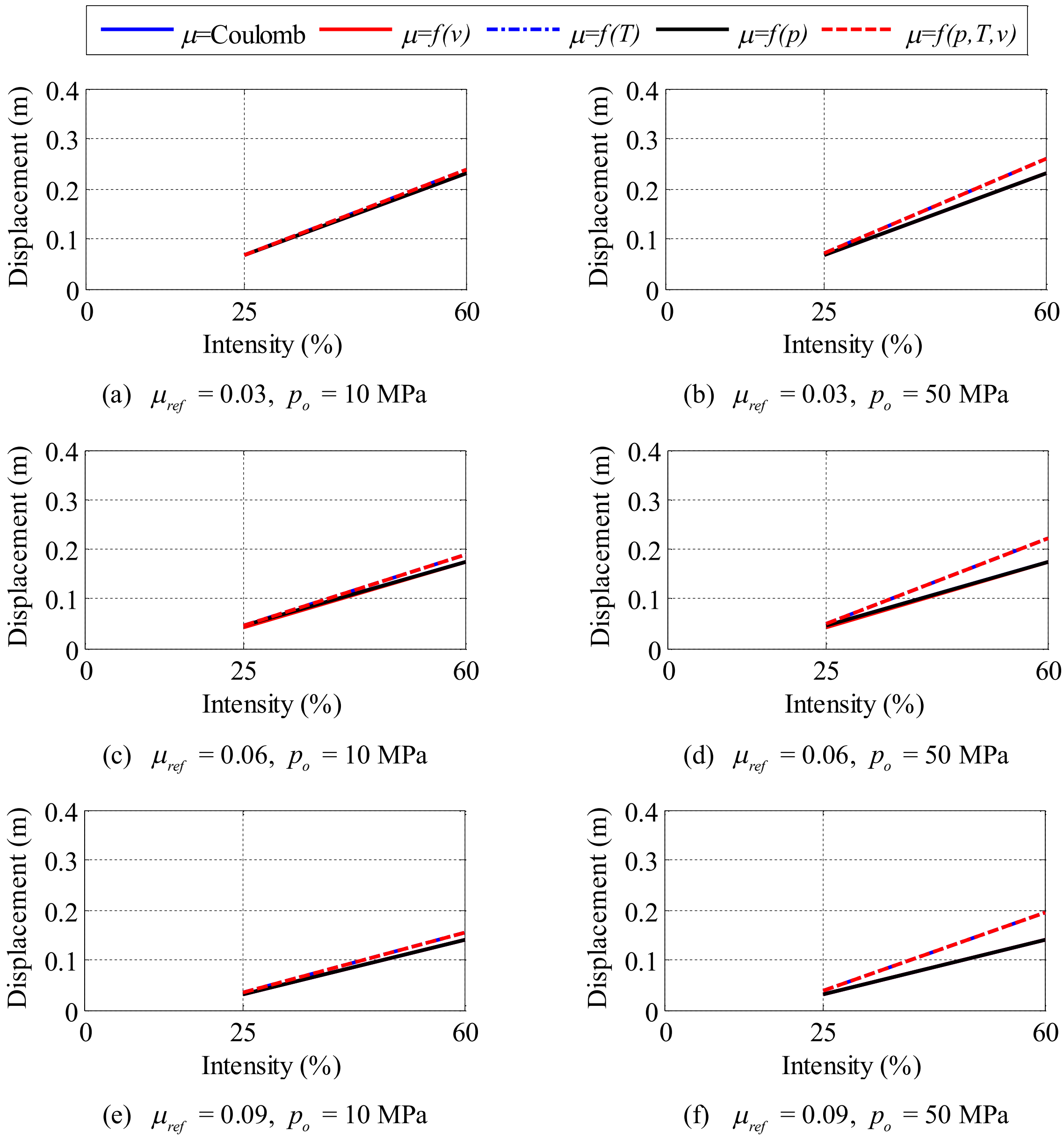

(a) μ_{ref} = 0.03, p_o = 10 MPa

(b) μ_{ref} = 0.03, p_o = 50 MPa

(c) μ_{ref} = 0.06, p_o = 10 MPa

(d) μ_{ref} = 0.06, p_o = 50 MPa

(e) μ_{ref} = 0.09, p_o = 10 MPa

(f) μ_{ref} = 0.09, p_o = 50 MPa

Figure 7-18: 90th percentile displacement demand on an FP bearing with a sliding period of 1.5 s subjected to the 30 ground motions amplitude scaled to different intensities

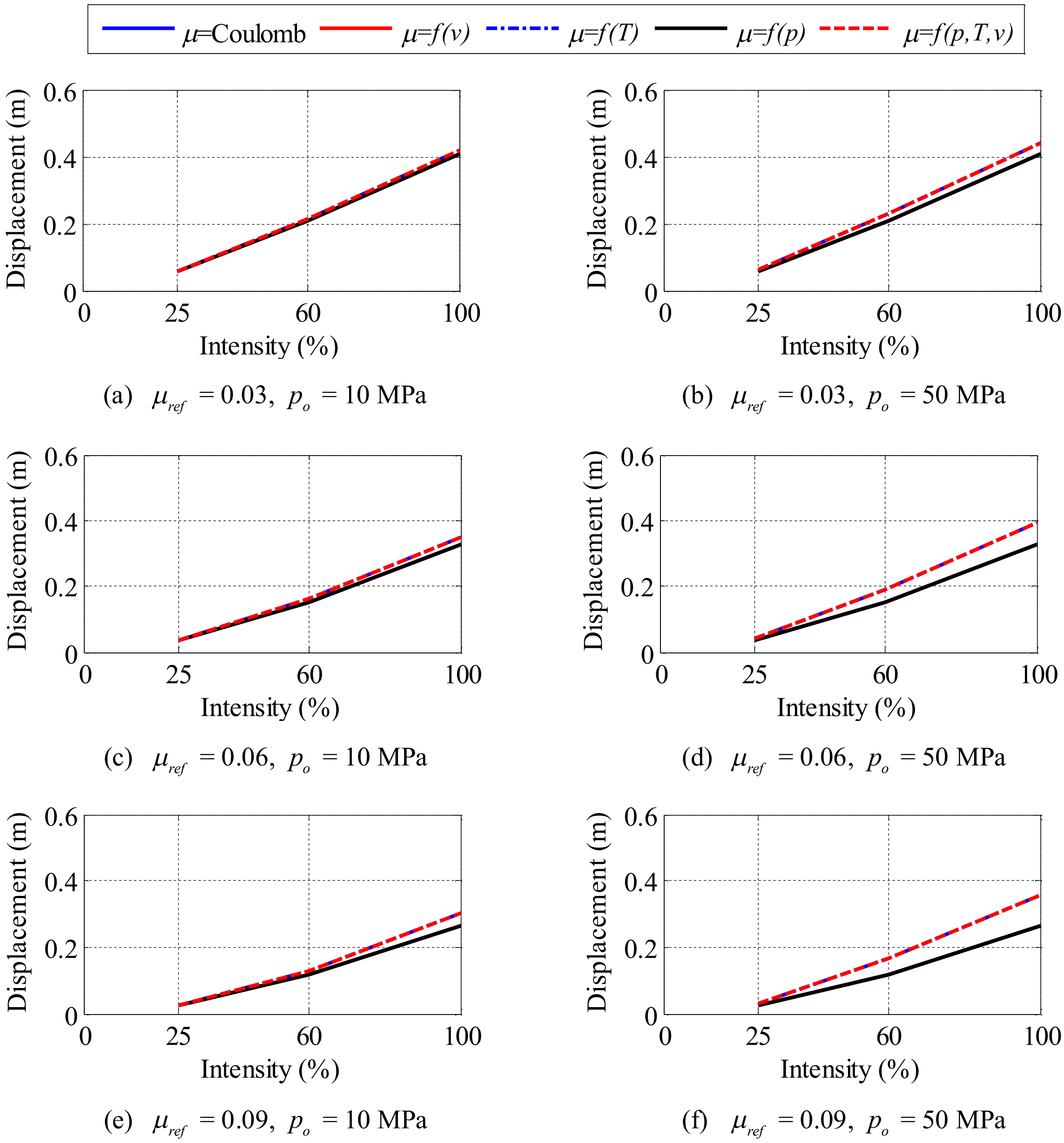

(a) $\mu_{ref} = 0.03$, $p_o = 10$ MPa

(b) $\mu_{ref} = 0.03$, $p_o = 50$ MPa

(c) $\mu_{ref} = 0.06$, $p_o = 10$ MPa

(d) $\mu_{ref} = 0.06$, $p_o = 50$ MPa

(e) $\mu_{ref} = 0.09$, $p_o = 10$ MPa

(f) $\mu_{ref} = 0.09$, $p_o = 50$ MPa

Figure 7-19: Median displacement demand on an FP bearing with a sliding period of 2 s subjected to the 30 ground motions amplitude scaled to different intensities

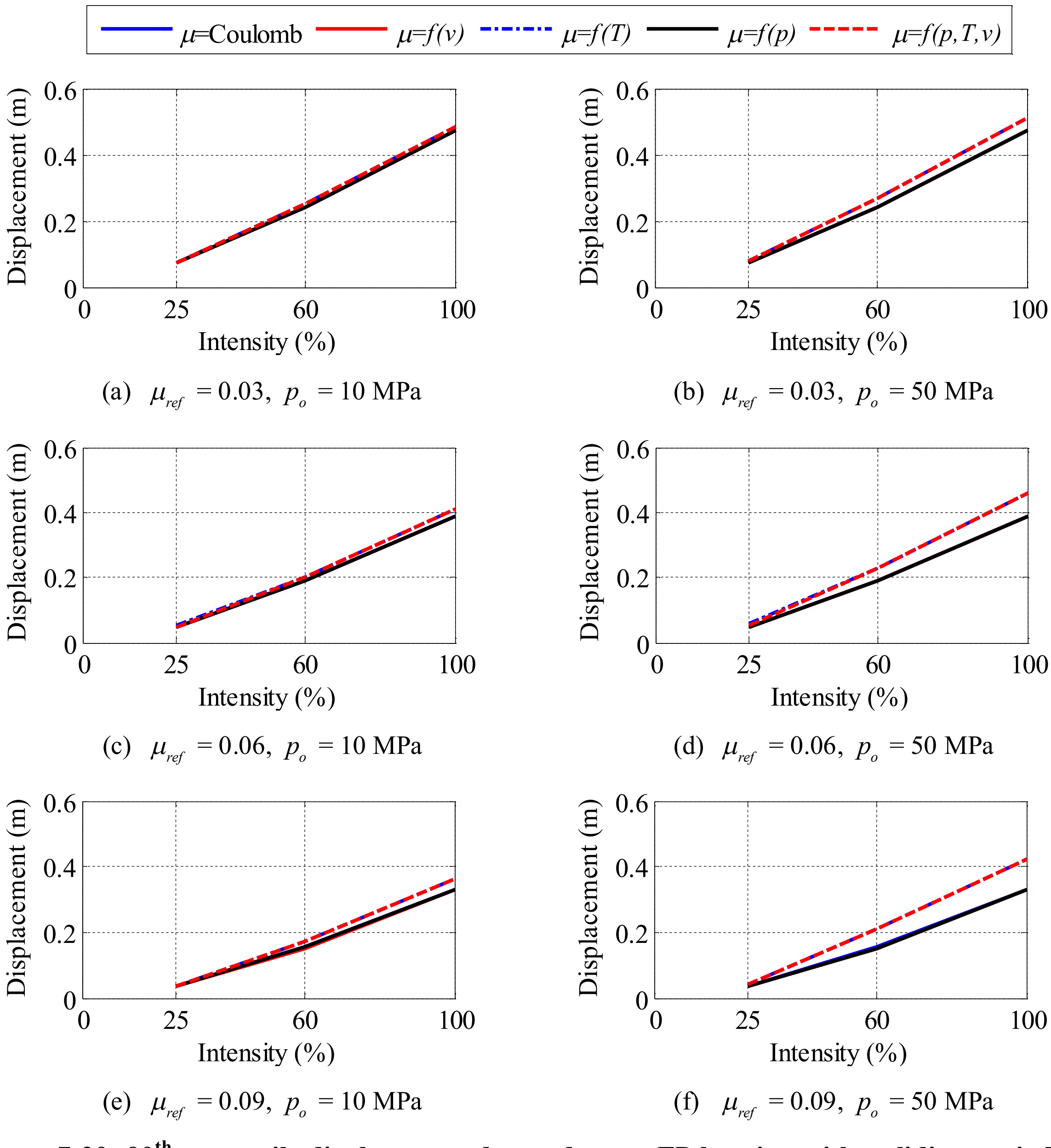

Figure 7-20: 90th percentile displacement demand on an FP bearing with a sliding period of 2 s subjected to the 30 ground motions amplitude scaled to different intensities

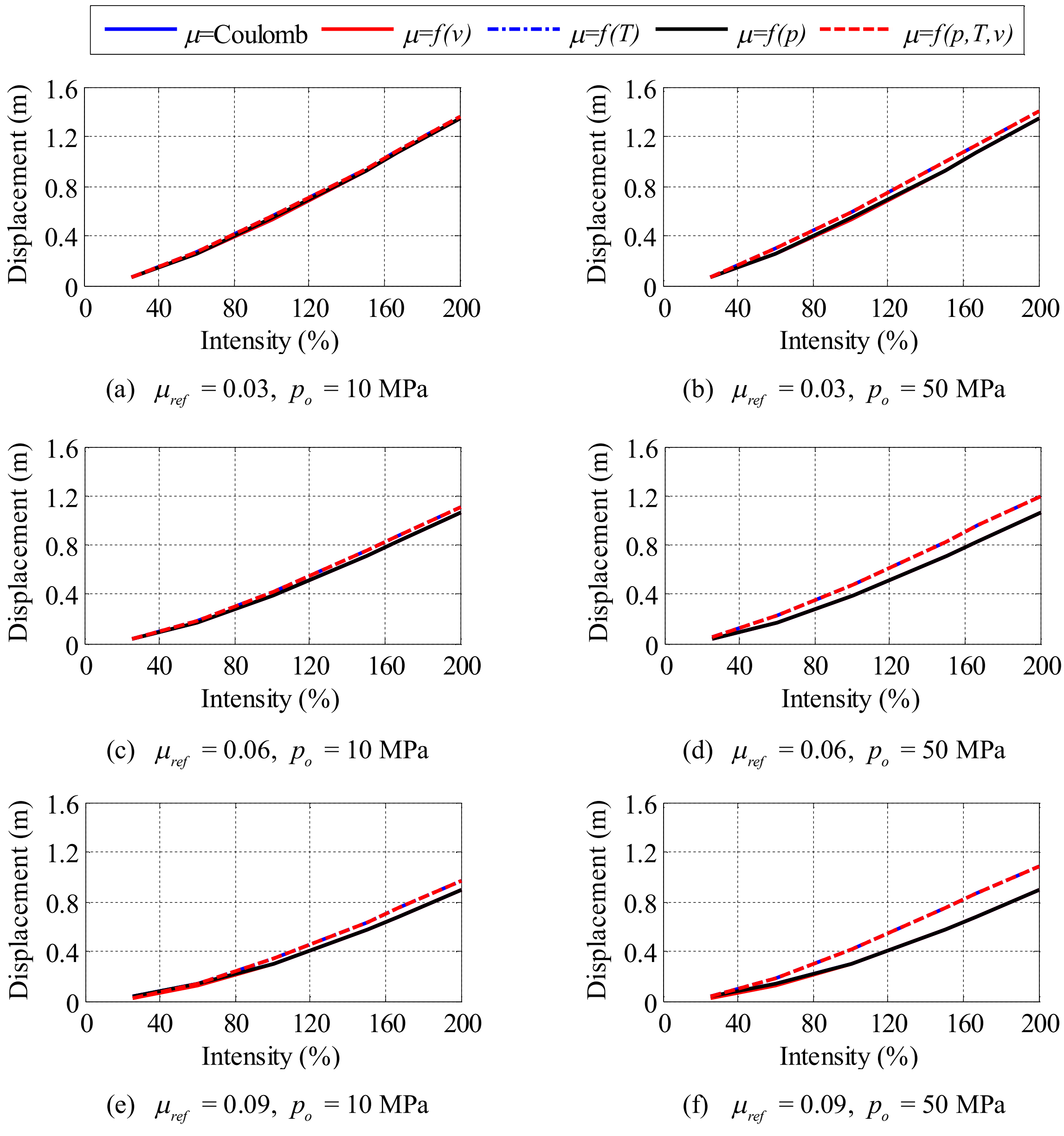

Figure 7-21: Median displacement demand on an FP bearing with a sliding period of 4 s subjected to the 30 ground motions amplitude scaled to different intensities

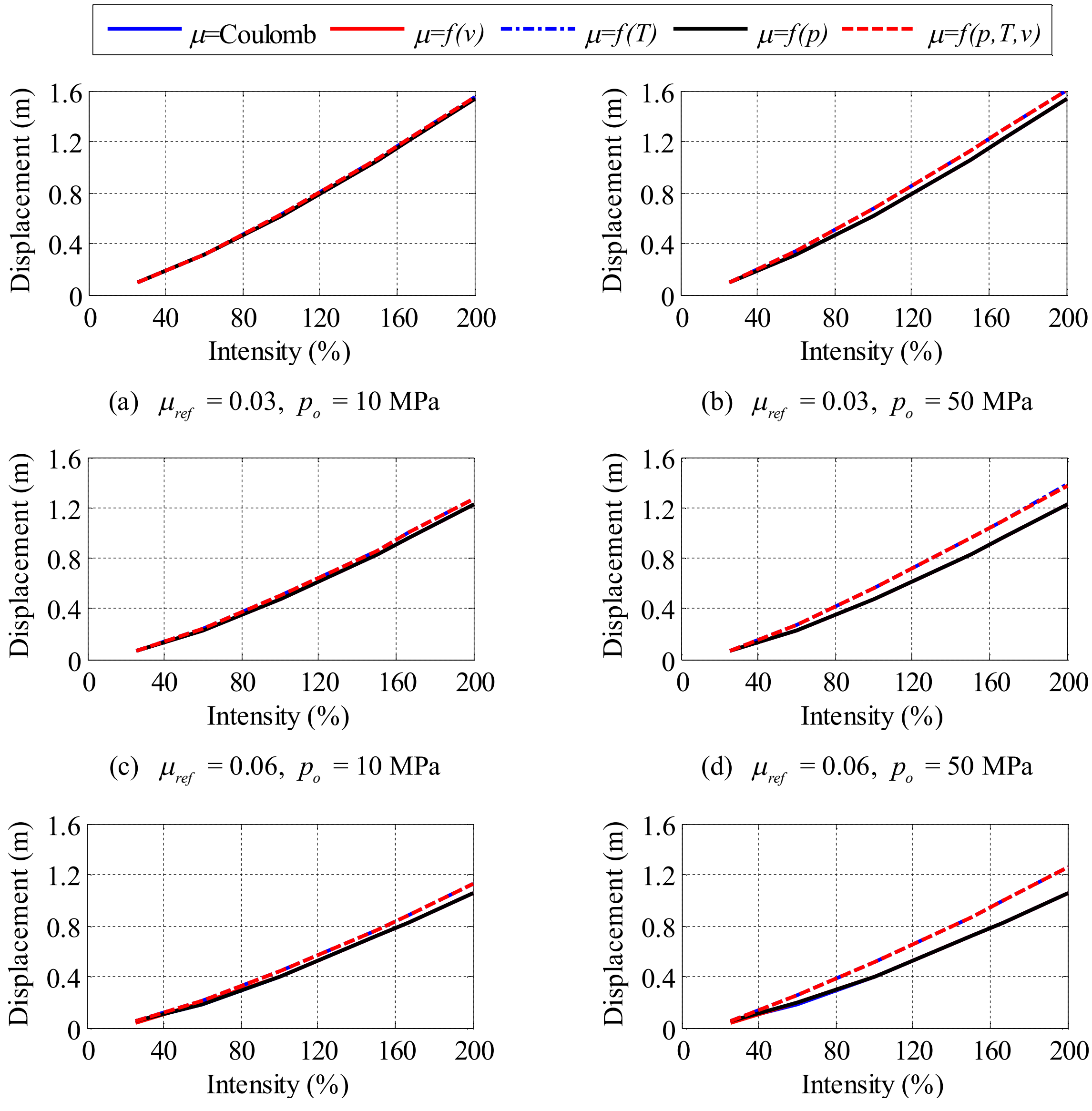

(a) $\mu_{ref} = 0.03,\ p_o = 10$ MPa (b) $\mu_{ref} = 0.03,\ p_o = 50$ MPa

(c) $\mu_{ref} = 0.06,\ p_o = 10$ MPa (d) $\mu_{ref} = 0.06,\ p_o = 50$ MPa

(e) $\mu_{ref} = 0.09,\ p_o = 10$ MPa (f) $\mu_{ref} = 0.09,\ p_o = 50$ MPa

Figure 7-22: 90th percentile displacement demand on an FP bearing with a sliding period of 4 s subjected to the 30 ground motions amplitude scaled to different intensities

7.5.3.1.1 Vogtle

Figure 7-23 presents the 99th (90th) percentile peak displacements for FP bearings with sliding periods, T_{sliding}, of 1.5 s, 2 s, 3 s and 4 s, p_o of 10 MPa and 50 MPa, and μ_{ref} of 0.03, 0.06 and 0.09, subjected to the 30 ground motions scaled by 0.25 (0.60). The 90th percentile peak displacements for the 100,000-year shaking are greater than the 99th percentile peak displacements for the 10,000-year shaking for all combinations of T_{sliding}, p_o, μ_{ref} and choice of friction model. In this figure, DBE (EDBE) denotes results for 10,000 (100,000)-year earthquake shaking.

7.5.3.1.2 Diablo Canyon

Figure 7-24 presents 99th (90th) percentile displacements for FP bearings with T_{sliding} of 3 s and 4 s, p_o of 10 MPa and 50 MPa, and μ_{ref} of 0.03, 0.06 and 0.09, subjected to ground motions at 100% (200%) shaking. The 90th percentile displacement for 100,000-year shaking is greater than the 99th percentile displacement for 10,000-year shaking. Similar to Figure 7-23, DBE (EDBE) represents 10,000 (100,000)-year shaking in Figure 7-24.

7.5.3.1.3 Clearance to the stop

The results presented in Figures 7-23 and 7-24 make it clear that the clearance to the hard stop is dictated by the 90th percentile displacement for 100,000-year earthquake shaking.

7.5.3.2 Relationships between median and 90th percentile displacements and hazard levels

Fragility curves were developed for individual isolators and safety-related umbilical lines in Chapter 6, which assumed that the clearance to the hard stop (90th percentile displacement for 100,000-year shaking) is greater than or equal to the median displacement for 1.1 times 100,000-year shaking. The assumption is verified below for three sites spanning the range of seismic hazard considered herein (see Table 6-3): Diablo Canyon, Vogtle and North Anna.

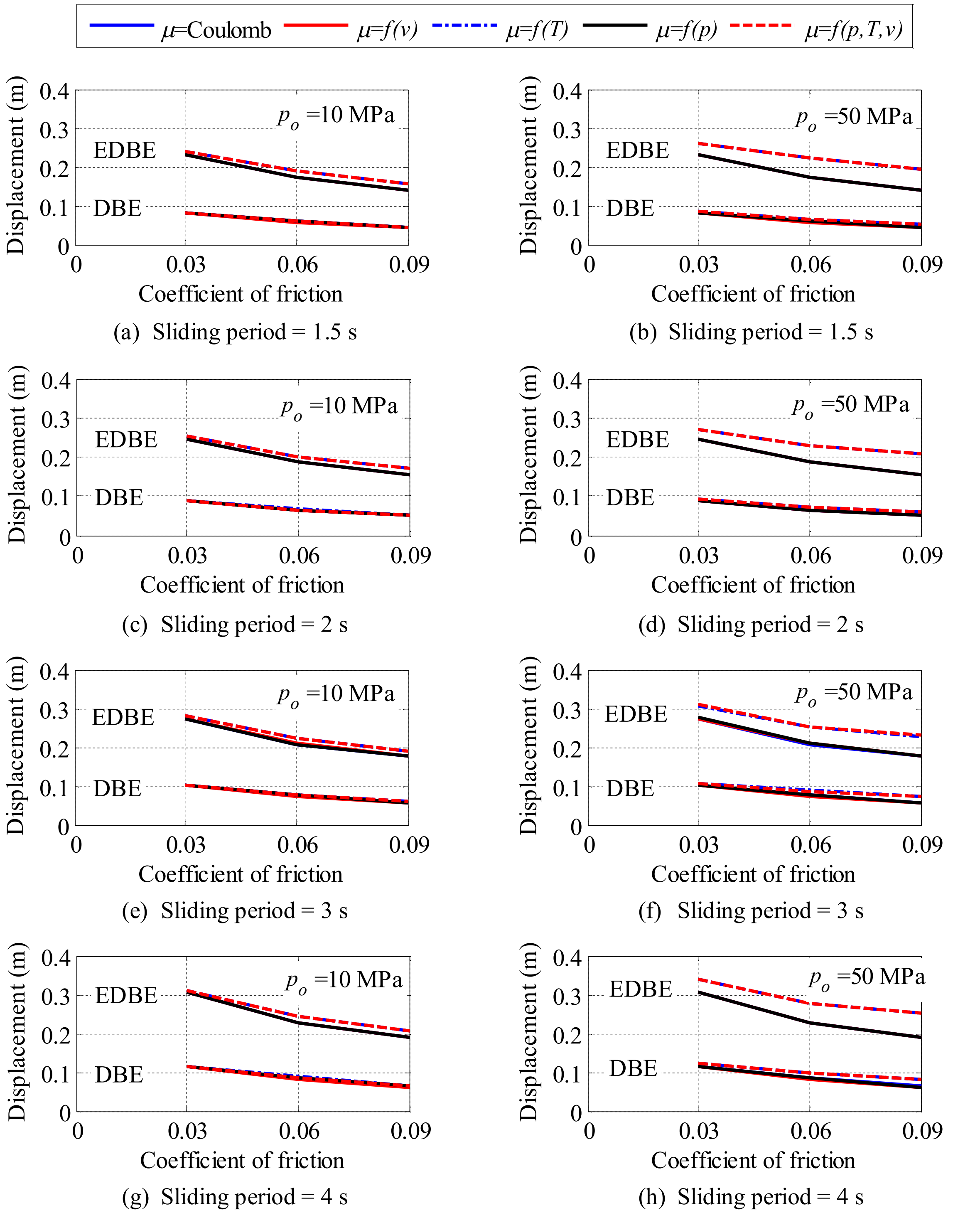

(a) Sliding period = 1.5 s

(b) Sliding period = 1.5 s

(c) Sliding period = 2 s

(d) Sliding period = 2 s

(e) Sliding period = 3 s

(f) Sliding period = 3 s

(g) Sliding period = 4 s

(h) Sliding period = 4 s

Figure 7-23: 99th percentile displacement for DBE shaking and 90th percentile displacement for EDBE shaking at Vogtle

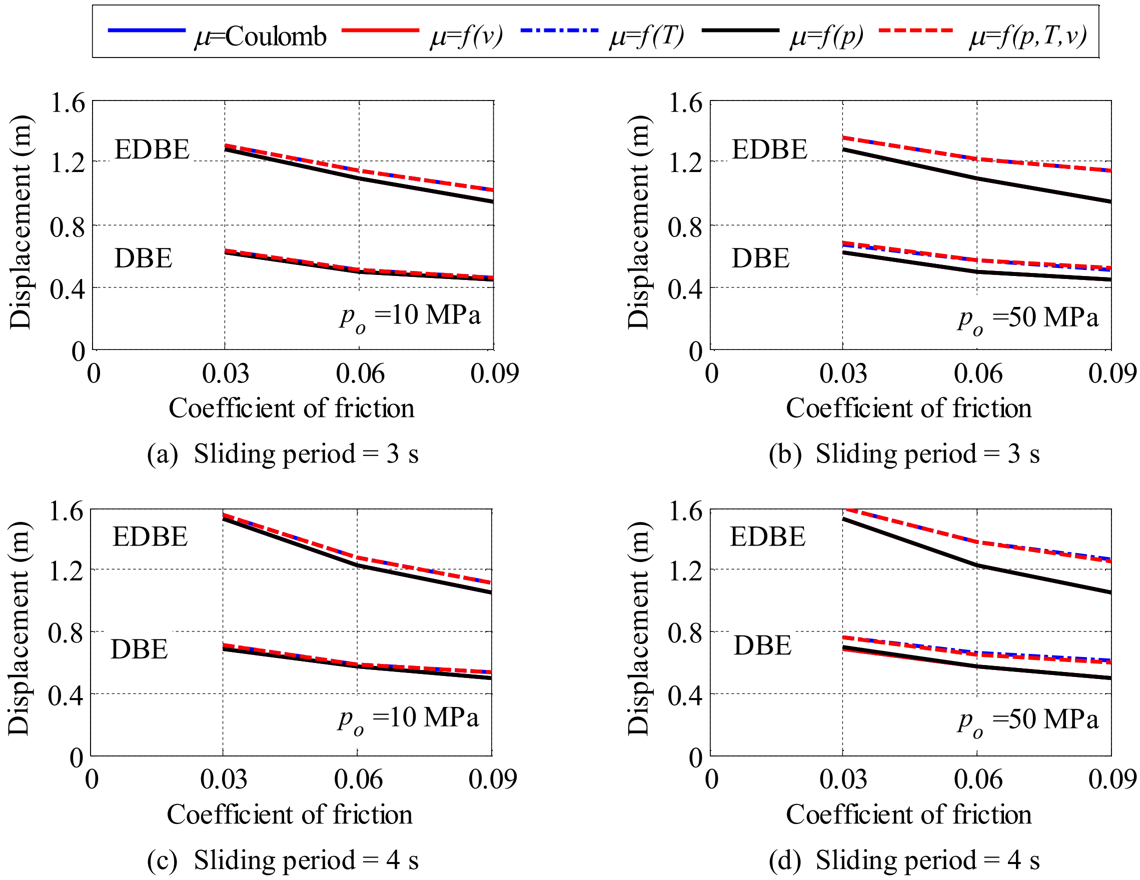

Figure 7-24: 99th percentile displacement for DBE shaking and 90th percentile displacement for EDBE shaking at Diablo Canyon

Spectrally matched ground motions consistent with 10,000-year shaking were developed for Diablo Canyon in Section 7.2. These ground motions were amplitude scaled to represent 100,000-year shaking at Diablo Canyon (×2), and 10,000-year (×0.25) and 100,000-year (×0.60) shaking at Vogtle; see Sections 7.2 and 7.3. Ground motions for 100,000-year shaking at North Anna are generated by amplitude scaling the 10,000-year Diablo Canyon motions by 0.50, which is the average of the ratios of the 1 s and 2 s spectral ordinates for 100,000-year shaking at North Anna to those for 10,000-year shaking at Diablo Canyon; see Table 6-3.

Single FP bearings with sliding periods of 3 s and 4 s, μ_{ref} of 0.06 and 0.09, p_o of 50 MPa and friction at the sliding surface described using Coulomb model and $\mu = f\left(p,T,v\right)$ model subjected to the ground motions with shaking intensities of 25%, 50%, 75%, 100%, 125%, 150%, 175%, 200%, 225%, 250%, 275% and 300%. The median displacements are plotted against shaking intensity in Figures 7-25 and 7-26 for the bearings with friction at the sliding surface described using the Coulomb and $\mu = f(p, T, v)$ models, respectively.

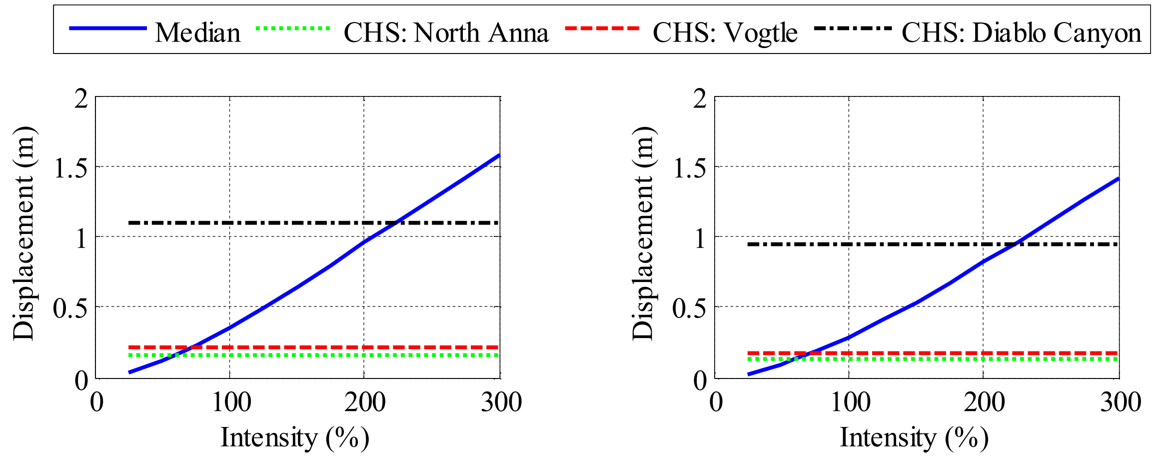

(a) Sliding period = 3 s; μ_{ref} = 0.06

(b) Sliding period = 3 s; μ_{ref} = 0.09

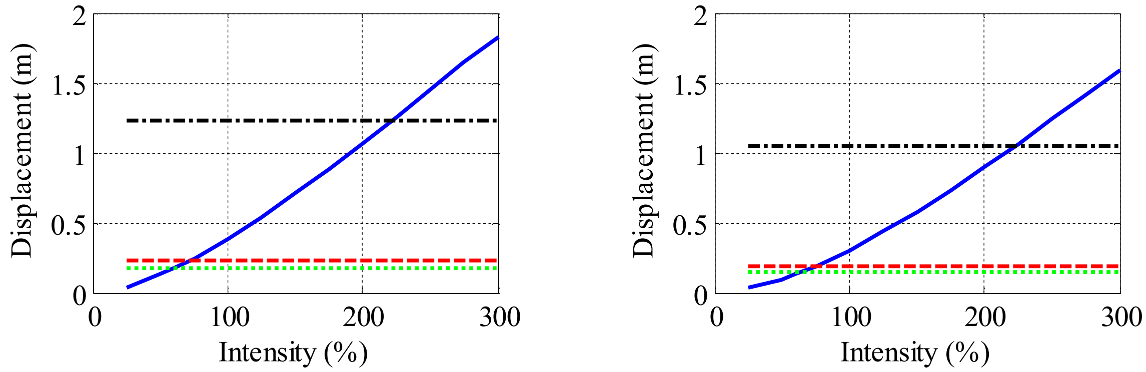

(c) Sliding period = 4 s; μ_{ref} = 0.06

(d) Sliding period = 4 s; μ_{ref} = 0.09

Figure 7-25: Median displacement plotted against intensity of shaking for a single FP bearing with friction at the sliding surface described using the Coulomb model; clearance to the hard stop (CHS) corresponds to the 90th percentile displacement for 100,000-year shaking

The intensity at which the median displacement is equal to the 90th percentile displacement for 100,000-year shaking ranges between 1.10 and 1.13 times the 100,000-year shaking for Diablo

Canyon, 1.13 and 1.24 for Vogtle, and 1.16 and 1.25 for North Anna, across all combinations of sliding period, μ_{ref} and definitions of friction model considered in Figures 7-25 and 7-26. Therefore, it is conservative (overestimating risk) to assume that the median displacement for 1.1 times 100,000-year shaking is equal to the 90th percentile displacement for 100,000-year shaking for the purpose of developing fragility curves for individual isolator units or umbilical lines.

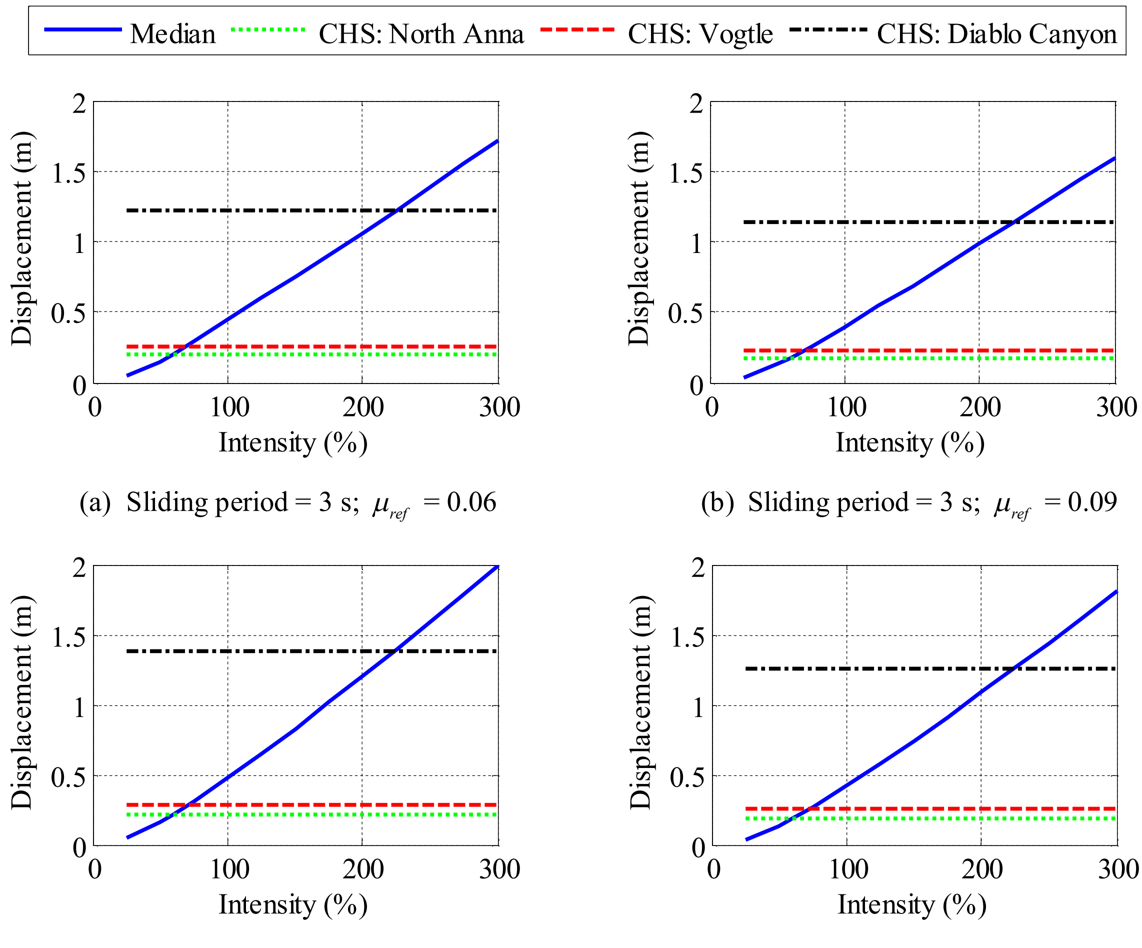

(a) Sliding period = 3 s; μ_{ref} = 0.06

(b) Sliding period = 3 s; μ_{ref} = 0.09

(c) Sliding period = 4 s; μ_{ref} = 0.06

(d) Sliding period = 4 s; μ_{ref} = 0.09

Figure 7-26: Median displacement plotted against intensity of shaking for a single FP bearing with friction at the sliding surface described using the *p-T-v* model; clearance to the hard stop (CHS) corresponds to the 90th percentile displacement at 100,000-year shaking

7.5.4 Temperature at the sliding surface

The temperature at the center of the sliding surface is considered appropriate to characterize heating effects (see Chapter 3). It is a function of the histories of axial pressure on the bearing, sliding velocity and coefficient of friction, in addition to the path of the slider relative to the sliding surface. This section reports temperature at the center of the sliding surface of FP bearings with different geometrical and material properties subjected to ground motions with a range of shaking intensities.

Figure 7-27 presents the percentiles of the temperature (assumed lognormal distribution; see Appendix H) at the center of the sliding surface of an FP bearing with a sliding period of 3 s, μ_{ref} of 0.03, 0.06 and 0.09, and p_o of 10 MPa and 50 MPa, subjected to the ground motions amplitude scaled by 1.0. The influence of choice of friction model is small on the temperature estimates at p_o of 10 MPa (Figures 7-27(a) through 7-27(c)). Results for p_o of 50 MPa are presented in Figures 7-27(d), 7-27(e) and 7-27(f) for μ_{ref} of 0.03, 0.06 and 0.09, respectively: the inclusion of heating effects influences the response significantly. The median peak temperatures for p_o of 50 MPa and μ_{ref} of 0.03, 0.06 and 0.09 are 210˚C, 350˚C and 480˚C, respectively, when the friction model ignores heating effects, and 150˚C, 220˚C and 280˚C, respectively, when it does. The 99th percentile peak temperatures for the three panels are 300˚C, 550˚C and 740˚C[1], respectively, when the heating effects are ignored and 200˚C, 290˚C and 380˚C, respectively, otherwise.

[1] There are no data available to characterize the performance of the FP composite at 740˚C.

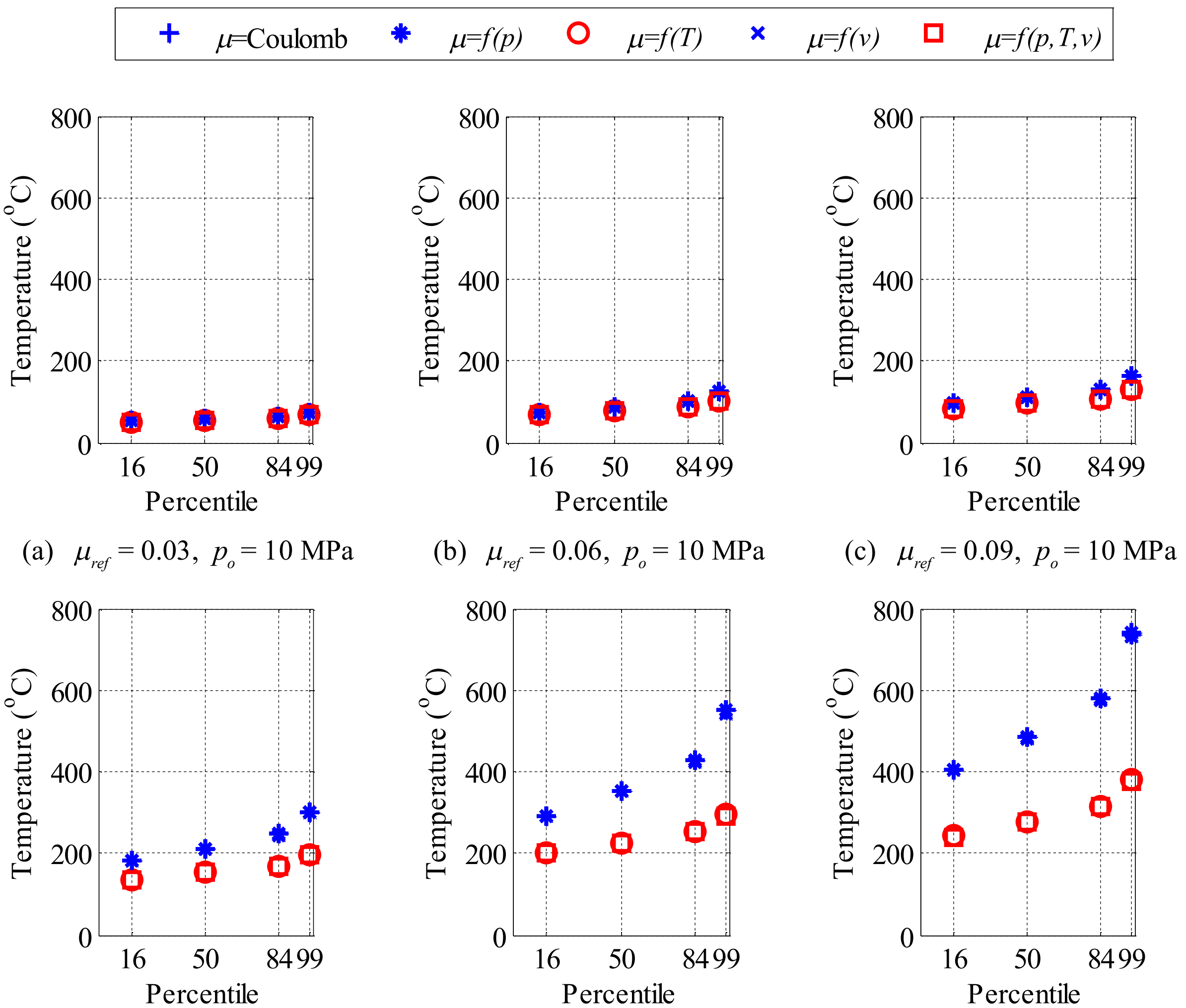

(a) $\mu_{ref} = 0.03,\ p_o = 10$ MPa (b) $\mu_{ref} = 0.06,\ p_o = 10$ MPa (c) $\mu_{ref} = 0.09,\ p_o = 10$ MPa

(d) $\mu_{ref} = 0.03,\ p_o = 50$ MPa (e) $\mu_{ref} = 0.06,\ p_o = 50$ MPa (f) $\mu_{ref} = 0.09,\ p_o = 50$ MPa

Figure 7-27: Distribution of peak temperature at the center of the sliding surface of the FP bearing with sliding period of 3 s subjected to the 30 ground motions with an amplitude scale factor of 1.0

Figure 7-28 (Figure 7-29) presents the median (90^{th} percentile) peak temperatures at the sliding surface of a 3 s FP bearing subjected to the set of 30 ground motions amplitude scaled by 0.25, 0.6, 1.0, 1.5, 1.67 and 2.0. The influence of the friction model is negligible at shaking intensity of 25%, irrespective of p_o and μ_{ref}. At p_o of 10 MPa (panels (a), (c) and (e)), the peak temperature is not sensitive to the choice of friction model. The median (90^{th} percentile) peak temperature can be greater by 70˚C (210˚C), 180˚C (250˚C) and 300˚C (400˚C) if the friction model ignores heating effects for μ_{ref} of 0.03, 0.06 and 0.09, respectively, at p_o of 50 MPa and a shaking intensity of 100% and greater. The peak temperature at the center of the sliding surface, and consequently the difference in the peak temperatures obtained using the two friction models, trends to a constant value at intensities greater than 100% because the slider traverses a path farther away from the center of the sliding surface during much of the strong shaking.

The median (90th percentile) peak temperatures at the center of the sliding surface of FP bearings with sliding periods of 1.5 s, 2 s and 4 s, subjected to ground motions with different amplitude scaling factors, are presented in Figures 7-30 (7-31), 7-32 (7-33) and 7-34 (7-35), respectively. The results for all of the cases considered in this section can be summarized as follows:

i. The peak temperatures are smaller when the friction model includes the temperature dependence of the coefficient of friction, because the coefficient of friction decreases with increase in temperature, leading to smaller heat generation and temperature rise.

ii. The velocity and axial pressure dependences of the coefficient of friction do not influence the peak temperature.

iii. The choice of friction model is not important for low amplitude shaking (shaking intensity of 25%) and small contact pressure (p_o = 10 MPa here).

iv. The importance of the choice of friction model increases with μ_{ref}.

v. The estimates of median and 90th percentile peak responses are most significantly affected by whether the friction model includes temperature dependence of friction, when shaking intensity is greater than or equal to 100%, p_o is 50 MPa and μ_{ref} is 0.09. The difference in the median (90th percentile) peak temperature due to choice of friction model can be as great as 300^{o}C (400^{o}C).

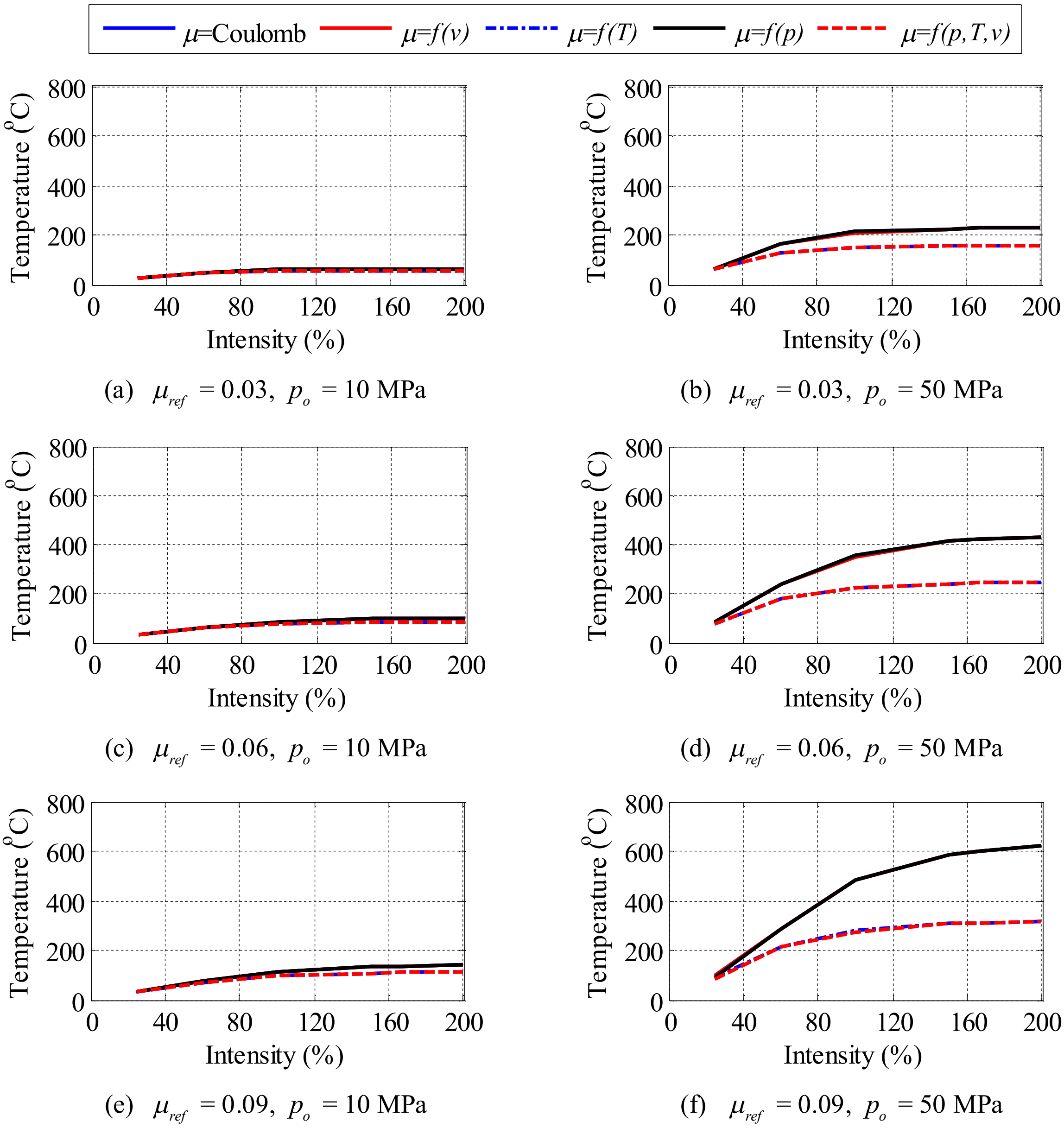

Figure 7-28: Median peak temperature at the center of the sliding surface of the FP bearing with a sliding period of 3 s subjected to the 30 ground motions amplitude scaled to different intensities

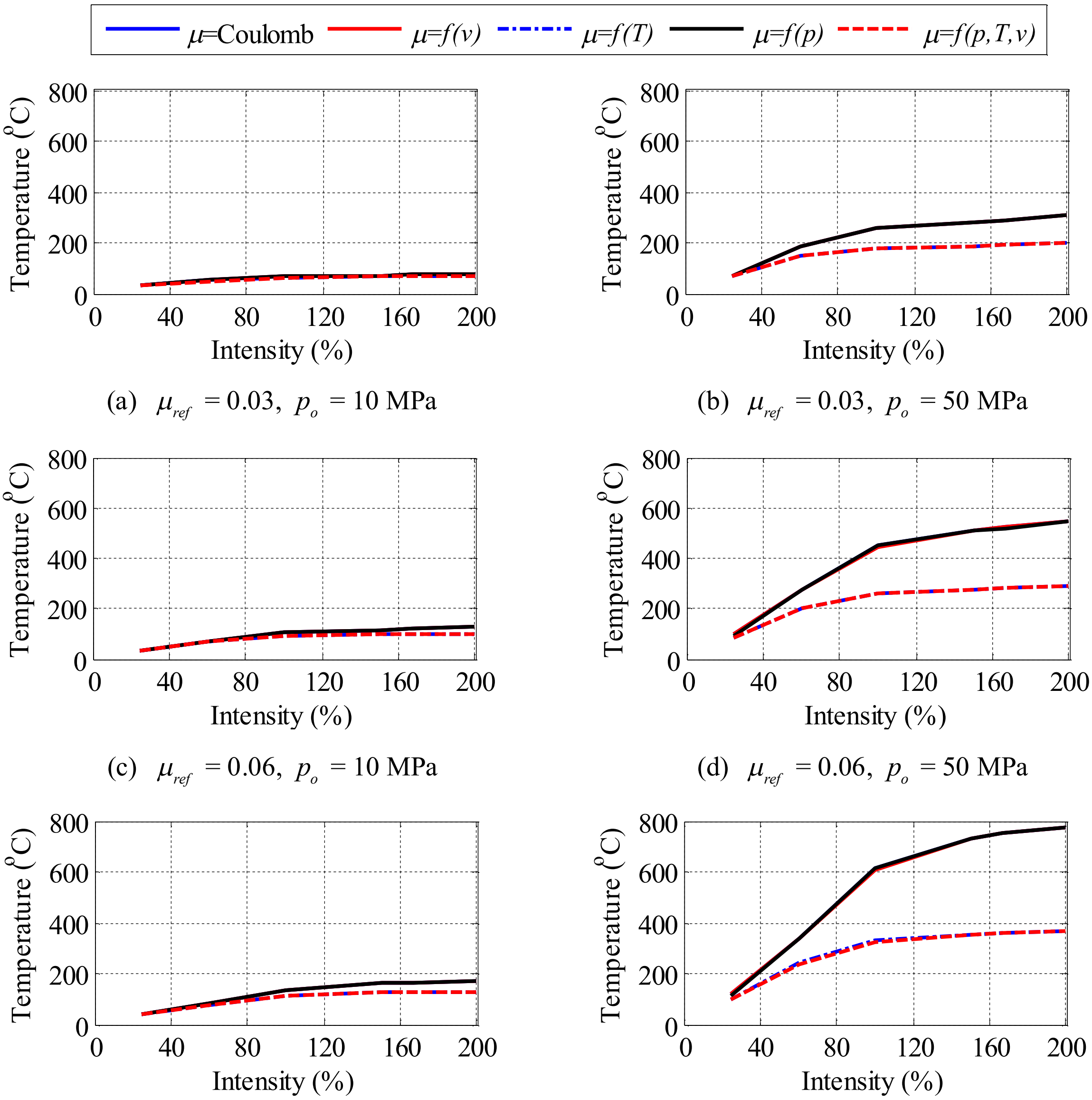

(a) $\mu_{ref} = 0.03,\ p_o = 10$ MPa

(b) $\mu_{ref} = 0.03,\ p_o = 50$ MPa

(c) $\mu_{ref} = 0.06,\ p_o = 10$ MPa

(d) $\mu_{ref} = 0.06,\ p_o = 50$ MPa

(e) $\mu_{ref} = 0.09,\ p_o = 10$ MPa

(f) $\mu_{ref} = 0.09,\ p_o = 50$ MPa

Figure 7-29: 90th percentile peak temperature at the center of the sliding surface of the FP bearing with a sliding period of 3 s subjected to the 30 ground motions amplitude scaled to different intensities

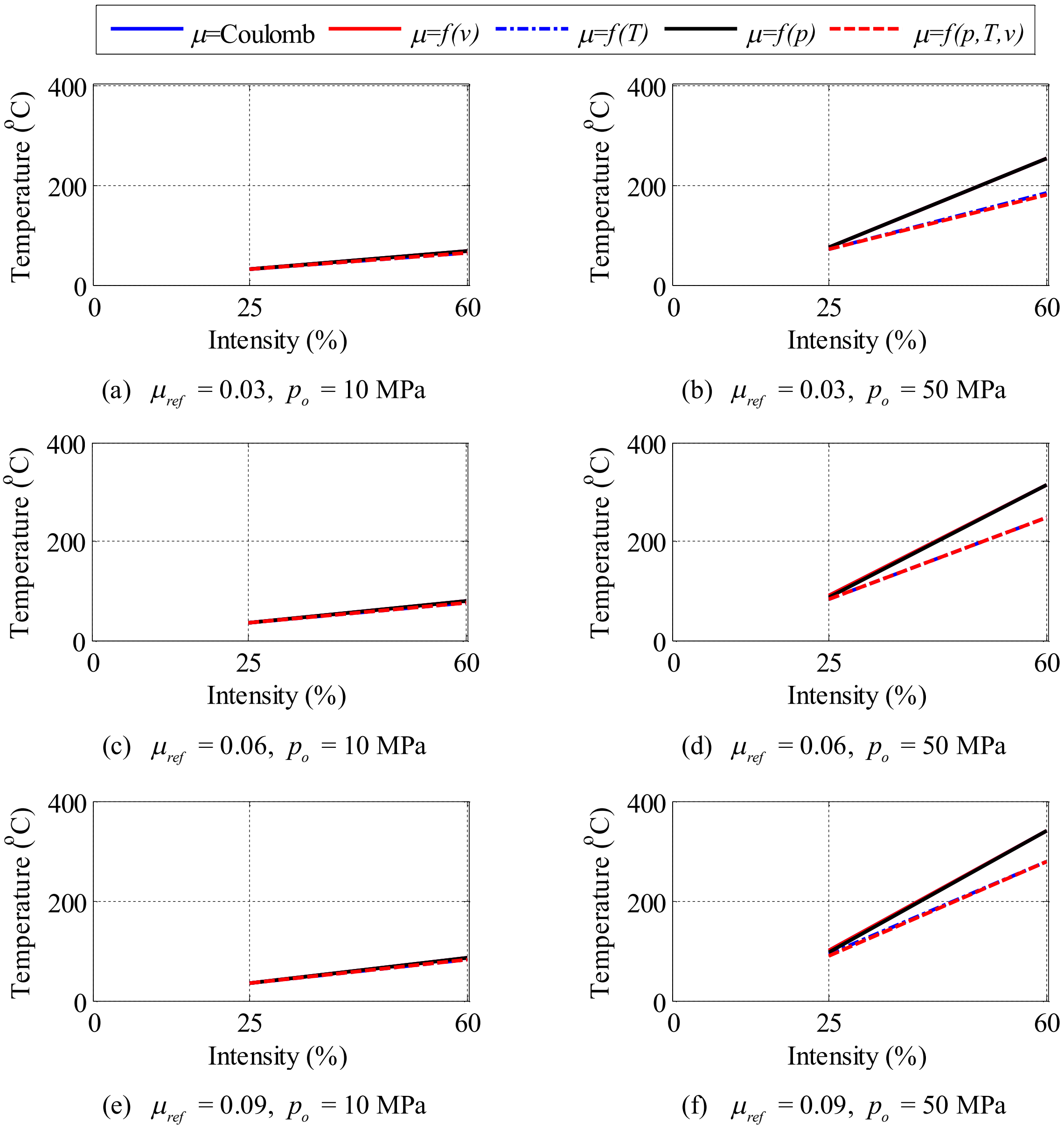

Figure 7-30: Median peak temperature at the center of the sliding surface of the FP bearing with a sliding period of 1.5 s subjected to the 30 ground motions amplitude scaled to different intensities

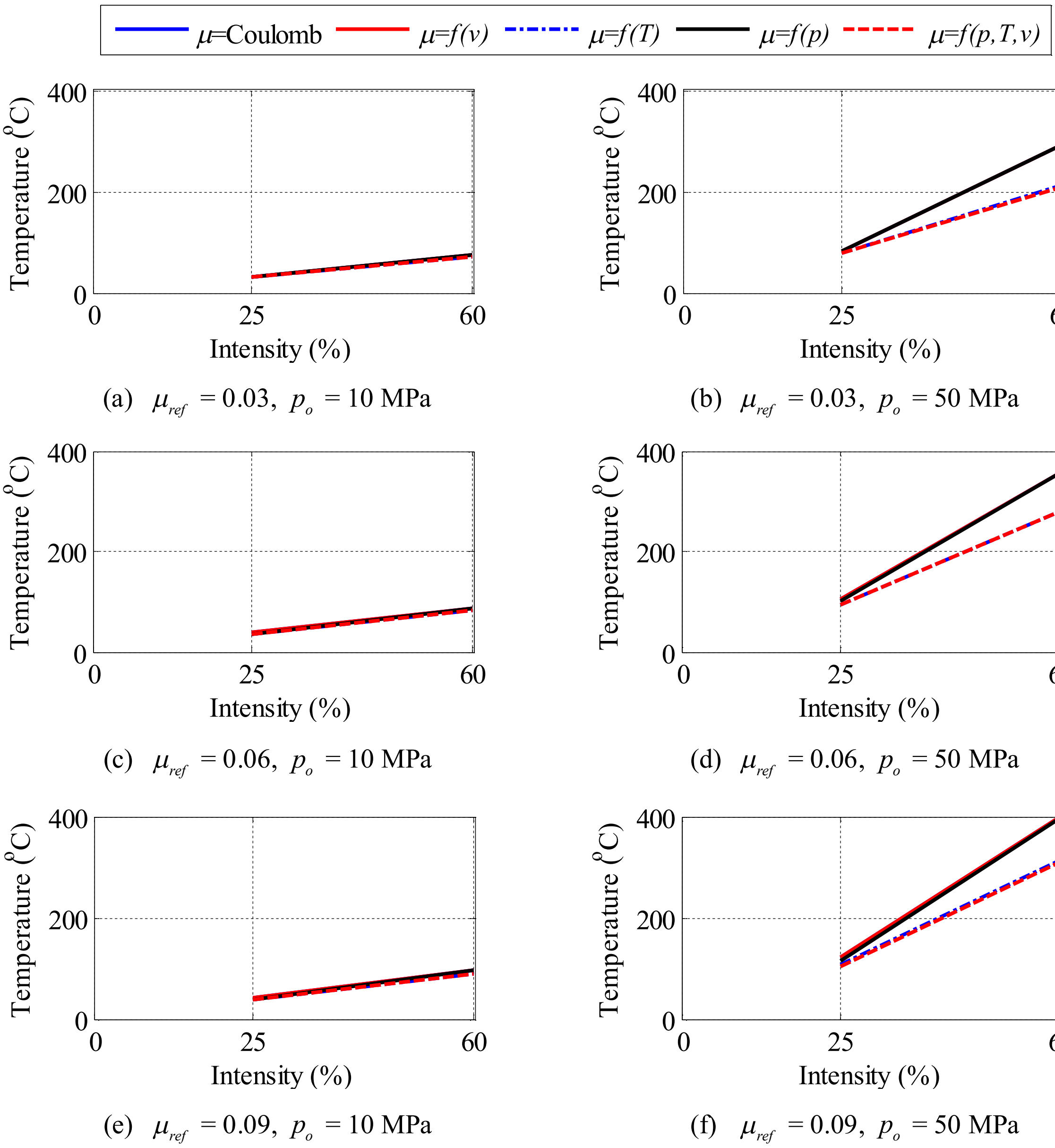

Figure 7-31: 90th percentile peak temperature at the center of the sliding surface of the FP bearing with a sliding period of 1.5 s subjected to the 30 ground motions amplitude scaled to different intensities

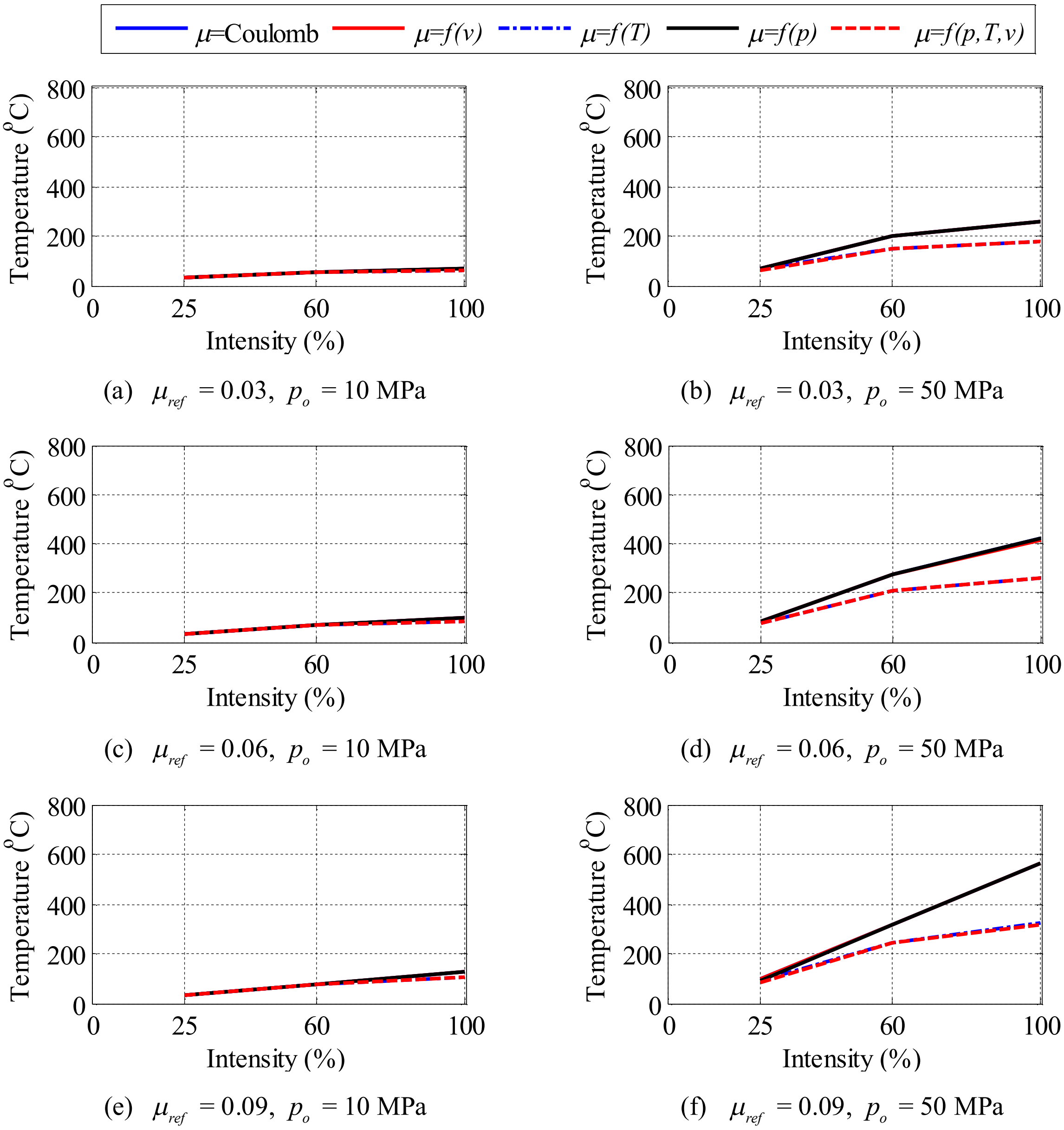

Figure 7-32: Median peak temperature at the center of the sliding surface of the FP bearing with a sliding period of 2 s subjected to the 30 ground motions amplitude scaled to different intensities

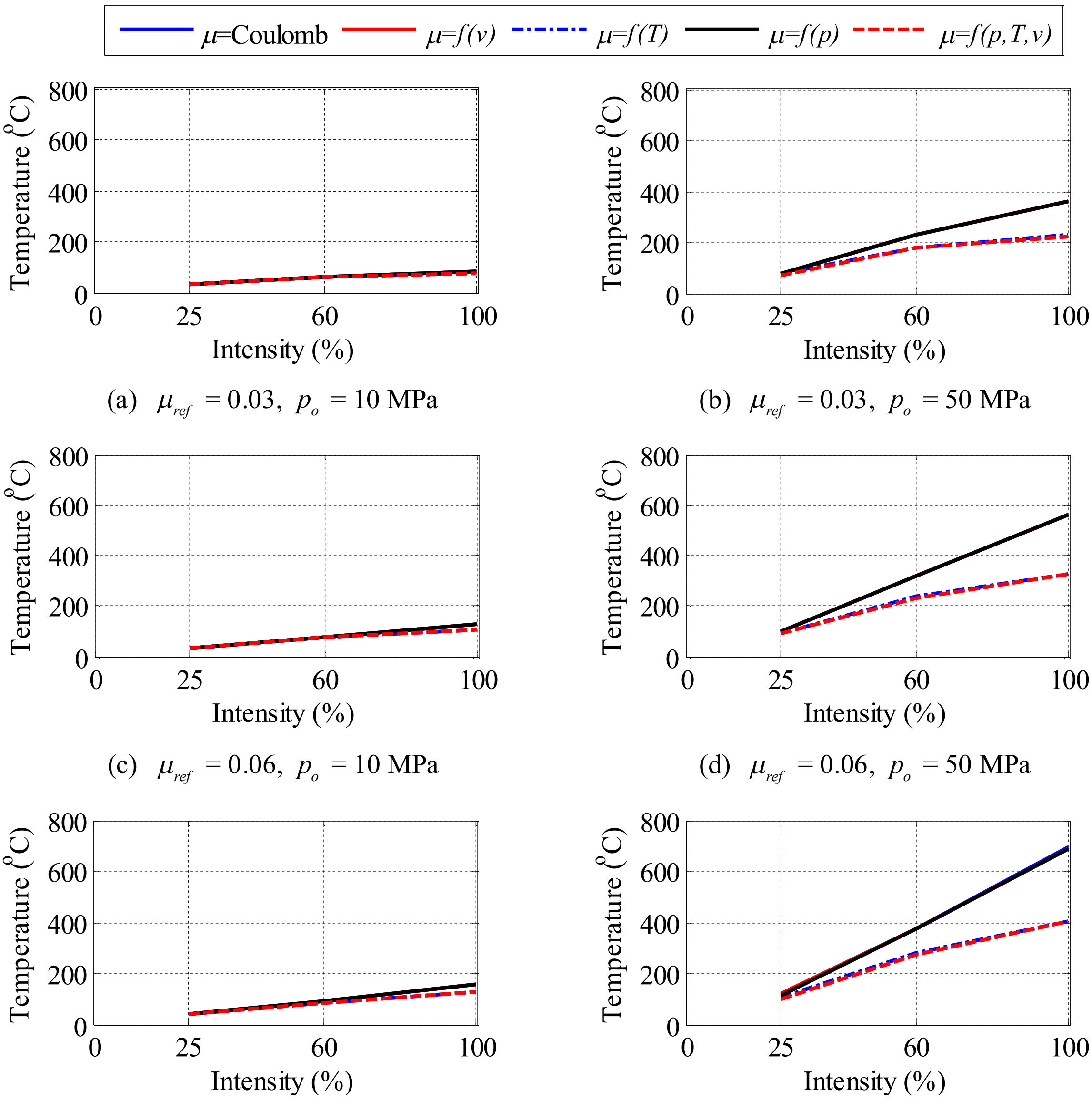

Figure 7-33: 90th percentile peak temperature at the center of the sliding surface of the FP bearing with a sliding period of 2 s subjected to the 30 ground motions amplitude scaled to different intensities

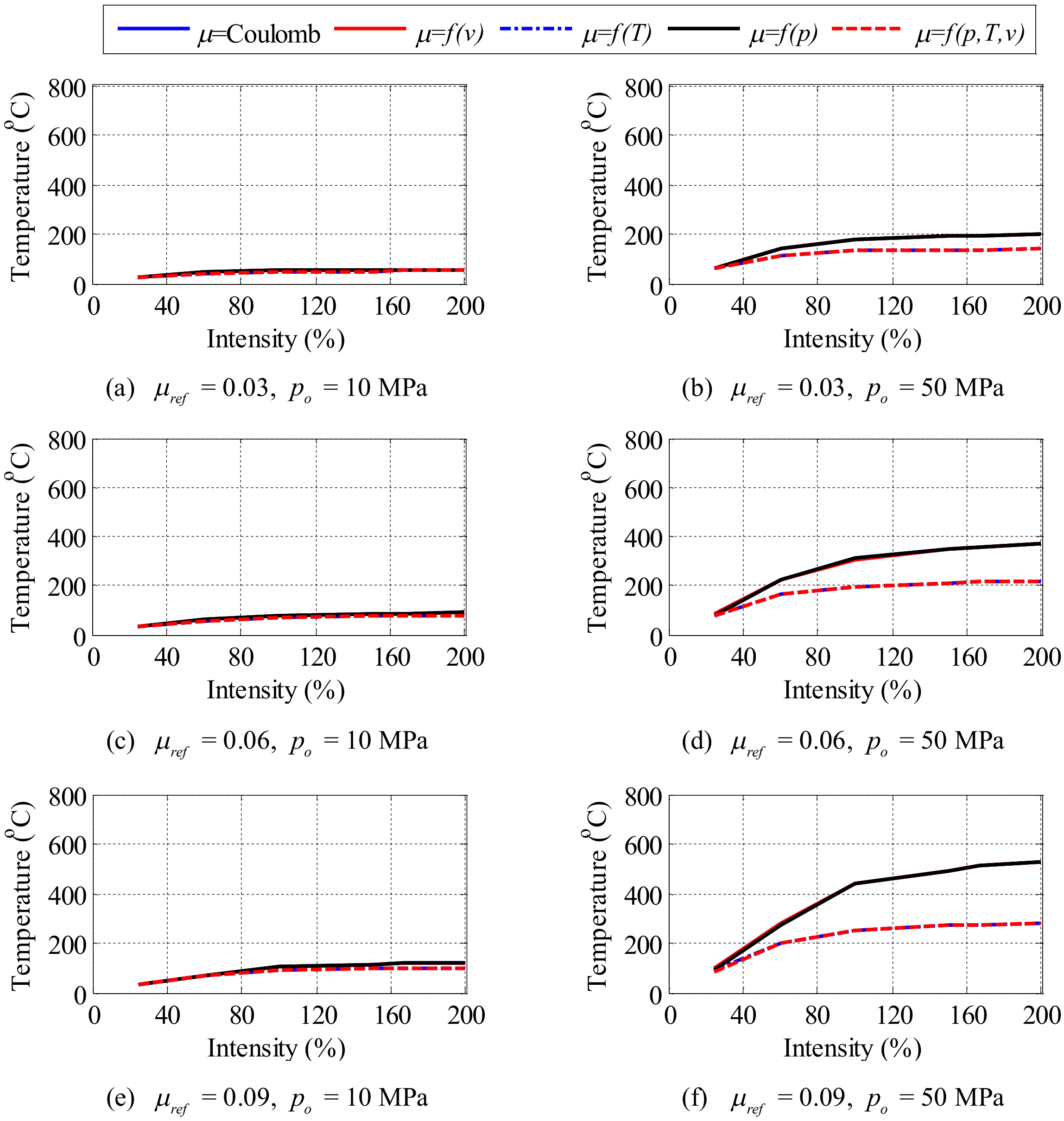

Figure 7-34: Median peak temperature at the center of the sliding surface of the FP bearing with a sliding period of 4 s subjected to the 30 ground motions amplitude scaled to different intensities

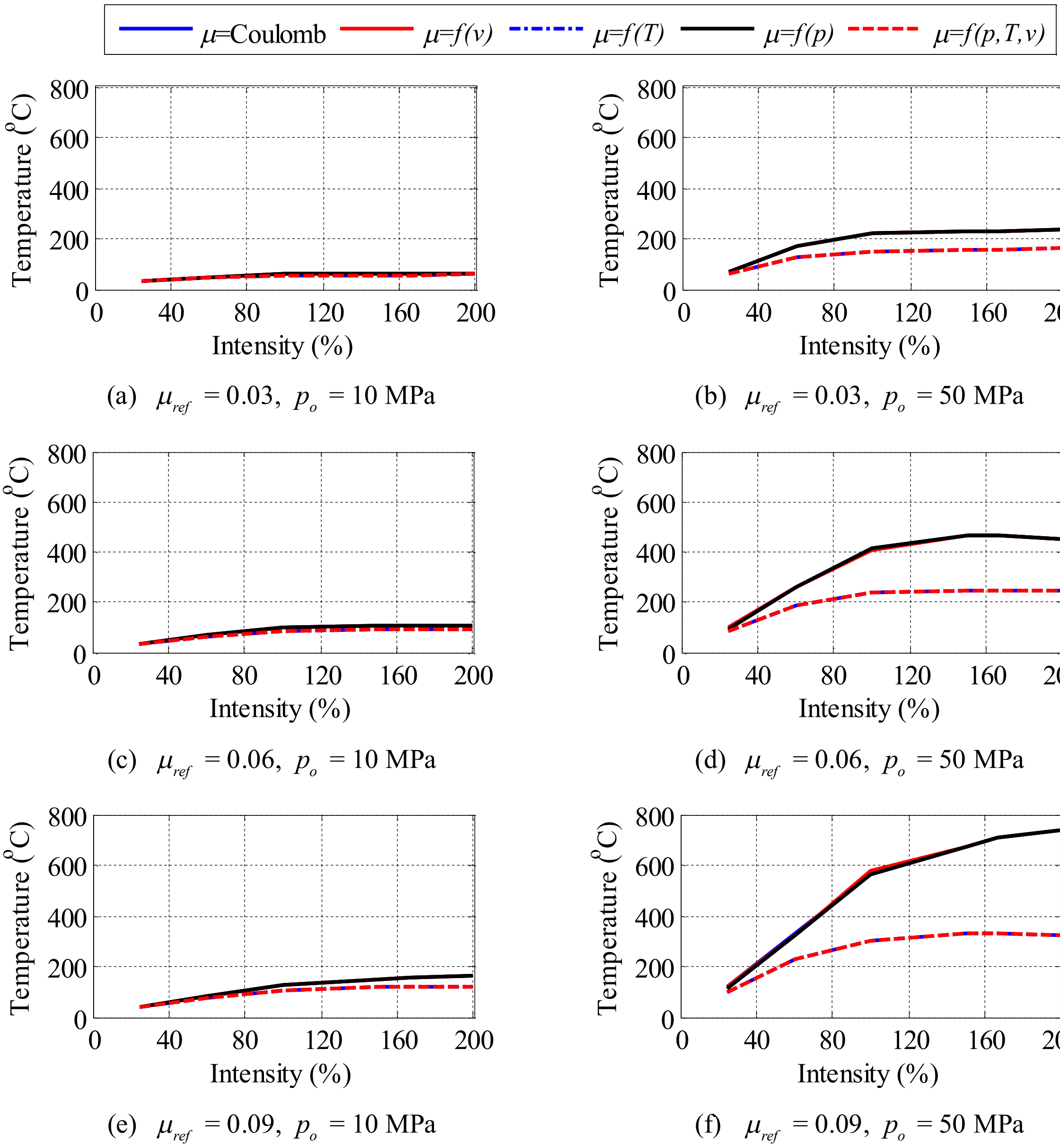

Figure 7-35: 90th percentile peak temperature at the center of the sliding surface of the FP bearing with a sliding period of 4 s subjected to the 30 ground motions amplitude scaled to different intensities

7.5.5 Floor response spectra

Figure 7-36(a) (7-36(b)) presents the 50th and 99th percentile response spectra in a horizontal direction (say X) corresponding to the absolute acceleration of the slider of the FP bearing with a sliding period of 3 s, μ_{ref} of 0.03 and p_o of 10 MPa (50 MPa) subjected to the 30 ground motions amplitude scaled by 1.0. The 30 values of response spectral ordinates (one for each set of ground motions) are assumed to distribute lognormally; see Appendix H. The influence of the choice of friction model is negligible for μ_{ref} of 0.03.

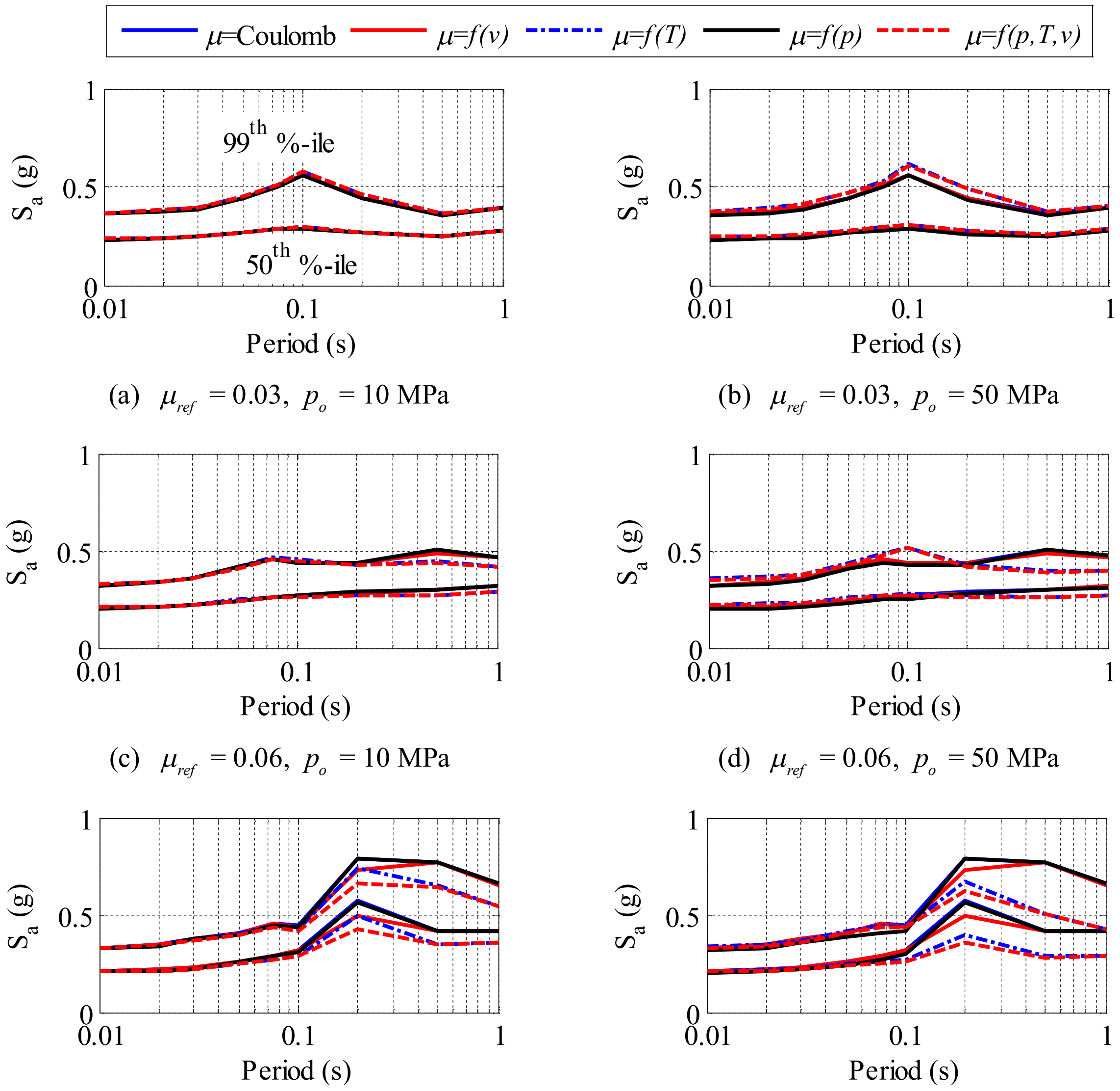

(a) $\mu_{ref} = 0.03$, $p_o = 10$ MPa

(b) $\mu_{ref} = 0.03$, $p_o = 50$ MPa

(c) $\mu_{ref} = 0.06$, $p_o = 10$ MPa

(d) $\mu_{ref} = 0.06$, $p_o = 50$ MPa

(e) $\mu_{ref} = 0.09$, $p_o = 10$ MPa

(f) $\mu_{ref} = 0.09$, $p_o = 50$ MPa

Figure 7-36: Five percent damped response spectra in X direction corresponding to the absolute acceleration of the slider of the FP bearing with sliding period of 3 s subjected to the 30 ground motions with amplitude scaling factor of 1.0

Figures 7-36(c) and 7-36(d) present results for μ_{ref} of 0.06. The spectral ordinates vary by up to ±20% for different choices of friction model, relative to those computed using Coulomb model, at periods longer than 0.07 s, noting that only heating affects the ordinates.

Figures 7-36(e) and 7-36(f) present results for μ_{ref} of 0.09. The floor spectral ordinates are not affected by the choice of friction model at periods shorter than 0.07 s, irrespective of p_o and μ_{ref}. The friction model affects the spectral ordinates at periods longer than 0.1 s. Consideration of heating can reduce the spectral demand by 0.1 g (0.2 g) or 20% (35%) for p_o of 10 MPa (50 MPa), at the higher percentiles. Consideration of the dependence of friction on pressure and velocity has no meaningful effect on spectral response.

Figure 7-37 presents the 5%-damped 50th and 90th percentile peak floor spectral accelerations in a horizontal direction (say X) at 0.01 s, 0.1 s and 0.5 s corresponding to the absolute acceleration of the slider of the 3 s FP bearing with p_o of 10 MPa and 50 MPa, and μ_{ref} of 0.06, subjected to the 30 ground motions amplitude scaled by the six factors of Table 7-3. Figure 7-37(a) presents spectral ordinates at 0.01 s for p_o of 10 MPa. The spectral ordinates are not influenced by the choice of friction model. The significance of the friction model is seen at p_o of 50 MPa (Figure 7-37(b)), although the effect is small. Figures 7-37(c) and 7-37(d) present spectral accelerations at 0.1 s for p_o of 10 MPa and 50 MPa, respectively; spectral ordinates at 0.5 s are presented in Figures 7-37(e) and 7-37(f). Figure 7-38 presents companion results to Figure 7-37 in the orthogonal horizontal direction (say Y). The magnitude of ordinates and influences of the choice of friction model on floor spectral ordinates are comparable to those with Figure 7-37.

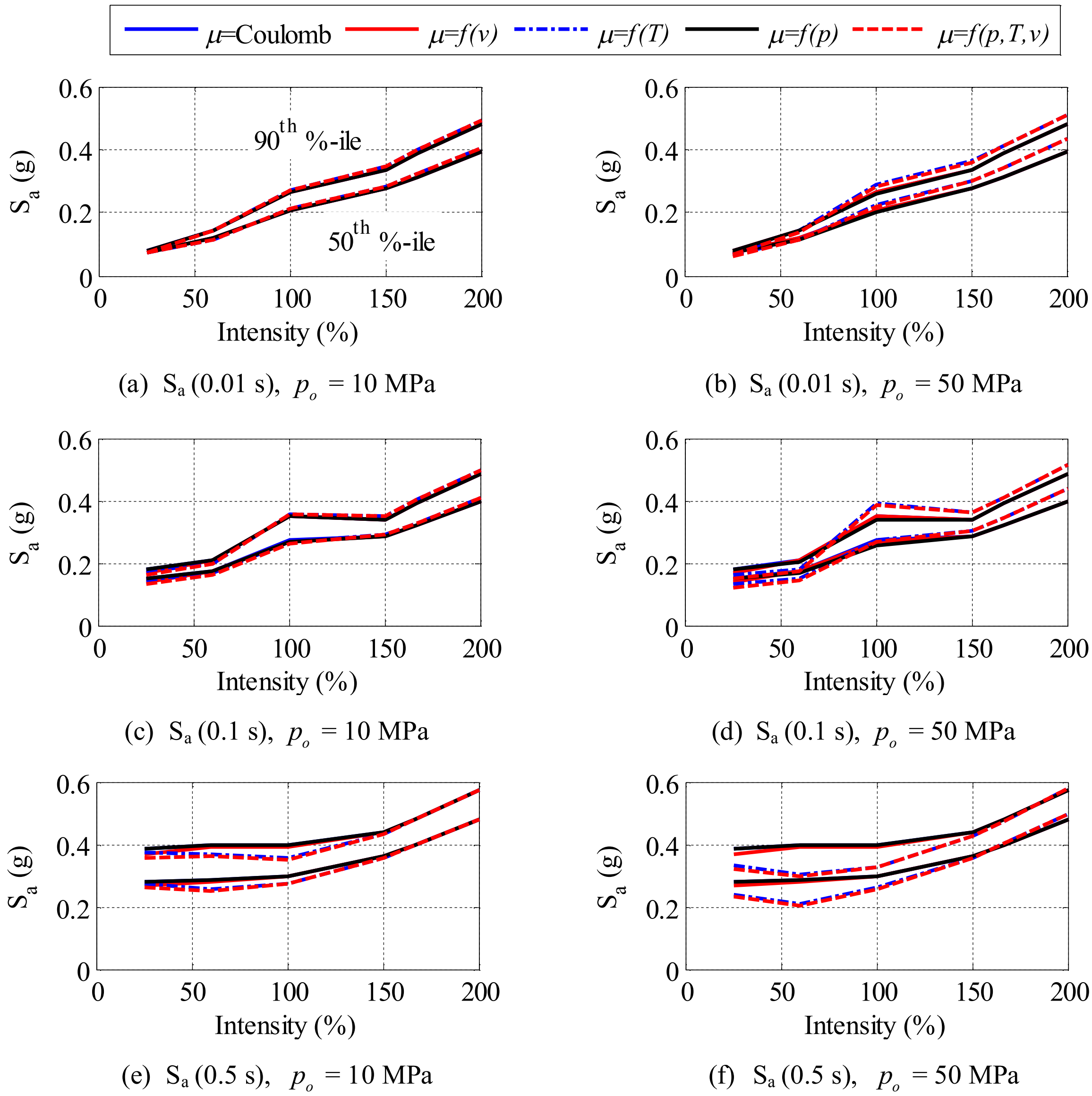

Figure 7-37: Five percent damped 50th and 90th percentile peak floor spectral ordinates at periods of 0.01 s, 0.1 s and 0.5 s, corresponding to the absolute acceleration response of the slider in the X direction of an FP bearing with a sliding period of 3 s, reference axial pressures of 10 MPa and 50 MPa, and reference coefficient of friction of 0.06, subjected to the 30 ground motions amplitude scaled to different intensities

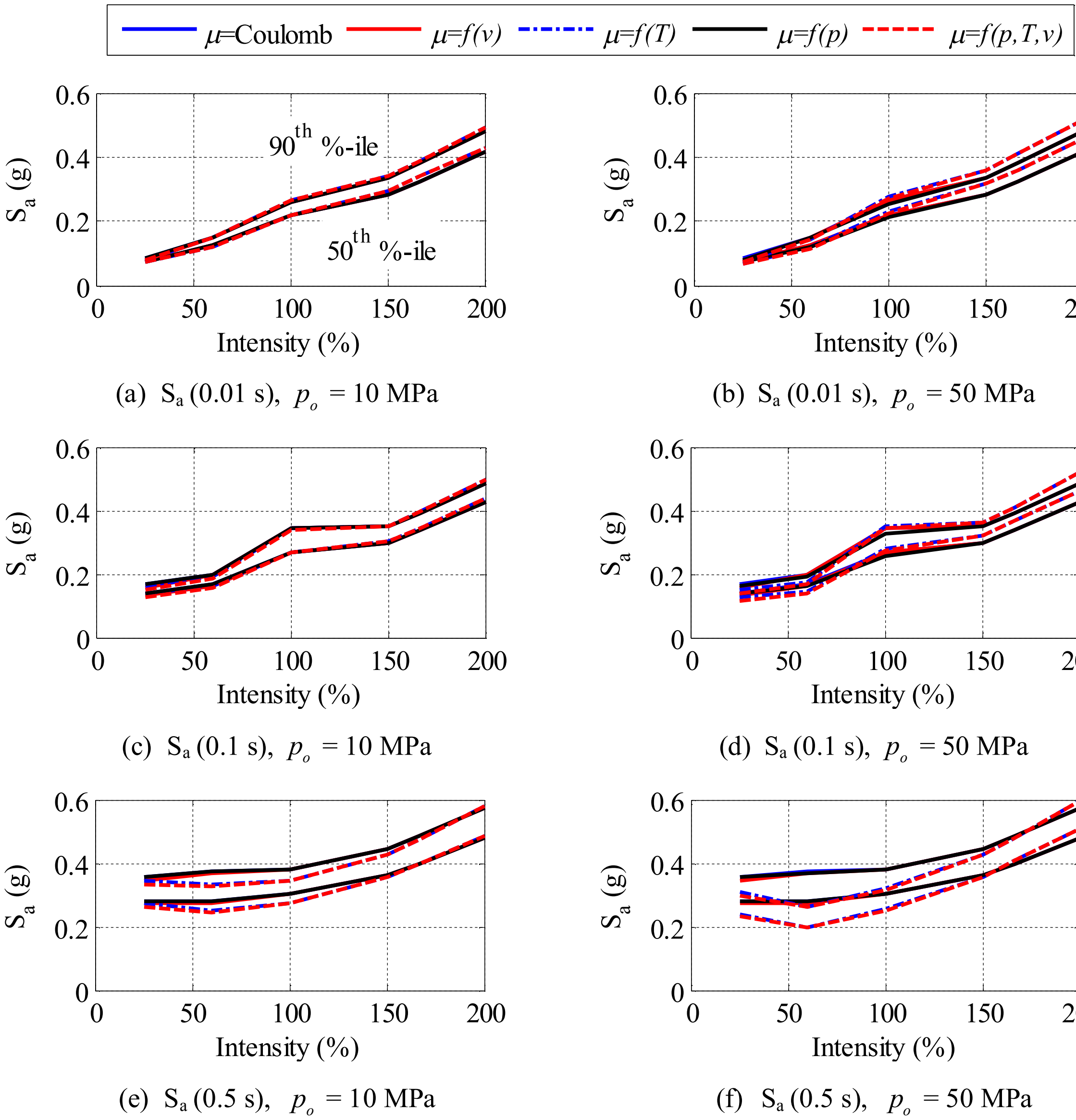

Figure 7-38: Five percent damped 50th and 90th percentile peak floor spectral ordinates at periods of 0.01 s, 0.1 s and 0.5 s, corresponding to the absolute acceleration response of the slider in the Y direction of an FP bearing with a sliding period of 3 s, reference axial pressures of 10 MPa and 50 MPa, and reference coefficient of friction of 0.06, subjected to the 30 ground motions amplitude scaled to different intensities

Panels (b), (d) and (f) of Figure 7-37 (and Figure 7-38) present the spectral ordinates for p_o of 50 MPa at periods 0.01 s, 0.1 s and 0.5 s, respectively. The spectral acceleration at a very short period (e.g., 0.01 s) is equal to the peak floor acceleration, which is approximately the ratio of the peak lateral force to the mass associated with the slider. It is seen in panels (b) of the two figures that the 0.01 s ordinates for different friction models are comparable, implying that the peak lateral force in the bearing is not influenced by the choice of friction model. The observations for spectral acceleration at 0.1 s (see panel (d)) are similar to those at 0.01 s. The ordinates at 0.5 s are sensitive to whether the friction model includes heating effects, especially at intensities smaller than 100%. The period of 0.5 s can be seen as a *transition* period between the pre-sliding regime (0.3 s) and the sliding regime (3 s). The trends seen in Figures 7-37(f) and 7-38(f) are consistent with prior observations regarding the intensity of shaking (0.6 or 1.0) for which the heating effects are greatest.

Figures 7-39 through 7-44 present floor spectral ordinates in the two horizontal directions corresponding to the absolute acceleration of slider of the 1.5 s FP bearing with μ_{ref} of 0.03, 0.06 and 0.09, p_o of 10 MPa and 50 MPa, subjected to the ground motions with amplitude scale factors of 0.25 and 0.60. Figures 7-45 through 7-50 present the spectral ordinates for the 2 s bearing with amplitude scale factors of 0.25, 0.60 and 1.00[1], Figures 7-51 through 7-60 present results for 3 s and 4 s bearings.

Figure 7-61 (7-62) presents the median (90th percentile) peak floor spectral ordinates at 0.01 s, 0.1 s and 0.5 s periods corresponding to the absolute acceleration in the X direction of the slider of the 3 s FP bearing with p_o of 50 MPa as a function of μ_{ref} at different levels of shaking intensity. In terms of floor spectra, the key observations from Figures 7-37 through 7-62 are:

i. The choice of friction model is unimportant at μ_{ref} = 0.03.

[1] Higher scale factors are not considered because the displacement demands on the bearing are considerably greater than 0.5*R*, which is impractical for FP bearings.

ii. The choice of friction model is unimportant for p_o = 10 MPa, and shorter periods (i.e., 0.01 s and 0.1 s).

iii. The differences in the spectral ordinates relative to those computed using the Coulomb model due to choice of friction model are less than 0.1 g (or 15%) at 0.01 s (and 0.1 s) for p_o of 50 MPa.

iv. For amplitude scale factors of 1.5 and smaller, the spectral ordinates at 0.5 s computed using a friction model that considers heating are smaller than those computed using a Coulomb (no heating) model: up to 35% smaller for p_o of 50 MPa and μ_{ref} of 0.09.

v. The velocity and pressure dependencies of the coefficient of friction do not materially influence floor spectra.

vi. The spectral acceleration ordinates at a short period (e.g., 0.01 s), which is also the peak floor acceleration, do not change considerably with increase in μ_{ref}.

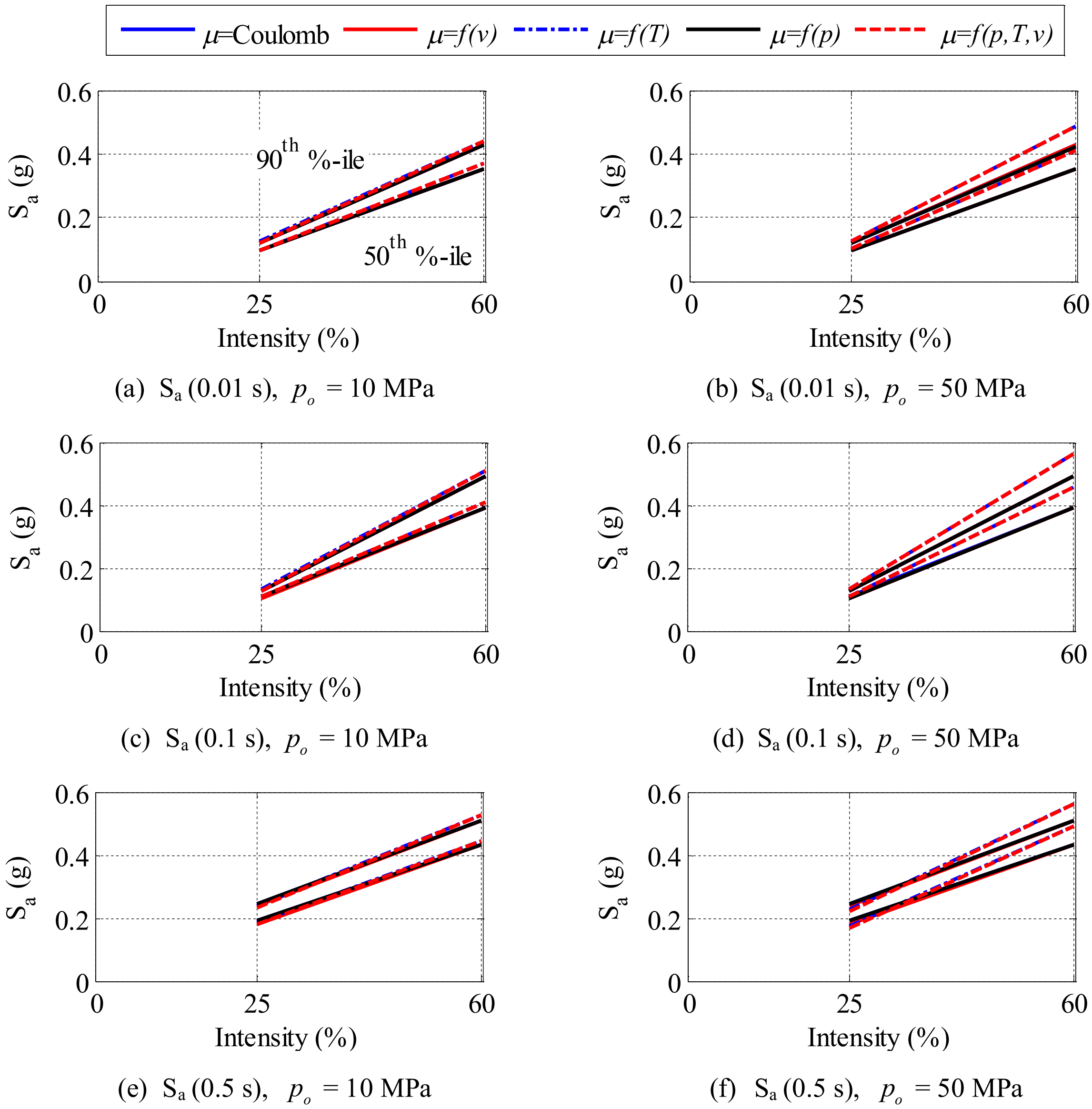

Figure 7-39: Five percent damped 50th and 90th percentile peak floor spectral ordinates at periods of 0.01 s, 0.1 s and 0.5 s, corresponding to the absolute acceleration response of the slider in the X direction of an FP bearing with a sliding period of 1.5 s, reference axial pressures of 10 MPa and 50 MPa, and reference coefficient of friction of 0.03, subjected to the 30 ground motions amplitude scaled to different intensities

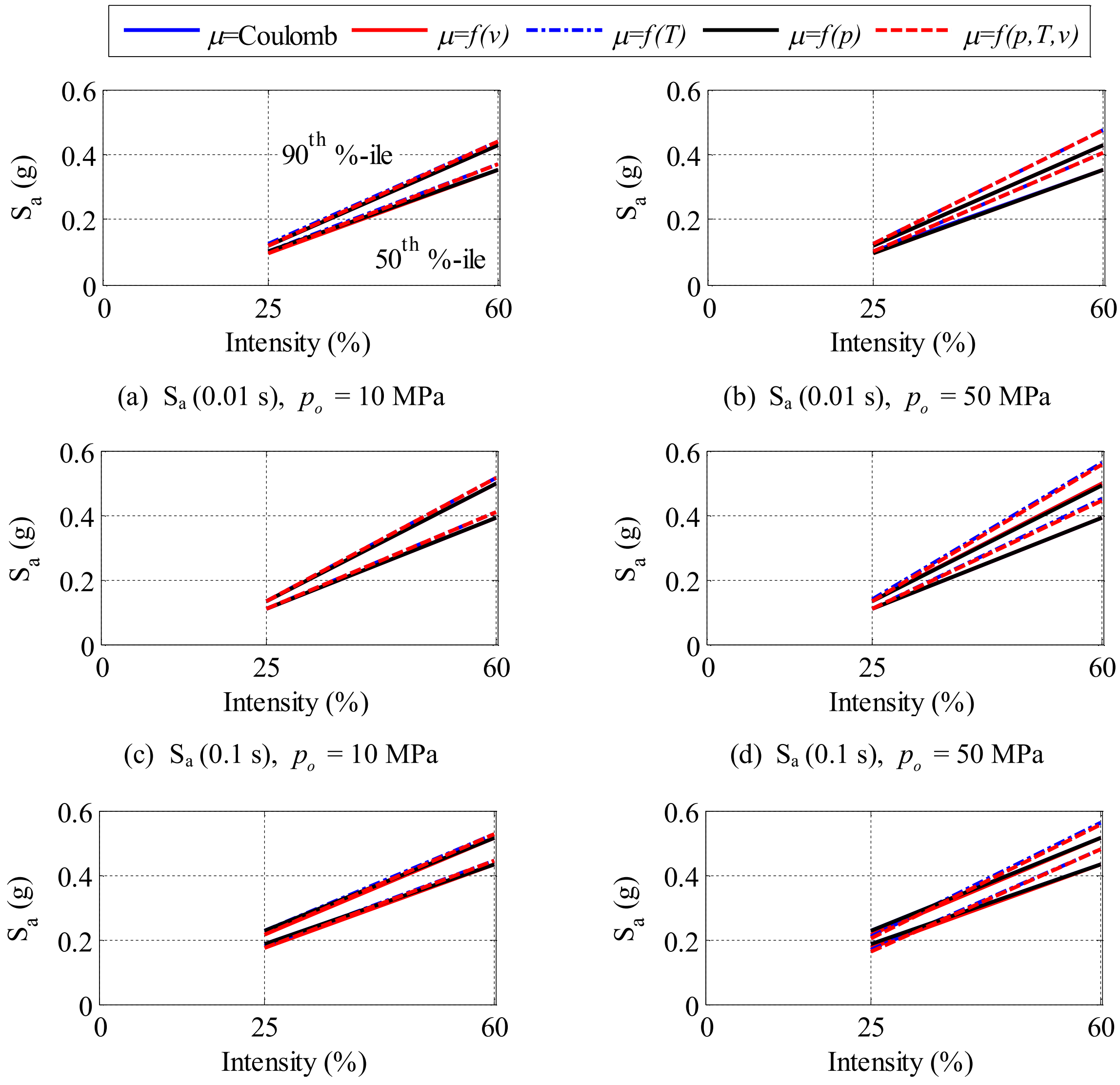

(a) S_a (0.01 s), p_o = 10 MPa (b) S_a (0.01 s), p_o = 50 MPa

(c) S_a (0.1 s), p_o = 10 MPa (d) S_a (0.1 s), p_o = 50 MPa

(e) S_a (0.5 s), p_o = 10 MPa (f) S_a (0.5 s), p_o = 50 MPa

Figure 7-40: Five percent damped 50th and 90th percentile peak floor spectral ordinates at periods of 0.01 s, 0.1 s and 0.5 s, corresponding to the absolute acceleration response of the slider in the Y direction of an FP bearing with a sliding period of 1.5 s, reference axial pressures of 10 MPa and 50 MPa, and reference coefficient of friction of 0.03, subjected to the 30 ground motions amplitude scaled to different intensities

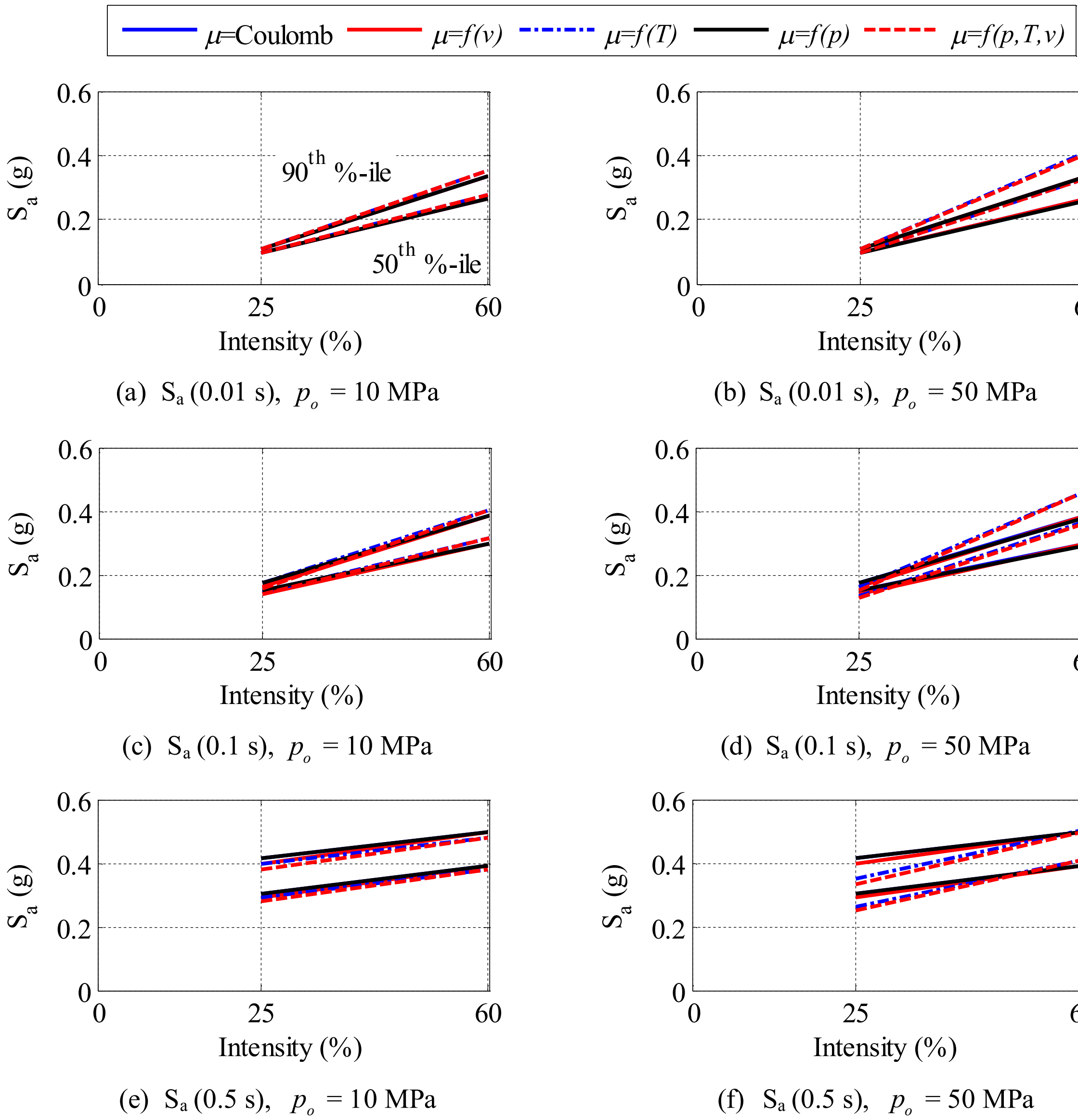

Figure 7-41: Five percent damped 50th and 90th percentile peak floor spectral ordinates at periods of 0.01 s, 0.1 s and 0.5 s, corresponding to the absolute acceleration response of the slider in the X direction of an FP bearing with a sliding period of 1.5 s, reference axial pressures of 10 MPa and 50 MPa, and reference coefficient of friction of 0.06, subjected to the 30 ground motions amplitude scaled to different intensities

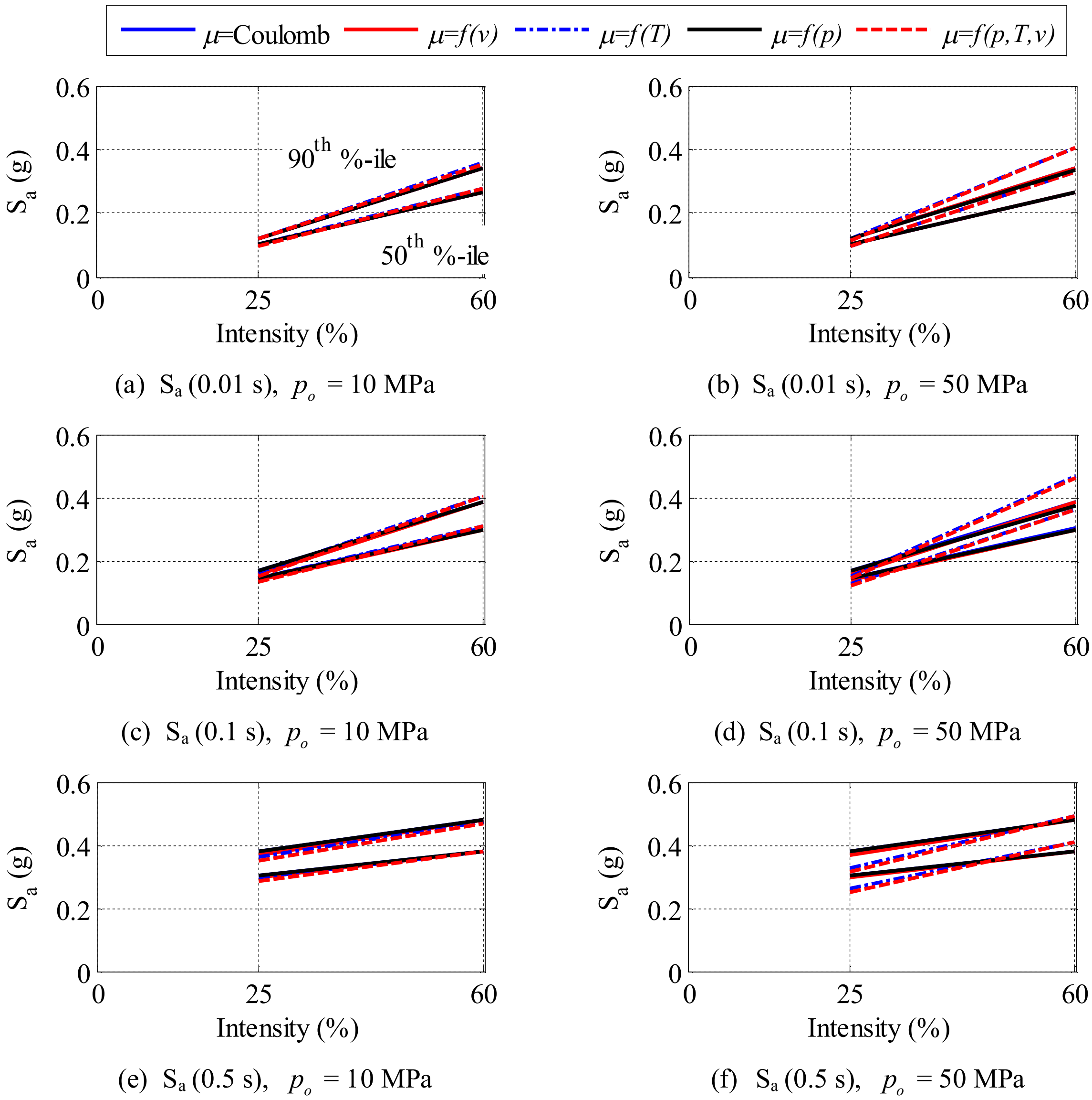

Figure 7-42: Five percent damped 50th and 90th percentile peak floor spectral ordinates at periods of 0.01 s, 0.1 s and 0.5 s, corresponding to the absolute acceleration response of the slider in the Y direction of an FP bearing with a sliding period of 1.5 s, reference axial pressures of 10 MPa and 50 MPa, and reference coefficient of friction of 0.06, subjected to the 30 ground motions amplitude scaled to different intensities

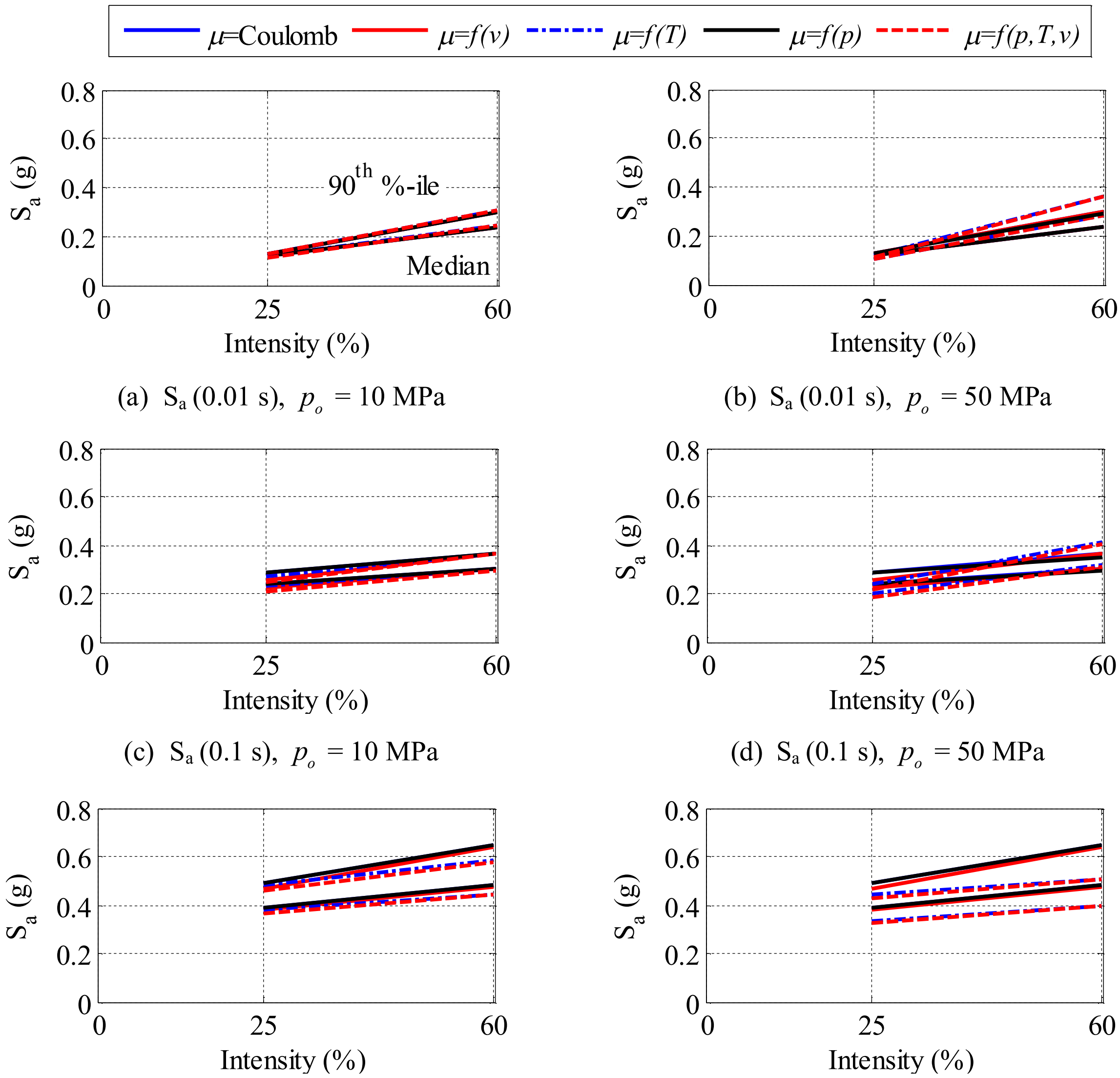

(a) S_a (0.01 s), p_o = 10 MPa

(b) S_a (0.01 s), p_o = 50 MPa

(c) S_a (0.1 s), p_o = 10 MPa

(d) S_a (0.1 s), p_o = 50 MPa

(e) S_a (0.5 s), p_o = 10 MPa

(f) S_a (0.5 s), p_o = 50 MPa

Figure 7-43: Five percent damped 50th and 90th percentile peak floor spectral ordinates at periods of 0.01 s, 0.1 s and 0.5 s, corresponding to the absolute acceleration response of the slider in the X direction of an FP bearing with a sliding period of 1.5 s, reference axial pressures of 10 MPa and 50 MPa, and reference coefficient of friction of 0.09, subjected to the 30 ground motions amplitude scaled to different intensities

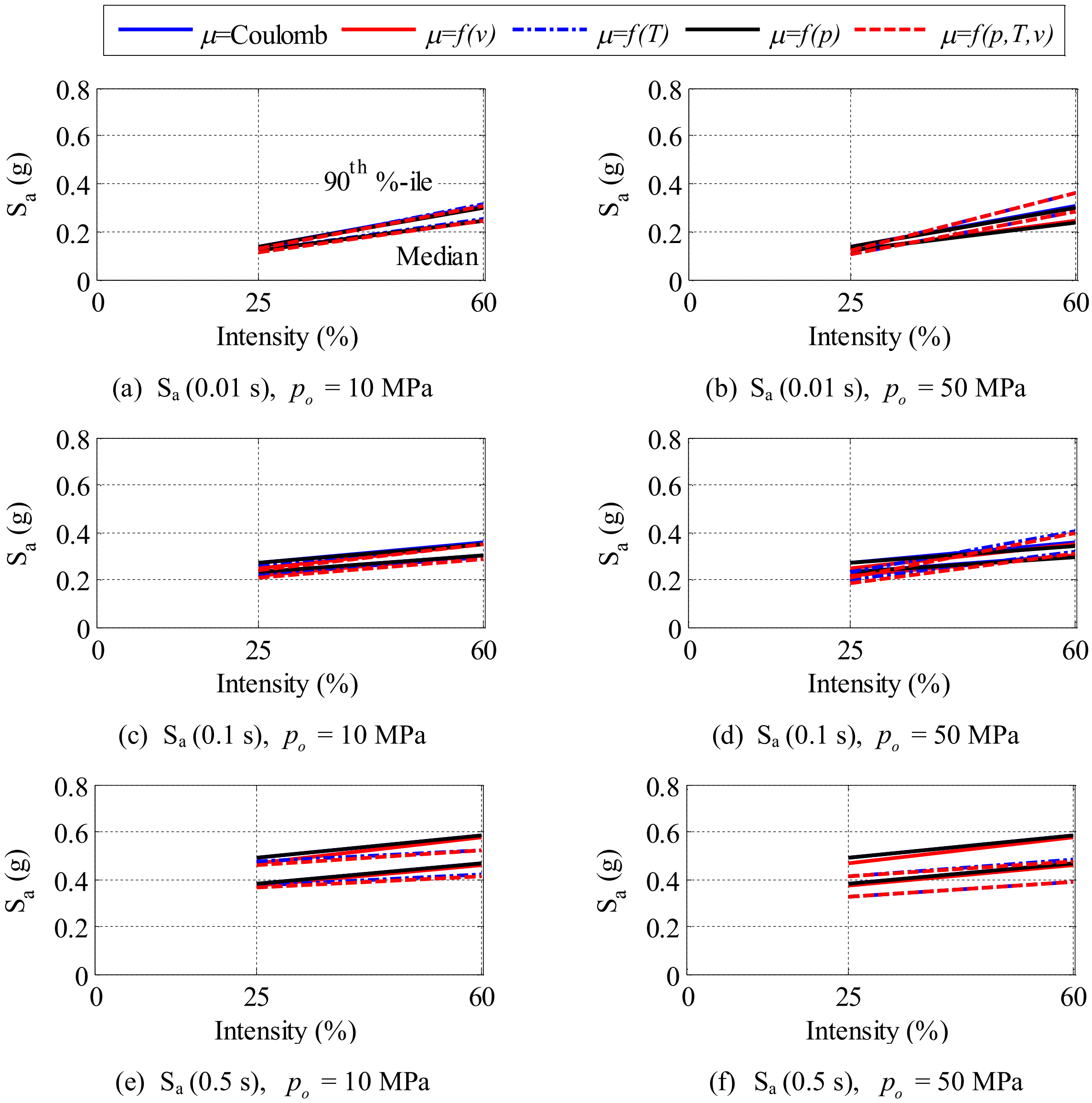

(a) S_a (0.01 s), p_o = 10 MPa (b) S_a (0.01 s), p_o = 50 MPa

(c) S_a (0.1 s), p_o = 10 MPa (d) S_a (0.1 s), p_o = 50 MPa

(e) S_a (0.5 s), p_o = 10 MPa (f) S_a (0.5 s), p_o = 50 MPa

Figure 7-44: Five percent damped 50th and 90th percentile peak floor spectral ordinates at periods of 0.01 s, 0.1 s and 0.5 s, corresponding to the absolute acceleration response of the slider in the Y direction of an FP bearing with a sliding period of 1.5 s, reference axial pressures of 10 MPa and 50 MPa, and reference coefficient of friction of 0.09, subjected to the 30 ground motions amplitude scaled to different intensities

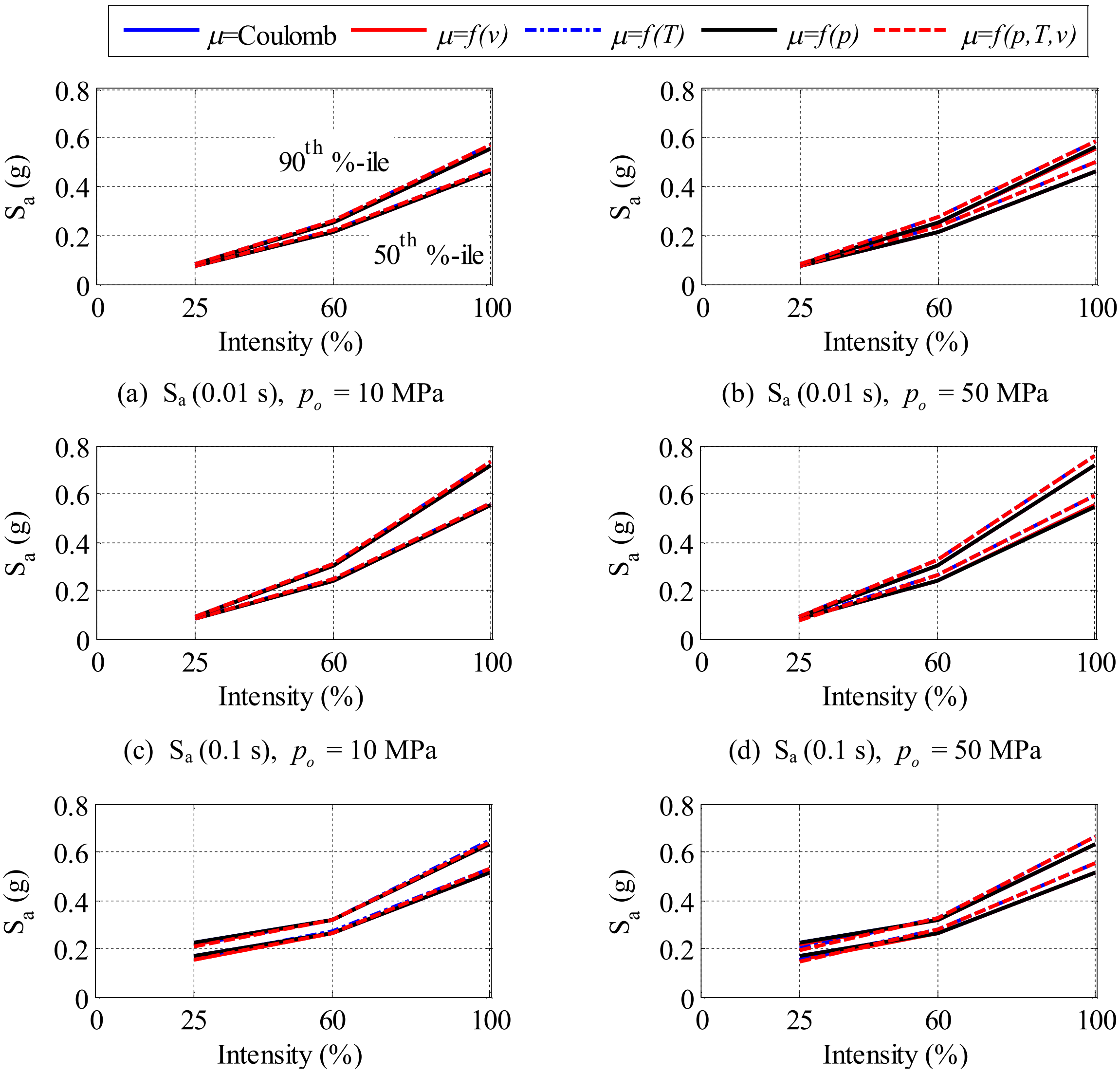

(a) S$_a$ (0.01 s), p_o = 10 MPa

(b) S$_a$ (0.01 s), p_o = 50 MPa

(c) S$_a$ (0.1 s), p_o = 10 MPa

(d) S$_a$ (0.1 s), p_o = 50 MPa

(e) S$_a$ (0.5 s), p_o = 10 MPa

(f) S$_a$ (0.5 s), p_o = 50 MPa

Figure 7-45: Five percent damped 50th and 90th percentile peak floor spectral ordinates at periods of 0.01 s, 0.1 s and 0.5 s, corresponding to the absolute acceleration response of the slider in the X direction of an FP bearing with a sliding period of 2 s, reference axial pressures of 10 MPa and 50 MPa, and reference coefficient of friction of 0.03, subjected to the 30 ground motions amplitude scaled to different intensities

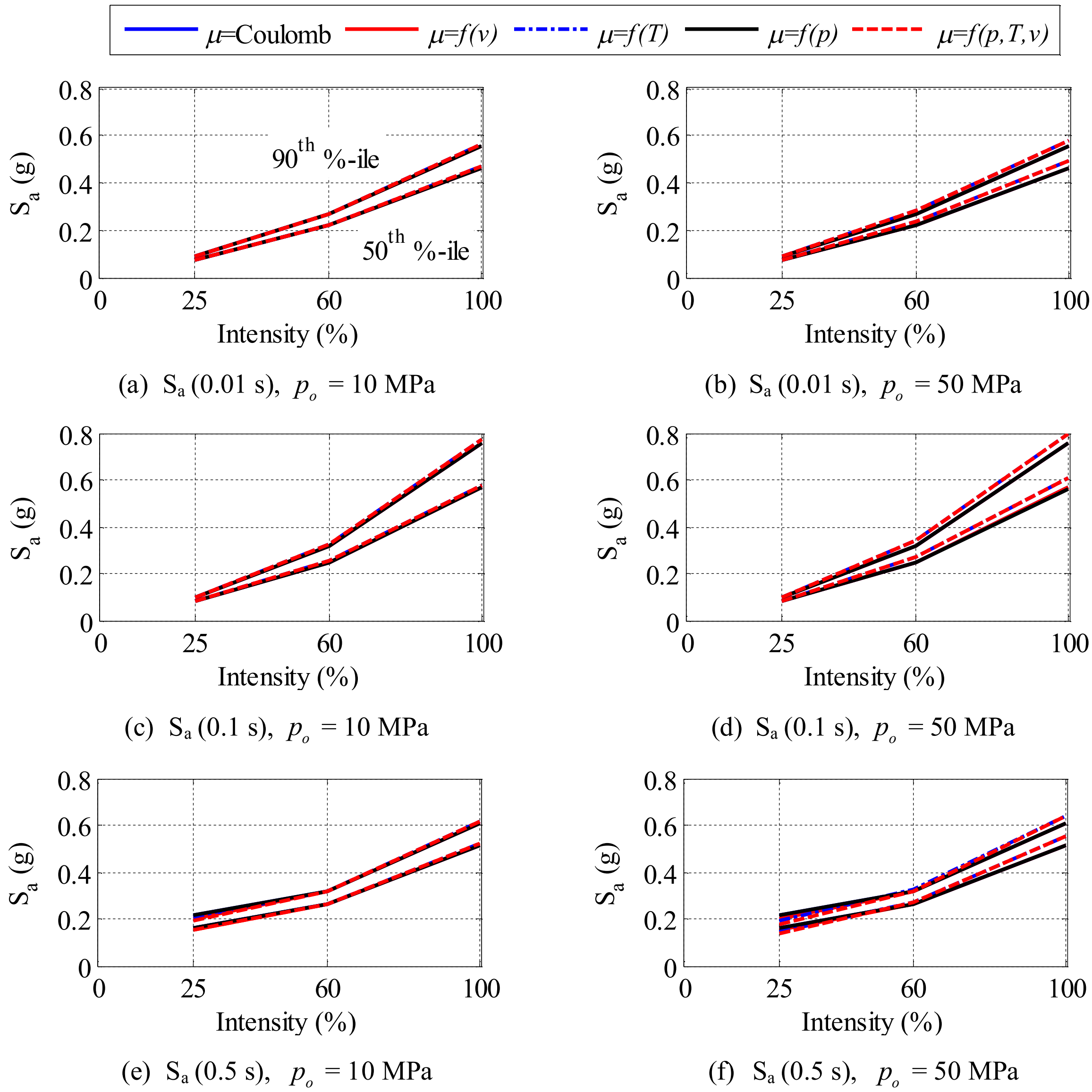

Figure 7-46: Five percent damped 50th and 90th percentile peak floor spectral ordinates at periods of 0.01 s, 0.1 s and 0.5 s, corresponding to the absolute acceleration response of the slider in the Y direction of an FP bearing with a sliding period of 2 s, reference axial pressures of 10 MPa and 50 MPa, and reference coefficient of friction of 0.03, subjected to the 30 ground motions amplitude scaled to different intensities

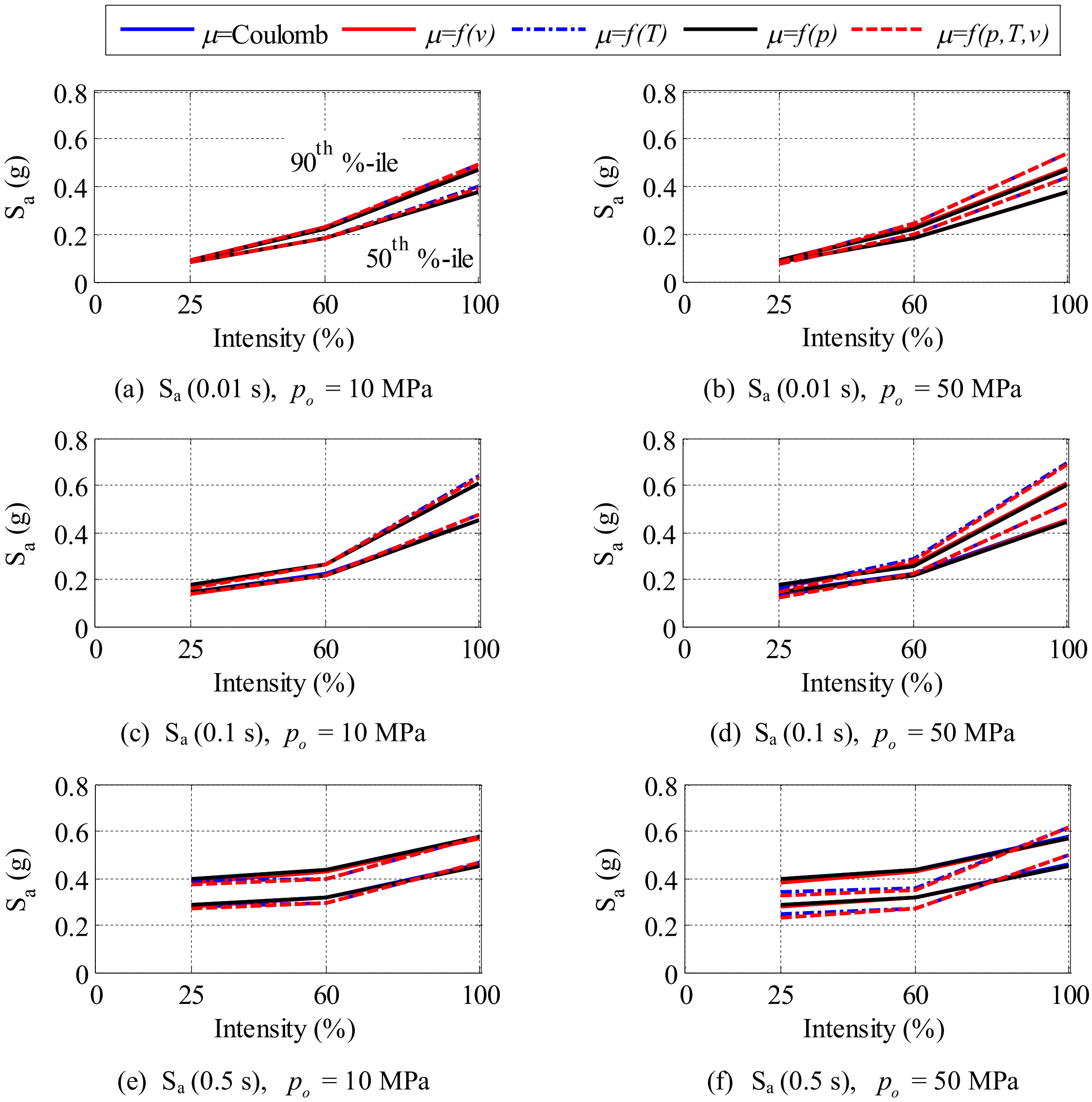

Figure 7-47: Five percent damped 50th and 90th percentile peak floor spectral ordinates at periods of 0.01 s, 0.1 s and 0.5 s, corresponding to the absolute acceleration response of the slider in the X direction of an FP bearing with a sliding period of 2 s, reference axial pressures of 10 MPa and 50 MPa, and reference coefficient of friction of 0.06, subjected to the 30 ground motions amplitude scaled to different intensities

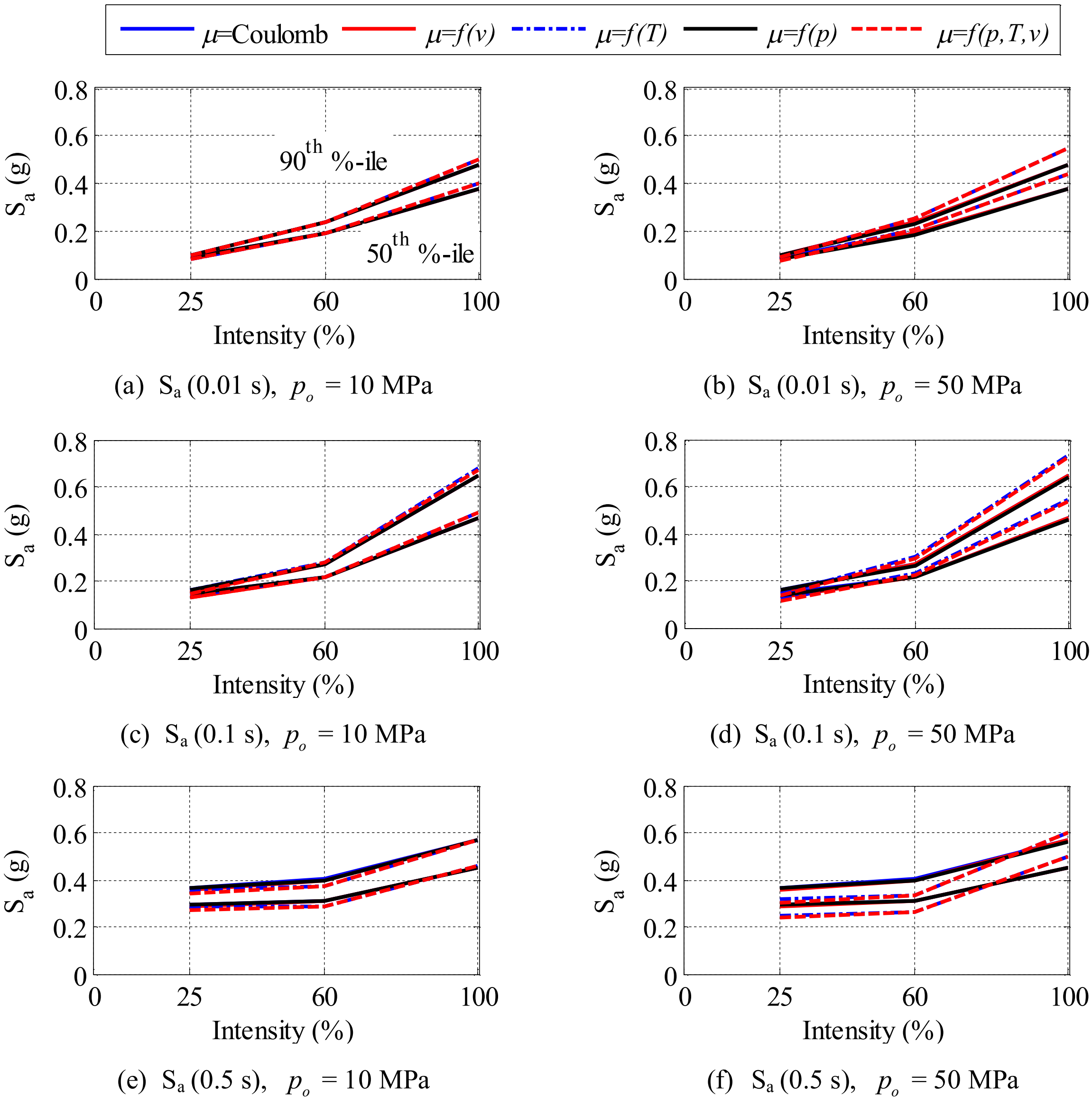

Figure 7-48: Five percent damped 50th and 90th percentile peak floor spectral ordinates at periods of 0.01 s, 0.1 s and 0.5 s, corresponding to the absolute acceleration response of the slider in the Y direction of an FP bearing with a sliding period of 2 s, reference axial pressures of 10 MPa and 50 MPa, and reference coefficient of friction of 0.06, subjected to the 30 ground motions amplitude scaled to different intensities

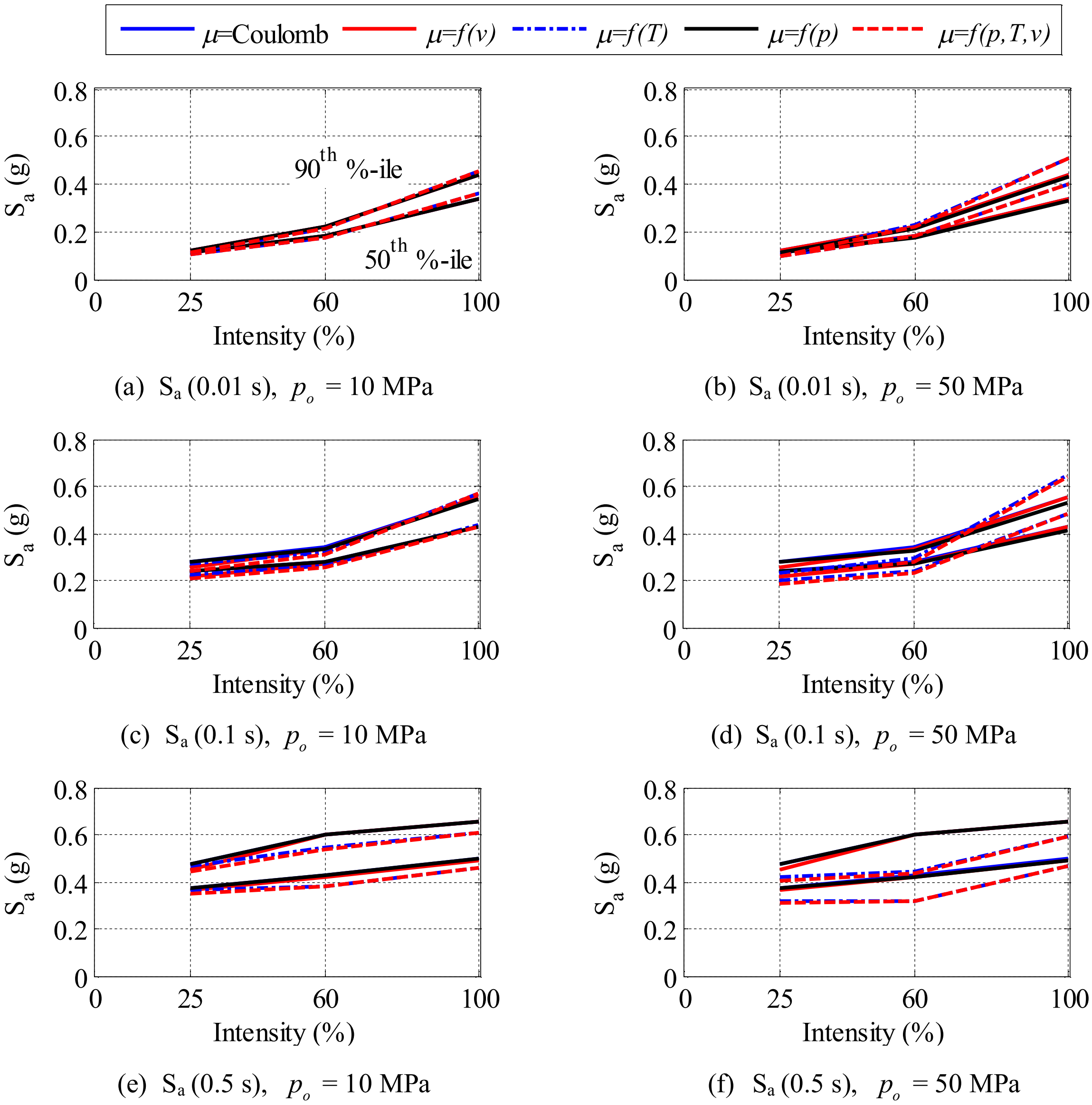

Figure 7-49: Five percent damped 50th and 90th percentile peak floor spectral ordinates at periods of 0.01 s, 0.1 s and 0.5 s, corresponding to the absolute acceleration response of the slider in the X direction of an FP bearing with a sliding period of 2 s, reference axial pressures of 10 MPa and 50 MPa, and reference coefficient of friction of 0.09, subjected to the 30 ground motions amplitude scaled to different intensities

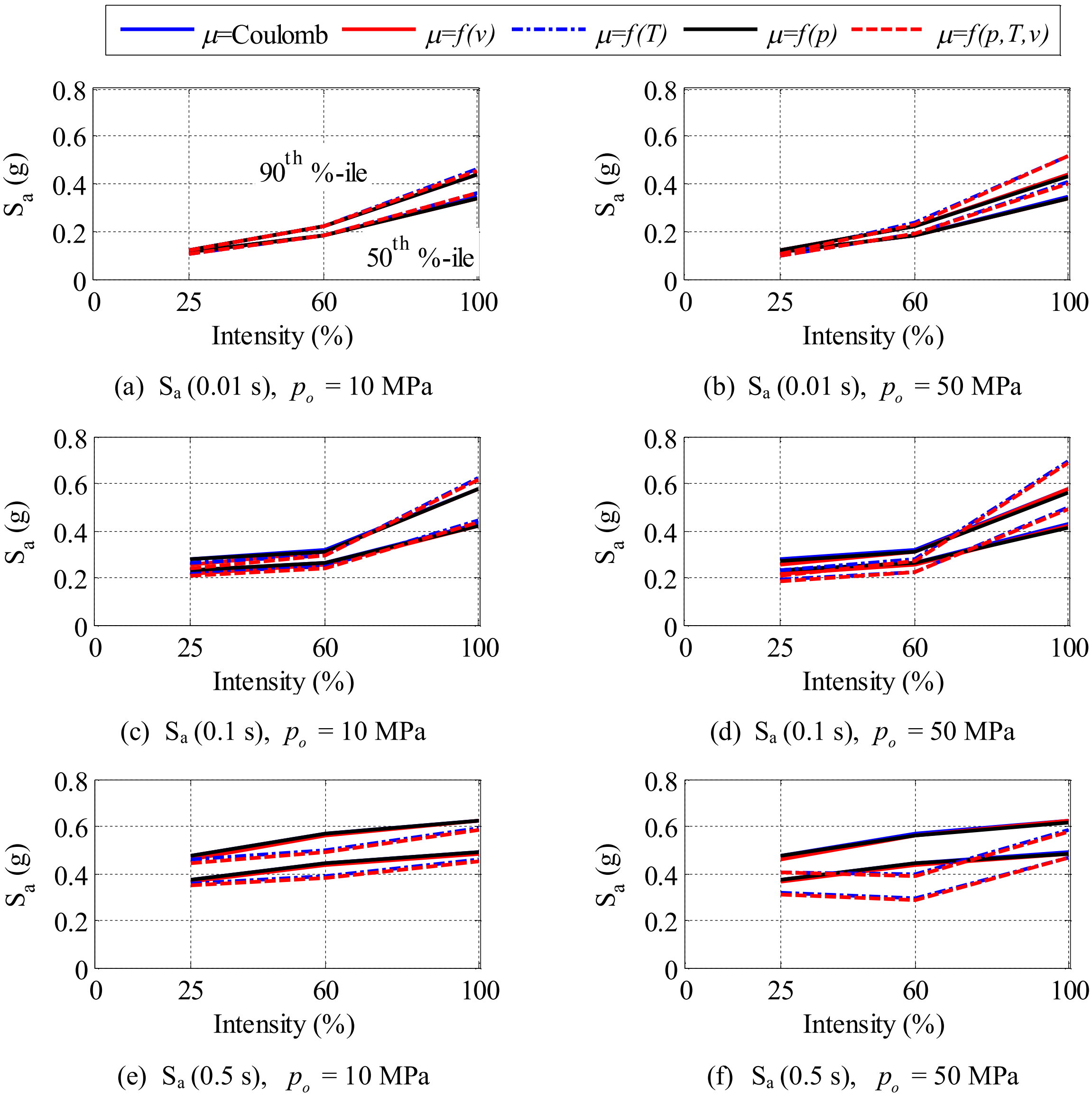

(a) S_a (0.01 s), p_o = 10 MPa
(b) S_a (0.01 s), p_o = 50 MPa
(c) S_a (0.1 s), p_o = 10 MPa
(d) S_a (0.1 s), p_o = 50 MPa
(e) S_a (0.5 s), p_o = 10 MPa
(f) S_a (0.5 s), p_o = 50 MPa

Figure 7-50: Five percent damped 50th and 90th percentile peak floor spectral ordinates at periods of 0.01 s, 0.1 s and 0.5 s, corresponding to the absolute acceleration response of the slider in the Y direction of an FP bearing with a sliding period of 2 s, reference axial pressures of 10 MPa and 50 MPa, and reference coefficient of friction of 0.09, subjected to the 30 ground motions amplitude scaled to different intensities

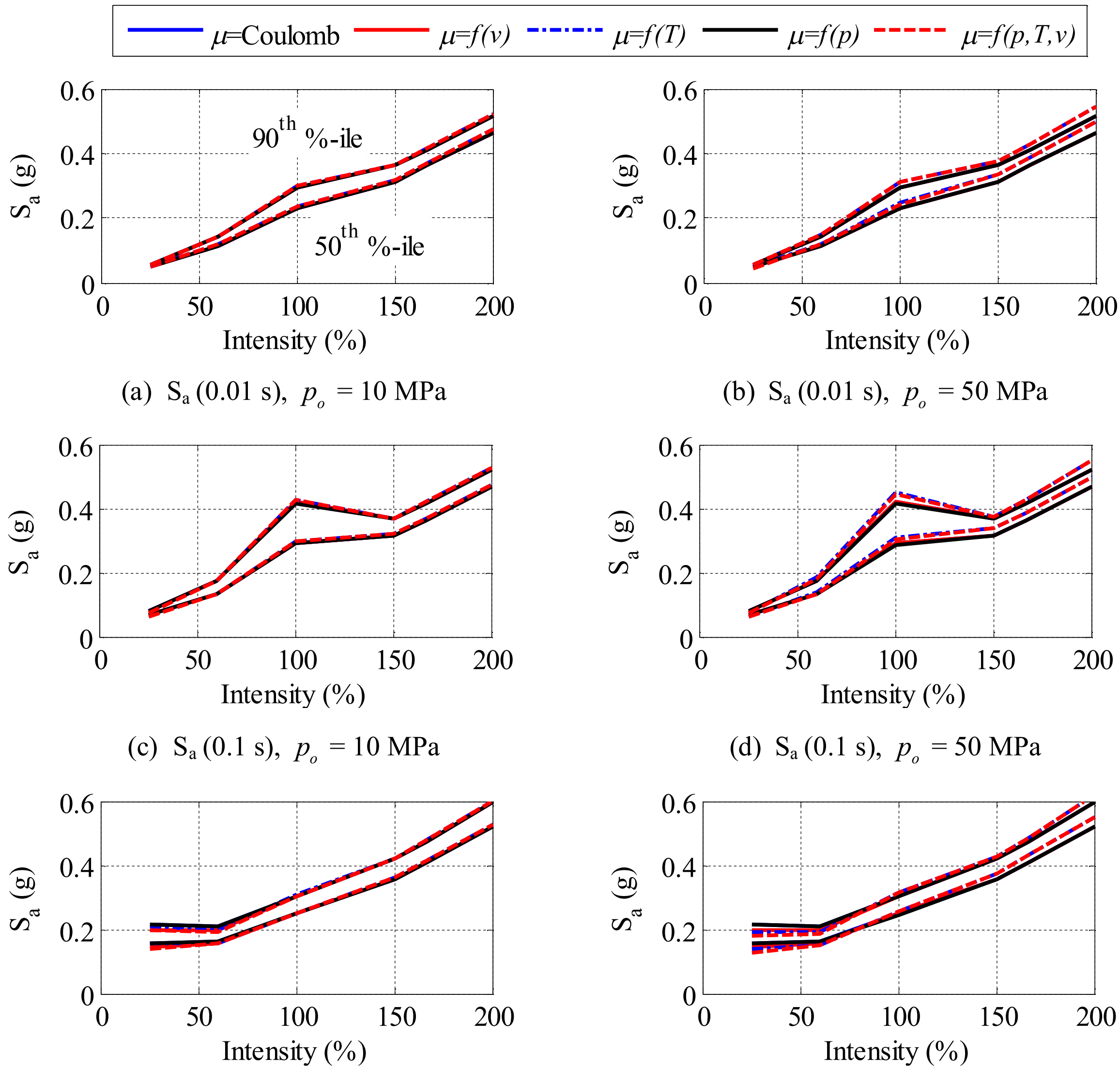

(a) S_a (0.01 s), p_o = 10 MPa

(b) S_a (0.01 s), p_o = 50 MPa

(c) S_a (0.1 s), p_o = 10 MPa

(d) S_a (0.1 s), p_o = 50 MPa

(e) S_a (0.5 s), p_o = 10 MPa

(f) S_a (0.5 s), p_o = 50 MPa

Figure 7-51: Five percent damped 50th and 90th percentile peak floor spectral ordinates at periods of 0.01 s, 0.1 s and 0.5 s, corresponding to the absolute acceleration response of the slider in the X direction of an FP bearing with a sliding period of 3 s, reference axial pressures of 10 MPa and 50 MPa, and reference coefficient of friction of 0.03, subjected to the 30 ground motions amplitude scaled to different intensities

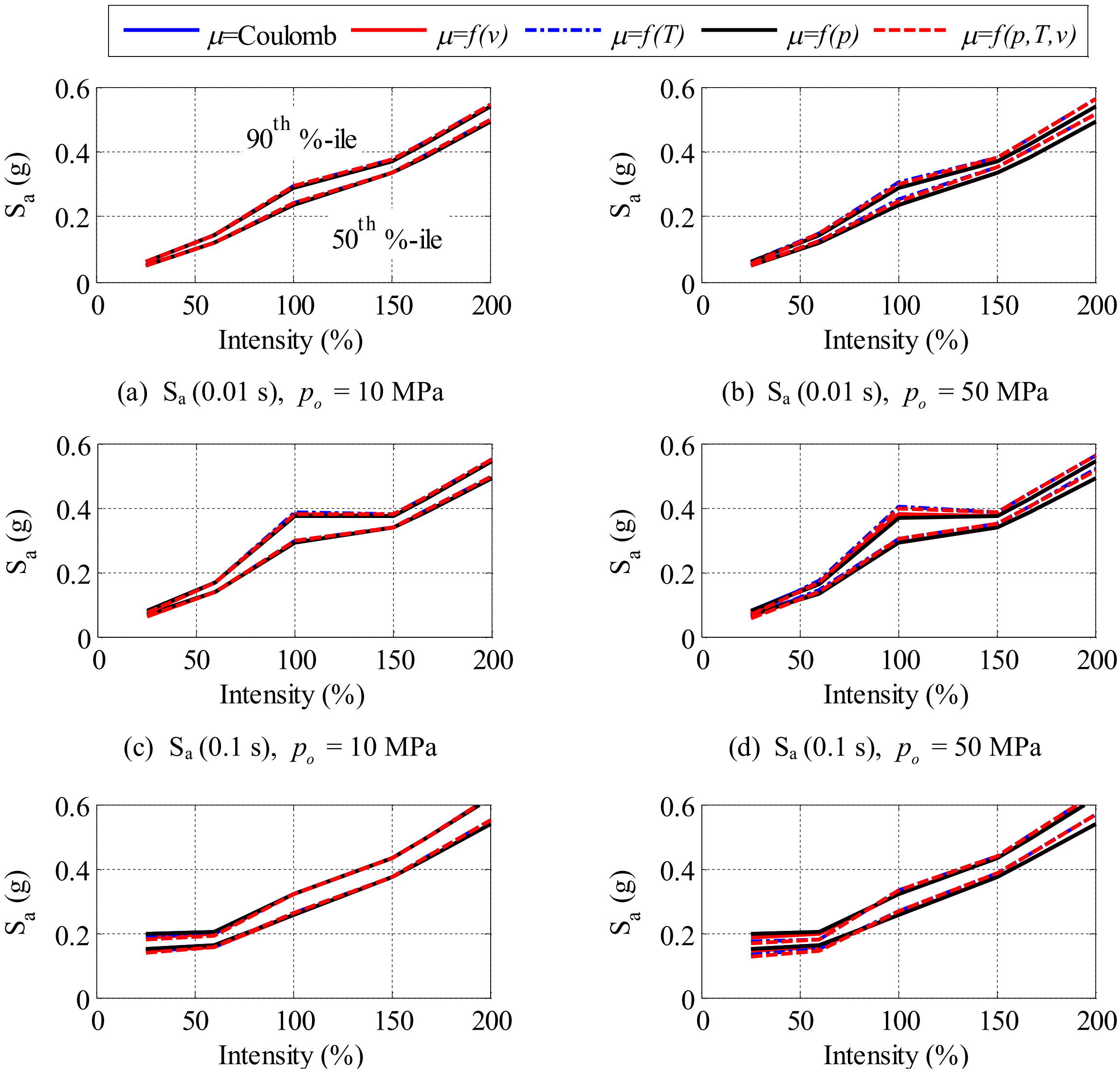

(a) S_a (0.01 s), p_o = 10 MPa

(b) S_a (0.01 s), p_o = 50 MPa

(c) S_a (0.1 s), p_o = 10 MPa

(d) S_a (0.1 s), p_o = 50 MPa

(e) S_a (0.5 s), p_o = 10 MPa

(f) S_a (0.5 s), p_o = 50 MPa

Figure 7-52: Five percent damped 50th and 90th percentile peak floor spectral ordinates at periods of 0.01 s, 0.1 s and 0.5 s, corresponding to the absolute acceleration response of the slider in the Y direction of an FP bearing with a sliding period of 3 s, reference axial pressures of 10 MPa and 50 MPa, and reference coefficient of friction of 0.03, subjected to the 30 ground motions amplitude scaled to different intensities

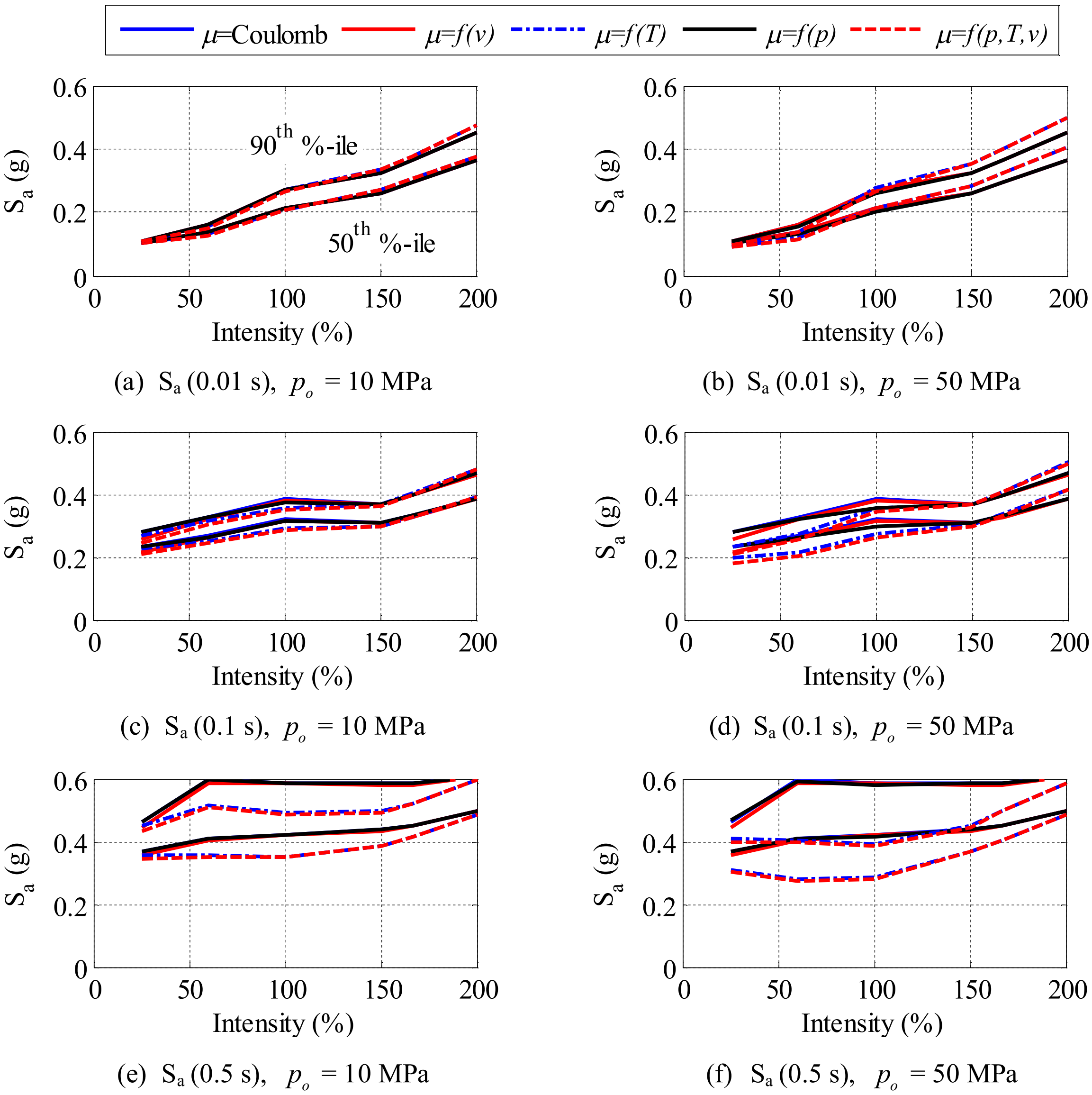

Figure 7-53: Five percent damped 50th and 90th percentile peak floor spectral ordinates at periods of 0.01 s, 0.1 s and 0.5 s, corresponding to the absolute acceleration response of the slider in the X direction of an FP bearing with a sliding period of 3 s, reference axial pressures of 10 MPa and 50 MPa, and reference coefficient of friction of 0.09, subjected to the 30 ground motions amplitude scaled to different intensities

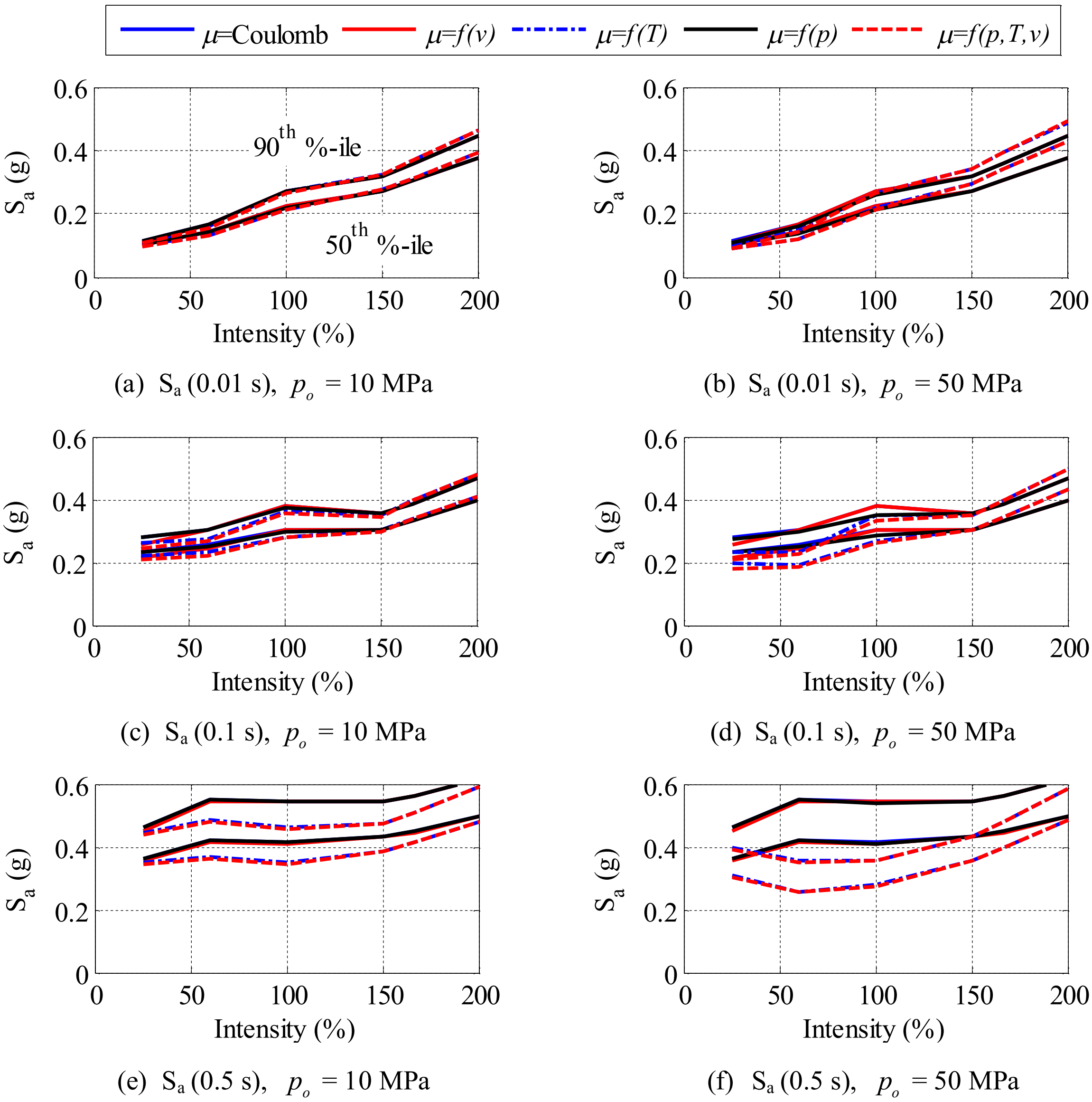

(a) S_a (0.01 s), p_o = 10 MPa

(b) S_a (0.01 s), p_o = 50 MPa

(c) S_a (0.1 s), p_o = 10 MPa

(d) S_a (0.1 s), p_o = 50 MPa

(e) S_a (0.5 s), p_o = 10 MPa

(f) S_a (0.5 s), p_o = 50 MPa

Figure 7-54: Five percent damped 50th and 90th percentile peak floor spectral ordinates at periods of 0.01 s, 0.1 s and 0.5 s, corresponding to the absolute acceleration response of the slider in the Y direction of an FP bearing with a sliding period of 3 s, reference axial pressures of 10 MPa and 50 MPa, and reference coefficient of friction of 0.09, subjected to the 30 ground motions amplitude scaled to different intensities

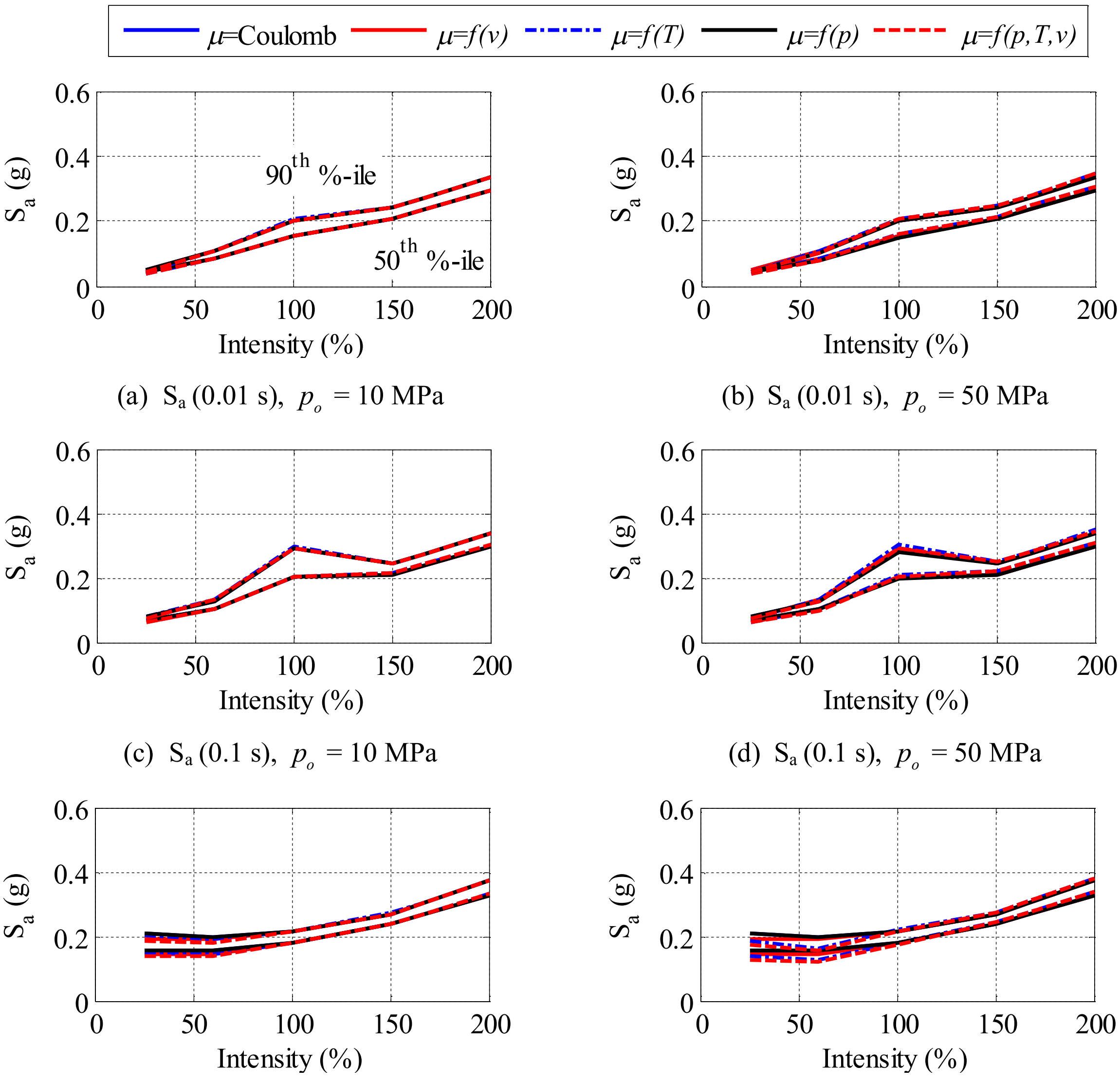

(a) S_a (0.01 s), p_o = 10 MPa
(b) S_a (0.01 s), p_o = 50 MPa
(c) S_a (0.1 s), p_o = 10 MPa
(d) S_a (0.1 s), p_o = 50 MPa
(e) S_a (0.5 s), p_o = 10 MPa
(f) S_a (0.5 s), p_o = 50 MPa

Figure 7-55: Five percent damped 50th and 90th percentile peak floor spectral ordinates at periods of 0.01 s, 0.1 s and 0.5 s, corresponding to the absolute acceleration response of the slider in the X direction of an FP bearing with a sliding period of 4 s, reference axial pressures of 10 MPa and 50 MPa, and reference coefficient of friction of 0.03, subjected to the 30 ground motions amplitude scaled to different intensities

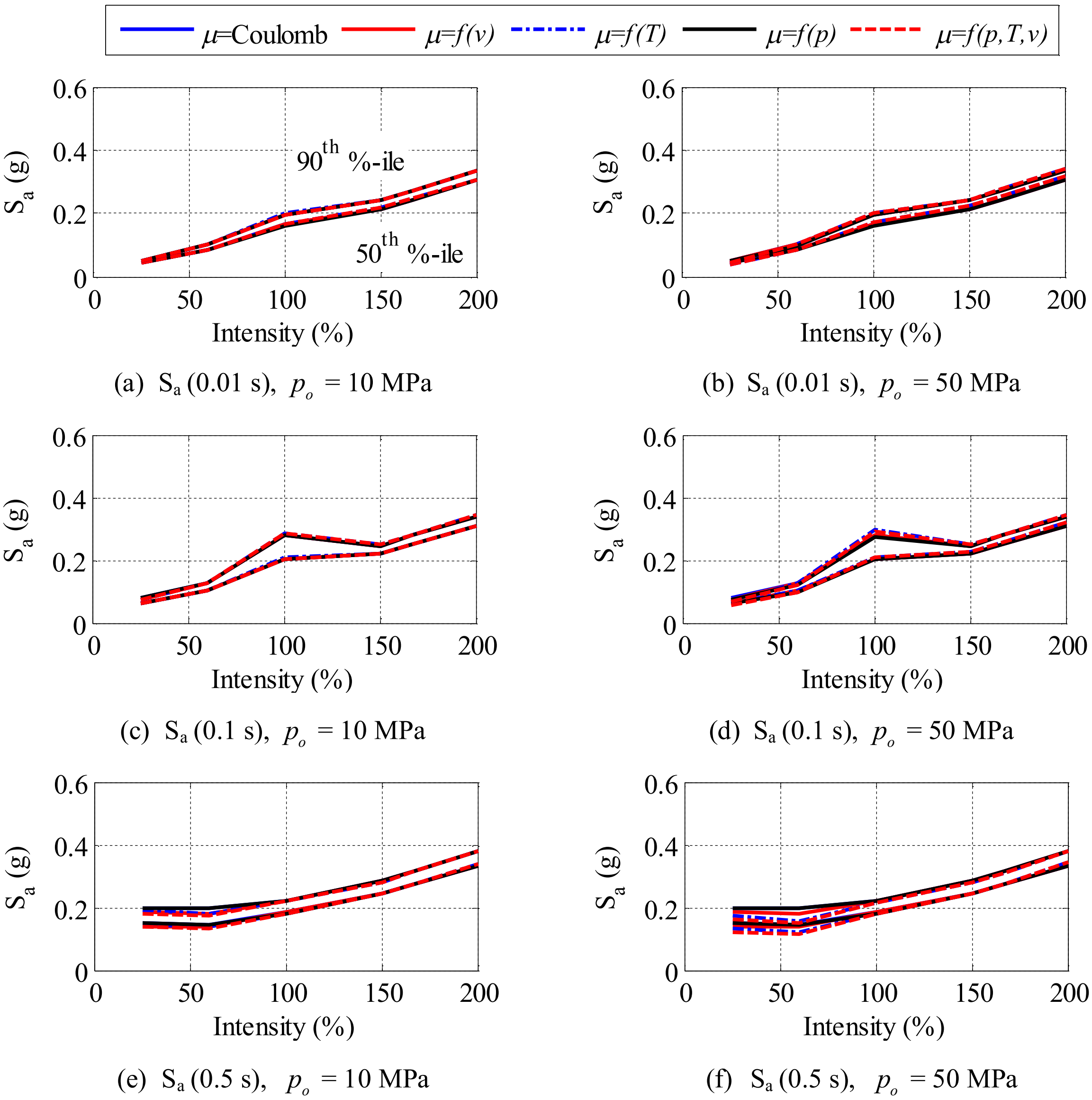

Figure 7-56: Five percent damped 50th and 90th percentile peak floor spectral ordinates at periods of 0.01 s, 0.1 s and 0.5 s, corresponding to the absolute acceleration response of the slider in the Y direction of an FP bearing with a sliding period of 4 s, reference axial pressures of 10 MPa and 50 MPa, and reference coefficient of friction of 0.03, subjected to the 30 ground motions amplitude scaled to different intensities

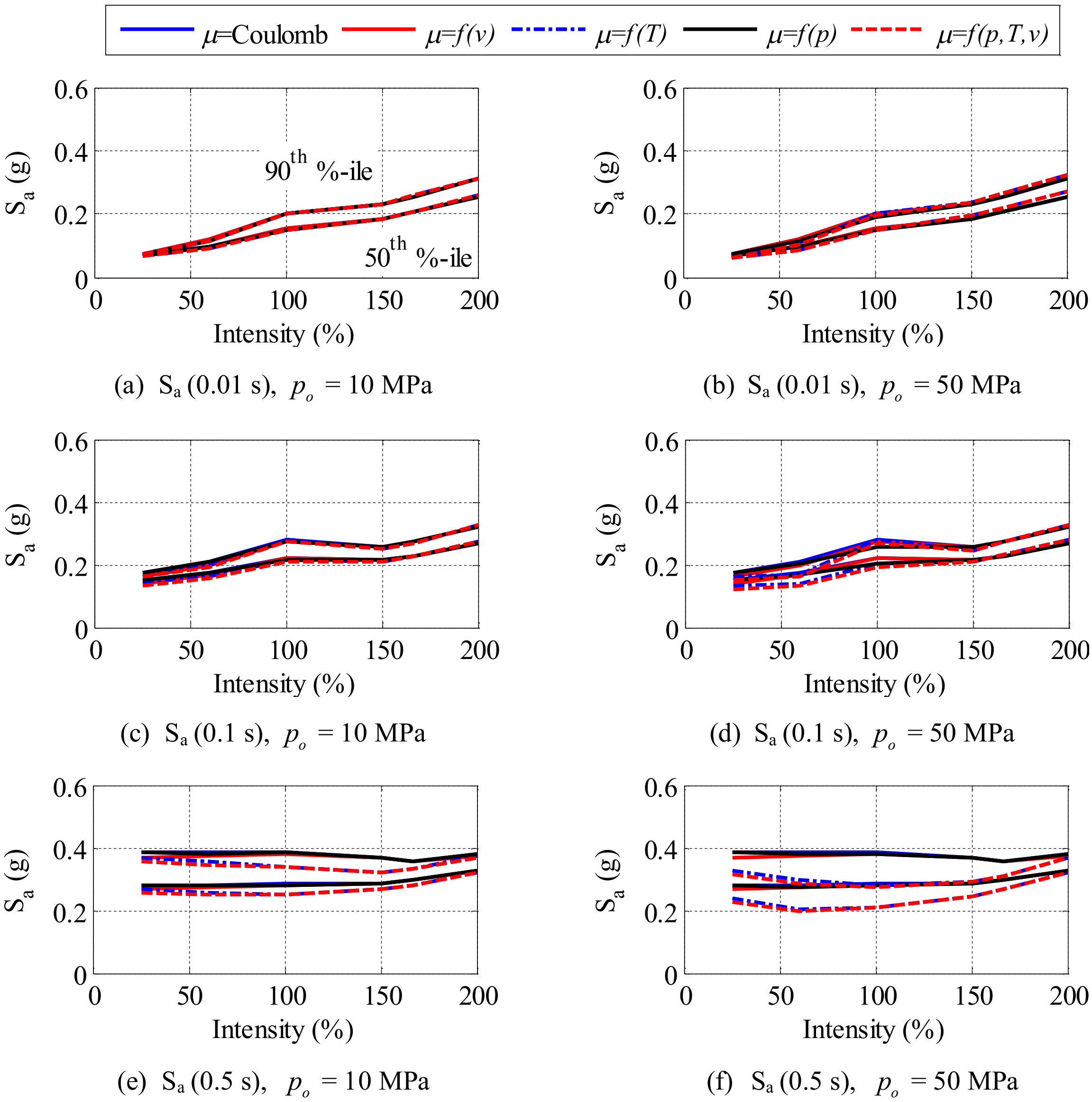

Figure 7-57: Five percent damped 50th and 90th percentile peak floor spectral ordinates at periods of 0.01 s, 0.1 s and 0.5 s, corresponding to the absolute acceleration response of the slider in the X direction of an FP bearing with a sliding period of 4 s, reference axial pressures of 10 MPa and 50 MPa, and reference coefficient of friction of 0.06, subjected to the 30 ground motions amplitude scaled to different intensities

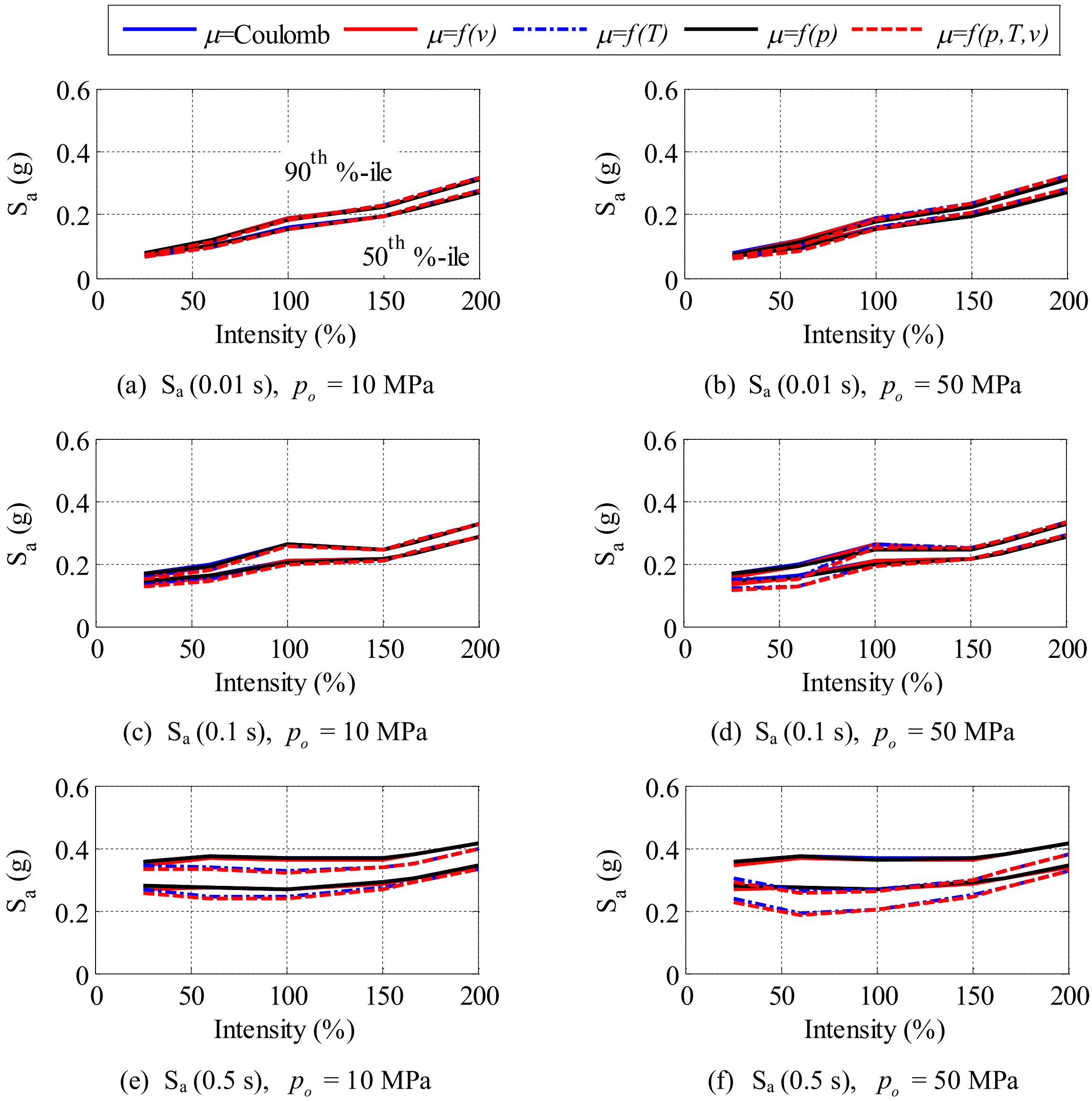

Figure 7-58: Five percent damped 50th and 90th percentile peak floor spectral ordinates at periods of 0.01 s, 0.1 s and 0.5 s, corresponding to the absolute acceleration response of the slider in the Y direction of an FP bearing with a sliding period of 4 s, reference axial pressures of 10 MPa and 50 MPa, and reference coefficient of friction of 0.06, subjected to the 30 ground motions amplitude scaled to different intensities

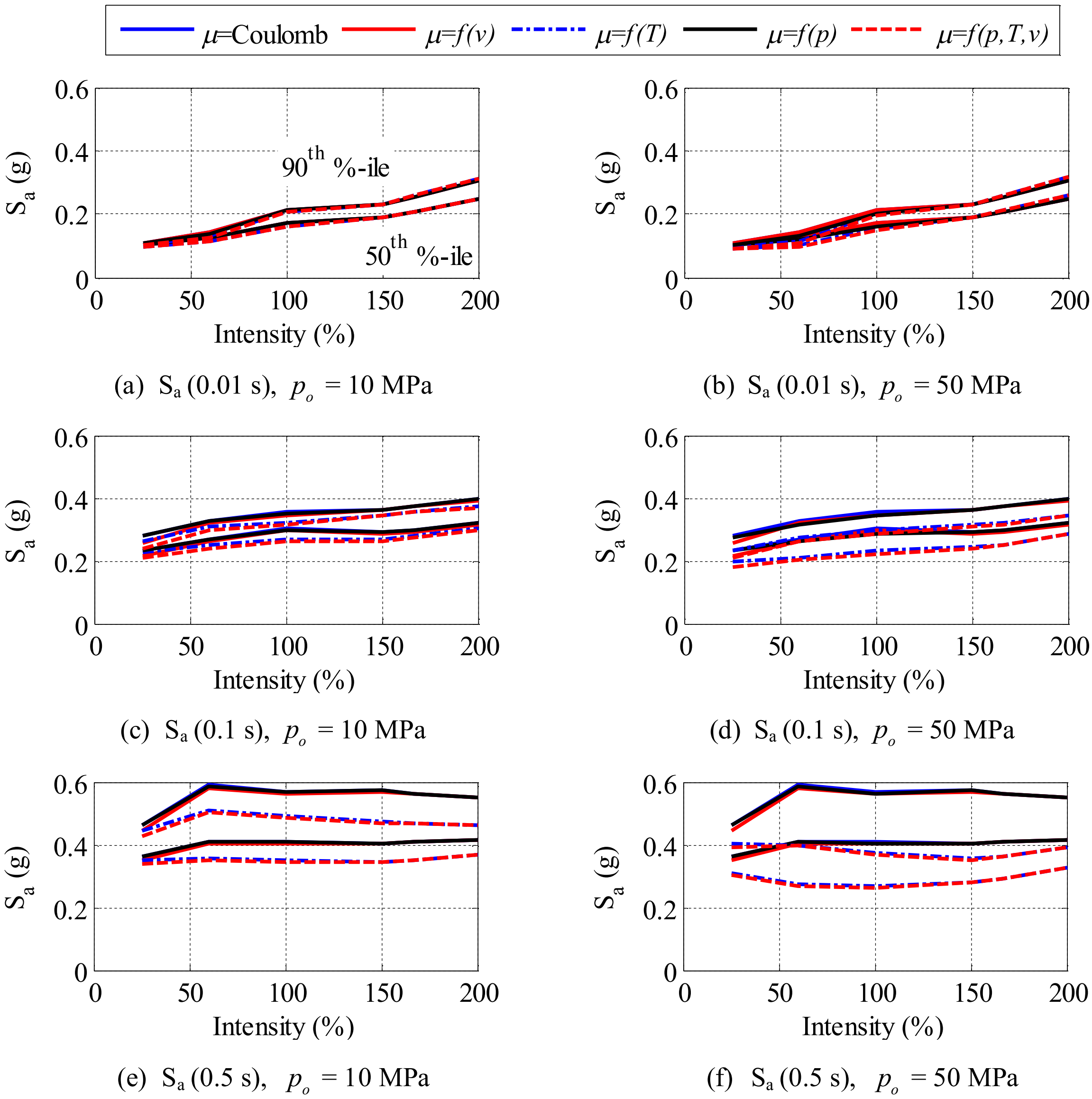

Figure 7-59: Five percent damped 50th and 90th percentile peak floor spectral ordinates at periods of 0.01 s, 0.1 s and 0.5 s, corresponding to the absolute acceleration response of the slider in the X direction of an FP bearing with a sliding period of 4 s, reference axial pressures of 10 MPa and 50 MPa, and reference coefficient of friction of 0.09, subjected to the 30 ground motions amplitude scaled to different intensities

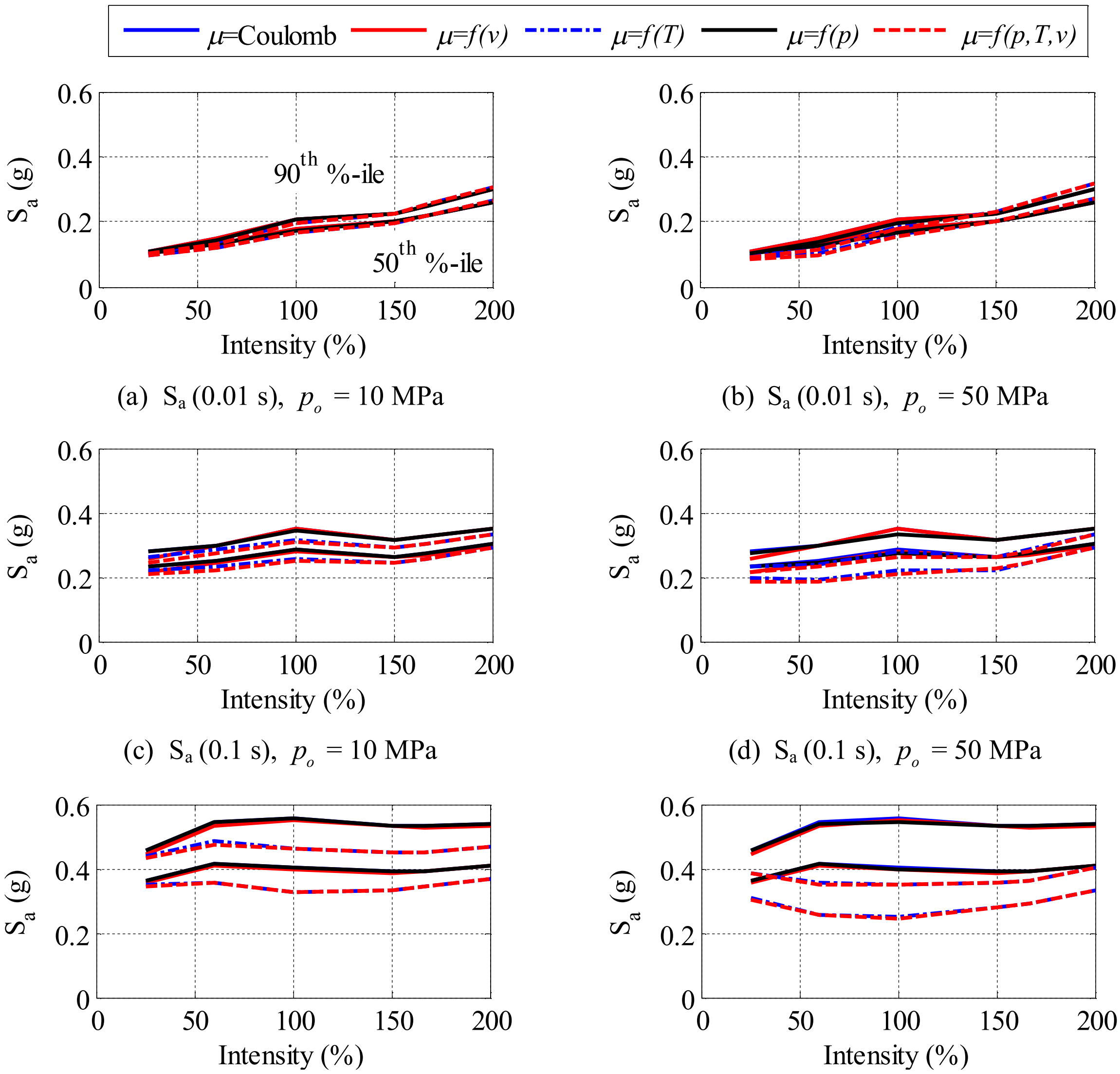

(a) S_a (0.01 s), p_o = 10 MPa

(b) S_a (0.01 s), p_o = 50 MPa

(c) S_a (0.1 s), p_o = 10 MPa

(d) S_a (0.1 s), p_o = 50 MPa

(e) S_a (0.5 s), p_o = 10 MPa

(f) S_a (0.5 s), p_o = 50 MPa

Figure 7-60: Five percent damped 50th and 90th percentile peak floor spectral ordinates at periods of 0.01 s, 0.1 s and 0.5 s, corresponding to the absolute acceleration response of the slider in the Y direction of an FP bearing with a sliding period of 4 s, reference axial pressures of 10 MPa and 50 MPa, and reference coefficient of friction of 0.09, subjected to the 30 ground motions amplitude scaled to different intensities

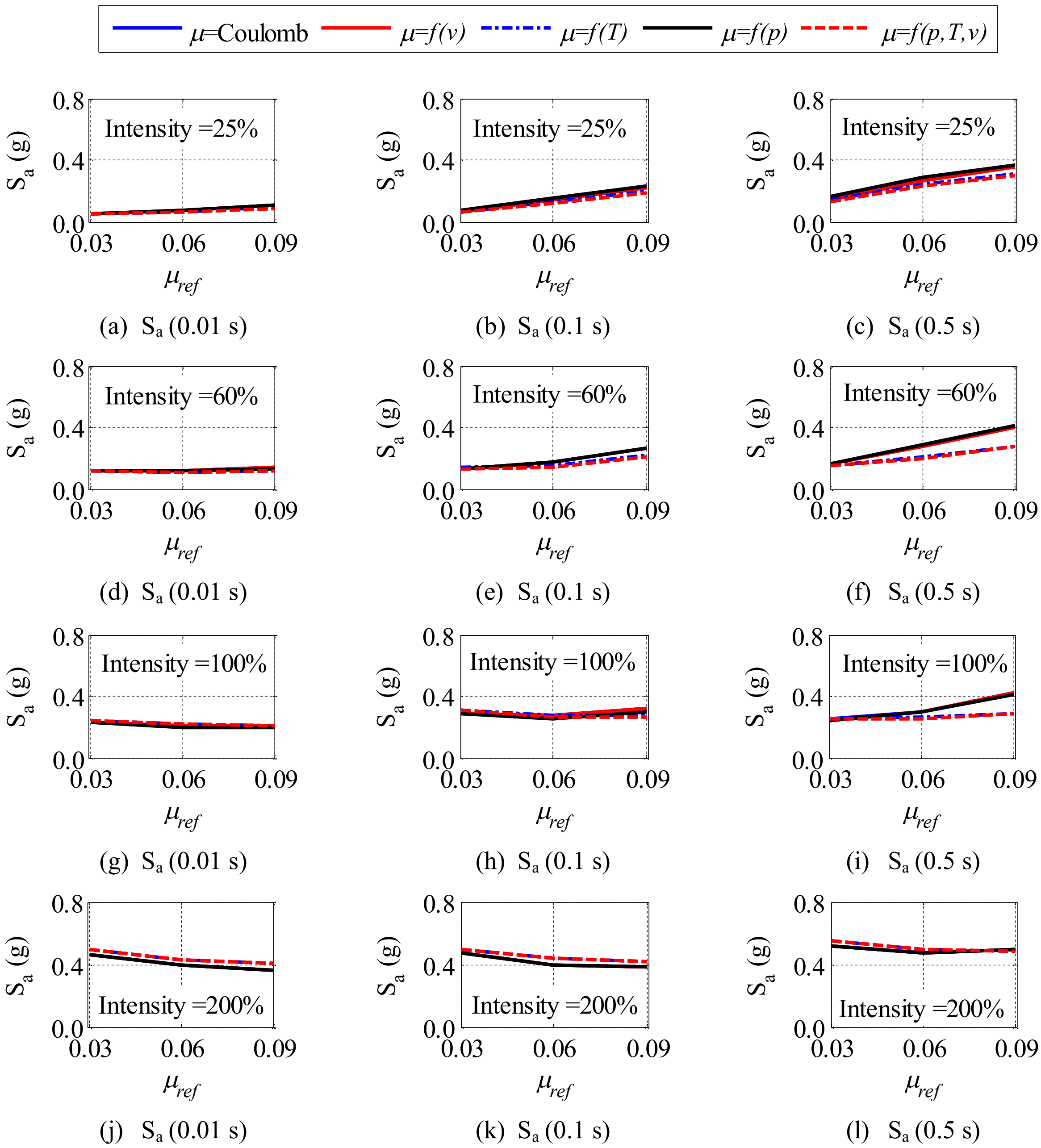

Figure 7-61: Five percent damped 50th percentile peak floor spectral ordinates at periods of 0.01 s, 0.1 s and 0.5 s, corresponding to the absolute acceleration response of the slider in the X direction of an FP bearing with a sliding period of 3 s, reference axial pressure of 50 MPa, and reference coefficients of friction of 0.03, 0.06 and 0.09, subjected to the 30 ground motions amplitude scaled to different intensities

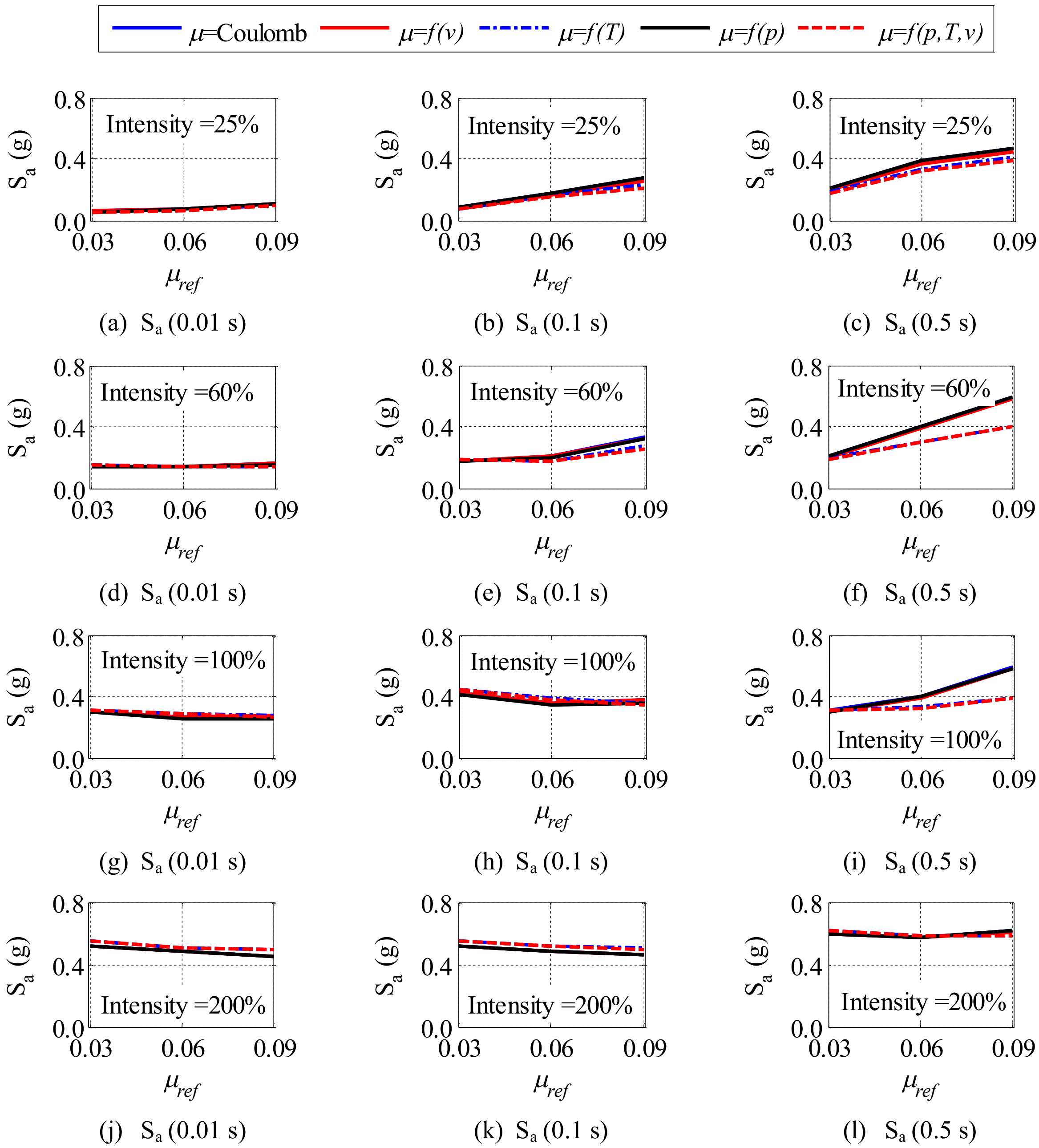

Figure 7-62: Five percent damped 90th percentile peak floor spectral ordinates at periods of 0.01 s, 0.1 s and 0.5 s, corresponding to the absolute acceleration response of the slider in the X direction of an FP bearing with a sliding period of 3 s, reference axial pressure of 50 MPa, and reference coefficients of friction of 0.03, 0.06 and 0.09, subjected to the 30 ground motions amplitude scaled to different intensities

CHAPTER 8

RESPONSE OF A NUCLEAR POWER PLANT SEISMICALLY ISOLATED USING FRICTION PENDULUM™ BEARINGS

8.1 Introduction

This chapter presents results of response-history analyses performed using different models of a seismically isolated nuclear power plant (NPP). The results of the analysis are used to answer three practical questions: 1) How significantly does the choice of friction model affect horizontal displacement response?, 2) How significantly does the vertical component of ground motion affect the displacement response of an FP-isolation system, and 3) Can key response quantities be estimated with a macro model of the isolation system?

An NPP typically includes three major structures: auxiliary and shield building (ASB), containment steel structure (CIS) and steel containment vessel (SCV). The ASB considered herein is a 140,000-ton concrete structure with a footprint of 97 m $\times$ 60 m, and a total height of 89 m (Roche, 2013). The CIS weighs 41,000 tons with a total height of 33 m (Short *et al.*, 2007). The SCV weighs 3,700 tons and is ignored in this study due to its relatively small mass (see Short *et al.* (2007)).

The first model of the NPP is the ASB and CIS supported on a common isolation system comprising single Friction Pendulum™ (FP) bearings. The second model of the NPP involves a macro (single) FP isolator, similar to that used in Chapter 7. Friction at the sliding surface is described using all five models listed in Table 7-2. Two response quantities are studied: 1) isolation-system displacement, and 2) floor spectral ordinates at different locations in the CIS.

The two NPP models are subjected to the ground motions consistent with seismic hazard at the two sites considered in Chapter 7: Diablo Canyon and Vogtle. Model 1 is subjected to the two horizontal and/or vertical components of ground motions. Model 2 is subjected only to the two horizontal components of ground motions.

The geometric properties of the ASB and the CIS considered in this study are presented in Section 8.2. The ASB and CIS models are described in Section 8.3. Two models of the seismically isolated NPP are presented in Section 8.4 and these are subjected to the ground motions of Section 8.5. Results of response-history analyses performed using the models of Section 8.4 subjected to ground motions of Section 8.5 are presented in Section 8.6.

8.2 Geometric Properties of the Nuclear Power Plant

This section presents the geometric properties of the ASB and CIS.

8.2.1 Auxiliary and shield building (ASB)

Figures 8-1 and 8-2 present plan and elevation views of the ASB, respectively. The dimensions of the ASB were provided by Roche (2013). The ASB is 97 m × 60 m in plan and its height is 89 m measured from the bottom of the basemat. The interior walls, floors and roof are 0.6 m (2 ft) thick. The exterior walls and the walls along the horizontal axes of symmetry are 0.9 m (3 ft) thick. The ASB is constructed of reinforced concrete with a density of 2400 kg/m^3, a characteristic concrete strength of 41 MPa and an elastic modulus of 30 GPa. The total mass of the ASB is 140,000 ton, with the 49,000 ton in the basemat, which is shown stippled in Figure 8-2.

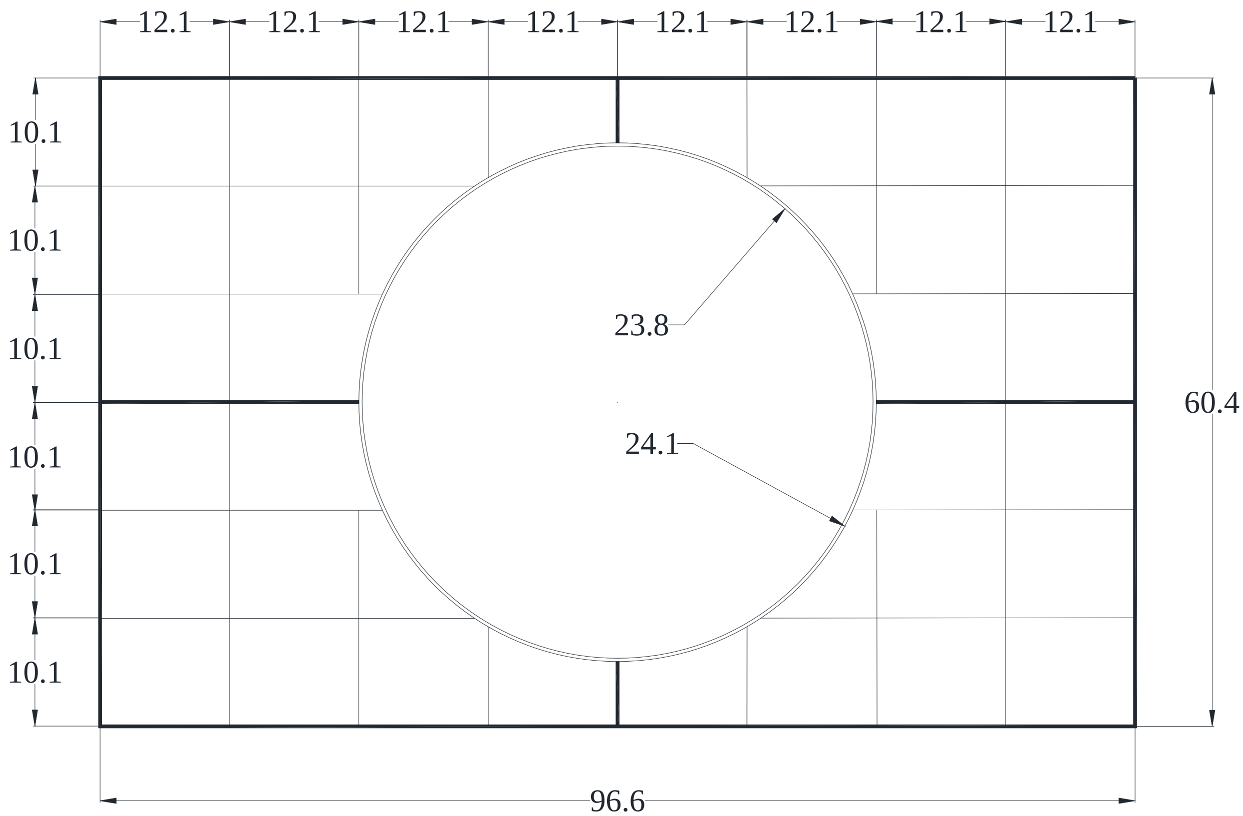

- Dimensions are in meters.
- Exterior walls and the walls along the two horizontal axes of symmetry are 0.9 m (3 ft) thick.
- Other walls are 0.6 m (2 ft) thick.
- The circle of radius 24.1 m (80 ft) indicates the 1.2 m (4 ft) thick cylindrical wall.
- The circle of radius 23.8 m (79 ft) indicates the 0.9 m (3 ft) thick hemispherical dome.

Figure 8-1: Plan view of auxiliary and shield building (adapted from Roche (2013))

8.2.2 Containment internal structure (CIS)

The CIS considered herein comprises a vertical stick with masses lumped at different heights and at three outrigger nodes. Figure 8-3 is a schematic of the 33 m-tall CIS. The circles indicate the locations of concentrated masses. The total mass of CIS[1] is 41,000 ton. The CIS model used in this study is from Short *et al.* (2007).

[1] The total mass of SCV considered by Short *et al.* (2007) is 3,700 ton, which is small compared to the masses of ASB (140,000 ton) and CIS (41,000 ton) considered in this study.

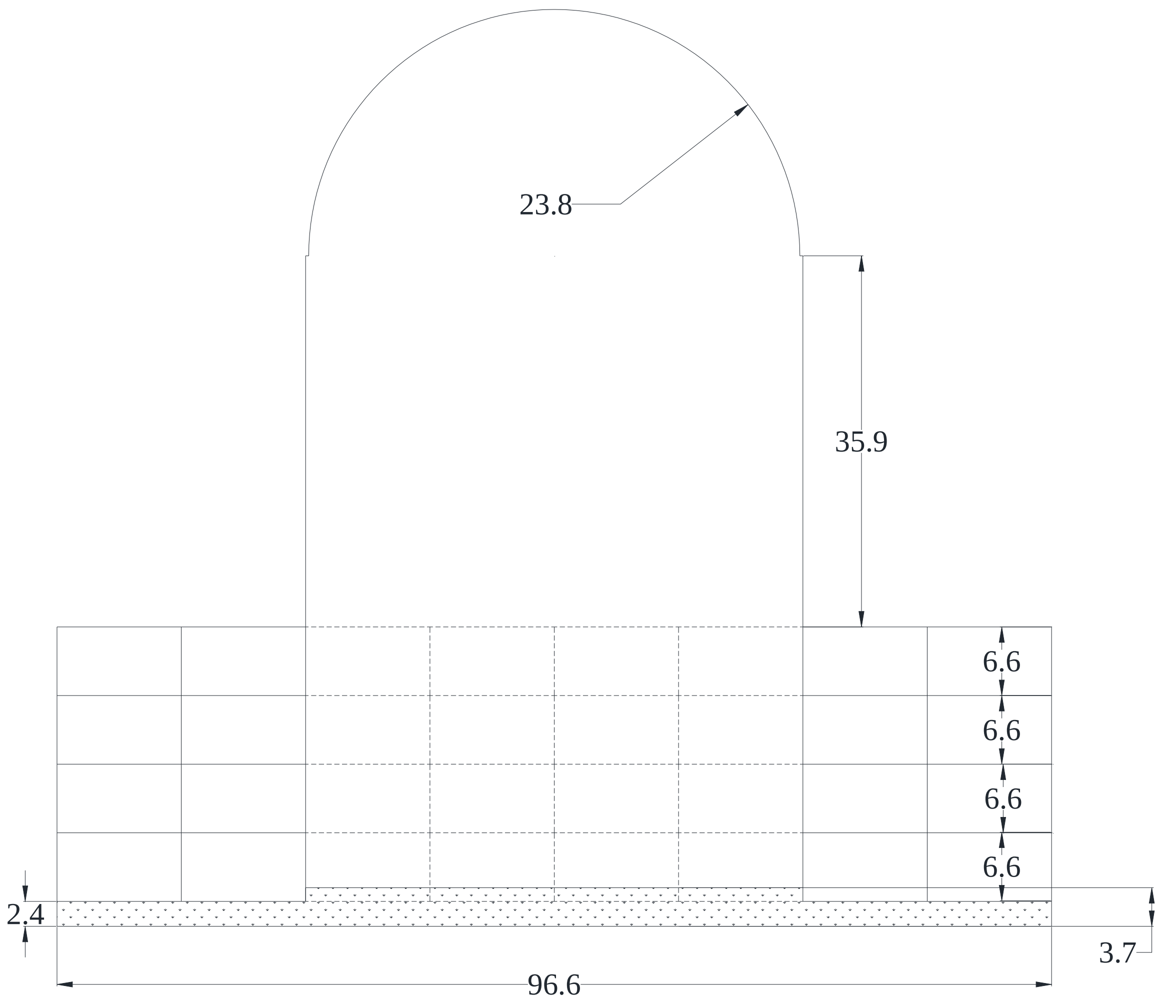

- Dimensions are in meters.
- Floors and roof are 0.6 m (2 ft) thick.
- Thickness of cylindrical wall is 1.2 m (4 ft).
- Thickness of hemispherical dome is 0.9 m (3 ft).

Figure 8-2: Elevation view of the auxiliary and shield building (adapted from Roche (2013))

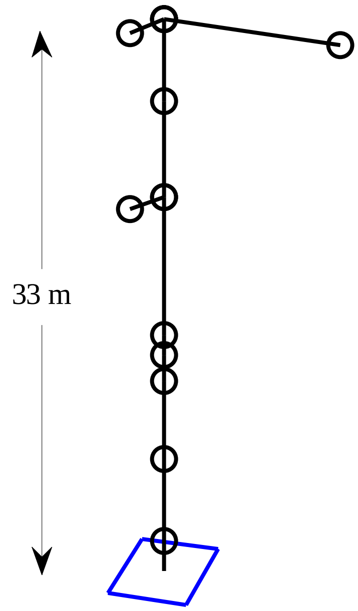

Figure 8-3: Containment internal structure (adapted from Short *et al.* (2007))

8.3 Modeling ASB and CIS for Response-history Analysis

8.3.1 Introduction

This section summarizes the approach used to model the ASB for response-history analysis using OpenSees (PEER, 2014). The distribution of the mass to the walls, floors, roof, cylindrical wall and hemispherical dome, and of the lateral stiffness contributed by the walls, cylinder and dome is discussed. The mass associated with the nodes and the stiffness of the elements used in the OpenSees model are listed. The dynamic properties (e.g., natural period and corresponding mode shape) of the ASB modeled in OpenSees are computed and compared with those obtained for the ASB modeled in LS-DYNA (LSTC, 2011), where the LS-DYNA model for the ASB was provided by Roche (2013).

The containment internal structure is modeled in OpenSees using the mass and stiffness data presented in Short *et al.* (2007).

8.3.2 Auxiliary and shield building (ASB)

8.3.2.1 LS-DYNA model

The nuclear power plant structure with plan and elevation views shown in Figures 8-1 and 8-2 was modeled in LS-DYNA (LSTC, 2011) by Roche (2013). Figure 8-4 shows the model of the ASB. The concrete characteristic strength was 41.3 MPa and its elastic modulus was 30.4 GPa.

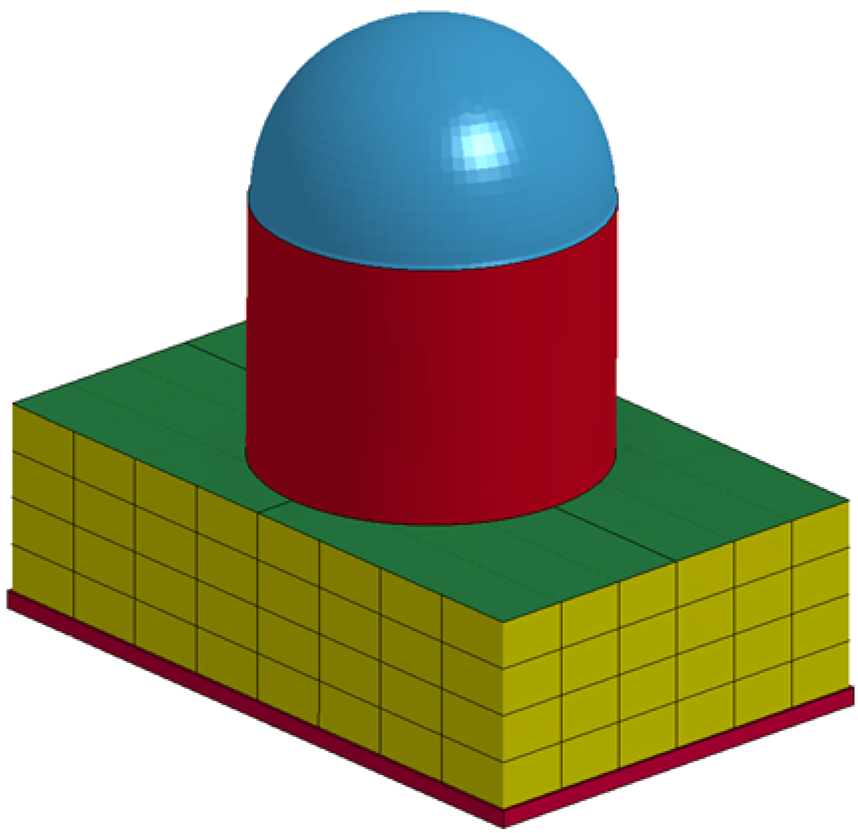

Figure 8-4: LS-DYNA model of the ASB (adapted from Roche (2013))

The natural periods for the first two modes of vibration of the ASB modeled using LS-DYNA are listed in Table 8-1. The first two mode shapes are shown in Figure 8-5.

Table 8-1: Natural periods of the ASB

Mode	LS-DYNA	OpenSees
1	0.23 s	0.15 s
2	0.22 s	0.15 s

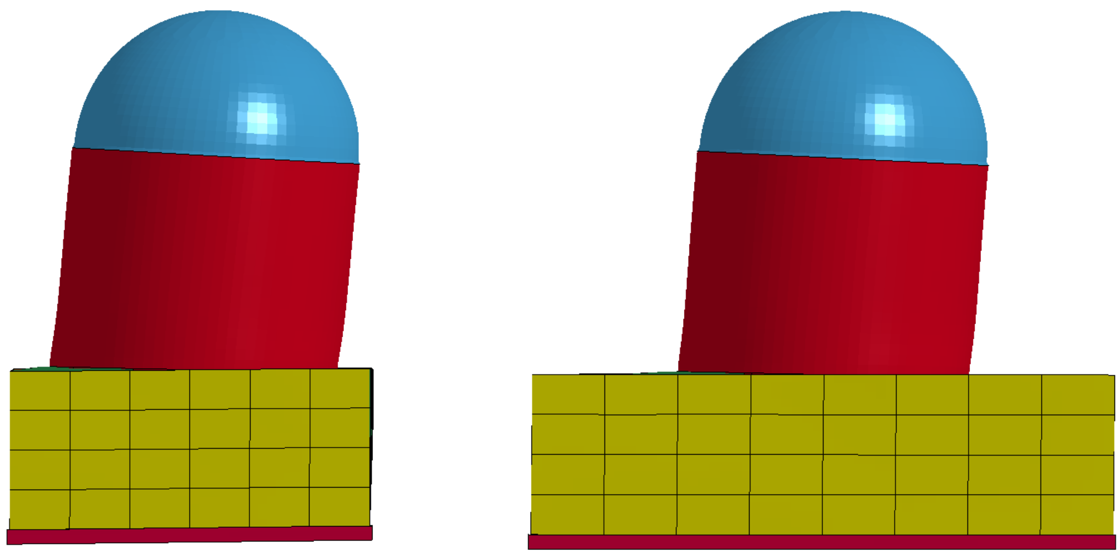

(a) First mode (b) Second mode

Figure 8-5: Mode shapes of the ASB

8.3.2.2 OpenSees model

8.3.2.2.1 Modeling of mass

The auxiliary and shield building is divided into three segments to facilitate modeling in OpenSees. The three segments are shown in Figure 8-6. Segment 2 is the central portion of the ASB comprising the cylindrical wall and its dome, with plan dimensions of 48 m × 60 m.

Segments 1 and 3 are symmetrically placed with respect to Segment 2; each has plan dimensions of 24 m $\times$ 60 m.

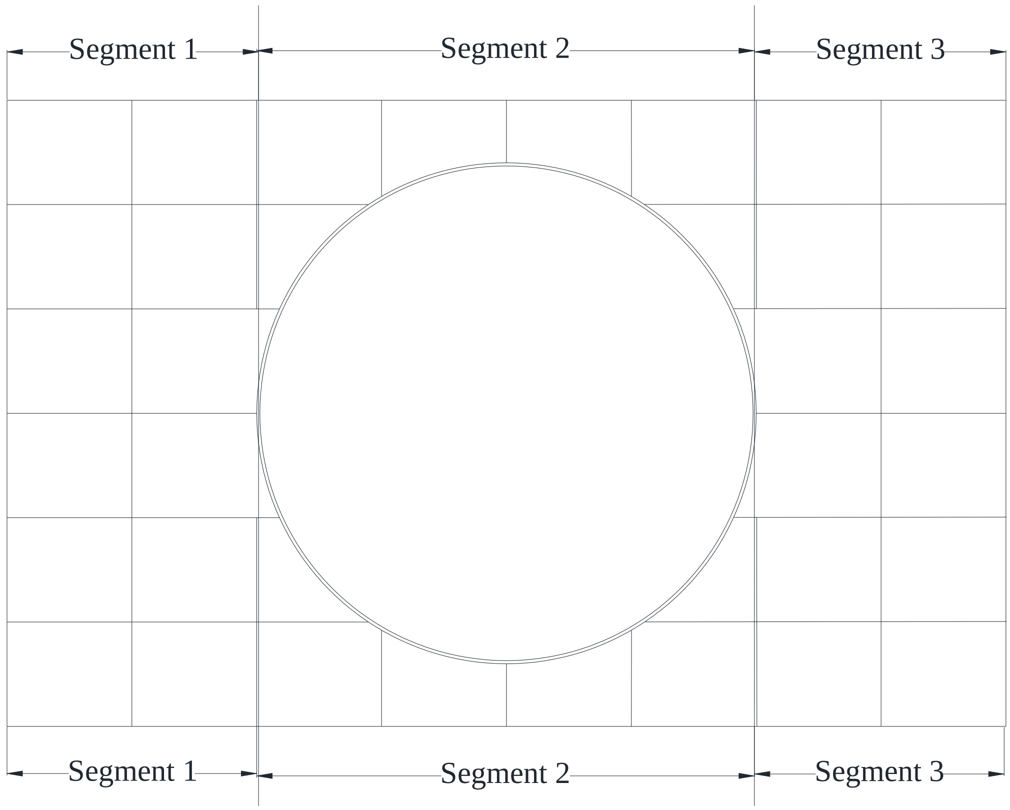

Figure 8-6: Segments of auxiliary and shield building (ASB)

Segment 1 of the ASB comprises a 2.4 m-thick basemat and four floors (including the roof), each 0.6 m-thick. The total length of 0.9 m-thick external walls, 0.9 m-thick internal walls and 0.6 m-thick internal walls is 109 m, 24 m and 198 m, respectively. The story height is 6.6 m. Five elevations are considered in the segment, namely, 1.2 m, 9.1 m, 15.8 m, 22.6 m and 29.3 m, which represent the locations of the basemat and the floors. Masses are lumped at the floors and the basemat. The mass of each wall is split between the floors above and below. The mass at each level is listed in Table 8-2.

Segment 2 of the ASB comprises 1) a 1.2 m-thick cylindrical wall with a radius and a height of 24 m and 62 m, respectively, 2) a 0.9 m-thick hemisphere with a radius of 24 m, 3) 0.9 m-thick exterior walls with a total length 97 m, 4) 0.9 m-thick interior walls with a total length of 12 m, 5) 0.6 m-thick interior walls with a total length of 89 m, 6) a 2.4 m-thick basemat with plan dimensions of 48 m $\times$ 60 m, 7) a 1.3 m-thick circular basemat on top of the rectangular basemat with a radius of 24 m, and 8) 0.6 m-thick floors at four levels (same as Segments 1 and 3) with a plan area of 1,100 m^2. In addition to the five elevations considered for Segments 1 and 3, four elevations, at heights of 41.5 m, 53.6 m, 65.8 m and 71.3 m measured from the bottom of the basemat, are considered for Segment 2. Mass is assigned to levels per the method adopted for Segments 1 and 3. The mass at the nine elevations of Segment 2 are listed in Table 8-2.

Table 8-2: Distribution of mass in the ASB

Level	**Height from bottom of basemat (m)**	**Mass (tonnes)**		
		Segment 1	Segment 2	Segment 3
1	1.2	11,000	27,000	11,000
2	9.1	5,800	6,700	5,800
3	15.8	5,800	7,000	5,800
4	22.6	5,800	7,000	5,800
5	29.3	4,000	6,600	4,000
6	41.5	-	5,300	-
7	53.6	-	5,300	-
8	65.8	-	3,800	-
9	71.3	-	6,700	-
	Total	32,000	75,000	32,000

The mass associated with an elevation in a segment is then distributed across nodes that are equispaced in plan. For this study, the spacing between nodes is 6 m for all three segments of the ASB. Consequently, there are 187 nodes at each of the five elevations lower than 30 m, and 99 nodes at each of the four higher elevations: a total of 1331 nodes ($5\times187+4\times99$) for the ASB. Figure 8-7 presents the locations of the nodes in plan. Figure 8-8 presents the location of nodes in elevation.

A small value of mass moment of inertia is assigned about the three axes to all 1,331 nodes in the OpenSees model of the ASB to avoid numerical instability. The locations of nodes, and the masses and mass moments of inertia associated with the nodes are listed in Appendix I.

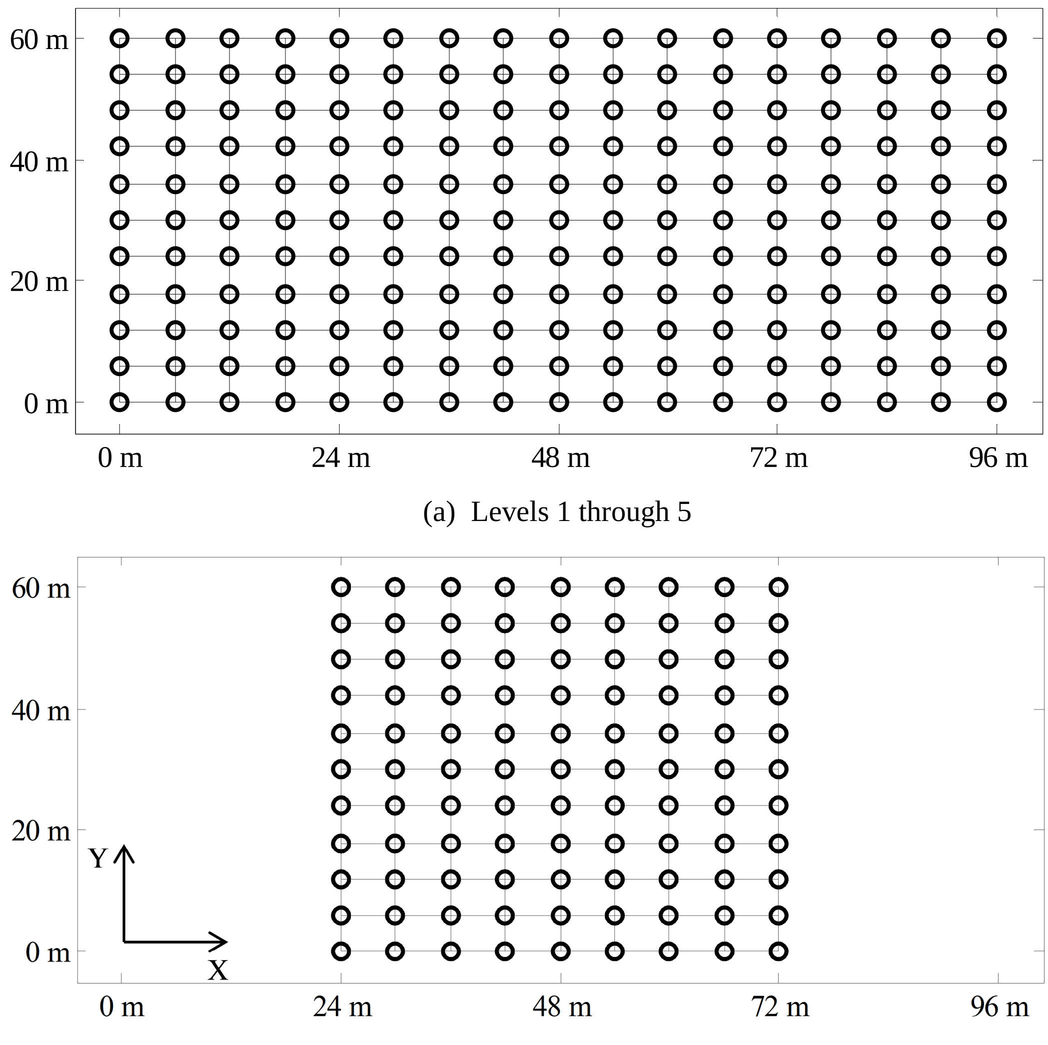

(b) Levels 6 through 9

Figure 8-7: Locations of nodes (indicated by circles) in the ASB in plan

8.3.2.2.2 Modeling of stiffness

The lateral stiffness of the ASB is modeled using discrete beam-column elements to speed the calculations. The ASB is assumed to be rigid in the vertical direction because its *true* dynamic response would not significantly affect the horizontal displacement response of the isolation systems and the assumption speeds calculations.

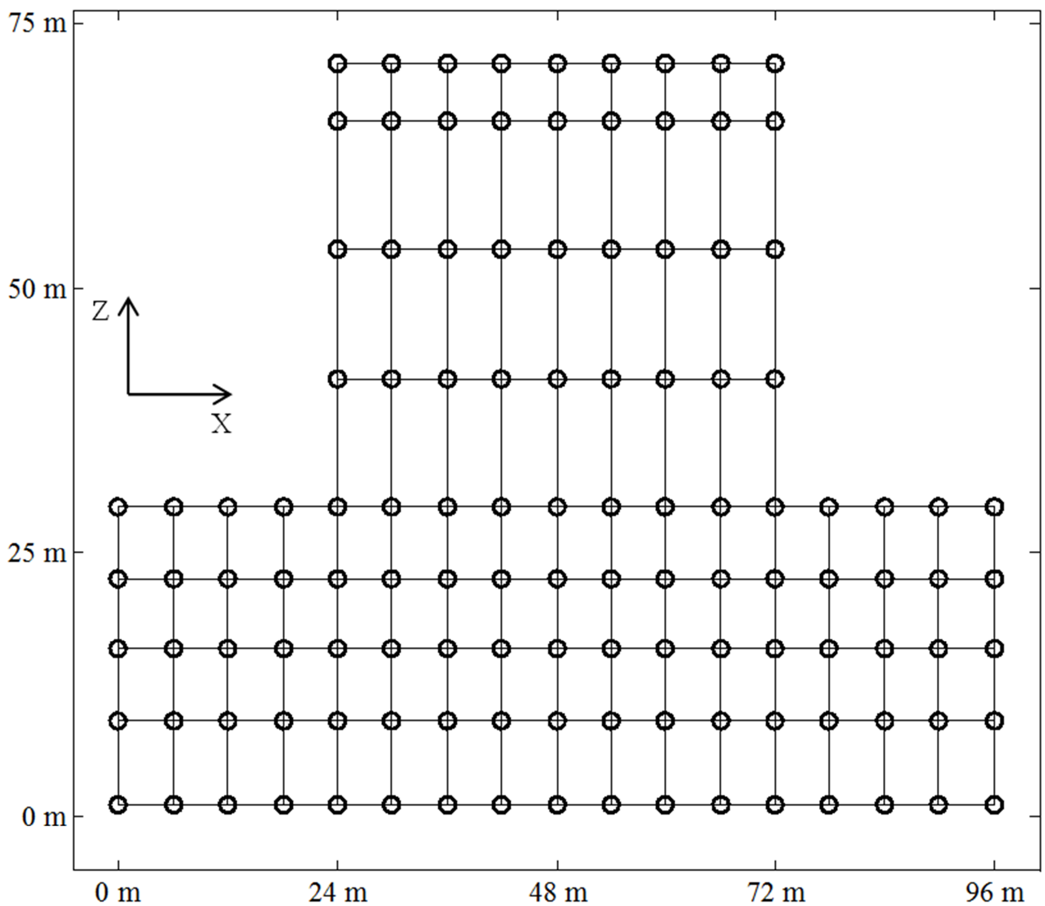

Figure 8-8: Locations of nodes (indicated by circles) in the ASB in elevation

The lateral stiffness of the ASB is summarized in Table 8-3 by segment and story. The stiffness for each story-segment pair is distributed equally between the columns in that pair. The number of columns in a story-segment pair is equal to the number of nodes at a floor level in the segment (e.g., 44 vertical columns in the first segment of ASB between any two adjacent floors).

8.3.2.2.3 *Implementation*

A total of 1331 nodes are used to discretize the ASB. Rigid horizontal beams along the two principal horizontal directions connect the nodes. These beams are modeled using *elasticBeamColumn* element in OpenSees (PEER, 2014). The connectivity of the horizontal beams is listed in Appendix I.

Table 8-3: Segment and story distribution of total stiffness of the auxiliary and shield building in the two orthogonal horizontal directions (X and Y)

Story	**Elevation level (m)**		**Stiffness ($\times 10^{11}$ N/m)**					
	Start	End	Segment 1		Segment 2		Segment 3	
			X	Y	X	Y	X	Y
1	1.2	9.1	2.4	1.8	6.3	5.5	2.4	1.8
2	9.1	15.8	2.4	1.8	5.5	4.7	2.4	1.8
3	15.8	22.6	2.4	1.8	5.5	4.7	2.4	1.8
4	22.6	29.3	2.4	1.8	5.5	4.7	2.4	1.8
5	29.3	41.5	-	-	1.0	1.0	-	-
6	41.5	53.6	-	-	1.0	1.0	-	-
7	53.6	65.8	-	-	1.0	1.0	-	-
8	65.8	71.3	-	-	2.2	2.2	-	-

The columns are modeled using the *elasticBeamColumn* element. The key user-defined input parameters for this element are: cross-sectional area, elastic modulus, shear modulus, and area moment of inertia about three orthogonal axes. The axial rigidity is achieved using a large cross-sectional area, which results in high shear stiffness. The lateral stiffness of each column is defined in terms of flexural stiffness. The area moments of inertia in the two orthogonal horizontal directions are selected so that its total lateral stiffness is equal to its flexural stiffness. The node connectivity of the columns and their area moments of inertia about the two horizontal axes are listed in Appendix I.

8.3.2.2.4 Dynamic properties

Table 8-1 lists the first two natural periods of the LS-DYNA and OpenSees models. The OpenSees mode shapes are plotted in Figure 8-9. The first translational mode is in the short direction (60 m, see Figure 8-1) of the ASB; the second translational mode is in the long direction. The natural periods compare sufficiently well for the purpose of the study, namely, to answer the three questions posed in Section 8.1. The OpenSees and LS-DYNA mode shapes are similar.

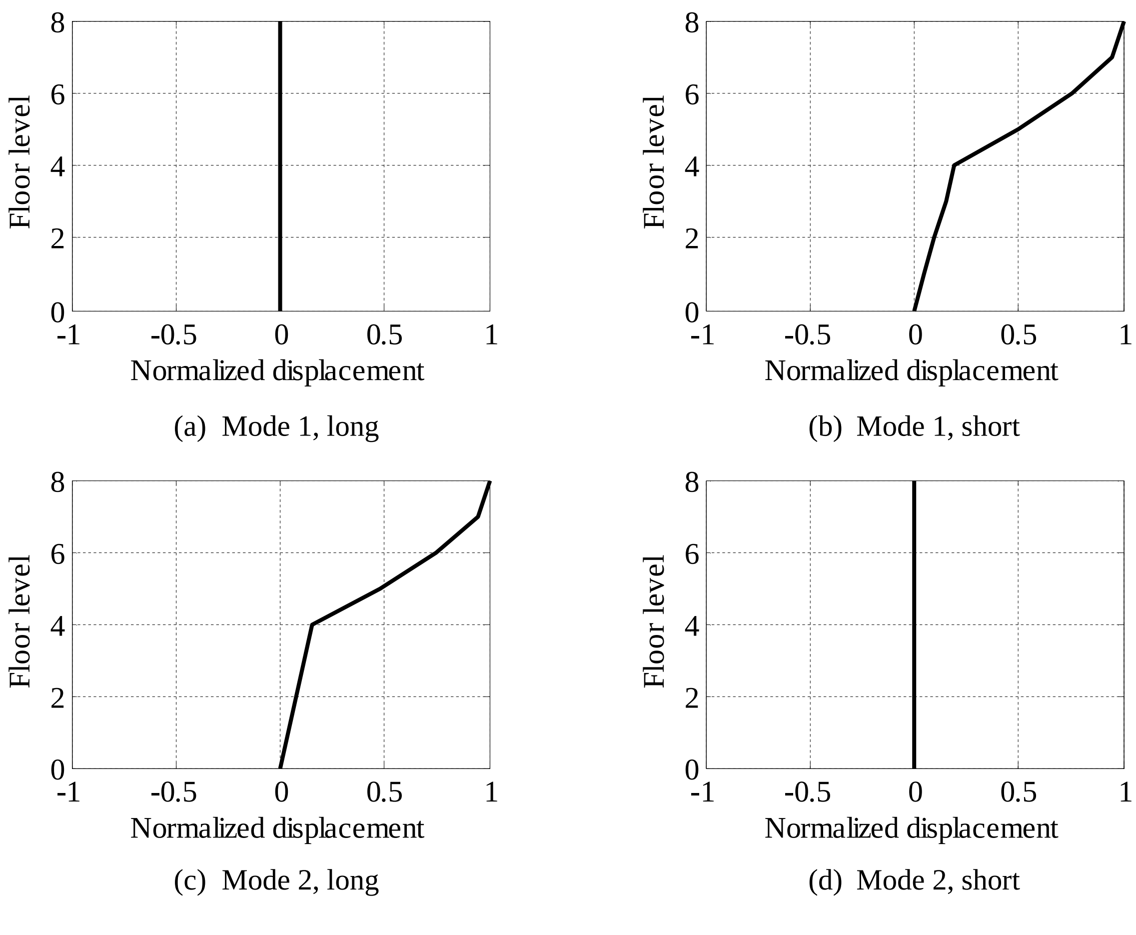

Figure 8-9: Mode shapes corresponding to the first two natural periods of vibration of the ASB

8.3.3 Containment internal structure (CIS)

The containment internal structure (CIS) is modeled in OpenSees as a vertical stick with three outrigger nodes (see Figure 8-3). This fixed-base CIS model is identical to that of Short *et al.* (2007). The coordinates of the nodes of the CIS model are listed in Table 8-4 and the masses lumped at the nodes are listed in Table 8-5. The directions X, Y and Z are shown in Figures 8-7 and 8-8. Node 109060 is at the center of the basemat in plan (see Figure 8-7 and Appendix I). Because the inertial effects of the vertical mass of the CIS accumulate at this node, the vertical inertial forces are unrealistically high. The CIS model responds dynamically in the vertical and horizontal directions, but only the horizontal dynamic response is studied in this chapter.

Table 8-4: Location of nodes in the CIS

Node	Coordinates (m)		
	X	Y	Z
109060	48.00	30.00	1.22
500	48.00	30.00	3.05
531	48.00	30.00	7.93
532	48.00	30.00	12.65
533	48.00	30.00	14.17
534	48.00	30.00	15.45
535	48.00	30.00	23.70
5351	44.95	26.95	23.70
536	48.00	30.00	29.41
537	48.00	30.00	29.41
538	48.00	30.00	34.29
5381	70.86	30.00	34.29
5382	44.95	26.95	34.29

The columns in the CIS are modeled using the *forceBeamColumn* element. The sections associated with the *forceBeamColumn* elements are *Elastic* and the properties of the section are listed in Table 8-6. The horizontal outriggers are modeled using the *rigidLink* element; the two nodes at the ends of the element are constrained to translate and rotate identically.

Table 8-5: Mass associated with the nodes in the CIS

Node	Mass in direction (in 100,000 kg)			Mass moment of inertia about axis (in 100,000 kg-m^2)		
	X	Y	Z	X	Y	Z
500	87	87	87	7701	7701	15402
531	135	135	135	19279	1859	21138
532	68	68	68	960	9219	10179
533	21	21	21	2508	2400	4908
534	47	47	47	4866	4327	9193
535	0	0	0	3825	3465	7290
5351	44	44	44	0	0	0
536	2	2	2	27	34	61
537	4	4	4	82	59	141
538	0	0	0	10	9	20
5381	0	0	0	0	0	0
5382	1	1	1	0	0	0

Table 8-6: Properties of elements connecting nodes in the CIS

Element	Connecting nodes		Properties of elastic section					
	Start	End	Cross sectional area (m^2)	Area moment of inertia about axes (in 10,000 m^4)			Ratio of shear area to cross sectional area	
				X	Y	Z	X	Y
500	109060	500	1409.8	11.0	9.6	20.5	0.55	0.61
501	500	531	1409.8	10.7	9.6	20.3	0.55	0.61
502	531	532	625.4	3.9	2.9	6.8	0.44	0.44
503	532	533	738.0	5.8	5.1	11.0	0.50	0.56
504	533	534	479.4	4.0	2.5	6.5	0.52	0.59
505	534	535	158.4	0.7	0.5	1.2	0.24	0.36
506	535	536	30.3	0.0	0.0	0.0	0.21	0.04
507	535	537	45.0	0.0	0.0	0.0	0.13	0.19
508	537	538	15.2	0.0	0.0	0.0	0.10	0.18

The natural periods of the CIS associated with the motion in the horizontal directions are listed in Table 8-7. These periods compare well with the values reported in Short *et al.* (2007).

8.4 Description of the Seismically Isolated Models

Two models of a seismically isolated nuclear power plant are analyzed to compute isolation-system displacement and horizontal floor spectra for nodes at different locations in the CIS. Table 8-8 maps the computed response quantities to the models. Note that Model 2 is subjected to horizontal components of ground motion only.

Table 8-7: Natural period of containment internal structure

	Period (s)	
Mode	Present study	Short *et al.* (2007)
1	0.082	0.083
2	0.078	0.075
3	0.061	0.067
4	0.053	0.057
5	0.048	0.050
6	0.042	0.035

Two percent Rayleigh damping is assigned at periods of 0.05 s and 3 s (the sliding period for this study). The displacement at which sliding commences is set equal to 1 mm.

Table 8-8: Response quantities estimated using the two models

Model	**Description**	**Response quantity**		
		Isolation-system displacement	Acceleration of basemat	Acceleration of nodes of CIS
1	Isolated ASB-CIS	✓	✓	✓
2	Macro model	✓	✓	×

8.4.1 Model 1: seismically isolated ASB and CIS

The ASB model comprises 187 nodes at the basemat level; the base of the CIS is represented by one node. One node is common to both the ASB and the CIS (109060). One hundred and eight seven single FP bearings are used to isolate the ASB and CIS. Each of the bottommost 187 nodes (height = 1.2 m; see Table 8-2 and Figure 8-7(a)) of the common basemat represents the slider of an FP bearing. One hundred and eighty seven additional nodes, each of which represents the sliding surface of an FP bearing, are introduced at the plan locations of the bottommost 187 nodes of the ASB. The nodes representing the sliding surface are restrained from translation and rotation; the nodes representing the slider are free to translate but restrained from rotation (a boundary condition enforced by the stiff basemat).

Gravity and inertial forces associated with the entire mass of the CIS are transferred at node 109060, which represents the slider of the FP bearing at the geometrical center of the basemat. The axial force on this bearing, and consequently the shear force and horizontal floor spectral ordinates, would be unrealistically high. The gravity force due to the CIS is therefore distributed equally among all 99 nodes of Segment 2 of the ASB (see Figure 8-6) representing sliders of FP bearings. The vertical inertial mass of the CIS is ignored in this study.

Model 1 is subjected to a) three components of ground motion, and b) two horizontal components of ground motions, to help answer the questions posed in Section 8.1.

8.4.1.1 Seismic isolation system

The seismic isolation system comprises 187 single FP bearings with a sliding period of 3 s, reference coefficient of friction of 0.06, static axial pressure of 50 MPa and friction at the sliding surface defined using the five friction models of Table 7-2. The center-to-center distance between adjacent bearings is 6 m. The bearings are placed at the nodes shown in Figure 8-7(a). The static axial load on each FP bearing in Segments 1 and 3 (see Figure 8-6) is 7,100 kN (32,000 tons distributed between 44 bearings; see Table 8-2). The static axial load on the bearings in Segment 2 is 11,000 kN (75,000 tons from the ASB and 41,000 tons from the CIS, distributed between 99 bearings). The radius of the contact area for each of the 44 FP bearings in Segments 1 and 3 is 0.21 m, and 0.26 m for each of the 99 FP bearings in Segment 2.

8.4.2 Model 2: macro model (single FP bearing)

Model 2 is a macro-model of the NPP comprising a single FP bearing and a lumped mass to describe the superstructure. A sliding period of 3 s, reference coefficient of friction of 0.06, static axial pressure of 50 MPa and friction at the sliding surface defined using the five models of Table 7-2 are considered. The static axial load on the bearing is the weighted average[1] of the static axial loads on the 187 FP bearings of Model 1: 9,200 kN. The radius of the contact area at the sliding surface is 0.24 m. The inertial masses associated with motion in the three translational directions are equal to the gravity load.

8.5 Ground Motions

A set of thirty three-component ground motions consistent with 10,000-year hazard at Diablo Canyon site is developed in Chapter 7. Sets of ground motions with four amplitude scale factors are considered in this chapter: 0.6, 1.0, 1.5 and 2.0, which approximately represent 100,000-year shaking at Vogtle, 10,000-year shaking at Diablo Canyon, 150% of 10,000-year shaking at Diablo Canyon, and 100,000-year shaking at Diablo Canyon, respectively (see Chapter 7).

[1] The static axial force on each of the 44 FP bearings of the seismically isolated ASB-CIS (Section 8.4.1) in Segments 1 and 3 is 7,100 kN. The force on each of the 99 bearings in Segment 2 of this model is 11,000 kN.

8.6 Results

This section presents results of the response-history analyses performed on Models 1 and 2. Distributions of peak isolation-system displacement and floor spectral accelerations are presented and studied.

8.6.1 Distribution of peak displacements

Figure 8-10(a) presents the distributions of displacements of the center of the isolation system for Models 1 and 2, with friction at the sliding surface of FP bearings described using the Coulomb model, subjected to the set of 30 ground motions amplitude scaled by 0.6. Model 1 is subjected to ground motions with and without the vertical component. Expectedly, the distributions of the isolation-system displacements obtained using the two models are virtually identical with less than a 2 mm (5 mm) difference in the median (99^{th} percentile) displacement. Including the vertical component of the ground motion in the response-history analysis of Model 1 alters the median (99^{th} percentile) isolation system displacement estimate by 0.1 mm (1 mm).

Figures 8-10(b) through 8-10(e) present results for Model 1 and Model 2, with friction at the sliding surface described using the pressure-dependent, temperature-dependent, velocity-dependent, and *p-T-v* model, respectively. The distributions of the isolation-system displacement computed using the two NPP models are virtually identical. Figures 8-11, 8-12 and 8-13 present results for ground motions amplitude scaled by 1.0, 1.5 and 2.0, respectively. The distributions of isolation-system displacement are similar, for a given intensity level and friction model. Including the vertical component of the ground motion in the response-history analysis of Model 1 does not change the distributions of horizontal displacement.

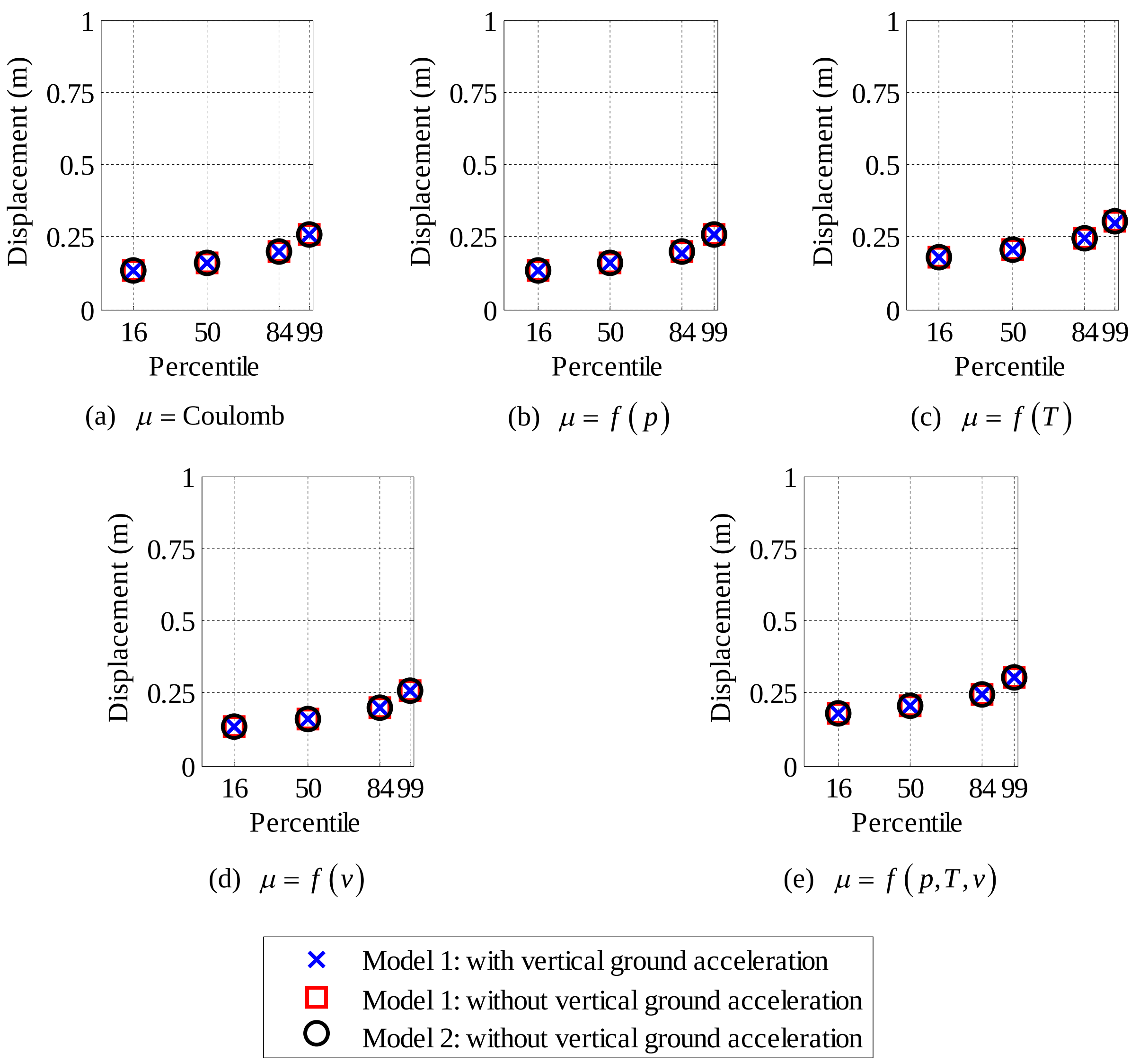

Figure 8-10: Distributions of isolation-system displacement for the three models subjected to the set of ground motions amplitude scaled by 0.6

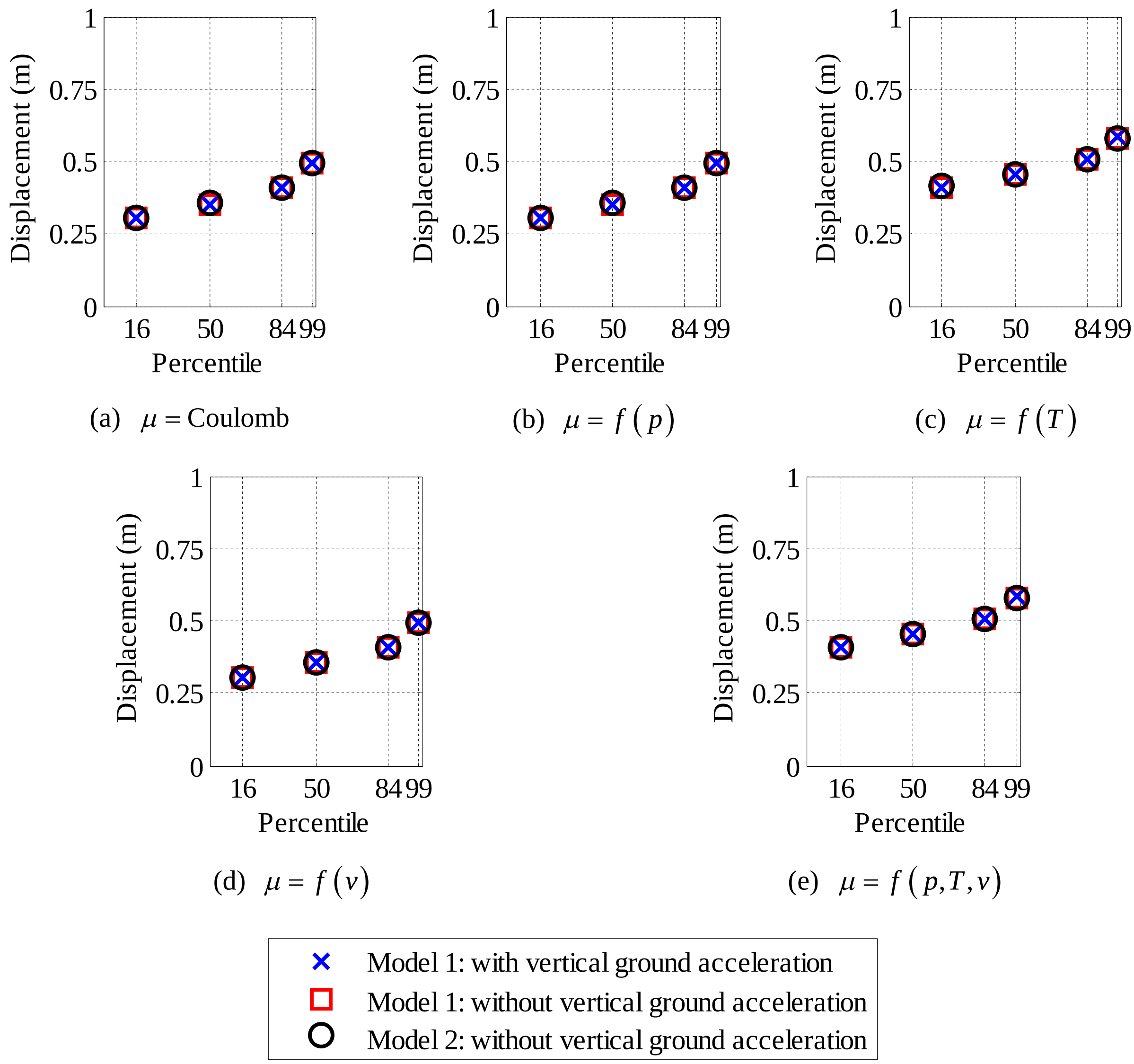

Figure 8-11: Distributions of isolation-system displacement for the three models subjected to the set of ground motions amplitude scaled by 1.0

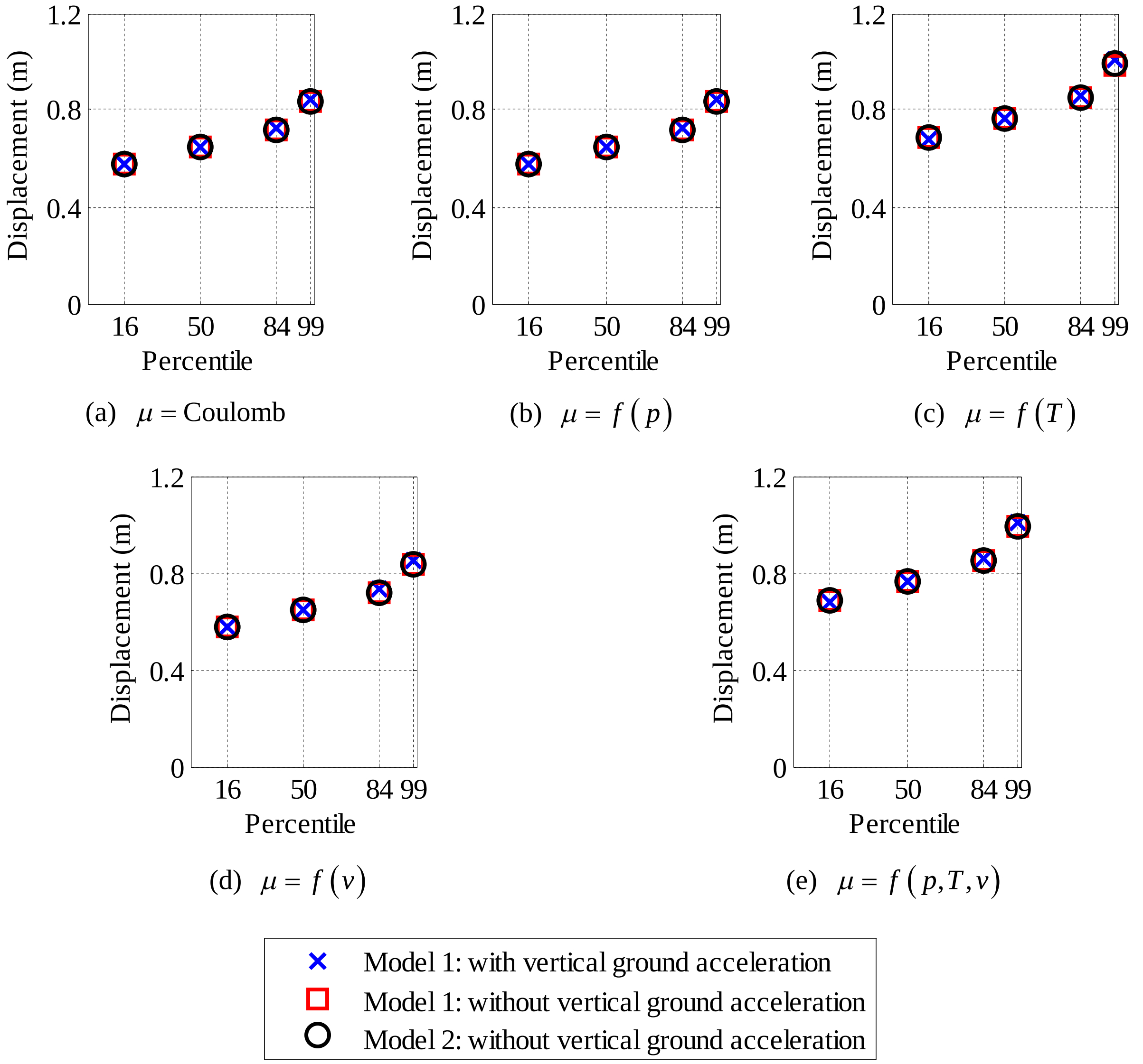

Figure 8-12: Distributions of isolation-system displacement for the three models subjected to the set of ground motions amplitude scaled by 1.5

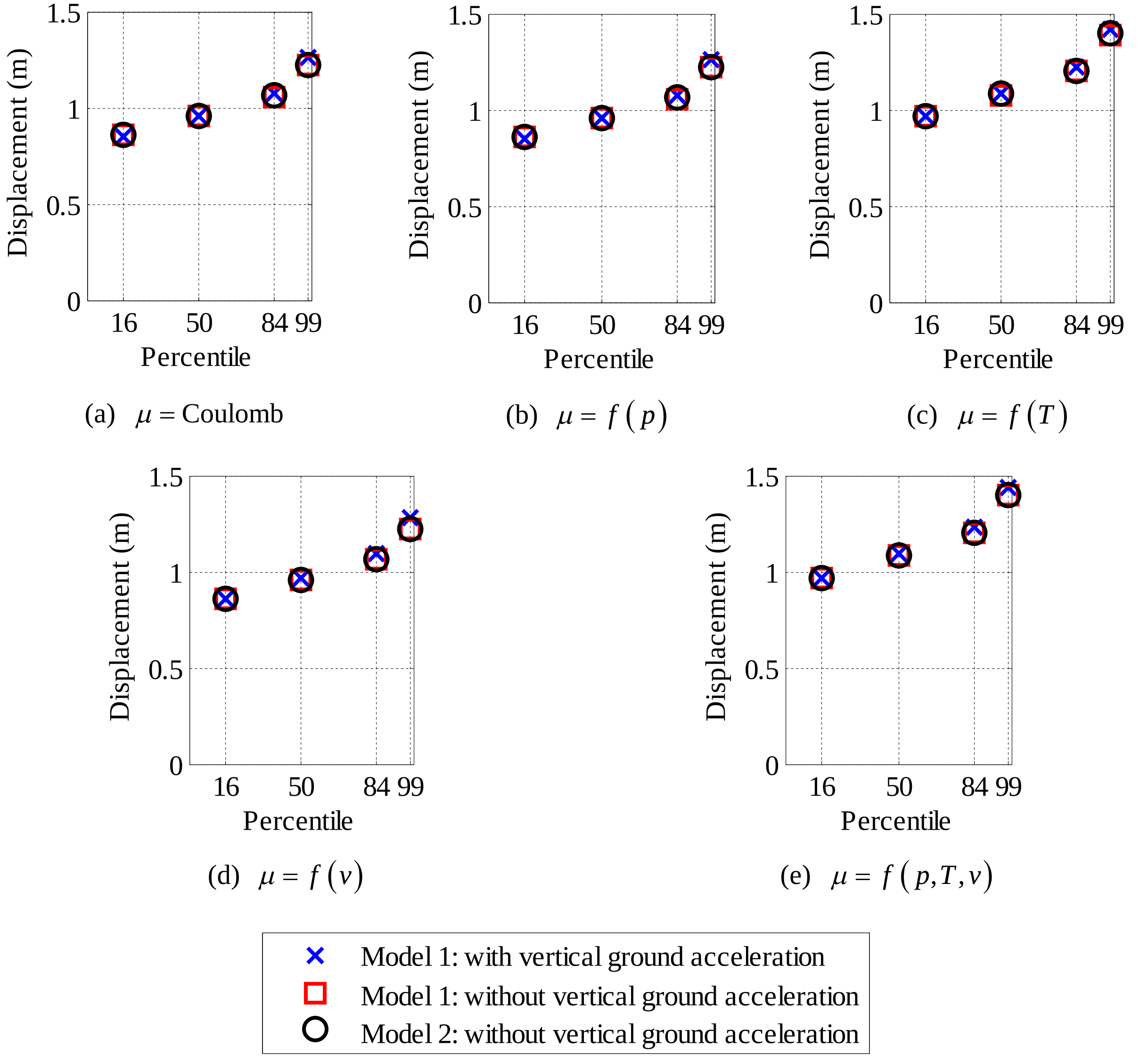

Figure 8-13: Distributions of isolation-system displacement for the three models subjected to the set of ground motions amplitude scaled by 2.0

8.6.1.1 Influence of definition of friction at the sliding surface

Large changes in the coefficient of friction are observed during the course of an analysis for bearings at different locations, when friction at the sliding surface is defined using the pressure-dependent model. Consider the seismically isolated ASB-CIS model (Model 1) with a reference coefficient of friction of 0.06 and friction at the sliding surface described using the pressure-dependent friction model subjected to the two horizontal and vertical components of ground motion 1 (GM1) with an amplitude scale factor of 1.0. The coefficient of friction at the sliding surface of the bearing at a corner of the isolation system varies between 0.046 and 0.082[1] during the course of shaking, and that at the center of the isolation system varies between 0.052 and 0.071. When the isolated ASB-CIS model is subjected only to the horizontal components of GM1, the coefficient varies between 0.051 and 0.069 for the bearing at the corner, and between 0.060 and 0.060 for the bearing at the center of the isolation system. These changes[2] in the coefficient of friction do not alter the distribution of isolation-system displacement[3] relative to that calculated ignoring the pressure-dependence of friction.

The calculated displacements are not materially affected by the velocity dependence of the coefficient of friction.

Inclusion of temperature dependency in the friction model significantly changes the estimate of isolation system displacement. The influence of heating on displacements, which is a function of shaking intensity, static axial pressure and reference coefficient of friction, is discussed in Chapter 7.

8.6.2 Floor spectra

This section presents floor spectra at the nodes 109060 (basemat level), 532 (height of 13 m), 5351 (height of 24 m) and 5382 (height of 34 m) of the CIS (see Table 8-4) computed using the

---

[1] As discussed in Chapter 3, the coefficient of friction increases with a decrease in axial pressure. The axial pressure on a bearing at a given location in the isolation system changes over the course of earthquake shaking due to the vertical component of ground motion and the response of the supported superstructure to the three components of ground motion.

[2] The average coefficient of friction for a bearing is 0.06 over the course of shaking, irrespective of the location.

[3] The median (99th percentile) displacements for Coulomb and pressure-dependent friction models differ by less than 0.5 mm.

two NPP models with friction at the sliding surface of the FP bearings defined using the five models of Table 7-2 subjected to the set of 30 ground motions amplitude scaled by 0.6, 1.0, 1.5 and 2.0.

Figure 8-14(a) presents the median floor spectrum in the X direction at node 109060 obtained using Model 1 with friction at the sliding surface of the FP bearings described using Coulomb model subjected to the two horizontal and vertical components of the 30 ground motions amplitude scaled by 0.6. The results for Model 1 subjected to the 30 sets of three-components ground motions are referred to as *benchmark* results in this section. Also plotted in the figure are the floor spectra for Models 1 and 2 subjected to only two horizontal components of the ground motions. The floor spectral ordinates at 0.01 s at node 109060 (basemat) indicate the peak floor acceleration and the shear force generated in the isolated superstructure. These ordinates are smaller than the *benchmark* results by 7% and 20% for the two models subjected to the horizontal components of the ground motions, respectively. These differences are 12% and 44% at 0.05 s, 3% and 18% at 0.1 s, and 1% and 3% at 1 s. Three components of motion are needed to generate horizontal floor spectra.

Figures 8-14(d) through 8-14(l) present the 50th, 90th and 99th percentile floor response spectra for the nodes 532, 5351 and 5382 of the CIS computed using Model 1. The general observations are similar to those for node 109060, namely, ignoring the vertical component of the ground is unconservative. The floor spectra for the velocity-dependent, temperature-dependent, pressure-dependent and *p-T-v* friction models are presented in Figures 8-15 through 8-18, respectively. Figures 8-19 through 8-23 present floor spectra in the X direction for the NPP models with the five friction models subjected to the 30 ground motions amplitude scaled by 1.0. Figures 8-24 through 8-33 present the floor spectra for amplitude scale factors of 1.5 and 2.0. The spectral ordinates in the Y direction are similar to those in the X direction and are not reported here. The results presented in Figures 8-14 through 8-33 can be summarized as follows:

i. The horizontal spectral ordinates computed using Model 1 subjected to the two horizontal components of ground motions are considerably smaller than those obtained for the model subjected to three components of ground motions.

ii. The differences between the *benchmark* horizontal ordinates and those calculated for the two models subjected to only the two horizontal components of ground motions

    a. increase substantially with increase in shaking intensity at periods 0.01 s, 0.05 s and 0.1 s (see Figures 8-34 through 8-36).

    b. are small at 1 s irrespective of shaking intensity (see Figures 8-34 through 8-36).

    c. are greater at the higher percentiles.

    d. are generally greater for nodes at higher elevations inside containment.

iii. The choice of friction model does not considerably influence the floor spectral ordinates (see Figures 8-37 and 8-38).

The following recommendations are made for modeling, analysis and design of a nuclear power plant isolated with single concave FP bearings:

i. The friction model for the FP isolator must account for heating effects.

ii. Isolation-system horizontal displacement can be estimated for preliminary analysis and design using a macro model.

iii. A complete three-dimensional model will be required for final analysis and design to account for torsion and rocking, to accommodate soil-structure-interaction analysis, to compute member forces and generate floor spectra.

iv. Vertical ground motion must be included to generate floor spectra.

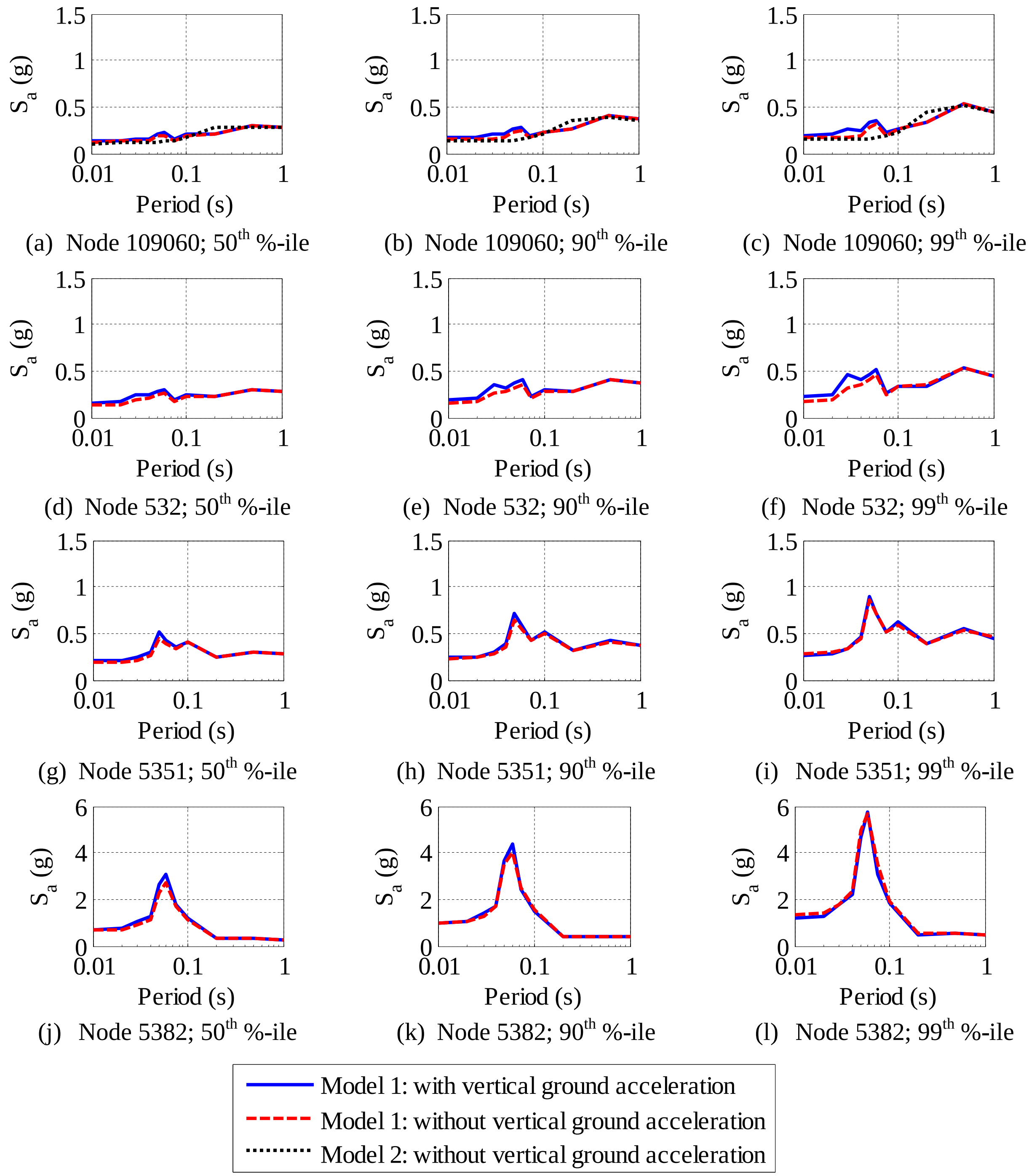

Figure 8-14: Floor spectra in the X direction at different nodes of the CIS computed using the two NPP models with friction at the sliding surface described using the Coulomb model subjected to the set of 30 ground motions amplitude scaled by 0.6

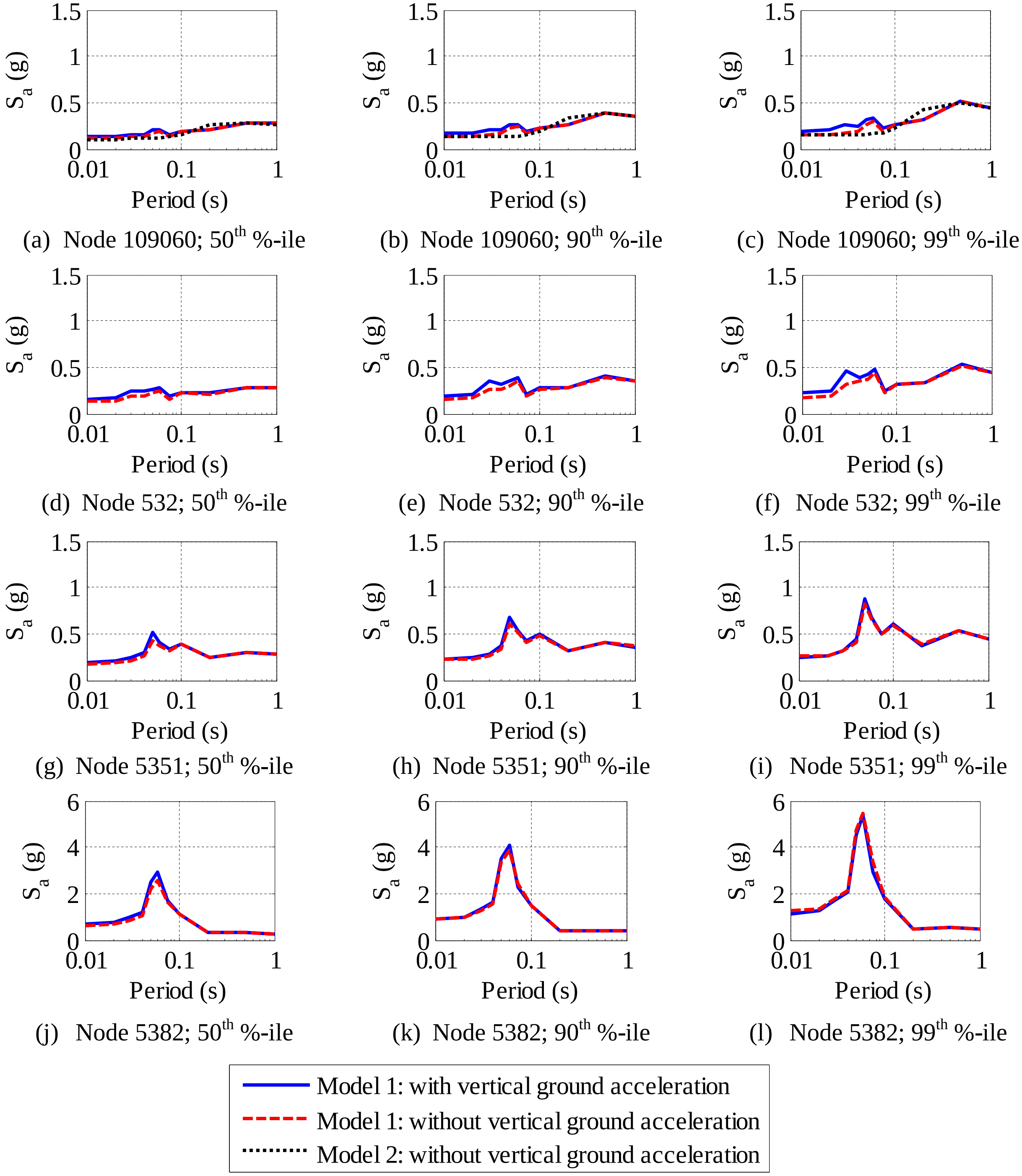

Figure 8-15: Floor spectra in the X direction at different nodes of the CIS computed using the two NPP models with friction at the sliding surface described using the velocity-dependent model subjected to the set of 30 ground motions amplitude scaled by 0.6

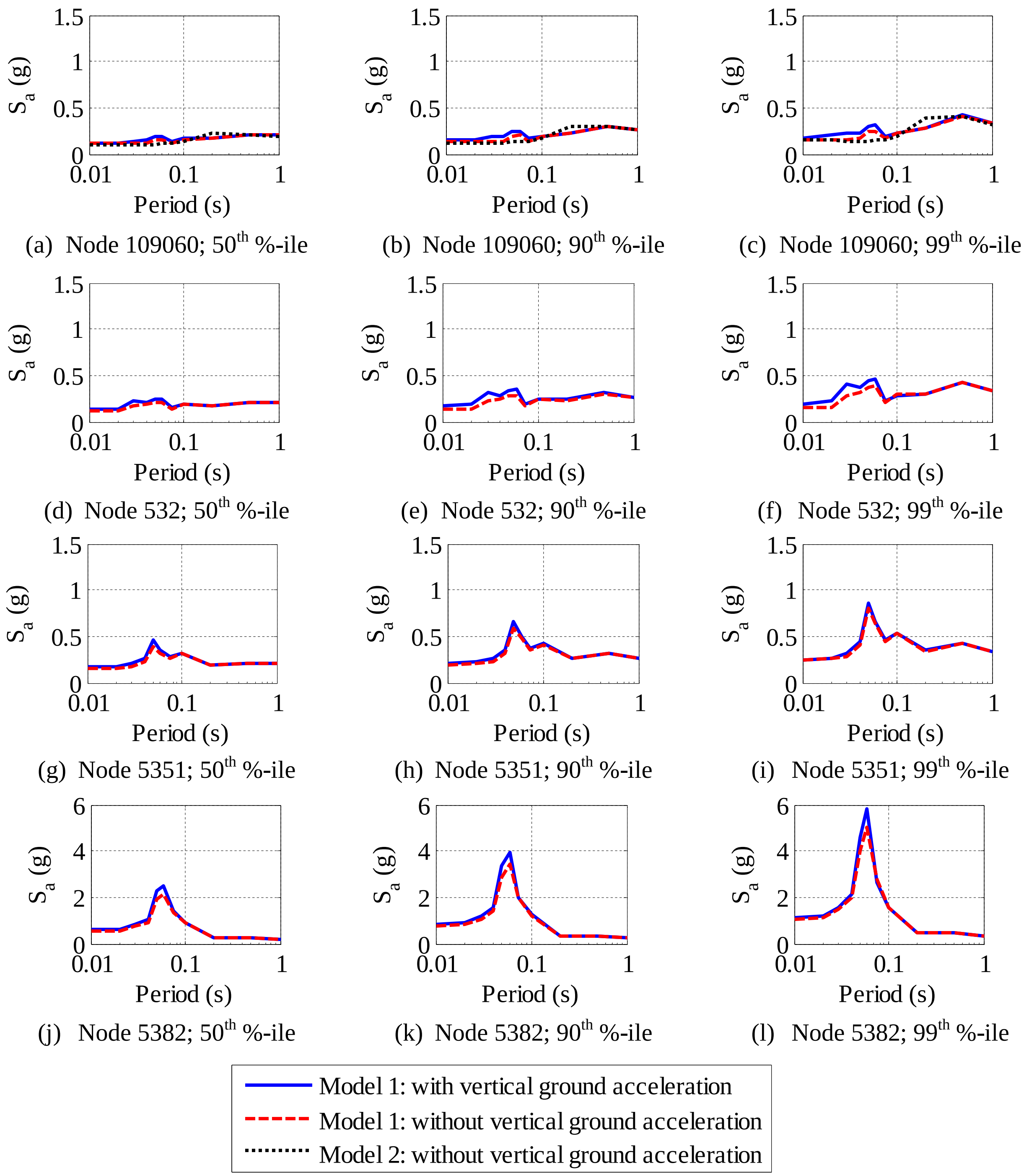

Figure 8-16: Floor spectra in the X direction at different nodes of the CIS computed using the two NPP models with friction at the sliding surface described using the temperature-dependent model subjected to the set of 30 ground motions amplitude scaled by 0.6

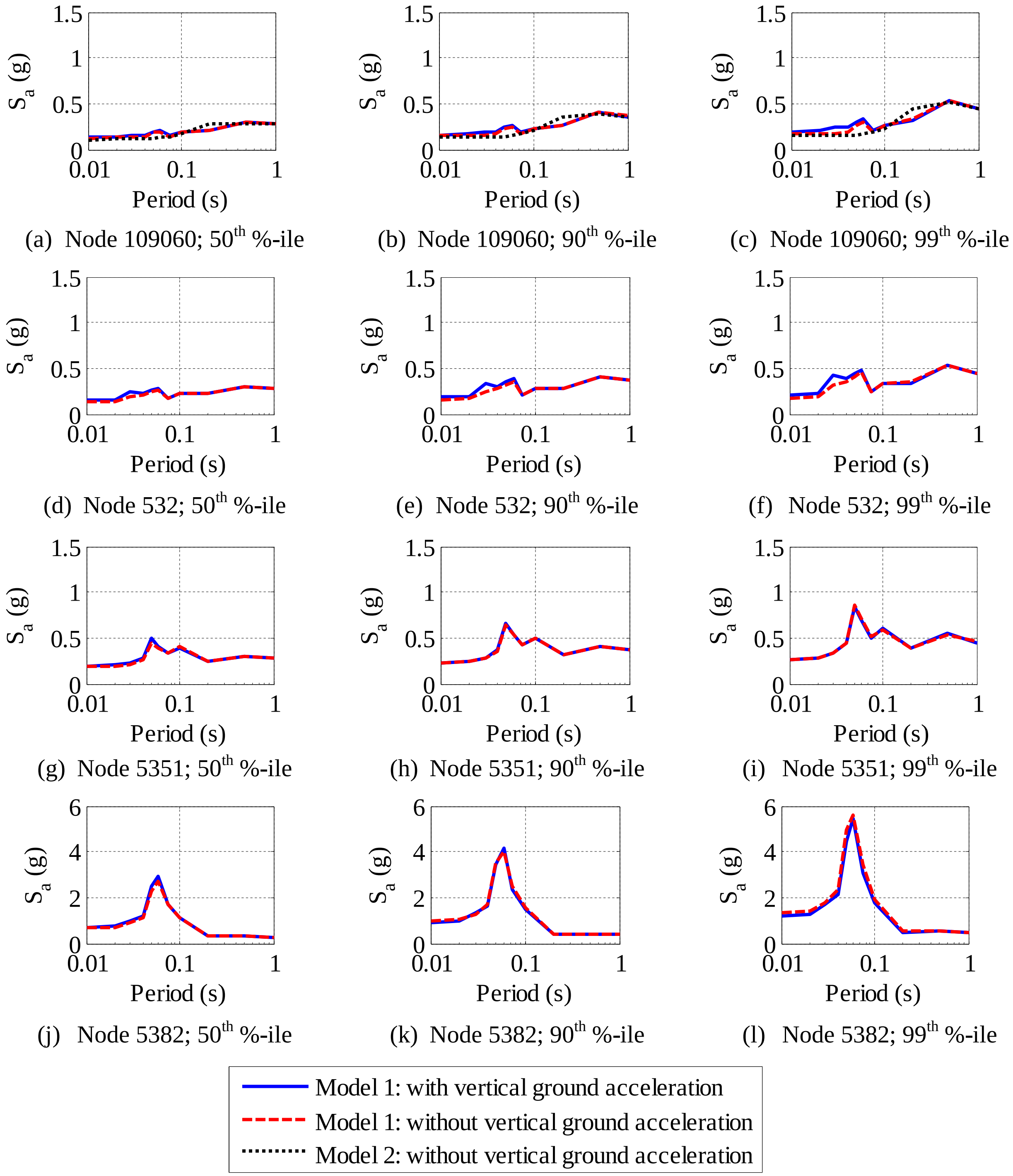

Figure 8-17: Floor spectra in the X direction at different nodes of the CIS computed using the two NPP models with friction at the sliding surface described using the pressure-dependent model subjected to the set of 30 ground motions with amplitude scaling factor of 0.6

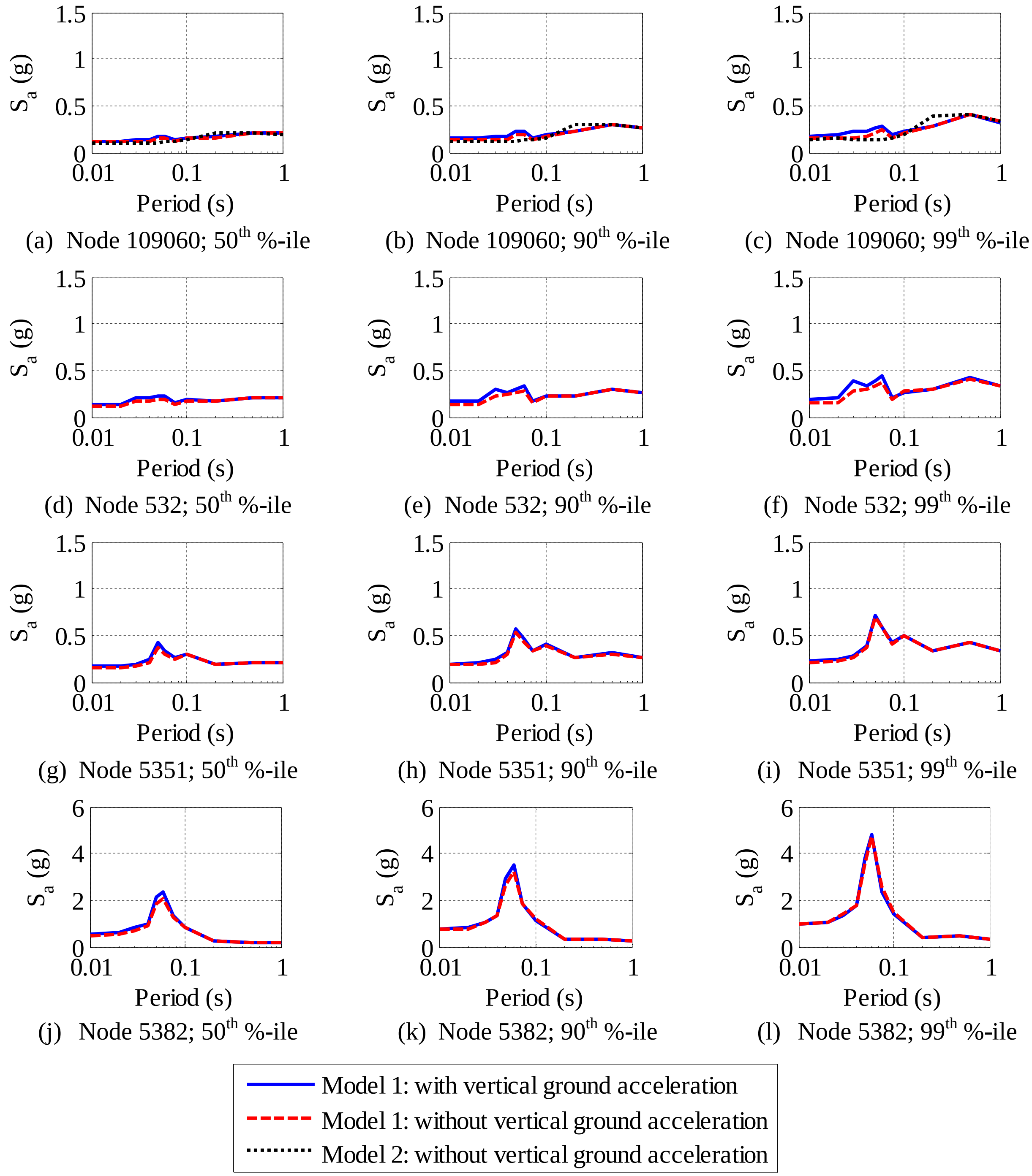

Figure 8-18: Floor spectra in the X direction at different nodes of the CIS computed using the two NPP models with friction at the sliding surface described using the *p-T-v* model subjected to the set of 30 ground motions with amplitude scaling factor of 0.6

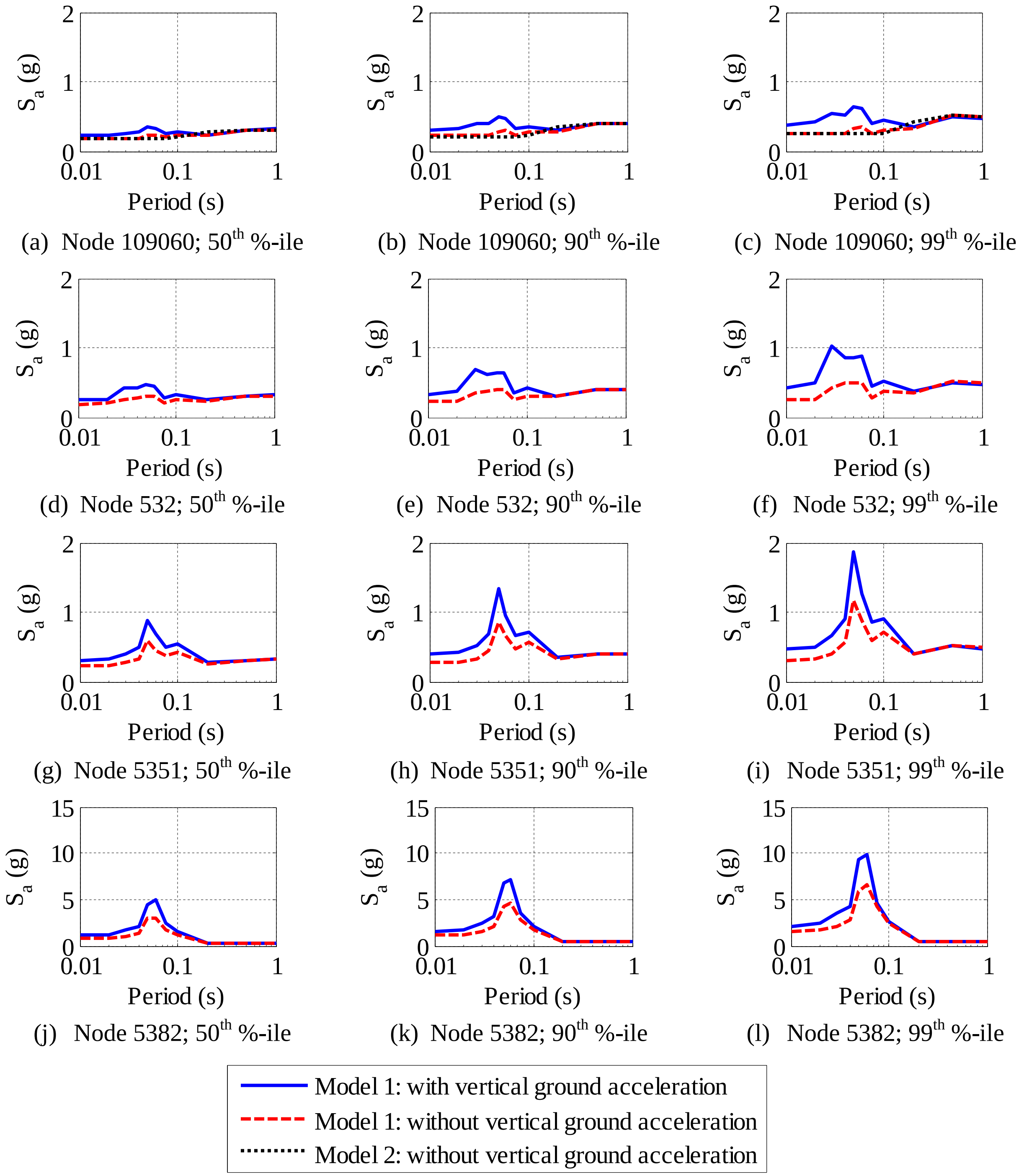

(a) Node 109060; 50th %-ile
(b) Node 109060; 90th %-ile
(c) Node 109060; 99th %-ile
(d) Node 532; 50th %-ile
(e) Node 532; 90th %-ile
(f) Node 532; 99th %-ile
(g) Node 5351; 50th %-ile
(h) Node 5351; 90th %-ile
(i) Node 5351; 99th %-ile
(j) Node 5382; 50th %-ile
(k) Node 5382; 90th %-ile
(l) Node 5382; 99th %-ile

Figure 8-19: Floor spectra in the X direction at different nodes of the CIS computed using the two NPP models with friction at the sliding surface described using the Coulomb model subjected to the set of 30 ground motions amplitude scaled by 1.0

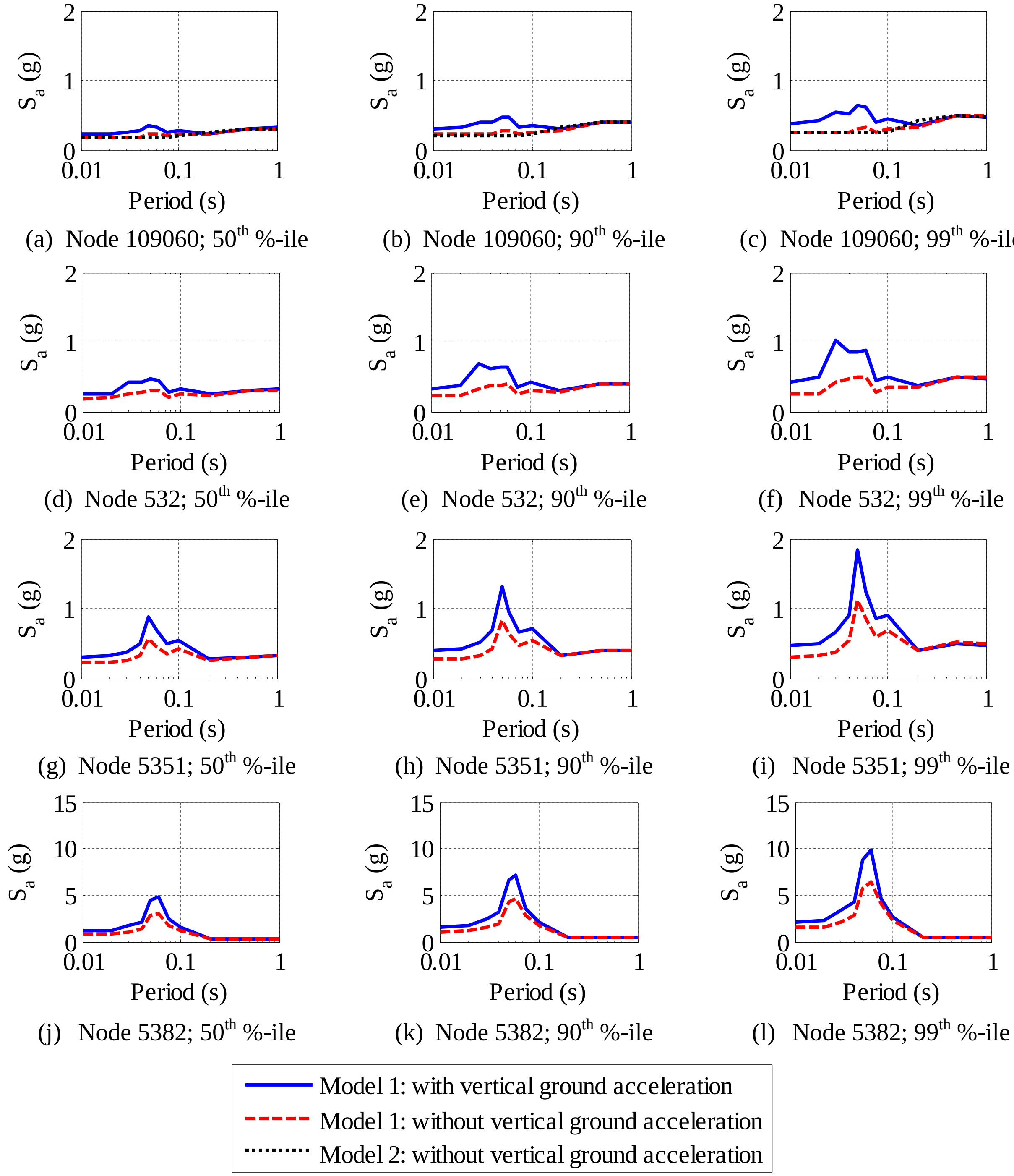

Figure 8-20: Floor spectra in the X direction at different nodes of the CIS computed using the two NPP models with friction at the sliding surface described using the velocity-dependent model subjected to the set of 30 ground motions amplitude scaled by 1.0

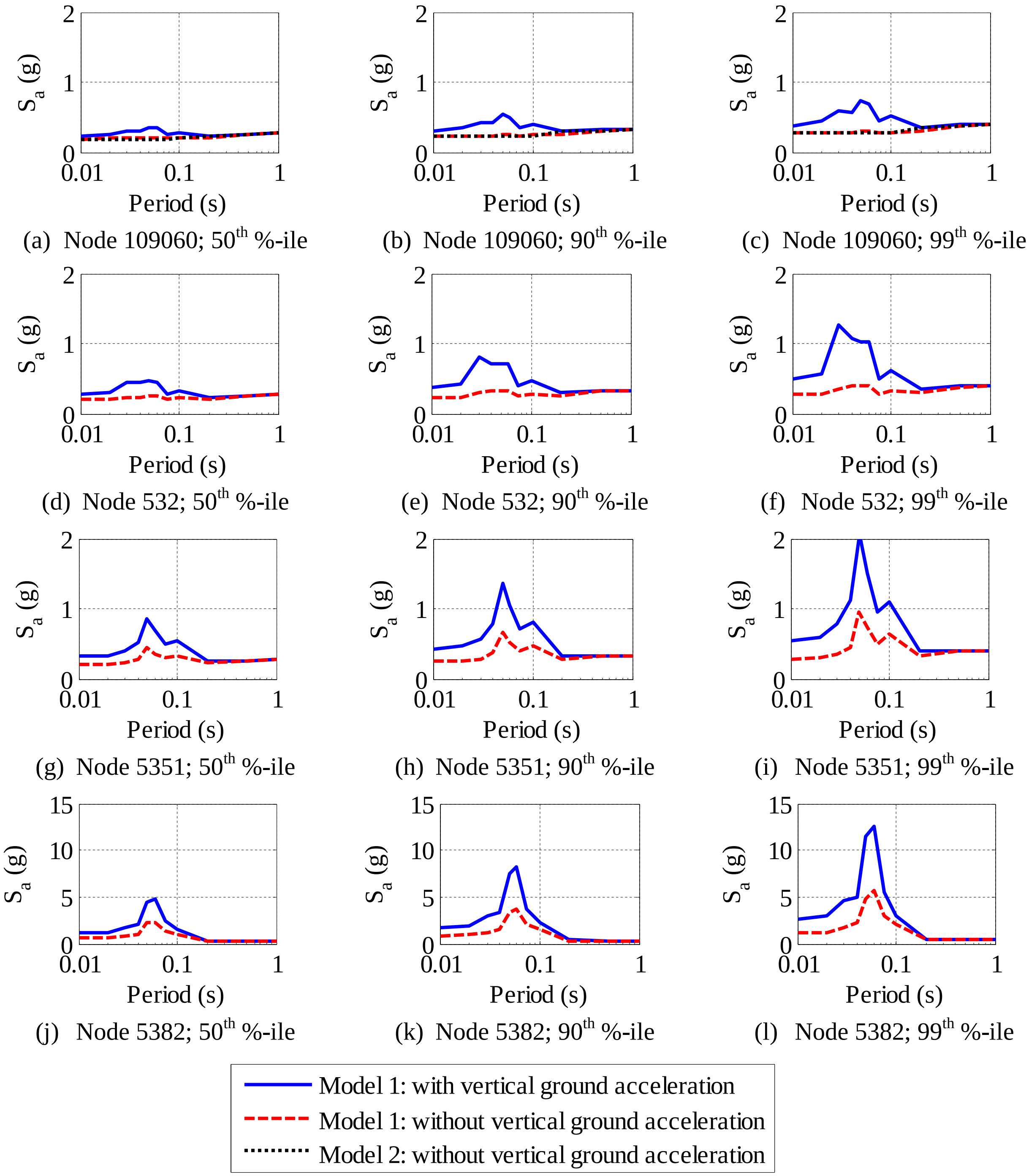

Figure 8-21: Floor spectra in the X direction at different nodes of the CIS computed using the two NPP models with friction at the sliding surface described using the temperature-dependent model subjected to the set of 30 ground motions amplitude scaled by 1.0

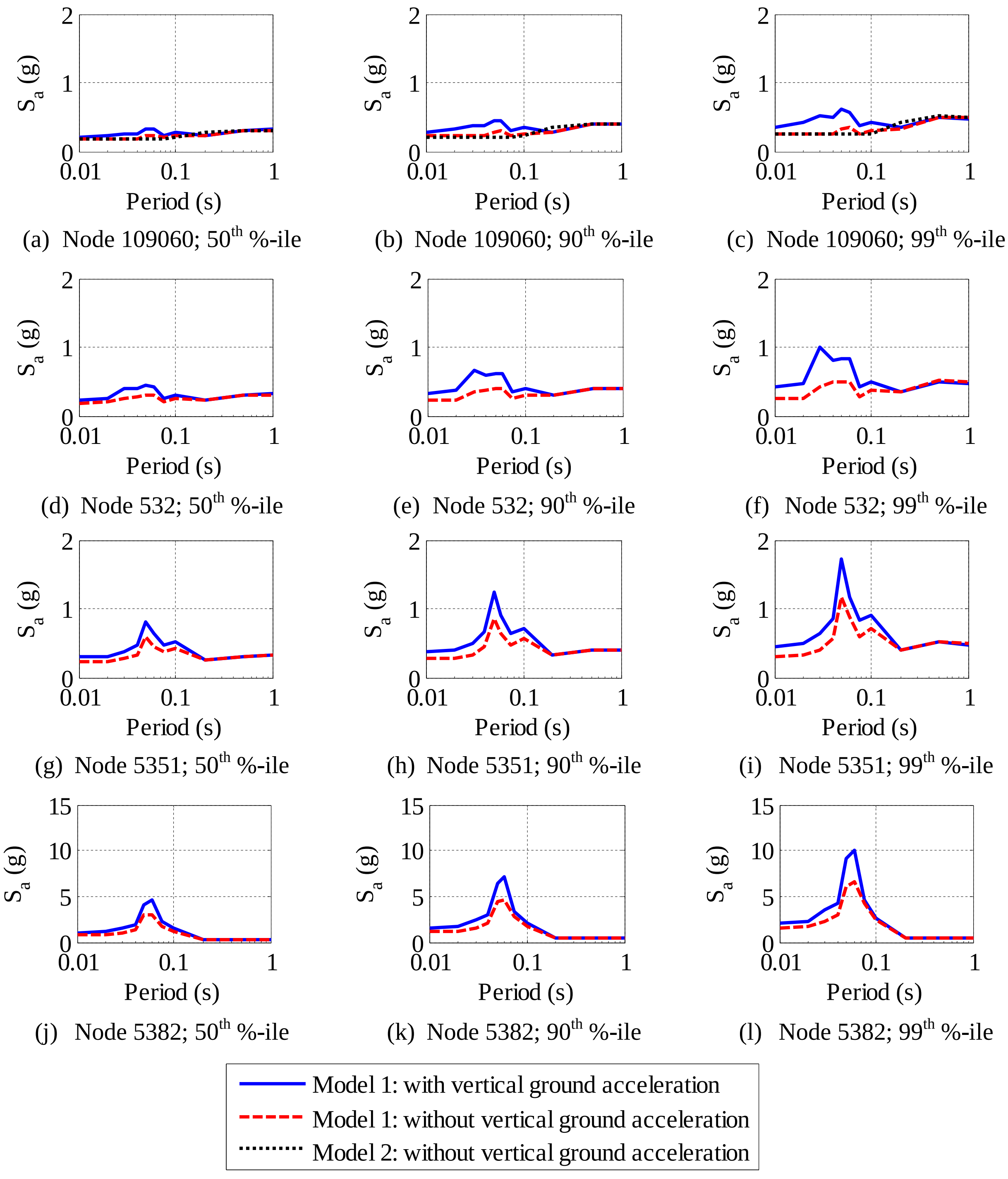

Figure 8-22: Floor spectra in the X direction at different nodes of the CIS computed using the two NPP models with friction at the sliding surface described using the pressure-dependent model subjected to the set of 30 ground motions amplitude scaled by 1.0

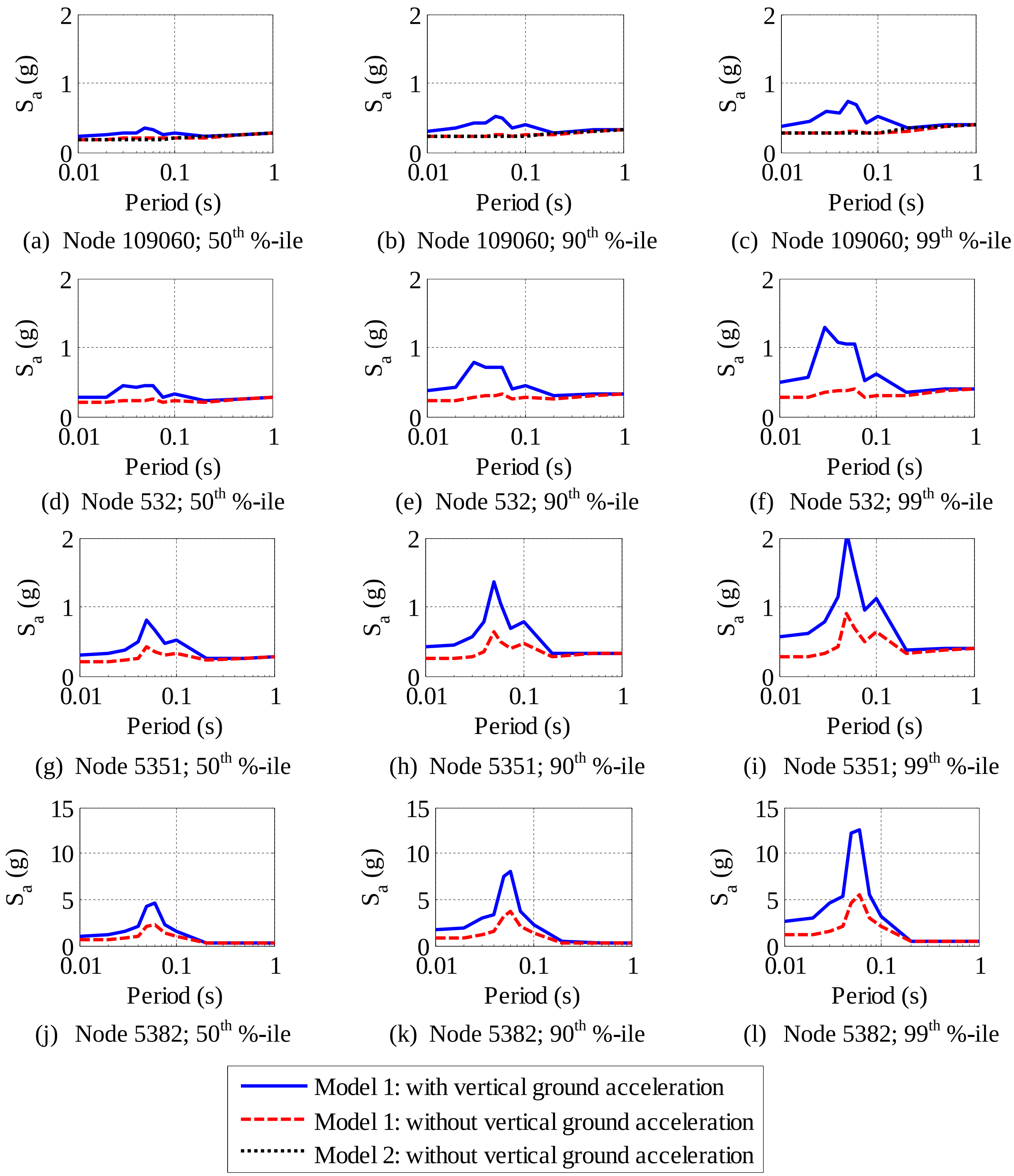

Figure 8-23: Floor spectra in the X direction at different nodes of the CIS computed using the two NPP models with friction at the sliding surface described using the *p-T-v* model subjected to the set of 30 ground motions amplitude scaled by 1.0

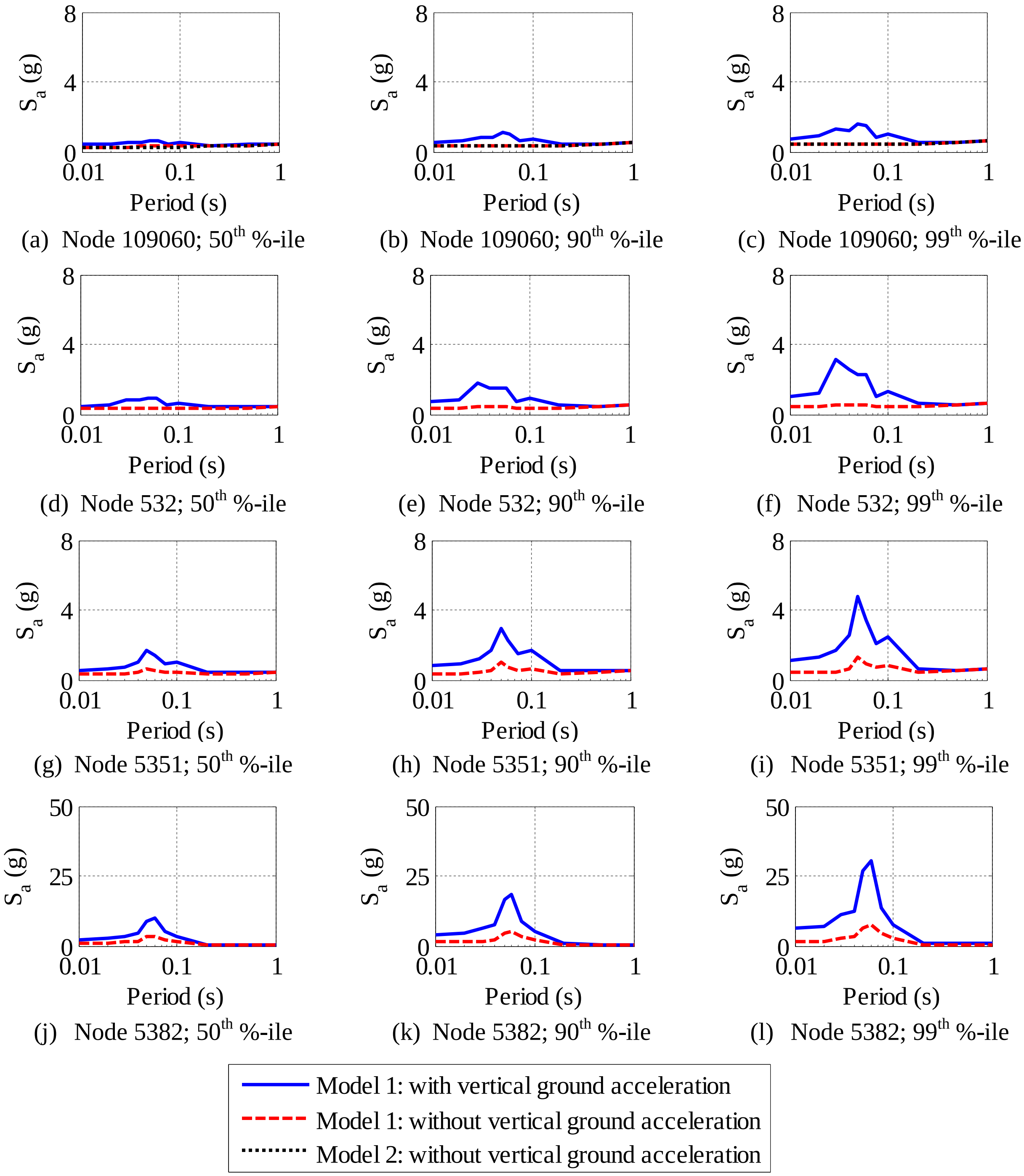

Figure 8-24: Floor spectra in the X direction at different nodes of the CIS computed using the two NPP models with friction at the sliding surface described using the Coulomb model subjected to the set of 30 ground motions amplitude scaled by 1.5

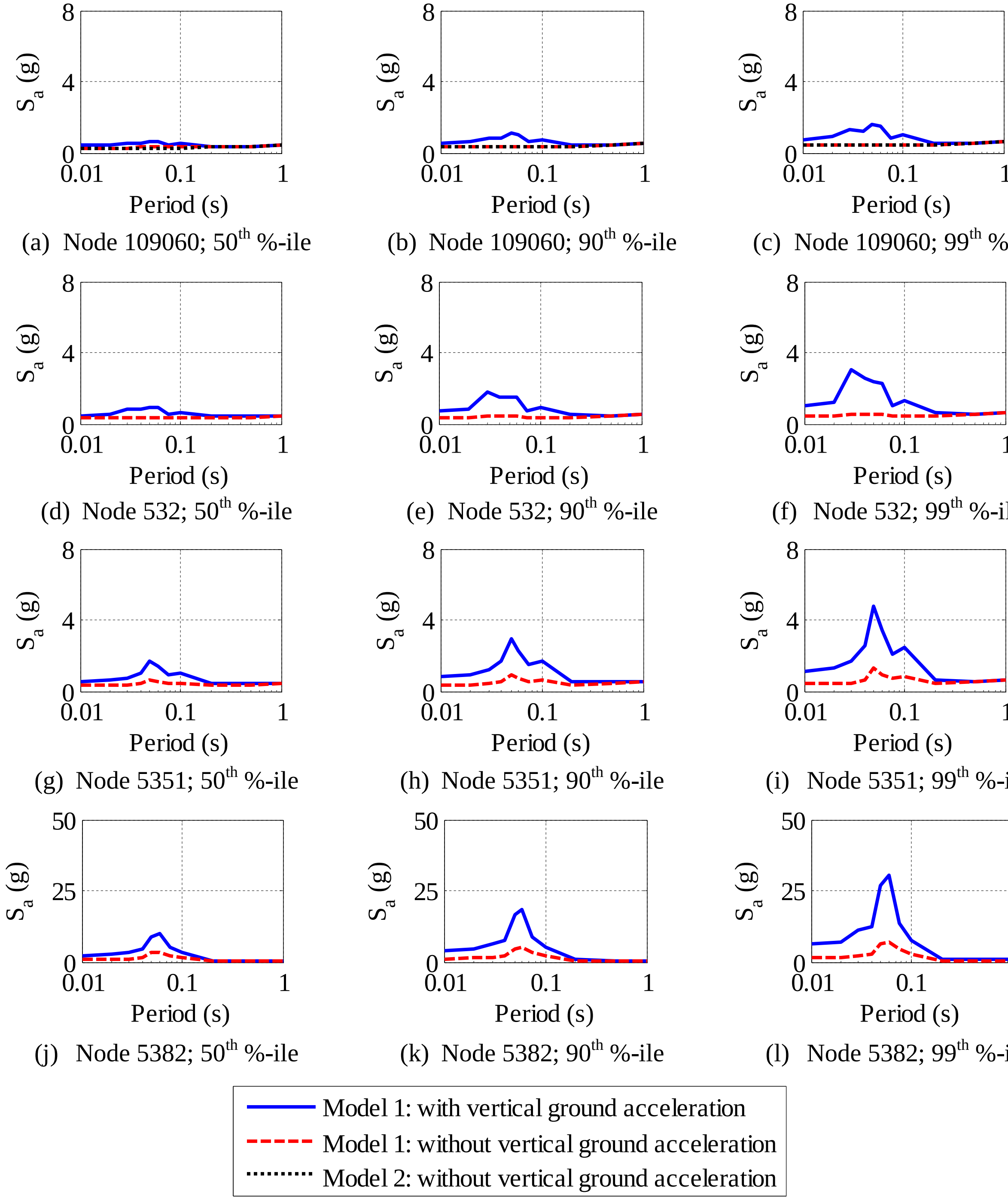

Figure 8-25: Floor spectra in the X direction at different nodes of the CIS computed using the two NPP models with friction at the sliding surface described using the velocity-dependent model subjected to the set of 30 ground motions amplitude scaled by 1.5

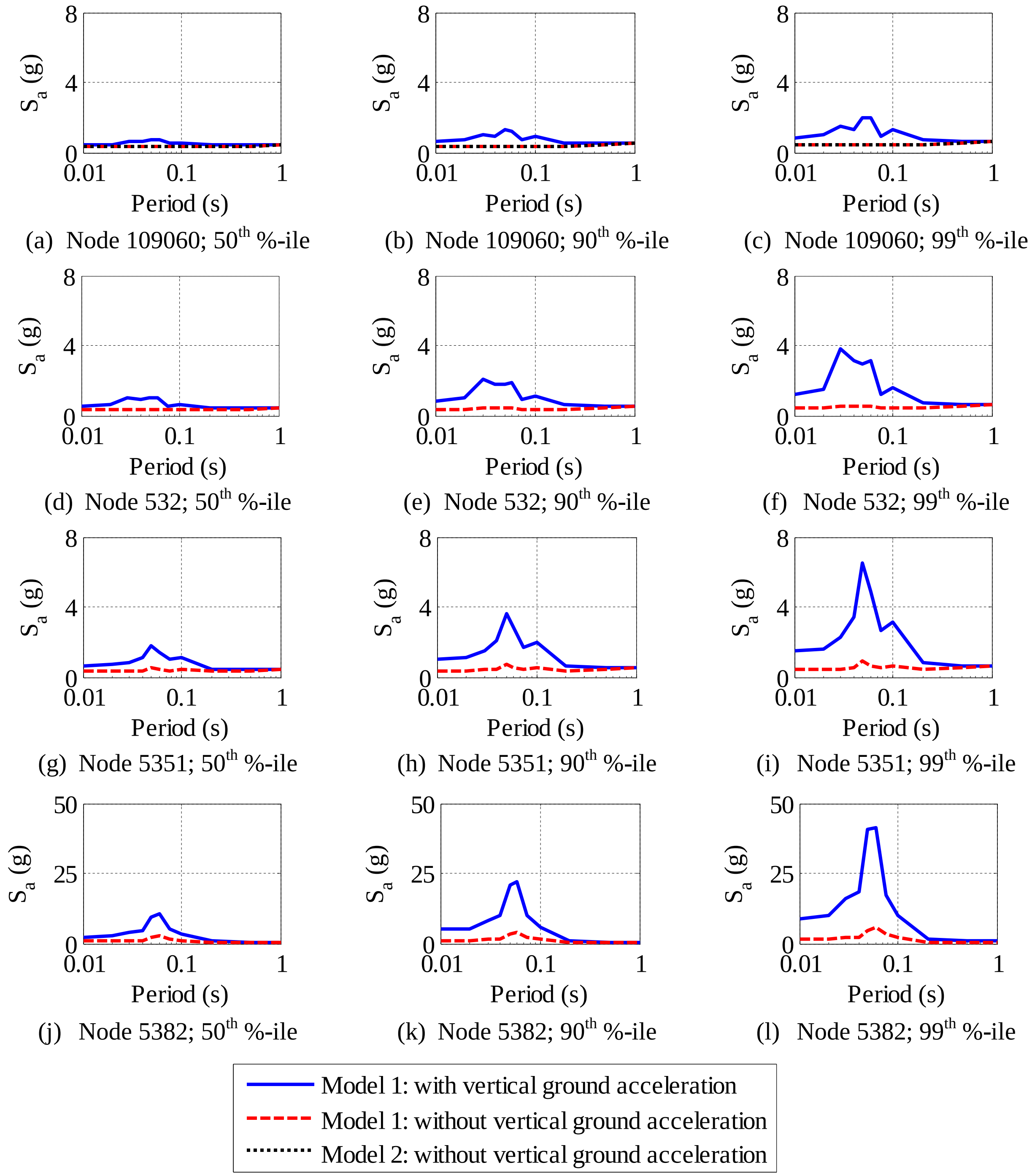

Figure 8-26: Floor spectra in the X direction at different nodes of the CIS computed using the two NPP models with friction at the sliding surface described using the temperature-dependent model subjected to the set of 30 ground motions amplitude scaled by 1.5

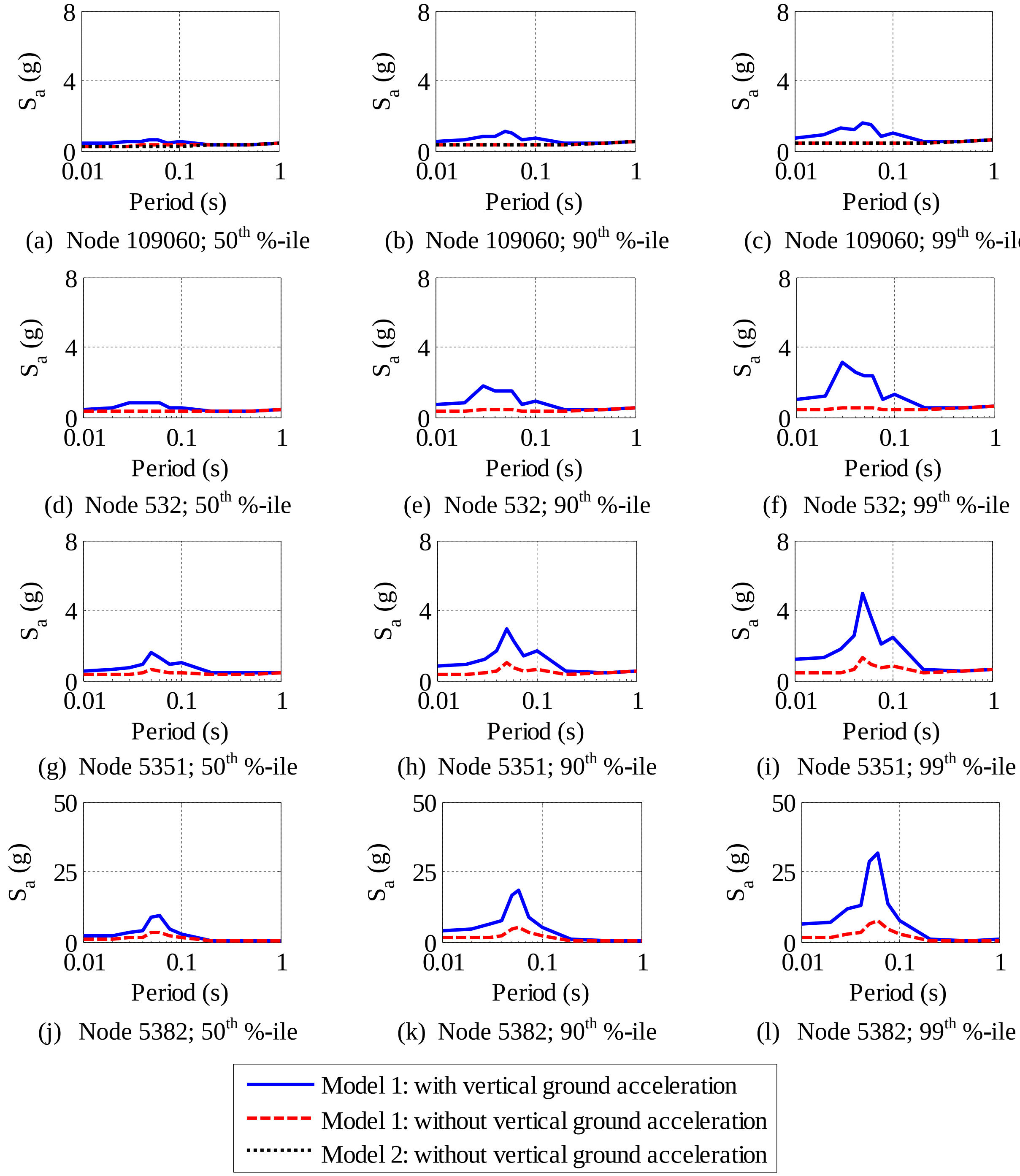

Figure 8-27: Floor spectra in the X direction at different nodes of the CIS computed using the two NPP models with friction at the sliding surface described using the pressure-dependent model subjected to the set of 30 ground motions amplitude scaled by 1.5

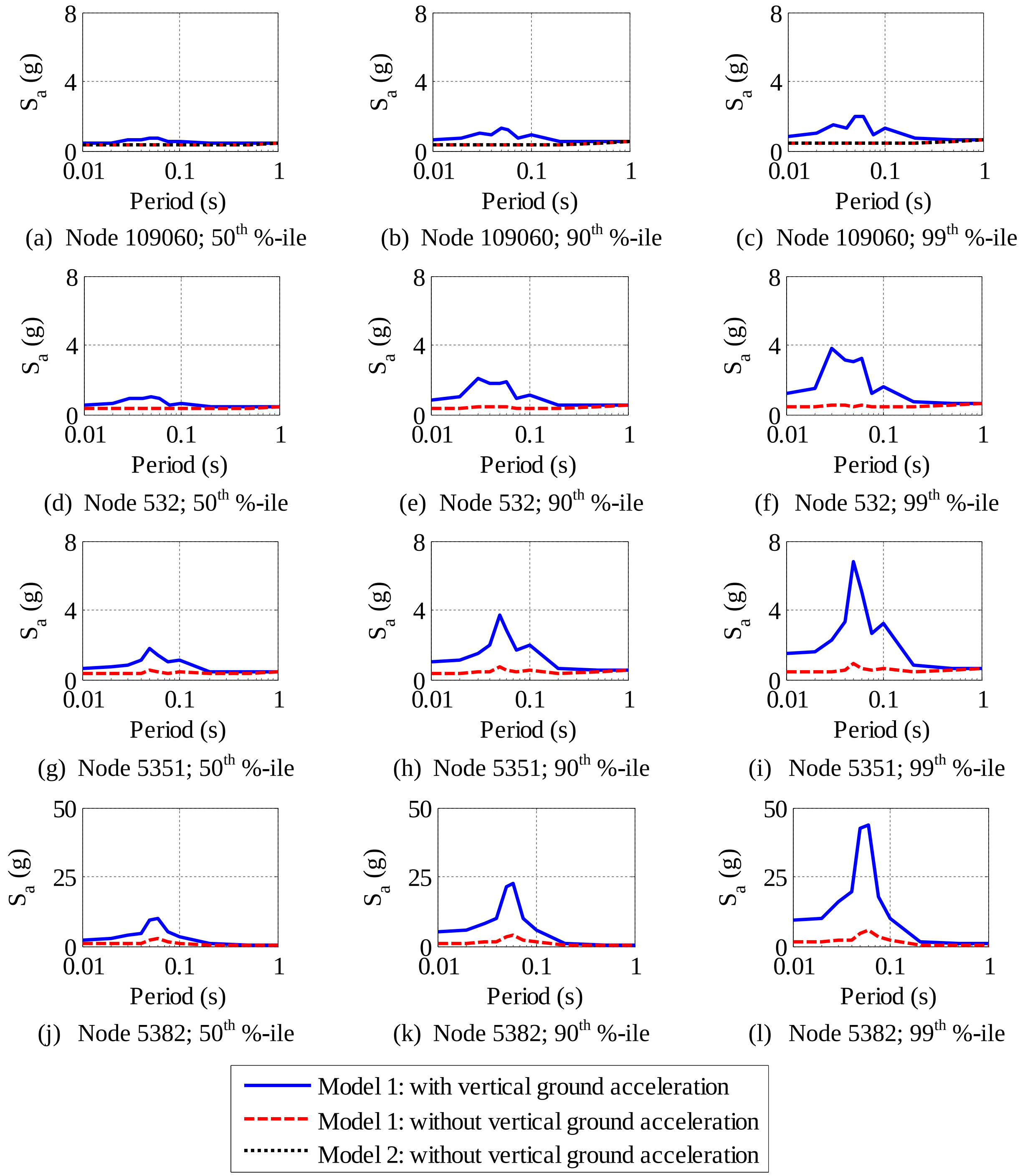

(a) Node 109060; 50th %-ile (b) Node 109060; 90th %-ile (c) Node 109060; 99th %-ile

(d) Node 532; 50th %-ile (e) Node 532; 90th %-ile (f) Node 532; 99th %-ile

(g) Node 5351; 50th %-ile (h) Node 5351; 90th %-ile (i) Node 5351; 99th %-ile

(j) Node 5382; 50th %-ile (k) Node 5382; 90th %-ile (l) Node 5382; 99th %-ile

Figure 8-28: Floor spectra in the X direction at different nodes of the CIS computed using the two NPP models with friction at the sliding surface described using the *p-T-v* model subjected to the set of 30 ground motions amplitude scaled by 1.5

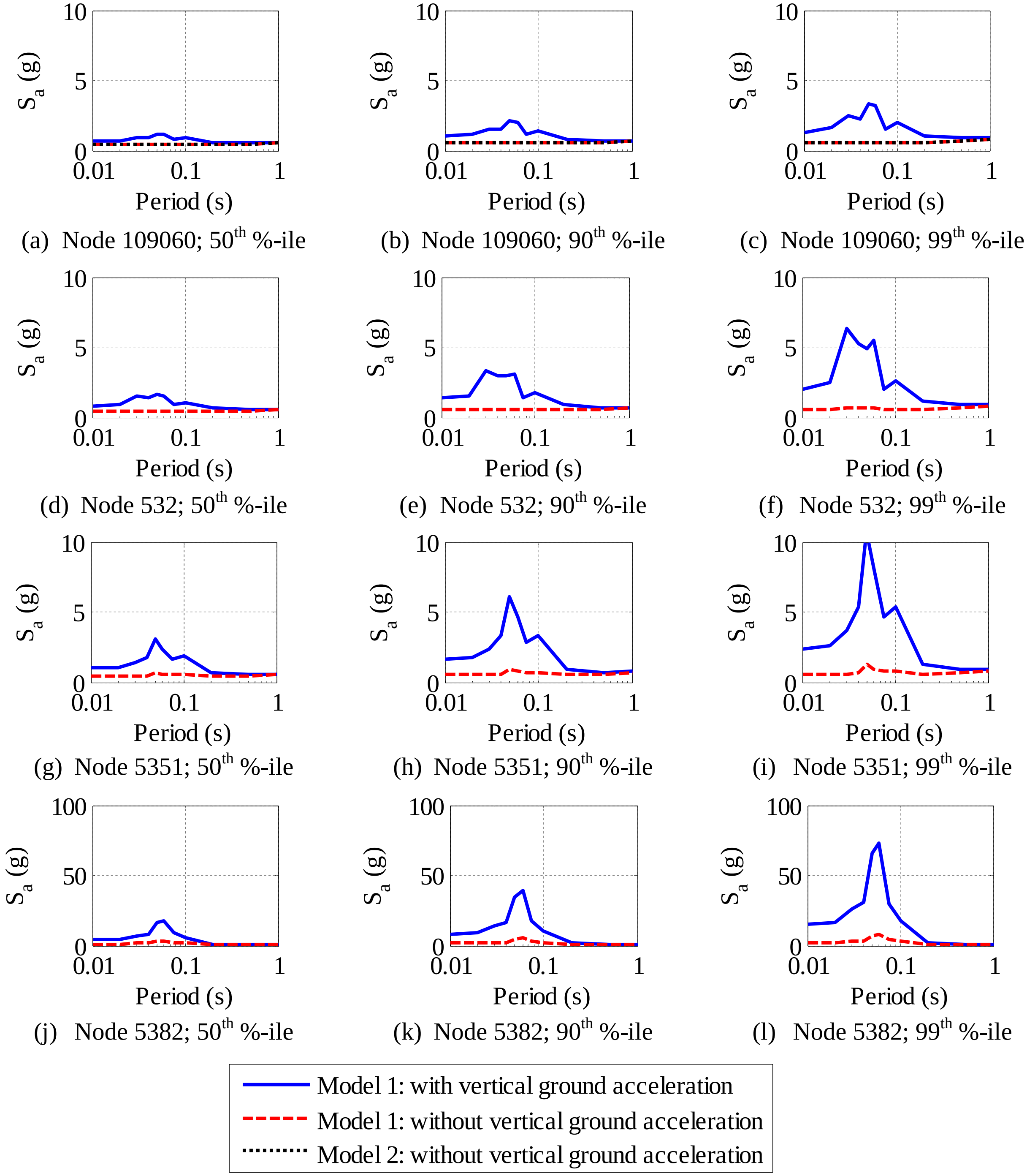

Figure 8-29: Floor spectra in the X direction at different nodes of the CIS computed using the two NPP models with friction at the sliding surface described using the Coulomb model subjected to the set of 30 ground motions amplitude scaled by 2.0

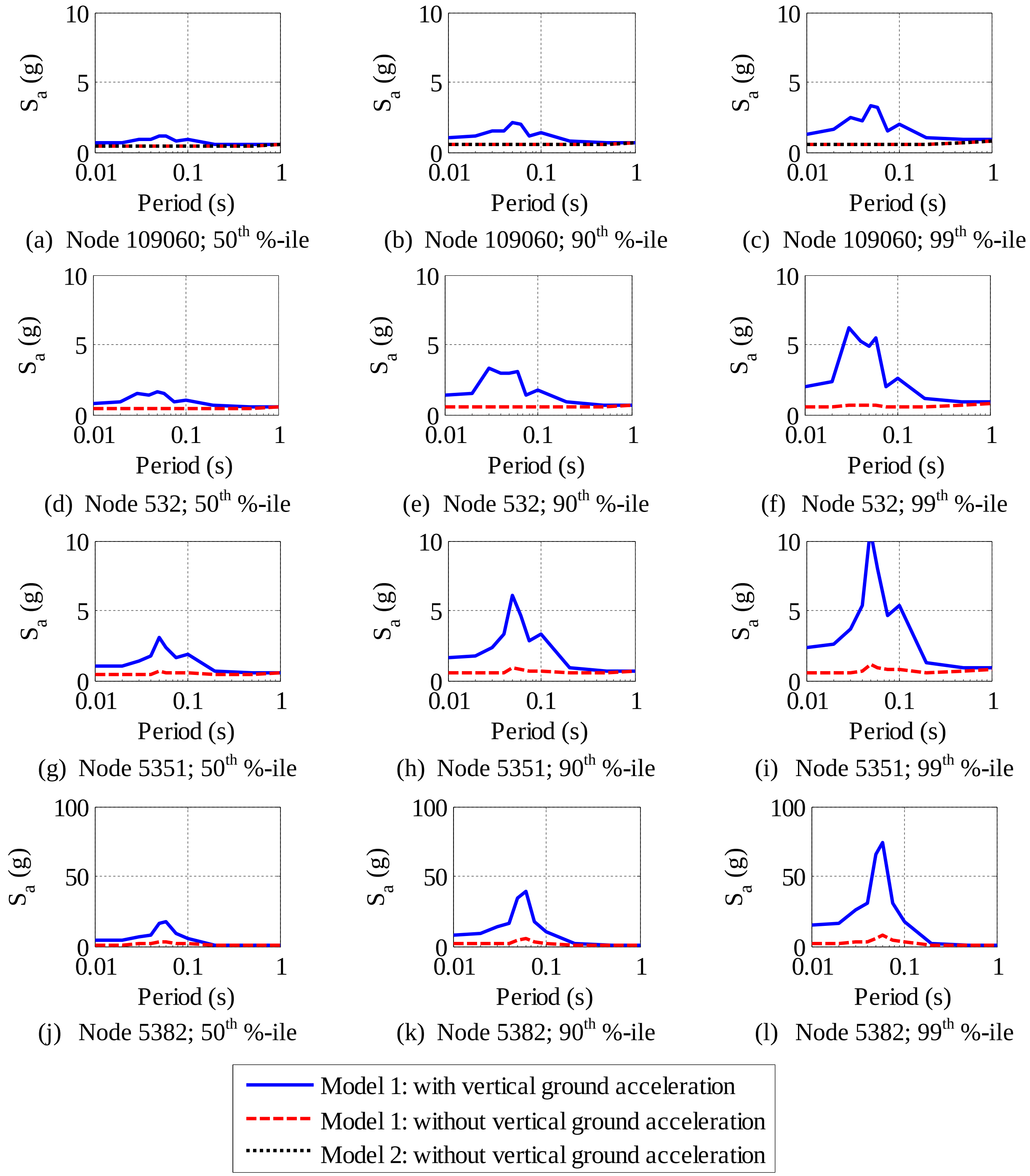

Figure 8-30: Floor spectra in the X direction at different nodes of the CIS computed using the two NPP models with friction at the sliding surface described using the velocity-dependent model subjected to the set of 30 ground motions amplitude scaled by 2.0

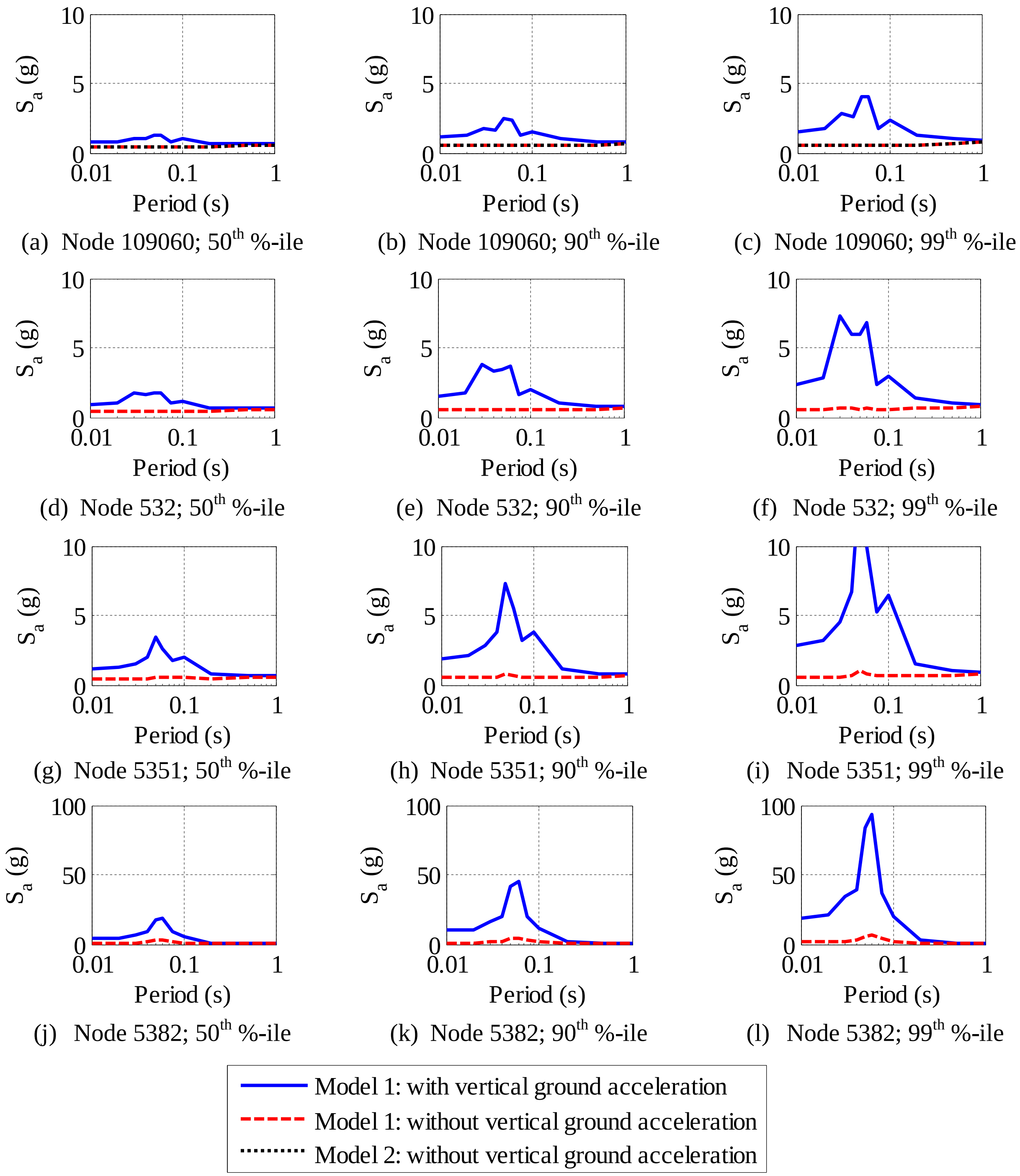

Figure 8-31: Floor spectra in the X direction at different nodes of the CIS computed using the two NPP models with friction at the sliding surface described using the temperature-dependent model subjected to the set of 30 ground motions amplitude scaled by 2.0

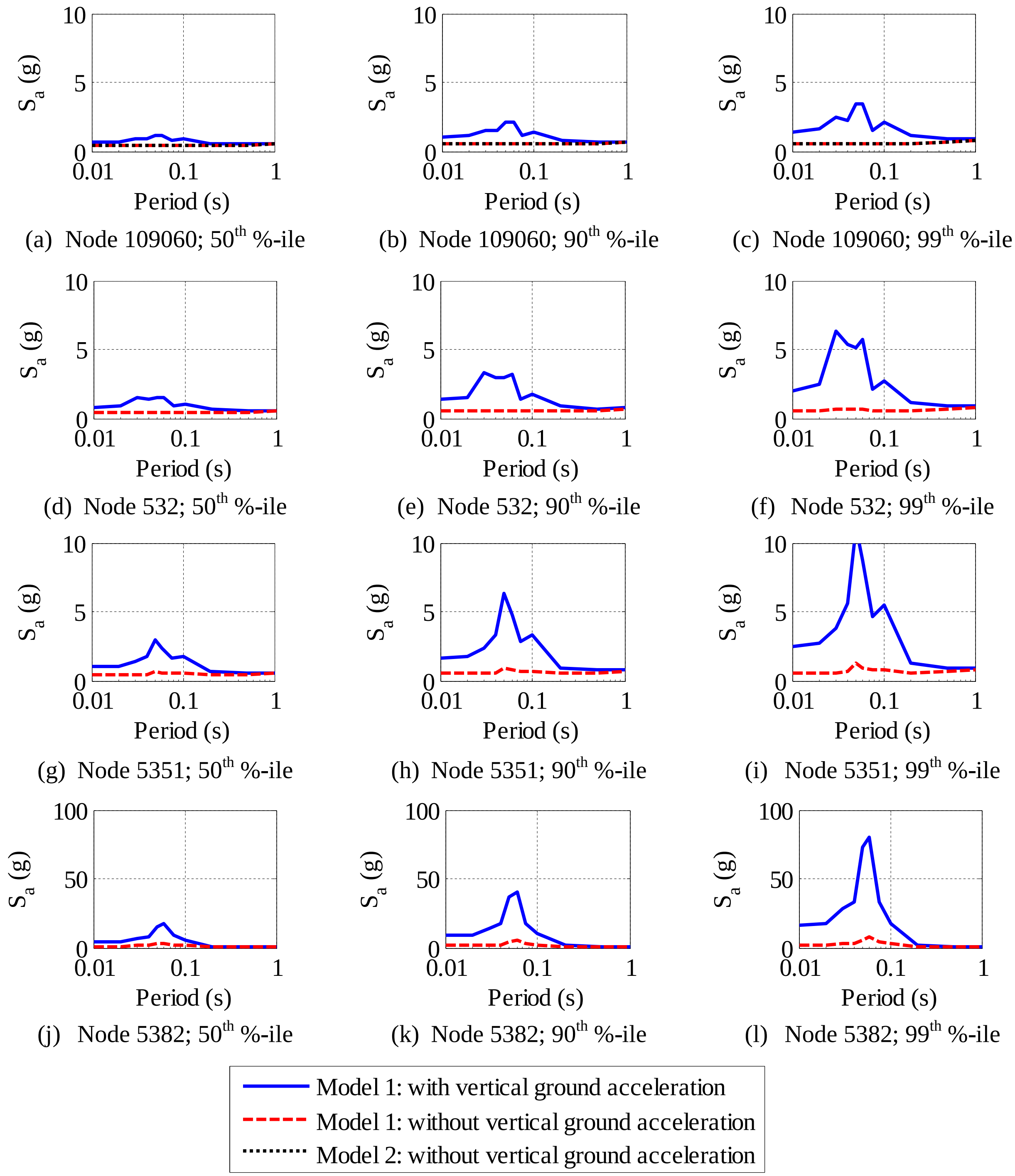

Figure 8-32: Floor spectra in the X direction at different nodes of the CIS computed using the two NPP models with friction at the sliding surface described using the pressure-dependent model subjected to the set of 30 ground motions amplitude scaled by 2.0

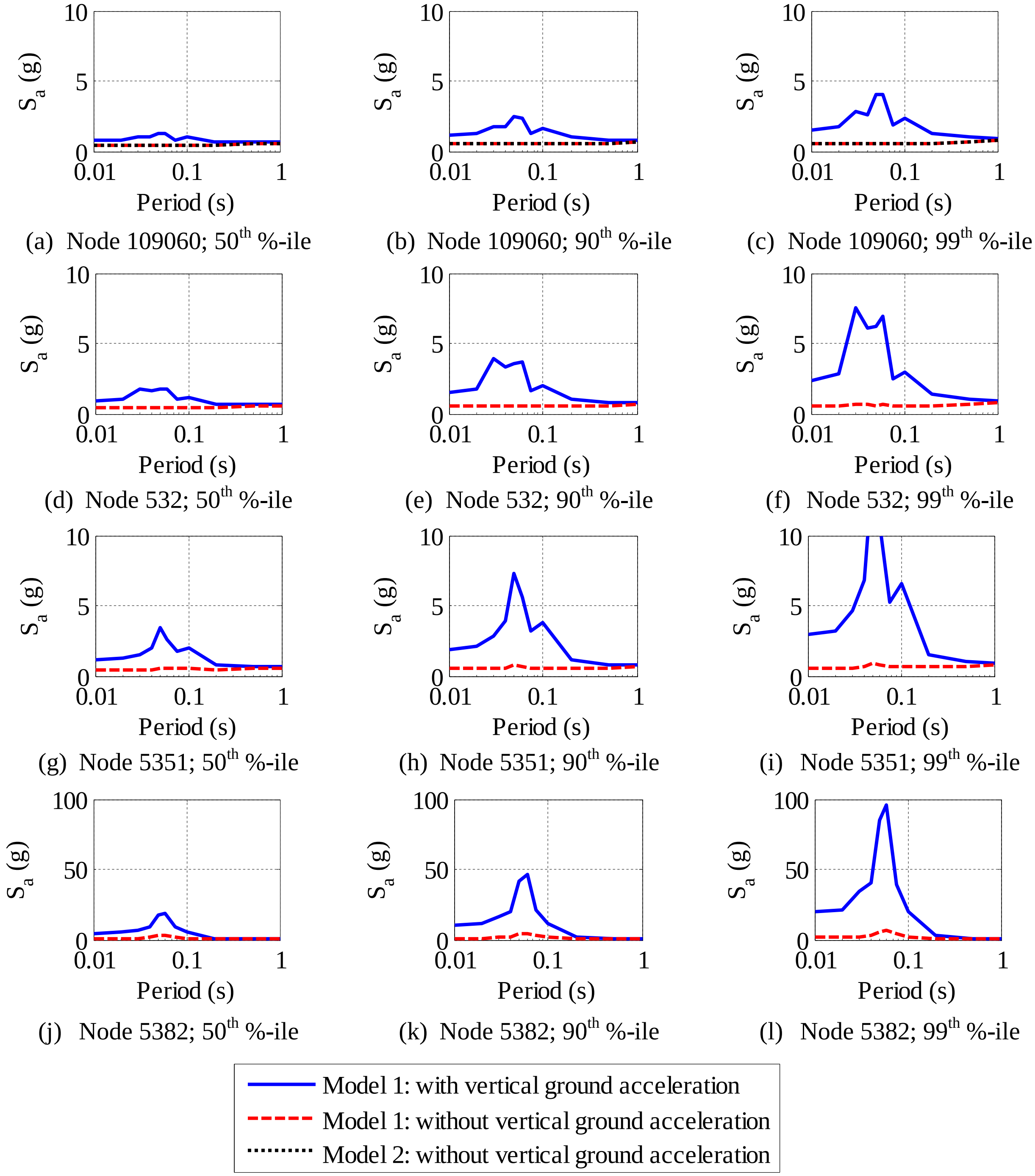

Figure 8-33: Floor spectra in the X direction at different nodes of the CIS computed using the two NPP models with friction at the sliding surface described using the *p-T-v* model subjected to the set of 30 ground motions amplitude scaled by 2.0

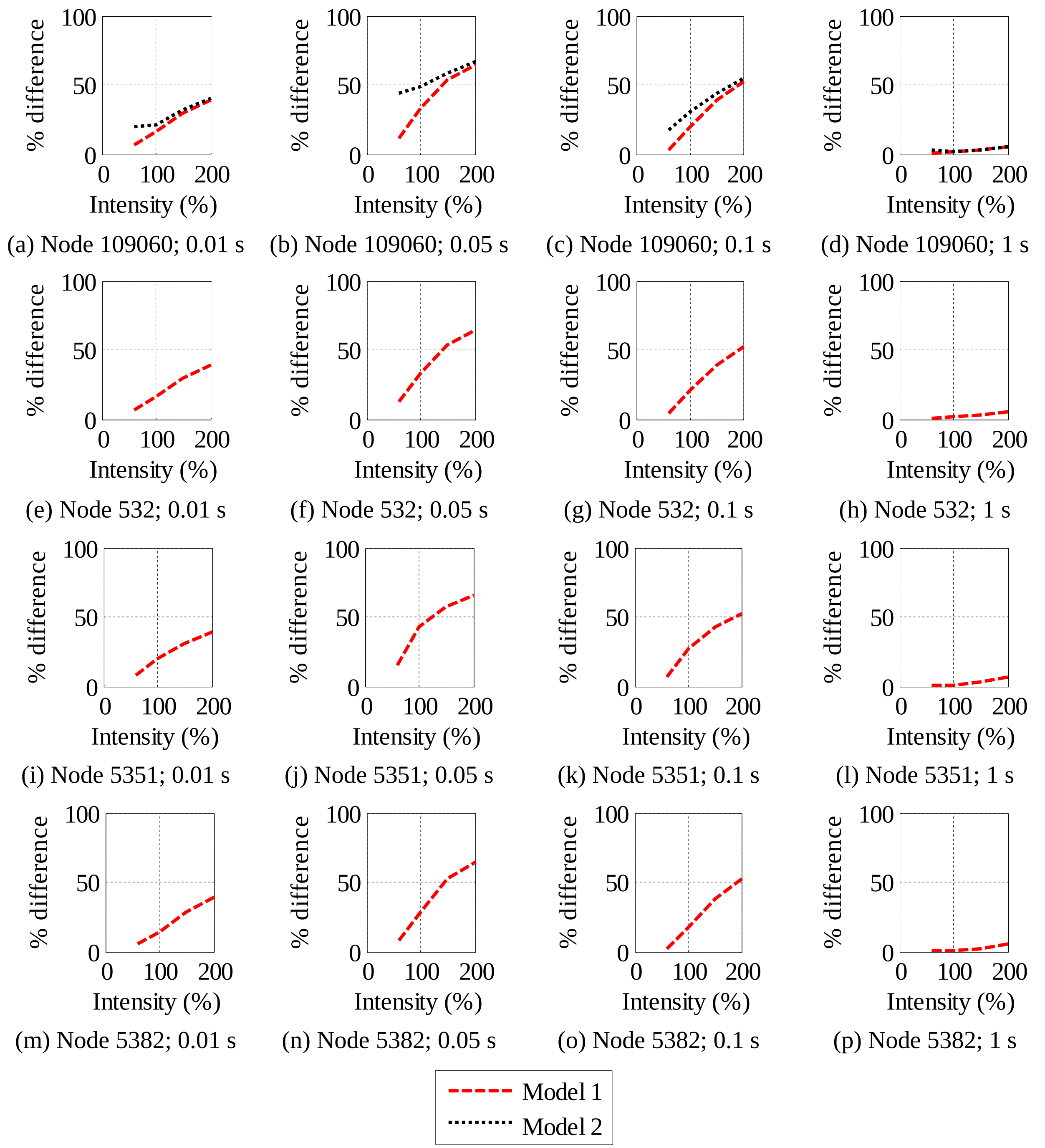

Figure 8-34: Percentage difference between the median floor spectral ordinates computed using the two NPP models subjected to two horizontal components of ground motions relative to that computed using Model 1 subjected to three components of the ground motion

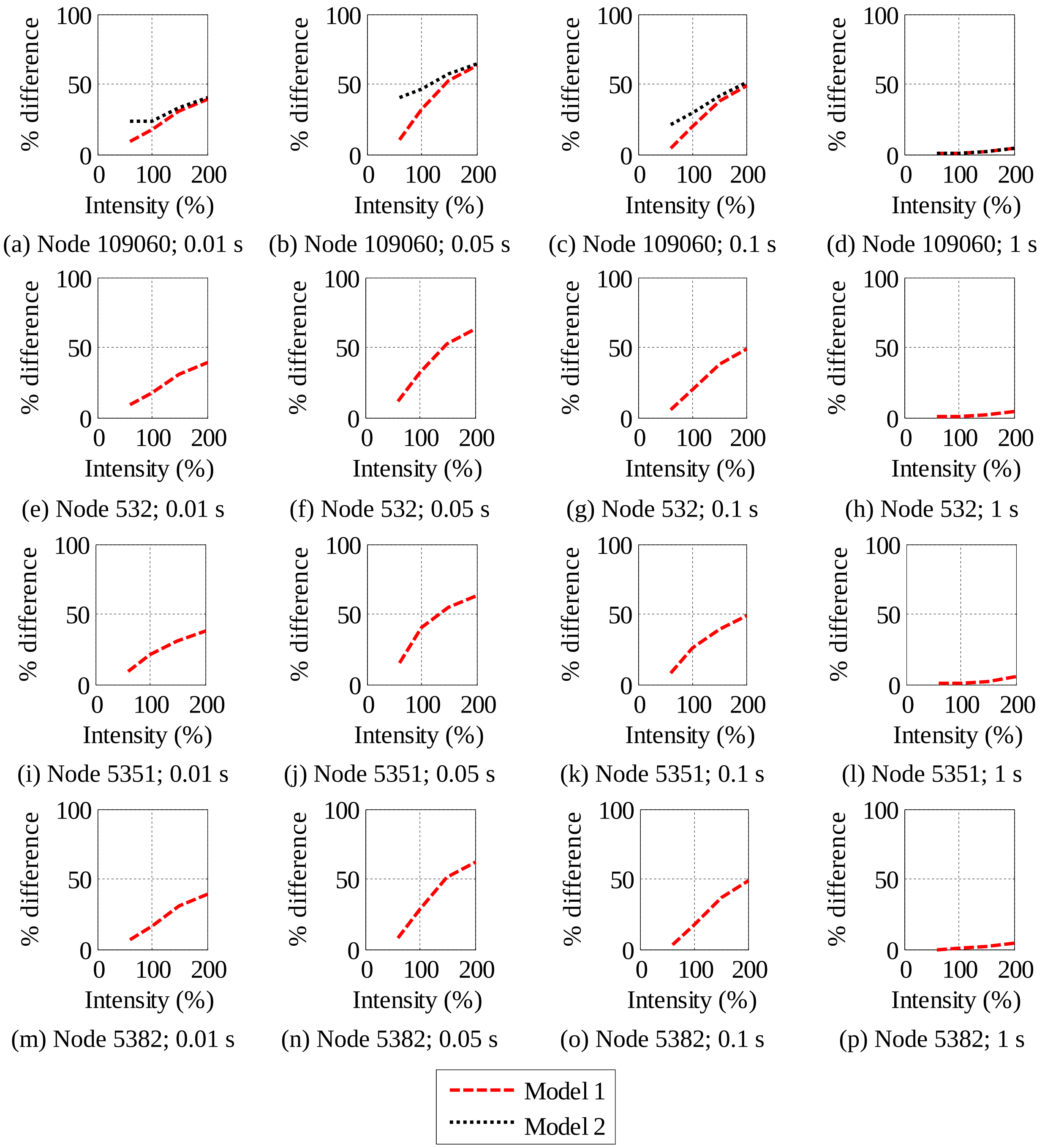

Figure 8-35: Percentage difference between the 90th percentile floor spectral ordinates computed using the two NPP models subjected to two horizontal components of ground motions relative to that computed using Model 1 subjected to three components of the ground motion

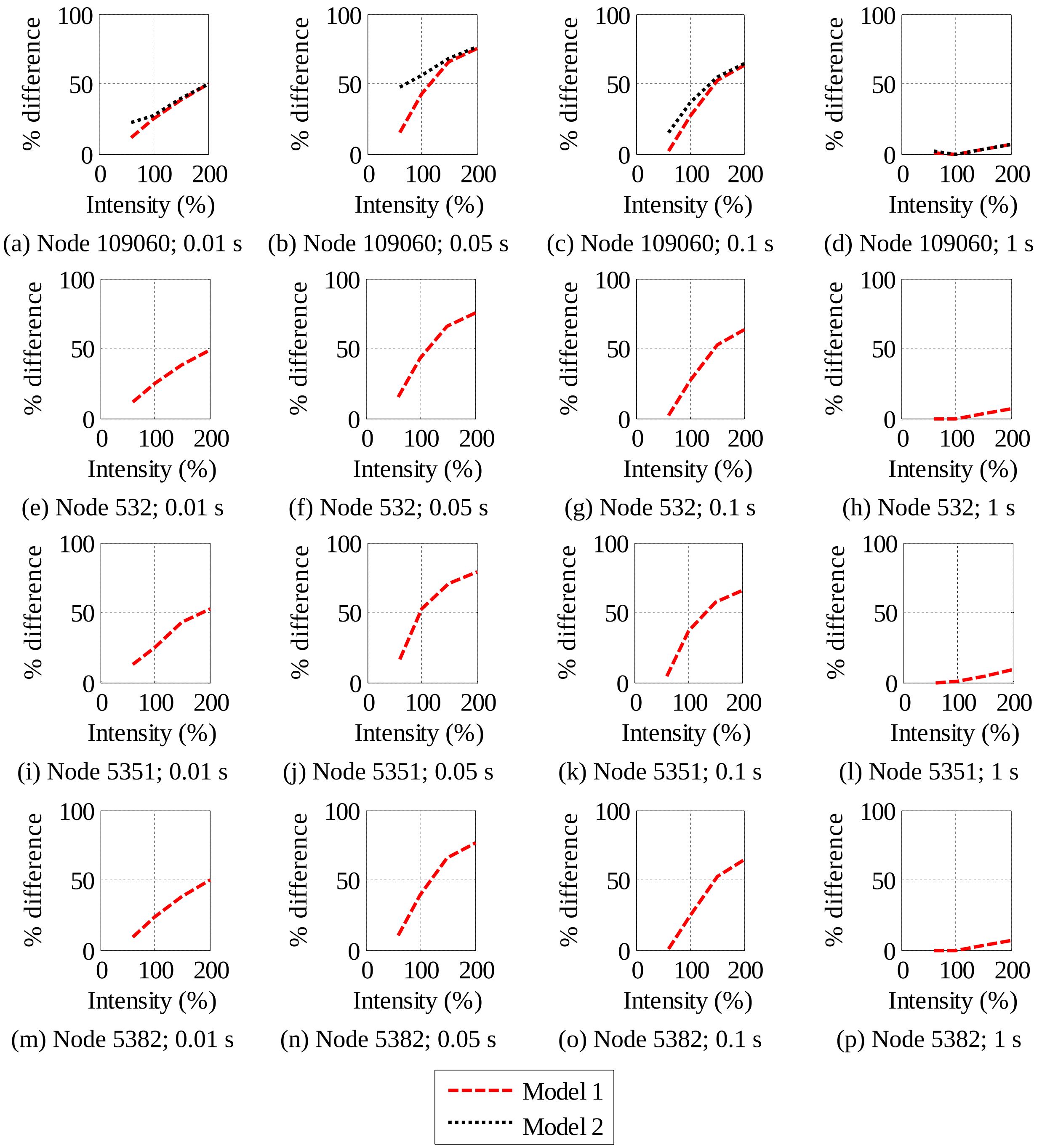

Figure 8-36: Percentage difference between the 99th percentile floor spectral ordinates computed using the two NPP models subjected to two horizontal components of ground motions relative to that computed using Model 1 subjected to three components of the ground motion

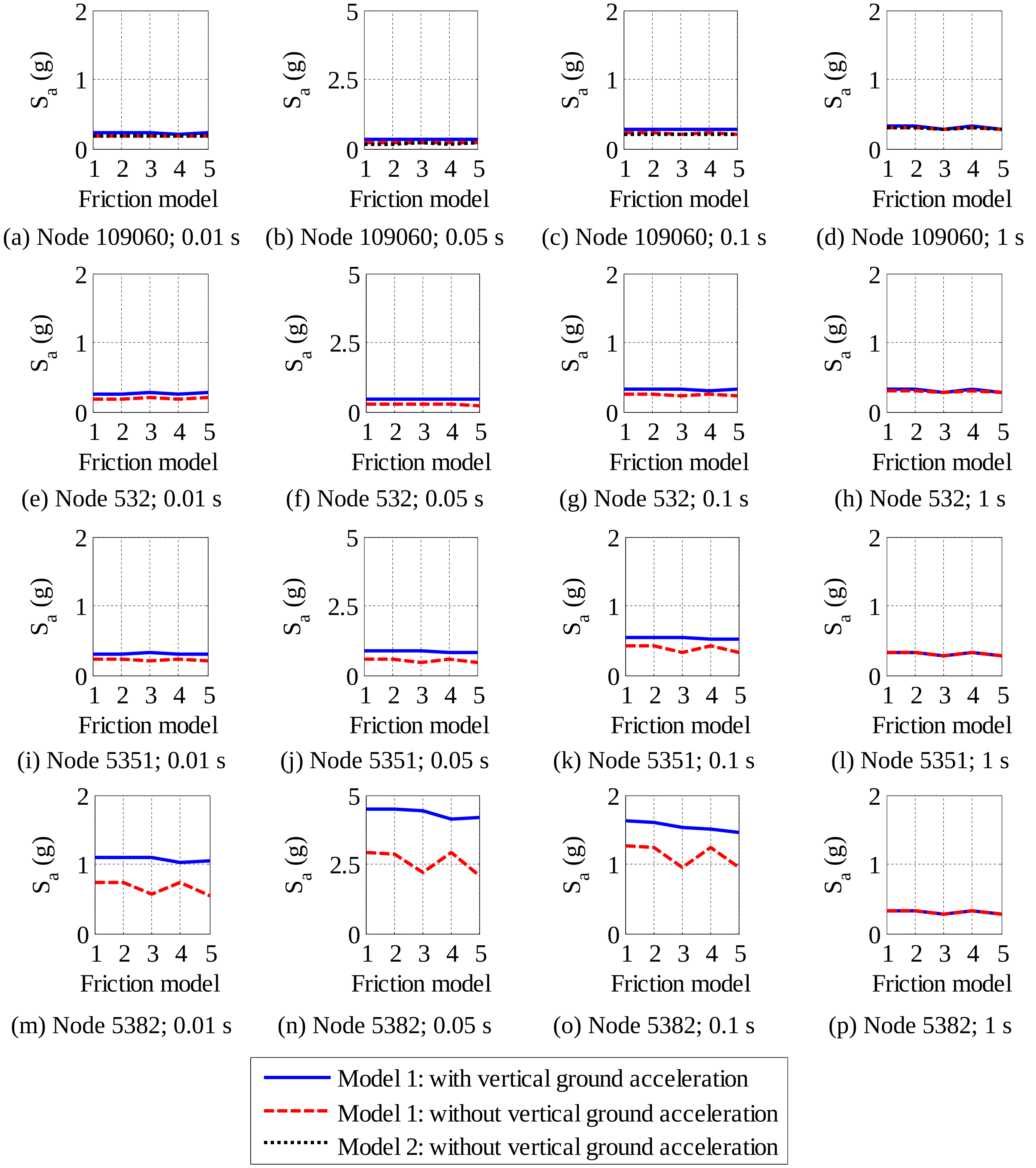

Figure 8-37: Median spectral accelerations in the X direction for four nodes of the CIS subjected to 30 ground motions amplitude scaled by 1.0; friction models 1 through 5, respectively, denote Coulomb, pressure-dependent, temperature-dependent, velocity-dependent and *p-T-v* models

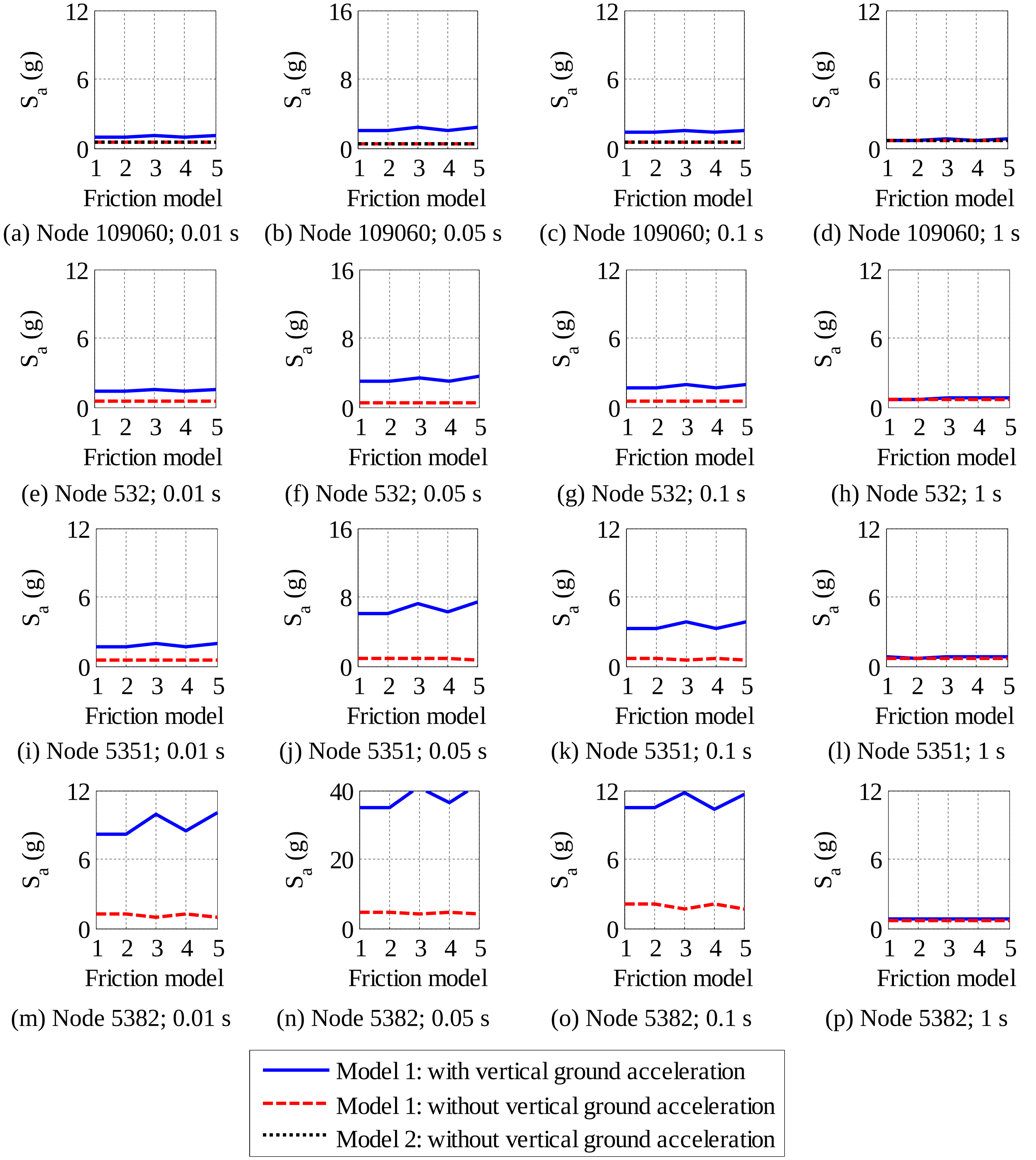

Figure 8-38: Spectral accelerations at the 90th percentile in the X direction for four nodes of the CIS subjected to 30 ground motions amplitude scaled by 2.0; friction models 1 through 5, respectively, denote Coulomb, pressure-dependent, temperature-dependent, velocity-dependent and *p*-*T*-*v* models

CHAPTER 9

SUMMARY AND CONCLUSIONS

9.1 Introduction

In the United States, nuclear power plants (NPPs) are designed for severe internal and external natural and man-made hazards, including earthquakes. Severe earthquakes can challenge new and existing NPPs, with large forces expected in their internal structures, systems and components (SSCs) in design basis shaking. Base isolation is a viable strategy to seismically protect SSCs in NPPs, since it effectively filters a significant fraction of the high frequency, horizontal earthquake shaking, and it facilitates standardization of plant designs. Sliding isolators, here single concave Friction Pendulum™ (FP) bearings, are one type of hardware that could be used in the United States for safety-related nuclear structures, including nuclear power plants.

This report is composed of three key parts: 1) modeling of the coefficient of friction at the sliding surface of a single concave FP bearing, 2) characterization of seismic hazard for a seismically isolated nuclear power plants, and 3) results of response-history analyses performed using different models of FP isolated nuclear power plants.

9.2 Characterizing Friction in Sliding Isolation Bearings

9.2.1 Summary

Expressions to define the relationships between the coefficient of sliding friction and sliding velocity, axial pressure and temperature at the sliding surface are developed based in large part on past experiments. These expressions are coded into a new OpenSees element *FPBearingPTV*, which simulates the behavior of a single FP bearing. The assumptions involved in the modeling of the bearing are studied and the software is *verified* and *validated* using the procedure outlined in ASME (2006) and presented in Oberkampf and Roy (2010).

9.2.2 Conclusions

The key conclusions from the study on the characterization of the coefficient of friction are:

i. The assumption that the small-velocity coefficient of friction is half the high-velocity coefficient of friction does not affect the displacement response of a seismically isolated nuclear power plant, except for very low intensity shaking, which is of no practical importance.
ii. The temperature at the center of the sliding surface can be considered to represent the temperature of the sliding surface for the purpose of response-history analyses of the isolated structures.
iii. The infinite half-space assumption for the temperature calculations leads to reasonable predictions of the force-displacement response of FP bearings. Radiation losses are small and need not be considered in the temperature calculations.
iv. The new OpenSees element *FPBearingPTV* simulates the lateral force-displacement response of single FP bearings.

9.3 Representations of Seismic Hazard for Isolated Nuclear Power Plants

9.3.1 Summary

The US Nuclear Regulatory Commission will require two levels of seismic hazard to be considered for the analysis and design of seismically isolated NPPs in the United States (see Kammerer *et al.* (forthcoming)): a ground motion response spectrum+ (GMRS+) and an extended design basis (EDB) GMRS. The GMRS is defined as the product of a design factor and the uniform hazard response spectrum (UHRS) with a mean annual frequency of exceedance (MAFE) of 10^{-4} (return period of 10,000 years). The GMRS+ is the envelope of the GMRS and a regulator-specific minimum response spectrum (e.g., an appropriate spectral shape anchored to a peak ground acceleration of 0.1 g). The EDB GMRS is the UHRS at an MAFE of 10^{-5} (return period of 100,000 years) but can be no less than 1.67 times GMRS+.

The forthcoming seismic isolation NUREG requires the inclusion of a hard stop to allow the seismic isolation system to be screened out of earthquake-induced accident sequences that lead to core damage or large release of radiation. Prototype isolators are to be tested at a horizontal displacement corresponding to the clearance between the isolated superstructure and the stop: the clearance to the hard stop (CHS). The distance CHS is determined by nonlinear response-history analysis and the NUREG will require it to be greater than the 99^{th} (90^{th}) percentile displacement for GMRS+ (EDB GMRS shaking). Distributions of peak isolation-system displacement (and thus the CHS) can be substantially influenced by the definition of seismic hazard. Three alternate representations of seismic hazard are considered herein: UHRS, conditional mean spectrum (CMS) and conditional spectra (CS). The horizontal spectrum for each representation is a geometric mean spectrum of the two horizontal components. Sets of spectrally matched ground motions consistent with the 10,000-year and 100,000-year UHRS, CMS and CS are developed for the site of the Diablo Canyon Nuclear Generating Station, a site of high seismicity. An additional set of ground motions, UHRS with *maximum* and *minimum* components (UHRS-MaxMin), is generated for each return period, to recognize the difference in shaking along perpendicular horizontal axes that is observed in recorded ground motions. Single FP bearings with a range of geometrical and material properties are subjected to these four representations of ground shaking and the distributions of peak displacement are studied.

9.3.2 Conclusions

The following conclusions are drawn from the study on alternate representations of seismic hazard:

i. Distributions of peak displacement are significantly influenced by the choice of target spectrum. The choice of seed ground motions does not affect the distributions.
ii. The 90th percentile peak displacement for 100,000-year shaking is greater than the 99th percentile peak displacement for 10,000-year shaking, for a given target spectrum (or spectra), and dictates the required clearance to the hard stop.
iii. The UHRS-, CMS- and CS- displacements are comparable at the 90th percentile for the two levels of shaking. The 90th percentile UHRS-MaxMin displacements are substantially greater than those for the UHRS, CMS or CS, at the two levels of shaking. Seismic hazard for isolated nuclear power plants should be defined using a UHRS appropriately considering the differences between the two orthogonal horizontal components (i.e., UHRS-MaxMin motions).

iv. The choice of friction model has a considerable influence on the peak displacement of the isolation system, especially for sites of intense shaking and isolators with high contact pressures and high reference coefficient of friction. The temperature dependence of the coefficient of friction should be addressed in the calculation of the clearance to the hard stop: 90^{th} percentile displacement for 100,000-year shaking.

9.4 Earthquake Risk for Seismically Isolated Nuclear Power Plants

9.4.1 Summary

The key performance goals for seismically isolated nuclear power plants as outlined in the forthcoming seismic isolation NUREG (Kammerer *et al.*, forthcoming) are: 1) the probability of the isolated superstructure striking the hard stop should be less than 10% for EDB GMRS shaking, 2) the probability of loss of axial load capacity of an individual isolator unit should be less than 10% at the 90^{th} percentile EDB GMRS displacement, and 3) the probability of loss of function of a safety-related umbilical line should be less than 10% at the 90^{th} percentile EDB GMRS displacement. The first goal is achieved by installing the hard stop (see Section 9.3.1) at a clear distance from the isolated superstructure at a displacement no less than the 90^{th} percentile EDB GMRS displacement. The performance goal for individual isolators is achieved by prototype testing. The performance goal for the safety-related umbilical lines can be realized by a combination of analysis and testing. In this report, the mean annual frequencies of unacceptable performance of isolation systems (and umbilical lines) are calculated for eight sites of nuclear facilities across the United States, representing regions of low, moderate and high seismic hazard. The purpose of the calculations are two-fold, namely, 1) provide a roadmap for an applicant to calculate the earthquake risk associated with a seismic isolation system with a given horizontal displacement capacity, and 2) provide the US Nuclear Regulatory Commission (Chapter 6) and the US Department of Energy (Appendix F) with insight into the risk associated with a seismic isolation system, with and without a hard stop present.

Median fragility curves are developed for isolators tested at different displacements (e.g., 90^{th} percentile displacement for EDB GMRS shaking in Chapter 6 and 90^{th} percentile displacement for 150% DBE shaking in Appendix F) at different confidence levels (e.g., 90%). The hard stop is accounted for by truncating the fragility curve at the failure probability with which the isolators are tested (e.g., 10%). To enable the risk calculations, the hazard curves are defined in Chapter 6 as multiples of the GMRS (equal to the UHRS at an MAFE of 10^{-4}), which is taken as the average of the multiples of the GMRS ordinates at 1 s and 2 s. The fragility and hazard curves for the umbilical lines are identical to those for the individual isolators.

The earthquake risk associated with individual isolators is quantified in terms of annual frequency of unacceptable performance: providing a benchmark against which to compare risk reduction strategies. The risk associated with the isolation system is (very) conservatively set equal to the mean annual frequency of failure for individual isolators, noting that although isolator capacities are likely highly correlated if nuclear-industry quality assurance/quality control procedures are followed, isolator demands are likely weakly correlated. Three risk-reduction strategies are considered: 1) testing the prototype isolators with a greater confidence at a given displacement, 2) testing the isolators for a greater displacement and corresponding axial force at a given confidence level, and 3) providing a hard stop (which is required for USNRC-regulated isolated nuclear power plants). The annual frequency of unacceptable performance of individual bearings (loss of axial load capacity at the CHS displacement) is calculated in Chapter 6 at eight sites of nuclear facility located across the United States.

Companion calculations for Seismic Design Category 5 nuclear structures per ASCE Standard 43-05 (ASCE, 2005) are presented in Appendix F. Median fragility curves are conservatively derived (overestimating risk) by setting the 90th percentile displacement for EDB GMRS shaking (or 150% DBE shaking in ASCE 43 space) equal to the median displacement for 110% EDB GMRS shaking (or 165% DBE shaking in ASCE 43 space).

9.4.2 Conclusions

The following conclusions are drawn on the subject of earthquake risk of seismically isolated nuclear power plants:

i. The mean annual frequency of unacceptable performance of individual isolators (and umbilical lines) tested in accordance with the forthcoming seismic isolation NUREG (i.e., 90% confidence at 90th percentile displacement for EDB GMRS shaking) ranges between 4.7×10^{-6} and 7.3×10^{-6} for a log standard deviation of 0.05: values substantially greater than a target goal of 1×10^{-6}. The risk is reduced in a meaningful manner if testing is performed to either the same displacement but higher confidence or the same confidence and greater displacement, but remains greater than 1×10^{-6}. The introduction of a hard stop at the 90th percentile displacement for EDB GMRS shaking achieves the goal of driving the risk below 1×10^{-6}. If the confidence level is increased from 90% to 99%, the risk drops well below 1×10^{-7}.

ii. A hard stop is generally needed to reduce the annual frequency of unacceptable performance of a DoE-regulated SDC 5 isolated safety-related nuclear structure below the target goal of 1×10^{-5}.

iii. The ground motion response spectrum in NRC space and the design response spectrum in DOE space are calculated for design of nuclear power plants (and other SDC 5 structures) by multiplying the ordinates of a uniform hazard response spectrum at the specified hazard exceedance frequency by a design factor that is greater than or equal to 1.0. The factor can be set equal to 1.0 for design of a seismically isolated nuclear power plant if the earthquake risk is dominated by horizontal ground shaking and a hard stop is provided.

9.5 Response of Seismically Isolated Nuclear Power Plants

9.5.1 Summary

The response of a sample nuclear power plant isolated on single concave FP™ bearings is studied to understand what design decisions most affect behavior. Two sites are considered, namely, Diablo Canyon and Vogtle, sites of high and moderate seismicity, respectively. Alternate models of the sample power plant are considered. Friction Pendulum bearings with a range of sliding periods, reference coefficients of friction, and reference axial pressures are considered with friction at the sliding surface defined using models that account for the pressure-, temperature- and/or velocity-dependencies.

9.5.2 Conclusions

The following conclusions are drawn from the response-history analyses presented in Chapters 7 and 8 and are specific to the type of composite material used in the FP bearing:

i. Isolation-system horizontal displacement can be estimated for preliminary design using a macro model (single bearing) of the isolation system. Considering the vertical component of ground motion in the response-history analysis does not change the horizontal displacement response, which was first observed in the experiments of Mosqueda *et al.* (2004).

ii. The friction model used to compute isolation-system displacement should include the heating effects. Displacements may be significantly underestimated if the heating effects are ignored and if the reference axial pressure, reference coefficient of friction and/or shaking intensity are high.

iii. The friction model need not consider the velocity- and pressure-dependence of the coefficient of friction to compute isolation-system displacement.

iv. Floor spectra in isolated nuclear structures should be computed using a detailed 3D finite element model of the isolated superstructure. Vertical ground motion must be included to compute horizontal floor spectra. The choice of friction model does not significantly influence the floor spectral ordinates.

CHAPTER 10

REFERENCES

Aiken, I. D., Nims, D. K., Whittaker, A. S., and Kelly, J. M. (1993). "Testing of passive energy dissipation systems." *Earthquake Spectra*, 9(3), 335-370.

Al-Hussaini, T. M., Zayas, V. A., and Constantinou, M. C. (1994). "Seismic isolation of multi-story frame structures using spherical sliding isolation systems." Report NCEER-94-0007, University at Buffalo, State University of New York, Buffalo, NY.

Almazán, J. L., De La Llera, J. C., and Inaudi, J. A. (1998). "Modeling aspects of structures isolated with the frictional pendulum system." *Earthquake Engineering & Structural Dynamics*, 27(8), 845-867.

American Concrete Institute (ACI). (2013a). "Code requirements for nuclear safety-related concrete structures and commentary." ACI Standard 349-13, Farmington Hills, MI.

American Concrete Institute (ACI). (2013b). "Code for concrete containments ", ACI Standard 359-13, Farmington Hills, MI.

American Institute of Steel Construction (AISC). (2012). "Specification for safety-related steel structures for nuclear facilities." ANSI/AISC N690-12, Chicago, IL.

American Nuclear Society (ANS). (2010). "Categorization of nuclear facility structures, systems, and components for seismic design." ANSI/ANS-2.26-2004, La Grange Park, IL.

American Society of Civil Engineers (ASCE). (2005). "Seismic design criteria for structures, systems and components in nuclear facilities." ASCE Standard 43-05, Reston, VA.

American Society of Civil Engineers (ASCE). (2010). "Minimum design loads for buildings and other structures." ASCE Standard 7-10, Reston, VA.

American Society of Civil Engineers (ASCE). (2016). "Seismic analysis of safety-related nuclear structures and commentary." ASCE Standard 4, Reston, VA.

Arya, A. S. (1984). "Sliding concept for mitigation of earthquake disaster to masonry buildings." *Proceedings, Eighth World Conference on Earthquake Engineering*, San Francisco, CA.

American Society of Mechanical Engineers (ASME). (2006). "Guide for verification and validation in computational solid mechanics." ASME Standard V&V 10-2006, New York, NY.

Badillo-Almaraz, H., Whittaker, A. S., and Reinhorn, A. M. (2007). "Seismic fragility of suspended ceiling systems." *Earthquake Spectra*, 23(1), 21-40.

Baker, J. W., and Cornell, C. A. (2006). "Spectral shape, epsilon and record selection." *Earthquake Engineering & Structural Dynamics*, 35(9), 1077-1095.

Baker, J. W., and Jayaram, N. (2008). "Correlation of spectral acceleration values from NGA ground motion models." *Earthquake Spectra*, 24(1), 299-317.

Bathe, K. J. (1996). "Finite element procedures." Prentice-Hall, NJ.

Benjamin, J. R., and Cornell, C. A. (1970). "Probability, statistics, and decision for Civil engineers." McGraw-Hill, New York, NY.

Beyer, K., and Bommer, J. J. (2006). "Relationships between median values and between aleatory variabilities for different definitions of the horizontal component of motion." *Bulletin of the Seismological Society of America*, 96(4A), 1512-1522.

Boore, D. M., Watson-Lamprey, J., and Abrahamson, N. (2006). "Orientation-independent measures of ground motion." *Bulletin of the Seismological Society of America*, 96(4A), 1502-1511.

Buckle, I. G. (1985). "New Zealand seismic base isolation concepts and their application to nuclear engineering." *Nuclear Engineering and Design*, 84(3), 313-326.

Buckle, I. G., and Mayes, R. L. (1990). "Seismic isolation: history, application and performance-a world view." *Earthquake Spectra*, 6(2), 161-201.

Burningham, C., Mosqueda, G., and Saavedra, R. R. (2007). "Comparison of seismic fragility of free standing equipment using current testing protocols and recorded building floor motions." *Proceedings, Earthquake Engineering Symposium for Young Researchers*, August 8-12, Seattle, WA.

Campbell, K. W., and Bozorgnia, Y. (2008). "NGA ground motion model for the geometric mean horizontal component of PGA, PGV, PGD and 5% damped linear elastic response spectra for periods ranging from 0.01 to 10 s." *Earthquake Spectra*, 24(1), 139-171.

Civil Engineering Research Foundation (CERF). (1998). "Evaluation findings for Earthquake Protection Systems, Inc. Friction Pendulum bearings.", Report HITEC 98-07#40370, Highway Innovative Technology Evaluation Center, Washington, D.C.

Chang, K. C., Hwang, J. S., and Lee, G. C. (1990). "Analytical model for sliding behavior of Teflon-stainless steel interfaces." *Journal of Engineering Mechanics*, 116(12), 2749-2763.

Chopra, A. (2007). "Dynamics of structure–Theory and applications to earthquake engineering." Pearson Education, Upper Saddle River, NJ.

Christopoulos, C., and Filiatrault, A. (2006). "Principles of passive supplemental damping and seismic isolation." IUSS Press, Pavia, Italy.

Chung, J., and Hulbert, G. M. (1993). "A time-integration algorithm for structural dynamics with improved numerical dissipation: the generalized-α method." *ASME Journal of Applied Mechanics*, 60, 371-375.

Cizelj, L., and Simonovski, I. (2011). "Fatigue relevance of stratified flows in pipes: A parametric study." *Nuclear Engineering and Design*, 241(4), 1191-1195.

Clark, P. W., Aiken, I. D., Nakashima, M., Miyazaki, M., and Midorikawa, M. (1999). "The 1995 Kobe (Hyogo-ken Nanbu) earthquake as a trigger for implementing new seismic design technologies in Japan." *Lessons Learned Over Time, Learning From Earthquakes Series*, Vol. III, Earthquake Engineering Research Institute, CA.

Clark, P. W., Higashino, M., and Kelly, J. M. (1996). "Performance of seismically isolated structures in the January 17, 1994 Northridge earthquake." *Proceedings, Sixth U.S.-Japan Workshop on the Improvement of Building Structural Design and Construction Practices in the United States and Japan*, Victoria, B.C., Canada.

Clarke, C. S. J., Buchanan, R., Efthymiou, M., and Shaw, C. (2005). "Structural platform solution for seismic arctic environments--Sakhalin II offshore facilities." *Proceedings, Offshore Technology Conference*, Houston, TX.

Constantinou, M. C., and Symans, M. D. (1992). "Experimental and analytical investigation of seismic response of structures with supplemental fluid viscous dampers." Report NCEER-92-0032, University at Buffalo, State University of New York, Buffalo, NY.

Constantinou, M. C., Kalpakidis, I., Filiatrault, A., and Lay, R. A. E. (2011). "LRFD-based analysis and design procedures for bridge bearings and seismic isolators." Report MCEER-11-0004, University at Buffalo, State University of New York, Buffalo, NY.

Constantinou, M. C., Tsopelas, P., Kasalanati, A., and Wolff, E. D. (1999). "Property modification factors for seismic isolation bearings." Report MCEER-99-0012, University at Buffalo, State University of New York, Buffalo, NY.

Constantinou, M. C., Tsopelas, P., Kim, Y.-S., and Okamoto, S. (1993). "NCEER-Taisei Corporation research program on sliding seismic isolation systems for bridges: Experimental and analytical study of a Friction Pendulum System (FPS)." Report NCEER-93-0020, University at Buffalo, State University of New York, Buffalo, NY.

Constantinou, M. C., Whittaker, A. S., Kalpakidis, Y., Fenz, D. M., and Warn, G. P. (2007). "Performance of seismic isolation hardware under service and seismic loading." Report MCEER-07-0012, University at Buffalo, State University of New York, Buffalo, NY.

Computers and Structures Incorporated (CSI). (2013). SAP2000 (Version 15.2.1) [Computer Program], Berkeley, CA.

Dao, N. D., Ryan, K. L., Sato, E., and Sasaki, T. (2013). "Predicting the displacement of triple pendulum™ bearings in a full-scale shaking experiment using a three-dimensional element." *Earthquake Engineering & Structural Dynamics*, 42(11), 1677-1695.

Dassault Systemes (DS). (2013). ABAQUS/CAE 6.10-EF2 (Version 6.10-EF2) [Computer program], Waltham, MA.

Drozdov, Y. N., Nadein, V. A., and Puchkov, V. N. (2007). "The effect of earthquake parameters on the tribological characteristics of friction pendulum bearings (seismic isolators)." *Journal of Machinery Manufacture and Reliability*, 36(2), 143-152.

Drozdov, Y. N., Nadein, V. A., and Puchkov, V. N. (2010). "Seismic isolators for petroleum and gas platforms of the “Sakhalin-2” project." *Journal of Machinery Manufacture and Reliability*, 39(6), 591-604.

Earthquake Protection Systems (EPS). (2011). "Earthquake protection systems", <http://www.earthquakeprotection.com/index.html>. (May 18, 2012).

Federal Emergency Management Agency (FEMA). (2012). "Seismic performance assessment of buildings, Volume 1: methodology." FEMA P-58-1, Washington, D.C.

Fenz, D. M., and Constantinou, M. C. (2006). "Behaviour of the double concave Friction Pendulum bearing." *Earthquake Engineering & Structural Dynamics*, 35(11), 1403-1424.

Fenz, D. M., and Constantinou, M. C. (2008a). "Modeling Triple Friction Pendulum bearings for response-history analysis." *Earthquake Spectra*, 24(4), 1011.

Fenz, D. M., and Constantinou, M. C. (2008b). "Mechanical behavior of multi-spherical sliding bearings." Report MCEER-08-0007, University at Buffalo, State University of New York, Buffalo, NY.

Fenz, D. M., Seed, R., Slatnick, S., Stewart, H. R., and Constantinou, M. C. (2011). "Development of performance-based testing specifications for the Arkutun-Dagi Friction Pendulum bearings." *Proceedings, Arctic Technology Conference*, February 7-9, Houston, TX.

Filiatrault, A., Kuan, S., and Tremblay, R. (2004). "Shake table testing of bookcase – partition wall systems." *Canadian Journal of Civil Engineering*, 31(4), 664-676.

Grandis, S. D., Forni, M., Bruyn, D. D., and Cardini, S. (2011). "Seismic isolation of Gen IV lead-cooled reactors." *Transactions, 21st International Conference on Structural Mechanics in Reactor Technology (SMiRT21)*, November 6-11, New Delhi, India.

Gülerce, Z., and Abrahamson, N. A. (2011). "Site-specific design spectra for vertical ground motion." *Earthquake Spectra*, 27(4), 1023-1047.

Hancock, J., Watson-Lamprey, J., Abrahamson, N., Bommer, J., Markatis, A., McCoy, E., and Mendis, R. (2006). "An improved method of matching response spectra of recorded earthquake ground motion using wavelets." *Journal of Earthquake Engineering*, 10 (Special Issue 1), 67-89.

Hilber, H. M., Hughes, T. J., and Taylor, R. L. (1977). "Improved numerical dissipation for time integration algorithms in structural dynamics." *Earthquake Engineering & Structural Dynamics*, 5(3), 283-292.

Huang, Y.-N. (2008). "Performance assessment of conventional and base-isolated nuclear power plants for earthquake and blast loadings." PhD dissertation, University at Buffalo, State University of New York, Buffalo, NY.

Huang, Y.-N., Whittaker, A. S., and Luco, N. (2010). "Seismic performance assessment of base-isolated safety-related nuclear structures." *Earthquake Engineering & Structural Dynamics*, 39(13), 1421-1442.

Huang, Y.-N., Whittaker, A. S., Constantinou, M. C., and Malushte, S. (2007). "Seismic demands on secondary systems in base-isolated nuclear power plants." *Earthquake Engineering & Structural Dynamics*, 36(12), 1741-1761.

Huang, Y.-N., Whittaker, A. S., Kennedy, R. P., and Mayes, R. L. (2013). "Response of base-isolated nuclear structures for design and beyond-design basis earthquake shaking." *Earthquake Engineering & Structural Dynamics*, 42(3), 339-356.

Huang, Y.-N., Whittaker, A. S., Kennedy, R. P., and Mayes, R. L. (2009). "Assessment of base-isolated nuclear structures for design and beyond-design basis earthquake shaking." Report MCEER-09-0008, University at Buffalo, State University of New York, Buffalo, NY.

Inagaki, Y., Kunitomi, K., Futakawa, M., Ikuo, I., and Kaji, Y. (2004). "R&D on high temperature components." *Nuclear Engineering and Design*, 233(1–3), 211-223.

Incropera, F. P., and Dewitt, D. P. (1985). "Introduction to heat transfer." John Wiley & Sons, New York, NY.

Izumi, M. (1988). "State-of-the art report: Base isolation and passive seismic response control." *Proceedings, Ninth World Conference on Earthquake Engineering*, August 2-9, 1988, Tokyo, Japan.

Jarque, C. M., and Bera, A. K. (1987). "A test for normality of observations and regression residuals." *International Statistical Review / Revue Internationale de Statistique*, 55(2), 163-172.

Jayaram, N., Lin, T., and Baker, J. W. (2011). "A computationally efficient ground-motion selection algorithm for matching a target response spectrum mean and variance." *Earthquake Spectra*, 27(3), 797-815.

Kadak, A. C. B., Ronald G.; Driscoll, Michael J.; Yip, Sidney; Wilson, David Gordon; No, Hee Cheon; Wang, Jing; MacLean, Heather; Galen, Tamara; Wang, Chunyun; Lebenhaft, Julian; Zhai, Tieliang; Petti, David A.; Terry, William K.; Gougar, Hans D.; Ougouag, Abderrafi M.; Oh, Chang H.; Moore, Richard L.; Miller, Gregory K.; Maki, John T.; Smolik, Galen R.; Varacalle, Dominic J. (2000). "Modular pebble bed reactor." Report INEEL/EXT-2000-01034, Center for Advanced Nuclear Energy Systems, Massachusetts Institute of Technology, Cambridge, MA.

Kammerer, A., Whittaker, A., and Constantinou, M. (forthcoming). "Technical considerations for seismic isolation of nuclear facilities." Report NUREG-****, United States Nuclear Regulatory Commission, Washington, D.C.

Kat, C.-J., and Els, P. S. (2012). "Validation metric based on relative error." *Mathematical and Computer Modelling of Dynamical Systems*, 18(5), 487-520.

Kelly, J. M. (1986). "Aseismic base isolation: review and bibliography." *Soil Dynamics and Earthquake Engineering*, 5(4), 202-216.

Kelly, J. M. (1993). "The implementation of base isolation in the United States." *Proceedings, 6th Symposium on Seismic, Shock, and Vibration Isolation, ASME Pressure Vessel and Piping Conference*, Denver, CO.

Kelly, J. (2004). "Seismic isolation." Chapter II in *Earthquake engineering: From engineering seismology to performance-based engineering* eds. Y. Bozorgnia, and V. V. Bertero, CRC Press.

Kelly, J. M., Skinner, R. I., and Heine, A. J. (1972). "Mechanisms of energy absorption in special devices for use in earthquake resistant structures." *Bulletin of the New Zealand Society for Earthquake Engineering*, 5(3), 63-88.

Kumar, M., Whittaker, A., and Constantinou, M. (2014). "An advanced numerical model of elastomeric seismic isolation bearings." *Earthquake Engineering & Structural Dynamics*, 43(13), 1955-1974.

Lilliefors, H. W. (1969). "On the Kolmogorov-Smirnov test for the exponential distribution with mean unknown." *Journal of the American Statistical Association*, 64(325), 387-389.

Lomiento, G., Bonessio, N., and Benzoni, G. (2013). "Friction model for sliding bearings under seismic excitation." *Journal of Earthquake Engineering*, 17(8), 1162-1191.

Livermore Software Technology Corporation (LSTC). (2011). LS-DYNA (Version 5.1.1) [Computer program], Livermore, CA.

Makris, N., and Deoskar, H. S. (1996). "Prediction of observed response of base-isolated structure." *Journal of Structural Engineering*, 122(5), 485-493.

Martelli, A., Clemente, P., Saitta, F., and Forni, M. (2012). "Recent worldwide application of seismic isolation and energy dissipation to steel and other materials structures and conditions for their correct use." *Behavior of Steel Structures in Seismic Areas*, *Stessa 2012*, eds. F. Mazzolani, and R. Herrera, Taylor & Francis Group, London, UK.

McGuire, R. K. (2004). "Seismic hazard and risk analysis." Monograph MNO-10, Earthquake Engineering Research Institute, Oakland, CA.

Mokha, A. S., Amin, N., Constantinou, M. C., and Zayas, V. (1996). "Seismic isolation retrofit of large historic building." *Journal of Structural Engineering*, 122(3), 298-308.

Mokha, A., Constantinou, M. C., and Reinhorn, A. M. (1988). "Teflon bearings in aseismic base isolation: Experimental studies and mathematical modeling." Report NCEER-88-0038, University at Buffalo, State University of New York, Buffalo, NY.

Morita, K., and Takayama, M. (2008). "Performance of seismic isolated buildings due to 2005 Fukuoka earthquake in Japan." *Proceedings, Fourteenth World Conference on Earthquake Engineering*, Beijing, China.

Mosqueda, G., Whittaker, A. S., and Fenves, G. L. (2004). "Characterization and modeling of Friction Pendulum bearings subjected to multiple components of excitation." *Journal of Structural Engineering*, 130(3), 433-442.

Naeim, F., and Kelly, J. M. (1999). "Design of seismic isolated structures: From theory to practice." John Wiley & Sons, New York, NY.

Nagarajaiah, S., and Sun, X. (2001). "Base-isolated FCC building: impact response in Northridge earthquake." *Journal of Structural Engineering*, 127(9), 1063-1075.

Nakashima, M., and Chulisp, P. (2003). "A partial view of Japanese post-Kobe seismic design and construction practices." *Earthquake Engineering and Engineering Seismology*, 4(1), 3-13.

National Institute of Standards and Technology (NIST) (2011). "Selecting and scaling earthquake ground motions for performing response-history analyses." NIST GCR 11-917-15, Gaithersburg, MD.

Nazin, V. V. (1978). "Buildings on gravitational seismoisolation system in Sevastopol." *Proceedings, VI Symposium on Earthquake Engineering*, Vol. I, Roorkee, India.

Oberkampf, W. L., and Barone, M. F. (2006). "Measures of agreement between computation and experiment: Validation metrics." *Journal of Computational Physics*, 217(1), 5-36.

Oberkampf, W. L., and Roy, C. J. (2010). "Verification and validation in scientific computing." Cambridge University Press, UK.

Pall, A. S., and Marsh, C. (1982). "Response of friction damped braced frames." *Journal of the Structural Division,* 108(ST6), 1313-1323.

Pacific Earthquake Engineering Research Center (PEER). (2014). Open System for Earthquake Engineering Simulation (Version 2.4.3) [Computer program], Berkeley, CA.

Ray, T. (2013). "Modeling of multi-dimensional inelastic and nonlinear elastic structural systems." PhD dissertation, University at Buffalo, State University of New York, Buffalo, NY.

Robinson, W. H. (1982). "Lead-rubber hysteretic bearings suitable for protecting structures during earthquakes." *Earthquake Engineering & Structural Dynamics*, 10(4), 593-604.

Roche, R. (2013). "Nuclear power plant testbeds for seismic isolation." *Personal Communication* to A. Whittaker.

Roy, C. J., McWherter-Payne, M. A., and Oberkampf, W. L. (2003). "Verification and validation for laminar hypersonic flowfields, part 1: verification." *AIAA Journal*, 41(10), 1934-1943.

Sarin, H., Kokkolaras, M., Hulbert, G., Papalambros, P., Barbat, S., and Yang, R. J. (2010). "Comparing time histories for validation of simulation models: Error measures and metrics." *Journal of Dynamic Systems, Measurement, and Control*, 132(6), 061401.

Sarkisian, M., Lee, P., Hu, L., Doo, C., Zayas, V., Constantinou, M., and Bachman, R. (2012). "Property verification of Triple Pendulum™ seismic isolation bearings." *Proceedings: 20th Analysis & Computational Specialty Conference, Structures Congress 2012*, March 29-31, Chicago, IL.

Sarlis, A. A., and Constantinou, M. C. (2013). "Model of Triple Friction Pendulum bearing for general geometric and frictional parameters and for uplift conditions." Report MCEER-13-0010, University at Buffalo, State University of New York, Buffalo, NY.

Schulz, T. L. (2006). "Westinghouse AP1000 advanced passive plant." *Nuclear Engineering and Design*, 236(14–16), 1547-1557.

Schwer, L. E. (2007). "Validation metrics for response histories: perspectives and case studies." *Engineering with Computers*, 23(4), 295-309.

Short, S., Hardy, G., Merz, K., and Johnson, J. (2007). "Program on technology innovation: validation of CLASSI and SASSI codes to treat seismic wave incoherence in soil-structure interaction (SSI) analysis of nuclear power plant structures." Report 1015111, Electric Power Research Institute, Palo Alto, CA.

Simo, J. C., and Hughes, T. J. (1998). "Computational inelasticity." Springer, New York, NY.

Sivaselvan, M. V., and Reinhorn, A. M. (2004). "Nonlinear structural analysis towards collapse simulation: a dynamical systems approach." Report MCEER-2004-05, University at Buffalo, State University of New York, Buffalo, NY.

Skinner, R. I., Robinson, W. H., and McVerry, G. H. (1991). "Seismic isolation in New Zealand." *Nuclear Engineering and Design*, 127(3), 281-289.

Syed, M. B., Patisson, L., Curtido, M., Slee, B., and Diaz, S. (2014). "The challenging requirements of the ITER anti seismic bearings." *Nuclear Engineering and Design*, 269(0), 212-216.

Tajirian, F. F., Kelly, J. M., and Aiken, I. D. (1990). "Seismic isolation for advanced nuclear power stations." *Earthquake Spectra*, 6(2), 371-401.

Tassios, T. P. (2009). "Seismic engineering contributions and trends to face future 1755 event." *The 1755 Lisbon Earthquake: Revisited*, Ed. A. Ansal, Springer.

Trifunac, M. D., and Brady, A. G. (1975). "A study on the duration of strong earthquake ground motion." *Bulletin of the Seismological Society of America*, 65(3), 581-626.

Tsai, C. S. (1997). "Finite element formulations for Friction Pendulum seismic isolation bearings." *International Journal for Numerical Methods in Engineering*, 40(1), 29-49.

Tsopelas, P., Okamoto, S., Constantinou, M. C., Ozaki, D., and Fujii, S. (1994a). "NCEER-Taisei Corporation research program on sliding seismic isolation systems for bridges: Experimental & analytical study of systems consisting of sliding bearings, rubber restoring force devices and fluid dampers." Report NCEER-94-0002, University at Buffalo, State University of New York, Buffalo, NY.

Tsopelas, P. C., Constantinou, M. C., and Reinhorn, A. M. (1994b). "3D-BASIS-ME: Computer program for nonlinear dynamic analysis of seismically isolated single and multiple structures and liquid storage tanks." Report NCEER-94-0010, University at Buffalo, State University of New York, Buffalo, NY.

United States Atomic Energy Commission (USAEC). (1973). "Design response spectra for seismic design of nuclear power plants." Regulatory Guide 1.60, Washington, D.C.

United States Department of Energy (DOE). (1994). "Natural phenomena hazards design and evaluation criteria for Department of Energy facilities." DOE-STD-1020-94, Washington, D.C.

United States Nuclear Regulatory Commission (USNRC). (2007a). "A performance-based approach to define the site-specific earthquake ground motion." Regulatory Guide 1.208, Washington, D.C.

United States Nuclear Regulatory Commission (USNRC). (2007b). "Standard review plan for the review of safety analysis reports for nuclear power plants." NUREG-0800, Washington, D.C.

United States Nuclear Regulatory Commission (USNRC). (2014). "Design response spectra for seismic design of nuclear power plants." Regulatory Guide 1.60, Washington, D.C.

United States Nuclear Regulatory Commission (USNRC). (2012). "Nuclear reactors", <http://www.nrc.gov/reading-rm/doc-collections/nuregs/staff/sr1350/v23/sr1350v23-sec-3.pdf>. (June 4, 2012).

United States Nuclear Regulatory Commission (USNRC). (2013). "Information digest." Report NUREG-1350, Washington D.C.

Wolff, E. (1999). "Frictional heating in sliding bearings and an experimental study of high friction materials." MS thesis, University at Buffalo, State University of New York, Buffalo, NY.

Wolff, E. (2003). "Experimental study of seismic isolation systems with emphasis on secondary system response and verification of accuracy of dynamic response history analysis methods." PhD dissertation, University at Buffalo, State University of New York, Buffalo, NY.

Wright, F. L. (1977). "An autobiography: Frank Llyod Wright." Horizon Press, New York, NY.

Zayas, V. A., Low, S. S., and Mahin, S. A. (1987). "The FPS earthquake resisting system experimental report." Report UCB/EERC-87/01, Earthquake Engineering Research Center, Berkeley, CA.

Zayas, V. A., Low, S., Mokha, A. S., and Imbsen, R. A. (2001). "Seismic isolation of Benicia-Martinez Bridge." *Proceedings, Structures Congress 2001*, American Society of Civil Engineers, May 21-23, Washington, D.C.

Zekioglu, A., Huseyin, D., and Erkus, B. (2009). "Performance-based seismic design of a large seismically isolated structure: Istanbul Sabiha Gokcen International Airport Terminal Building." *Proceedings, Structural Engineers Association of California 2009 Convention*, September, San Diego, CA.

APPENDIX A

GROUND MOTIONS USED IN THE VERIFICATION STUDIES

A.1 Description of Ground Motion Records

This section presents details on the ground motions used in the analyses presented in chapters 3 and 4, and Appendix B. These chapters deal with verification of assumptions in modeling Friction Pendulum™ (FP) bearings. Thirty ground motions scaled to match a geomean spectrum with a mean annual frequency of exceedance of 10^{-4} for the site of the nuclear power plant at Diablo Canyon in California were considered. These motions are expected to impose significant displacement demand on isolators, considering the proximity of the site to San Andreas and Hosgri faults. The procedure for selection and scaling the ground motions is described in Huang *et al.* (2009). Figure A-1 shows the response spectra of the spectrally matched ground motions in the three orthogonal directions. Figure A-2 shows the duration of strong shaking for the thirty ground motions estimated using the approach suggested by Trifunac and Brady (1975). The duration of strong shaking is the greater of the values computed in the two horizontal directions. Of the thirty ground motions considered, the minimum duration of strong shaking is for ground motion number 20 (=6.6 s) and the maximum duration is for ground motion number 29 (=28.2 s).

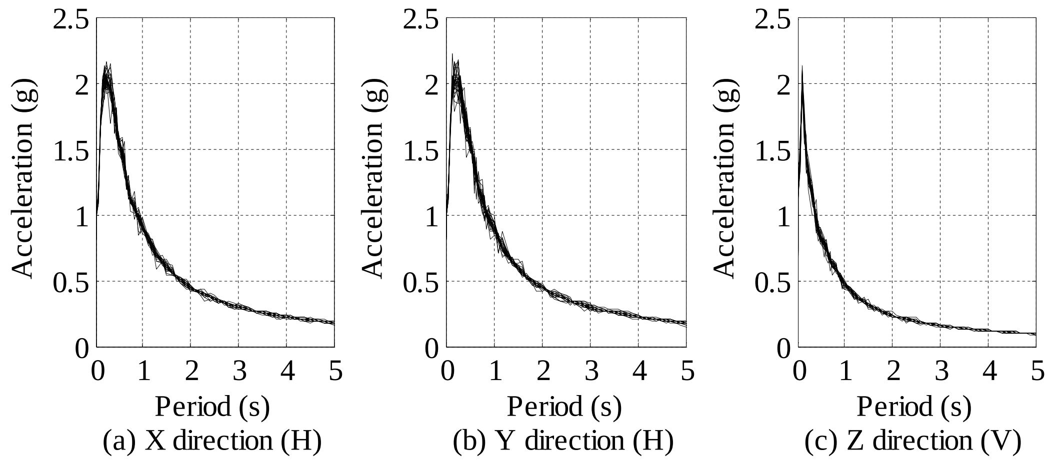

Figure A-1: Response spectral of the ground motions for Diablo Canyon Nuclear Generating Station

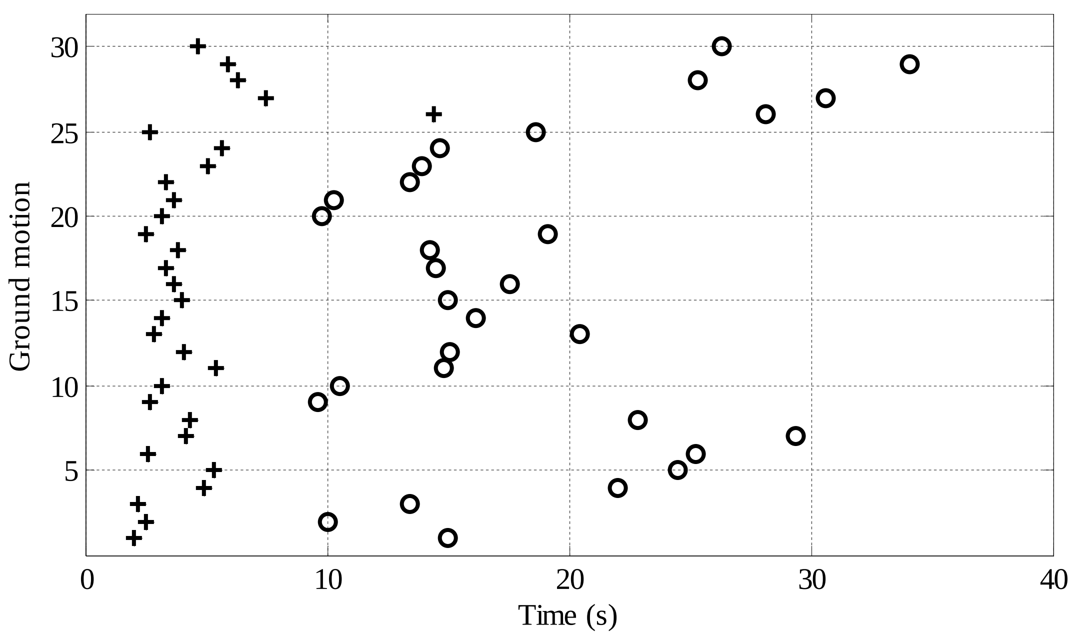

Figure A-2: Duration of shaking for the ground motions, + = beginning, o = end

APPENDIX B

EFFECT OF AN ASSUMPTION RELATED TO THE DEPENDENCE OF THE COEFFICIENT OF FRICTION ON THE VELOCITY OF SLIDING

B.1 Introduction

The relationship between the coefficient of sliding friction of a single concave Friction Pendulum™ (FP) bearing and the velocity of sliding at the interface is given in terms of the coefficients of friction at very small and very high velocities, and a rate parameter. The coefficient of friction at a high velocity is a function of axial pressure, while the coefficient does not vary significantly with change in the axial pressure on the bearing when measured at a small velocity (see Chapter 3). To decouple the influence of velocity and axial pressure on the coefficient of friction, an assumption is made that the coefficient of friction at a very small velocity also depends on the axial pressure and is half that at a very high velocity for all values of axial pressure. This appendix examines the effect of the assumption on the maximum displacement demand and the maximum absolute acceleration response and the maximum temperature at the sliding interface of an FP bearing subjected to earthquake ground motions of different intensities.

B.2 Analysis Scheme

A single FP bearing is considered for the analysis. The sliding period for the bearing is 3 s and the coefficient of friction measured at a reference axial pressure on the bearing p_o and at a high sliding velocity is 0.06. The radius of the area of contact is 200 mm. Two values of p_o, 10 MPa and 50 MPa, are considered, and masses associated with the slider are 128,000 kg and

640,000 kg, respectively. Thirty ground motions compatible with the geometric mean spectrum for the Diablo Canyon nuclear power generating site corresponding to a return period of 10,000 years (see Huang *et al.* (2009)) are considered. The details on the ground motions are given in the Appendix A. The ground motions are amplitude scaled to 100%, 50%, 25% and 5% of their original intensities.

Analyses were performed for two cases. Case 1 considers that the coefficient of friction at a small velocity $(\mu_{\min})$ remains constant as the axial pressure on the bearing changes. The coefficient of friction at a small velocity is fixed at one half that measured at a high velocity with the bearing subjected to a reference axial pressure of p_o. The variation in the coefficient of sliding friction $(\mu(v))$ with sliding velocity (v) is defined by the following equation

$$\mu(v) = \mu_{\max} \times \left(1 - \left(1 - \frac{\mu_{\min}}{\mu_{\max}}\right) e^{-av}\right) \tag{B-1}$$

where $\mu_{\max}$ is the coefficient of sliding friction measure at a very high velocity, a is the rate parameter which defines the rate of transition between $\mu_{\min}$ and $\mu_{\max}$. Case 2 assumes that the coefficient of friction at a very small velocity of sliding is half that measured at a high velocity at all values of axial pressure. With this assumption the above equation becomes

$$\mu(v) = \mu_{\max} \times \left(1 - 0.5e^{-av}\right) \tag{B-2}$$

The variation in $\mu_{\max}$ with axial pressure (p) is given by the following equation.

$$\mu_{\max} = \mu_{p=p_o} \times 0.7^{0.02(p-p_o)} \tag{B-3}$$

where $\mu_{p=p_o}$ is the coefficient of friction at a reference axial pressure of p_o measured at a high velocity of sliding. Pressure is measured in MPa units. Case 1 represents the "exact" coupled relationship between coefficient of friction, sliding velocity and axial pressure, whereas Case 2 represents an "approximate" relationship between the three quantities. The effect of temperature on the coefficient of sliding friction is ignored for the two cases. Panel (a) of Figure B-1 shows the variation in $\mu_{\min}$ and $\mu_{\max}$ with axial pressure for Case 1, with p_o set equal to 10 MPa. Panel (b) presents the curves for a p_o of 50 MPa. Panels (c) and (d) present the variation in $\mu_{\min}$ and $\mu_{\max}$ with axial pressure for Case 2, with p_o set equal to 10 MPa and 50 MPa, respectively.

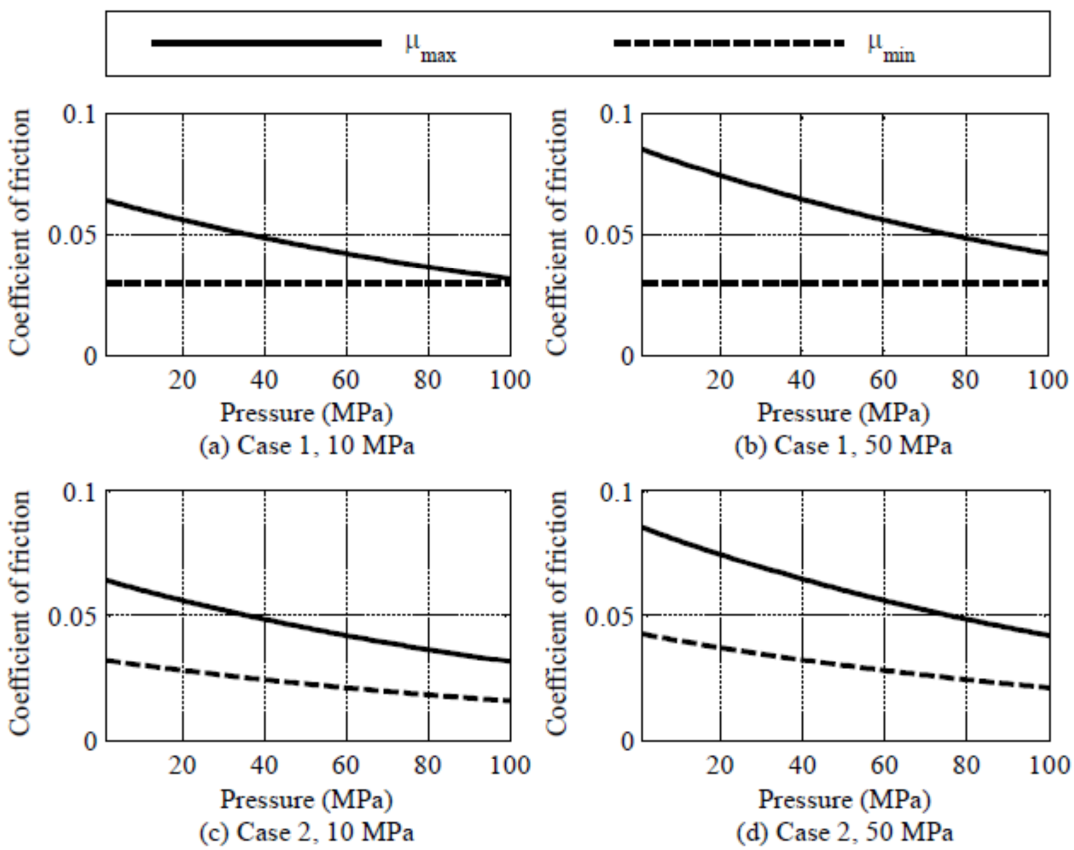

Figure B-1: "Exact" (Case 1) and "approximate" (Case 2) relationships between coefficient of friction and axial pressure on Friction Pendulum™ bearings

B.3 Results

Figure B-2 presents the differences in the maximum displacement of the FP bearing, when the friction at the sliding surface is defined using "exact" (Case 1) and "approximate" (Case 2) models. p_o set at 10 MPa for panel (a) and 50 MPa for panel (b). The maximum difference is smaller than 0.3 mm for all combinations of ground motions, shaking intensities and p_o. The peak displacement of the bearing with either 10 MPa or 50 MPa of static axial pressure subjected to the 30 ground motions scaled to 100% of their original intensities ranges between 260 mm and 690 mm. The analyses were also run for the FP bearing with the sliding period of 2 s. The maximum difference in the peak displacements due to the choice of the friction model across all combinations of static axial pressure, intensity level and ground motions is less than 0.15 mm, whereas the peak displacement of the bearing ranges between 310 mm and 570 mm, when the bearing is subjected to the 30 ground motions scaled to their original intensities irrespective of the level of axial pressure on the bearing. Hence, the choice of the "exact" or "approximate" relation between coefficient of sliding friction, axial pressure and sliding velocity does not considerably affect the maximum displacement response.

Figure B-3 presents the difference in peak acceleration response in a horizontal direction for the two approaches of defining the coefficient of friction for the bearing with the sliding period of 3 s. The maximum difference among all combinations of ground motions, intensities and p_o is less than 0.00015 g, which is very small compared to the peak acceleration of the original ground motions of about 1 g.

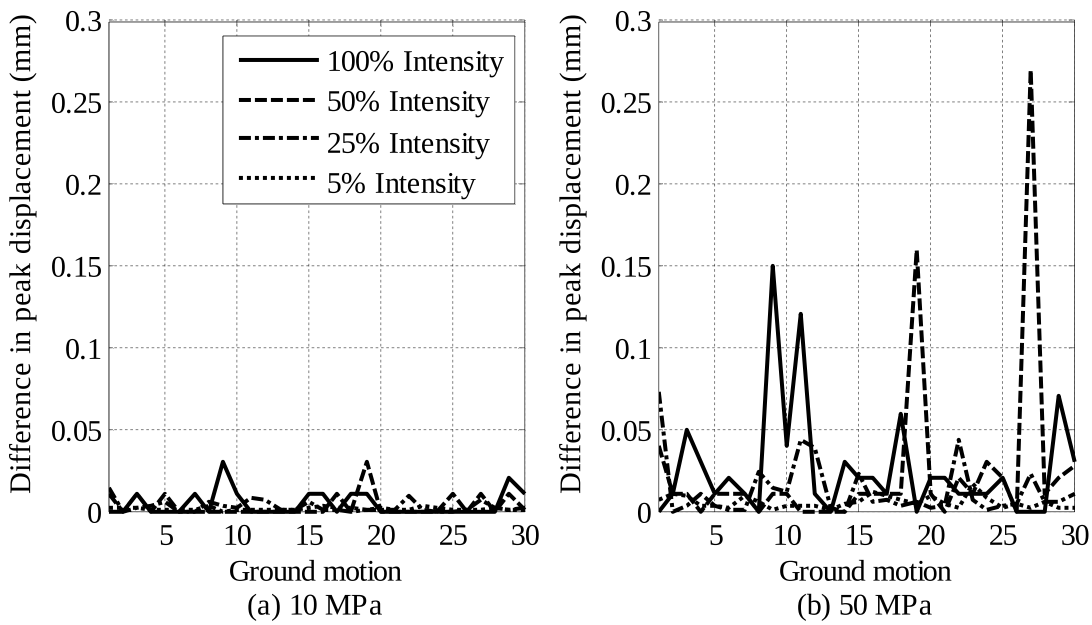

Figure B-2: Difference in the peak displacement for the FP bearing with sliding period of 3 s obtained using "exact" (Case 1) and "approximate" (Case 2) relationships between coefficient of friction, sliding velocity and axial pressure

B.4 Summary

Two methods to define the coupled influence of axial pressure and sliding velocity on the coefficient of sliding friction are considered. In the "exact" method the high-velocity coefficient of friction is expressed as a function of axial pressure, whereas the small-velocity coefficient of friction remains fixed. It is assumed in the "approximate" method that the small-velocity coefficient of friction is half the high-velocity coefficient of friction at all levels of axial pressure. An FP bearing with a sliding period of isolation of 3 s and coefficient of friction at a reference axial pressure of 0.06 was subjected to ground motions scaled to different intensities. The results show that for all combinations of p_o, ground motion and intensity levels, the difference in the maximum displacement response of bearing is smaller than 0.3 mm, and that in the maximum absolute acceleration response is smaller than 0.00015 g, when the two methods to define the coefficient of friction are considered.

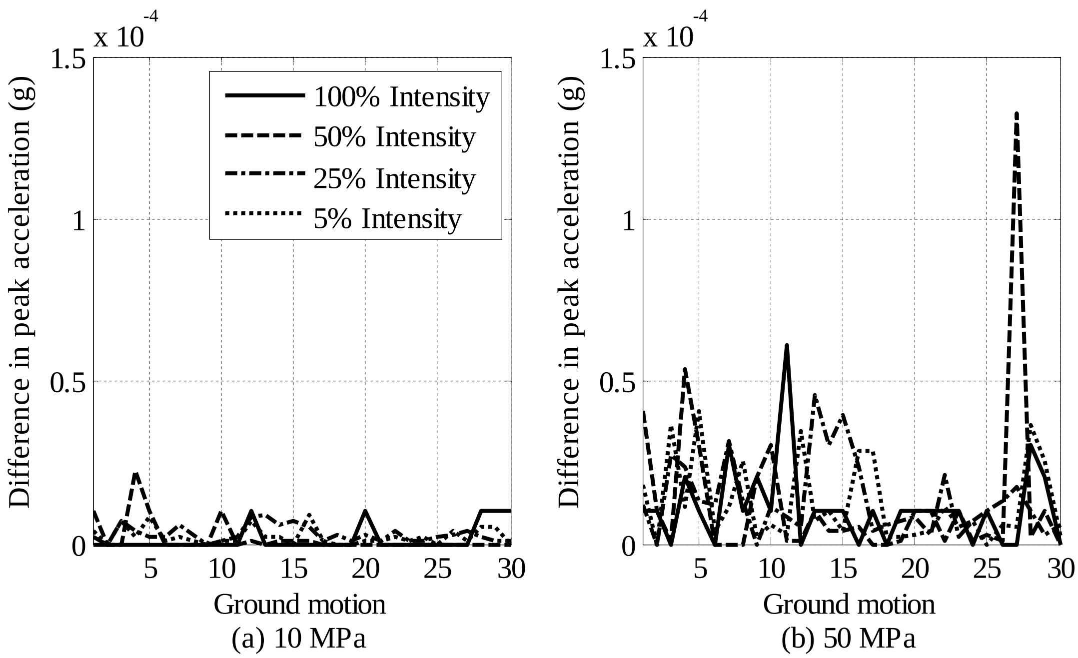

Figure B-3: Difference in the peak acceleration response of the FP bearing with a sliding period of 3 s in a horizontal direction obtained using "exact" (Case 1) and "approximate" (Case 2) relationships between coefficient of friction, sliding velocity and axial pressure

APPENDIX C

ACCELERATION OF THE SLIDER OF A FRICTION PENDULUM BEARING IN THE VERTICAL DIRECTION

C.1 Introduction

The motion of the slider across the sliding surface of a Friction Pendulum™ (FP) bearing is coupled in the vertical and horizontal directions. The total acceleration of the slider in the vertical direction at a given instant in time is the sum of the vertical ground acceleration and the vertical acceleration of the slider due to its motion relative to the sliding surface. The relative contributions to the total acceleration of the slider in the vertical direction are studied in this appendix.

C.2 Modeling and Analysis Scheme

FP bearings with a sliding period of oscillation 2 s, 3 s and 4 s, a reference coefficient of friction 0.06 and a reference pressure (= static axial pressure) of 50 MPa were subjected to the 30 ground motions of Appendix A. Friction on the sliding surface was described by the Coulomb model. The radius of the area of contact at the sliding surface was 200 mm. The entire mass associated with the static axial load was considered to be active in the three orthogonal directions. Mass proportional damping of 2% of critical was assigned to the system with the proportionality constant updated at every step of analysis based on the instantaneous fundamental frequency of the system.

C.3 Vertical Acceleration of the Slider

There are two components of the vertical acceleration of the slider of an FP bearing, namely, 1) the acceleration due to relative motion at the sliding surface, and 2) the ground acceleration; see Figure C-1. This section presents a method to estimate the acceleration of the slider relative to the sliding surface.

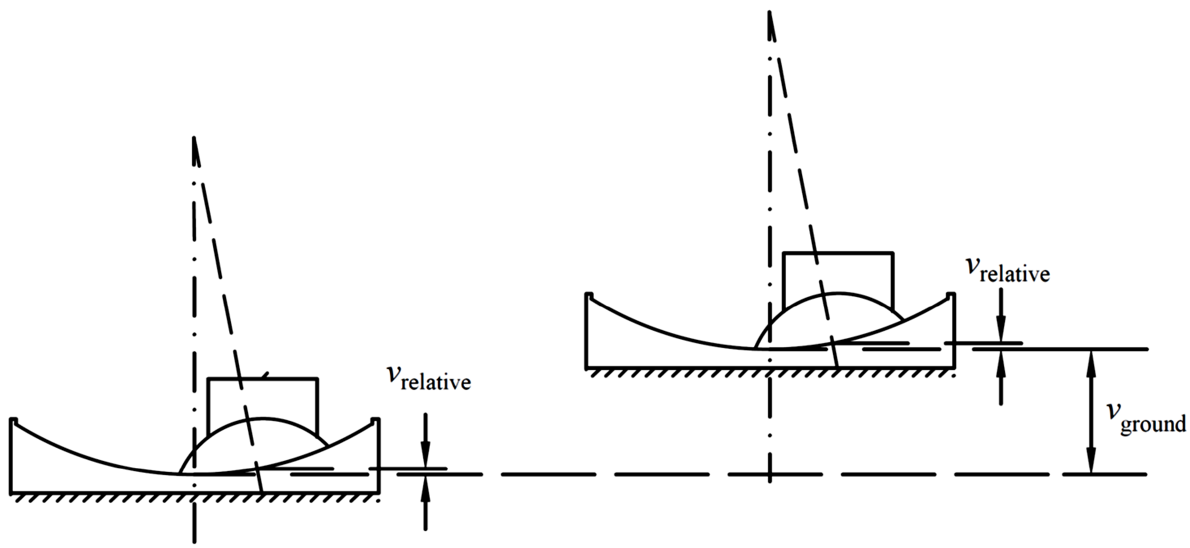

(a) Translation of slider relative to sliding surface, v_{relative}

(b) Ground translation, v_{ground}, and v_{relative}

Figure C-1: Vertical translation of the slider of an FP bearing

An estimate of the vertical displacement of the slider relative to its position at the beginning of the motion, $v_{\text{relative},t}$, at the time t is obtained using the following expression.

$$v_{\text{relative},t} = R - \sqrt{\left(R^2 - u^2_{\text{horizontal},t}\right)} \tag{C-1}$$

where $u_{\text{horizontal},t}$ is the horizontal displacement of the slider relative to the center of sliding surface at time t and R is the radius of curvature of the sliding surface. The velocity in the vertical direction, $\dot{v}_{\text{relative},t}$, at time t is calculated as the change in vertical displacement of the slider in time interval Δt.

$$\dot{v}_{\text{relative},t} = \frac{v_{\text{relative},t} - v_{\text{relative},t-\Delta t}}{\Delta t} \tag{C-2}$$

where all parameters were defined previously. The acceleration of the slider relative to the sliding surface, $\ddot{v}_{\text{relative},t}$, at time t is calculated similarly:

$$\ddot{v}_{\text{relative},t} = \frac{\dot{v}_{\text{relative},t} - \dot{v}_{\text{relative},t-\Delta t}}{\Delta t} \tag{C-3}$$

where all parameters were defined previously. The total acceleration history of the slider is obtained by summing the relative acceleration and ground acceleration histories.

C.4 Effect on Total Vertical Acceleration Histories

Figure C-2a presents the maximum and minimum values of the vertical ground acceleration (VGA) histories and the vertical total acceleration (VTA) histories of the slider of the 2 s FP bearing subjected to the 30 sets of ground motions. Also plotted in the panel are values for the vertical acceleration history of the slider relative (VRA) to the sliding surface. Panels (b) and (c) present information for 3 s and 4 s bearings, respectively.

The peak values of VRA decrease for bearings with longer sliding periods. The greatest absolute value of the peak VRA (= 6.5 m/s^2 or 0.7 g) is observed for the 2 s bearing subjected to ground motion number 1 (GM1). Although this value of VRA is comparable to the corresponding peak VGA of 6.8 m/s^2, the peak VTA (= 7.0 m/s^2) is not significantly affected by the relative acceleration of the slider because the peaks do not occur simultaneously. Figure C-3 presents the ground, relative and total acceleration histories for the 2 s bearing and GM1, for which the peak values occur at 3.39 s, 3.825 s and 3.77 s, respectively.

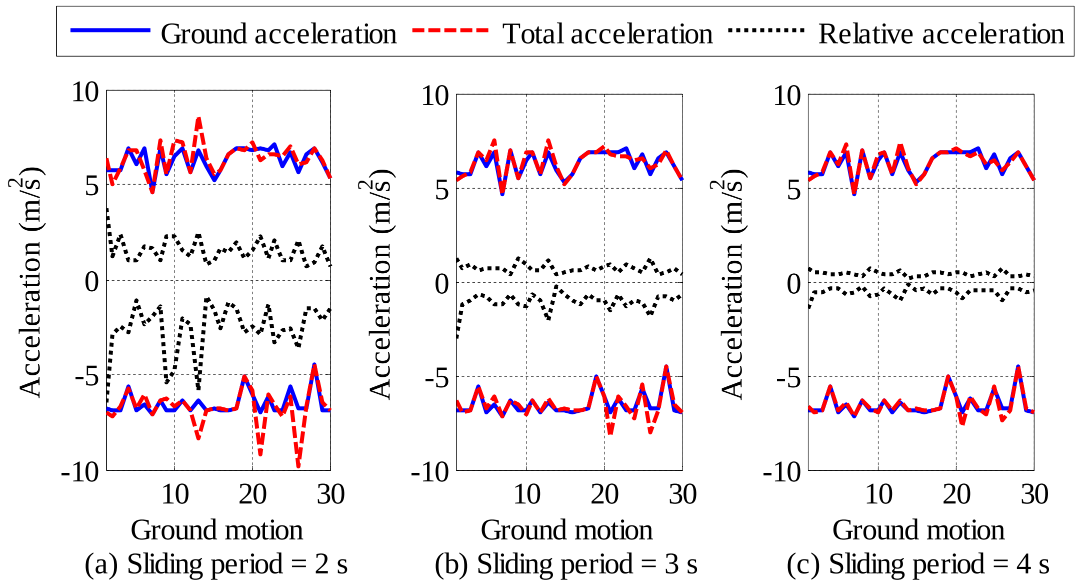

Figure C-2: Maximum and minimum values of the vertical components of the ground acceleration histories, total acceleration histories of the slider, and acceleration histories of the slider relative to the sliding surface

The vertical relative acceleration (VRA) influences VTA significantly for some values of sliding period and some ground motions. For example, for the 2 s bearing, the peak values of VGA and VTA are 7.0 m/s^2 and 9.2 m/s^2, respectively, when the bearing is subjected to GM21, and 6.7 m/s^2 and 9.8 m/s^2, respectively, when the bearing is subjected to GM26. The peak VTA for the two cases is greater by 30% and 50%, respectively, than the corresponding peak VGA. However, averaged across all ground motions, the percentage difference is relatively small: 7% for the 2 s bearing, 4% for the 3 s bearing, and 2% for the 4 s bearing.

Figure C-4 plots the data of Figure C-2 computed using three time steps, namely, 0.001 s, 0.002 s, and 0.005 s. The choice of time step has no influence on the results, for the values considered.

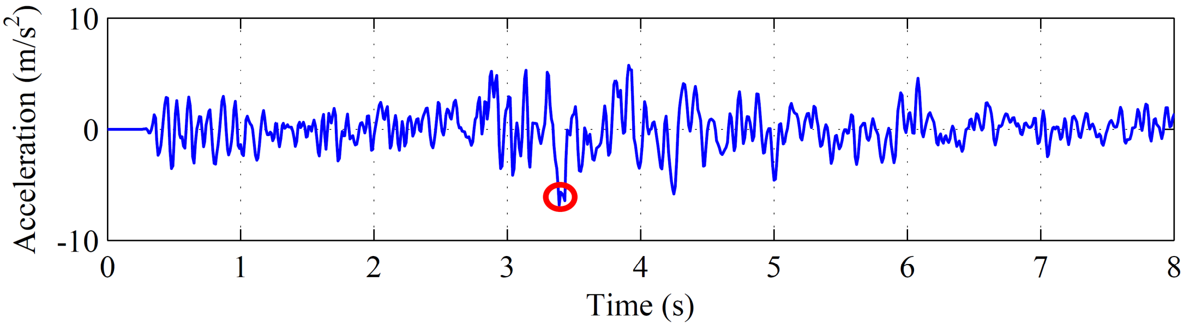

(a) Ground acceleration

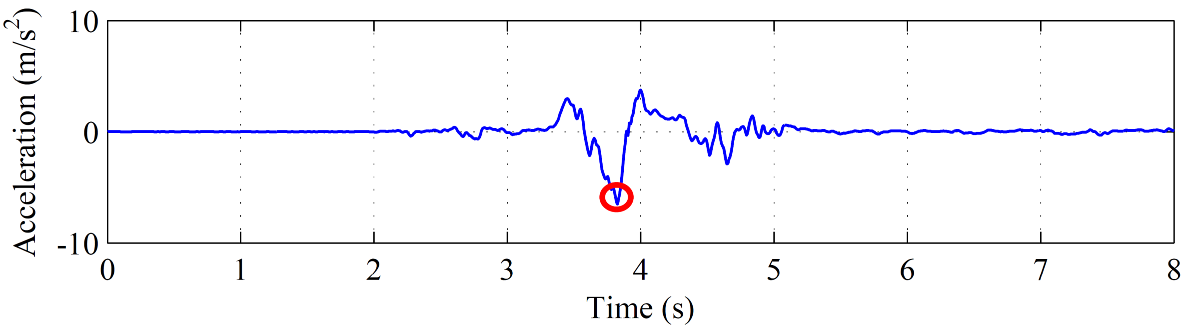

(b) Relative acceleration

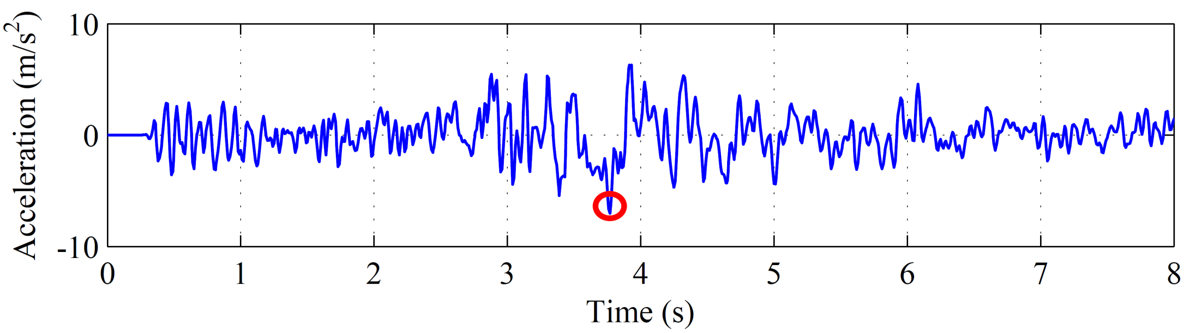

(c) Total acceleration

Figure C-3: Histories of vertical ground acceleration, acceleration of the slider relative to the sliding surface and the total acceleration of the slider of the FP bearing with a sliding period of 2 s subjected to GM1

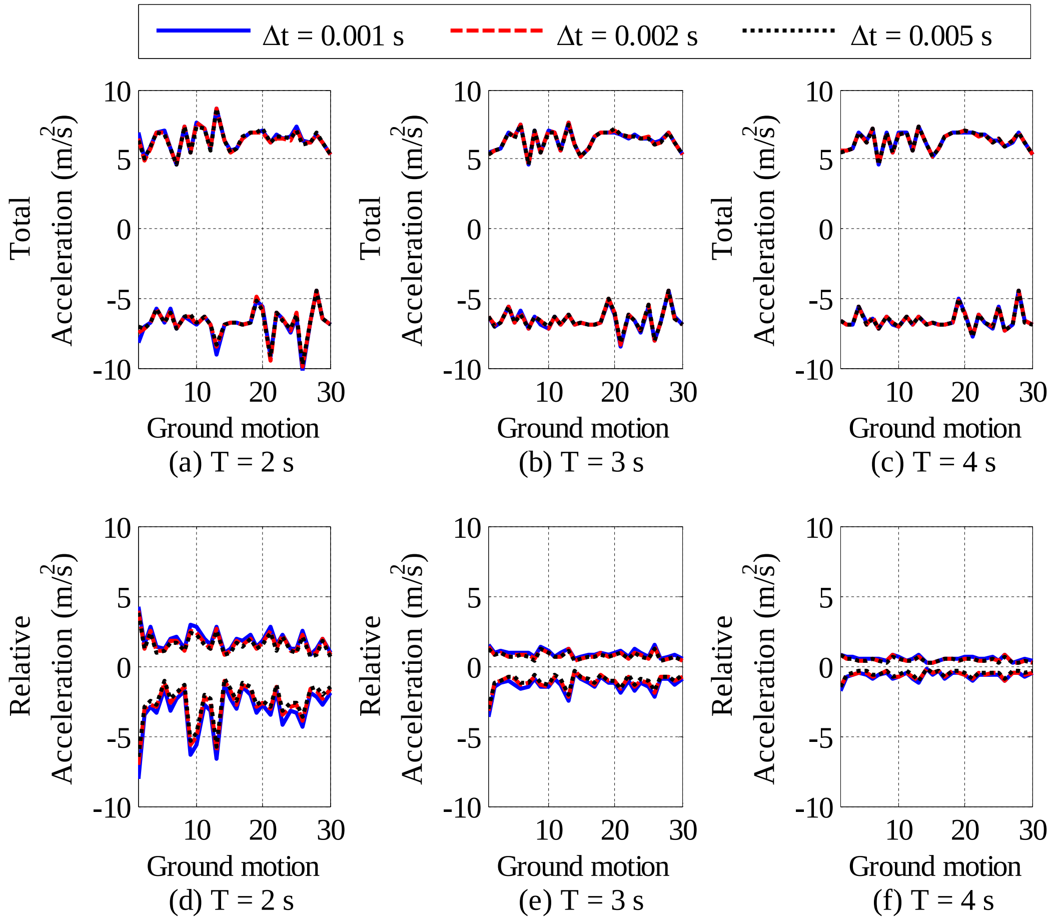

Figure C-4: Influence of analysis time step on peak accelerations

C.5 Effect on Vertical Floor Spectra

The maximum value of VRA was observed for the 2 s bearing subjected to GM1. The peak VTA was most influenced by VRA for the 2 s bearing subjected to GM21 and GM26, as noted previously. The vertical relative acceleration most influenced the peak VTA for the 3 s and 4 s bearings subjected to GM21 and GM26. Figure C-5 presents response spectra for VGA, VRA and VTA for GM1, GM21 and GM26, and sliding periods of 2 s, 3 s and 4 s. The floor spectral ordinates for VTA are comparable to those for VGA, indicating that the vertical motion of slider relative to the sliding surface does not significantly influence the floor spectral ordinates in the vertical direction.

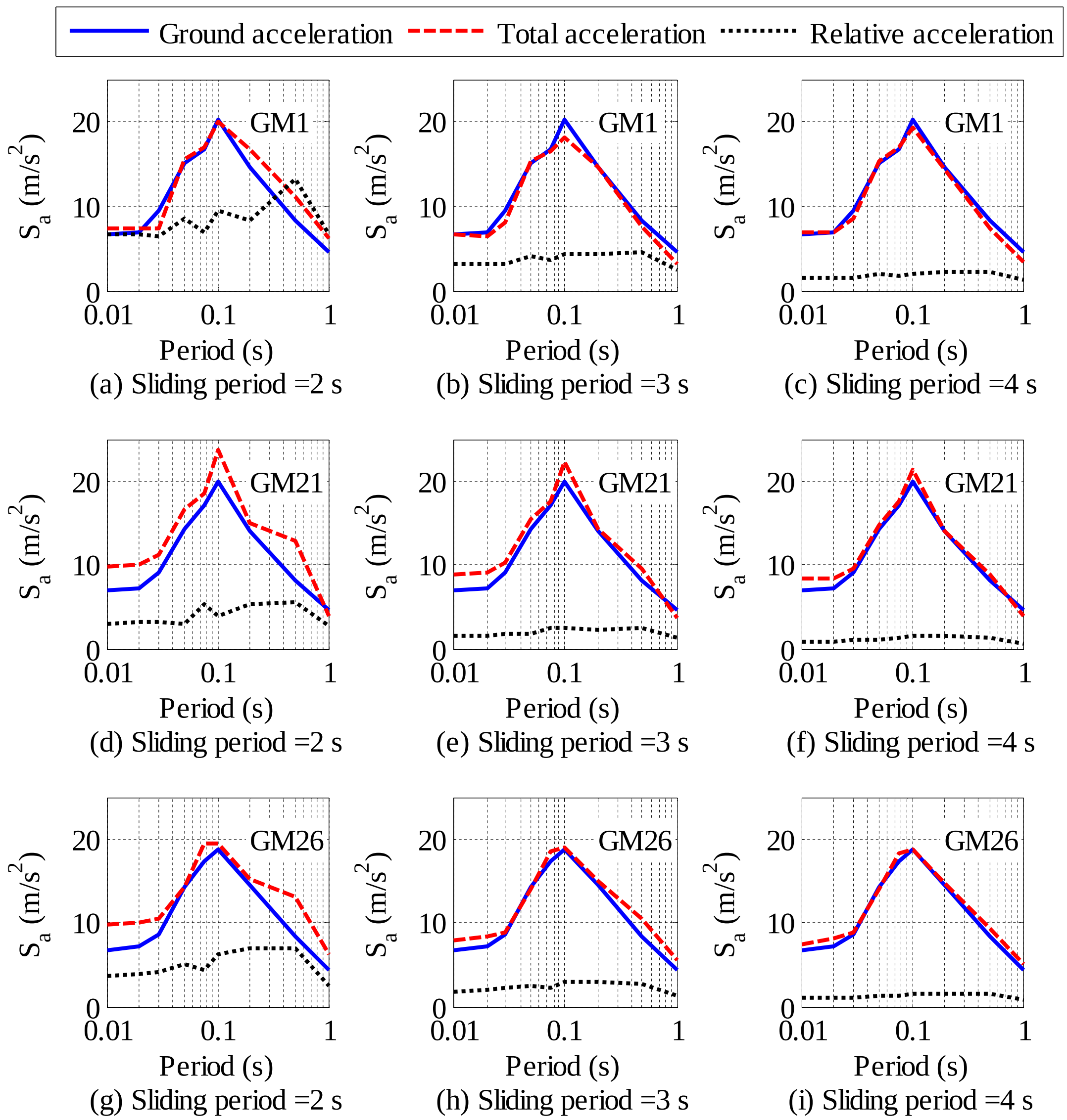

Figure C-5: Response spectra for the vertical components of ground acceleration histories, total acceleration histories of the slider, and acceleration histories of the slider relative to the sliding surface

C.6 Summary

Friction Pendulum™ (FP) bearings with sliding periods of 2 s, 3 s and 4 s, a Coulomb-type coefficient of friction of 0.06, and a static axial pressure of 50 MPa were subjected to the 30 ground motions of Appendix A. The peak values of vertical ground acceleration, vertical acceleration of the slider relative to the sliding surface and total vertical acceleration of the slider were computed. The acceleration of the slider relative to the sliding surface does not significantly influence the total peak acceleration of the slider or vertical response spectral ordinates, especially for sliding periods of 3 s and longer.

APPENDIX D

RELATIVE VERTICAL DISPLACEMENTS IN FRICTION PENDULUM™ SEISMIC ISOLATION SYSTEMS

D.1 Introduction

A Friction Pendulum™ (FP) bearing undergoes vertical and horizontal displacement during earthquake shaking due to the curvature of the sliding surface. The vertical displacement is a function of the translation and rotation in the isolation system, and the location of the bearing in the isolation system. The relative vertical displacement between adjacent FP bearings will produce internal forces in the supported superstructure. Unlike elastomeric bearings that shorten when displaced laterally, the overall height of the FP bearing increases with horizontal displacement.

This appendix presents a study on the vertical displacements in isolation systems comprised of uniformly spaced FP bearings. A procedure to compute the displacement in individual bearings of an isolation system subjected to translation and rotation is presented. Two isolation systems with different geometric properties are subjected to differing levels of translational and rotational displacements. Vertical displacements in individual bearings are reported.

D.2 Procedure to Compute Change in Elevation of a Bearing

An isolation system with FP bearings installed in a square pattern is considered for this study. Panel (a) of Figure D-1 shows the undeformed isolation system. Panels (b) and (c) present the isolation system after translation and rotation, respectively. This section describes the procedure to compute the increase in height of the bearings in the isolation system subjected to combined translation and rotation.

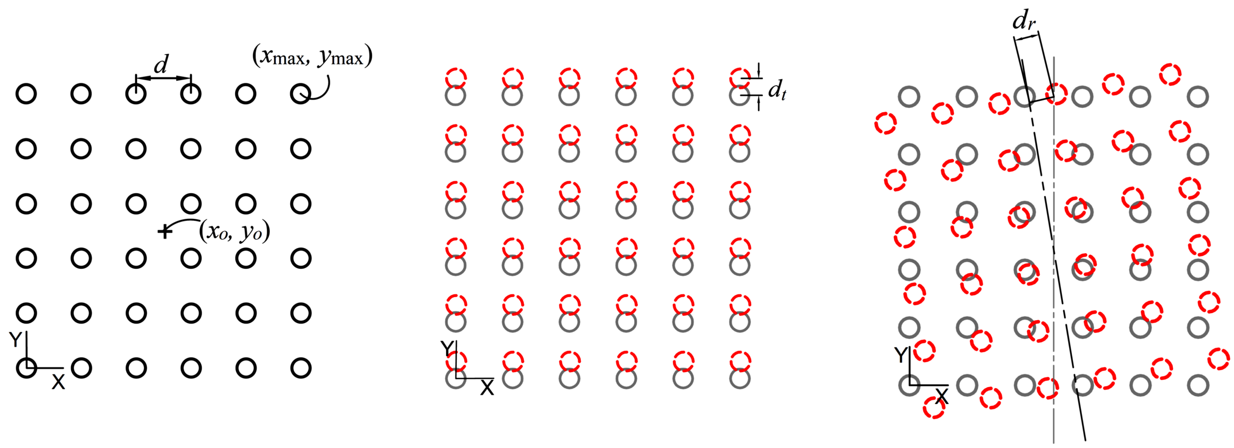

(a) Undeformed (b) After translation (c) After rotation

Figure D-1: Schematic of the seismic isolation system in different configurations

The angle of rotation, θ_{rot}, corresponding to a perimeter displacement, d_r, (panel (c) of Figure D-1) in the isolation system can be given by

$$\theta_{rot} = \tan^{-1}\left(\frac{|d_r|}{y_{\max} - y_o}\right) \approx \frac{|d_r|}{y_{\max} - y_o} \tag{D-1}$$

where $|d_r|$ is the magnitude of d_r, y_o is the Y coordinate of the geometrical center of the undeformed isolation system and $y_{\max}$ is the Y coordinate of the center of bearings in the farthest row of the undeformed system (see panel (a) of Figure D-1). Assume r_{orient} is the distance between the center of the sliding surface of a bearing with coordinates (x, y) and the geometrical center of the isolation system with coordinates (x_o, y_o). The angle, θ_{orient}, between the line joining the center of the sliding surface of an FP bearing to the geometrical center of isolation system and the Y axis is

$$\theta_{orient} = \tan^{-1}\left|\frac{x - x_o}{y - y_o}\right| \tag{D-2}$$

Following rotation of the isolation system, the relative horizontal displacement between the slider and the sliding surface of the bearing is the product of r_{orient} and θ_{rot}. The resulting changes in the X and Y coordinates (Δx_{rot} and Δy_{rot}) of the slider are given by the following expressions:

$$\Delta x_{rot} = -sign(y - y_o)(r_{orient} \times \theta_{rot})\cos(\theta_{orient}) \tag{D-3}$$

$$\Delta y_{rot} = sign(x - x_o)(r_{orient} \times \theta_{rot})\sin(\theta_{orient}) \tag{D-4}$$

where $sign(a) = 1$ if $a > 0$ and $sign(a) = -1$ if $a < 0$. All other parameters are defined previously.

If Δx_{trans} and Δy_{trans} are the change in the X and Y coordinates, respectively, of the slider of the bearing due to translation, then the new coordinate of the center of the slider of the bearing (x_{new}, y_{new}) is given by

$$x_{new} = x + \Delta x_{trans} + \Delta x_{rot} \tag{D-5}$$

$$y_{new} = y + \Delta y_{trans} + \Delta y_{rot} \tag{D-6}$$

The next step is to compute the rise (or increase in height) at the center of the slider, Δz, of an FP bearing with sliding period, T, and radius of curvature, R. If the coordinates of center of its sliding surface are (x, y) and that of the center of its slider are (x_{new}, y_{new}), then Δz is given by

$$\Delta z = R - \sqrt{R^2 - (x_{new} - x)^2 - (y_{new} - y)^2} \tag{D-7}$$

where the radius of curvature R is related to the sliding period T by

$$R = \frac{T^2}{4\pi^2} g \tag{D-8}$$

where g is the acceleration due to gravity.

D.3 Analysis Results

This section describes the geometrical properties of isolation systems and individual bearings, the translation and rotation imposed on the isolation systems, and results of the analysis. The closest distance d between two bearings (see Figure D-1a) is 6 m. Each row and column of the system has a total of 17 bearings, for a total of 289 bearings in an area of 96 m × 96 m, measured center to center of the bearings at the corners of the isolation system. Two values of sliding period are considered: 2 s and 4 s. Table D-1 lists the translations and rotations imposed on the isolation system, and points to results, presented in terms of increase in height, by figure number. The magnitudes of imposed translations and rotations are selected so that the peak displacement of an individual bearing of the system is greater than $0.2R$, which is a widely accepted limit on the displacement capacity of an FP bearing (see Constantinou *et al.* (2011)). Substantial amount of rotations are considered $(d_r = 0.5d_t)$, despite the fact that this type of isolation system does not experience significant rotational motion during earthquake-induced shaking because the centers of gravity and lateral stiffness tend to coincide.

Table D-1: Translation and rotation imposed on isolation systems

Case	Isolation System	Sliding period (s)	Radius of curvature (m)	Translation (m)		Rotation	Results
				X	Y		
1	1	2	1	0	0.200	d_r = 0.000 m	Figure D-2
2	1	2	1	0	0.000	d_r = 0.100 m	Figure D-3
3	1	2	1	0	0.200	d_r = 0.100 m	Figure D-4
4	2	4	4	0	0.600	d_r = 0.000 m	Figure D-5
5	2	4	4	0	0.000	d_r = 0.300 m	Figure D-6
6	2	4	4	0	0.600	d_r = 0.300 m	Figure D-7

The height of all bearings in an isolation system rises by the same amount when only translation is imposed. For the system with 2 s isolators subjected to a translation of 0.200 m (Case 1, see Figure D-2), the increase in height is 0.020 m. The increase is 0.046 m for the 4 s isolator subjected to a translation of 0.600 m (Case 4, see Figure D-5).

Figure D-3 shows the increase in the height of the bearings in the 2 s isolation system subjected to a rotation described by d_r = 0.100 m (Case 2). There is no increase in height at the geometrical center of the system. The bearings at the corners of the 96 m × 96 m isolation system increase in height by 0.010 m. The maximum relative change in height between adjacent bearings is observed at the corners of the isolation system. The maximum gradient between two adjacent bearings is 0.002 m over a horizontal distance of 8.500 m or 1/4250. Figure D-6 shows the results for 4 s isolation system subjected to rotation described by d_r = 0.300 m (Case 5). The maximum gradient between two adjacent bearings is 6 mm over a distance of 8.500 m or 1/1416.

For all the cases considered, the maximum increase in height is 0.116 m (Case 6) and the maximum gradient between two adjacent bearings is 1/667.

D.4 Summary

Seismic isolation bearings change in height when they are displaced laterally: elastomeric bearings shorten and the FP bearings rise. Basemats and diaphragms installed atop isolation systems could be structurally challenged if the relative change in height between adjacent bearings is significant.

Single concave FP isolation systems with plan dimensions of 96 m × 96 m and a 6 m spacing between the bearings (on center) were subjected to combinations of translation and torsion, noting that torsional response of FP isolation systems is generally small because the lateral stiffness of an FP isolator is a function of the supported mass. Friction Pendulum isolators are often sized such that the maximum lateral displacement, due to any combination of system translation and rotation, is less than $0.2R$, where R is the radius of curvature of the sliding surface. Effectively, this limits the displacement capacity of a 2 s isolation system to 0.200 m and a 4 s isolation system to 0.800 m.

For this study, the maximum lateral displacement imposed on the 2 (4) s isolation system was 0.300 (0.900) m: values greater than $0.2R$. The maximum increase in height in all of the isolators and displaced configurations considered was 0.116 m, the maximum relative difference in height between adjacent bearings was 0.009 m, and the maximum vertical gradient was 1/667. Given that the relative vertical displacement and gradient would be experienced in only beyond design basis shaking, and their small magnitudes, basemat or diaphragm design need not consider the relative change in height of the adjacent FP bearings.

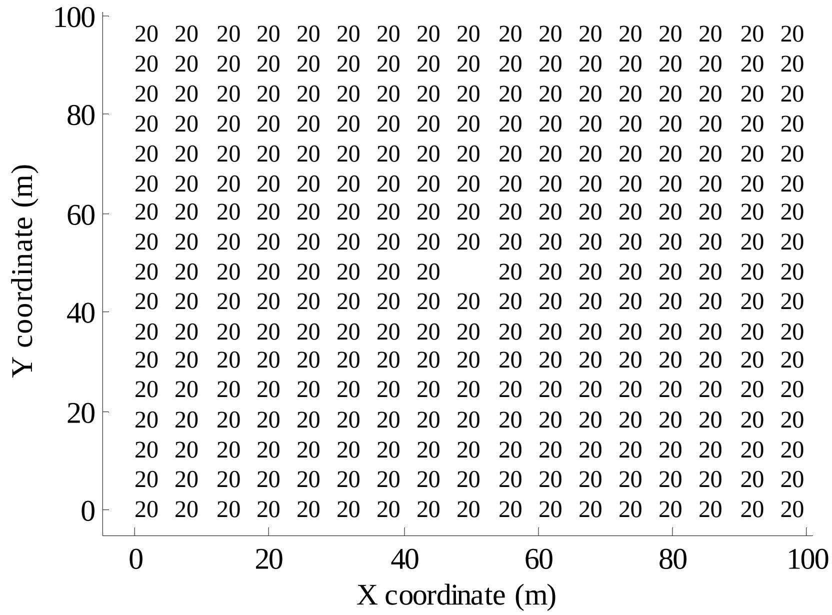

Figure D-2: Elevation in bearings (mm) of the isolation system comprising FP bearings with a sliding period of 2 s subjected to a translation of 0.200 m (Case 1)

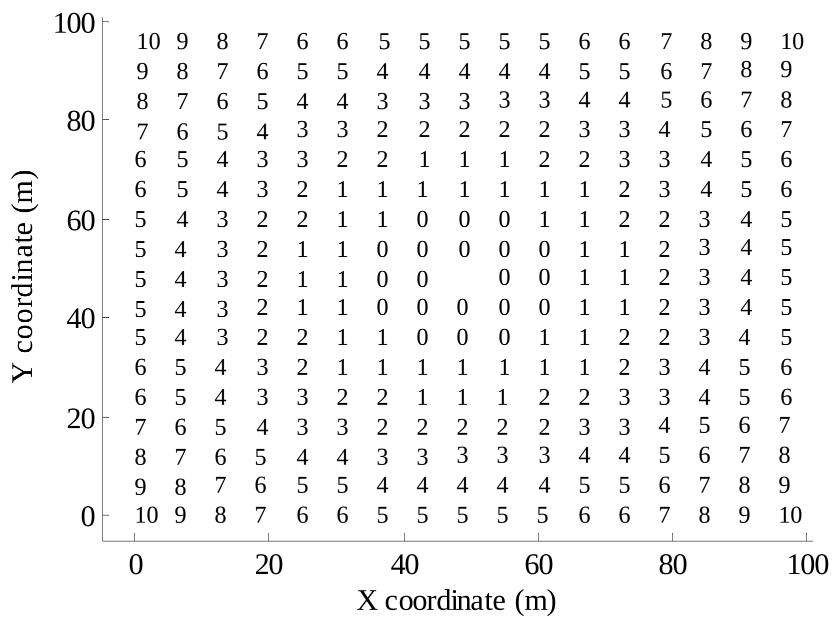

Figure D-3: Elevation in bearings (mm) of the isolation system comprising FP bearings with a sliding period of 2 s subjected to a rotation of 0.100 m (Case 2)

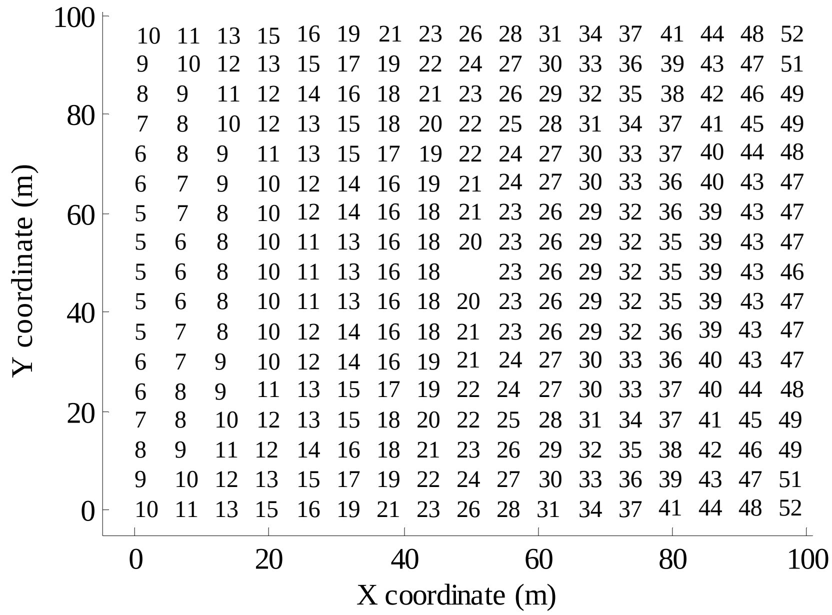

Figure D-4: Elevation in bearings (mm) of the isolation system comprising FP bearings with a sliding period of 2 s subjected to a translation of 0.200 m and a rotation of 0.100 m (Case 3)

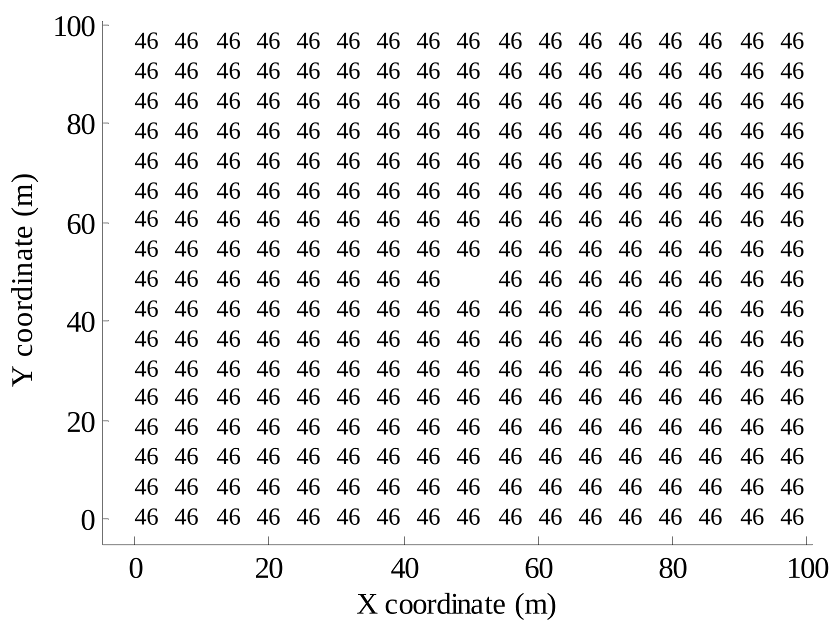

Figure D-5: Elevation in bearings (mm) of the isolation system comprising FP bearings with a sliding period of 4 s subjected to a translation of 0.600 m (Case 4)

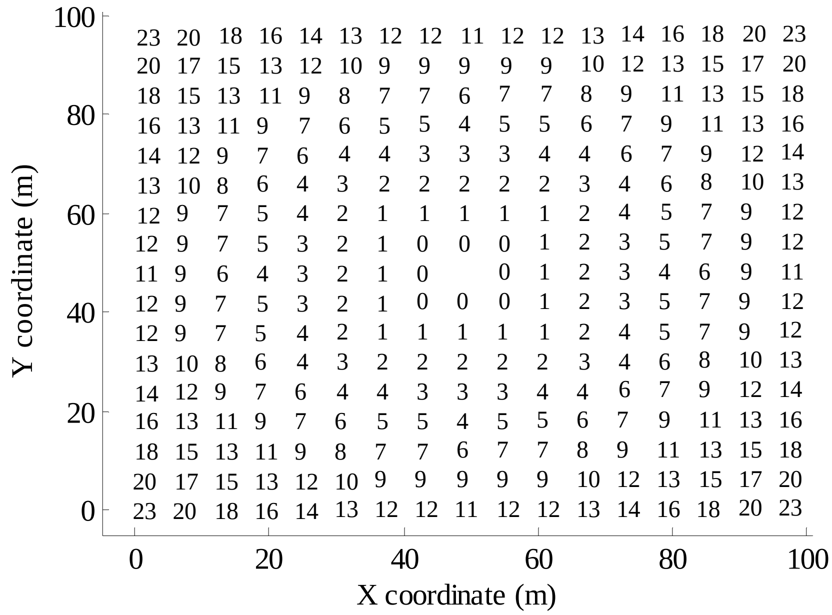

Figure D-6: Elevation in bearings (mm) of the isolation system comprising FP bearings with a sliding period of 4 s subjected to a rotation of 0.300 m (Case 5)

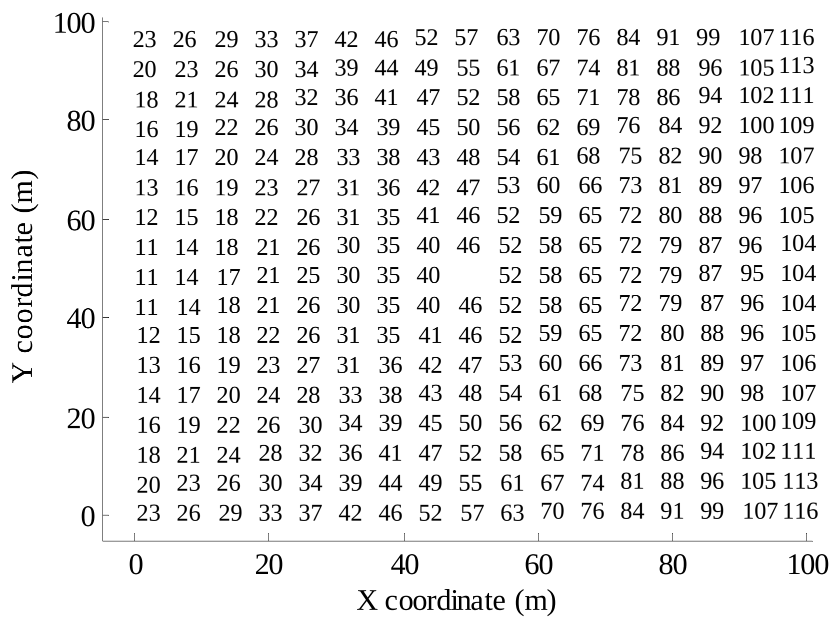

Figure D-7: Elevation in bearings (mm) of the isolation system comprising FP bearings with a sliding period of 4 s subjected to a translation of 0.600 m and a rotation of 0.300 m (Case 6)

APPENDIX E

SEED GROUND MOTIONS FOR RESPONSE-HISTORY ANALYSIS

E.1 Introduction

Three representations of seismic hazard at the site of Diablo Canyon Nuclear Generating Station (DCNGS) are considered in Chapter 5: uniform hazard spectrum (UHRS), conditional mean spectrum (CMS), and conditional spectra (CS). This appendix presents the lists of seed ground motions that were spectrally matched to the three representations of the 10,000-year seismic hazard at the DCNGS site. The seed motions are downloaded from the Pacific Earthquake Engineering Research (PEER) Center, Next Generation Attenuation (NGA) database from the webpage http://peer.berkeley.edu/peer_ground_motion_database (accessed on June 15, 2014).

E.2 Lists of Seed Motions

Table E-1 lists the 30 seeds scaled to the UHRS. Table E-2 lists the 30 seed motions spectrally matched to the CMS with conditioning periods of 2 s, 3 s and 4 s. Table E-3 (E-4, E-5) lists the set of 30 seed ground motions spectrally matched to the set of 30 CS with a conditioning period of 2 s (3 s, 4 s).

Table E-1: Set of seed motions to be scaled to a uniform hazard spectrum representing the seismic hazard at Diablo Canyon for a return period of 10,000 years

Sl No	NGA Number	Event	Year	Magnitude	Epicentral Distance (km)
1	72	San Fernando	1971	6.6	24
2	77	San Fernando	1971	6.6	12
3	80	San Fernando	1971	6.6	39
4	143	Tabas	1978	7.4	55
5	284	Irpinia	1980	6.9	33
6	285	Irpinia	1980	6.9	23
7	286	Irpinia	1980	6.9	23
8	292	Irpinia	1980	6.9	30
9	763	Loma Prieta	1989	6.9	29
10	765	Loma Prieta	1989	6.9	29
11	2704	Chi-Chi	1999	6.2	30
12	810	Loma Prieta	1989	6.9	16
13	828	Cape Mendocino	1992	7.0	5
14	957	Northridge	1994	6.7	64
15	989	Northridge	1994	6.7	15
16	994	Northridge	1994	6.7	25
17	1011	Northridge	1994	6.7	19
18	1012	Northridge	1994	6.7	14
19	1021	Northridge	1994	6.7	50
20	1050	Northridge	1994	6.7	20
21	1051	Northridge	1994	6.7	20
22	1078	Northridge	1994	6.7	15
23	1091	Northridge	1994	6.7	38
24	1161	Kocaeli	1999	7.5	47
25	1165	Kocaeli	1999	7.5	5
26	1485	Chi-Chi	1999	7.6	78
27	1107	Kobe	1995	6.9	24
28	1509	Chi-Chi	1999	7.6	19
29	1633	Manjil	1990	7.4	40
30	3548	Loma Prieta	1989	6.9	20

Table E-2: Set of seed motions to be scaled to conditional mean spectra representing the seismic hazard at Diablo Canyon for a return period of 10,000 years

Sl No	NGA Number	Event	Year	Magnitude	Epicentral Distance (km)
1	1051	Northridge	1994	6.7	20
2	1508	Chi-Chi	1999	7.6	21
3	68	San Fernando	1971	6.6	39
4	1511	Chi-Chi	1999	7.6	16
5	180	Imperial Valley	1979	6.5	28
6	1115	Kobe	1995	6.9	42
7	3282	Chi-Chi	1999	6.3	71
8	2704	Chi-Chi	1999	6.2	30
9	187	Imperial Valley	1979	6.5	49
10	184	Imperial Valley	1979	6.5	27
11	1118	Kobe	1995	6.9	39
12	3269	Chi-Chi	1999	6.3	57
13	2457	Chi-Chi	1999	6.2	26
14	879	Landers	1992	7.3	44
15	285	Irpinia	1980	6.9	23
16	159	Imperial Valley	1979	6.5	3
17	1510	Chi-Chi	1999	7.6	21
18	737	Loma Prieta	1989	6.9	40
19	1107	Kobe	1995	6.9	24
20	1633	Manjil	1990	7.4	40
21	1528	Chi-Chi	1999	7.6	45
22	1144	Gulf of Aqaba	1995	7.2	93
23	802	Loma Prieta	1989	6.9	27
24	169	Imperial Valley	1979	6.5	34
25	3512	Chi-Chi	1999	6.3	56
26	183	Imperial Valley	1979	6.5	28
27	1244	Chi-Chi	1999	7.6	32
28	3286	Chi-Chi	1999	6.3	101
29	3264	Chi-Chi	1999	6.3	108
30	292	Irpinia	1980	6.9	30

Table E-3: Set 1 of seed motions scaled to 30 conditional spectra representing the seismic hazard at Diablo Canyon for a return period of 10,000 years

Sl No	NGA Number	Event	Year	Magnitude	Epicentral Distance (km)	Scaled to conditional spectrum number
1	1202	Chi-Chi	1999	7.6	44	1
2	1051	Northridge	1994	6.7	20	2
3	1787	Hector Mine	1999	7.1	27	3
4	884	Landers	1992	7.3	42	4
5	180	Imperial Valley	1979	6.5	28	5
6	1115	Kobe	1995	6.9	42	6
7	3282	Chi-Chi	1999	6.3	71	7
8	1762	Hector Mine	1999	7.1	48	8
9	187	Imperial Valley	1979	6.5	49	9
10	6	Imperial Valley	1940	7.0	13	10
11	1118	Kobe	1995	6.9	39	11
12	3269	Chi-Chi	1999	6.3	57	12
13	2457	Chi-Chi	1999	6.2	26	13
14	755	Loma Prieta	1989	6.9	31	14
15	285	Irpinia	1980	6.9	23	15
16	1209	Chi-Chi	1999	7.6	55	16
17	1078	Northridge	1994	6.7	15	17
18	737	Loma Prieta	1989	6.9	40	18
19	1503	Chi-Chi	1999	7.6	27	19
20	2458	Chi-Chi	1999	6.2	34	20
21	1528	Chi-Chi	1999	7.6	45	21
22	806	Loma Prieta	1989	6.9	42	22
23	802	Loma Prieta	1989	6.9	27	23
24	169	Imperial Valley	1979	6.5	34	24
25	3512	Chi-Chi	1999	6.3	56	25
26	183	Imperial Valley	1979	6.5	28	26
27	143	Tabas	1978	7.3	55	27
28	3286	Chi-Chi	1999	6.3	101	28
29	3264	Chi-Chi	1999	6.3	108	29
30	292	Trinidad	1980	7.2	77	30

Table E-4: Set 2 of seed motions scaled to 30 conditional spectra representing the seismic hazard at Diablo Canyon for a return period of 10,000 years

Sl No	NGA Number	Event	Year	Magnitude	Epicentral Distance (km)	Scaled to conditional spectrum number
1	1009	Northridge	1994	6.7	20	1
2	881	Landers	1992	7.3	21	2
3	179	Imperial Valley	1979	6.5	27	3
4	68	San Fernando	1971	6.6	39	4
5	1511	Chi-Chi	1999	7.6	16	5
6	173	Imperial Valley	1979	6.5	26	6
7	1611	Duzce	1999	7.1	13	7
8	2899	Chi-Chi	1999	6.2	45	8
9	1107	Kobe	1995	6.9	24	9
10	1100	Kobe	1995	6.9	47	10
11	1540	Chi-Chi	1999	7.6	38	11
12	1488	Chi-Chi	1999	7.6	43	12
13	184	Imperial Valley	1979	6.5	27	13
14	1508	Chi-Chi	1999	7.6	21	14
15	3319	Chi-Chi	1999	6.3	97	15
16	879	Landers	1992	7.3	44	16
17	1633	Manjil	1990	7.4	40	17
18	1144	Gulf of Aqaba	1995	7.2	93	18
19	3271	Chi-Chi	1999	6.3	80	19
20	159	Imperial Valley	1979	6.5	3	20
21	170	Imperial Valley	1979	6.5	29	21
22	754	Loma Prieta	1989	6.9	31	22
23	1545	Chi-Chi	1999	7.6	26	23
24	1509	Chi-Chi	1999	7.6	19	24
25	174	Imperial Valley	1979	6.5	29	25
26	1111	Kobe	1995	6.9	9	26
27	1077	Northridge	1994	6.7	22	27
28	800	Loma Prieta	1989	6.9	46	28
29	1084	Northridge	1994	6.7	13	29
30	1183	Chi-Chi	1999	7.6	69	30

Table E-5: Set 3 of seed motions scaled to 30 conditional spectra representing the seismic hazard at Diablo Canyon for a return period of 10,000 years

Sl No	NGA Number	Event	Year	Magnitude	Epicentral Distance (km)	Scaled to conditional spectrum number
1	1201	Chi-Chi	1999	7.6	46	1
2	2705	Chi-Chi	1999	6.2	35	2
3	1013	Northridge	1994	6.7	12	3
4	3317	Chi-Chi	1999	6.3	50	4
5	3302	Chi-Chi	1999	6.3	84	5
6	3275	Chi-Chi	1999	6.3	62	6
7	2752	Chi-Chi	1999	6.2	28	7
8	527	N. Palm Springs	1986	6.1	6	8
9	2655	Chi-Chi	1999	6.2	24	9
10	1487	Chi-Chi	1999	7.6	86	10
11	2495	Chi-Chi	1999	6.2	29	11
12	2897	Chi-Chi	1999	6.2	43	12
13	1085	Northridge	1994	6.7	14	13
14	1330	Chi-Chi	1999	7.6	137	14
15	885	Landers	1992	7.3	122	15
16	1460	Chi-Chi	1999	7.6	167	16
17	985	Northridge	1994	6.7	28	17
18	1636	Manjil	1990	7.4	84	18
19	2462	Chi-Chi	1999	6.2	39	19
20	1110	Kobe	1995	6.9	52	20
21	1161	Kocaeli	1999	7.5	47	21
22	826	Cape Mendocino	1992	7.0	53	22
23	1521	Chi-Chi	1999	7.6	7	23
24	3281	Chi-Chi	1999	6.3	71	24
25	882	Landers	1992	7.3	32	25
26	2884	Chi-Chi	1999	6.2	48	26
27	185	Imperial Valley	1979	6.5	20	27
28	2699	Chi-Chi	1999	6.2	28	28
29	3272	Chi-Chi	1999	6.3	89	29
30	549	Chalfant Valley	1986	6.2	20	30

APPENDIX F

RISK CALCULATIONS FOR SEISMICALLY ISOLATED SDC 5 NUCLEAR STRUCTURES DESIGNED PER ASCE STANDARD 4

F.1 Introduction

The annual frequencies of unacceptable performance of isolation systems designed and tested per the forthcoming seismic isolation NUREG (Kammerer *et al.*, forthcoming) are calculated and presented in Chapter 6 for eight sites of nuclear facilities across the United States. This appendix presents companion calculations for isolation systems analyzed and tested per the forthcoming edition of ASCE Standard 4 (ASCE, forthcoming) for a Seismic Design Category 5 safety-related nuclear structure.

F.2 Annual Frequency of Unacceptable Performance of an Isolation System

F.2.1 ASCE Standard 4 for isolated nuclear structures

The US Department of Energy (DoE) uses ASCE Standard 4 and ASCE Standard 43 (ASCE, 2005) for seismic analysis and design of safety-related nuclear structures, which include nuclear power plants. Department of Energy-regulated nuclear power plants fall into Seismic Design Category (SDC) 5, which specifies the hazard exceedance frequency for the design earthquake (= 1×10^{-4}) and the target performance goal (1×10^{-5}).

Section 1.3 of ASCE 43-05 writes that the target performance can be achieved by satisfying two criteria, namely, 1) Less than about a 1% probability of unacceptable performance for the design basis earthquake (DBE) ground motion, and 2) Less than about a 10% probability of unacceptable performance for a ground motion equal to 150% of the DBE ground motion. In ASCE 43-05, the DBE ground motion is defined in terms of a design response spectrum with ordinates equal to the product of the uniform hazard response spectrum (UHRS) at the specified mean annual frequency of exceedance and a design factor. For a nuclear power plant, the UHRS is specified at a mean annual frequency of exceedance of 1×10^{-4}.

The forthcoming edition of ASCE Standard 4 (likely ASCE 4-14) will include a section on seismic isolation. The target performance goal of 1×10^{-5} for a seismically isolated SDC 5 safety-related nuclear structure is achieved using the two criteria listed above, where unacceptable performance of the isolation system is conservatively measured in terms of insufficient capacity of individual isolators, identical to Chapter 6. Herein, the design factor is assumed to be 1.0, which is confirmed through risk calculations.

The following sections present fragility curves and the calculation of annual frequency of unacceptable performance based on isolators being designed and tested per the provisions of the forthcoming edition of ASCE Standard 4 (ASCE, forthcoming), namely, there be 90+% confidence that the isolators can support axial loads at a horizontal displacement equal to the clearance to the stop, CS, where CS is no less than the 90th percentile horizontal displacement for 150% DBE shaking. The risk calculations are repeated for isolators tested with 90+% confidence at 90th percentile horizontal displacement for 200% DBE shaking. Similar to Chapter 6 (and confirmed in Chapter 7), the *median* fragility curves are developed assuming that the 90th percentile displacement for 150% (200%) DBE shaking is equal to the median displacement at 1.1 times 150% (200%) DBE shaking. The hazard curves plotted in Figure 6-7 are used for the risk calculations.

F.2.2 Isolators tested at 90th percentile displacement for 150+% DBE shaking

Figure F-1 presents fragility curves for isolators tested with 90% confidence at median displacement for 165% DBE shaking (or 90th percentile displacement for 150% DBE shaking) with no hard stop. Figure F-2 presents the disaggregation of risk for log standard deviation, β, equal to 0.01 at Diablo Canyon and North Anna. Figures F-3 and F-4 present fragility curves for isolators tested at median displacement for 165% DBE shaking with 95% and 99% confidence, respectively. Figure F-5 presents fragility curves for isolators tested with 90% confidence at median displacement for 187.5% DBE shaking. The annual frequencies of unacceptable performance for isolators with fragility curves of Figures F-1, F-3, F-4 and F-5 are listed in Tables F-1, F-2, F-3 and F-4, respectively. A small reduction in risk is achieved if the confidence level on isolator performance is increased from 90% to 99% (see Tables F-1 and F-3). The meaningful reduction in risk is achieved at 90% confidence if the isolators are tested (and perform acceptably) at the median displacement for 187.5% DBE shaking (compare the risk numbers in Tables F-1 and F-4). The annual frequencies of unacceptable performance reported in Tables F-1 through F-4 are greater than 1×10^{-5} for all bar one combinations considered here: a hard stop is most likely needed in isolated SDC 5 nuclear structures to achieve the target performance goal.

The above calculations were performed assuming no hard stop was present. The fragility curves of Figures F-1, F-3, F-4 and F-5 are truncated at the specified level of confidence to acknowledge the presence of a hard stop at the given median displacement in Figures F-6, F-7, F-8 and F-9, respectively. The annual frequencies of unacceptable performance for the hard-stop-enabled fragility curves of Figures F-6 through F-9 are listed in Tables F-5 through

F-8, respectively. All of the listed frequencies are considerably smaller than 1×10^{-5} for all combinations of site, confidence, test displacement and log standard deviation. A value of the design factor equal to 1.0 is appropriate for seismically isolated SDC 5 nuclear structures, provided the effects of vertical shaking do not control the design. A substantial reduction in risk is achieved if the confidence on isolator performance is increased from 90% to 99% (see Tables F-5 and F-7).

Chapter 6 identified the ratio of 5% damped spectral demand of 100,000- to 10,000-year earthquake shaking for periods of 1 s and 2 s and eight sites of nuclear facilities in the United States. The ratio is smaller in regions of high seismic hazard (e.g., = 2 for Diablo Canyon at 2 s, see Table 6-3) than low seismic hazard (e.g., = 3.1 for North Anna at 2 s, see Table 6-3). The seismic isolation NUREG requires bearings to be tested at the 90th percentile displacement for 100,000-year shaking (and not a constant fraction of DBE shaking). The variation in risk across the eight sites, assuming no hard stop is present, is relatively small: 4.7×10^{-6} for Diablo Canyon to 7.3×10^{-6} for North Anna (see Table 6-7, $\beta = 0.05$). The greatest difference in risk is by a factor of 1.5, which increases to 2.5 when the beyond design basis earthquake is presented as a contact fraction (=1.5) of design basis earthquake shaking: 14.7×10^{-6} for Diablo Canyon to 34.8×10^{-6} for North Anna (see Table F-1, $\beta = 0.05$).

F.2.3 Isolators tested at 90th percentile displacement for 200% DBE shaking

The 2 s seismic demand at the site of Diablo Canyon is greater by more than a factor of 2 than the demand at the other sites considered in this report, with the exception of Los Alamos: see Table 6-3. Isolators with capacity just sufficient for Diablo Canyon would have excess capacity at all other sites, leading to the question, “By how much is risk reduced if the beyond design basis shaking is assumed to be 2.0 times design basis shaking?". This question is addressed below.

The fragility curves and risk disaggregation plots of Figures F-1, F-2, F-3, F-4, F-6, F-7 and F-8 are re-generated for isolators tested with 90%, 95% and 99% confidence at median displacement for 220% (= 1.1 times 200%: converting 90th percentile displacements to median displacements, as described previously) DBE shaking, and are plotted in Figures F-10 through F-16, respectively. The corresponding annual frequencies of unacceptable performance are listed in Tables F-9 through F-14, respectively. The frequencies are greater than 1×10^{-5} for five of the eight sites if a hard stop is not provided and considerably less than 1×10^{-5} for all eight sites if a hard stop is provided. (The risk numbers in the last column of Tables F-9 through F-11 are similar to those in the corresponding column of Tables 6-7 through 6-9, because 2.0 times DBE shaking for Diablo Canyon is approximately equal to shaking with a mean annual frequency of exceedance of 1×10^{-5}: the seismic isolation NUREG definition of beyond design basis shaking.)

The increase in shaking intensity from 150% DBE to 200% DBE for the purpose of establishing displacements for testing isolators leads to a significant reduction in risk, with the greatest reductions for the sites of highest seismic hazard (e.g., Diablo Canyon, a factor of between 3.5 and 4) and the smallest reductions for the sites of lowest seismic hazard (e.g., North Anna, a factor of approximately 1.7). The significant difference in the slope on the seismic hazard curves for sites of low and high seismicity is the reason why the risk reductions are not uniform for a consistent increase in the shaking intensity from 150% DBE to 200% DBE. However, the annual frequency of unacceptable performance is greater than the target performance goal of 1×10^{-5} for five of the eight sites. A hard stop would still be needed for these five sites if 200% DBE shaking rather than 150% DBE shaking is used to define beyond design basis shaking. There is no practical risk-based benefit to increasing the shaking intensity used to define beyond design basis shaking.

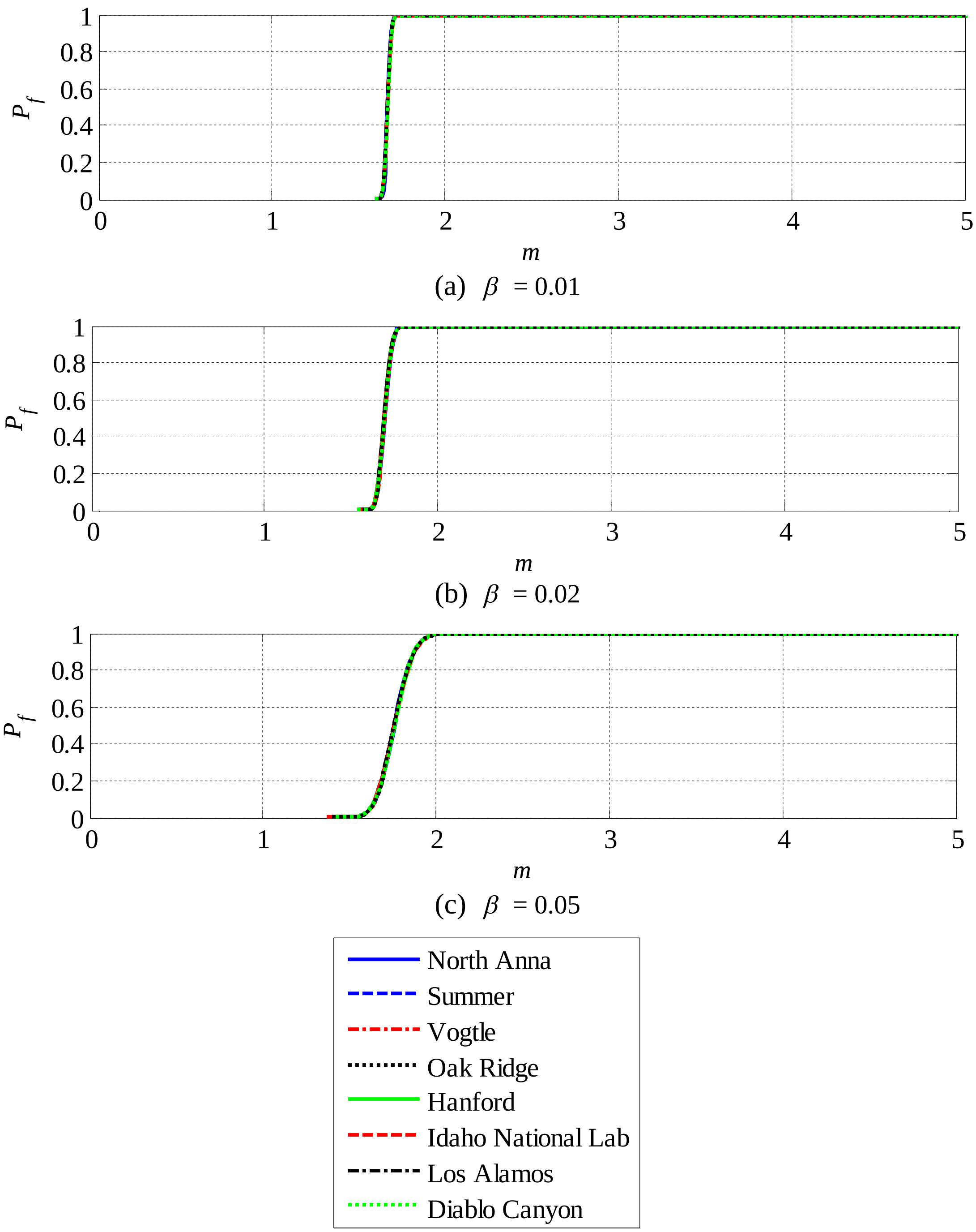

Figure F-1: Probability of unacceptable performance, P_f, of individual isolator units for 90% confidence at median displacement for 165% DBE shaking plotted against multiples, *m*, of UHRS shaking with MAFE of 10^{-4}, without a hard stop

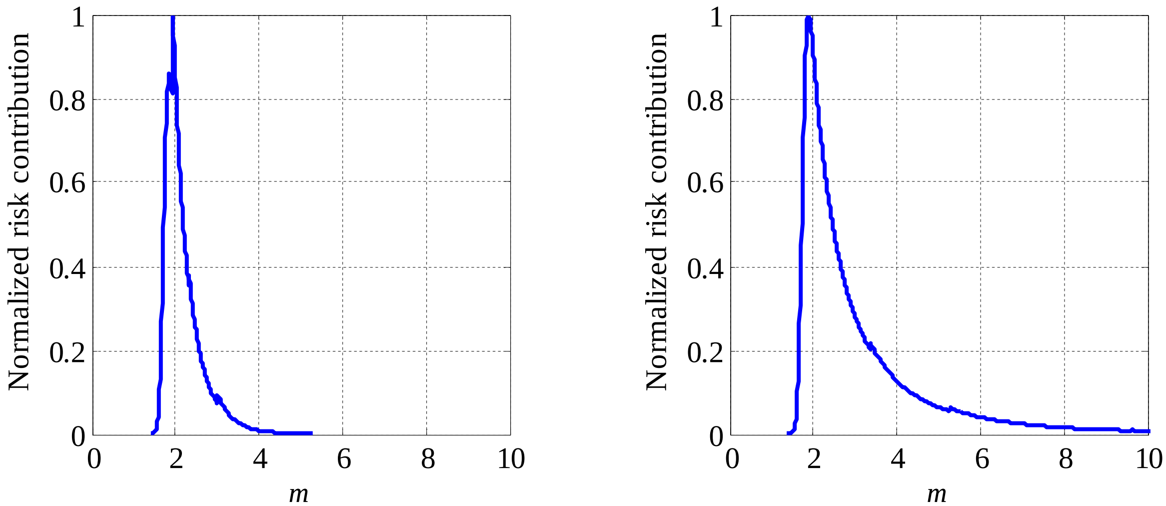

(a) Diablo Canyon (b) North Anna

Figure F-2: Disaggregation of risk corresponding to Figure F-1(a) for two sites

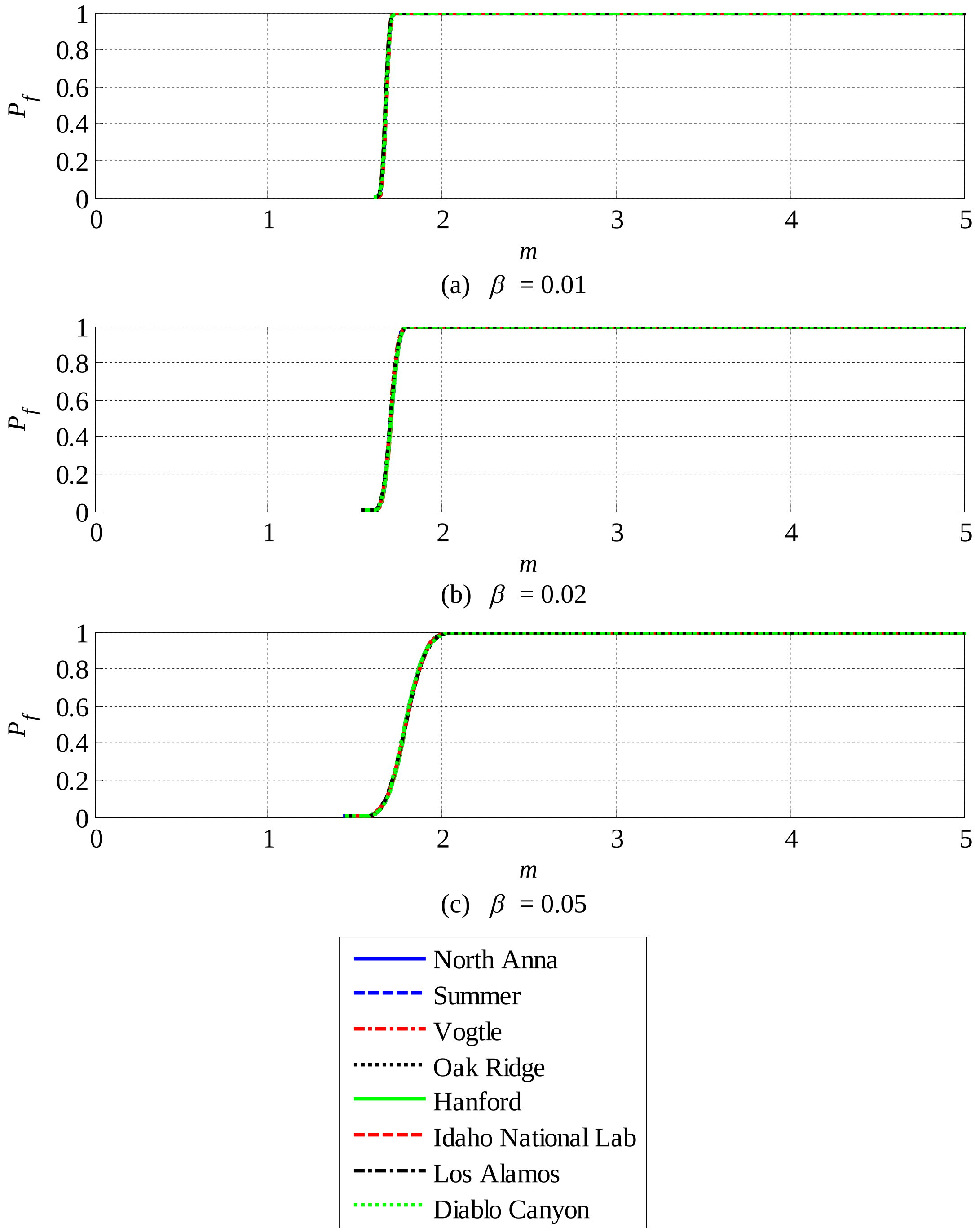

Figure F-3: Probability of unacceptable performance, P_f, of individual isolator units for 95% confidence at median displacement for 165% DBE shaking plotted against multiples, m, of UHRS shaking with MAFE of 10^{-4}, without a hard stop

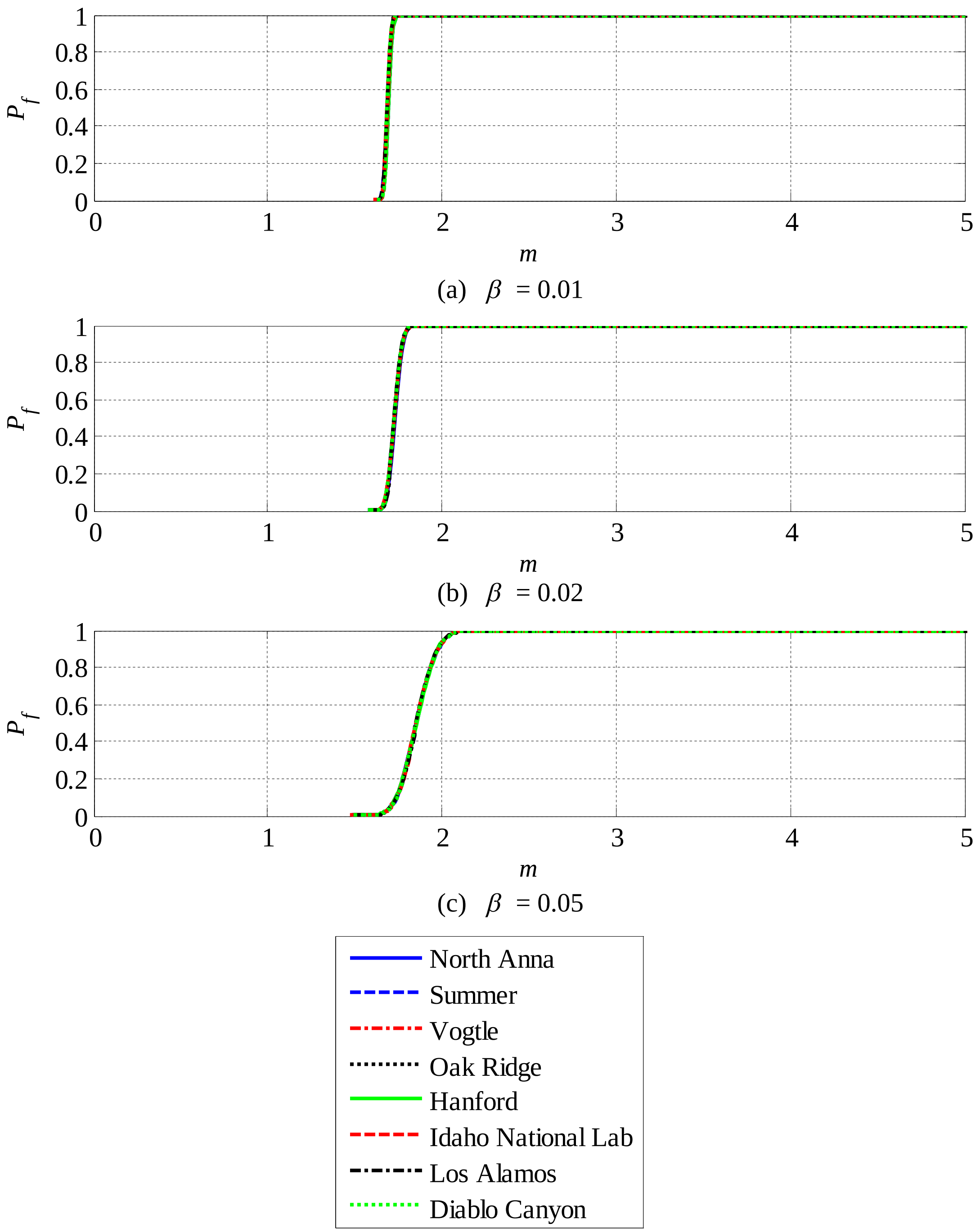

Figure F-4: Probability of unacceptable performance, P_f, of individual isolator units for 99% confidence at median displacement for 165% DBE shaking plotted against multiples, *m*, of UHRS shaking with MAFE of 10^{-4}, without a hard stop

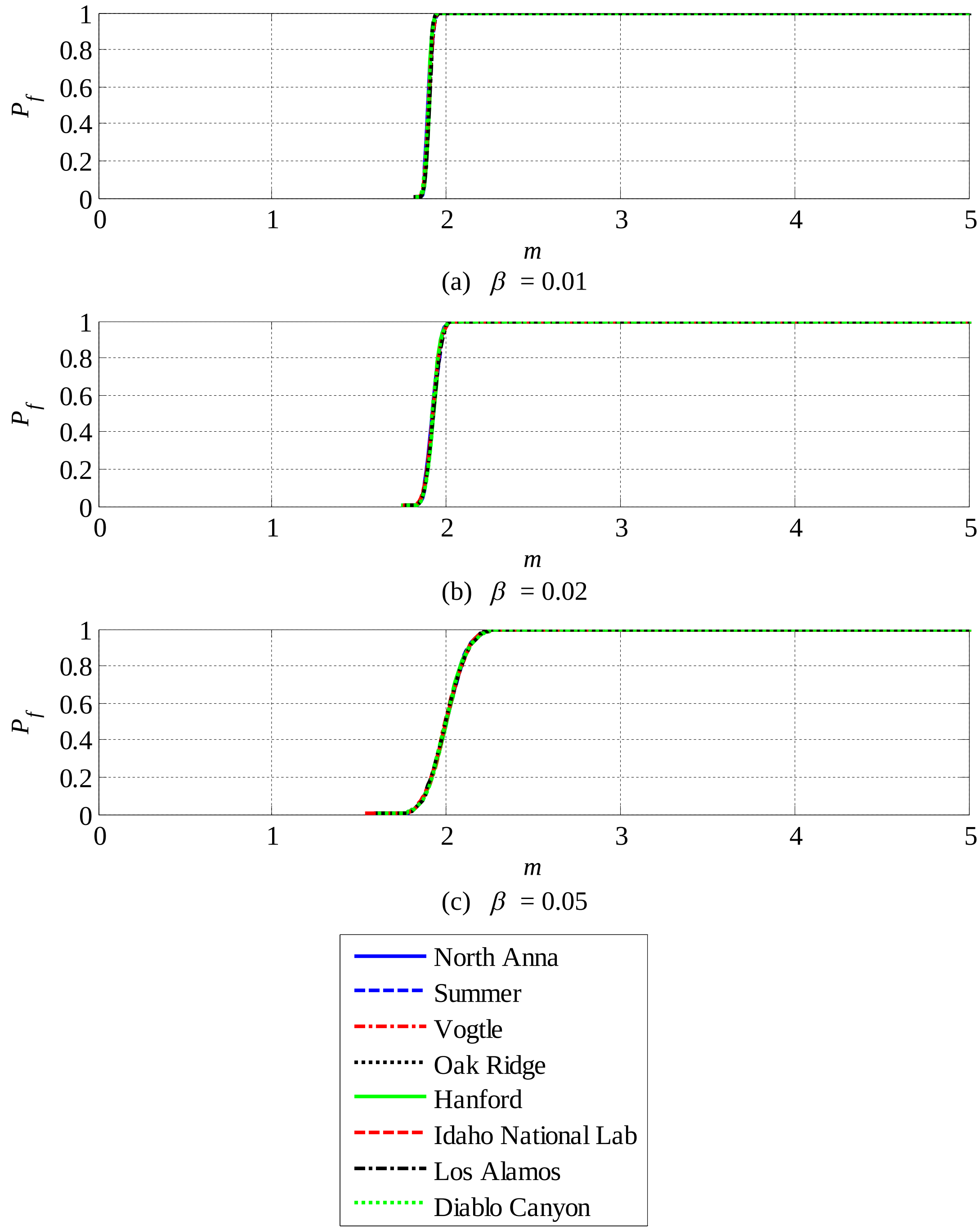

Figure F-5: Probability of unacceptable performance, P_f, of individual isolator units for 90% confidence at median displacement for 187.5% DBE shaking plotted against multiples, *m*, of UHRS shaking with MAFE of 10^{-4}, without a hard stop

Table F-1: Annual frequency of unacceptable performance ($\times 10^{-6}$) of individual isolator units tested with 90% confidence at median displacement for 165% DBE shaking, without a hard stop

	Site							
	North Anna	Summer	Vogtle	Oak Ridge	Hanford	Idaho	Los Alamos	Diablo Canyon
$\beta = 0.01$	38.2	28.4	26.2	33.8	21.0	17.9	38.6	17.6
$\beta = 0.02$	37.2	27.6	25.2	32.9	20.1	17.2	37.4	16.8
$\beta = 0.05$	34.8	25.2	22.8	30.5	17.9	15.2	34.3	14.7

Table F-2: Annual frequency of unacceptable performance ($\times 10^{-6}$) of individual isolator units tested with 95% confidence at median displacement for 165% DBE shaking, without a hard stop

	Site							
	North Anna	Summer	Vogtle	Oak Ridge	Hanford	Idaho	Los Alamos	Diablo Canyon
$\beta = 0.01$	37.7	28.2	25.9	33.5	20.7	17.7	38.3	17.4
$\beta = 0.02$	36.6	27.2	24.8	32.4	19.6	16.8	36.9	16.3
$\beta = 0.05$	33.5	24.2	21.7	29.4	16.8	14.2	33.0	13.7

Table F-3: Annual frequency of unacceptable performance ($\times 10^{-6}$) of individual isolator units tested with 99% confidence at median displacement for 165% DBE shaking, without a hard stop

	Site							
	North Anna	Summer	Vogtle	Oak Ridge	Hanford	Idaho	Los Alamos	Diablo Canyon
$\beta = 0.01$	37.3	27.7	25.4	33.1	20.2	17.2	37.7	16.8
$\beta = 0.02$	35.8	26.2	23.8	31.5	18.6	16.0	35.6	15.4
$\beta = 0.05$	31.4	22.0	19.8	27.2	15.0	12.6	30.3	12.0

Table F-4: Annual frequency of unacceptable performance ($\times 10^{-6}$) of individual isolator units tested with 90% confidence at median displacement for 187.5% DBE shaking, without a hard stop

	Site							
	North Anna	Summer	Vogtle	Oak Ridge	Hanford	Idaho	Los Alamos	Diablo Canyon
$\beta = 0.01$	29.8	20.5	18.3	25.6	13.6	11.4	28.5	10.7
$\beta = 0.02$	29.1	19.9	17.7	25.0	13.0	10.9	27.5	10.2
$\beta = 0.05$	27.2	18.1	16.1	23.1	11.5	9.6	25.3	8.7

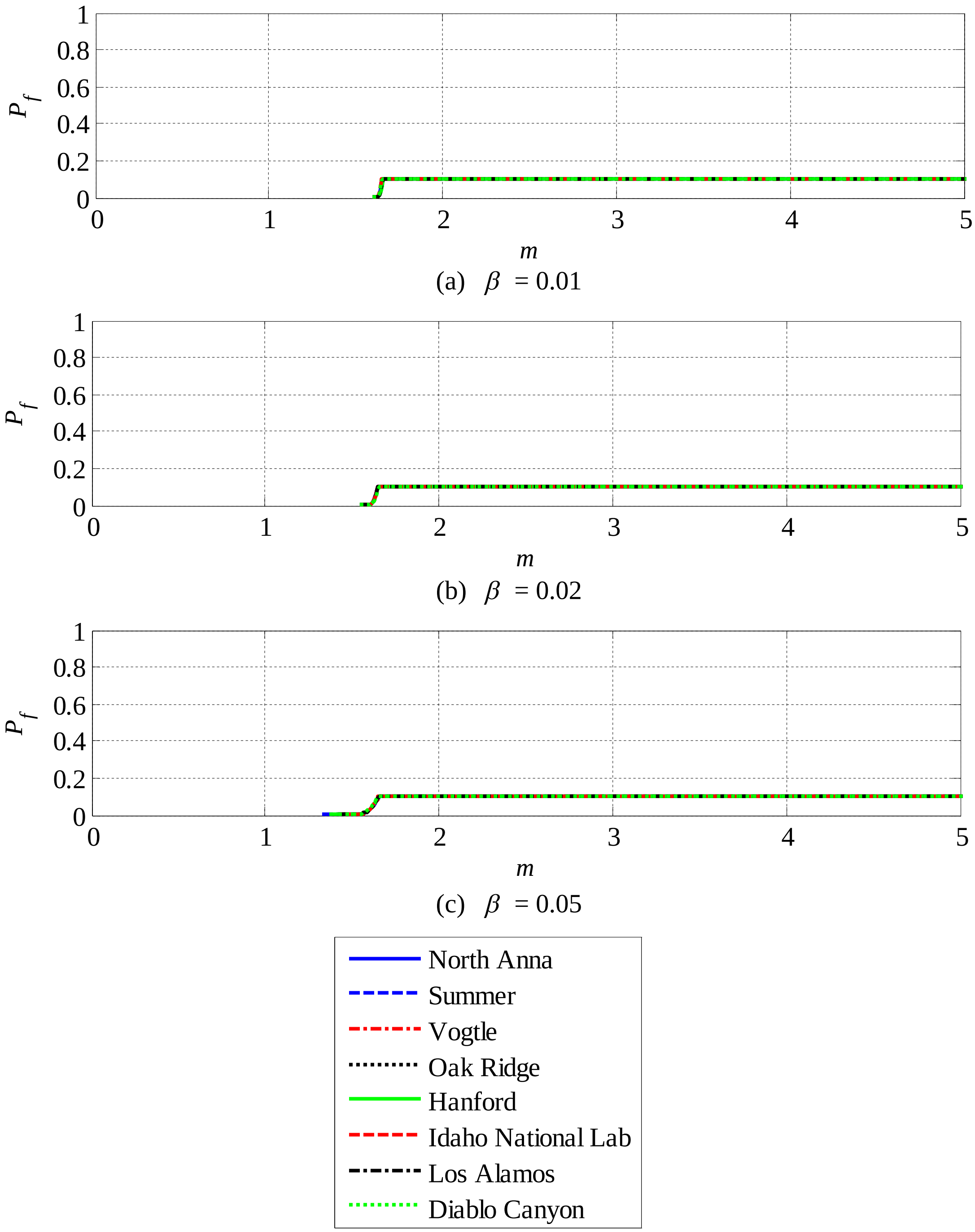

Figure F-6: Probability of unacceptable performance, P_f, of individual isolator units for 90% confidence at median displacement for 165% DBE shaking plotted against multiples, *m*, of UHRS shaking with MAFE of 10^{-4}, with a hard stop at median displacement for 165% DBE shaking

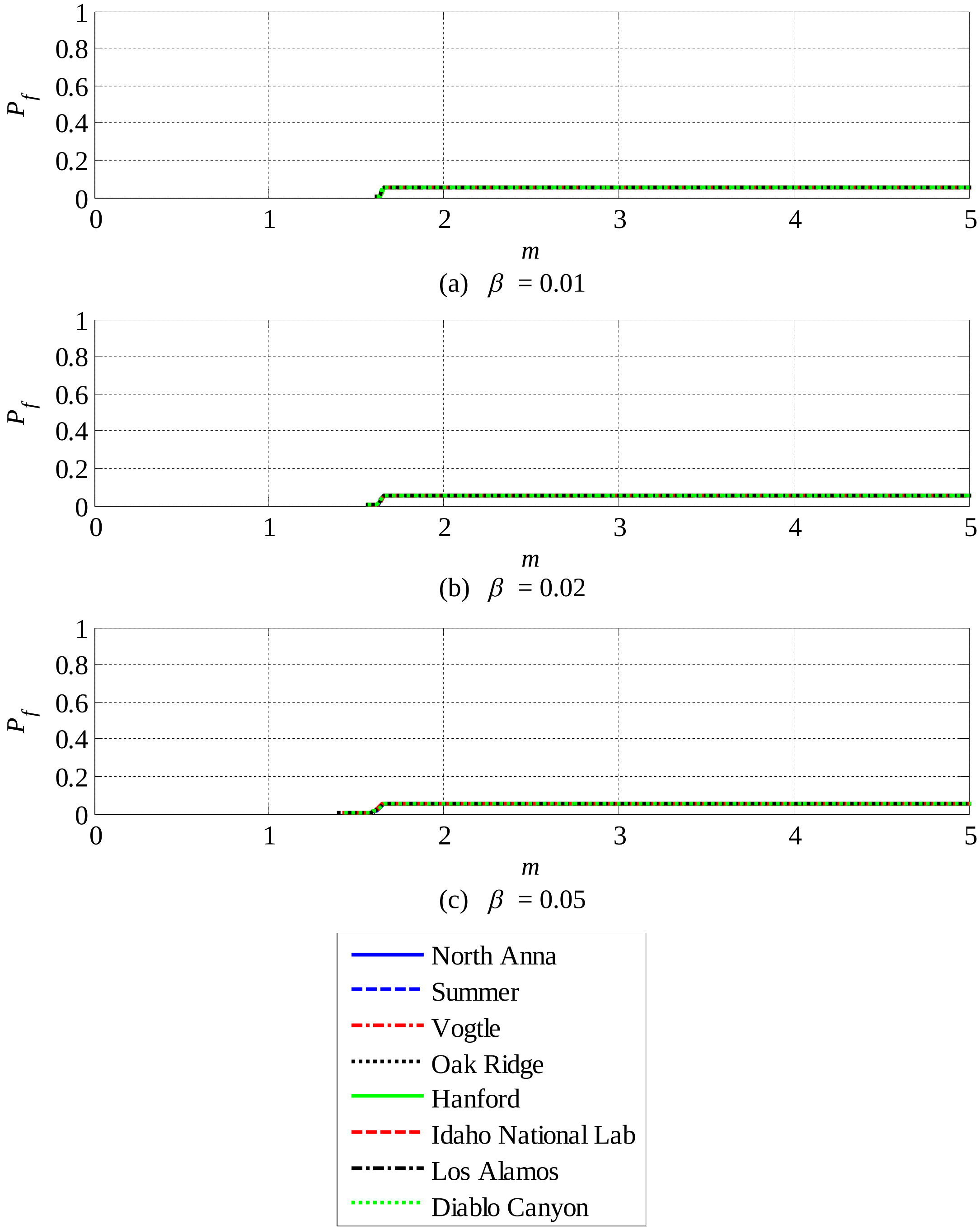

Figure F-7: Probability of unacceptable performance, P_f, of individual isolator units for 95% confidence at median displacement for 165% DBE shaking plotted against multiples, *m*, of UHRS shaking with MAFE of 10^{-4}, with a hard stop at median displacement for 165% DBE shaking

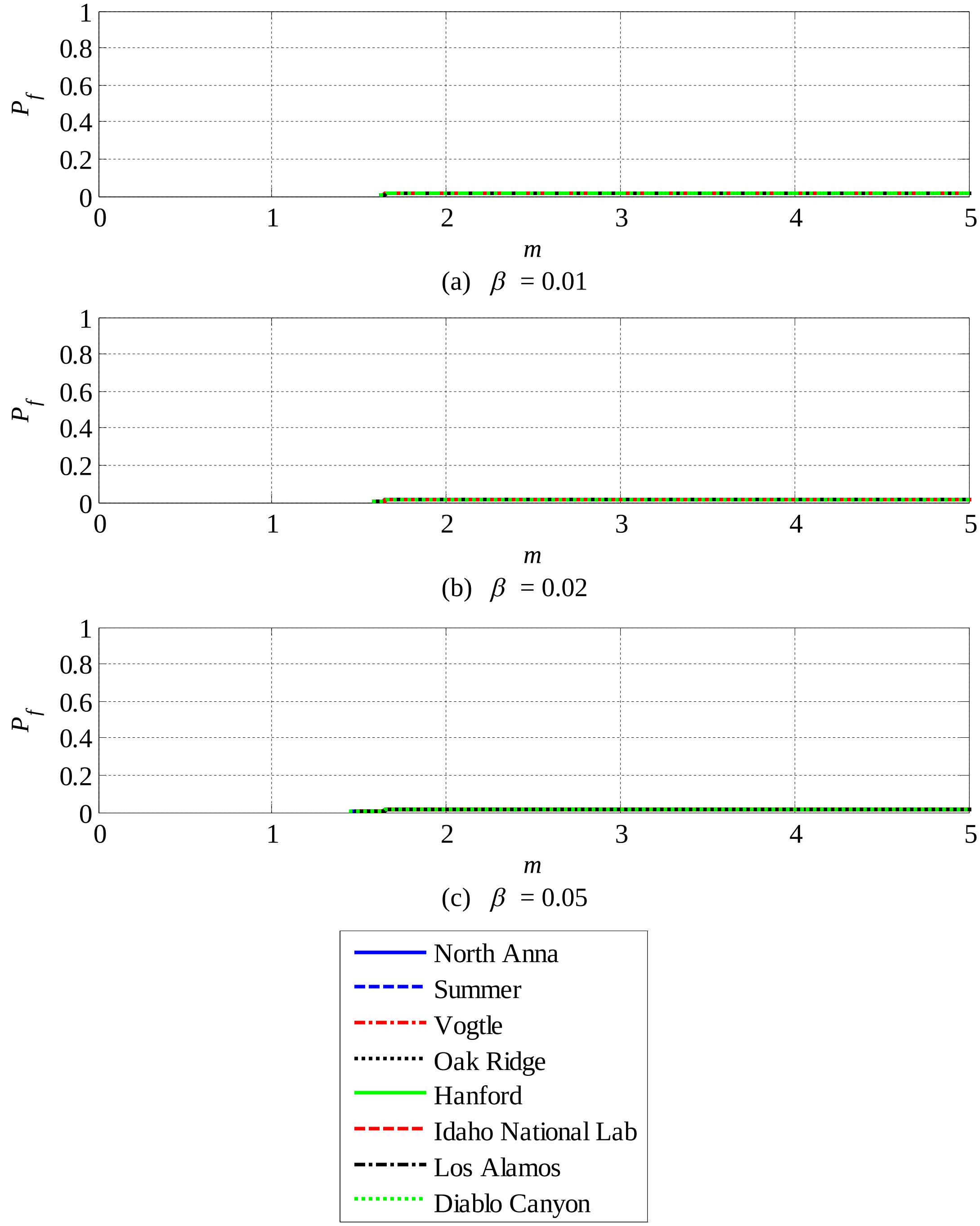

Figure F-8: Probability of unacceptable performance, P_f, of individual isolator units for 99% confidence at median displacement for 165% GMRS shaking plotted against multiples, *m*, of UHRS shaking with MAFE of 10^{-4}, with a hard stop at median displacement for 165% DBE shaking

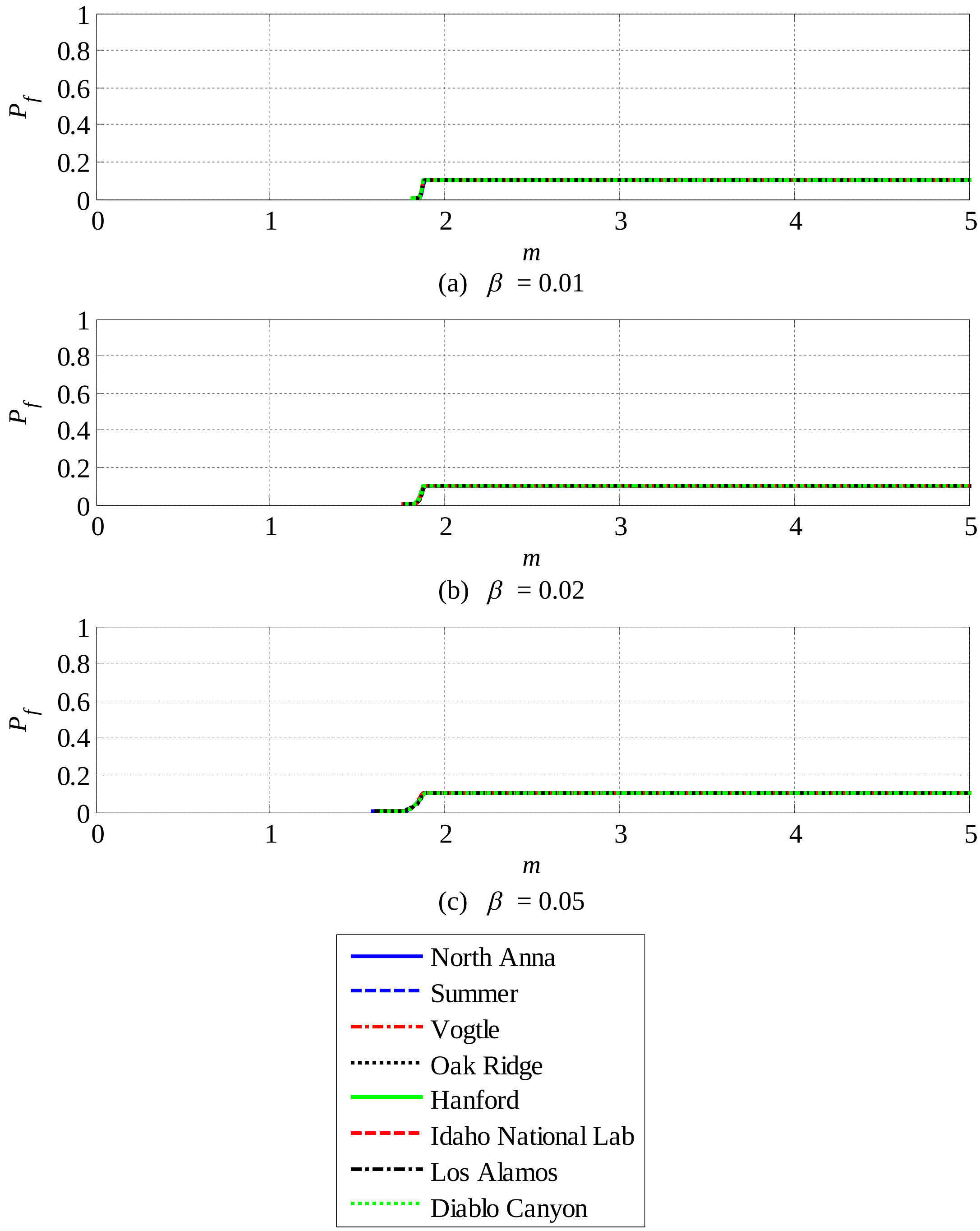

Figure F-9: Probability of unacceptable performance, P_f, of individual isolator units for 90% confidence at median displacement for 187.5% EDB DBE shaking plotted against multiples, *m*, of UHRS shaking with MAFE of 10^{-4}, with a hard stop at median displacement for 187.5% DBE shaking

Table F-5: Annual frequency of unacceptable performance ($\times 10^{-6}$) of individual isolator units tested with 90% confidence at median displacement for 165% DBE shaking, with a hard stop at median displacement for 165% DBE shaking

	Site							
	North Anna	Summer	Vogtle	Oak Ridge	Hanford	Idaho	Los Alamos	Diablo Canyon
$\beta = 0.01$	3.9	3.0	2.7	3.5	2.2	1.9	4.0	1.9
$\beta = 0.02$	4.0	3.0	2.8	3.6	2.3	1.9	4.1	1.9
$\beta = 0.05$	4.1	3.1	2.9	3.7	2.4	2.1	4.2	2.0

Table F-6: Annual frequency of unacceptable performance ($\times 10^{-6}$) of individual isolator units tested with 95% confidence at median displacement for 165% DBE shaking, with a hard stop at median displacement for 165% DBE shaking

	Site							
	North Anna	Summer	Vogtle	Oak Ridge	Hanford	Idaho	Los Alamos	Diablo Canyon
$\beta = 0.01$	2.0	1.5	1.4	1.8	1.1	1.0	2.0	0.9
$\beta = 0.02$	2.0	1.5	1.4	1.8	1.1	1.0	2.0	0.9
$\beta = 0.05$	2.0	1.6	1.4	1.8	1.2	1.0	2.1	1.0

Table F-7: Annual frequency of unacceptable performance ($\times 10^{-6}$) of individual isolator units tested with 99% confidence at median displacement for 165% DBE shaking, with a hard stop at median displacement for 165% DBE shaking

	Site							
	North Anna	Summer	Vogtle	Oak Ridge	Hanford	Idaho	Los Alamos	Diablo Canyon
$\beta = 0.01$	0.4	0.3	0.3	0.4	0.2	0.2	0.4	0.2
$\beta = 0.02$	0.4	0.3	0.3	0.4	0.2	0.2	0.4	0.2
$\beta = 0.05$	0.4	0.3	0.3	0.4	0.2	0.2	0.4	0.2

Table F-8: Annual frequency of unacceptable performance ($\times 10^{-6}$) of individual isolator units tested with 90% confidence at median displacement for 187.5% DBE shaking, with a hard stop at median displacement for 187.5% DBE shaking

	Site							
	North Anna	Summer	Vogtle	Oak Ridge	Hanford	Idaho	Los Alamos	Diablo Canyon
$\beta = 0.01$	3.1	2.2	1.9	2.7	1.4	1.2	3.0	1.2
$\beta = 0.02$	3.1	2.2	1.9	2.7	1.5	1.2	3.0	1.2
$\beta = 0.05$	3.2	2.3	2.0	2.8	1.5	1.3	3.1	1.2

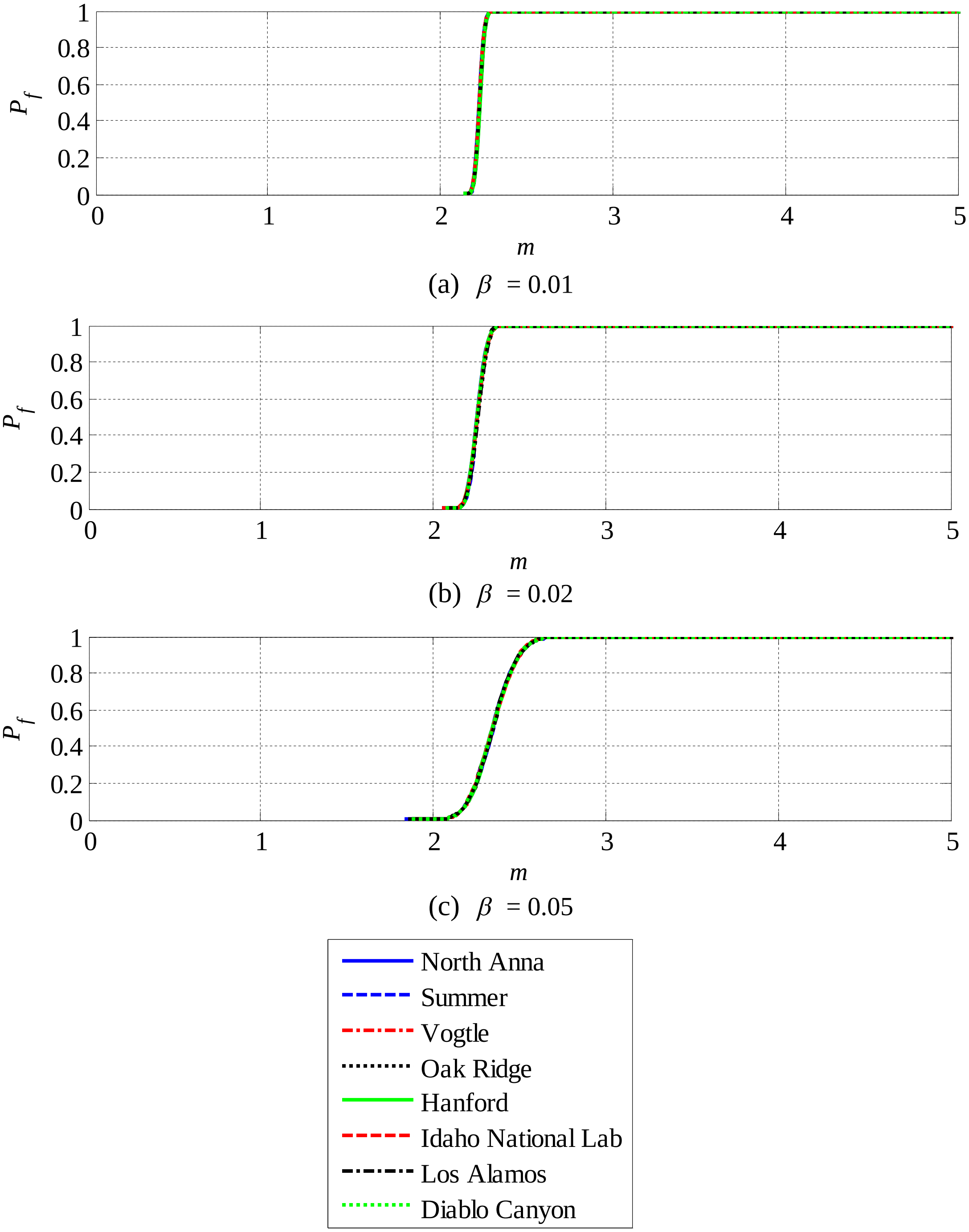

Figure F-10: Probability of unacceptable performance, P_f, of individual isolator units for 90% confidence at median displacement for 220% DBE shaking plotted against multiples, *m*, of UHRS shaking with MAFE of 10^{-4}, without a hard stop

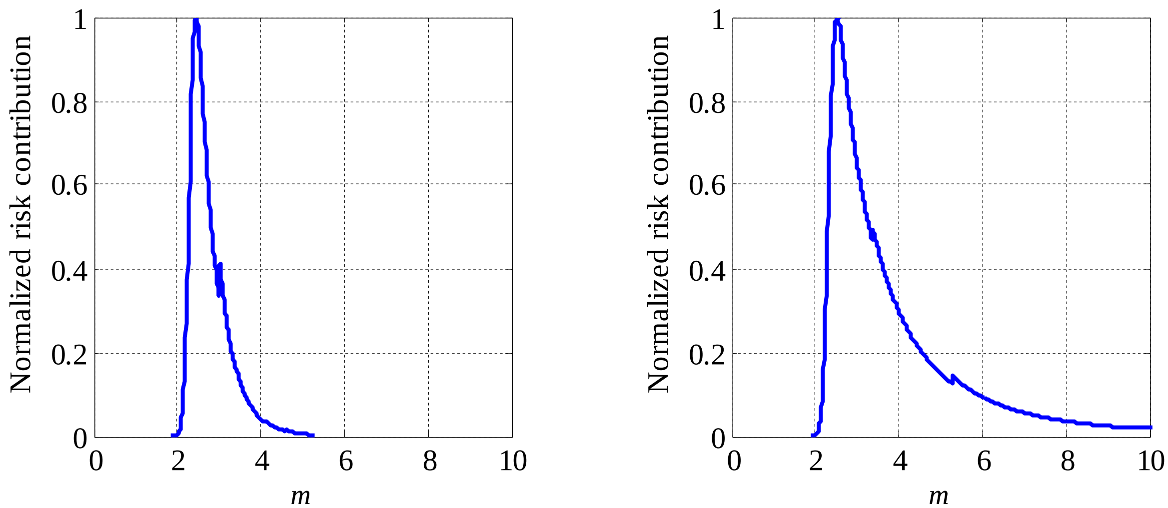

(a) Diablo Canyon (b) North Anna

Figure F-11: Disaggregation of risk corresponding to Figure F-10(a) for two sites

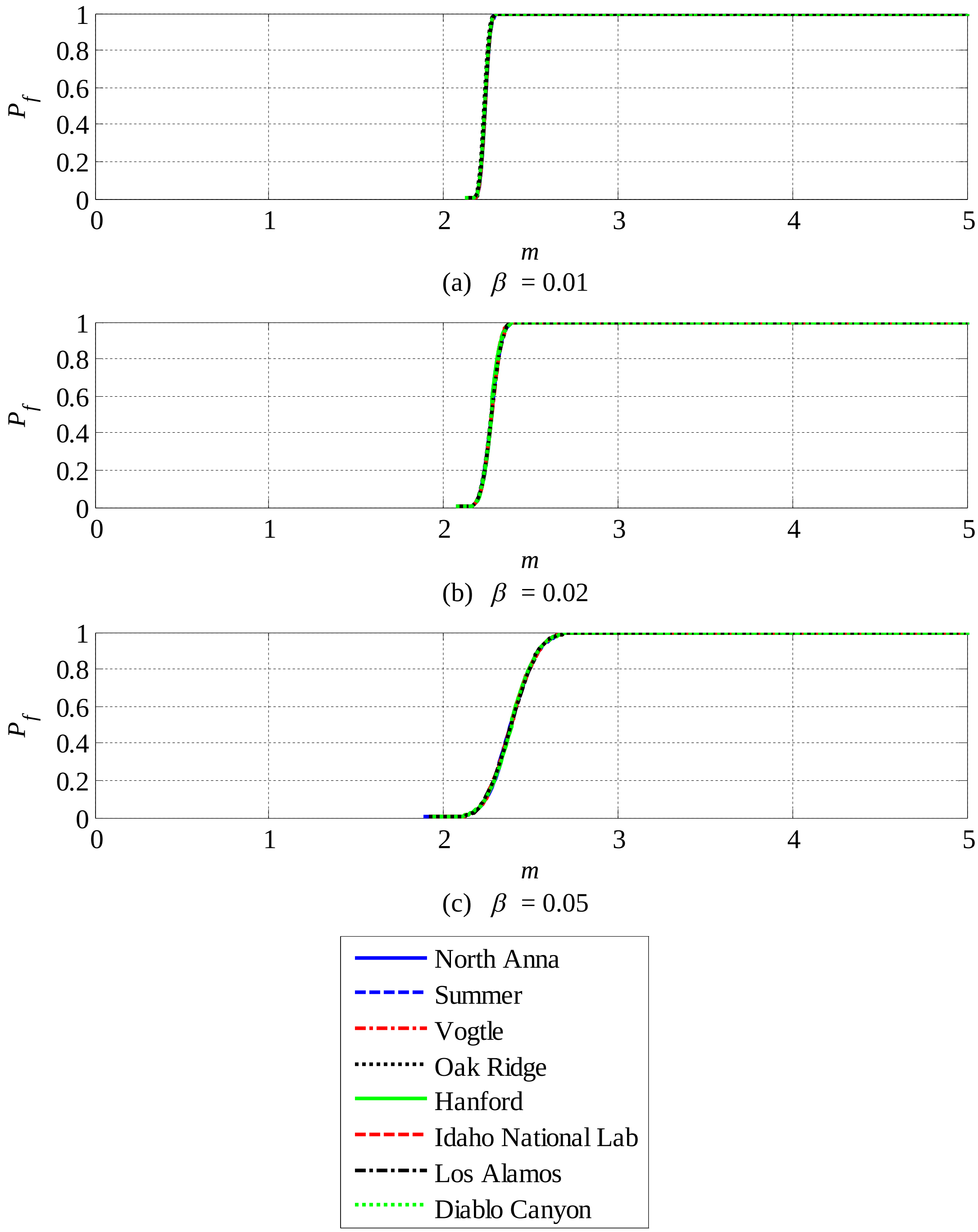

Figure F-12: Probability of unacceptable performance, P_f, of individual isolator units for 95% confidence at median displacement for 220% DBE shaking plotted against multiples, m, of UHRS shaking with MAFE of 10^{-4}, without a hard stop

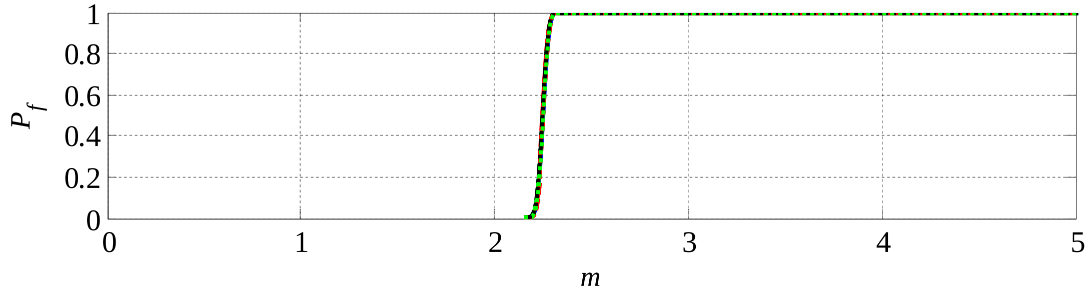

(a) β = 0.01

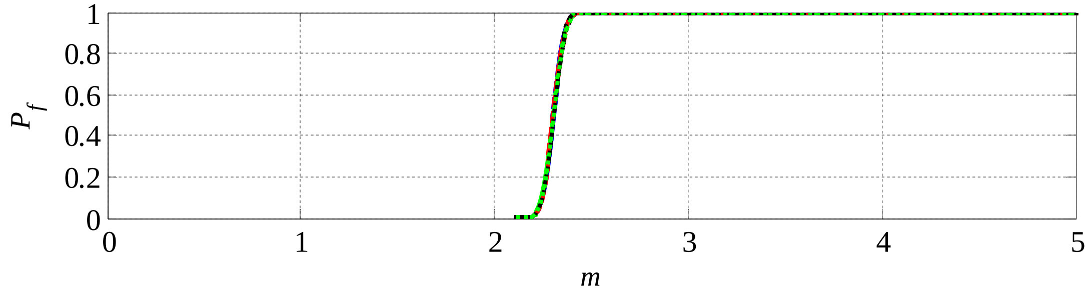

(b) β = 0.02

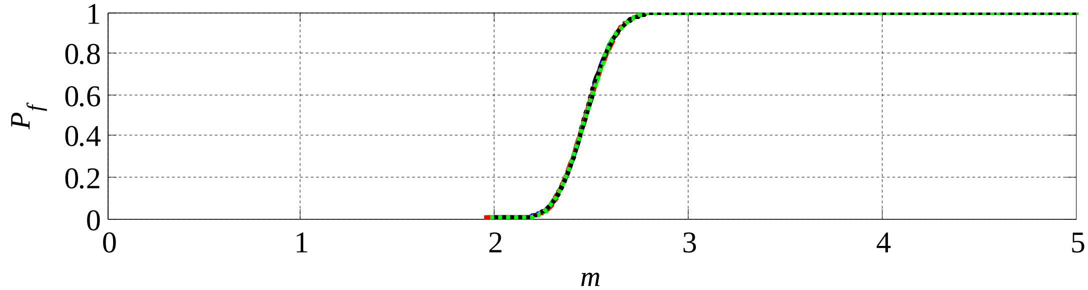

(c) β = 0.05

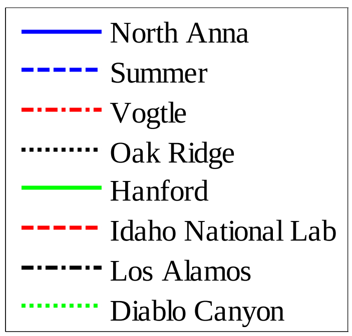

Figure F-13: Probability of unacceptable performance, P_f, of individual isolator units for 99% confidence at median displacement for 220% DBE shaking plotted against multiples, *m*, of UHRS shaking with MAFE of 10^{-4}, without a hard stop

Table F-9: Annual frequency of unacceptable performance ($\times 10^{-6}$) of individual isolator units tested with 90% confidence at median displacement for 220% DBE shaking, without a hard stop

	Site							
	North Anna	Summer	Vogtle	Oak Ridge	Hanford	Idaho	Los Alamos	Diablo Canyon
$\beta = 0.01$	22.0	13.7	11.8	18.1	7.5	6.1	19.4	5.0
$\beta = 0.02$	21.5	13.3	11.4	17.6	7.1	5.8	18.8	4.7
$\beta = 0.05$	20.1	12.1	10.2	16.3	6.2	5.0	17.3	4.0

Table F-10: Annual frequency of unacceptable performance ($\times 10^{-6}$) of individual isolator units tested with 95% confidence at median displacement for 220% DBE shaking, without a hard stop

	Site							
	North Anna	Summer	Vogtle	Oak Ridge	Hanford	Idaho	Los Alamos	Diablo Canyon
$\beta = 0.01$	21.9	13.5	11.7	18.0	7.4	6.0	19.2	4.9
$\beta = 0.02$	21.2	13.0	11.1	17.3	6.9	5.6	18.5	4.5
$\beta = 0.05$	19.4	11.5	9.7	15.7	5.8	4.7	16.5	3.6

Table F-11: Annual frequency of unacceptable performance ($\times 10^{-6}$) of individual isolator units tested with 99% confidence at median displacement for 220% DBE shaking, without a hard stop

	Site							
	North Anna	Summer	Vogtle	Oak Ridge	Hanford	Idaho	Los Alamos	Diablo Canyon
$\beta = 0.01$	21.6	13.3	11.4	17.7	7.2	5.8	18.9	4.7
$\beta = 0.02$	20.7	12.5	10.7	16.9	6.5	5.3	17.9	4.2
$\beta = 0.05$	18.2	10.5	8.8	14.5	5.0	4.1	15.2	3.0

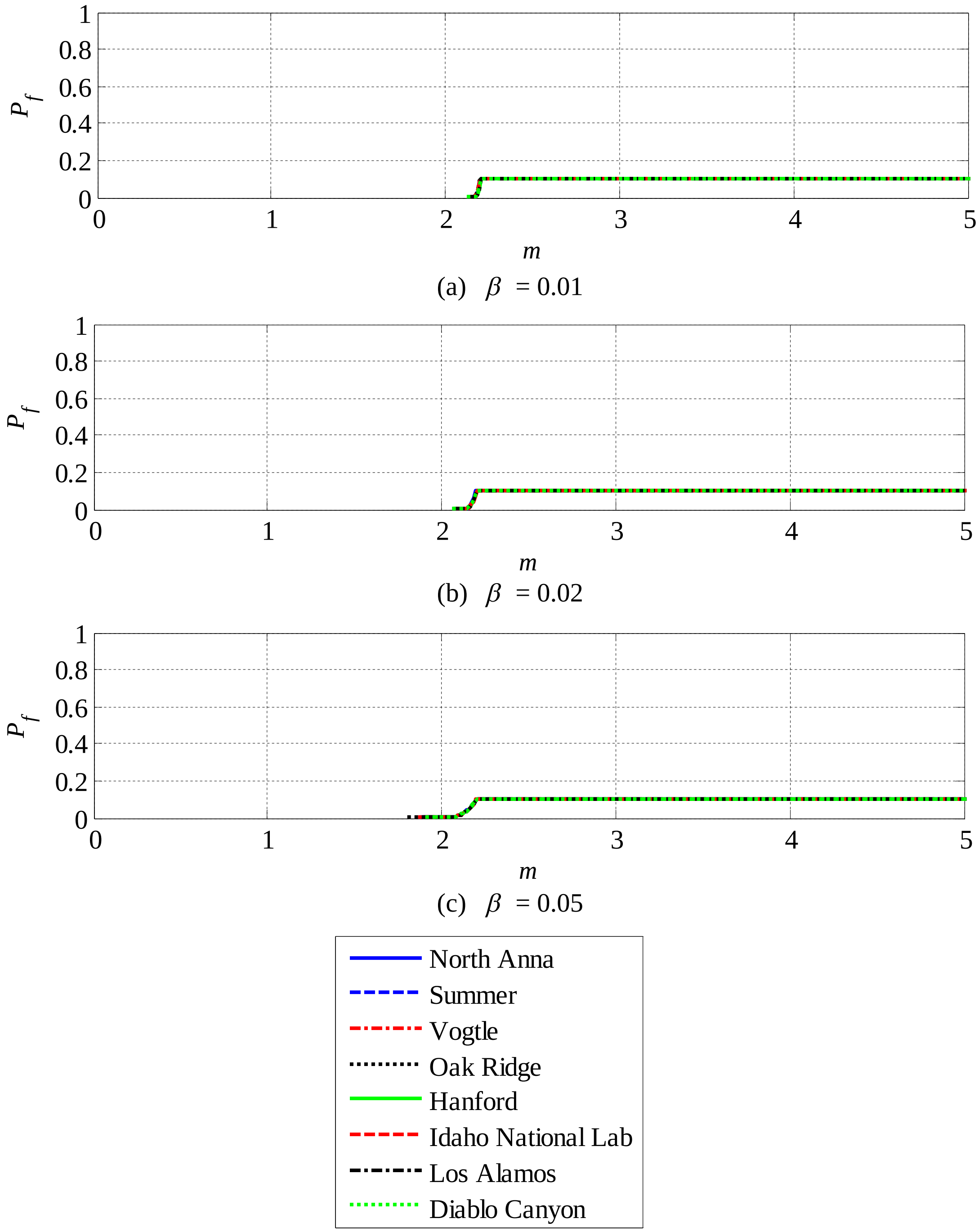

Figure F-14: Probability of unacceptable performance, P_f, of individual isolator units for 90% confidence at median displacement for 220% DBE shaking plotted against multiples, m, of UHRS shaking with MAFE of 10^{-4}, with a hard stop at median displacement for 220% DBE shaking

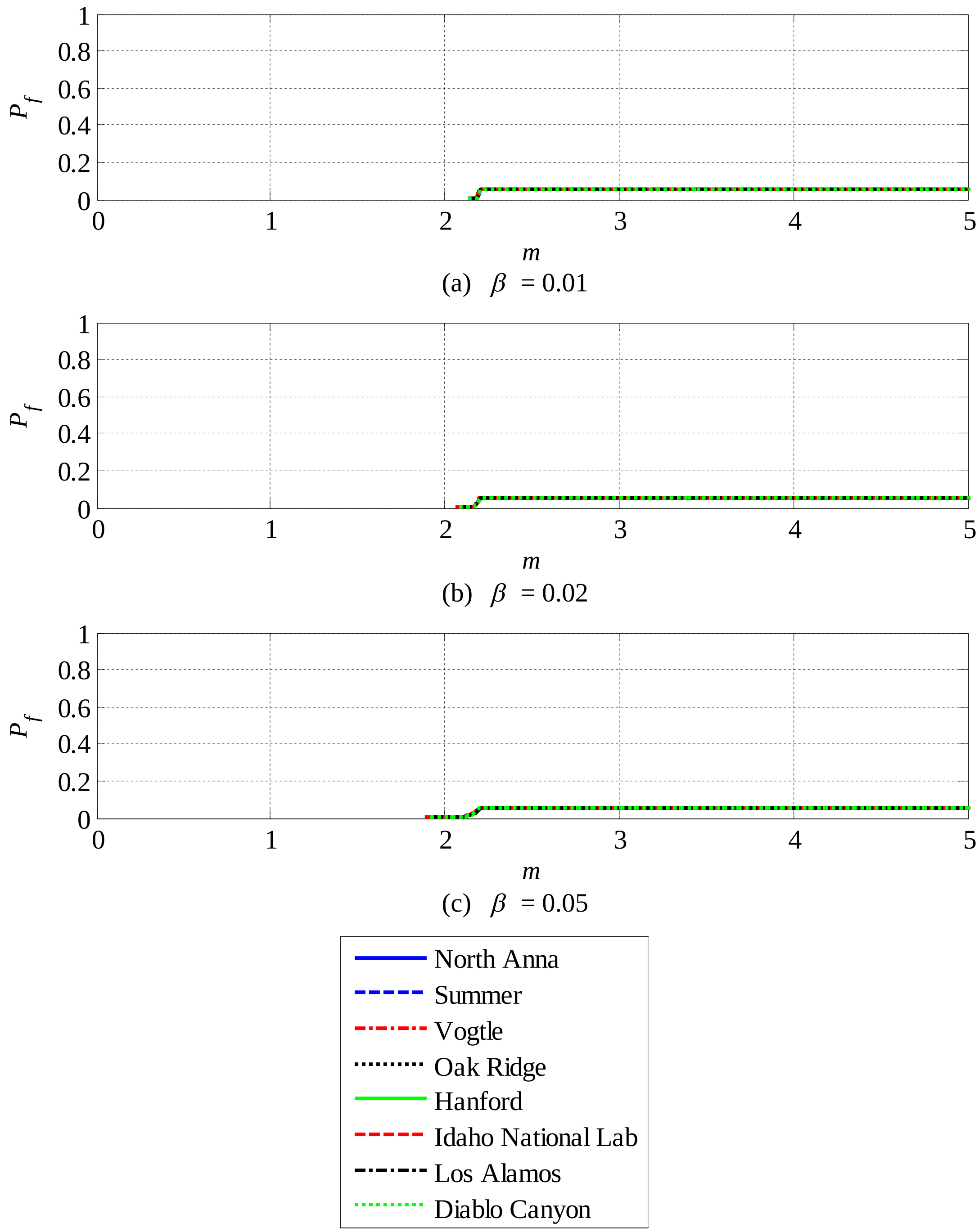

Figure F-15: Probability of unacceptable performance, P_f, of individual isolator units for 95% confidence at median displacement for 220% DBE shaking plotted against multiples, m, of UHRS shaking with MAFE of 10^{-4}, with a hard stop at median displacement for 220% DBE shaking

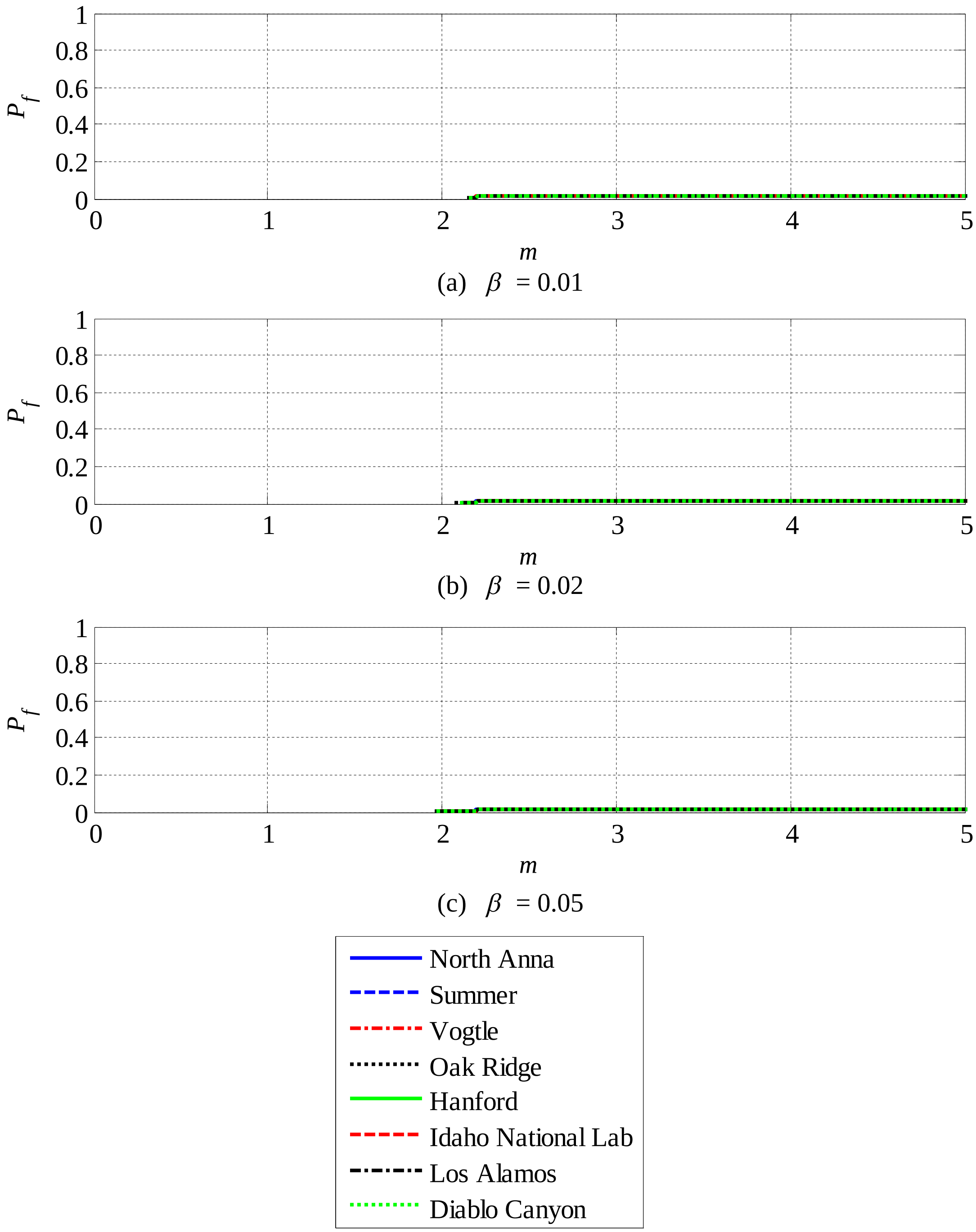

Figure F-16: Probability of unacceptable performance, P_f, of individual isolator units for 99% confidence at median displacement for 220% DBE shaking plotted against multiples, m, of UHRS shaking with MAFE of 10^{-4}, with a hard stop at median displacement for 220% DBE shaking

Table F-12: Annual frequency of unacceptable performance ($\times 10^{-6}$) of individual isolator units tested with 90% confidence at median displacement for 220% DBE shaking, with a hard stop at median displacement for 220% DBE shaking

	Site							
	North Anna	Summer	Vogtle	Oak Ridge	Hanford	Idaho	Los Alamos	Diablo Canyon
$\beta = 0.01$	2.3	1.4	1.2	1.9	0.8	0.6	2.0	0.5
$\beta = 0.02$	2.3	1.4	1.3	1.9	0.8	0.7	2.0	0.6
$\beta = 0.05$	2.4	1.5	1.3	2.0	0.9	0.7	2.1	0.6

Table F-13: Annual frequency of unacceptable performance ($\times 10^{-6}$) of individual isolator units tested with 95% confidence at median displacement for 220% DBE shaking, with a hard stop at median displacement for 220% DBE shaking

	Site							
	North Anna	Summer	Vogtle	Oak Ridge	Hanford	Idaho	Los Alamos	Diablo Canyon
$\beta = 0.01$	1.1	0.7	0.6	0.9	0.4	0.3	1.0	0.3
$\beta = 0.02$	1.1	0.7	0.6	0.9	0.4	0.3	1.0	0.3
$\beta = 0.05$	1.2	0.7	0.6	1.0	0.4	0.4	1.1	0.3

Table F-14: Annual frequency of unacceptable performance ($\times 10^{-6}$) of individual isolator units tested with 99% confidence at median displacement for 220% DBE shaking, with a hard stop at median displacement for 220% DBE shaking

	Site							
	North Anna	Summer	Vogtle	Oak Ridge	Hanford	Idaho	Los Alamos	Diablo Canyon
$\beta = 0.01$	0.2	0.1	0.1	0.2	0.1	0.1	0.2	0.1
$\beta = 0.02$	0.2	0.1	0.1	0.2	0.1	0.1	0.2	0.1
$\beta = 0.05$	0.2	0.1	0.1	0.2	0.1	0.1	0.2	0.1

APPENDIX G

SCALING GROUND MOTIONS FOR RESPONSE-HISTORY ANALYSIS

G.1 Introduction

Ground motions for three sites of nuclear facilities in the United States, namely, Diablo Canyon, Vogtle and North Anna, representing 10,000-year and 100,000-year shaking are used to perform the analyses presented in Chapters 6, 7 and 8. These ground motions are developed by either spectral matching or amplitude scaling. The appropriateness of amplitude scaling ground motions to represent seismic hazard at different sites and return periods is discussed here.

G.2 Response Spectral Shapes for Different Sites and Shaking Levels

The NIST report GCR 11-917-15, "Selecting and scaling earthquake ground motions for performing response-history analysis" (NIST, 2011) presents the state-of-knowledge and state-of-practice on generating sets of ground motions for response-history analysis of buildings (and nuclear power plants). The NIST report includes detailed discussions of probabilistic seismic hazard analysis; near-field effects, which is important for the Diablo Canyon site; and spectral matching of ground motions. Herein, one set of seed motions is selected for scaling to match or be consistent with response spectra at different sites. This decision is questionable for different return periods and different sites and should be justified.

In this report, ground motions are scaled to be consistent with spectral demands at three sites of nuclear facilities in the United States. The ground motions are used in Chapters 6, 7 and 8 to qualitatively understand a) the annual frequency of unacceptable performance of isolated nuclear structures designed in accordance with the forthcoming seismic isolation NUREG (Kammerer *et* *al.*, forthcoming), b) the importance of pressure, velocity, and temperature on the coefficient of sliding friction of Friction Pendulum™ bearings, and c) the displacement response of sample isolated nuclear power plants located at Diablo Canyon and Vogtle. Site class B per ASCE 7-10 (ASCE, 2010) is assumed for each location to enable the reader to compare the risks at different sites and to provide insight into the impact of hazard-curve slope on the calculated risk.

Consider Figure G-1 that plots normalized uniform hazard response spectra for three of the sites of Figure 6-2: Diablo Canyon, Vogtle and North Anna. The latitude and longitude for the three sites are

- Diablo Canyon: latitude 35.2116 N, longitude 120.8556 W
- Vogtle: latitude 33.1433 N, longitude 81.7606 W
- North Anna: latitude 38.0606 N, longitude 77.7894 W

Two return periods are considered: 10,000 and 100,000 years. The three sites represent regions of high, moderate and low seismicity, and Western United States, Central United States and Eastern United States, respectively. The acceleration response spectra were generated from data available at the USGS website http://geohazards.usgs.gov/hazardtool/application.php (accessed on December 30, 2014) and normalized to 1.0 g at a period of 1.5 s. Of the three sites, only Diablo Canyon would possibly be associated with site class B for site-specific calculations.

In the period range between 1.0 s and 2.0 s, which is important for calculating isolation-system displacements, the spectral shapes are sufficiently similar to justify the use at all three sites and two return periods of one set of seed ground motions scaled to be consistent with 10,000-year shaking at Diablo Canyon. If floor spectral demands were the primary focus of the response-history analysis, attention would have to be paid to spectral demands in the period range from 0.02 s to 0.50 s, and alternate scaling procedures would have to be adopted.

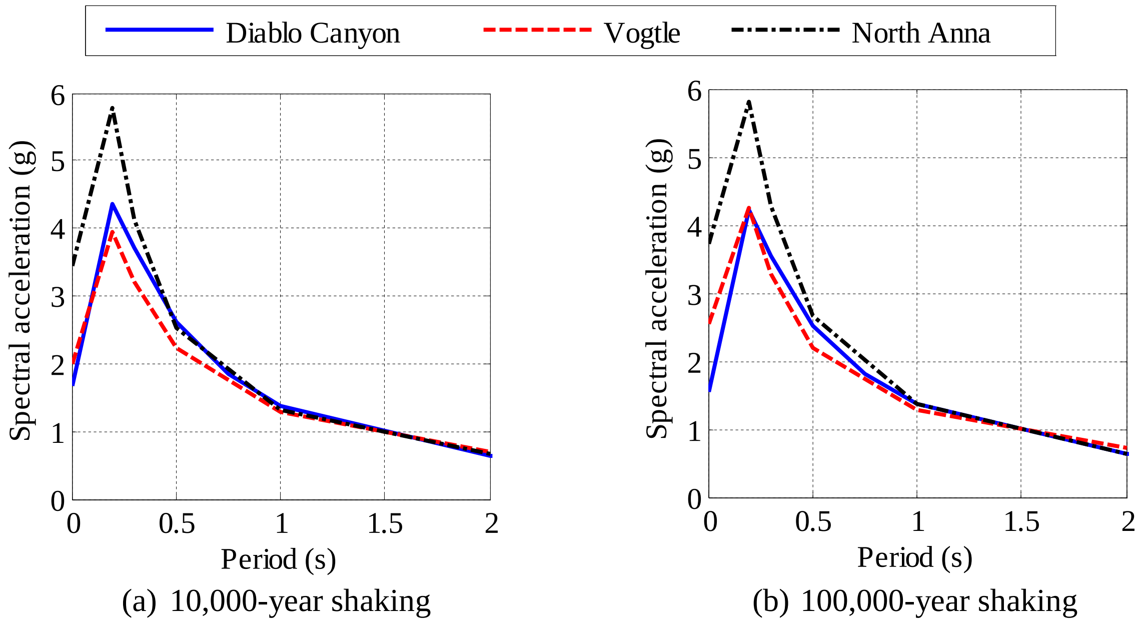

Figure G-1: Normalized 5% damped uniform hazard response spectra

Using 1.5 seconds as an anchor point, the factors of Table G-1 can be used to scale the 10,000-year ground motions at Diablo Canyon to other sites and return periods. A factor is not provided for 10,000 years and North Anna because risk computations in Chapter 6 are not required for this return period.

Table G-1: Ground motion amplitude scale factors

Site	Return period (years)	Scale factor
Diablo Canyon	10,000	1.00
	100,000	2.00
Vogtle	10,000	0.25
	100,000	0.60
North Anna	100,000	0.50

APPENDIX H

PROBABILITY DISTRIBUTIONS OF RESPONSES IN ISOLATED STRUCTURES

H.1 Introduction

Chapter 7 reports the results of response-history analyses performed on Friction Pendulum™ (FP) bearings with a range of geometrical and material properties, and static axial pressures. Three-component sets of thirty ground motions consistent with fractions of the seismic hazard at the site of a nuclear power plant in the United States were used for the analyses. The responses to each set of ground motions, namely, peak isolator displacements, peak temperature at the sliding surface, and floor spectral ordinates were assumed to distribute lognormally. This assumption is verified in this appendix.

H.2 Analysis Scheme

Single FP bearings with sliding periods of 1.5 s, 2 s, 3 s and 4 s, reference coefficients of friction of 0.03, 0.06 and 0.09, and reference axial pressures of 10 MPa and 50 MPa, were subjected to the sets of 30 ground motions consistent with 10,000-year return period seismic hazard (design basis earthquake, DBE) at Diablo Canyon. See Chapter 7 for details. The ground motions were amplitude scaled to six intensities: 25%, 60%, 100%, 150%, 167% and 200% DBE. Five models that consider the dependencies of the instantaneous values of axial pressure, sliding velocity and temperature at the sliding surface, on the coefficient of sliding friction were used to define friction at the sliding surface. Response-history analyses for some combinations of sliding period, reference coefficient of friction and shaking intensity could not be completed because of high displacements, for which converged solutions could not be obtained. These combinations are identified in Chapter 7.

H.3 Tests to Determine Normality

Three tests to determine the normality of a data set are considered: Lilliefors, Chi-square and Jarque-Bera. The test statistics for the data set are compared with corresponding values for a normally distributed data set. The statistics are briefly discussed below.

The statistic, LT, used in the Lilliefors test (Lilliefors, 1969) is the maximum absolute difference between the empirical cumulative distribution function, O_{CDF}, of the data and the cumulative distribution function, E_{CDF}, for a normal distribution with the same mean and variance:

$$LT = \max\left|O_{CDF} - E_{CDF}\right| \quad \text{(H-1)}$$

where all terms were defined previously.

The Chi-square test (e.g., Benjamin and Cornell (1970)) is performed by grouping the data into bins and comparing the observed and expected counts in the bins. The test statistic, χ^2, is given by

$$\chi^2 = \sum_{j=1}^{n_{bin}} \frac{\left(O_j - E_j\right)^2}{E_j} \quad \text{(H-2)}$$

where O_j and E_j are observed and expected counts in the bins, respectively, and n_{bin} is number of bins.

The test statistic, JB, for the Jarque-Bera test for normality of a data set (Jarque and Bera, 1987) is given by

$$JB = \frac{n}{6}\left(s^2 + \frac{\left(k-3\right)^2}{4} \right) \quad \text{(H-3)}$$

where n is number of data points in the sample, s is the sample skewness given by

$$s = \frac{\mu_3^2}{\mu_2^3} \quad \text{(H-4)}$$

and k is sample kurtosis given by

$$k = \frac{\mu_4}{\mu_2^2} \quad \text{(H-5)}$$

where μ_i $\left(i = 2, 3, 4\right)$ is given by

$$\mu_i = \frac{1}{n}\sum_{j=1}^{n}\left(v_j - \overline{v}\right)^i \quad \text{(H-6)}$$

where v_j is the j^{th} data point in the sample of size n and $\overline{v}$ is the average of the sample.

The three tests are performed on the log of the response quantities (e.g., peak displacement) at 5% significance level[1,2] to determine if the sets of data distribute lognormally.

[1] A significance level of 5% means that there is a less than 5% probability of the distribution not being normal if the test indicates that the distribution is normal. A detailed discussion on the topic can be found in Benjamin and Cornell (1970).

[2] A significance level of 5% is used traditionally. A test conducted at a smaller significance level is more likely to lead to the conclusion that the data is lognormally distributed.

H.4 Results

Figure H-1(a) presents the cumulative distribution of the 30 values of peak displacements of the FP bearing with a sliding period of 3 s, a reference coefficient of friction of 0.03, friction at sliding surface defined using Model 1 (Coulomb model) of Table 6-1, and a reference axial pressure of 50 MPa, subjected to the 30 ground motions at 100% amplitude. Also plotted in the panel is the lognormal fit to the data. Figures H-1(b), H-1(c), H-1(d) and H-1(e) present results for the other four friction models of Table 6-1. The five sets of data distribute lognormally per the three tests of Section H.3, with the exception of the data of Figures H-1(c) and H-1(e) that do not distribute lognormally per the Lilliefors test at 5% significance level.

Figure H-2(a) presents the outputs of Lilliefors test performed on the 550 sets of 30 values of the log of peak displacements of FP bearings with different geometries, liners and loadings. A total of 513 (93%) of the 550 sets of data distribute lognormally per this test. Figures H-2(b) and H-2(c) present the results for Chi-square and Jarque-Bera tests, respectively. The sets of 30 peak displacements distribute lognormally for 100% and 94% of the 550 combinations, respectively.

Figure H-3 presents the cumulative distributions for the five sets of 30 values of peak temperatures at the sliding surface of the FP bearing considered in Figure H-1. All five sets of data distribute lognormally per the three tests. Figure H-4 presents the results of the three tests for all the 550 combinations. The 30 values of temperatures distribute lognormally for 80% to 90% of the combinations.

Figure H-5 presents the cumulative distribution for the 30 values of spectral acceleration at 0.05 s corresponding to the absolute horizontal acceleration response of the slider of the FP bearing considered in Figures H-1 and H-3. All five sets of 30 values distribute lognormally per the three tests. Figure H-6 presents the results of the normality tests on the log of the spectral ordinates at nine periods (= 0.01 s, 0.02 s, 0.03 s, 0.05 s, 0.075 s, 0.1 s, 0.2 s, 0.5 s and 1 s) corresponding to the absolute acceleration of the slider in the vertical and two horizontal directions for all 550 combinations of Figure H-2 (and Figure H-4). The 30 values of spectral ordinates distribute lognormally for 90% to 95% of the 14850 cases ($3\times9\times550$).

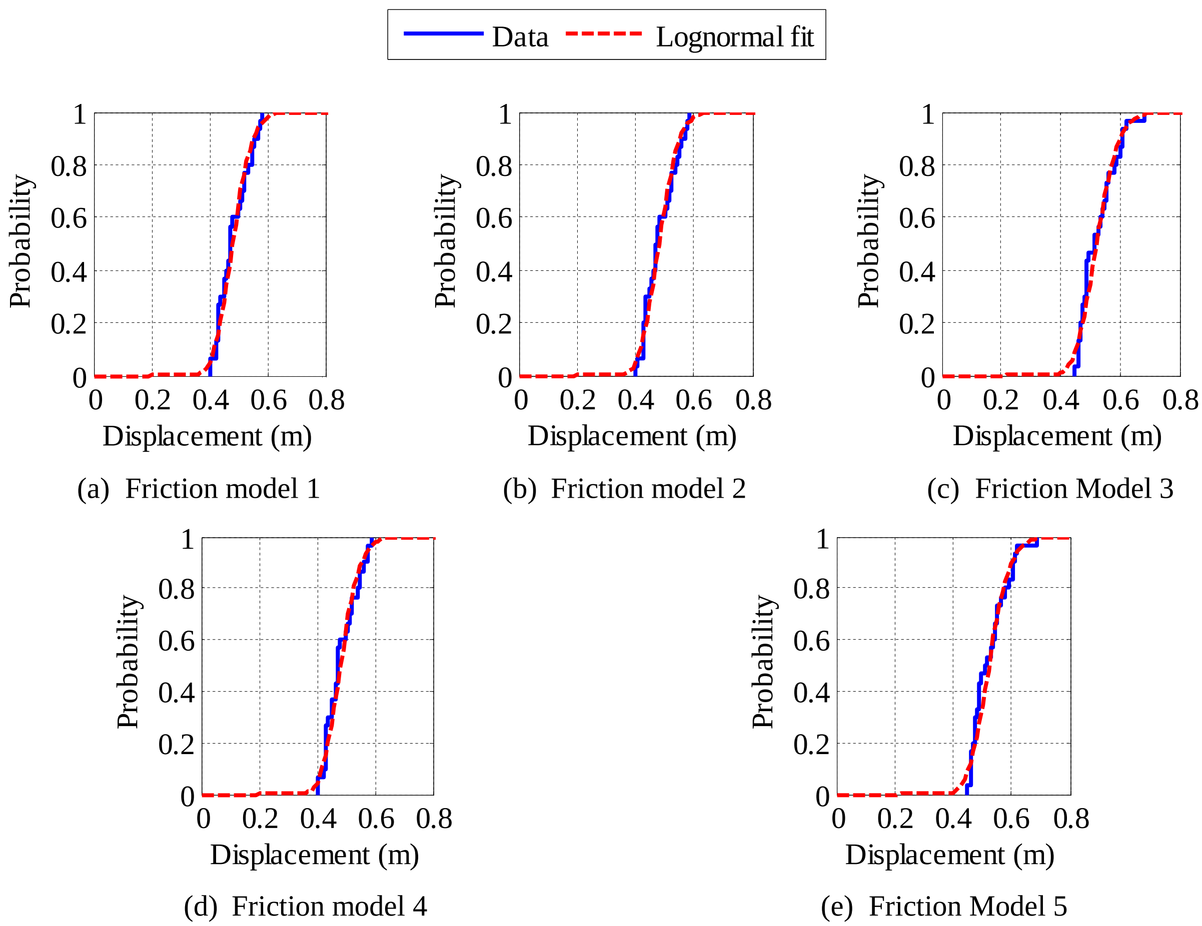

Figure H-1: Empirical cumulative distribution of the 30 values of peak displacement and the lognormal fits

H.5 Summary

The distributions of the response quantities (e.g., peak temperature at sliding surface) of FP bearings with a range of geometrical and material properties, and static axial loads, subjected to ground motions consistent with different fractions of seismic hazards at the site of the Diablo Canyon nuclear power plant are studied. The Lilliefors, Chi-square and Jarque-Bera tests for normality are used to determine if the log of the response quantities distribute normally. The peak isolator displacements, peak temperatures at the sliding surface, and floor spectral accelerations distribute lognormally in at least 90%, 80% and 90% of the cases, respectively, according to the three tests performed at the 5% significance level. Therefore, the distributions can be assumed to be lognormal for all combinations of natural period, reference coefficient of friction, friction model, reference axial pressure and sets of ground motions.

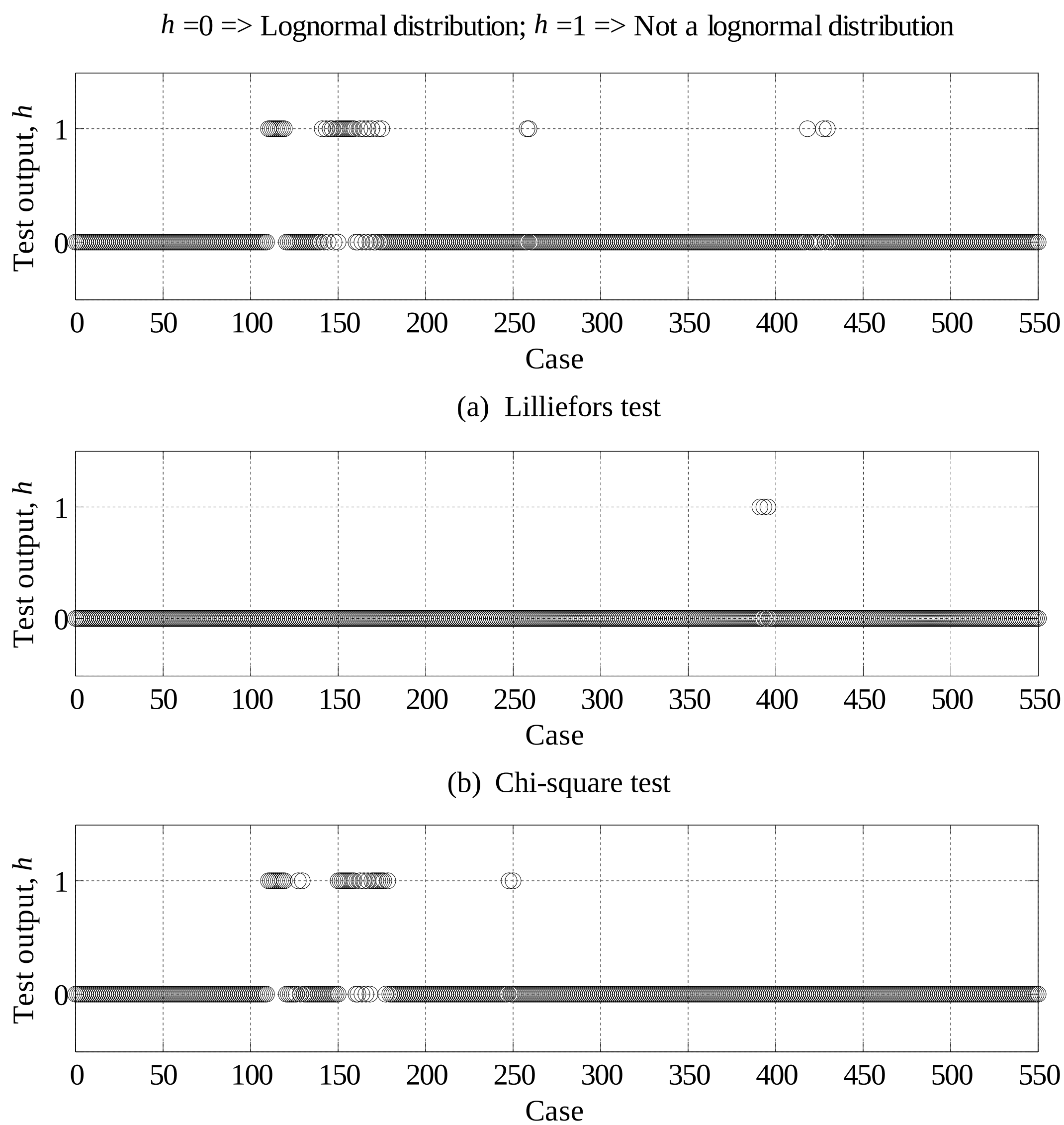

(a) Lilliefors test

(b) Chi-square test

(c) Jarque-Bera test

Figure H-2: Results of normality tests performed on the sets of the logs of the 30 values of peak displacements of FP bearings

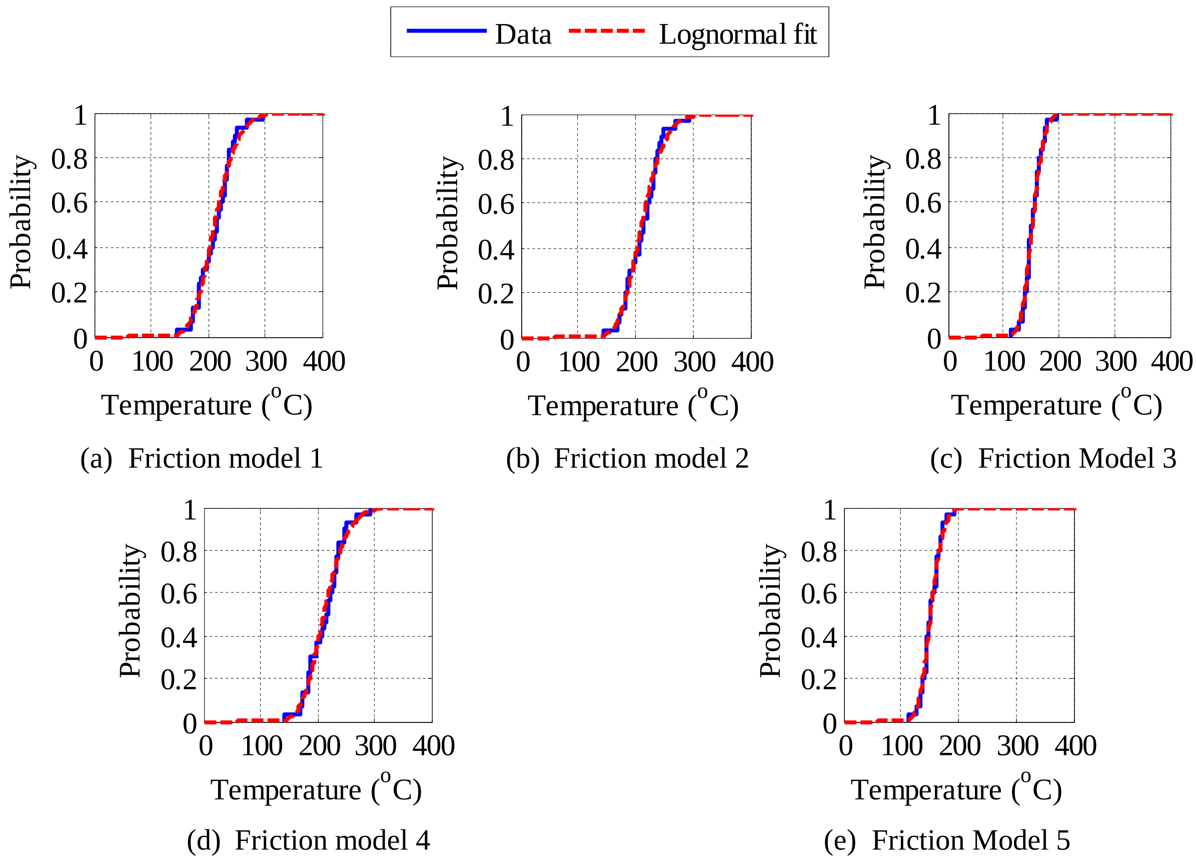

Figure H-3: Empirical cumulative distribution of the 30 values of peak temperature and the lognormal fits

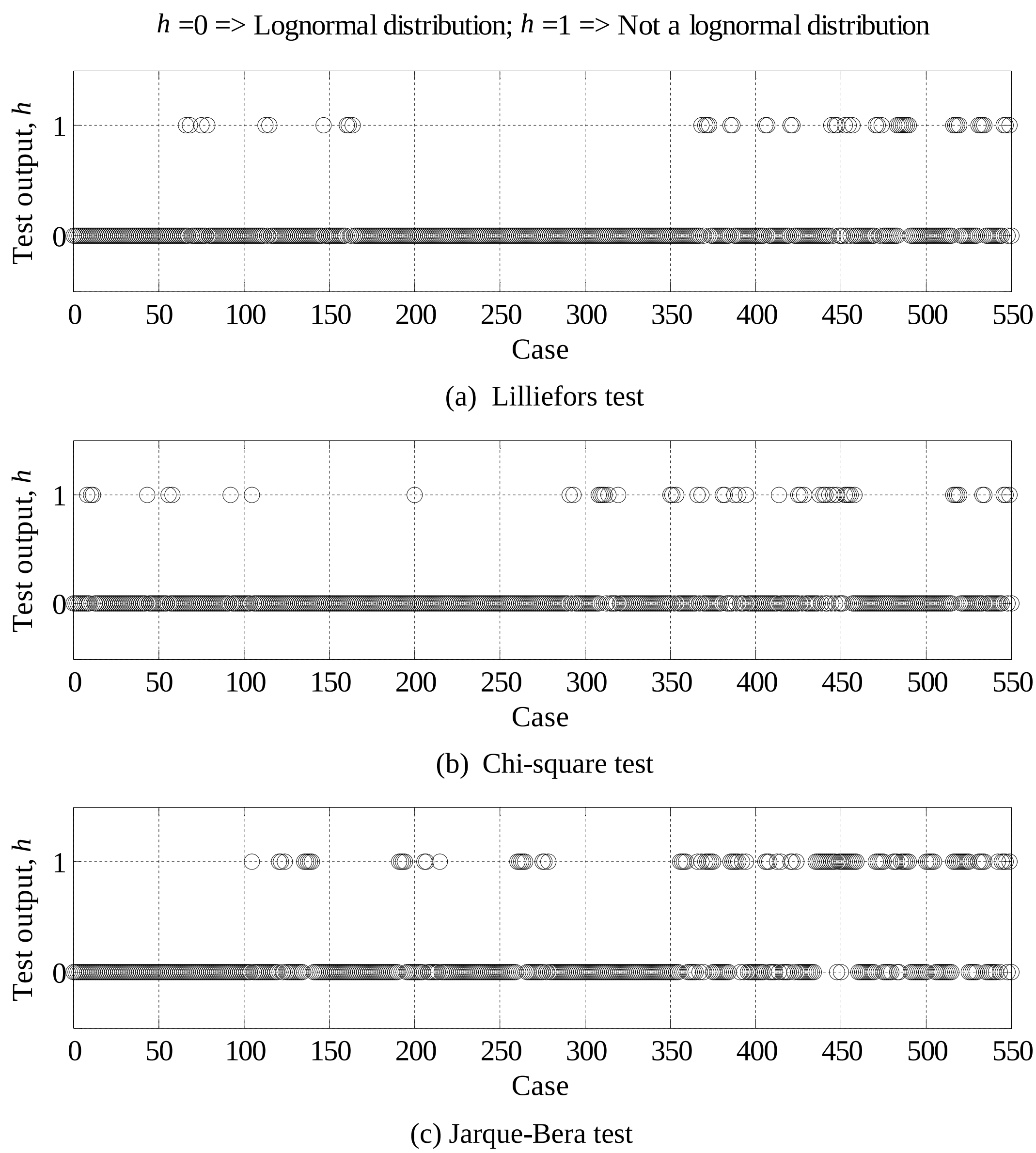

Figure H-4: Results of normality tests performed on the sets of the logs of the 30 values of peak temperature at the sliding surface of FP bearings

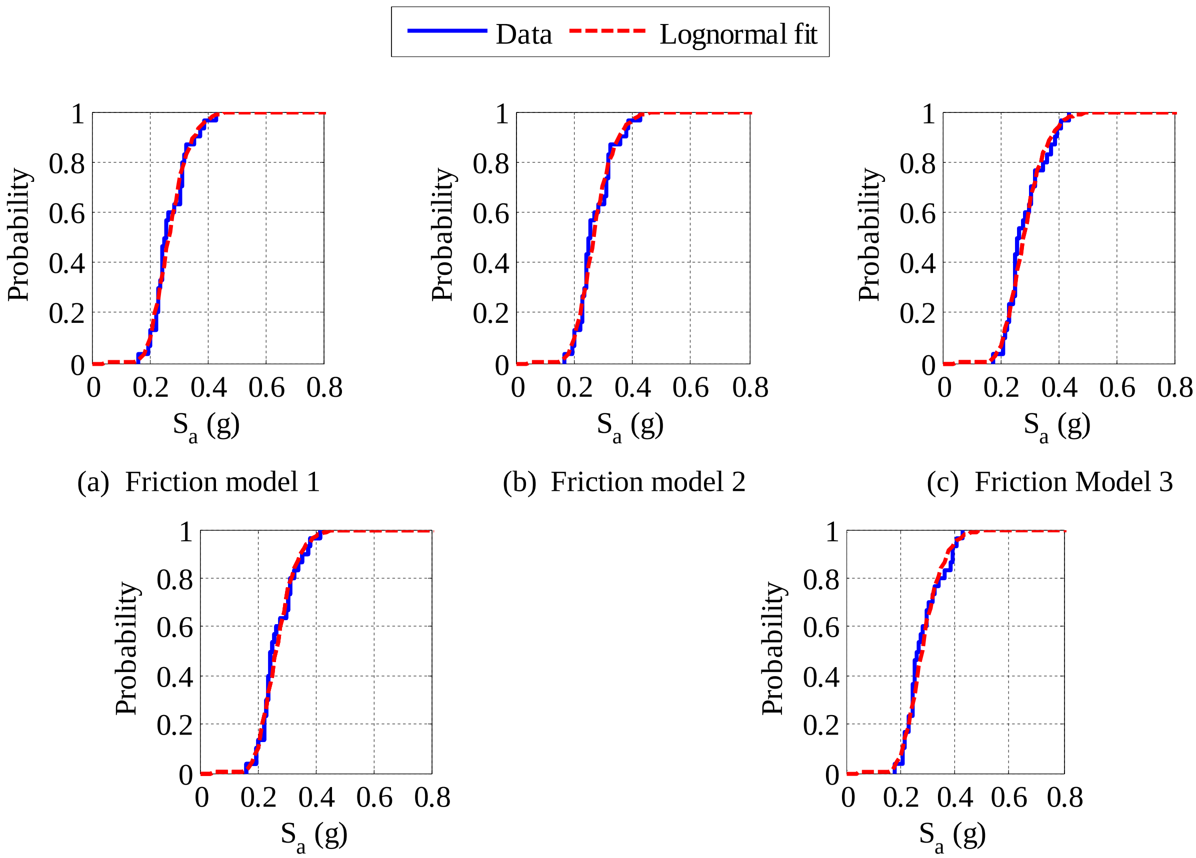

(a) Friction model 1 (b) Friction model 2 (c) Friction Model 3

(d) Friction model 4 (e) Friction Model 5

Figure H-5: Empirical cumulative distribution of the 30 values of floor spectral acceleration and the lognormal fits

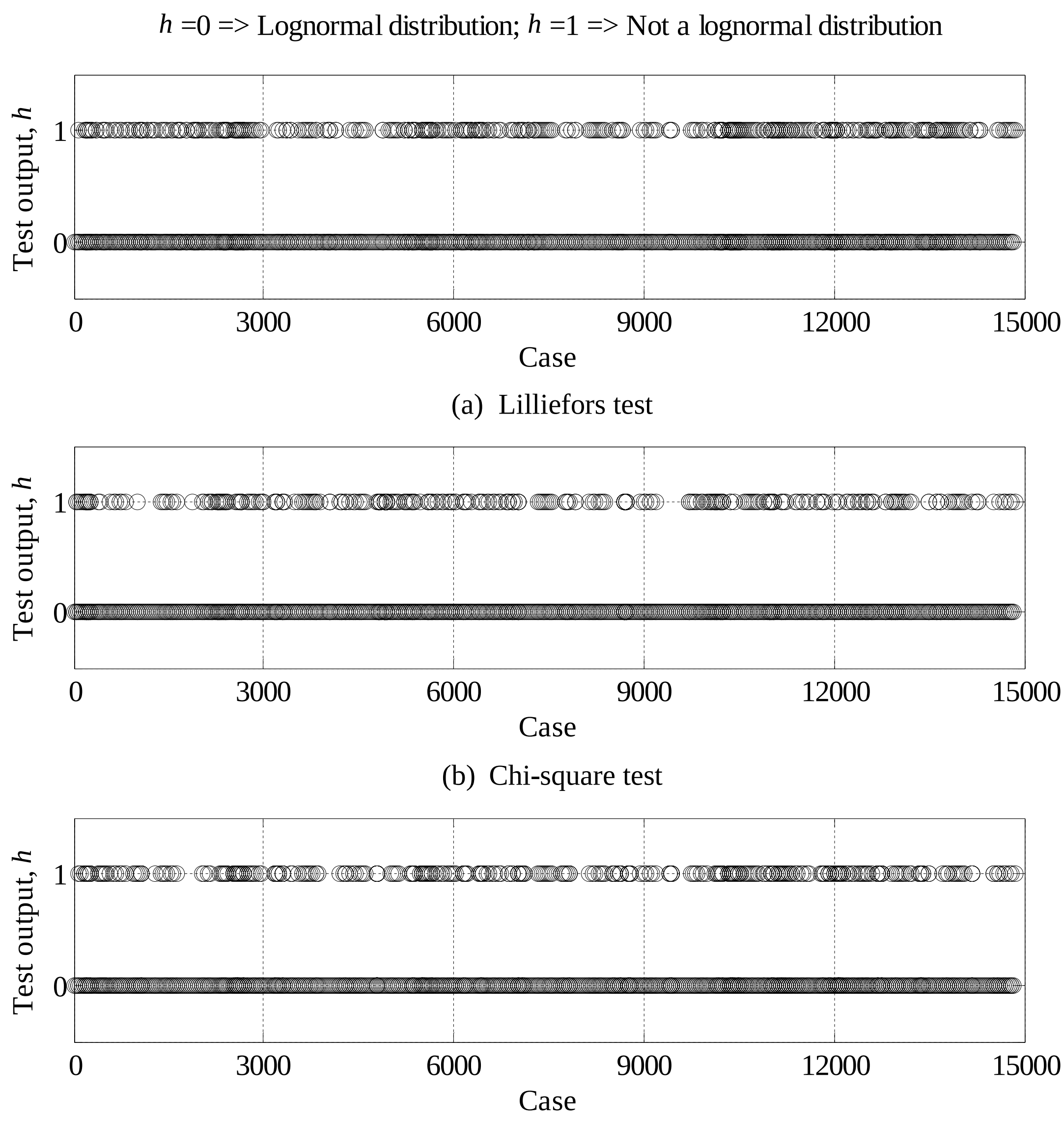

(a) Lilliefors test

(b) Chi-square test

(c) Jarque-Bera test

Figure H-6: Results of normality tests performed on the sets of the logs of the 30 values of floor spectral acceleration

APPENDIX I

OPENSEES MODEL OF THE AUXILIARY AND SHIELD BUILDINGS

I.1 Introduction

A detailed model of auxiliary and shield building (ASB) of a nuclear power plant (NPP) is developed and analyzed. Results are reported in Chapter 8. This appendix presents the details of the OpenSees (PEER, 2014) model of the ASB: coordinates of nodes, mass associated with nodes, connectivity of elements and properties of elements between nodes.

I.2 Features of the OpenSees model for the ASB

Table I-1 list the nodes (and their coordinates) in the OpenSees model of the ASB. Table I-2 presents the mass associated with each node in three orthogonal directions (two horizontal and vertical) and the inertial mass about the axes through the three directions. Table I-3 lists the node connectivity of the horizontal elements in the ASB. Table I-4 lists the connectivity of the vertical elements of the ASB, together with the area moments of inertia of the elements (columns) about the two principal (orthogonal) horizontal directions.

Table I-1: Coordinates of nodes in the OpenSees model of the ASB

Node	Coordinates (m)			Node	Coordinates (m)		
	X	Y	Z		X	Y	Z
101010	0.0	0.0	1.2	105020	24.0	6.0	1.2
101020	0.0	6.0	1.2	105030	24.0	12.0	1.2
101030	0.0	12.0	1.2	105040	24.0	18.0	1.2
101040	0.0	18.0	1.2	105050	24.0	24.0	1.2
101050	0.0	24.0	1.2	105060	24.0	30.0	1.2
101060	0.0	30.0	1.2	105070	24.0	36.0	1.2
101070	0.0	36.0	1.2	105080	24.0	42.0	1.2
101080	0.0	42.0	1.2	105090	24.0	48.0	1.2
101090	0.0	48.0	1.2	105100	24.0	54.0	1.2
101100	0.0	54.0	1.2	105110	24.0	60.0	1.2
101110	0.0	60.0	1.2	106010	30.0	0.0	1.2
102010	6.0	0.0	1.2	106020	30.0	6.0	1.2
102020	6.0	6.0	1.2	106030	30.0	12.0	1.2
102030	6.0	12.0	1.2	106040	30.0	18.0	1.2
102040	6.0	18.0	1.2	106050	30.0	24.0	1.2
102050	6.0	24.0	1.2	106060	30.0	30.0	1.2
102060	6.0	30.0	1.2	106070	30.0	36.0	1.2
102070	6.0	36.0	1.2	106080	30.0	42.0	1.2
102080	6.0	42.0	1.2	106090	30.0	48.0	1.2
102090	6.0	48.0	1.2	106100	30.0	54.0	1.2
102100	6.0	54.0	1.2	106110	30.0	60.0	1.2
102110	6.0	60.0	1.2	107010	36.0	0.0	1.2
103010	12.0	0.0	1.2	107020	36.0	6.0	1.2
103020	12.0	6.0	1.2	107030	36.0	12.0	1.2
103030	12.0	12.0	1.2	107040	36.0	18.0	1.2
103040	12.0	18.0	1.2	107050	36.0	24.0	1.2
103050	12.0	24.0	1.2	107060	36.0	30.0	1.2
103060	12.0	30.0	1.2	107070	36.0	36.0	1.2
103070	12.0	36.0	1.2	107080	36.0	42.0	1.2
103080	12.0	42.0	1.2	107090	36.0	48.0	1.2
103090	12.0	48.0	1.2	107100	36.0	54.0	1.2
103100	12.0	54.0	1.2	107110	36.0	60.0	1.2
103110	12.0	60.0	1.2	108010	42.0	0.0	1.2
104010	18.0	0.0	1.2	108020	42.0	6.0	1.2
104020	18.0	6.0	1.2	108030	42.0	12.0	1.2
104030	18.0	12.0	1.2	108040	42.0	18.0	1.2
104040	18.0	18.0	1.2	108050	42.0	24.0	1.2
104050	18.0	24.0	1.2	108060	42.0	30.0	1.2
104060	18.0	30.0	1.2	108070	42.0	36.0	1.2
104070	18.0	36.0	1.2	108080	42.0	42.0	1.2
104080	18.0	42.0	1.2	108090	42.0	48.0	1.2
104090	18.0	48.0	1.2	108100	42.0	54.0	1.2
104100	18.0	54.0	1.2	108110	42.0	60.0	1.2
104110	18.0	60.0	1.2	109010	48.0	0.0	1.2
105010	24.0	0.0	1.2	109020	48.0	6.0	1.2

Table I-1 (continued)

Node	Coordinates (m)			Node	Coordinates (m)		
	X	Y	Z		X	Y	Z
109030	48.0	12.0	1.2	113040	72.0	18.0	1.2
109040	48.0	18.0	1.2	113050	72.0	24.0	1.2
109050	48.0	24.0	1.2	113060	72.0	30.0	1.2
109060	48.0	30.0	1.2	113070	72.0	36.0	1.2
109070	48.0	36.0	1.2	113080	72.0	42.0	1.2
109080	48.0	42.0	1.2	113090	72.0	48.0	1.2
109090	48.0	48.0	1.2	113100	72.0	54.0	1.2
109100	48.0	54.0	1.2	113110	72.0	60.0	1.2
109110	48.0	60.0	1.2	114010	78.0	0.0	1.2
110010	54.0	0.0	1.2	114020	78.0	6.0	1.2
110020	54.0	6.0	1.2	114030	78.0	12.0	1.2
110030	54.0	12.0	1.2	114040	78.0	18.0	1.2
110040	54.0	18.0	1.2	114050	78.0	24.0	1.2
110050	54.0	24.0	1.2	114060	78.0	30.0	1.2
110060	54.0	30.0	1.2	114070	78.0	36.0	1.2
110070	54.0	36.0	1.2	114080	78.0	42.0	1.2
110080	54.0	42.0	1.2	114090	78.0	48.0	1.2
110090	54.0	48.0	1.2	114100	78.0	54.0	1.2
110100	54.0	54.0	1.2	114110	78.0	60.0	1.2
110110	54.0	60.0	1.2	115010	84.0	0.0	1.2
111010	60.0	0.0	1.2	115020	84.0	6.0	1.2
111020	60.0	6.0	1.2	115030	84.0	12.0	1.2
111030	60.0	12.0	1.2	115040	84.0	18.0	1.2
111040	60.0	18.0	1.2	115050	84.0	24.0	1.2
111050	60.0	24.0	1.2	115060	84.0	30.0	1.2
111060	60.0	30.0	1.2	115070	84.0	36.0	1.2
111070	60.0	36.0	1.2	115080	84.0	42.0	1.2
111080	60.0	42.0	1.2	115090	84.0	48.0	1.2
111090	60.0	48.0	1.2	115100	84.0	54.0	1.2
111100	60.0	54.0	1.2	115110	84.0	60.0	1.2
111110	60.0	60.0	1.2	116010	90.0	0.0	1.2
112010	66.0	0.0	1.2	116020	90.0	6.0	1.2
112020	66.0	6.0	1.2	116030	90.0	12.0	1.2
112030	66.0	12.0	1.2	116040	90.0	18.0	1.2
112040	66.0	18.0	1.2	116050	90.0	24.0	1.2
112050	66.0	24.0	1.2	116060	90.0	30.0	1.2
112060	66.0	30.0	1.2	116070	90.0	36.0	1.2
112070	66.0	36.0	1.2	116080	90.0	42.0	1.2
112080	66.0	42.0	1.2	116090	90.0	48.0	1.2
112090	66.0	48.0	1.2	116100	90.0	54.0	1.2
112100	66.0	54.0	1.2	116110	90.0	60.0	1.2
112110	66.0	60.0	1.2	117010	96.0	0.0	1.2
113010	72.0	0.0	1.2	117020	96.0	6.0	1.2
113020	72.0	6.0	1.2	117030	96.0	12.0	1.2
113030	72.0	12.0	1.2	117040	96.0	18.0	1.2

Table I-1 (continued)

Node	Coordinates (m)			Node	Coordinates (m)		
	X	Y	Z		X	Y	Z
117050	96.0	24.0	1.2	204060	18.0	30.0	9.1
117060	96.0	30.0	1.2	204070	18.0	36.0	9.1
117070	96.0	36.0	1.2	204080	18.0	42.0	9.1
117080	96.0	42.0	1.2	204090	18.0	48.0	9.1
117090	96.0	48.0	1.2	204100	18.0	54.0	9.1
117100	96.0	54.0	1.2	204110	18.0	60.0	9.1
117110	96.0	60.0	1.2	205010	24.0	0.0	9.1
201010	0.0	0.0	9.1	205020	24.0	6.0	9.1
201020	0.0	6.0	9.1	205030	24.0	12.0	9.1
201030	0.0	12.0	9.1	205040	24.0	18.0	9.1
201040	0.0	18.0	9.1	205050	24.0	24.0	9.1
201050	0.0	24.0	9.1	205060	24.0	30.0	9.1
201060	0.0	30.0	9.1	205070	24.0	36.0	9.1
201070	0.0	36.0	9.1	205080	24.0	42.0	9.1
201080	0.0	42.0	9.1	205090	24.0	48.0	9.1
201090	0.0	48.0	9.1	205100	24.0	54.0	9.1
201100	0.0	54.0	9.1	205110	24.0	60.0	9.1
201110	0.0	60.0	9.1	206010	30.0	0.0	9.1
202010	6.0	0.0	9.1	206020	30.0	6.0	9.1
202020	6.0	6.0	9.1	206030	30.0	12.0	9.1
202030	6.0	12.0	9.1	206040	30.0	18.0	9.1
202040	6.0	18.0	9.1	206050	30.0	24.0	9.1
202050	6.0	24.0	9.1	206060	30.0	30.0	9.1
202060	6.0	30.0	9.1	206070	30.0	36.0	9.1
202070	6.0	36.0	9.1	206080	30.0	42.0	9.1
202080	6.0	42.0	9.1	206090	30.0	48.0	9.1
202090	6.0	48.0	9.1	206100	30.0	54.0	9.1
202100	6.0	54.0	9.1	206110	30.0	60.0	9.1
202110	6.0	60.0	9.1	207010	36.0	0.0	9.1
203010	12.0	0.0	9.1	207020	36.0	6.0	9.1
203020	12.0	6.0	9.1	207030	36.0	12.0	9.1
203030	12.0	12.0	9.1	207040	36.0	18.0	9.1
203040	12.0	18.0	9.1	207050	36.0	24.0	9.1
203050	12.0	24.0	9.1	207060	36.0	30.0	9.1
203060	12.0	30.0	9.1	207070	36.0	36.0	9.1
203070	12.0	36.0	9.1	207080	36.0	42.0	9.1
203080	12.0	42.0	9.1	207090	36.0	48.0	9.1
203090	12.0	48.0	9.1	207100	36.0	54.0	9.1
203100	12.0	54.0	9.1	207110	36.0	60.0	9.1
203110	12.0	60.0	9.1	208010	42.0	0.0	9.1
204010	18.0	0.0	9.1	208020	42.0	6.0	9.1
204020	18.0	6.0	9.1	208030	42.0	12.0	9.1
204030	18.0	12.0	9.1	208040	42.0	18.0	9.1
204040	18.0	18.0	9.1	208050	42.0	24.0	9.1
204050	18.0	24.0	9.1	208060	42.0	30.0	9.1

Table I-1 (continued)

Node	Coordinates (m)			Node	Coordinates (m)		
	X	Y	Z		X	Y	Z
208070	42.0	36.0	9.1	212080	66.0	42.0	9.1
208080	42.0	42.0	9.1	212090	66.0	48.0	9.1
208090	42.0	48.0	9.1	212100	66.0	54.0	9.1
208100	42.0	54.0	9.1	212110	66.0	60.0	9.1
208110	42.0	60.0	9.1	213010	72.0	0.0	9.1
209010	48.0	0.0	9.1	213020	72.0	6.0	9.1
209020	48.0	6.0	9.1	213030	72.0	12.0	9.1
209030	48.0	12.0	9.1	213040	72.0	18.0	9.1
209040	48.0	18.0	9.1	213050	72.0	24.0	9.1
209050	48.0	24.0	9.1	213060	72.0	30.0	9.1
209060	48.0	30.0	9.1	213070	72.0	36.0	9.1
209070	48.0	36.0	9.1	213080	72.0	42.0	9.1
209080	48.0	42.0	9.1	213090	72.0	48.0	9.1
209090	48.0	48.0	9.1	213100	72.0	54.0	9.1
209100	48.0	54.0	9.1	213110	72.0	60.0	9.1
209110	48.0	60.0	9.1	214010	78.0	0.0	9.1
210010	54.0	0.0	9.1	214020	78.0	6.0	9.1
210020	54.0	6.0	9.1	214030	78.0	12.0	9.1
210030	54.0	12.0	9.1	214040	78.0	18.0	9.1
210040	54.0	18.0	9.1	214050	78.0	24.0	9.1
210050	54.0	24.0	9.1	214060	78.0	30.0	9.1
210060	54.0	30.0	9.1	214070	78.0	36.0	9.1
210070	54.0	36.0	9.1	214080	78.0	42.0	9.1
210080	54.0	42.0	9.1	214090	78.0	48.0	9.1
210090	54.0	48.0	9.1	214100	78.0	54.0	9.1
210100	54.0	54.0	9.1	214110	78.0	60.0	9.1
210110	54.0	60.0	9.1	215010	84.0	0.0	9.1
211010	60.0	0.0	9.1	215020	84.0	6.0	9.1
211020	60.0	6.0	9.1	215030	84.0	12.0	9.1
211030	60.0	12.0	9.1	215040	84.0	18.0	9.1
211040	60.0	18.0	9.1	215050	84.0	24.0	9.1
211050	60.0	24.0	9.1	215060	84.0	30.0	9.1
211060	60.0	30.0	9.1	215070	84.0	36.0	9.1
211070	60.0	36.0	9.1	215080	84.0	42.0	9.1
211080	60.0	42.0	9.1	215090	84.0	48.0	9.1
211090	60.0	48.0	9.1	215100	84.0	54.0	9.1
211100	60.0	54.0	9.1	215110	84.0	60.0	9.1
211110	60.0	60.0	9.1	216010	90.0	0.0	9.1
212010	66.0	0.0	9.1	216020	90.0	6.0	9.1
212020	66.0	6.0	9.1	216030	90.0	12.0	9.1
212030	66.0	12.0	9.1	216040	90.0	18.0	9.1
212040	66.0	18.0	9.1	216050	90.0	24.0	9.1
212050	66.0	24.0	9.1	216060	90.0	30.0	9.1
212060	66.0	30.0	9.1	216070	90.0	36.0	9.1
212070	66.0	36.0	9.1	216080	90.0	42.0	9.1

Table I-1 (continued)

Node	Coordinates (m)			Node	Coordinates (m)		
	X	Y	Z		X	Y	Z
216090	90.0	48.0	9.1	303100	12.0	54.0	15.9
216100	90.0	54.0	9.1	303110	12.0	60.0	15.9
216110	90.0	60.0	9.1	304010	18.0	0.0	15.9
217010	96.0	0.0	9.1	304020	18.0	6.0	15.9
217020	96.0	6.0	9.1	304030	18.0	12.0	15.9
217030	96.0	12.0	9.1	304040	18.0	18.0	15.9
217040	96.0	18.0	9.1	304050	18.0	24.0	15.9
217050	96.0	24.0	9.1	304060	18.0	30.0	15.9
217060	96.0	30.0	9.1	304070	18.0	36.0	15.9
217070	96.0	36.0	9.1	304080	18.0	42.0	15.9
217080	96.0	42.0	9.1	304090	18.0	48.0	15.9
217090	96.0	48.0	9.1	304100	18.0	54.0	15.9
217100	96.0	54.0	9.1	304110	18.0	60.0	15.9
217110	96.0	60.0	9.1	305010	24.0	0.0	15.9
301010	0.0	0.0	15.9	305020	24.0	6.0	15.9
301020	0.0	6.0	15.9	305030	24.0	12.0	15.9
301030	0.0	12.0	15.9	305040	24.0	18.0	15.9
301040	0.0	18.0	15.9	305050	24.0	24.0	15.9
301050	0.0	24.0	15.9	305060	24.0	30.0	15.9
301060	0.0	30.0	15.9	305070	24.0	36.0	15.9
301070	0.0	36.0	15.9	305080	24.0	42.0	15.9
301080	0.0	42.0	15.9	305090	24.0	48.0	15.9
301090	0.0	48.0	15.9	305100	24.0	54.0	15.9
301100	0.0	54.0	15.9	305110	24.0	60.0	15.9
301110	0.0	60.0	15.9	306010	30.0	0.0	15.9
302010	6.0	0.0	15.9	306020	30.0	6.0	15.9
302020	6.0	6.0	15.9	306030	30.0	12.0	15.9
302030	6.0	12.0	15.9	306040	30.0	18.0	15.9
302040	6.0	18.0	15.9	306050	30.0	24.0	15.9
302050	6.0	24.0	15.9	306060	30.0	30.0	15.9
302060	6.0	30.0	15.9	306070	30.0	36.0	15.9
302070	6.0	36.0	15.9	306080	30.0	42.0	15.9
302080	6.0	42.0	15.9	306090	30.0	48.0	15.9
302090	6.0	48.0	15.9	306100	30.0	54.0	15.9
302100	6.0	54.0	15.9	306110	30.0	60.0	15.9
302110	6.0	60.0	15.9	307010	36.0	0.0	15.9
303010	12.0	0.0	15.9	307020	36.0	6.0	15.9
303020	12.0	6.0	15.9	307030	36.0	12.0	15.9
303030	12.0	12.0	15.9	307040	36.0	18.0	15.9
303040	12.0	18.0	15.9	307050	36.0	24.0	15.9
303050	12.0	24.0	15.9	307060	36.0	30.0	15.9
303060	12.0	30.0	15.9	307070	36.0	36.0	15.9
303070	12.0	36.0	15.9	307080	36.0	42.0	15.9
303080	12.0	42.0	15.9	307090	36.0	48.0	15.9
303090	12.0	48.0	15.9	307100	36.0	54.0	15.9

Table I-1 (continued)

Node	Coordinates (m)			Node	Coordinates (m)		
	X	Y	Z		X	Y	Z
307110	36.0	60.0	15.9	312010	66.0	0.0	15.9
308010	42.0	0.0	15.9	312020	66.0	6.0	15.9
308020	42.0	6.0	15.9	312030	66.0	12.0	15.9
308030	42.0	12.0	15.9	312040	66.0	18.0	15.9
308040	42.0	18.0	15.9	312050	66.0	24.0	15.9
308050	42.0	24.0	15.9	312060	66.0	30.0	15.9
308060	42.0	30.0	15.9	312070	66.0	36.0	15.9
308070	42.0	36.0	15.9	312080	66.0	42.0	15.9
308080	42.0	42.0	15.9	312090	66.0	48.0	15.9
308090	42.0	48.0	15.9	312100	66.0	54.0	15.9
308100	42.0	54.0	15.9	312110	66.0	60.0	15.9
308110	42.0	60.0	15.9	313010	72.0	0.0	15.9
309010	48.0	0.0	15.9	313020	72.0	6.0	15.9
309020	48.0	6.0	15.9	313030	72.0	12.0	15.9
309030	48.0	12.0	15.9	313040	72.0	18.0	15.9
309040	48.0	18.0	15.9	313050	72.0	24.0	15.9
309050	48.0	24.0	15.9	313060	72.0	30.0	15.9
309060	48.0	30.0	15.9	313070	72.0	36.0	15.9
309070	48.0	36.0	15.9	313080	72.0	42.0	15.9
309080	48.0	42.0	15.9	313090	72.0	48.0	15.9
309090	48.0	48.0	15.9	313100	72.0	54.0	15.9
309100	48.0	54.0	15.9	313110	72.0	60.0	15.9
309110	48.0	60.0	15.9	314010	78.0	0.0	15.9
310010	54.0	0.0	15.9	314020	78.0	6.0	15.9
310020	54.0	6.0	15.9	314030	78.0	12.0	15.9
310030	54.0	12.0	15.9	314040	78.0	18.0	15.9
310040	54.0	18.0	15.9	314050	78.0	24.0	15.9
310050	54.0	24.0	15.9	314060	78.0	30.0	15.9
310060	54.0	30.0	15.9	314070	78.0	36.0	15.9
310070	54.0	36.0	15.9	314080	78.0	42.0	15.9
310080	54.0	42.0	15.9	314090	78.0	48.0	15.9
310090	54.0	48.0	15.9	314100	78.0	54.0	15.9
310100	54.0	54.0	15.9	314110	78.0	60.0	15.9
310110	54.0	60.0	15.9	315010	84.0	0.0	15.9
311010	60.0	0.0	15.9	315020	84.0	6.0	15.9
311020	60.0	6.0	15.9	315030	84.0	12.0	15.9
311030	60.0	12.0	15.9	315040	84.0	18.0	15.9
311040	60.0	18.0	15.9	315050	84.0	24.0	15.9
311050	60.0	24.0	15.9	315060	84.0	30.0	15.9
311060	60.0	30.0	15.9	315070	84.0	36.0	15.9
311070	60.0	36.0	15.9	315080	84.0	42.0	15.9
311080	60.0	42.0	15.9	315090	84.0	48.0	15.9
311090	60.0	48.0	15.9	315100	84.0	54.0	15.9
311100	60.0	54.0	15.9	315110	84.0	60.0	15.9
311110	60.0	60.0	15.9	316010	90.0	0.0	15.9

Table I-1 (continued)

Node	Coordinates (m)			Node	Coordinates (m)		
	X	Y	Z		X	Y	Z
316020	90.0	6.0	15.9	403030	12.0	12.0	22.6
316030	90.0	12.0	15.9	403040	12.0	18.0	22.6
316040	90.0	18.0	15.9	403050	12.0	24.0	22.6
316050	90.0	24.0	15.9	403060	12.0	30.0	22.6
316060	90.0	30.0	15.9	403070	12.0	36.0	22.6
316070	90.0	36.0	15.9	403080	12.0	42.0	22.6
316080	90.0	42.0	15.9	403090	12.0	48.0	22.6
316090	90.0	48.0	15.9	403100	12.0	54.0	22.6
316100	90.0	54.0	15.9	403110	12.0	60.0	22.6
316110	90.0	60.0	15.9	404010	18.0	0.0	22.6
317010	96.0	0.0	15.9	404020	18.0	6.0	22.6
317020	96.0	6.0	15.9	404030	18.0	12.0	22.6
317030	96.0	12.0	15.9	404040	18.0	18.0	22.6
317040	96.0	18.0	15.9	404050	18.0	24.0	22.6
317050	96.0	24.0	15.9	404060	18.0	30.0	22.6
317060	96.0	30.0	15.9	404070	18.0	36.0	22.6
317070	96.0	36.0	15.9	404080	18.0	42.0	22.6
317080	96.0	42.0	15.9	404090	18.0	48.0	22.6
317090	96.0	48.0	15.9	404100	18.0	54.0	22.6
317100	96.0	54.0	15.9	404110	18.0	60.0	22.6
317110	96.0	60.0	15.9	405010	24.0	0.0	22.6
401010	0.0	0.0	22.6	405020	24.0	6.0	22.6
401020	0.0	6.0	22.6	405030	24.0	12.0	22.6
401030	0.0	12.0	22.6	405040	24.0	18.0	22.6
401040	0.0	18.0	22.6	405050	24.0	24.0	22.6
401050	0.0	24.0	22.6	405060	24.0	30.0	22.6
401060	0.0	30.0	22.6	405070	24.0	36.0	22.6
401070	0.0	36.0	22.6	405080	24.0	42.0	22.6
401080	0.0	42.0	22.6	405090	24.0	48.0	22.6
401090	0.0	48.0	22.6	405100	24.0	54.0	22.6
401100	0.0	54.0	22.6	405110	24.0	60.0	22.6
401110	0.0	60.0	22.6	406010	30.0	0.0	22.6
402010	6.0	0.0	22.6	406020	30.0	6.0	22.6
402020	6.0	6.0	22.6	406030	30.0	12.0	22.6
402030	6.0	12.0	22.6	406040	30.0	18.0	22.6
402040	6.0	18.0	22.6	406050	30.0	24.0	22.6
402050	6.0	24.0	22.6	406060	30.0	30.0	22.6
402060	6.0	30.0	22.6	406070	30.0	36.0	22.6
402070	6.0	36.0	22.6	406080	30.0	42.0	22.6
402080	6.0	42.0	22.6	406090	30.0	48.0	22.6
402090	6.0	48.0	22.6	406100	30.0	54.0	22.6
402100	6.0	54.0	22.6	406110	30.0	60.0	22.6
402110	6.0	60.0	22.6	407010	36.0	0.0	22.6
403010	12.0	0.0	22.6	407020	36.0	6.0	22.6
403020	12.0	6.0	22.6	407030	36.0	12.0	22.6

Table I-1 (continued)

Node	Coordinates (m)			Node	Coordinates (m)		
	X	Y	Z		X	Y	Z
407040	36.0	18.0	22.6	411050	60.0	24.0	22.6
407050	36.0	24.0	22.6	411060	60.0	30.0	22.6
407060	36.0	30.0	22.6	411070	60.0	36.0	22.6
407070	36.0	36.0	22.6	411080	60.0	42.0	22.6
407080	36.0	42.0	22.6	411090	60.0	48.0	22.6
407090	36.0	48.0	22.6	411100	60.0	54.0	22.6
407100	36.0	54.0	22.6	411110	60.0	60.0	22.6
407110	36.0	60.0	22.6	412010	66.0	0.0	22.6
408010	42.0	0.0	22.6	412020	66.0	6.0	22.6
408020	42.0	6.0	22.6	412030	66.0	12.0	22.6
408030	42.0	12.0	22.6	412040	66.0	18.0	22.6
408040	42.0	18.0	22.6	412050	66.0	24.0	22.6
408050	42.0	24.0	22.6	412060	66.0	30.0	22.6
408060	42.0	30.0	22.6	412070	66.0	36.0	22.6
408070	42.0	36.0	22.6	412080	66.0	42.0	22.6
408080	42.0	42.0	22.6	412090	66.0	48.0	22.6
408090	42.0	48.0	22.6	412100	66.0	54.0	22.6
408100	42.0	54.0	22.6	412110	66.0	60.0	22.6
408110	42.0	60.0	22.6	413010	72.0	0.0	22.6
409010	48.0	0.0	22.6	413020	72.0	6.0	22.6
409020	48.0	6.0	22.6	413030	72.0	12.0	22.6
409030	48.0	12.0	22.6	413040	72.0	18.0	22.6
409040	48.0	18.0	22.6	413050	72.0	24.0	22.6
409050	48.0	24.0	22.6	413060	72.0	30.0	22.6
409060	48.0	30.0	22.6	413070	72.0	36.0	22.6
409070	48.0	36.0	22.6	413080	72.0	42.0	22.6
409080	48.0	42.0	22.6	413090	72.0	48.0	22.6
409090	48.0	48.0	22.6	413100	72.0	54.0	22.6
409100	48.0	54.0	22.6	413110	72.0	60.0	22.6
409110	48.0	60.0	22.6	414010	78.0	0.0	22.6
410010	54.0	0.0	22.6	414020	78.0	6.0	22.6
410020	54.0	6.0	22.6	414030	78.0	12.0	22.6
410030	54.0	12.0	22.6	414040	78.0	18.0	22.6
410040	54.0	18.0	22.6	414050	78.0	24.0	22.6
410050	54.0	24.0	22.6	414060	78.0	30.0	22.6
410060	54.0	30.0	22.6	414070	78.0	36.0	22.6
410070	54.0	36.0	22.6	414080	78.0	42.0	22.6
410080	54.0	42.0	22.6	414090	78.0	48.0	22.6
410090	54.0	48.0	22.6	414100	78.0	54.0	22.6
410100	54.0	54.0	22.6	414110	78.0	60.0	22.6
410110	54.0	60.0	22.6	415010	84.0	0.0	22.6
411010	60.0	0.0	22.6	415020	84.0	6.0	22.6
411020	60.0	6.0	22.6	415030	84.0	12.0	22.6
411030	60.0	12.0	22.6	415040	84.0	18.0	22.6
411040	60.0	18.0	22.6	415050	84.0	24.0	22.6

Table I-1 (continued)

Node	Coordinates (m)			Node	Coordinates (m)		
	X	Y	Z		X	Y	Z
415060	84.0	30.0	22.6	502070	6.0	36.0	29.3
415070	84.0	36.0	22.6	502080	6.0	42.0	29.3
415080	84.0	42.0	22.6	502090	6.0	48.0	29.3
415090	84.0	48.0	22.6	502100	6.0	54.0	29.3
415100	84.0	54.0	22.6	502110	6.0	60.0	29.3
415110	84.0	60.0	22.6	503010	12.0	0.0	29.3
416010	90.0	0.0	22.6	503020	12.0	6.0	29.3
416020	90.0	6.0	22.6	503030	12.0	12.0	29.3
416030	90.0	12.0	22.6	503040	12.0	18.0	29.3
416040	90.0	18.0	22.6	503050	12.0	24.0	29.3
416050	90.0	24.0	22.6	503060	12.0	30.0	29.3
416060	90.0	30.0	22.6	503070	12.0	36.0	29.3
416070	90.0	36.0	22.6	503080	12.0	42.0	29.3
416080	90.0	42.0	22.6	503090	12.0	48.0	29.3
416090	90.0	48.0	22.6	503100	12.0	54.0	29.3
416100	90.0	54.0	22.6	503110	12.0	60.0	29.3
416110	90.0	60.0	22.6	504010	18.0	0.0	29.3
417010	96.0	0.0	22.6	504020	18.0	6.0	29.3
417020	96.0	6.0	22.6	504030	18.0	12.0	29.3
417030	96.0	12.0	22.6	504040	18.0	18.0	29.3
417040	96.0	18.0	22.6	504050	18.0	24.0	29.3
417050	96.0	24.0	22.6	504060	18.0	30.0	29.3
417060	96.0	30.0	22.6	504070	18.0	36.0	29.3
417070	96.0	36.0	22.6	504080	18.0	42.0	29.3
417080	96.0	42.0	22.6	504090	18.0	48.0	29.3
417090	96.0	48.0	22.6	504100	18.0	54.0	29.3
417100	96.0	54.0	22.6	504110	18.0	60.0	29.3
417110	96.0	60.0	22.6	505010	24.0	0.0	29.3
501010	0.0	0.0	29.3	505020	24.0	6.0	29.3
501020	0.0	6.0	29.3	505030	24.0	12.0	29.3
501030	0.0	12.0	29.3	505040	24.0	18.0	29.3
501040	0.0	18.0	29.3	505050	24.0	24.0	29.3
501050	0.0	24.0	29.3	505060	24.0	30.0	29.3
501060	0.0	30.0	29.3	505070	24.0	36.0	29.3
501070	0.0	36.0	29.3	505080	24.0	42.0	29.3
501080	0.0	42.0	29.3	505090	24.0	48.0	29.3
501090	0.0	48.0	29.3	505100	24.0	54.0	29.3
501100	0.0	54.0	29.3	505110	24.0	60.0	29.3
501110	0.0	60.0	29.3	506010	30.0	0.0	29.3
502010	6.0	0.0	29.3	506020	30.0	6.0	29.3
502020	6.0	6.0	29.3	506030	30.0	12.0	29.3
502030	6.0	12.0	29.3	506040	30.0	18.0	29.3
502040	6.0	18.0	29.3	506050	30.0	24.0	29.3
502050	6.0	24.0	29.3	506060	30.0	30.0	29.3
502060	6.0	30.0	29.3	506070	30.0	36.0	29.3

Table I-1 (continued)

Node	Coordinates (m)			Node	Coordinates (m)		
	X	Y	Z		X	Y	Z
506080	30.0	42.0	29.3	510090	54.0	48.0	29.3
506090	30.0	48.0	29.3	510100	54.0	54.0	29.3
506100	30.0	54.0	29.3	510110	54.0	60.0	29.3
506110	30.0	60.0	29.3	511010	60.0	0.0	29.3
507010	36.0	0.0	29.3	511020	60.0	6.0	29.3
507020	36.0	6.0	29.3	511030	60.0	12.0	29.3
507030	36.0	12.0	29.3	511040	60.0	18.0	29.3
507040	36.0	18.0	29.3	511050	60.0	24.0	29.3
507050	36.0	24.0	29.3	511060	60.0	30.0	29.3
507060	36.0	30.0	29.3	511070	60.0	36.0	29.3
507070	36.0	36.0	29.3	511080	60.0	42.0	29.3
507080	36.0	42.0	29.3	511090	60.0	48.0	29.3
507090	36.0	48.0	29.3	511100	60.0	54.0	29.3
507100	36.0	54.0	29.3	511110	60.0	60.0	29.3
507110	36.0	60.0	29.3	512010	66.0	0.0	29.3
508010	42.0	0.0	29.3	512020	66.0	6.0	29.3
508020	42.0	6.0	29.3	512030	66.0	12.0	29.3
508030	42.0	12.0	29.3	512040	66.0	18.0	29.3
508040	42.0	18.0	29.3	512050	66.0	24.0	29.3
508050	42.0	24.0	29.3	512060	66.0	30.0	29.3
508060	42.0	30.0	29.3	512070	66.0	36.0	29.3
508070	42.0	36.0	29.3	512080	66.0	42.0	29.3
508080	42.0	42.0	29.3	512090	66.0	48.0	29.3
508090	42.0	48.0	29.3	512100	66.0	54.0	29.3
508100	42.0	54.0	29.3	512110	66.0	60.0	29.3
508110	42.0	60.0	29.3	513010	72.0	0.0	29.3
509010	48.0	0.0	29.3	513020	72.0	6.0	29.3
509020	48.0	6.0	29.3	513030	72.0	12.0	29.3
509030	48.0	12.0	29.3	513040	72.0	18.0	29.3
509040	48.0	18.0	29.3	513050	72.0	24.0	29.3
509050	48.0	24.0	29.3	513060	72.0	30.0	29.3
509060	48.0	30.0	29.3	513070	72.0	36.0	29.3
509070	48.0	36.0	29.3	513080	72.0	42.0	29.3
509080	48.0	42.0	29.3	513090	72.0	48.0	29.3
509090	48.0	48.0	29.3	513100	72.0	54.0	29.3
509100	48.0	54.0	29.3	513110	72.0	60.0	29.3
509110	48.0	60.0	29.3	514010	78.0	0.0	29.3
510010	54.0	0.0	29.3	514020	78.0	6.0	29.3
510020	54.0	6.0	29.3	514030	78.0	12.0	29.3
510030	54.0	12.0	29.3	514040	78.0	18.0	29.3
510040	54.0	18.0	29.3	514050	78.0	24.0	29.3
510050	54.0	24.0	29.3	514060	78.0	30.0	29.3
510060	54.0	30.0	29.3	514070	78.0	36.0	29.3
510070	54.0	36.0	29.3	514080	78.0	42.0	29.3
510080	54.0	42.0	29.3	514090	78.0	48.0	29.3

Table I-1 (continued)

Node	Coordinates (m)			Node	Coordinates (m)		
	X	Y	Z		X	Y	Z
514100	78.0	54.0	29.3	605110	24.0	60.0	41.5
514110	78.0	60.0	29.3	606010	30.0	0.0	41.5
515010	84.0	0.0	29.3	606020	30.0	6.0	41.5
515020	84.0	6.0	29.3	606030	30.0	12.0	41.5
515030	84.0	12.0	29.3	606040	30.0	18.0	41.5
515040	84.0	18.0	29.3	606050	30.0	24.0	41.5
515050	84.0	24.0	29.3	606060	30.0	30.0	41.5
515060	84.0	30.0	29.3	606070	30.0	36.0	41.5
515070	84.0	36.0	29.3	606080	30.0	42.0	41.5
515080	84.0	42.0	29.3	606090	30.0	48.0	41.5
515090	84.0	48.0	29.3	606100	30.0	54.0	41.5
515100	84.0	54.0	29.3	606110	30.0	60.0	41.5
515110	84.0	60.0	29.3	607010	36.0	0.0	41.5
516010	90.0	0.0	29.3	607020	36.0	6.0	41.5
516020	90.0	6.0	29.3	607030	36.0	12.0	41.5
516030	90.0	12.0	29.3	607040	36.0	18.0	41.5
516040	90.0	18.0	29.3	607050	36.0	24.0	41.5
516050	90.0	24.0	29.3	607060	36.0	30.0	41.5
516060	90.0	30.0	29.3	607070	36.0	36.0	41.5
516070	90.0	36.0	29.3	607080	36.0	42.0	41.5
516080	90.0	42.0	29.3	607090	36.0	48.0	41.5
516090	90.0	48.0	29.3	607100	36.0	54.0	41.5
516100	90.0	54.0	29.3	607110	36.0	60.0	41.5
516110	90.0	60.0	29.3	608010	42.0	0.0	41.5
517010	96.0	0.0	29.3	608020	42.0	6.0	41.5
517020	96.0	6.0	29.3	608030	42.0	12.0	41.5
517030	96.0	12.0	29.3	608040	42.0	18.0	41.5
517040	96.0	18.0	29.3	608050	42.0	24.0	41.5
517050	96.0	24.0	29.3	608060	42.0	30.0	41.5
517060	96.0	30.0	29.3	608070	42.0	36.0	41.5
517070	96.0	36.0	29.3	608080	42.0	42.0	41.5
517080	96.0	42.0	29.3	608090	42.0	48.0	41.5
517090	96.0	48.0	29.3	608100	42.0	54.0	41.5
517100	96.0	54.0	29.3	608110	42.0	60.0	41.5
517110	96.0	60.0	29.3	609010	48.0	0.0	41.5
605010	24.0	0.0	41.5	609020	48.0	6.0	41.5
605020	24.0	6.0	41.5	609030	48.0	12.0	41.5
605030	24.0	12.0	41.5	609040	48.0	18.0	41.5
605040	24.0	18.0	41.5	609050	48.0	24.0	41.5
605050	24.0	24.0	41.5	609060	48.0	30.0	41.5
605060	24.0	30.0	41.5	609070	48.0	36.0	41.5
605070	24.0	36.0	41.5	609080	48.0	42.0	41.5
605080	24.0	42.0	41.5	609090	48.0	48.0	41.5
605090	24.0	48.0	41.5	609100	48.0	54.0	41.5
605100	24.0	54.0	41.5	609110	48.0	60.0	41.5

Table I-1 (continued)

Node	Coordinates (m)			Node	Coordinates (m)		
	X	Y	Z		X	Y	Z
610010	54.0	0.0	41.5	705020	24.0	6.0	53.6
610020	54.0	6.0	41.5	705030	24.0	12.0	53.6
610030	54.0	12.0	41.5	705040	24.0	18.0	53.6
610040	54.0	18.0	41.5	705050	24.0	24.0	53.6
610050	54.0	24.0	41.5	705060	24.0	30.0	53.6
610060	54.0	30.0	41.5	705070	24.0	36.0	53.6
610070	54.0	36.0	41.5	705080	24.0	42.0	53.6
610080	54.0	42.0	41.5	705090	24.0	48.0	53.6
610090	54.0	48.0	41.5	705100	24.0	54.0	53.6
610100	54.0	54.0	41.5	705110	24.0	60.0	53.6
610110	54.0	60.0	41.5	706010	30.0	0.0	53.6
611010	60.0	0.0	41.5	706020	30.0	6.0	53.6
611020	60.0	6.0	41.5	706030	30.0	12.0	53.6
611030	60.0	12.0	41.5	706040	30.0	18.0	53.6
611040	60.0	18.0	41.5	706050	30.0	24.0	53.6
611050	60.0	24.0	41.5	706060	30.0	30.0	53.6
611060	60.0	30.0	41.5	706070	30.0	36.0	53.6
611070	60.0	36.0	41.5	706080	30.0	42.0	53.6
611080	60.0	42.0	41.5	706090	30.0	48.0	53.6
611090	60.0	48.0	41.5	706100	30.0	54.0	53.6
611100	60.0	54.0	41.5	706110	30.0	60.0	53.6
611110	60.0	60.0	41.5	707010	36.0	0.0	53.6
612010	66.0	0.0	41.5	707020	36.0	6.0	53.6
612020	66.0	6.0	41.5	707030	36.0	12.0	53.6
612030	66.0	12.0	41.5	707040	36.0	18.0	53.6
612040	66.0	18.0	41.5	707050	36.0	24.0	53.6
612050	66.0	24.0	41.5	707060	36.0	30.0	53.6
612060	66.0	30.0	41.5	707070	36.0	36.0	53.6
612070	66.0	36.0	41.5	707080	36.0	42.0	53.6
612080	66.0	42.0	41.5	707090	36.0	48.0	53.6
612090	66.0	48.0	41.5	707100	36.0	54.0	53.6
612100	66.0	54.0	41.5	707110	36.0	60.0	53.6
612110	66.0	60.0	41.5	708010	42.0	0.0	53.6
613010	72.0	0.0	41.5	708020	42.0	6.0	53.6
613020	72.0	6.0	41.5	708030	42.0	12.0	53.6
613030	72.0	12.0	41.5	708040	42.0	18.0	53.6
613040	72.0	18.0	41.5	708050	42.0	24.0	53.6
613050	72.0	24.0	41.5	708060	42.0	30.0	53.6
613060	72.0	30.0	41.5	708070	42.0	36.0	53.6
613070	72.0	36.0	41.5	708080	42.0	42.0	53.6
613080	72.0	42.0	41.5	708090	42.0	48.0	53.6
613090	72.0	48.0	41.5	708100	42.0	54.0	53.6
613100	72.0	54.0	41.5	708110	42.0	60.0	53.6
613110	72.0	60.0	41.5	709010	48.0	0.0	53.6
705010	24.0	0.0	53.6	709020	48.0	6.0	53.6

Table I-1 (continued)

Node	Coordinates (m)			Node	Coordinates (m)		
	X	Y	Z		X	Y	Z
709030	48.0	12.0	53.6	713040	72.0	18.0	53.6
709040	48.0	18.0	53.6	713050	72.0	24.0	53.6
709050	48.0	24.0	53.6	713060	72.0	30.0	53.6
709060	48.0	30.0	53.6	713070	72.0	36.0	53.6
709070	48.0	36.0	53.6	713080	72.0	42.0	53.6
709080	48.0	42.0	53.6	713090	72.0	48.0	53.6
709090	48.0	48.0	53.6	713100	72.0	54.0	53.6
709100	48.0	54.0	53.6	713110	72.0	60.0	53.6
709110	48.0	60.0	53.6	805010	24.0	0.0	65.8
710010	54.0	0.0	53.6	805020	24.0	6.0	65.8
710020	54.0	6.0	53.6	805030	24.0	12.0	65.8
710030	54.0	12.0	53.6	805040	24.0	18.0	65.8
710040	54.0	18.0	53.6	805050	24.0	24.0	65.8
710050	54.0	24.0	53.6	805060	24.0	30.0	65.8
710060	54.0	30.0	53.6	805070	24.0	36.0	65.8
710070	54.0	36.0	53.6	805080	24.0	42.0	65.8
710080	54.0	42.0	53.6	805090	24.0	48.0	65.8
710090	54.0	48.0	53.6	805100	24.0	54.0	65.8
710100	54.0	54.0	53.6	805110	24.0	60.0	65.8
710110	54.0	60.0	53.6	806010	30.0	0.0	65.8
711010	60.0	0.0	53.6	806020	30.0	6.0	65.8
711020	60.0	6.0	53.6	806030	30.0	12.0	65.8
711030	60.0	12.0	53.6	806040	30.0	18.0	65.8
711040	60.0	18.0	53.6	806050	30.0	24.0	65.8
711050	60.0	24.0	53.6	806060	30.0	30.0	65.8
711060	60.0	30.0	53.6	806070	30.0	36.0	65.8
711070	60.0	36.0	53.6	806080	30.0	42.0	65.8
711080	60.0	42.0	53.6	806090	30.0	48.0	65.8
711090	60.0	48.0	53.6	806100	30.0	54.0	65.8
711100	60.0	54.0	53.6	806110	30.0	60.0	65.8
711110	60.0	60.0	53.6	807010	36.0	0.0	65.8
712010	66.0	0.0	53.6	807020	36.0	6.0	65.8
712020	66.0	6.0	53.6	807030	36.0	12.0	65.8
712030	66.0	12.0	53.6	807040	36.0	18.0	65.8
712040	66.0	18.0	53.6	807050	36.0	24.0	65.8
712050	66.0	24.0	53.6	807060	36.0	30.0	65.8
712060	66.0	30.0	53.6	807070	36.0	36.0	65.8
712070	66.0	36.0	53.6	807080	36.0	42.0	65.8
712080	66.0	42.0	53.6	807090	36.0	48.0	65.8
712090	66.0	48.0	53.6	807100	36.0	54.0	65.8
712100	66.0	54.0	53.6	807110	36.0	60.0	65.8
712110	66.0	60.0	53.6	808010	42.0	0.0	65.8
713010	72.0	0.0	53.6	808020	42.0	6.0	65.8
713020	72.0	6.0	53.6	808030	42.0	12.0	65.8
713030	72.0	12.0	53.6	808040	42.0	18.0	65.8

Table I-1 (continued)

Node	Coordinates (m)			Node	Coordinates (m)		
	X	Y	Z		X	Y	Z
808050	42.0	24.0	65.8	812060	66.0	30.0	65.8
808060	42.0	30.0	65.8	812070	66.0	36.0	65.8
808070	42.0	36.0	65.8	812080	66.0	42.0	65.8
808080	42.0	42.0	65.8	812090	66.0	48.0	65.8
808090	42.0	48.0	65.8	812100	66.0	54.0	65.8
808100	42.0	54.0	65.8	812110	66.0	60.0	65.8
808110	42.0	60.0	65.8	813010	72.0	0.0	65.8
809010	48.0	0.0	65.8	813020	72.0	6.0	65.8
809020	48.0	6.0	65.8	813030	72.0	12.0	65.8
809030	48.0	12.0	65.8	813040	72.0	18.0	65.8
809040	48.0	18.0	65.8	813050	72.0	24.0	65.8
809050	48.0	24.0	65.8	813060	72.0	30.0	65.8
809060	48.0	30.0	65.8	813070	72.0	36.0	65.8
809070	48.0	36.0	65.8	813080	72.0	42.0	65.8
809080	48.0	42.0	65.8	813090	72.0	48.0	65.8
809090	48.0	48.0	65.8	813100	72.0	54.0	65.8
809100	48.0	54.0	65.8	813110	72.0	60.0	65.8
809110	48.0	60.0	65.8	905010	24.0	0.0	71.3
810010	54.0	0.0	65.8	905020	24.0	6.0	71.3
810020	54.0	6.0	65.8	905030	24.0	12.0	71.3
810030	54.0	12.0	65.8	905040	24.0	18.0	71.3
810040	54.0	18.0	65.8	905050	24.0	24.0	71.3
810050	54.0	24.0	65.8	905060	24.0	30.0	71.3
810060	54.0	30.0	65.8	905070	24.0	36.0	71.3
810070	54.0	36.0	65.8	905080	24.0	42.0	71.3
810080	54.0	42.0	65.8	905090	24.0	48.0	71.3
810090	54.0	48.0	65.8	905100	24.0	54.0	71.3
810100	54.0	54.0	65.8	905110	24.0	60.0	71.3
810110	54.0	60.0	65.8	906010	30.0	0.0	71.3
811010	60.0	0.0	65.8	906020	30.0	6.0	71.3
811020	60.0	6.0	65.8	906030	30.0	12.0	71.3
811030	60.0	12.0	65.8	906040	30.0	18.0	71.3
811040	60.0	18.0	65.8	906050	30.0	24.0	71.3
811050	60.0	24.0	65.8	906060	30.0	30.0	71.3
811060	60.0	30.0	65.8	906070	30.0	36.0	71.3
811070	60.0	36.0	65.8	906080	30.0	42.0	71.3
811080	60.0	42.0	65.8	906090	30.0	48.0	71.3
811090	60.0	48.0	65.8	906100	30.0	54.0	71.3
811100	60.0	54.0	65.8	906110	30.0	60.0	71.3
811110	60.0	60.0	65.8	907010	36.0	0.0	71.3
812010	66.0	0.0	65.8	907020	36.0	6.0	71.3
812020	66.0	6.0	65.8	907030	36.0	12.0	71.3
812030	66.0	12.0	65.8	907040	36.0	18.0	71.3
812040	66.0	18.0	65.8	907050	36.0	24.0	71.3
812050	66.0	24.0	65.8	907060	36.0	30.0	71.3

Table I-1 (continued)

Node	Coordinates (m)			Node	Coordinates (m)		
	X	Y	Z		X	Y	Z
907070	36.0	36.0	71.3	911080	60.0	42.0	71.3
907080	36.0	42.0	71.3	911090	60.0	48.0	71.3
907090	36.0	48.0	71.3	911100	60.0	54.0	71.3
907100	36.0	54.0	71.3	911110	60.0	60.0	71.3
907110	36.0	60.0	71.3	912010	66.0	0.0	71.3
908010	42.0	0.0	71.3	912020	66.0	6.0	71.3
908020	42.0	6.0	71.3	912030	66.0	12.0	71.3
908030	42.0	12.0	71.3	912040	66.0	18.0	71.3
908040	42.0	18.0	71.3	912050	66.0	24.0	71.3
908050	42.0	24.0	71.3	912060	66.0	30.0	71.3
908060	42.0	30.0	71.3	912070	66.0	36.0	71.3
908070	42.0	36.0	71.3	912080	66.0	42.0	71.3
908080	42.0	42.0	71.3	912090	66.0	48.0	71.3
908090	42.0	48.0	71.3	912100	66.0	54.0	71.3
908100	42.0	54.0	71.3	912110	66.0	60.0	71.3
908110	42.0	60.0	71.3	913010	72.0	0.0	71.3
909010	48.0	0.0	71.3	913020	72.0	6.0	71.3
909020	48.0	6.0	71.3	913030	72.0	12.0	71.3
909030	48.0	12.0	71.3	913040	72.0	18.0	71.3
909040	48.0	18.0	71.3	913050	72.0	24.0	71.3
909050	48.0	24.0	71.3	913060	72.0	30.0	71.3
909060	48.0	30.0	71.3	913070	72.0	36.0	71.3
909070	48.0	36.0	71.3	913080	72.0	42.0	71.3
909080	48.0	42.0	71.3	913090	72.0	48.0	71.3
909090	48.0	48.0	71.3	913100	72.0	54.0	71.3
909100	48.0	54.0	71.3	913110	72.0	60.0	71.3
909110	48.0	60.0	71.3				
910010	54.0	0.0	71.3				
910020	54.0	6.0	71.3				
910030	54.0	12.0	71.3				
910040	54.0	18.0	71.3				
910050	54.0	24.0	71.3				
910060	54.0	30.0	71.3				
910070	54.0	36.0	71.3				
910080	54.0	42.0	71.3				
910090	54.0	48.0	71.3				
910100	54.0	54.0	71.3				
910110	54.0	60.0	71.3				
911010	60.0	0.0	71.3				
911020	60.0	6.0	71.3				
911030	60.0	12.0	71.3				
911040	60.0	18.0	71.3				
911050	60.0	24.0	71.3				
911060	60.0	30.0	71.3				
911070	60.0	36.0	71.3				

Table I-2: Masses assigned to nodes in the OpenSees model of the ASB

Node	Mass in direction (kg)			Mass moment of inertia about axis (kg-m^2)		
	X	Y	Z	X	Y	Z
101010	242945.5	242945.5	242945.5	100.0	100.0	100.0
101020	242945.5	242945.5	242945.5	100.0	100.0	100.0
101030	242945.5	242945.5	242945.5	100.0	100.0	100.0
101040	242945.5	242945.5	242945.5	100.0	100.0	100.0
101050	242945.5	242945.5	242945.5	100.0	100.0	100.0
101060	242945.5	242945.5	242945.5	100.0	100.0	100.0
101070	242945.5	242945.5	242945.5	100.0	100.0	100.0
101080	242945.5	242945.5	242945.5	100.0	100.0	100.0
101090	242945.5	242945.5	242945.5	100.0	100.0	100.0
101100	242945.5	242945.5	242945.5	100.0	100.0	100.0
101110	242945.5	242945.5	242945.5	100.0	100.0	100.0
102010	242945.5	242945.5	242945.5	100.0	100.0	100.0
102020	242945.5	242945.5	242945.5	100.0	100.0	100.0
102030	242945.5	242945.5	242945.5	100.0	100.0	100.0
102040	242945.5	242945.5	242945.5	100.0	100.0	100.0
102050	242945.5	242945.5	242945.5	100.0	100.0	100.0
102060	242945.5	242945.5	242945.5	100.0	100.0	100.0
102070	242945.5	242945.5	242945.5	100.0	100.0	100.0
102080	242945.5	242945.5	242945.5	100.0	100.0	100.0
102090	242945.5	242945.5	242945.5	100.0	100.0	100.0
102100	242945.5	242945.5	242945.5	100.0	100.0	100.0
102110	242945.5	242945.5	242945.5	100.0	100.0	100.0
103010	242945.5	242945.5	242945.5	100.0	100.0	100.0
103020	242945.5	242945.5	242945.5	100.0	100.0	100.0
103030	242945.5	242945.5	242945.5	100.0	100.0	100.0
103040	242945.5	242945.5	242945.5	100.0	100.0	100.0
103050	242945.5	242945.5	242945.5	100.0	100.0	100.0
103060	242945.5	242945.5	242945.5	100.0	100.0	100.0
103070	242945.5	242945.5	242945.5	100.0	100.0	100.0
103080	242945.5	242945.5	242945.5	100.0	100.0	100.0
103090	242945.5	242945.5	242945.5	100.0	100.0	100.0
103100	242945.5	242945.5	242945.5	100.0	100.0	100.0
103110	242945.5	242945.5	242945.5	100.0	100.0	100.0
104010	242945.5	242945.5	242945.5	100.0	100.0	100.0
104020	242945.5	242945.5	242945.5	100.0	100.0	100.0
104030	242945.5	242945.5	242945.5	100.0	100.0	100.0
104040	242945.5	242945.5	242945.5	100.0	100.0	100.0
104050	242945.5	242945.5	242945.5	100.0	100.0	100.0
104060	242945.5	242945.5	242945.5	100.0	100.0	100.0
104070	242945.5	242945.5	242945.5	100.0	100.0	100.0
104080	242945.5	242945.5	242945.5	100.0	100.0	100.0
104090	242945.5	242945.5	242945.5	100.0	100.0	100.0

Table I-2 (continued)

Node	Mass in direction (kg)			Mass moment of inertia about axis (kg-m^2)		
	X	Y	Z	X	Y	Z
104100	242945.5	242945.5	242945.5	100.0	100.0	100.0
104110	242945.5	242945.5	242945.5	100.0	100.0	100.0
105010	268969.7	268969.7	268969.7	100.0	100.0	100.0
105020	268969.7	268969.7	268969.7	100.0	100.0	100.0
105030	268969.7	268969.7	268969.7	100.0	100.0	100.0
105040	268969.7	268969.7	268969.7	100.0	100.0	100.0
105050	268969.7	268969.7	268969.7	100.0	100.0	100.0
105060	268969.7	268969.7	268969.7	100.0	100.0	100.0
105070	268969.7	268969.7	268969.7	100.0	100.0	100.0
105080	268969.7	268969.7	268969.7	100.0	100.0	100.0
105090	268969.7	268969.7	268969.7	100.0	100.0	100.0
105100	268969.7	268969.7	268969.7	100.0	100.0	100.0
105110	268969.7	268969.7	268969.7	100.0	100.0	100.0
106010	268969.7	268969.7	268969.7	100.0	100.0	100.0
106020	268969.7	268969.7	268969.7	100.0	100.0	100.0
106030	268969.7	268969.7	268969.7	100.0	100.0	100.0
106040	268969.7	268969.7	268969.7	100.0	100.0	100.0
106050	268969.7	268969.7	268969.7	100.0	100.0	100.0
106060	268969.7	268969.7	268969.7	100.0	100.0	100.0
106070	268969.7	268969.7	268969.7	100.0	100.0	100.0
106080	268969.7	268969.7	268969.7	100.0	100.0	100.0
106090	268969.7	268969.7	268969.7	100.0	100.0	100.0
106100	268969.7	268969.7	268969.7	100.0	100.0	100.0
106110	268969.7	268969.7	268969.7	100.0	100.0	100.0
107010	268969.7	268969.7	268969.7	100.0	100.0	100.0
107020	268969.7	268969.7	268969.7	100.0	100.0	100.0
107030	268969.7	268969.7	268969.7	100.0	100.0	100.0
107040	268969.7	268969.7	268969.7	100.0	100.0	100.0
107050	268969.7	268969.7	268969.7	100.0	100.0	100.0
107060	268969.7	268969.7	268969.7	100.0	100.0	100.0
107070	268969.7	268969.7	268969.7	100.0	100.0	100.0
107080	268969.7	268969.7	268969.7	100.0	100.0	100.0
107090	268969.7	268969.7	268969.7	100.0	100.0	100.0
107100	268969.7	268969.7	268969.7	100.0	100.0	100.0
107110	268969.7	268969.7	268969.7	100.0	100.0	100.0
108010	268969.7	268969.7	268969.7	100.0	100.0	100.0
108020	268969.7	268969.7	268969.7	100.0	100.0	100.0
108030	268969.7	268969.7	268969.7	100.0	100.0	100.0
108040	268969.7	268969.7	268969.7	100.0	100.0	100.0
108050	268969.7	268969.7	268969.7	100.0	100.0	100.0
108060	268969.7	268969.7	268969.7	100.0	100.0	100.0
108070	268969.7	268969.7	268969.7	100.0	100.0	100.0
108080	268969.7	268969.7	268969.7	100.0	100.0	100.0

Table I-2 (continued)

Node	Mass in direction (kg)			Mass moment of inertia about axis (kg-m^2)		
	X	Y	Z	X	Y	Z
108090	268969.7	268969.7	268969.7	100.0	100.0	100.0
108100	268969.7	268969.7	268969.7	100.0	100.0	100.0
108110	268969.7	268969.7	268969.7	100.0	100.0	100.0
109010	268969.7	268969.7	268969.7	100.0	100.0	100.0
109020	268969.7	268969.7	268969.7	100.0	100.0	100.0
109030	268969.7	268969.7	268969.7	100.0	100.0	100.0
109040	268969.7	268969.7	268969.7	100.0	100.0	100.0
109050	268969.7	268969.7	268969.7	100.0	100.0	100.0
109060	268969.7	268969.7	268969.7	100.0	100.0	100.0
109070	268969.7	268969.7	268969.7	100.0	100.0	100.0
109080	268969.7	268969.7	268969.7	100.0	100.0	100.0
109090	268969.7	268969.7	268969.7	100.0	100.0	100.0
109100	268969.7	268969.7	268969.7	100.0	100.0	100.0
109110	268969.7	268969.7	268969.7	100.0	100.0	100.0
110010	268969.7	268969.7	268969.7	100.0	100.0	100.0
110020	268969.7	268969.7	268969.7	100.0	100.0	100.0
110030	268969.7	268969.7	268969.7	100.0	100.0	100.0
110040	268969.7	268969.7	268969.7	100.0	100.0	100.0
110050	268969.7	268969.7	268969.7	100.0	100.0	100.0
110060	268969.7	268969.7	268969.7	100.0	100.0	100.0
110070	268969.7	268969.7	268969.7	100.0	100.0	100.0
110080	268969.7	268969.7	268969.7	100.0	100.0	100.0
110090	268969.7	268969.7	268969.7	100.0	100.0	100.0
110100	268969.7	268969.7	268969.7	100.0	100.0	100.0
110110	268969.7	268969.7	268969.7	100.0	100.0	100.0
111010	268969.7	268969.7	268969.7	100.0	100.0	100.0
111020	268969.7	268969.7	268969.7	100.0	100.0	100.0
111030	268969.7	268969.7	268969.7	100.0	100.0	100.0
111040	268969.7	268969.7	268969.7	100.0	100.0	100.0
111050	268969.7	268969.7	268969.7	100.0	100.0	100.0
111060	268969.7	268969.7	268969.7	100.0	100.0	100.0
111070	268969.7	268969.7	268969.7	100.0	100.0	100.0
111080	268969.7	268969.7	268969.7	100.0	100.0	100.0
111090	268969.7	268969.7	268969.7	100.0	100.0	100.0
111100	268969.7	268969.7	268969.7	100.0	100.0	100.0
111110	268969.7	268969.7	268969.7	100.0	100.0	100.0
112010	268969.7	268969.7	268969.7	100.0	100.0	100.0
112020	268969.7	268969.7	268969.7	100.0	100.0	100.0
112030	268969.7	268969.7	268969.7	100.0	100.0	100.0
112040	268969.7	268969.7	268969.7	100.0	100.0	100.0
112050	268969.7	268969.7	268969.7	100.0	100.0	100.0
112060	268969.7	268969.7	268969.7	100.0	100.0	100.0
112070	268969.7	268969.7	268969.7	100.0	100.0	100.0
112080	268969.7	268969.7	268969.7	100.0	100.0	100.0
112090	268969.7	268969.7	268969.7	100.0	100.0	100.0

Table I-2 (continued)

Node	Mass in direction (kg)			Mass moment of inertia about axis (kg-m^2)		
	X	Y	Z	X	Y	Z
112100	268969.7	268969.7	268969.7	100.0	100.0	100.0
112110	268969.7	268969.7	268969.7	100.0	100.0	100.0
113010	268969.7	268969.7	268969.7	100.0	100.0	100.0
113020	268969.7	268969.7	268969.7	100.0	100.0	100.0
113030	268969.7	268969.7	268969.7	100.0	100.0	100.0
113040	268969.7	268969.7	268969.7	100.0	100.0	100.0
113050	268969.7	268969.7	268969.7	100.0	100.0	100.0
113060	268969.7	268969.7	268969.7	100.0	100.0	100.0
113070	268969.7	268969.7	268969.7	100.0	100.0	100.0
113080	268969.7	268969.7	268969.7	100.0	100.0	100.0
113090	268969.7	268969.7	268969.7	100.0	100.0	100.0
113100	268969.7	268969.7	268969.7	100.0	100.0	100.0
113110	268969.7	268969.7	268969.7	100.0	100.0	100.0
114010	242945.5	242945.5	242945.5	100.0	100.0	100.0
114020	242945.5	242945.5	242945.5	100.0	100.0	100.0
114030	242945.5	242945.5	242945.5	100.0	100.0	100.0
114040	242945.5	242945.5	242945.5	100.0	100.0	100.0
114050	242945.5	242945.5	242945.5	100.0	100.0	100.0
114060	242945.5	242945.5	242945.5	100.0	100.0	100.0
114070	242945.5	242945.5	242945.5	100.0	100.0	100.0
114080	242945.5	242945.5	242945.5	100.0	100.0	100.0
114090	242945.5	242945.5	242945.5	100.0	100.0	100.0
114100	242945.5	242945.5	242945.5	100.0	100.0	100.0
114110	242945.5	242945.5	242945.5	100.0	100.0	100.0
115010	242945.5	242945.5	242945.5	100.0	100.0	100.0
115020	242945.5	242945.5	242945.5	100.0	100.0	100.0
115030	242945.5	242945.5	242945.5	100.0	100.0	100.0
115040	242945.5	242945.5	242945.5	100.0	100.0	100.0
115050	242945.5	242945.5	242945.5	100.0	100.0	100.0
115060	242945.5	242945.5	242945.5	100.0	100.0	100.0
115070	242945.5	242945.5	242945.5	100.0	100.0	100.0
115080	242945.5	242945.5	242945.5	100.0	100.0	100.0
115090	242945.5	242945.5	242945.5	100.0	100.0	100.0
115100	242945.5	242945.5	242945.5	100.0	100.0	100.0
115110	242945.5	242945.5	242945.5	100.0	100.0	100.0
116010	242945.5	242945.5	242945.5	100.0	100.0	100.0
116020	242945.5	242945.5	242945.5	100.0	100.0	100.0
116030	242945.5	242945.5	242945.5	100.0	100.0	100.0
116040	242945.5	242945.5	242945.5	100.0	100.0	100.0
116050	242945.5	242945.5	242945.5	100.0	100.0	100.0
116060	242945.5	242945.5	242945.5	100.0	100.0	100.0
116070	242945.5	242945.5	242945.5	100.0	100.0	100.0
116080	242945.5	242945.5	242945.5	100.0	100.0	100.0
116090	242945.5	242945.5	242945.5	100.0	100.0	100.0
116100	242945.5	242945.5	242945.5	100.0	100.0	100.0

Table I-2 (continued)

Node	Mass in direction (kg)			Mass moment of inertia about axis (kg-m^2)		
	X	Y	Z	X	Y	Z
116110	242945.5	242945.5	242945.5	100.0	100.0	100.0
117010	242945.5	242945.5	242945.5	100.0	100.0	100.0
117020	242945.5	242945.5	242945.5	100.0	100.0	100.0
117030	242945.5	242945.5	242945.5	100.0	100.0	100.0
117040	242945.5	242945.5	242945.5	100.0	100.0	100.0
117050	242945.5	242945.5	242945.5	100.0	100.0	100.0
117060	242945.5	242945.5	242945.5	100.0	100.0	100.0
117070	242945.5	242945.5	242945.5	100.0	100.0	100.0
117080	242945.5	242945.5	242945.5	100.0	100.0	100.0
117090	242945.5	242945.5	242945.5	100.0	100.0	100.0
117100	242945.5	242945.5	242945.5	100.0	100.0	100.0
117110	242945.5	242945.5	242945.5	100.0	100.0	100.0
201010	130963.6	130963.6	130963.6	100.0	100.0	100.0
201020	130963.6	130963.6	130963.6	100.0	100.0	100.0
201030	130963.6	130963.6	130963.6	100.0	100.0	100.0
201040	130963.6	130963.6	130963.6	100.0	100.0	100.0
201050	130963.6	130963.6	130963.6	100.0	100.0	100.0
201060	130963.6	130963.6	130963.6	100.0	100.0	100.0
201070	130963.6	130963.6	130963.6	100.0	100.0	100.0
201080	130963.6	130963.6	130963.6	100.0	100.0	100.0
201090	130963.6	130963.6	130963.6	100.0	100.0	100.0
201100	130963.6	130963.6	130963.6	100.0	100.0	100.0
201110	130963.6	130963.6	130963.6	100.0	100.0	100.0
202010	130963.6	130963.6	130963.6	100.0	100.0	100.0
202020	130963.6	130963.6	130963.6	100.0	100.0	100.0
202030	130963.6	130963.6	130963.6	100.0	100.0	100.0
202040	130963.6	130963.6	130963.6	100.0	100.0	100.0
202050	130963.6	130963.6	130963.6	100.0	100.0	100.0
202060	130963.6	130963.6	130963.6	100.0	100.0	100.0
202070	130963.6	130963.6	130963.6	100.0	100.0	100.0
202080	130963.6	130963.6	130963.6	100.0	100.0	100.0
202090	130963.6	130963.6	130963.6	100.0	100.0	100.0
202100	130963.6	130963.6	130963.6	100.0	100.0	100.0
202110	130963.6	130963.6	130963.6	100.0	100.0	100.0
203010	130963.6	130963.6	130963.6	100.0	100.0	100.0
203020	130963.6	130963.6	130963.6	100.0	100.0	100.0
203030	130963.6	130963.6	130963.6	100.0	100.0	100.0
203040	130963.6	130963.6	130963.6	100.0	100.0	100.0
203050	130963.6	130963.6	130963.6	100.0	100.0	100.0
203060	130963.6	130963.6	130963.6	100.0	100.0	100.0
203070	130963.6	130963.6	130963.6	100.0	100.0	100.0
203080	130963.6	130963.6	130963.6	100.0	100.0	100.0
203090	130963.6	130963.6	130963.6	100.0	100.0	100.0
203100	130963.6	130963.6	130963.6	100.0	100.0	100.0
203110	130963.6	130963.6	130963.6	100.0	100.0	100.0

Table I-2 (continued)

Node	Mass in direction (kg)			Mass moment of inertia about axis (kg-m^2)		
	X	Y	Z	X	Y	Z
204010	130963.6	130963.6	130963.6	100.0	100.0	100.0
204020	130963.6	130963.6	130963.6	100.0	100.0	100.0
204030	130963.6	130963.6	130963.6	100.0	100.0	100.0
204040	130963.6	130963.6	130963.6	100.0	100.0	100.0
204050	130963.6	130963.6	130963.6	100.0	100.0	100.0
204060	130963.6	130963.6	130963.6	100.0	100.0	100.0
204070	130963.6	130963.6	130963.6	100.0	100.0	100.0
204080	130963.6	130963.6	130963.6	100.0	100.0	100.0
204090	130963.6	130963.6	130963.6	100.0	100.0	100.0
204100	130963.6	130963.6	130963.6	100.0	100.0	100.0
204110	130963.6	130963.6	130963.6	100.0	100.0	100.0
205010	67878.8	67878.8	67878.8	100.0	100.0	100.0
205020	67878.8	67878.8	67878.8	100.0	100.0	100.0
205030	67878.8	67878.8	67878.8	100.0	100.0	100.0
205040	67878.8	67878.8	67878.8	100.0	100.0	100.0
205050	67878.8	67878.8	67878.8	100.0	100.0	100.0
205060	67878.8	67878.8	67878.8	100.0	100.0	100.0
205070	67878.8	67878.8	67878.8	100.0	100.0	100.0
205080	67878.8	67878.8	67878.8	100.0	100.0	100.0
205090	67878.8	67878.8	67878.8	100.0	100.0	100.0
205100	67878.8	67878.8	67878.8	100.0	100.0	100.0
205110	67878.8	67878.8	67878.8	100.0	100.0	100.0
206010	67878.8	67878.8	67878.8	100.0	100.0	100.0
206020	67878.8	67878.8	67878.8	100.0	100.0	100.0
206030	67878.8	67878.8	67878.8	100.0	100.0	100.0
206040	67878.8	67878.8	67878.8	100.0	100.0	100.0
206050	67878.8	67878.8	67878.8	100.0	100.0	100.0
206060	67878.8	67878.8	67878.8	100.0	100.0	100.0
206070	67878.8	67878.8	67878.8	100.0	100.0	100.0
206080	67878.8	67878.8	67878.8	100.0	100.0	100.0
206090	67878.8	67878.8	67878.8	100.0	100.0	100.0
206100	67878.8	67878.8	67878.8	100.0	100.0	100.0
206110	67878.8	67878.8	67878.8	100.0	100.0	100.0
207010	67878.8	67878.8	67878.8	100.0	100.0	100.0
207020	67878.8	67878.8	67878.8	100.0	100.0	100.0
207030	67878.8	67878.8	67878.8	100.0	100.0	100.0
207040	67878.8	67878.8	67878.8	100.0	100.0	100.0
207050	67878.8	67878.8	67878.8	100.0	100.0	100.0
207060	67878.8	67878.8	67878.8	100.0	100.0	100.0
207070	67878.8	67878.8	67878.8	100.0	100.0	100.0
207080	67878.8	67878.8	67878.8	100.0	100.0	100.0
207090	67878.8	67878.8	67878.8	100.0	100.0	100.0
207100	67878.8	67878.8	67878.8	100.0	100.0	100.0
207110	67878.8	67878.8	67878.8	100.0	100.0	100.0
208010	67878.8	67878.8	67878.8	100.0	100.0	100.0

Table I-2 (continued)

Node	Mass in direction (kg)			Mass moment of inertia about axis (kg-m^2)		
	X	Y	Z	X	Y	Z
208020	67878.8	67878.8	67878.8	100.0	100.0	100.0
208030	67878.8	67878.8	67878.8	100.0	100.0	100.0
208040	67878.8	67878.8	67878.8	100.0	100.0	100.0
208050	67878.8	67878.8	67878.8	100.0	100.0	100.0
208060	67878.8	67878.8	67878.8	100.0	100.0	100.0
208070	67878.8	67878.8	67878.8	100.0	100.0	100.0
208080	67878.8	67878.8	67878.8	100.0	100.0	100.0
208090	67878.8	67878.8	67878.8	100.0	100.0	100.0
208100	67878.8	67878.8	67878.8	100.0	100.0	100.0
208110	67878.8	67878.8	67878.8	100.0	100.0	100.0
209010	67878.8	67878.8	67878.8	100.0	100.0	100.0
209020	67878.8	67878.8	67878.8	100.0	100.0	100.0
209030	67878.8	67878.8	67878.8	100.0	100.0	100.0
209040	67878.8	67878.8	67878.8	100.0	100.0	100.0
209050	67878.8	67878.8	67878.8	100.0	100.0	100.0
209060	67878.8	67878.8	67878.8	100.0	100.0	100.0
209070	67878.8	67878.8	67878.8	100.0	100.0	100.0
209080	67878.8	67878.8	67878.8	100.0	100.0	100.0
209090	67878.8	67878.8	67878.8	100.0	100.0	100.0
209100	67878.8	67878.8	67878.8	100.0	100.0	100.0
209110	67878.8	67878.8	67878.8	100.0	100.0	100.0
210010	67878.8	67878.8	67878.8	100.0	100.0	100.0
210020	67878.8	67878.8	67878.8	100.0	100.0	100.0
210030	67878.8	67878.8	67878.8	100.0	100.0	100.0
210040	67878.8	67878.8	67878.8	100.0	100.0	100.0
210050	67878.8	67878.8	67878.8	100.0	100.0	100.0
210060	67878.8	67878.8	67878.8	100.0	100.0	100.0
210070	67878.8	67878.8	67878.8	100.0	100.0	100.0
210080	67878.8	67878.8	67878.8	100.0	100.0	100.0
210090	67878.8	67878.8	67878.8	100.0	100.0	100.0
210100	67878.8	67878.8	67878.8	100.0	100.0	100.0
210110	67878.8	67878.8	67878.8	100.0	100.0	100.0
211010	67878.8	67878.8	67878.8	100.0	100.0	100.0
211020	67878.8	67878.8	67878.8	100.0	100.0	100.0
211030	67878.8	67878.8	67878.8	100.0	100.0	100.0
211040	67878.8	67878.8	67878.8	100.0	100.0	100.0
211050	67878.8	67878.8	67878.8	100.0	100.0	100.0
211060	67878.8	67878.8	67878.8	100.0	100.0	100.0
211070	67878.8	67878.8	67878.8	100.0	100.0	100.0
211080	67878.8	67878.8	67878.8	100.0	100.0	100.0
211090	67878.8	67878.8	67878.8	100.0	100.0	100.0
211100	67878.8	67878.8	67878.8	100.0	100.0	100.0
211110	67878.8	67878.8	67878.8	100.0	100.0	100.0
212010	67878.8	67878.8	67878.8	100.0	100.0	100.0
212020	67878.8	67878.8	67878.8	100.0	100.0	100.0

Table I-2 (continued)

Node	Mass in direction (kg)			Mass moment of inertia about axis (kg-m^2)		
	X	Y	Z	X	Y	Z
212030	67878.8	67878.8	67878.8	100.0	100.0	100.0
212040	67878.8	67878.8	67878.8	100.0	100.0	100.0
212050	67878.8	67878.8	67878.8	100.0	100.0	100.0
212060	67878.8	67878.8	67878.8	100.0	100.0	100.0
212070	67878.8	67878.8	67878.8	100.0	100.0	100.0
212080	67878.8	67878.8	67878.8	100.0	100.0	100.0
212090	67878.8	67878.8	67878.8	100.0	100.0	100.0
212100	67878.8	67878.8	67878.8	100.0	100.0	100.0
212110	67878.8	67878.8	67878.8	100.0	100.0	100.0
213010	67878.8	67878.8	67878.8	100.0	100.0	100.0
213020	67878.8	67878.8	67878.8	100.0	100.0	100.0
213030	67878.8	67878.8	67878.8	100.0	100.0	100.0
213040	67878.8	67878.8	67878.8	100.0	100.0	100.0
213050	67878.8	67878.8	67878.8	100.0	100.0	100.0
213060	67878.8	67878.8	67878.8	100.0	100.0	100.0
213070	67878.8	67878.8	67878.8	100.0	100.0	100.0
213080	67878.8	67878.8	67878.8	100.0	100.0	100.0
213090	67878.8	67878.8	67878.8	100.0	100.0	100.0
213100	67878.8	67878.8	67878.8	100.0	100.0	100.0
213110	67878.8	67878.8	67878.8	100.0	100.0	100.0
214010	130963.6	130963.6	130963.6	100.0	100.0	100.0
214020	130963.6	130963.6	130963.6	100.0	100.0	100.0
214030	130963.6	130963.6	130963.6	100.0	100.0	100.0
214040	130963.6	130963.6	130963.6	100.0	100.0	100.0
214050	130963.6	130963.6	130963.6	100.0	100.0	100.0
214060	130963.6	130963.6	130963.6	100.0	100.0	100.0
214070	130963.6	130963.6	130963.6	100.0	100.0	100.0
214080	130963.6	130963.6	130963.6	100.0	100.0	100.0
214090	130963.6	130963.6	130963.6	100.0	100.0	100.0
214100	130963.6	130963.6	130963.6	100.0	100.0	100.0
214110	130963.6	130963.6	130963.6	100.0	100.0	100.0
215010	130963.6	130963.6	130963.6	100.0	100.0	100.0
215020	130963.6	130963.6	130963.6	100.0	100.0	100.0
215030	130963.6	130963.6	130963.6	100.0	100.0	100.0
215040	130963.6	130963.6	130963.6	100.0	100.0	100.0
215050	130963.6	130963.6	130963.6	100.0	100.0	100.0
215060	130963.6	130963.6	130963.6	100.0	100.0	100.0
215070	130963.6	130963.6	130963.6	100.0	100.0	100.0
215080	130963.6	130963.6	130963.6	100.0	100.0	100.0
215090	130963.6	130963.6	130963.6	100.0	100.0	100.0
215100	130963.6	130963.6	130963.6	100.0	100.0	100.0
215110	130963.6	130963.6	130963.6	100.0	100.0	100.0
216010	130963.6	130963.6	130963.6	100.0	100.0	100.0
216020	130963.6	130963.6	130963.6	100.0	100.0	100.0
216030	130963.6	130963.6	130963.6	100.0	100.0	100.0

Table I-2 (continued)

Node	Mass in direction (kg)			Mass moment of inertia about axis (kg-m^2)		
	X	Y	Z	X	Y	Z
216040	130963.6	130963.6	130963.6	100.0	100.0	100.0
216050	130963.6	130963.6	130963.6	100.0	100.0	100.0
216060	130963.6	130963.6	130963.6	100.0	100.0	100.0
216070	130963.6	130963.6	130963.6	100.0	100.0	100.0
216080	130963.6	130963.6	130963.6	100.0	100.0	100.0
216090	130963.6	130963.6	130963.6	100.0	100.0	100.0
216100	130963.6	130963.6	130963.6	100.0	100.0	100.0
216110	130963.6	130963.6	130963.6	100.0	100.0	100.0
217010	130963.6	130963.6	130963.6	100.0	100.0	100.0
217020	130963.6	130963.6	130963.6	100.0	100.0	100.0
217030	130963.6	130963.6	130963.6	100.0	100.0	100.0
217040	130963.6	130963.6	130963.6	100.0	100.0	100.0
217050	130963.6	130963.6	130963.6	100.0	100.0	100.0
217060	130963.6	130963.6	130963.6	100.0	100.0	100.0
217070	130963.6	130963.6	130963.6	100.0	100.0	100.0
217080	130963.6	130963.6	130963.6	100.0	100.0	100.0
217090	130963.6	130963.6	130963.6	100.0	100.0	100.0
217100	130963.6	130963.6	130963.6	100.0	100.0	100.0
217110	130963.6	130963.6	130963.6	100.0	100.0	100.0
301010	130963.6	130963.6	130963.6	100.0	100.0	100.0
301020	130963.6	130963.6	130963.6	100.0	100.0	100.0
301030	130963.6	130963.6	130963.6	100.0	100.0	100.0
301040	130963.6	130963.6	130963.6	100.0	100.0	100.0
301050	130963.6	130963.6	130963.6	100.0	100.0	100.0
301060	130963.6	130963.6	130963.6	100.0	100.0	100.0
301070	130963.6	130963.6	130963.6	100.0	100.0	100.0
301080	130963.6	130963.6	130963.6	100.0	100.0	100.0
301090	130963.6	130963.6	130963.6	100.0	100.0	100.0
301100	130963.6	130963.6	130963.6	100.0	100.0	100.0
301110	130963.6	130963.6	130963.6	100.0	100.0	100.0
302010	130963.6	130963.6	130963.6	100.0	100.0	100.0
302020	130963.6	130963.6	130963.6	100.0	100.0	100.0
302030	130963.6	130963.6	130963.6	100.0	100.0	100.0
302040	130963.6	130963.6	130963.6	100.0	100.0	100.0
302050	130963.6	130963.6	130963.6	100.0	100.0	100.0
302060	130963.6	130963.6	130963.6	100.0	100.0	100.0
302070	130963.6	130963.6	130963.6	100.0	100.0	100.0
302080	130963.6	130963.6	130963.6	100.0	100.0	100.0
302090	130963.6	130963.6	130963.6	100.0	100.0	100.0
302100	130963.6	130963.6	130963.6	100.0	100.0	100.0
302110	130963.6	130963.6	130963.6	100.0	100.0	100.0
303010	130963.6	130963.6	130963.6	100.0	100.0	100.0
303020	130963.6	130963.6	130963.6	100.0	100.0	100.0
303030	130963.6	130963.6	130963.6	100.0	100.0	100.0
303040	130963.6	130963.6	130963.6	100.0	100.0	100.0

Table I-2 (continued)

Node	Mass in direction (kg)			Mass moment of inertia about axis (kg-m^2)		
	X	Y	Z	X	Y	Z
303050	130963.6	130963.6	130963.6	100.0	100.0	100.0
303060	130963.6	130963.6	130963.6	100.0	100.0	100.0
303070	130963.6	130963.6	130963.6	100.0	100.0	100.0
303080	130963.6	130963.6	130963.6	100.0	100.0	100.0
303090	130963.6	130963.6	130963.6	100.0	100.0	100.0
303100	130963.6	130963.6	130963.6	100.0	100.0	100.0
303110	130963.6	130963.6	130963.6	100.0	100.0	100.0
304010	130963.6	130963.6	130963.6	100.0	100.0	100.0
304020	130963.6	130963.6	130963.6	100.0	100.0	100.0
304030	130963.6	130963.6	130963.6	100.0	100.0	100.0
304040	130963.6	130963.6	130963.6	100.0	100.0	100.0
304050	130963.6	130963.6	130963.6	100.0	100.0	100.0
304060	130963.6	130963.6	130963.6	100.0	100.0	100.0
304070	130963.6	130963.6	130963.6	100.0	100.0	100.0
304080	130963.6	130963.6	130963.6	100.0	100.0	100.0
304090	130963.6	130963.6	130963.6	100.0	100.0	100.0
304100	130963.6	130963.6	130963.6	100.0	100.0	100.0
304110	130963.6	130963.6	130963.6	100.0	100.0	100.0
305010	70836.4	70836.4	70836.4	100.0	100.0	100.0
305020	70836.4	70836.4	70836.4	100.0	100.0	100.0
305030	70836.4	70836.4	70836.4	100.0	100.0	100.0
305040	70836.4	70836.4	70836.4	100.0	100.0	100.0
305050	70836.4	70836.4	70836.4	100.0	100.0	100.0
305060	70836.4	70836.4	70836.4	100.0	100.0	100.0
305070	70836.4	70836.4	70836.4	100.0	100.0	100.0
305080	70836.4	70836.4	70836.4	100.0	100.0	100.0
305090	70836.4	70836.4	70836.4	100.0	100.0	100.0
305100	70836.4	70836.4	70836.4	100.0	100.0	100.0
305110	70836.4	70836.4	70836.4	100.0	100.0	100.0
306010	70836.4	70836.4	70836.4	100.0	100.0	100.0
306020	70836.4	70836.4	70836.4	100.0	100.0	100.0
306030	70836.4	70836.4	70836.4	100.0	100.0	100.0
306040	70836.4	70836.4	70836.4	100.0	100.0	100.0
306050	70836.4	70836.4	70836.4	100.0	100.0	100.0
306060	70836.4	70836.4	70836.4	100.0	100.0	100.0
306070	70836.4	70836.4	70836.4	100.0	100.0	100.0
306080	70836.4	70836.4	70836.4	100.0	100.0	100.0
306090	70836.4	70836.4	70836.4	100.0	100.0	100.0
306100	70836.4	70836.4	70836.4	100.0	100.0	100.0
306110	70836.4	70836.4	70836.4	100.0	100.0	100.0
307010	70836.4	70836.4	70836.4	100.0	100.0	100.0
307020	70836.4	70836.4	70836.4	100.0	100.0	100.0
307030	70836.4	70836.4	70836.4	100.0	100.0	100.0
307040	70836.4	70836.4	70836.4	100.0	100.0	100.0
307050	70836.4	70836.4	70836.4	100.0	100.0	100.0

Table I-2 (continued)

Node	Mass in direction (kg)			Mass moment of inertia about axis (kg-m^2)		
	X	Y	Z	X	Y	Z
307060	70836.4	70836.4	70836.4	100.0	100.0	100.0
307070	70836.4	70836.4	70836.4	100.0	100.0	100.0
307080	70836.4	70836.4	70836.4	100.0	100.0	100.0
307090	70836.4	70836.4	70836.4	100.0	100.0	100.0
307100	70836.4	70836.4	70836.4	100.0	100.0	100.0
307110	70836.4	70836.4	70836.4	100.0	100.0	100.0
308010	70836.4	70836.4	70836.4	100.0	100.0	100.0
308020	70836.4	70836.4	70836.4	100.0	100.0	100.0
308030	70836.4	70836.4	70836.4	100.0	100.0	100.0
308040	70836.4	70836.4	70836.4	100.0	100.0	100.0
308050	70836.4	70836.4	70836.4	100.0	100.0	100.0
308060	70836.4	70836.4	70836.4	100.0	100.0	100.0
308070	70836.4	70836.4	70836.4	100.0	100.0	100.0
308080	70836.4	70836.4	70836.4	100.0	100.0	100.0
308090	70836.4	70836.4	70836.4	100.0	100.0	100.0
308100	70836.4	70836.4	70836.4	100.0	100.0	100.0
308110	70836.4	70836.4	70836.4	100.0	100.0	100.0
309010	70836.4	70836.4	70836.4	100.0	100.0	100.0
309020	70836.4	70836.4	70836.4	100.0	100.0	100.0
309030	70836.4	70836.4	70836.4	100.0	100.0	100.0
309040	70836.4	70836.4	70836.4	100.0	100.0	100.0
309050	70836.4	70836.4	70836.4	100.0	100.0	100.0
309060	70836.4	70836.4	70836.4	100.0	100.0	100.0
309070	70836.4	70836.4	70836.4	100.0	100.0	100.0
309080	70836.4	70836.4	70836.4	100.0	100.0	100.0
309090	70836.4	70836.4	70836.4	100.0	100.0	100.0
309100	70836.4	70836.4	70836.4	100.0	100.0	100.0
309110	70836.4	70836.4	70836.4	100.0	100.0	100.0
310010	70836.4	70836.4	70836.4	100.0	100.0	100.0
310020	70836.4	70836.4	70836.4	100.0	100.0	100.0
310030	70836.4	70836.4	70836.4	100.0	100.0	100.0
310040	70836.4	70836.4	70836.4	100.0	100.0	100.0
310050	70836.4	70836.4	70836.4	100.0	100.0	100.0
310060	70836.4	70836.4	70836.4	100.0	100.0	100.0
310070	70836.4	70836.4	70836.4	100.0	100.0	100.0
310080	70836.4	70836.4	70836.4	100.0	100.0	100.0
310090	70836.4	70836.4	70836.4	100.0	100.0	100.0
310100	70836.4	70836.4	70836.4	100.0	100.0	100.0
310110	70836.4	70836.4	70836.4	100.0	100.0	100.0
311010	70836.4	70836.4	70836.4	100.0	100.0	100.0
311020	70836.4	70836.4	70836.4	100.0	100.0	100.0
311030	70836.4	70836.4	70836.4	100.0	100.0	100.0
311040	70836.4	70836.4	70836.4	100.0	100.0	100.0
311050	70836.4	70836.4	70836.4	100.0	100.0	100.0
311060	70836.4	70836.4	70836.4	100.0	100.0	100.0

Table I-2 (continued)

Node	Mass in direction (kg)			Mass moment of inertia about axis (kg-m^2)		
	X	Y	Z	X	Y	Z
311070	70836.4	70836.4	70836.4	100.0	100.0	100.0
311080	70836.4	70836.4	70836.4	100.0	100.0	100.0
311090	70836.4	70836.4	70836.4	100.0	100.0	100.0
311100	70836.4	70836.4	70836.4	100.0	100.0	100.0
311110	70836.4	70836.4	70836.4	100.0	100.0	100.0
312010	70836.4	70836.4	70836.4	100.0	100.0	100.0
312020	70836.4	70836.4	70836.4	100.0	100.0	100.0
312030	70836.4	70836.4	70836.4	100.0	100.0	100.0
312040	70836.4	70836.4	70836.4	100.0	100.0	100.0
312050	70836.4	70836.4	70836.4	100.0	100.0	100.0
312060	70836.4	70836.4	70836.4	100.0	100.0	100.0
312070	70836.4	70836.4	70836.4	100.0	100.0	100.0
312080	70836.4	70836.4	70836.4	100.0	100.0	100.0
312090	70836.4	70836.4	70836.4	100.0	100.0	100.0
312100	70836.4	70836.4	70836.4	100.0	100.0	100.0
312110	70836.4	70836.4	70836.4	100.0	100.0	100.0
313010	70836.4	70836.4	70836.4	100.0	100.0	100.0
313020	70836.4	70836.4	70836.4	100.0	100.0	100.0
313030	70836.4	70836.4	70836.4	100.0	100.0	100.0
313040	70836.4	70836.4	70836.4	100.0	100.0	100.0
313050	70836.4	70836.4	70836.4	100.0	100.0	100.0
313060	70836.4	70836.4	70836.4	100.0	100.0	100.0
313070	70836.4	70836.4	70836.4	100.0	100.0	100.0
313080	70836.4	70836.4	70836.4	100.0	100.0	100.0
313090	70836.4	70836.4	70836.4	100.0	100.0	100.0
313100	70836.4	70836.4	70836.4	100.0	100.0	100.0
313110	70836.4	70836.4	70836.4	100.0	100.0	100.0
314010	130963.6	130963.6	130963.6	100.0	100.0	100.0
314020	130963.6	130963.6	130963.6	100.0	100.0	100.0
314030	130963.6	130963.6	130963.6	100.0	100.0	100.0
314040	130963.6	130963.6	130963.6	100.0	100.0	100.0
314050	130963.6	130963.6	130963.6	100.0	100.0	100.0
314060	130963.6	130963.6	130963.6	100.0	100.0	100.0
314070	130963.6	130963.6	130963.6	100.0	100.0	100.0
314080	130963.6	130963.6	130963.6	100.0	100.0	100.0
314090	130963.6	130963.6	130963.6	100.0	100.0	100.0
314100	130963.6	130963.6	130963.6	100.0	100.0	100.0
314110	130963.6	130963.6	130963.6	100.0	100.0	100.0
315010	130963.6	130963.6	130963.6	100.0	100.0	100.0
315020	130963.6	130963.6	130963.6	100.0	100.0	100.0
315030	130963.6	130963.6	130963.6	100.0	100.0	100.0
315040	130963.6	130963.6	130963.6	100.0	100.0	100.0
315050	130963.6	130963.6	130963.6	100.0	100.0	100.0
315060	130963.6	130963.6	130963.6	100.0	100.0	100.0
315070	130963.6	130963.6	130963.6	100.0	100.0	100.0

Table I-2 (continued)

Node	Mass in direction (kg)			Mass moment of inertia about axis (kg-m^2)		
	X	Y	Z	X	Y	Z
315080	130963.6	130963.6	130963.6	100.0	100.0	100.0
315090	130963.6	130963.6	130963.6	100.0	100.0	100.0
315100	130963.6	130963.6	130963.6	100.0	100.0	100.0
315110	130963.6	130963.6	130963.6	100.0	100.0	100.0
316010	130963.6	130963.6	130963.6	100.0	100.0	100.0
316020	130963.6	130963.6	130963.6	100.0	100.0	100.0
316030	130963.6	130963.6	130963.6	100.0	100.0	100.0
316040	130963.6	130963.6	130963.6	100.0	100.0	100.0
316050	130963.6	130963.6	130963.6	100.0	100.0	100.0
316060	130963.6	130963.6	130963.6	100.0	100.0	100.0
316070	130963.6	130963.6	130963.6	100.0	100.0	100.0
316080	130963.6	130963.6	130963.6	100.0	100.0	100.0
316090	130963.6	130963.6	130963.6	100.0	100.0	100.0
316100	130963.6	130963.6	130963.6	100.0	100.0	100.0
316110	130963.6	130963.6	130963.6	100.0	100.0	100.0
317010	130963.6	130963.6	130963.6	100.0	100.0	100.0
317020	130963.6	130963.6	130963.6	100.0	100.0	100.0
317030	130963.6	130963.6	130963.6	100.0	100.0	100.0
317040	130963.6	130963.6	130963.6	100.0	100.0	100.0
317050	130963.6	130963.6	130963.6	100.0	100.0	100.0
317060	130963.6	130963.6	130963.6	100.0	100.0	100.0
317070	130963.6	130963.6	130963.6	100.0	100.0	100.0
317080	130963.6	130963.6	130963.6	100.0	100.0	100.0
317090	130963.6	130963.6	130963.6	100.0	100.0	100.0
317100	130963.6	130963.6	130963.6	100.0	100.0	100.0
317110	130963.6	130963.6	130963.6	100.0	100.0	100.0
401010	130963.6	130963.6	130963.6	100.0	100.0	100.0
401020	130963.6	130963.6	130963.6	100.0	100.0	100.0
401030	130963.6	130963.6	130963.6	100.0	100.0	100.0
401040	130963.6	130963.6	130963.6	100.0	100.0	100.0
401050	130963.6	130963.6	130963.6	100.0	100.0	100.0
401060	130963.6	130963.6	130963.6	100.0	100.0	100.0
401070	130963.6	130963.6	130963.6	100.0	100.0	100.0
401080	130963.6	130963.6	130963.6	100.0	100.0	100.0
401090	130963.6	130963.6	130963.6	100.0	100.0	100.0
401100	130963.6	130963.6	130963.6	100.0	100.0	100.0
401110	130963.6	130963.6	130963.6	100.0	100.0	100.0
402010	130963.6	130963.6	130963.6	100.0	100.0	100.0
402020	130963.6	130963.6	130963.6	100.0	100.0	100.0
402030	130963.6	130963.6	130963.6	100.0	100.0	100.0
402040	130963.6	130963.6	130963.6	100.0	100.0	100.0
402050	130963.6	130963.6	130963.6	100.0	100.0	100.0
402060	130963.6	130963.6	130963.6	100.0	100.0	100.0
402070	130963.6	130963.6	130963.6	100.0	100.0	100.0
402080	130963.6	130963.6	130963.6	100.0	100.0	100.0

Table I-2 (continued)

Node	Mass in direction (kg)			Mass moment of inertia about axis (kg-m^2)		
	X	Y	Z	X	Y	Z
402090	130963.6	130963.6	130963.6	100.0	100.0	100.0
402100	130963.6	130963.6	130963.6	100.0	100.0	100.0
402110	130963.6	130963.6	130963.6	100.0	100.0	100.0
403010	130963.6	130963.6	130963.6	100.0	100.0	100.0
403020	130963.6	130963.6	130963.6	100.0	100.0	100.0
403030	130963.6	130963.6	130963.6	100.0	100.0	100.0
403040	130963.6	130963.6	130963.6	100.0	100.0	100.0
403050	130963.6	130963.6	130963.6	100.0	100.0	100.0
403060	130963.6	130963.6	130963.6	100.0	100.0	100.0
403070	130963.6	130963.6	130963.6	100.0	100.0	100.0
403080	130963.6	130963.6	130963.6	100.0	100.0	100.0
403090	130963.6	130963.6	130963.6	100.0	100.0	100.0
403100	130963.6	130963.6	130963.6	100.0	100.0	100.0
403110	130963.6	130963.6	130963.6	100.0	100.0	100.0
404010	130963.6	130963.6	130963.6	100.0	100.0	100.0
404020	130963.6	130963.6	130963.6	100.0	100.0	100.0
404030	130963.6	130963.6	130963.6	100.0	100.0	100.0
404040	130963.6	130963.6	130963.6	100.0	100.0	100.0
404050	130963.6	130963.6	130963.6	100.0	100.0	100.0
404060	130963.6	130963.6	130963.6	100.0	100.0	100.0
404070	130963.6	130963.6	130963.6	100.0	100.0	100.0
404080	130963.6	130963.6	130963.6	100.0	100.0	100.0
404090	130963.6	130963.6	130963.6	100.0	100.0	100.0
404100	130963.6	130963.6	130963.6	100.0	100.0	100.0
404110	130963.6	130963.6	130963.6	100.0	100.0	100.0
405010	70836.4	70836.4	70836.4	100.0	100.0	100.0
405020	70836.4	70836.4	70836.4	100.0	100.0	100.0
405030	70836.4	70836.4	70836.4	100.0	100.0	100.0
405040	70836.4	70836.4	70836.4	100.0	100.0	100.0
405050	70836.4	70836.4	70836.4	100.0	100.0	100.0
405060	70836.4	70836.4	70836.4	100.0	100.0	100.0
405070	70836.4	70836.4	70836.4	100.0	100.0	100.0
405080	70836.4	70836.4	70836.4	100.0	100.0	100.0
405090	70836.4	70836.4	70836.4	100.0	100.0	100.0
405100	70836.4	70836.4	70836.4	100.0	100.0	100.0
405110	70836.4	70836.4	70836.4	100.0	100.0	100.0
406010	70836.4	70836.4	70836.4	100.0	100.0	100.0
406020	70836.4	70836.4	70836.4	100.0	100.0	100.0
406030	70836.4	70836.4	70836.4	100.0	100.0	100.0
406040	70836.4	70836.4	70836.4	100.0	100.0	100.0
406050	70836.4	70836.4	70836.4	100.0	100.0	100.0
406060	70836.4	70836.4	70836.4	100.0	100.0	100.0
406070	70836.4	70836.4	70836.4	100.0	100.0	100.0
406080	70836.4	70836.4	70836.4	100.0	100.0	100.0
406090	70836.4	70836.4	70836.4	100.0	100.0	100.0

Table I-2 (continued)

Node	Mass in direction (kg)			Mass moment of inertia about axis (kg-m^2)		
	X	Y	Z	X	Y	Z
406100	70836.4	70836.4	70836.4	100.0	100.0	100.0
406110	70836.4	70836.4	70836.4	100.0	100.0	100.0
407010	70836.4	70836.4	70836.4	100.0	100.0	100.0
407020	70836.4	70836.4	70836.4	100.0	100.0	100.0
407030	70836.4	70836.4	70836.4	100.0	100.0	100.0
407040	70836.4	70836.4	70836.4	100.0	100.0	100.0
407050	70836.4	70836.4	70836.4	100.0	100.0	100.0
407060	70836.4	70836.4	70836.4	100.0	100.0	100.0
407070	70836.4	70836.4	70836.4	100.0	100.0	100.0
407080	70836.4	70836.4	70836.4	100.0	100.0	100.0
407090	70836.4	70836.4	70836.4	100.0	100.0	100.0
407100	70836.4	70836.4	70836.4	100.0	100.0	100.0
407110	70836.4	70836.4	70836.4	100.0	100.0	100.0
408010	70836.4	70836.4	70836.4	100.0	100.0	100.0
408020	70836.4	70836.4	70836.4	100.0	100.0	100.0
408030	70836.4	70836.4	70836.4	100.0	100.0	100.0
408040	70836.4	70836.4	70836.4	100.0	100.0	100.0
408050	70836.4	70836.4	70836.4	100.0	100.0	100.0
408060	70836.4	70836.4	70836.4	100.0	100.0	100.0
408070	70836.4	70836.4	70836.4	100.0	100.0	100.0
408080	70836.4	70836.4	70836.4	100.0	100.0	100.0
408090	70836.4	70836.4	70836.4	100.0	100.0	100.0
408100	70836.4	70836.4	70836.4	100.0	100.0	100.0
408110	70836.4	70836.4	70836.4	100.0	100.0	100.0
409010	70836.4	70836.4	70836.4	100.0	100.0	100.0
409020	70836.4	70836.4	70836.4	100.0	100.0	100.0
409030	70836.4	70836.4	70836.4	100.0	100.0	100.0
409040	70836.4	70836.4	70836.4	100.0	100.0	100.0
409050	70836.4	70836.4	70836.4	100.0	100.0	100.0
409060	70836.4	70836.4	70836.4	100.0	100.0	100.0
409070	70836.4	70836.4	70836.4	100.0	100.0	100.0
409080	70836.4	70836.4	70836.4	100.0	100.0	100.0
409090	70836.4	70836.4	70836.4	100.0	100.0	100.0
409100	70836.4	70836.4	70836.4	100.0	100.0	100.0
409110	70836.4	70836.4	70836.4	100.0	100.0	100.0
410010	70836.4	70836.4	70836.4	100.0	100.0	100.0
410020	70836.4	70836.4	70836.4	100.0	100.0	100.0
410030	70836.4	70836.4	70836.4	100.0	100.0	100.0
410040	70836.4	70836.4	70836.4	100.0	100.0	100.0
410050	70836.4	70836.4	70836.4	100.0	100.0	100.0
410060	70836.4	70836.4	70836.4	100.0	100.0	100.0
410070	70836.4	70836.4	70836.4	100.0	100.0	100.0
410080	70836.4	70836.4	70836.4	100.0	100.0	100.0
410090	70836.4	70836.4	70836.4	100.0	100.0	100.0
410100	70836.4	70836.4	70836.4	100.0	100.0	100.0

Table I-2 (continued)

Node	Mass in direction (kg)			Mass moment of inertia about axis (kg-m^2)		
	X	Y	Z	X	Y	Z
410110	70836.4	70836.4	70836.4	100.0	100.0	100.0
411010	70836.4	70836.4	70836.4	100.0	100.0	100.0
411020	70836.4	70836.4	70836.4	100.0	100.0	100.0
411030	70836.4	70836.4	70836.4	100.0	100.0	100.0
411040	70836.4	70836.4	70836.4	100.0	100.0	100.0
411050	70836.4	70836.4	70836.4	100.0	100.0	100.0
411060	70836.4	70836.4	70836.4	100.0	100.0	100.0
411070	70836.4	70836.4	70836.4	100.0	100.0	100.0
411080	70836.4	70836.4	70836.4	100.0	100.0	100.0
411090	70836.4	70836.4	70836.4	100.0	100.0	100.0
411100	70836.4	70836.4	70836.4	100.0	100.0	100.0
411110	70836.4	70836.4	70836.4	100.0	100.0	100.0
412010	70836.4	70836.4	70836.4	100.0	100.0	100.0
412020	70836.4	70836.4	70836.4	100.0	100.0	100.0
412030	70836.4	70836.4	70836.4	100.0	100.0	100.0
412040	70836.4	70836.4	70836.4	100.0	100.0	100.0
412050	70836.4	70836.4	70836.4	100.0	100.0	100.0
412060	70836.4	70836.4	70836.4	100.0	100.0	100.0
412070	70836.4	70836.4	70836.4	100.0	100.0	100.0
412080	70836.4	70836.4	70836.4	100.0	100.0	100.0
412090	70836.4	70836.4	70836.4	100.0	100.0	100.0
412100	70836.4	70836.4	70836.4	100.0	100.0	100.0
412110	70836.4	70836.4	70836.4	100.0	100.0	100.0
413010	70836.4	70836.4	70836.4	100.0	100.0	100.0
413020	70836.4	70836.4	70836.4	100.0	100.0	100.0
413030	70836.4	70836.4	70836.4	100.0	100.0	100.0
413040	70836.4	70836.4	70836.4	100.0	100.0	100.0
413050	70836.4	70836.4	70836.4	100.0	100.0	100.0
413060	70836.4	70836.4	70836.4	100.0	100.0	100.0
413070	70836.4	70836.4	70836.4	100.0	100.0	100.0
413080	70836.4	70836.4	70836.4	100.0	100.0	100.0
413090	70836.4	70836.4	70836.4	100.0	100.0	100.0
413100	70836.4	70836.4	70836.4	100.0	100.0	100.0
413110	70836.4	70836.4	70836.4	100.0	100.0	100.0
414010	130963.6	130963.6	130963.6	100.0	100.0	100.0
414020	130963.6	130963.6	130963.6	100.0	100.0	100.0
414030	130963.6	130963.6	130963.6	100.0	100.0	100.0
414040	130963.6	130963.6	130963.6	100.0	100.0	100.0
414050	130963.6	130963.6	130963.6	100.0	100.0	100.0
414060	130963.6	130963.6	130963.6	100.0	100.0	100.0
414070	130963.6	130963.6	130963.6	100.0	100.0	100.0
414080	130963.6	130963.6	130963.6	100.0	100.0	100.0
414090	130963.6	130963.6	130963.6	100.0	100.0	100.0
414100	130963.6	130963.6	130963.6	100.0	100.0	100.0
414110	130963.6	130963.6	130963.6	100.0	100.0	100.0

Table I-2 (continued)

Node	Mass in direction (kg)			Mass moment of inertia about axis (kg-m^2)		
	X	Y	Z	X	Y	Z
415010	130963.6	130963.6	130963.6	100.0	100.0	100.0
415020	130963.6	130963.6	130963.6	100.0	100.0	100.0
415030	130963.6	130963.6	130963.6	100.0	100.0	100.0
415040	130963.6	130963.6	130963.6	100.0	100.0	100.0
415050	130963.6	130963.6	130963.6	100.0	100.0	100.0
415060	130963.6	130963.6	130963.6	100.0	100.0	100.0
415070	130963.6	130963.6	130963.6	100.0	100.0	100.0
415080	130963.6	130963.6	130963.6	100.0	100.0	100.0
415090	130963.6	130963.6	130963.6	100.0	100.0	100.0
415100	130963.6	130963.6	130963.6	100.0	100.0	100.0
415110	130963.6	130963.6	130963.6	100.0	100.0	100.0
416010	130963.6	130963.6	130963.6	100.0	100.0	100.0
416020	130963.6	130963.6	130963.6	100.0	100.0	100.0
416030	130963.6	130963.6	130963.6	100.0	100.0	100.0
416040	130963.6	130963.6	130963.6	100.0	100.0	100.0
416050	130963.6	130963.6	130963.6	100.0	100.0	100.0
416060	130963.6	130963.6	130963.6	100.0	100.0	100.0
416070	130963.6	130963.6	130963.6	100.0	100.0	100.0
416080	130963.6	130963.6	130963.6	100.0	100.0	100.0
416090	130963.6	130963.6	130963.6	100.0	100.0	100.0
416100	130963.6	130963.6	130963.6	100.0	100.0	100.0
416110	130963.6	130963.6	130963.6	100.0	100.0	100.0
417010	130963.6	130963.6	130963.6	100.0	100.0	100.0
417020	130963.6	130963.6	130963.6	100.0	100.0	100.0
417030	130963.6	130963.6	130963.6	100.0	100.0	100.0
417040	130963.6	130963.6	130963.6	100.0	100.0	100.0
417050	130963.6	130963.6	130963.6	100.0	100.0	100.0
417060	130963.6	130963.6	130963.6	100.0	100.0	100.0
417070	130963.6	130963.6	130963.6	100.0	100.0	100.0
417080	130963.6	130963.6	130963.6	100.0	100.0	100.0
417090	130963.6	130963.6	130963.6	100.0	100.0	100.0
417100	130963.6	130963.6	130963.6	100.0	100.0	100.0
417110	130963.6	130963.6	130963.6	100.0	100.0	100.0
501010	90545.5	90545.5	90545.5	100.0	100.0	100.0
501020	90545.5	90545.5	90545.5	100.0	100.0	100.0
501030	90545.5	90545.5	90545.5	100.0	100.0	100.0
501040	90545.5	90545.5	90545.5	100.0	100.0	100.0
501050	90545.5	90545.5	90545.5	100.0	100.0	100.0
501060	90545.5	90545.5	90545.5	100.0	100.0	100.0
501070	90545.5	90545.5	90545.5	100.0	100.0	100.0
501080	90545.5	90545.5	90545.5	100.0	100.0	100.0
501090	90545.5	90545.5	90545.5	100.0	100.0	100.0
501100	90545.5	90545.5	90545.5	100.0	100.0	100.0
501110	90545.5	90545.5	90545.5	100.0	100.0	100.0
502010	90545.5	90545.5	90545.5	100.0	100.0	100.0

Table I-2 (continued)

Node	Mass in direction (kg)			Mass moment of inertia about axis (kg-m^2)		
	X	Y	Z	X	Y	Z
502020	90545.5	90545.5	90545.5	100.0	100.0	100.0
502030	90545.5	90545.5	90545.5	100.0	100.0	100.0
502040	90545.5	90545.5	90545.5	100.0	100.0	100.0
502050	90545.5	90545.5	90545.5	100.0	100.0	100.0
502060	90545.5	90545.5	90545.5	100.0	100.0	100.0
502070	90545.5	90545.5	90545.5	100.0	100.0	100.0
502080	90545.5	90545.5	90545.5	100.0	100.0	100.0
502090	90545.5	90545.5	90545.5	100.0	100.0	100.0
502100	90545.5	90545.5	90545.5	100.0	100.0	100.0
502110	90545.5	90545.5	90545.5	100.0	100.0	100.0
503010	90545.5	90545.5	90545.5	100.0	100.0	100.0
503020	90545.5	90545.5	90545.5	100.0	100.0	100.0
503030	90545.5	90545.5	90545.5	100.0	100.0	100.0
503040	90545.5	90545.5	90545.5	100.0	100.0	100.0
503050	90545.5	90545.5	90545.5	100.0	100.0	100.0
503060	90545.5	90545.5	90545.5	100.0	100.0	100.0
503070	90545.5	90545.5	90545.5	100.0	100.0	100.0
503080	90545.5	90545.5	90545.5	100.0	100.0	100.0
503090	90545.5	90545.5	90545.5	100.0	100.0	100.0
503100	90545.5	90545.5	90545.5	100.0	100.0	100.0
503110	90545.5	90545.5	90545.5	100.0	100.0	100.0
504010	90545.5	90545.5	90545.5	100.0	100.0	100.0
504020	90545.5	90545.5	90545.5	100.0	100.0	100.0
504030	90545.5	90545.5	90545.5	100.0	100.0	100.0
504040	90545.5	90545.5	90545.5	100.0	100.0	100.0
504050	90545.5	90545.5	90545.5	100.0	100.0	100.0
504060	90545.5	90545.5	90545.5	100.0	100.0	100.0
504070	90545.5	90545.5	90545.5	100.0	100.0	100.0
504080	90545.5	90545.5	90545.5	100.0	100.0	100.0
504090	90545.5	90545.5	90545.5	100.0	100.0	100.0
504100	90545.5	90545.5	90545.5	100.0	100.0	100.0
504110	90545.5	90545.5	90545.5	100.0	100.0	100.0
505010	66569.7	66569.7	66569.7	100.0	100.0	100.0
505020	66569.7	66569.7	66569.7	100.0	100.0	100.0
505030	66569.7	66569.7	66569.7	100.0	100.0	100.0
505040	66569.7	66569.7	66569.7	100.0	100.0	100.0
505050	66569.7	66569.7	66569.7	100.0	100.0	100.0
505060	66569.7	66569.7	66569.7	100.0	100.0	100.0
505070	66569.7	66569.7	66569.7	100.0	100.0	100.0
505080	66569.7	66569.7	66569.7	100.0	100.0	100.0
505090	66569.7	66569.7	66569.7	100.0	100.0	100.0
505100	66569.7	66569.7	66569.7	100.0	100.0	100.0
505110	66569.7	66569.7	66569.7	100.0	100.0	100.0
506010	66569.7	66569.7	66569.7	100.0	100.0	100.0
506020	66569.7	66569.7	66569.7	100.0	100.0	100.0

Table I-2 (continued)

Node	Mass in direction (kg)			Mass moment of inertia about axis (kg-m^2)		
	X	Y	Z	X	Y	Z
506030	66569.7	66569.7	66569.7	100.0	100.0	100.0
506040	66569.7	66569.7	66569.7	100.0	100.0	100.0
506050	66569.7	66569.7	66569.7	100.0	100.0	100.0
506060	66569.7	66569.7	66569.7	100.0	100.0	100.0
506070	66569.7	66569.7	66569.7	100.0	100.0	100.0
506080	66569.7	66569.7	66569.7	100.0	100.0	100.0
506090	66569.7	66569.7	66569.7	100.0	100.0	100.0
506100	66569.7	66569.7	66569.7	100.0	100.0	100.0
506110	66569.7	66569.7	66569.7	100.0	100.0	100.0
507010	66569.7	66569.7	66569.7	100.0	100.0	100.0
507020	66569.7	66569.7	66569.7	100.0	100.0	100.0
507030	66569.7	66569.7	66569.7	100.0	100.0	100.0
507040	66569.7	66569.7	66569.7	100.0	100.0	100.0
507050	66569.7	66569.7	66569.7	100.0	100.0	100.0
507060	66569.7	66569.7	66569.7	100.0	100.0	100.0
507070	66569.7	66569.7	66569.7	100.0	100.0	100.0
507080	66569.7	66569.7	66569.7	100.0	100.0	100.0
507090	66569.7	66569.7	66569.7	100.0	100.0	100.0
507100	66569.7	66569.7	66569.7	100.0	100.0	100.0
507110	66569.7	66569.7	66569.7	100.0	100.0	100.0
508010	66569.7	66569.7	66569.7	100.0	100.0	100.0
508020	66569.7	66569.7	66569.7	100.0	100.0	100.0
508030	66569.7	66569.7	66569.7	100.0	100.0	100.0
508040	66569.7	66569.7	66569.7	100.0	100.0	100.0
508050	66569.7	66569.7	66569.7	100.0	100.0	100.0
508060	66569.7	66569.7	66569.7	100.0	100.0	100.0
508070	66569.7	66569.7	66569.7	100.0	100.0	100.0
508080	66569.7	66569.7	66569.7	100.0	100.0	100.0
508090	66569.7	66569.7	66569.7	100.0	100.0	100.0
508100	66569.7	66569.7	66569.7	100.0	100.0	100.0
508110	66569.7	66569.7	66569.7	100.0	100.0	100.0
509010	66569.7	66569.7	66569.7	100.0	100.0	100.0
509020	66569.7	66569.7	66569.7	100.0	100.0	100.0
509030	66569.7	66569.7	66569.7	100.0	100.0	100.0
509040	66569.7	66569.7	66569.7	100.0	100.0	100.0
509050	66569.7	66569.7	66569.7	100.0	100.0	100.0
509060	66569.7	66569.7	66569.7	100.0	100.0	100.0
509070	66569.7	66569.7	66569.7	100.0	100.0	100.0
509080	66569.7	66569.7	66569.7	100.0	100.0	100.0
509090	66569.7	66569.7	66569.7	100.0	100.0	100.0
509100	66569.7	66569.7	66569.7	100.0	100.0	100.0
509110	66569.7	66569.7	66569.7	100.0	100.0	100.0
510010	66569.7	66569.7	66569.7	100.0	100.0	100.0
510020	66569.7	66569.7	66569.7	100.0	100.0	100.0
510030	66569.7	66569.7	66569.7	100.0	100.0	100.0

Table I-2 (continued)

Node	Mass in direction (kg)			Mass moment of inertia about axis (kg-m^2)		
	X	Y	Z	X	Y	Z
510040	66569.7	66569.7	66569.7	100.0	100.0	100.0
510050	66569.7	66569.7	66569.7	100.0	100.0	100.0
510060	66569.7	66569.7	66569.7	100.0	100.0	100.0
510070	66569.7	66569.7	66569.7	100.0	100.0	100.0
510080	66569.7	66569.7	66569.7	100.0	100.0	100.0
510090	66569.7	66569.7	66569.7	100.0	100.0	100.0
510100	66569.7	66569.7	66569.7	100.0	100.0	100.0
510110	66569.7	66569.7	66569.7	100.0	100.0	100.0
511010	66569.7	66569.7	66569.7	100.0	100.0	100.0
511020	66569.7	66569.7	66569.7	100.0	100.0	100.0
511030	66569.7	66569.7	66569.7	100.0	100.0	100.0
511040	66569.7	66569.7	66569.7	100.0	100.0	100.0
511050	66569.7	66569.7	66569.7	100.0	100.0	100.0
511060	66569.7	66569.7	66569.7	100.0	100.0	100.0
511070	66569.7	66569.7	66569.7	100.0	100.0	100.0
511080	66569.7	66569.7	66569.7	100.0	100.0	100.0
511090	66569.7	66569.7	66569.7	100.0	100.0	100.0
511100	66569.7	66569.7	66569.7	100.0	100.0	100.0
511110	66569.7	66569.7	66569.7	100.0	100.0	100.0
512010	66569.7	66569.7	66569.7	100.0	100.0	100.0
512020	66569.7	66569.7	66569.7	100.0	100.0	100.0
512030	66569.7	66569.7	66569.7	100.0	100.0	100.0
512040	66569.7	66569.7	66569.7	100.0	100.0	100.0
512050	66569.7	66569.7	66569.7	100.0	100.0	100.0
512060	66569.7	66569.7	66569.7	100.0	100.0	100.0
512070	66569.7	66569.7	66569.7	100.0	100.0	100.0
512080	66569.7	66569.7	66569.7	100.0	100.0	100.0
512090	66569.7	66569.7	66569.7	100.0	100.0	100.0
512100	66569.7	66569.7	66569.7	100.0	100.0	100.0
512110	66569.7	66569.7	66569.7	100.0	100.0	100.0
513010	66569.7	66569.7	66569.7	100.0	100.0	100.0
513020	66569.7	66569.7	66569.7	100.0	100.0	100.0
513030	66569.7	66569.7	66569.7	100.0	100.0	100.0
513040	66569.7	66569.7	66569.7	100.0	100.0	100.0
513050	66569.7	66569.7	66569.7	100.0	100.0	100.0
513060	66569.7	66569.7	66569.7	100.0	100.0	100.0
513070	66569.7	66569.7	66569.7	100.0	100.0	100.0
513080	66569.7	66569.7	66569.7	100.0	100.0	100.0
513090	66569.7	66569.7	66569.7	100.0	100.0	100.0
513100	66569.7	66569.7	66569.7	100.0	100.0	100.0
513110	66569.7	66569.7	66569.7	100.0	100.0	100.0
514010	90545.5	90545.5	90545.5	100.0	100.0	100.0
514020	90545.5	90545.5	90545.5	100.0	100.0	100.0
514030	90545.5	90545.5	90545.5	100.0	100.0	100.0
514040	90545.5	90545.5	90545.5	100.0	100.0	100.0

Table I-2 (continued)

Node	Mass in direction (kg)			Mass moment of inertia about axis (kg-m^2)		
	X	Y	Z	X	Y	Z
514050	90545.5	90545.5	90545.5	100.0	100.0	100.0
514060	90545.5	90545.5	90545.5	100.0	100.0	100.0
514070	90545.5	90545.5	90545.5	100.0	100.0	100.0
514080	90545.5	90545.5	90545.5	100.0	100.0	100.0
514090	90545.5	90545.5	90545.5	100.0	100.0	100.0
514100	90545.5	90545.5	90545.5	100.0	100.0	100.0
514110	90545.5	90545.5	90545.5	100.0	100.0	100.0
515010	90545.5	90545.5	90545.5	100.0	100.0	100.0
515020	90545.5	90545.5	90545.5	100.0	100.0	100.0
515030	90545.5	90545.5	90545.5	100.0	100.0	100.0
515040	90545.5	90545.5	90545.5	100.0	100.0	100.0
515050	90545.5	90545.5	90545.5	100.0	100.0	100.0
515060	90545.5	90545.5	90545.5	100.0	100.0	100.0
515070	90545.5	90545.5	90545.5	100.0	100.0	100.0
515080	90545.5	90545.5	90545.5	100.0	100.0	100.0
515090	90545.5	90545.5	90545.5	100.0	100.0	100.0
515100	90545.5	90545.5	90545.5	100.0	100.0	100.0
515110	90545.5	90545.5	90545.5	100.0	100.0	100.0
516010	90545.5	90545.5	90545.5	100.0	100.0	100.0
516020	90545.5	90545.5	90545.5	100.0	100.0	100.0
516030	90545.5	90545.5	90545.5	100.0	100.0	100.0
516040	90545.5	90545.5	90545.5	100.0	100.0	100.0
516050	90545.5	90545.5	90545.5	100.0	100.0	100.0
516060	90545.5	90545.5	90545.5	100.0	100.0	100.0
516070	90545.5	90545.5	90545.5	100.0	100.0	100.0
516080	90545.5	90545.5	90545.5	100.0	100.0	100.0
516090	90545.5	90545.5	90545.5	100.0	100.0	100.0
516100	90545.5	90545.5	90545.5	100.0	100.0	100.0
516110	90545.5	90545.5	90545.5	100.0	100.0	100.0
517010	90545.5	90545.5	90545.5	100.0	100.0	100.0
517020	90545.5	90545.5	90545.5	100.0	100.0	100.0
517030	90545.5	90545.5	90545.5	100.0	100.0	100.0
517040	90545.5	90545.5	90545.5	100.0	100.0	100.0
517050	90545.5	90545.5	90545.5	100.0	100.0	100.0
517060	90545.5	90545.5	90545.5	100.0	100.0	100.0
517070	90545.5	90545.5	90545.5	100.0	100.0	100.0
517080	90545.5	90545.5	90545.5	100.0	100.0	100.0
517090	90545.5	90545.5	90545.5	100.0	100.0	100.0
517100	90545.5	90545.5	90545.5	100.0	100.0	100.0
517110	90545.5	90545.5	90545.5	100.0	100.0	100.0
605010	53818.2	53818.2	53818.2	100.0	100.0	100.0
605020	53818.2	53818.2	53818.2	100.0	100.0	100.0
605030	53818.2	53818.2	53818.2	100.0	100.0	100.0
605040	53818.2	53818.2	53818.2	100.0	100.0	100.0
605050	53818.2	53818.2	53818.2	100.0	100.0	100.0

Table I-2 (continued)

Node	Mass in direction (kg)			Mass moment of inertia about axis (kg-m^2)		
	X	Y	Z	X	Y	Z
605060	53818.2	53818.2	53818.2	100.0	100.0	100.0
605070	53818.2	53818.2	53818.2	100.0	100.0	100.0
605080	53818.2	53818.2	53818.2	100.0	100.0	100.0
605090	53818.2	53818.2	53818.2	100.0	100.0	100.0
605100	53818.2	53818.2	53818.2	100.0	100.0	100.0
605110	53818.2	53818.2	53818.2	100.0	100.0	100.0
606010	53818.2	53818.2	53818.2	100.0	100.0	100.0
606020	53818.2	53818.2	53818.2	100.0	100.0	100.0
606030	53818.2	53818.2	53818.2	100.0	100.0	100.0
606040	53818.2	53818.2	53818.2	100.0	100.0	100.0
606050	53818.2	53818.2	53818.2	100.0	100.0	100.0
606060	53818.2	53818.2	53818.2	100.0	100.0	100.0
606070	53818.2	53818.2	53818.2	100.0	100.0	100.0
606080	53818.2	53818.2	53818.2	100.0	100.0	100.0
606090	53818.2	53818.2	53818.2	100.0	100.0	100.0
606100	53818.2	53818.2	53818.2	100.0	100.0	100.0
606110	53818.2	53818.2	53818.2	100.0	100.0	100.0
607010	53818.2	53818.2	53818.2	100.0	100.0	100.0
607020	53818.2	53818.2	53818.2	100.0	100.0	100.0
607030	53818.2	53818.2	53818.2	100.0	100.0	100.0
607040	53818.2	53818.2	53818.2	100.0	100.0	100.0
607050	53818.2	53818.2	53818.2	100.0	100.0	100.0
607060	53818.2	53818.2	53818.2	100.0	100.0	100.0
607070	53818.2	53818.2	53818.2	100.0	100.0	100.0
607080	53818.2	53818.2	53818.2	100.0	100.0	100.0
607090	53818.2	53818.2	53818.2	100.0	100.0	100.0
607100	53818.2	53818.2	53818.2	100.0	100.0	100.0
607110	53818.2	53818.2	53818.2	100.0	100.0	100.0
608010	53818.2	53818.2	53818.2	100.0	100.0	100.0
608020	53818.2	53818.2	53818.2	100.0	100.0	100.0
608030	53818.2	53818.2	53818.2	100.0	100.0	100.0
608040	53818.2	53818.2	53818.2	100.0	100.0	100.0
608050	53818.2	53818.2	53818.2	100.0	100.0	100.0
608060	53818.2	53818.2	53818.2	100.0	100.0	100.0
608070	53818.2	53818.2	53818.2	100.0	100.0	100.0
608080	53818.2	53818.2	53818.2	100.0	100.0	100.0
608090	53818.2	53818.2	53818.2	100.0	100.0	100.0
608100	53818.2	53818.2	53818.2	100.0	100.0	100.0
608110	53818.2	53818.2	53818.2	100.0	100.0	100.0
609010	53818.2	53818.2	53818.2	100.0	100.0	100.0
609020	53818.2	53818.2	53818.2	100.0	100.0	100.0
609030	53818.2	53818.2	53818.2	100.0	100.0	100.0
609040	53818.2	53818.2	53818.2	100.0	100.0	100.0
609050	53818.2	53818.2	53818.2	100.0	100.0	100.0
609060	53818.2	53818.2	53818.2	100.0	100.0	100.0

Table I-2 (continued)

Node	Mass in direction (kg)			Mass moment of inertia about axis (kg-m^2)		
	X	Y	Z	X	Y	Z
609070	53818.2	53818.2	53818.2	100.0	100.0	100.0
609080	53818.2	53818.2	53818.2	100.0	100.0	100.0
609090	53818.2	53818.2	53818.2	100.0	100.0	100.0
609100	53818.2	53818.2	53818.2	100.0	100.0	100.0
609110	53818.2	53818.2	53818.2	100.0	100.0	100.0
610010	53818.2	53818.2	53818.2	100.0	100.0	100.0
610020	53818.2	53818.2	53818.2	100.0	100.0	100.0
610030	53818.2	53818.2	53818.2	100.0	100.0	100.0
610040	53818.2	53818.2	53818.2	100.0	100.0	100.0
610050	53818.2	53818.2	53818.2	100.0	100.0	100.0
610060	53818.2	53818.2	53818.2	100.0	100.0	100.0
610070	53818.2	53818.2	53818.2	100.0	100.0	100.0
610080	53818.2	53818.2	53818.2	100.0	100.0	100.0
610090	53818.2	53818.2	53818.2	100.0	100.0	100.0
610100	53818.2	53818.2	53818.2	100.0	100.0	100.0
610110	53818.2	53818.2	53818.2	100.0	100.0	100.0
611010	53818.2	53818.2	53818.2	100.0	100.0	100.0
611020	53818.2	53818.2	53818.2	100.0	100.0	100.0
611030	53818.2	53818.2	53818.2	100.0	100.0	100.0
611040	53818.2	53818.2	53818.2	100.0	100.0	100.0
611050	53818.2	53818.2	53818.2	100.0	100.0	100.0
611060	53818.2	53818.2	53818.2	100.0	100.0	100.0
611070	53818.2	53818.2	53818.2	100.0	100.0	100.0
611080	53818.2	53818.2	53818.2	100.0	100.0	100.0
611090	53818.2	53818.2	53818.2	100.0	100.0	100.0
611100	53818.2	53818.2	53818.2	100.0	100.0	100.0
611110	53818.2	53818.2	53818.2	100.0	100.0	100.0
612010	53818.2	53818.2	53818.2	100.0	100.0	100.0
612020	53818.2	53818.2	53818.2	100.0	100.0	100.0
612030	53818.2	53818.2	53818.2	100.0	100.0	100.0
612040	53818.2	53818.2	53818.2	100.0	100.0	100.0
612050	53818.2	53818.2	53818.2	100.0	100.0	100.0
612060	53818.2	53818.2	53818.2	100.0	100.0	100.0
612070	53818.2	53818.2	53818.2	100.0	100.0	100.0
612080	53818.2	53818.2	53818.2	100.0	100.0	100.0
612090	53818.2	53818.2	53818.2	100.0	100.0	100.0
612100	53818.2	53818.2	53818.2	100.0	100.0	100.0
612110	53818.2	53818.2	53818.2	100.0	100.0	100.0
613010	53818.2	53818.2	53818.2	100.0	100.0	100.0
613020	53818.2	53818.2	53818.2	100.0	100.0	100.0
613030	53818.2	53818.2	53818.2	100.0	100.0	100.0
613040	53818.2	53818.2	53818.2	100.0	100.0	100.0
613050	53818.2	53818.2	53818.2	100.0	100.0	100.0
613060	53818.2	53818.2	53818.2	100.0	100.0	100.0
613070	53818.2	53818.2	53818.2	100.0	100.0	100.0

Table I-2 (continued)

Node	Mass in direction (kg)			Mass moment of inertia about axis (kg-m^2)		
	X	Y	Z	X	Y	Z
613080	53818.2	53818.2	53818.2	100.0	100.0	100.0
613090	53818.2	53818.2	53818.2	100.0	100.0	100.0
613100	53818.2	53818.2	53818.2	100.0	100.0	100.0
613110	53818.2	53818.2	53818.2	100.0	100.0	100.0
705010	53818.2	53818.2	53818.2	100.0	100.0	100.0
705020	53818.2	53818.2	53818.2	100.0	100.0	100.0
705030	53818.2	53818.2	53818.2	100.0	100.0	100.0
705040	53818.2	53818.2	53818.2	100.0	100.0	100.0
705050	53818.2	53818.2	53818.2	100.0	100.0	100.0
705060	53818.2	53818.2	53818.2	100.0	100.0	100.0
705070	53818.2	53818.2	53818.2	100.0	100.0	100.0
705080	53818.2	53818.2	53818.2	100.0	100.0	100.0
705090	53818.2	53818.2	53818.2	100.0	100.0	100.0
705100	53818.2	53818.2	53818.2	100.0	100.0	100.0
705110	53818.2	53818.2	53818.2	100.0	100.0	100.0
706010	53818.2	53818.2	53818.2	100.0	100.0	100.0
706020	53818.2	53818.2	53818.2	100.0	100.0	100.0
706030	53818.2	53818.2	53818.2	100.0	100.0	100.0
706040	53818.2	53818.2	53818.2	100.0	100.0	100.0
706050	53818.2	53818.2	53818.2	100.0	100.0	100.0
706060	53818.2	53818.2	53818.2	100.0	100.0	100.0
706070	53818.2	53818.2	53818.2	100.0	100.0	100.0
706080	53818.2	53818.2	53818.2	100.0	100.0	100.0
706090	53818.2	53818.2	53818.2	100.0	100.0	100.0
706100	53818.2	53818.2	53818.2	100.0	100.0	100.0
706110	53818.2	53818.2	53818.2	100.0	100.0	100.0
707010	53818.2	53818.2	53818.2	100.0	100.0	100.0
707020	53818.2	53818.2	53818.2	100.0	100.0	100.0
707030	53818.2	53818.2	53818.2	100.0	100.0	100.0
707040	53818.2	53818.2	53818.2	100.0	100.0	100.0
707050	53818.2	53818.2	53818.2	100.0	100.0	100.0
707060	53818.2	53818.2	53818.2	100.0	100.0	100.0
707070	53818.2	53818.2	53818.2	100.0	100.0	100.0
707080	53818.2	53818.2	53818.2	100.0	100.0	100.0
707090	53818.2	53818.2	53818.2	100.0	100.0	100.0
707100	53818.2	53818.2	53818.2	100.0	100.0	100.0
707110	53818.2	53818.2	53818.2	100.0	100.0	100.0
708010	53818.2	53818.2	53818.2	100.0	100.0	100.0
708020	53818.2	53818.2	53818.2	100.0	100.0	100.0
708030	53818.2	53818.2	53818.2	100.0	100.0	100.0
708040	53818.2	53818.2	53818.2	100.0	100.0	100.0
708050	53818.2	53818.2	53818.2	100.0	100.0	100.0
708060	53818.2	53818.2	53818.2	100.0	100.0	100.0
708070	53818.2	53818.2	53818.2	100.0	100.0	100.0
708080	53818.2	53818.2	53818.2	100.0	100.0	100.0

Table I-2 (continued)

Node	Mass in direction (kg)			Mass moment of inertia about axis (kg-m^2)		
	X	Y	Z	X	Y	Z
708090	53818.2	53818.2	53818.2	100.0	100.0	100.0
708100	53818.2	53818.2	53818.2	100.0	100.0	100.0
708110	53818.2	53818.2	53818.2	100.0	100.0	100.0
709010	53818.2	53818.2	53818.2	100.0	100.0	100.0
709020	53818.2	53818.2	53818.2	100.0	100.0	100.0
709030	53818.2	53818.2	53818.2	100.0	100.0	100.0
709040	53818.2	53818.2	53818.2	100.0	100.0	100.0
709050	53818.2	53818.2	53818.2	100.0	100.0	100.0
709060	53818.2	53818.2	53818.2	100.0	100.0	100.0
709070	53818.2	53818.2	53818.2	100.0	100.0	100.0
709080	53818.2	53818.2	53818.2	100.0	100.0	100.0
709090	53818.2	53818.2	53818.2	100.0	100.0	100.0
709100	53818.2	53818.2	53818.2	100.0	100.0	100.0
709110	53818.2	53818.2	53818.2	100.0	100.0	100.0
710010	53818.2	53818.2	53818.2	100.0	100.0	100.0
710020	53818.2	53818.2	53818.2	100.0	100.0	100.0
710030	53818.2	53818.2	53818.2	100.0	100.0	100.0
710040	53818.2	53818.2	53818.2	100.0	100.0	100.0
710050	53818.2	53818.2	53818.2	100.0	100.0	100.0
710060	53818.2	53818.2	53818.2	100.0	100.0	100.0
710070	53818.2	53818.2	53818.2	100.0	100.0	100.0
710080	53818.2	53818.2	53818.2	100.0	100.0	100.0
710090	53818.2	53818.2	53818.2	100.0	100.0	100.0
710100	53818.2	53818.2	53818.2	100.0	100.0	100.0
710110	53818.2	53818.2	53818.2	100.0	100.0	100.0
711010	53818.2	53818.2	53818.2	100.0	100.0	100.0
711020	53818.2	53818.2	53818.2	100.0	100.0	100.0
711030	53818.2	53818.2	53818.2	100.0	100.0	100.0
711040	53818.2	53818.2	53818.2	100.0	100.0	100.0
711050	53818.2	53818.2	53818.2	100.0	100.0	100.0
711060	53818.2	53818.2	53818.2	100.0	100.0	100.0
711070	53818.2	53818.2	53818.2	100.0	100.0	100.0
711080	53818.2	53818.2	53818.2	100.0	100.0	100.0
711090	53818.2	53818.2	53818.2	100.0	100.0	100.0
711100	53818.2	53818.2	53818.2	100.0	100.0	100.0
711110	53818.2	53818.2	53818.2	100.0	100.0	100.0
712010	53818.2	53818.2	53818.2	100.0	100.0	100.0
712020	53818.2	53818.2	53818.2	100.0	100.0	100.0
712030	53818.2	53818.2	53818.2	100.0	100.0	100.0
712040	53818.2	53818.2	53818.2	100.0	100.0	100.0
712050	53818.2	53818.2	53818.2	100.0	100.0	100.0
712060	53818.2	53818.2	53818.2	100.0	100.0	100.0
712070	53818.2	53818.2	53818.2	100.0	100.0	100.0
712080	53818.2	53818.2	53818.2	100.0	100.0	100.0
712090	53818.2	53818.2	53818.2	100.0	100.0	100.0

Table I-2 (continued)

Node	Mass in direction (kg)			Mass moment of inertia about axis (kg-m^2)		
	X	Y	Z	X	Y	Z
712100	53818.2	53818.2	53818.2	100.0	100.0	100.0
712110	53818.2	53818.2	53818.2	100.0	100.0	100.0
713010	53818.2	53818.2	53818.2	100.0	100.0	100.0
713020	53818.2	53818.2	53818.2	100.0	100.0	100.0
713030	53818.2	53818.2	53818.2	100.0	100.0	100.0
713040	53818.2	53818.2	53818.2	100.0	100.0	100.0
713050	53818.2	53818.2	53818.2	100.0	100.0	100.0
713060	53818.2	53818.2	53818.2	100.0	100.0	100.0
713070	53818.2	53818.2	53818.2	100.0	100.0	100.0
713080	53818.2	53818.2	53818.2	100.0	100.0	100.0
713090	53818.2	53818.2	53818.2	100.0	100.0	100.0
713100	53818.2	53818.2	53818.2	100.0	100.0	100.0
713110	53818.2	53818.2	53818.2	100.0	100.0	100.0
805010	39030.3	39030.3	39030.3	100.0	100.0	100.0
805020	39030.3	39030.3	39030.3	100.0	100.0	100.0
805030	39030.3	39030.3	39030.3	100.0	100.0	100.0
805040	39030.3	39030.3	39030.3	100.0	100.0	100.0
805050	39030.3	39030.3	39030.3	100.0	100.0	100.0
805060	39030.3	39030.3	39030.3	100.0	100.0	100.0
805070	39030.3	39030.3	39030.3	100.0	100.0	100.0
805080	39030.3	39030.3	39030.3	100.0	100.0	100.0
805090	39030.3	39030.3	39030.3	100.0	100.0	100.0
805100	39030.3	39030.3	39030.3	100.0	100.0	100.0
805110	39030.3	39030.3	39030.3	100.0	100.0	100.0
806010	39030.3	39030.3	39030.3	100.0	100.0	100.0
806020	39030.3	39030.3	39030.3	100.0	100.0	100.0
806030	39030.3	39030.3	39030.3	100.0	100.0	100.0
806040	39030.3	39030.3	39030.3	100.0	100.0	100.0
806050	39030.3	39030.3	39030.3	100.0	100.0	100.0
806060	39030.3	39030.3	39030.3	100.0	100.0	100.0
806070	39030.3	39030.3	39030.3	100.0	100.0	100.0
806080	39030.3	39030.3	39030.3	100.0	100.0	100.0
806090	39030.3	39030.3	39030.3	100.0	100.0	100.0
806100	39030.3	39030.3	39030.3	100.0	100.0	100.0
806110	39030.3	39030.3	39030.3	100.0	100.0	100.0
807010	39030.3	39030.3	39030.3	100.0	100.0	100.0
807020	39030.3	39030.3	39030.3	100.0	100.0	100.0
807030	39030.3	39030.3	39030.3	100.0	100.0	100.0
807040	39030.3	39030.3	39030.3	100.0	100.0	100.0
807050	39030.3	39030.3	39030.3	100.0	100.0	100.0
807060	39030.3	39030.3	39030.3	100.0	100.0	100.0
807070	39030.3	39030.3	39030.3	100.0	100.0	100.0
807080	39030.3	39030.3	39030.3	100.0	100.0	100.0
807090	39030.3	39030.3	39030.3	100.0	100.0	100.0
807100	39030.3	39030.3	39030.3	100.0	100.0	100.0

Table I-2 (continued)

Node	Mass in direction (kg)			Mass moment of inertia about axis (kg-m^2)		
	X	Y	Z	X	Y	Z
807110	39030.3	39030.3	39030.3	100.0	100.0	100.0
808010	39030.3	39030.3	39030.3	100.0	100.0	100.0
808020	39030.3	39030.3	39030.3	100.0	100.0	100.0
808030	39030.3	39030.3	39030.3	100.0	100.0	100.0
808040	39030.3	39030.3	39030.3	100.0	100.0	100.0
808050	39030.3	39030.3	39030.3	100.0	100.0	100.0
808060	39030.3	39030.3	39030.3	100.0	100.0	100.0
808070	39030.3	39030.3	39030.3	100.0	100.0	100.0
808080	39030.3	39030.3	39030.3	100.0	100.0	100.0
808090	39030.3	39030.3	39030.3	100.0	100.0	100.0
808100	39030.3	39030.3	39030.3	100.0	100.0	100.0
808110	39030.3	39030.3	39030.3	100.0	100.0	100.0
809010	39030.3	39030.3	39030.3	100.0	100.0	100.0
809020	39030.3	39030.3	39030.3	100.0	100.0	100.0
809030	39030.3	39030.3	39030.3	100.0	100.0	100.0
809040	39030.3	39030.3	39030.3	100.0	100.0	100.0
809050	39030.3	39030.3	39030.3	100.0	100.0	100.0
809060	39030.3	39030.3	39030.3	100.0	100.0	100.0
809070	39030.3	39030.3	39030.3	100.0	100.0	100.0
809080	39030.3	39030.3	39030.3	100.0	100.0	100.0
809090	39030.3	39030.3	39030.3	100.0	100.0	100.0
809100	39030.3	39030.3	39030.3	100.0	100.0	100.0
809110	39030.3	39030.3	39030.3	100.0	100.0	100.0
810010	39030.3	39030.3	39030.3	100.0	100.0	100.0
810020	39030.3	39030.3	39030.3	100.0	100.0	100.0
810030	39030.3	39030.3	39030.3	100.0	100.0	100.0
810040	39030.3	39030.3	39030.3	100.0	100.0	100.0
810050	39030.3	39030.3	39030.3	100.0	100.0	100.0
810060	39030.3	39030.3	39030.3	100.0	100.0	100.0
810070	39030.3	39030.3	39030.3	100.0	100.0	100.0
810080	39030.3	39030.3	39030.3	100.0	100.0	100.0
810090	39030.3	39030.3	39030.3	100.0	100.0	100.0
810100	39030.3	39030.3	39030.3	100.0	100.0	100.0
810110	39030.3	39030.3	39030.3	100.0	100.0	100.0
811010	39030.3	39030.3	39030.3	100.0	100.0	100.0
811020	39030.3	39030.3	39030.3	100.0	100.0	100.0
811030	39030.3	39030.3	39030.3	100.0	100.0	100.0
811040	39030.3	39030.3	39030.3	100.0	100.0	100.0
811050	39030.3	39030.3	39030.3	100.0	100.0	100.0
811060	39030.3	39030.3	39030.3	100.0	100.0	100.0
811070	39030.3	39030.3	39030.3	100.0	100.0	100.0
811080	39030.3	39030.3	39030.3	100.0	100.0	100.0
811090	39030.3	39030.3	39030.3	100.0	100.0	100.0
811100	39030.3	39030.3	39030.3	100.0	100.0	100.0
811110	39030.3	39030.3	39030.3	100.0	100.0	100.0

Table I-2 (continued)

Node	Mass in direction (kg)			Mass moment of inertia about axis (kg-m^2)		
	X	Y	Z	X	Y	Z
812010	39030.3	39030.3	39030.3	100.0	100.0	100.0
812020	39030.3	39030.3	39030.3	100.0	100.0	100.0
812030	39030.3	39030.3	39030.3	100.0	100.0	100.0
812040	39030.3	39030.3	39030.3	100.0	100.0	100.0
812050	39030.3	39030.3	39030.3	100.0	100.0	100.0
812060	39030.3	39030.3	39030.3	100.0	100.0	100.0
812070	39030.3	39030.3	39030.3	100.0	100.0	100.0
812080	39030.3	39030.3	39030.3	100.0	100.0	100.0
812090	39030.3	39030.3	39030.3	100.0	100.0	100.0
812100	39030.3	39030.3	39030.3	100.0	100.0	100.0
812110	39030.3	39030.3	39030.3	100.0	100.0	100.0
813010	39030.3	39030.3	39030.3	100.0	100.0	100.0
813020	39030.3	39030.3	39030.3	100.0	100.0	100.0
813030	39030.3	39030.3	39030.3	100.0	100.0	100.0
813040	39030.3	39030.3	39030.3	100.0	100.0	100.0
813050	39030.3	39030.3	39030.3	100.0	100.0	100.0
813060	39030.3	39030.3	39030.3	100.0	100.0	100.0
813070	39030.3	39030.3	39030.3	100.0	100.0	100.0
813080	39030.3	39030.3	39030.3	100.0	100.0	100.0
813090	39030.3	39030.3	39030.3	100.0	100.0	100.0
813100	39030.3	39030.3	39030.3	100.0	100.0	100.0
813110	39030.3	39030.3	39030.3	100.0	100.0	100.0
905010	67321.2	67321.2	67321.2	100.0	100.0	100.0
905020	67321.2	67321.2	67321.2	100.0	100.0	100.0
905030	67321.2	67321.2	67321.2	100.0	100.0	100.0
905040	67321.2	67321.2	67321.2	100.0	100.0	100.0
905050	67321.2	67321.2	67321.2	100.0	100.0	100.0
905060	67321.2	67321.2	67321.2	100.0	100.0	100.0
905070	67321.2	67321.2	67321.2	100.0	100.0	100.0
905080	67321.2	67321.2	67321.2	100.0	100.0	100.0
905090	67321.2	67321.2	67321.2	100.0	100.0	100.0
905100	67321.2	67321.2	67321.2	100.0	100.0	100.0
905110	67321.2	67321.2	67321.2	100.0	100.0	100.0
906010	67321.2	67321.2	67321.2	100.0	100.0	100.0
906020	67321.2	67321.2	67321.2	100.0	100.0	100.0
906030	67321.2	67321.2	67321.2	100.0	100.0	100.0
906040	67321.2	67321.2	67321.2	100.0	100.0	100.0
906050	67321.2	67321.2	67321.2	100.0	100.0	100.0
906060	67321.2	67321.2	67321.2	100.0	100.0	100.0
906070	67321.2	67321.2	67321.2	100.0	100.0	100.0
906080	67321.2	67321.2	67321.2	100.0	100.0	100.0
906090	67321.2	67321.2	67321.2	100.0	100.0	100.0
906100	67321.2	67321.2	67321.2	100.0	100.0	100.0
906110	67321.2	67321.2	67321.2	100.0	100.0	100.0
907010	67321.2	67321.2	67321.2	100.0	100.0	100.0

Table I-2 (continued)

Node	Mass in direction (kg)			Mass moment of inertia about axis (kg-m^2)		
	X	Y	Z	X	Y	Z
907020	67321.2	67321.2	67321.2	100.0	100.0	100.0
907030	67321.2	67321.2	67321.2	100.0	100.0	100.0
907040	67321.2	67321.2	67321.2	100.0	100.0	100.0
907050	67321.2	67321.2	67321.2	100.0	100.0	100.0
907060	67321.2	67321.2	67321.2	100.0	100.0	100.0
907070	67321.2	67321.2	67321.2	100.0	100.0	100.0
907080	67321.2	67321.2	67321.2	100.0	100.0	100.0
907090	67321.2	67321.2	67321.2	100.0	100.0	100.0
907100	67321.2	67321.2	67321.2	100.0	100.0	100.0
907110	67321.2	67321.2	67321.2	100.0	100.0	100.0
908010	67321.2	67321.2	67321.2	100.0	100.0	100.0
908020	67321.2	67321.2	67321.2	100.0	100.0	100.0
908030	67321.2	67321.2	67321.2	100.0	100.0	100.0
908040	67321.2	67321.2	67321.2	100.0	100.0	100.0
908050	67321.2	67321.2	67321.2	100.0	100.0	100.0
908060	67321.2	67321.2	67321.2	100.0	100.0	100.0
908070	67321.2	67321.2	67321.2	100.0	100.0	100.0
908080	67321.2	67321.2	67321.2	100.0	100.0	100.0
908090	67321.2	67321.2	67321.2	100.0	100.0	100.0
908100	67321.2	67321.2	67321.2	100.0	100.0	100.0
908110	67321.2	67321.2	67321.2	100.0	100.0	100.0
909010	67321.2	67321.2	67321.2	100.0	100.0	100.0
909020	67321.2	67321.2	67321.2	100.0	100.0	100.0
909030	67321.2	67321.2	67321.2	100.0	100.0	100.0
909040	67321.2	67321.2	67321.2	100.0	100.0	100.0
909050	67321.2	67321.2	67321.2	100.0	100.0	100.0
909060	67321.2	67321.2	67321.2	100.0	100.0	100.0
909070	67321.2	67321.2	67321.2	100.0	100.0	100.0
909080	67321.2	67321.2	67321.2	100.0	100.0	100.0
909090	67321.2	67321.2	67321.2	100.0	100.0	100.0
909100	67321.2	67321.2	67321.2	100.0	100.0	100.0
909110	67321.2	67321.2	67321.2	100.0	100.0	100.0
910010	67321.2	67321.2	67321.2	100.0	100.0	100.0
910020	67321.2	67321.2	67321.2	100.0	100.0	100.0
910030	67321.2	67321.2	67321.2	100.0	100.0	100.0
910040	67321.2	67321.2	67321.2	100.0	100.0	100.0
910050	67321.2	67321.2	67321.2	100.0	100.0	100.0
910060	67321.2	67321.2	67321.2	100.0	100.0	100.0
910070	67321.2	67321.2	67321.2	100.0	100.0	100.0
910080	67321.2	67321.2	67321.2	100.0	100.0	100.0
910090	67321.2	67321.2	67321.2	100.0	100.0	100.0
910100	67321.2	67321.2	67321.2	100.0	100.0	100.0
910110	67321.2	67321.2	67321.2	100.0	100.0	100.0
911010	67321.2	67321.2	67321.2	100.0	100.0	100.0
911020	67321.2	67321.2	67321.2	100.0	100.0	100.0

Table I-2 (continued)

Node	Mass in direction (kg)			Mass moment of inertia about axis (kg-m^2)		
	X	Y	Z	X	Y	Z
911030	67321.2	67321.2	67321.2	100.0	100.0	100.0
911040	67321.2	67321.2	67321.2	100.0	100.0	100.0
911050	67321.2	67321.2	67321.2	100.0	100.0	100.0
911060	67321.2	67321.2	67321.2	100.0	100.0	100.0
911070	67321.2	67321.2	67321.2	100.0	100.0	100.0
911080	67321.2	67321.2	67321.2	100.0	100.0	100.0
911090	67321.2	67321.2	67321.2	100.0	100.0	100.0
911100	67321.2	67321.2	67321.2	100.0	100.0	100.0
911110	67321.2	67321.2	67321.2	100.0	100.0	100.0
912010	67321.2	67321.2	67321.2	100.0	100.0	100.0
912020	67321.2	67321.2	67321.2	100.0	100.0	100.0
912030	67321.2	67321.2	67321.2	100.0	100.0	100.0
912040	67321.2	67321.2	67321.2	100.0	100.0	100.0
912050	67321.2	67321.2	67321.2	100.0	100.0	100.0
912060	67321.2	67321.2	67321.2	100.0	100.0	100.0
912070	67321.2	67321.2	67321.2	100.0	100.0	100.0
912080	67321.2	67321.2	67321.2	100.0	100.0	100.0
912090	67321.2	67321.2	67321.2	100.0	100.0	100.0
912100	67321.2	67321.2	67321.2	100.0	100.0	100.0
912110	67321.2	67321.2	67321.2	100.0	100.0	100.0
913010	67321.2	67321.2	67321.2	100.0	100.0	100.0
913020	67321.2	67321.2	67321.2	100.0	100.0	100.0
913030	67321.2	67321.2	67321.2	100.0	100.0	100.0
913040	67321.2	67321.2	67321.2	100.0	100.0	100.0
913050	67321.2	67321.2	67321.2	100.0	100.0	100.0
913060	67321.2	67321.2	67321.2	100.0	100.0	100.0
913070	67321.2	67321.2	67321.2	100.0	100.0	100.0
913080	67321.2	67321.2	67321.2	100.0	100.0	100.0
913090	67321.2	67321.2	67321.2	100.0	100.0	100.0
913100	67321.2	67321.2	67321.2	100.0	100.0	100.0
913110	67321.2	67321.2	67321.2	100.0	100.0	100.0

Table I-3: Connectivity of the horizontal elements of the ASB

Element No	Connecting Nodes		Element No	Connecting Nodes	
	Node 1	Node 2		Node 1	Node 2
101010	101010	101020	105060	105060	105070
101020	101020	101030	105070	105070	105080
101030	101030	101040	105080	105080	105090
101040	101040	101050	105090	105090	105100
101050	101050	101060	105100	105100	105110
101060	101060	101070	106010	106010	106020
101070	101070	101080	106020	106020	106030
101080	101080	101090	106030	106030	106040
101090	101090	101100	106040	106040	106050
101100	101100	101110	106050	106050	106060
102010	102010	102020	106060	106060	106070
102020	102020	102030	106070	106070	106080
102030	102030	102040	106080	106080	106090
102040	102040	102050	106090	106090	106100
102050	102050	102060	106100	106100	106110
102060	102060	102070	107010	107010	107020
102070	102070	102080	107020	107020	107030
102080	102080	102090	107030	107030	107040
102090	102090	102100	107040	107040	107050
102100	102100	102110	107050	107050	107060
103010	103010	103020	107060	107060	107070
103020	103020	103030	107070	107070	107080
103030	103030	103040	107080	107080	107090
103040	103040	103050	107090	107090	107100
103050	103050	103060	107100	107100	107110
103060	103060	103070	108010	108010	108020
103070	103070	103080	108020	108020	108030
103080	103080	103090	108030	108030	108040
103090	103090	103100	108040	108040	108050
103100	103100	103110	108050	108050	108060
104010	104010	104020	108060	108060	108070
104020	104020	104030	108070	108070	108080
104030	104030	104040	108080	108080	108090
104040	104040	104050	108090	108090	108100
104050	104050	104060	108100	108100	108110
104060	104060	104070	109010	109010	109020
104070	104070	104080	109020	109020	109030
104080	104080	104090	109030	109030	109040
104090	104090	104100	109040	109040	109050
104100	104100	104110	109050	109050	109060
105010	105010	105020	109060	109060	109070
105020	105020	105030	109070	109070	109080
105030	105030	105040	109080	109080	109090
105040	105040	105050	109090	109090	109100
105050	105050	105060	109100	109100	109110

Table I-3 (continued)

Element No	Connecting Nodes		Element No	Connecting Nodes	
	Node 1	Node 2		Node 1	Node 2
110010	110010	110020	114060	114060	114070
110020	110020	110030	114070	114070	114080
110030	110030	110040	114080	114080	114090
110040	110040	110050	114090	114090	114100
110050	110050	110060	114100	114100	114110
110060	110060	110070	115010	115010	115020
110070	110070	110080	115020	115020	115030
110080	110080	110090	115030	115030	115040
110090	110090	110100	115040	115040	115050
110100	110100	110110	115050	115050	115060
111010	111010	111020	115060	115060	115070
111020	111020	111030	115070	115070	115080
111030	111030	111040	115080	115080	115090
111040	111040	111050	115090	115090	115100
111050	111050	111060	115100	115100	115110
111060	111060	111070	116010	116010	116020
111070	111070	111080	116020	116020	116030
111080	111080	111090	116030	116030	116040
111090	111090	111100	116040	116040	116050
111100	111100	111110	116050	116050	116060
112010	112010	112020	116060	116060	116070
112020	112020	112030	116070	116070	116080
112030	112030	112040	116080	116080	116090
112040	112040	112050	116090	116090	116100
112050	112050	112060	116100	116100	116110
112060	112060	112070	117010	117010	117020
112070	112070	112080	117020	117020	117030
112080	112080	112090	117030	117030	117040
112090	112090	112100	117040	117040	117050
112100	112100	112110	117050	117050	117060
113010	113010	113020	117060	117060	117070
113020	113020	113030	117070	117070	117080
113030	113030	113040	117080	117080	117090
113040	113040	113050	117090	117090	117100
113050	113050	113060	117100	117100	117110
113060	113060	113070	201010	201010	201020
113070	113070	113080	201020	201020	201030
113080	113080	113090	201030	201030	201040
113090	113090	113100	201040	201040	201050
113100	113100	113110	201050	201050	201060
114010	114010	114020	201060	201060	201070
114020	114020	114030	201070	201070	201080
114030	114030	114040	201080	201080	201090
114040	114040	114050	201090	201090	201100
114050	114050	114060	201100	201100	201110

Table I-3 (continued)

Element No	Connecting Nodes		Element No	Connecting Nodes	
	Node 1	Node 2		Node 1	Node 2
202010	202010	202020	206060	206060	206070
202020	202020	202030	206070	206070	206080
202030	202030	202040	206080	206080	206090
202040	202040	202050	206090	206090	206100
202050	202050	202060	206100	206100	206110
202060	202060	202070	207010	207010	207020
202070	202070	202080	207020	207020	207030
202080	202080	202090	207030	207030	207040
202090	202090	202100	207040	207040	207050
202100	202100	202110	207050	207050	207060
203010	203010	203020	207060	207060	207070
203020	203020	203030	207070	207070	207080
203030	203030	203040	207080	207080	207090
203040	203040	203050	207090	207090	207100
203050	203050	203060	207100	207100	207110
203060	203060	203070	208010	208010	208020
203070	203070	203080	208020	208020	208030
203080	203080	203090	208030	208030	208040
203090	203090	203100	208040	208040	208050
203100	203100	203110	208050	208050	208060
204010	204010	204020	208060	208060	208070
204020	204020	204030	208070	208070	208080
204030	204030	204040	208080	208080	208090
204040	204040	204050	208090	208090	208100
204050	204050	204060	208100	208100	208110
204060	204060	204070	209010	209010	209020
204070	204070	204080	209020	209020	209030
204080	204080	204090	209030	209030	209040
204090	204090	204100	209040	209040	209050
204100	204100	204110	209050	209050	209060
205010	205010	205020	209060	209060	209070
205020	205020	205030	209070	209070	209080
205030	205030	205040	209080	209080	209090
205040	205040	205050	209090	209090	209100
205050	205050	205060	209100	209100	209110
205060	205060	205070	210010	210010	210020
205070	205070	205080	210020	210020	210030
205080	205080	205090	210030	210030	210040
205090	205090	205100	210040	210040	210050
205100	205100	205110	210050	210050	210060
206010	206010	206020	210060	210060	210070
206020	206020	206030	210070	210070	210080
206030	206030	206040	210080	210080	210090
206040	206040	206050	210090	210090	210100
206050	206050	206060	210100	210100	210110

Table I-3 (continued)

Element No	Connecting Nodes		Element No	Connecting Nodes	
	Node 1	Node 2		Node 1	Node 2
211010	211010	211020	215060	215060	215070
211020	211020	211030	215070	215070	215080
211030	211030	211040	215080	215080	215090
211040	211040	211050	215090	215090	215100
211050	211050	211060	215100	215100	215110
211060	211060	211070	216010	216010	216020
211070	211070	211080	216020	216020	216030
211080	211080	211090	216030	216030	216040
211090	211090	211100	216040	216040	216050
211100	211100	211110	216050	216050	216060
212010	212010	212020	216060	216060	216070
212020	212020	212030	216070	216070	216080
212030	212030	212040	216080	216080	216090
212040	212040	212050	216090	216090	216100
212050	212050	212060	216100	216100	216110
212060	212060	212070	217010	217010	217020
212070	212070	212080	217020	217020	217030
212080	212080	212090	217030	217030	217040
212090	212090	212100	217040	217040	217050
212100	212100	212110	217050	217050	217060
213010	213010	213020	217060	217060	217070
213020	213020	213030	217070	217070	217080
213030	213030	213040	217080	217080	217090
213040	213040	213050	217090	217090	217100
213050	213050	213060	217100	217100	217110
213060	213060	213070	301010	301010	301020
213070	213070	213080	301020	301020	301030
213080	213080	213090	301030	301030	301040
213090	213090	213100	301040	301040	301050
213100	213100	213110	301050	301050	301060
214010	214010	214020	301060	301060	301070
214020	214020	214030	301070	301070	301080
214030	214030	214040	301080	301080	301090
214040	214040	214050	301090	301090	301100
214050	214050	214060	301100	301100	301110
214060	214060	214070	302010	302010	302020
214070	214070	214080	302020	302020	302030
214080	214080	214090	302030	302030	302040
214090	214090	214100	302040	302040	302050
214100	214100	214110	302050	302050	302060
215010	215010	215020	302060	302060	302070
215020	215020	215030	302070	302070	302080
215030	215030	215040	302080	302080	302090
215040	215040	215050	302090	302090	302100
215050	215050	215060	302100	302100	302110

Table I-3 (continued)

Element No	Connecting Nodes		Element No	Connecting Nodes	
	Node 1	Node 2		Node 1	Node 2
303010	303010	303020	307060	307060	307070
303020	303020	303030	307070	307070	307080
303030	303030	303040	307080	307080	307090
303040	303040	303050	307090	307090	307100
303050	303050	303060	307100	307100	307110
303060	303060	303070	308010	308010	308020
303070	303070	303080	308020	308020	308030
303080	303080	303090	308030	308030	308040
303090	303090	303100	308040	308040	308050
303100	303100	303110	308050	308050	308060
304010	304010	304020	308060	308060	308070
304020	304020	304030	308070	308070	308080
304030	304030	304040	308080	308080	308090
304040	304040	304050	308090	308090	308100
304050	304050	304060	308100	308100	308110
304060	304060	304070	309010	309010	309020
304070	304070	304080	309020	309020	309030
304080	304080	304090	309030	309030	309040
304090	304090	304100	309040	309040	309050
304100	304100	304110	309050	309050	309060
305010	305010	305020	309060	309060	309070
305020	305020	305030	309070	309070	309080
305030	305030	305040	309080	309080	309090
305040	305040	305050	309090	309090	309100
305050	305050	305060	309100	309100	309110
305060	305060	305070	310010	310010	310020
305070	305070	305080	310020	310020	310030
305080	305080	305090	310030	310030	310040
305090	305090	305100	310040	310040	310050
305100	305100	305110	310050	310050	310060
306010	306010	306020	310060	310060	310070
306020	306020	306030	310070	310070	310080
306030	306030	306040	310080	310080	310090
306040	306040	306050	310090	310090	310100
306050	306050	306060	310100	310100	310110
306060	306060	306070	311010	311010	311020
306070	306070	306080	311020	311020	311030
306080	306080	306090	311030	311030	311040
306090	306090	306100	311040	311040	311050
306100	306100	306110	311050	311050	311060
307010	307010	307020	311060	311060	311070
307020	307020	307030	311070	311070	311080
307030	307030	307040	311080	311080	311090
307040	307040	307050	311090	311090	311100
307050	307050	307060	311100	311100	311110

Table I-3 (continued)

Element No	Connecting Nodes		Element No	Connecting Nodes	
	Node 1	Node 2		Node 1	Node 2
312010	312010	312020	316060	316060	316070
312020	312020	312030	316070	316070	316080
312030	312030	312040	316080	316080	316090
312040	312040	312050	316090	316090	316100
312050	312050	312060	316100	316100	316110
312060	312060	312070	317010	317010	317020
312070	312070	312080	317020	317020	317030
312080	312080	312090	317030	317030	317040
312090	312090	312100	317040	317040	317050
312100	312100	312110	317050	317050	317060
313010	313010	313020	317060	317060	317070
313020	313020	313030	317070	317070	317080
313030	313030	313040	317080	317080	317090
313040	313040	313050	317090	317090	317100
313050	313050	313060	317100	317100	317110
313060	313060	313070	401010	401010	401020
313070	313070	313080	401020	401020	401030
313080	313080	313090	401030	401030	401040
313090	313090	313100	401040	401040	401050
313100	313100	313110	401050	401050	401060
314010	314010	314020	401060	401060	401070
314020	314020	314030	401070	401070	401080
314030	314030	314040	401080	401080	401090
314040	314040	314050	401090	401090	401100
314050	314050	314060	401100	401100	401110
314060	314060	314070	402010	402010	402020
314070	314070	314080	402020	402020	402030
314080	314080	314090	402030	402030	402040
314090	314090	314100	402040	402040	402050
314100	314100	314110	402050	402050	402060
315010	315010	315020	402060	402060	402070
315020	315020	315030	402070	402070	402080
315030	315030	315040	402080	402080	402090
315040	315040	315050	402090	402090	402100
315050	315050	315060	402100	402100	402110
315060	315060	315070	403010	403010	403020
315070	315070	315080	403020	403020	403030
315080	315080	315090	403030	403030	403040
315090	315090	315100	403040	403040	403050
315100	315100	315110	403050	403050	403060
316010	316010	316020	403060	403060	403070
316020	316020	316030	403070	403070	403080
316030	316030	316040	403080	403080	403090
316040	316040	316050	403090	403090	403100
316050	316050	316060	403100	403100	403110

Table I-3 (continued)

Element No	Connecting Nodes		Element No	Connecting Nodes	
	Node 1	Node 2		Node 1	Node 2
404010	404010	404020	408060	408060	408070
404020	404020	404030	408070	408070	408080
404030	404030	404040	408080	408080	408090
404040	404040	404050	408090	408090	408100
404050	404050	404060	408100	408100	408110
404060	404060	404070	409010	409010	409020
404070	404070	404080	409020	409020	409030
404080	404080	404090	409030	409030	409040
404090	404090	404100	409040	409040	409050
404100	404100	404110	409050	409050	409060
405010	405010	405020	409060	409060	409070
405020	405020	405030	409070	409070	409080
405030	405030	405040	409080	409080	409090
405040	405040	405050	409090	409090	409100
405050	405050	405060	409100	409100	409110
405060	405060	405070	410010	410010	410020
405070	405070	405080	410020	410020	410030
405080	405080	405090	410030	410030	410040
405090	405090	405100	410040	410040	410050
405100	405100	405110	410050	410050	410060
406010	406010	406020	410060	410060	410070
406020	406020	406030	410070	410070	410080
406030	406030	406040	410080	410080	410090
406040	406040	406050	410090	410090	410100
406050	406050	406060	410100	410100	410110
406060	406060	406070	411010	411010	411020
406070	406070	406080	411020	411020	411030
406080	406080	406090	411030	411030	411040
406090	406090	406100	411040	411040	411050
406100	406100	406110	411050	411050	411060
407010	407010	407020	411060	411060	411070
407020	407020	407030	411070	411070	411080
407030	407030	407040	411080	411080	411090
407040	407040	407050	411090	411090	411100
407050	407050	407060	411100	411100	411110
407060	407060	407070	412010	412010	412020
407070	407070	407080	412020	412020	412030
407080	407080	407090	412030	412030	412040
407090	407090	407100	412040	412040	412050
407100	407100	407110	412050	412050	412060
408010	408010	408020	412060	412060	412070
408020	408020	408030	412070	412070	412080
408030	408030	408040	412080	412080	412090
408040	408040	408050	412090	412090	412100
408050	408050	408060	412100	412100	412110

Table I-3 (continued)

Element No	Connecting Nodes		Element No	Connecting Nodes	
	Node 1	Node 2		Node 1	Node 2
413010	413010	413020	417060	417060	417070
413020	413020	413030	417070	417070	417080
413030	413030	413040	417080	417080	417090
413040	413040	413050	417090	417090	417100
413050	413050	413060	417100	417100	417110
413060	413060	413070	501010	501010	501020
413070	413070	413080	501020	501020	501030
413080	413080	413090	501030	501030	501040
413090	413090	413100	501040	501040	501050
413100	413100	413110	501050	501050	501060
414010	414010	414020	501060	501060	501070
414020	414020	414030	501070	501070	501080
414030	414030	414040	501080	501080	501090
414040	414040	414050	501090	501090	501100
414050	414050	414060	501100	501100	501110
414060	414060	414070	502010	502010	502020
414070	414070	414080	502020	502020	502030
414080	414080	414090	502030	502030	502040
414090	414090	414100	502040	502040	502050
414100	414100	414110	502050	502050	502060
415010	415010	415020	502060	502060	502070
415020	415020	415030	502070	502070	502080
415030	415030	415040	502080	502080	502090
415040	415040	415050	502090	502090	502100
415050	415050	415060	502100	502100	502110
415060	415060	415070	503010	503010	503020
415070	415070	415080	503020	503020	503030
415080	415080	415090	503030	503030	503040
415090	415090	415100	503040	503040	503050
415100	415100	415110	503050	503050	503060
416010	416010	416020	503060	503060	503070
416020	416020	416030	503070	503070	503080
416030	416030	416040	503080	503080	503090
416040	416040	416050	503090	503090	503100
416050	416050	416060	503100	503100	503110
416060	416060	416070	504010	504010	504020
416070	416070	416080	504020	504020	504030
416080	416080	416090	504030	504030	504040
416090	416090	416100	504040	504040	504050
416100	416100	416110	504050	504050	504060
417010	417010	417020	504060	504060	504070
417020	417020	417030	504070	504070	504080
417030	417030	417040	504080	504080	504090
417040	417040	417050	504090	504090	504100
417050	417050	417060	504100	504100	504110

Table I-3 (continued)

Element No	Connecting Nodes		Element No	Connecting Nodes	
	Node 1	Node 2		Node 1	Node 2
505010	505010	505020	509060	509060	509070
505020	505020	505030	509070	509070	509080
505030	505030	505040	509080	509080	509090
505040	505040	505050	509090	509090	509100
505050	505050	505060	509100	509100	509110
505060	505060	505070	510010	510010	510020
505070	505070	505080	510020	510020	510030
505080	505080	505090	510030	510030	510040
505090	505090	505100	510040	510040	510050
505100	505100	505110	510050	510050	510060
506010	506010	506020	510060	510060	510070
506020	506020	506030	510070	510070	510080
506030	506030	506040	510080	510080	510090
506040	506040	506050	510090	510090	510100
506050	506050	506060	510100	510100	510110
506060	506060	506070	511010	511010	511020
506070	506070	506080	511020	511020	511030
506080	506080	506090	511030	511030	511040
506090	506090	506100	511040	511040	511050
506100	506100	506110	511050	511050	511060
507010	507010	507020	511060	511060	511070
507020	507020	507030	511070	511070	511080
507030	507030	507040	511080	511080	511090
507040	507040	507050	511090	511090	511100
507050	507050	507060	511100	511100	511110
507060	507060	507070	512010	512010	512020
507070	507070	507080	512020	512020	512030
507080	507080	507090	512030	512030	512040
507090	507090	507100	512040	512040	512050
507100	507100	507110	512050	512050	512060
508010	508010	508020	512060	512060	512070
508020	508020	508030	512070	512070	512080
508030	508030	508040	512080	512080	512090
508040	508040	508050	512090	512090	512100
508050	508050	508060	512100	512100	512110
508060	508060	508070	513010	513010	513020
508070	508070	508080	513020	513020	513030
508080	508080	508090	513030	513030	513040
508090	508090	508100	513040	513040	513050
508100	508100	508110	513050	513050	513060
509010	509010	509020	513060	513060	513070
509020	509020	509030	513070	513070	513080
509030	509030	509040	513080	513080	513090
509040	509040	509050	513090	513090	513100
509050	509050	509060	513100	513100	513110

Table I-3 (continued)

Element No	Connecting Nodes		Element No	Connecting Nodes	
	Node 1	Node 2		Node 1	Node 2
514010	514010	514020	605060	605060	605070
514020	514020	514030	605070	605070	605080
514030	514030	514040	605080	605080	605090
514040	514040	514050	605090	605090	605100
514050	514050	514060	605100	605100	605110
514060	514060	514070	606010	606010	606020
514070	514070	514080	606020	606020	606030
514080	514080	514090	606030	606030	606040
514090	514090	514100	606040	606040	606050
514100	514100	514110	606050	606050	606060
515010	515010	515020	606060	606060	606070
515020	515020	515030	606070	606070	606080
515030	515030	515040	606080	606080	606090
515040	515040	515050	606090	606090	606100
515050	515050	515060	606100	606100	606110
515060	515060	515070	607010	607010	607020
515070	515070	515080	607020	607020	607030
515080	515080	515090	607030	607030	607040
515090	515090	515100	607040	607040	607050
515100	515100	515110	607050	607050	607060
516010	516010	516020	607060	607060	607070
516020	516020	516030	607070	607070	607080
516030	516030	516040	607080	607080	607090
516040	516040	516050	607090	607090	607100
516050	516050	516060	607100	607100	607110
516060	516060	516070	608010	608010	608020
516070	516070	516080	608020	608020	608030
516080	516080	516090	608030	608030	608040
516090	516090	516100	608040	608040	608050
516100	516100	516110	608050	608050	608060
517010	517010	517020	608060	608060	608070
517020	517020	517030	608070	608070	608080
517030	517030	517040	608080	608080	608090
517040	517040	517050	608090	608090	608100
517050	517050	517060	608100	608100	608110
517060	517060	517070	609010	609010	609020
517070	517070	517080	609020	609020	609030
517080	517080	517090	609030	609030	609040
517090	517090	517100	609040	609040	609050
517100	517100	517110	609050	609050	609060
605010	605010	605020	609060	609060	609070
605020	605020	605030	609070	609070	609080
605030	605030	605040	609080	609080	609090
605040	605040	605050	609090	609090	609100
605050	605050	605060	609100	609100	609110

Table I-3 (continued)

Element No	Connecting Nodes		Element No	Connecting Nodes	
	Node 1	Node 2		Node 1	Node 2
610010	610010	610020	705060	705060	705070
610020	610020	610030	705070	705070	705080
610030	610030	610040	705080	705080	705090
610040	610040	610050	705090	705090	705100
610050	610050	610060	705100	705100	705110
610060	610060	610070	706010	706010	706020
610070	610070	610080	706020	706020	706030
610080	610080	610090	706030	706030	706040
610090	610090	610100	706040	706040	706050
610100	610100	610110	706050	706050	706060
611010	611010	611020	706060	706060	706070
611020	611020	611030	706070	706070	706080
611030	611030	611040	706080	706080	706090
611040	611040	611050	706090	706090	706100
611050	611050	611060	706100	706100	706110
611060	611060	611070	707010	707010	707020
611070	611070	611080	707020	707020	707030
611080	611080	611090	707030	707030	707040
611090	611090	611100	707040	707040	707050
611100	611100	611110	707050	707050	707060
612010	612010	612020	707060	707060	707070
612020	612020	612030	707070	707070	707080
612030	612030	612040	707080	707080	707090
612040	612040	612050	707090	707090	707100
612050	612050	612060	707100	707100	707110
612060	612060	612070	708010	708010	708020
612070	612070	612080	708020	708020	708030
612080	612080	612090	708030	708030	708040
612090	612090	612100	708040	708040	708050
612100	612100	612110	708050	708050	708060
613010	613010	613020	708060	708060	708070
613020	613020	613030	708070	708070	708080
613030	613030	613040	708080	708080	708090
613040	613040	613050	708090	708090	708100
613050	613050	613060	708100	708100	708110
613060	613060	613070	709010	709010	709020
613070	613070	613080	709020	709020	709030
613080	613080	613090	709030	709030	709040
613090	613090	613100	709040	709040	709050
613100	613100	613110	709050	709050	709060
705010	705010	705020	709060	709060	709070
705020	705020	705030	709070	709070	709080
705030	705030	705040	709080	709080	709090
705040	705040	705050	709090	709090	709100
705050	705050	705060	709100	709100	709110

Table I-3 (continued)

Element No	Connecting Nodes		Element No	Connecting Nodes	
	Node 1	Node 2		Node 1	Node 2
710010	710010	710020	805060	805060	805070
710020	710020	710030	805070	805070	805080
710030	710030	710040	805080	805080	805090
710040	710040	710050	805090	805090	805100
710050	710050	710060	805100	805100	805110
710060	710060	710070	806010	806010	806020
710070	710070	710080	806020	806020	806030
710080	710080	710090	806030	806030	806040
710090	710090	710100	806040	806040	806050
710100	710100	710110	806050	806050	806060
711010	711010	711020	806060	806060	806070
711020	711020	711030	806070	806070	806080
711030	711030	711040	806080	806080	806090
711040	711040	711050	806090	806090	806100
711050	711050	711060	806100	806100	806110
711060	711060	711070	807010	807010	807020
711070	711070	711080	807020	807020	807030
711080	711080	711090	807030	807030	807040
711090	711090	711100	807040	807040	807050
711100	711100	711110	807050	807050	807060
712010	712010	712020	807060	807060	807070
712020	712020	712030	807070	807070	807080
712030	712030	712040	807080	807080	807090
712040	712040	712050	807090	807090	807100
712050	712050	712060	807100	807100	807110
712060	712060	712070	808010	808010	808020
712070	712070	712080	808020	808020	808030
712080	712080	712090	808030	808030	808040
712090	712090	712100	808040	808040	808050
712100	712100	712110	808050	808050	808060
713010	713010	713020	808060	808060	808070
713020	713020	713030	808070	808070	808080
713030	713030	713040	808080	808080	808090
713040	713040	713050	808090	808090	808100
713050	713050	713060	808100	808100	808110
713060	713060	713070	809010	809010	809020
713070	713070	713080	809020	809020	809030
713080	713080	713090	809030	809030	809040
713090	713090	713100	809040	809040	809050
713100	713100	713110	809050	809050	809060
805010	805010	805020	809060	809060	809070
805020	805020	805030	809070	809070	809080
805030	805030	805040	809080	809080	809090
805040	805040	805050	809090	809090	809100
805050	805050	805060	809100	809100	809110

Table I-3 (continued)

Element No	Connecting Nodes		Element No	Connecting Nodes	
	Node 1	Node 2		Node 1	Node 2
810010	810010	810020	905060	905060	905070
810020	810020	810030	905070	905070	905080
810030	810030	810040	905080	905080	905090
810040	810040	810050	905090	905090	905100
810050	810050	810060	905100	905100	905110
810060	810060	810070	906010	906010	906020
810070	810070	810080	906020	906020	906030
810080	810080	810090	906030	906030	906040
810090	810090	810100	906040	906040	906050
810100	810100	810110	906050	906050	906060
811010	811010	811020	906060	906060	906070
811020	811020	811030	906070	906070	906080
811030	811030	811040	906080	906080	906090
811040	811040	811050	906090	906090	906100
811050	811050	811060	906100	906100	906110
811060	811060	811070	907010	907010	907020
811070	811070	811080	907020	907020	907030
811080	811080	811090	907030	907030	907040
811090	811090	811100	907040	907040	907050
811100	811100	811110	907050	907050	907060
812010	812010	812020	907060	907060	907070
812020	812020	812030	907070	907070	907080
812030	812030	812040	907080	907080	907090
812040	812040	812050	907090	907090	907100
812050	812050	812060	907100	907100	907110
812060	812060	812070	908010	908010	908020
812070	812070	812080	908020	908020	908030
812080	812080	812090	908030	908030	908040
812090	812090	812100	908040	908040	908050
812100	812100	812110	908050	908050	908060
813010	813010	813020	908060	908060	908070
813020	813020	813030	908070	908070	908080
813030	813030	813040	908080	908080	908090
813040	813040	813050	908090	908090	908100
813050	813050	813060	908100	908100	908110
813060	813060	813070	909010	909010	909020
813070	813070	813080	909020	909020	909030
813080	813080	813090	909030	909030	909040
813090	813090	813100	909040	909040	909050
813100	813100	813110	909050	909050	909060
905010	905010	905020	909060	909060	909070
905020	905020	905030	909070	909070	909080
905030	905030	905040	909080	909080	909090
905040	905040	905050	909090	909090	909100
905050	905050	905060	909100	909100	909110

Table I-3 (continued)

Element No	Connecting Nodes		Element No	Connecting Nodes	
	Node 1	Node 2		Node 1	Node 2
910010	910010	910020	1006010	106010	107010
910020	910020	910030	1007010	107010	108010
910030	910030	910040	1008010	108010	109010
910040	910040	910050	1009010	109010	110010
910050	910050	910060	1010010	110010	111010
910060	910060	910070	1011010	111010	112010
910070	910070	910080	1012010	112010	113010
910080	910080	910090	1013010	113010	114010
910090	910090	910100	1014010	114010	115010
910100	910100	910110	1015010	115010	116010
911010	911010	911020	1016010	116010	117010
911020	911020	911030	1001020	101020	102020
911030	911030	911040	1002020	102020	103020
911040	911040	911050	1003020	103020	104020
911050	911050	911060	1004020	104020	105020
911060	911060	911070	1005020	105020	106020
911070	911070	911080	1006020	106020	107020
911080	911080	911090	1007020	107020	108020
911090	911090	911100	1008020	108020	109020
911100	911100	911110	1009020	109020	110020
912010	912010	912020	1010020	110020	111020
912020	912020	912030	1011020	111020	112020
912030	912030	912040	1012020	112020	113020
912040	912040	912050	1013020	113020	114020
912050	912050	912060	1014020	114020	115020
912060	912060	912070	1015020	115020	116020
912070	912070	912080	1016020	116020	117020
912080	912080	912090	1001030	101030	102030
912090	912090	912100	1002030	102030	103030
912100	912100	912110	1003030	103030	104030
913010	913010	913020	1004030	104030	105030
913020	913020	913030	1005030	105030	106030
913030	913030	913040	1006030	106030	107030
913040	913040	913050	1007030	107030	108030
913050	913050	913060	1008030	108030	109030
913060	913060	913070	1009030	109030	110030
913070	913070	913080	1010030	110030	111030
913080	913080	913090	1011030	111030	112030
913090	913090	913100	1012030	112030	113030
913100	913100	913110	1013030	113030	114030
1001010	101010	102010	1014030	114030	115030
1002010	102010	103010	1015030	115030	116030
1003010	103010	104010	1016030	116030	117030
1004010	104010	105010	1001040	101040	102040
1005010	105010	106010	1002040	102040	103040

Table I-3 (continued)

Element No	Connecting Nodes		Element No	Connecting Nodes	
	Node 1	Node 2		Node 1	Node 2
1003040	103040	104040	1016060	116060	117060
1004040	104040	105040	1001070	101070	102070
1005040	105040	106040	1002070	102070	103070
1006040	106040	107040	1003070	103070	104070
1007040	107040	108040	1004070	104070	105070
1008040	108040	109040	1005070	105070	106070
1009040	109040	110040	1006070	106070	107070
1010040	110040	111040	1007070	107070	108070
1011040	111040	112040	1008070	108070	109070
1012040	112040	113040	1009070	109070	110070
1013040	113040	114040	1010070	110070	111070
1014040	114040	115040	1011070	111070	112070
1015040	115040	116040	1012070	112070	113070
1016040	116040	117040	1013070	113070	114070
1001050	101050	102050	1014070	114070	115070
1002050	102050	103050	1015070	115070	116070
1003050	103050	104050	1016070	116070	117070
1004050	104050	105050	1001080	101080	102080
1005050	105050	106050	1002080	102080	103080
1006050	106050	107050	1003080	103080	104080
1007050	107050	108050	1004080	104080	105080
1008050	108050	109050	1005080	105080	106080
1009050	109050	110050	1006080	106080	107080
1010050	110050	111050	1007080	107080	108080
1011050	111050	112050	1008080	108080	109080
1012050	112050	113050	1009080	109080	110080
1013050	113050	114050	1010080	110080	111080
1014050	114050	115050	1011080	111080	112080
1015050	115050	116050	1012080	112080	113080
1016050	116050	117050	1013080	113080	114080
1001060	101060	102060	1014080	114080	115080
1002060	102060	103060	1015080	115080	116080
1003060	103060	104060	1016080	116080	117080
1004060	104060	105060	1001090	101090	102090
1005060	105060	106060	1002090	102090	103090
1006060	106060	107060	1003090	103090	104090
1007060	107060	108060	1004090	104090	105090
1008060	108060	109060	1005090	105090	106090
1009060	109060	110060	1006090	106090	107090
1010060	110060	111060	1007090	107090	108090
1011060	111060	112060	1008090	108090	109090
1012060	112060	113060	1009090	109090	110090
1013060	113060	114060	1010090	110090	111090
1014060	114060	115060	1011090	111090	112090
1015060	115060	116060	1012090	112090	113090

Table I-3 (continued)

Element No	Connecting Nodes		Element No	Connecting Nodes	
	Node 1	Node 2		Node 1	Node 2
1013090	113090	114090	2010010	210010	211010
1014090	114090	115090	2011010	211010	212010
1015090	115090	116090	2012010	212010	213010
1016090	116090	117090	2013010	213010	214010
1001100	101100	102100	2014010	214010	215010
1002100	102100	103100	2015010	215010	216010
1003100	103100	104100	2016010	216010	217010
1004100	104100	105100	2001020	201020	202020
1005100	105100	106100	2002020	202020	203020
1006100	106100	107100	2003020	203020	204020
1007100	107100	108100	2004020	204020	205020
1008100	108100	109100	2005020	205020	206020
1009100	109100	110100	2006020	206020	207020
1010100	110100	111100	2007020	207020	208020
1011100	111100	112100	2008020	208020	209020
1012100	112100	113100	2009020	209020	210020
1013100	113100	114100	2010020	210020	211020
1014100	114100	115100	2011020	211020	212020
1015100	115100	116100	2012020	212020	213020
1016100	116100	117100	2013020	213020	214020
1001110	101110	102110	2014020	214020	215020
1002110	102110	103110	2015020	215020	216020
1003110	103110	104110	2016020	216020	217020
1004110	104110	105110	2001030	201030	202030
1005110	105110	106110	2002030	202030	203030
1006110	106110	107110	2003030	203030	204030
1007110	107110	108110	2004030	204030	205030
1008110	108110	109110	2005030	205030	206030
1009110	109110	110110	2006030	206030	207030
1010110	110110	111110	2007030	207030	208030
1011110	111110	112110	2008030	208030	209030
1012110	112110	113110	2009030	209030	210030
1013110	113110	114110	2010030	210030	211030
1014110	114110	115110	2011030	211030	212030
1015110	115110	116110	2012030	212030	213030
1016110	116110	117110	2013030	213030	214030
2001010	201010	202010	2014030	214030	215030
2002010	202010	203010	2015030	215030	216030
2003010	203010	204010	2016030	216030	217030
2004010	204010	205010	2001040	201040	202040
2005010	205010	206010	2002040	202040	203040
2006010	206010	207010	2003040	203040	204040
2007010	207010	208010	2004040	204040	205040
2008010	208010	209010	2005040	205040	206040
2009010	209010	210010	2006040	206040	207040

Table I-3 (continued)

Element No	Connecting Nodes		Element No	Connecting Nodes	
	Node 1	Node 2		Node 1	Node 2
2007040	207040	208040	2004070	204070	205070
2008040	208040	209040	2005070	205070	206070
2009040	209040	210040	2006070	206070	207070
2010040	210040	211040	2007070	207070	208070
2011040	211040	212040	2008070	208070	209070
2012040	212040	213040	2009070	209070	210070
2013040	213040	214040	2010070	210070	211070
2014040	214040	215040	2011070	211070	212070
2015040	215040	216040	2012070	212070	213070
2016040	216040	217040	2013070	213070	214070
2001050	201050	202050	2014070	214070	215070
2002050	202050	203050	2015070	215070	216070
2003050	203050	204050	2016070	216070	217070
2004050	204050	205050	2001080	201080	202080
2005050	205050	206050	2002080	202080	203080
2006050	206050	207050	2003080	203080	204080
2007050	207050	208050	2004080	204080	205080
2008050	208050	209050	2005080	205080	206080
2009050	209050	210050	2006080	206080	207080
2010050	210050	211050	2007080	207080	208080
2011050	211050	212050	2008080	208080	209080
2012050	212050	213050	2009080	209080	210080
2013050	213050	214050	2010080	210080	211080
2014050	214050	215050	2011080	211080	212080
2015050	215050	216050	2012080	212080	213080
2016050	216050	217050	2013080	213080	214080
2001060	201060	202060	2014080	214080	215080
2002060	202060	203060	2015080	215080	216080
2003060	203060	204060	2016080	216080	217080
2004060	204060	205060	2001090	201090	202090
2005060	205060	206060	2002090	202090	203090
2006060	206060	207060	2003090	203090	204090
2007060	207060	208060	2004090	204090	205090
2008060	208060	209060	2005090	205090	206090
2009060	209060	210060	2006090	206090	207090
2010060	210060	211060	2007090	207090	208090
2011060	211060	212060	2008090	208090	209090
2012060	212060	213060	2009090	209090	210090
2013060	213060	214060	2010090	210090	211090
2014060	214060	215060	2011090	211090	212090
2015060	215060	216060	2012090	212090	213090
2016060	216060	217060	2013090	213090	214090
2001070	201070	202070	2014090	214090	215090
2002070	202070	203070	2015090	215090	216090
2003070	203070	204070	2016090	216090	217090

Table I-3 (continued)

Element No	Connecting Nodes		Element No	Connecting Nodes	
	Node 1	Node 2		Node 1	Node 2
2001100	201100	202100	3014010	314010	315010
2002100	202100	203100	3015010	315010	316010
2003100	203100	204100	3016010	316010	317010
2004100	204100	205100	3001020	301020	302020
2005100	205100	206100	3002020	302020	303020
2006100	206100	207100	3003020	303020	304020
2007100	207100	208100	3004020	304020	305020
2008100	208100	209100	3005020	305020	306020
2009100	209100	210100	3006020	306020	307020
2010100	210100	211100	3007020	307020	308020
2011100	211100	212100	3008020	308020	309020
2012100	212100	213100	3009020	309020	310020
2013100	213100	214100	3010020	310020	311020
2014100	214100	215100	3011020	311020	312020
2015100	215100	216100	3012020	312020	313020
2016100	216100	217100	3013020	313020	314020
2001110	201110	202110	3014020	314020	315020
2002110	202110	203110	3015020	315020	316020
2003110	203110	204110	3016020	316020	317020
2004110	204110	205110	3001030	301030	302030
2005110	205110	206110	3002030	302030	303030
2006110	206110	207110	3003030	303030	304030
2007110	207110	208110	3004030	304030	305030
2008110	208110	209110	3005030	305030	306030
2009110	209110	210110	3006030	306030	307030
2010110	210110	211110	3007030	307030	308030
2011110	211110	212110	3008030	308030	309030
2012110	212110	213110	3009030	309030	310030
2013110	213110	214110	3010030	310030	311030
2014110	214110	215110	3011030	311030	312030
2015110	215110	216110	3012030	312030	313030
2016110	216110	217110	3013030	313030	314030
3001010	301010	302010	3014030	314030	315030
3002010	302010	303010	3015030	315030	316030
3003010	303010	304010	3016030	316030	317030
3004010	304010	305010	3001040	301040	302040
3005010	305010	306010	3002040	302040	303040
3006010	306010	307010	3003040	303040	304040
3007010	307010	308010	3004040	304040	305040
3008010	308010	309010	3005040	305040	306040
3009010	309010	310010	3006040	306040	307040
3010010	310010	311010	3007040	307040	308040
3011010	311010	312010	3008040	308040	309040
3012010	312010	313010	3009040	309040	310040
3013010	313010	314010	3010040	310040	311040

Table I-3 (continued)

Element No	Connecting Nodes		Element No	Connecting Nodes	
	Node 1	Node 2		Node 1	Node 2
3011040	311040	312040	3008070	308070	309070
3012040	312040	313040	3009070	309070	310070
3013040	313040	314040	3010070	310070	311070
3014040	314040	315040	3011070	311070	312070
3015040	315040	316040	3012070	312070	313070
3016040	316040	317040	3013070	313070	314070
3001050	301050	302050	3014070	314070	315070
3002050	302050	303050	3015070	315070	316070
3003050	303050	304050	3016070	316070	317070
3004050	304050	305050	3001080	301080	302080
3005050	305050	306050	3002080	302080	303080
3006050	306050	307050	3003080	303080	304080
3007050	307050	308050	3004080	304080	305080
3008050	308050	309050	3005080	305080	306080
3009050	309050	310050	3006080	306080	307080
3010050	310050	311050	3007080	307080	308080
3011050	311050	312050	3008080	308080	309080
3012050	312050	313050	3009080	309080	310080
3013050	313050	314050	3010080	310080	311080
3014050	314050	315050	3011080	311080	312080
3015050	315050	316050	3012080	312080	313080
3016050	316050	317050	3013080	313080	314080
3001060	301060	302060	3014080	314080	315080
3002060	302060	303060	3015080	315080	316080
3003060	303060	304060	3016080	316080	317080
3004060	304060	305060	3001090	301090	302090
3005060	305060	306060	3002090	302090	303090
3006060	306060	307060	3003090	303090	304090
3007060	307060	308060	3004090	304090	305090
3008060	308060	309060	3005090	305090	306090
3009060	309060	310060	3006090	306090	307090
3010060	310060	311060	3007090	307090	308090
3011060	311060	312060	3008090	308090	309090
3012060	312060	313060	3009090	309090	310090
3013060	313060	314060	3010090	310090	311090
3014060	314060	315060	3011090	311090	312090
3015060	315060	316060	3012090	312090	313090
3016060	316060	317060	3013090	313090	314090
3001070	301070	302070	3014090	314090	315090
3002070	302070	303070	3015090	315090	316090
3003070	303070	304070	3016090	316090	317090
3004070	304070	305070	3001100	301100	302100
3005070	305070	306070	3002100	302100	303100
3006070	306070	307070	3003100	303100	304100
3007070	307070	308070	3004100	304100	305100

Table I-3 (continued)

Element No	Connecting Nodes		Element No	Connecting Nodes	
	Node 1	Node 2		Node 1	Node 2
3005100	305100	306100	4002020	402020	403020
3006100	306100	307100	4003020	403020	404020
3007100	307100	308100	4004020	404020	405020
3008100	308100	309100	4005020	405020	406020
3009100	309100	310100	4006020	406020	407020
3010100	310100	311100	4007020	407020	408020
3011100	311100	312100	4008020	408020	409020
3012100	312100	313100	4009020	409020	410020
3013100	313100	314100	4010020	410020	411020
3014100	314100	315100	4011020	411020	412020
3015100	315100	316100	4012020	412020	413020
3016100	316100	317100	4013020	413020	414020
3001110	301110	302110	4014020	414020	415020
3002110	302110	303110	4015020	415020	416020
3003110	303110	304110	4016020	416020	417020
3004110	304110	305110	4001030	401030	402030
3005110	305110	306110	4002030	402030	403030
3006110	306110	307110	4003030	403030	404030
3007110	307110	308110	4004030	404030	405030
3008110	308110	309110	4005030	405030	406030
3009110	309110	310110	4006030	406030	407030
3010110	310110	311110	4007030	407030	408030
3011110	311110	312110	4008030	408030	409030
3012110	312110	313110	4009030	409030	410030
3013110	313110	314110	4010030	410030	411030
3014110	314110	315110	4011030	411030	412030
3015110	315110	316110	4012030	412030	413030
3016110	316110	317110	4013030	413030	414030
4001010	401010	402010	4014030	414030	415030
4002010	402010	403010	4015030	415030	416030
4003010	403010	404010	4016030	416030	417030
4004010	404010	405010	4001040	401040	402040
4005010	405010	406010	4002040	402040	403040
4006010	406010	407010	4003040	403040	404040
4007010	407010	408010	4004040	404040	405040
4008010	408010	409010	4005040	405040	406040
4009010	409010	410010	4006040	406040	407040
4010010	410010	411010	4007040	407040	408040
4011010	411010	412010	4008040	408040	409040
4012010	412010	413010	4009040	409040	410040
4013010	413010	414010	4010040	410040	411040
4014010	414010	415010	4011040	411040	412040
4015010	415010	416010	4012040	412040	413040
4016010	416010	417010	4013040	413040	414040
4001020	401020	402020	4014040	414040	415040

Table I-3 (continued)

Element No	Connecting Nodes		Element No	Connecting Nodes	
	Node 1	Node 2		Node 1	Node 2
4015040	415040	416040	4012070	412070	413070
4016040	416040	417040	4013070	413070	414070
4001050	401050	402050	4014070	414070	415070
4002050	402050	403050	4015070	415070	416070
4003050	403050	404050	4016070	416070	417070
4004050	404050	405050	4001080	401080	402080
4005050	405050	406050	4002080	402080	403080
4006050	406050	407050	4003080	403080	404080
4007050	407050	408050	4004080	404080	405080
4008050	408050	409050	4005080	405080	406080
4009050	409050	410050	4006080	406080	407080
4010050	410050	411050	4007080	407080	408080
4011050	411050	412050	4008080	408080	409080
4012050	412050	413050	4009080	409080	410080
4013050	413050	414050	4010080	410080	411080
4014050	414050	415050	4011080	411080	412080
4015050	415050	416050	4012080	412080	413080
4016050	416050	417050	4013080	413080	414080
4001060	401060	402060	4014080	414080	415080
4002060	402060	403060	4015080	415080	416080
4003060	403060	404060	4016080	416080	417080
4004060	404060	405060	4001090	401090	402090
4005060	405060	406060	4002090	402090	403090
4006060	406060	407060	4003090	403090	404090
4007060	407060	408060	4004090	404090	405090
4008060	408060	409060	4005090	405090	406090
4009060	409060	410060	4006090	406090	407090
4010060	410060	411060	4007090	407090	408090
4011060	411060	412060	4008090	408090	409090
4012060	412060	413060	4009090	409090	410090
4013060	413060	414060	4010090	410090	411090
4014060	414060	415060	4011090	411090	412090
4015060	415060	416060	4012090	412090	413090
4016060	416060	417060	4013090	413090	414090
4001070	401070	402070	4014090	414090	415090
4002070	402070	403070	4015090	415090	416090
4003070	403070	404070	4016090	416090	417090
4004070	404070	405070	4001100	401100	402100
4005070	405070	406070	4002100	402100	403100
4006070	406070	407070	4003100	403100	404100
4007070	407070	408070	4004100	404100	405100
4008070	408070	409070	4005100	405100	406100
4009070	409070	410070	4006100	406100	407100
4010070	410070	411070	4007100	407100	408100
4011070	411070	412070	4008100	408100	409100

Table I-3 (continued)

Element No	Connecting Nodes		Element No	Connecting Nodes	
	Node 1	Node 2		Node 1	Node 2
4009100	409100	410100	5006020	506020	507020
4010100	410100	411100	5007020	507020	508020
4011100	411100	412100	5008020	508020	509020
4012100	412100	413100	5009020	509020	510020
4013100	413100	414100	5010020	510020	511020
4014100	414100	415100	5011020	511020	512020
4015100	415100	416100	5012020	512020	513020
4016100	416100	417100	5013020	513020	514020
4001110	401110	402110	5014020	514020	515020
4002110	402110	403110	5015020	515020	516020
4003110	403110	404110	5016020	516020	517020
4004110	404110	405110	5001030	501030	502030
4005110	405110	406110	5002030	502030	503030
4006110	406110	407110	5003030	503030	504030
4007110	407110	408110	5004030	504030	505030
4008110	408110	409110	5005030	505030	506030
4009110	409110	410110	5006030	506030	507030
4010110	410110	411110	5007030	507030	508030
4011110	411110	412110	5008030	508030	509030
4012110	412110	413110	5009030	509030	510030
4013110	413110	414110	5010030	510030	511030
4014110	414110	415110	5011030	511030	512030
4015110	415110	416110	5012030	512030	513030
4016110	416110	417110	5013030	513030	514030
5001010	501010	502010	5014030	514030	515030
5002010	502010	503010	5015030	515030	516030
5003010	503010	504010	5016030	516030	517030
5004010	504010	505010	5001040	501040	502040
5005010	505010	506010	5002040	502040	503040
5006010	506010	507010	5003040	503040	504040
5007010	507010	508010	5004040	504040	505040
5008010	508010	509010	5005040	505040	506040
5009010	509010	510010	5006040	506040	507040
5010010	510010	511010	5007040	507040	508040
5011010	511010	512010	5008040	508040	509040
5012010	512010	513010	5009040	509040	510040
5013010	513010	514010	5010040	510040	511040
5014010	514010	515010	5011040	511040	512040
5015010	515010	516010	5012040	512040	513040
5016010	516010	517010	5013040	513040	514040
5001020	501020	502020	5014040	514040	515040
5002020	502020	503020	5015040	515040	516040
5003020	503020	504020	5016040	516040	517040
5004020	504020	505020	5001050	501050	502050
5005020	505020	506020	5002050	502050	503050

Table I-3 (continued)

Element No	Connecting Nodes		Element No	Connecting Nodes	
	Node 1	Node 2		Node 1	Node 2
5003050	503050	504050	5016070	516070	517070
5004050	504050	505050	5001080	501080	502080
5005050	505050	506050	5002080	502080	503080
5006050	506050	507050	5003080	503080	504080
5007050	507050	508050	5004080	504080	505080
5008050	508050	509050	5005080	505080	506080
5009050	509050	510050	5006080	506080	507080
5010050	510050	511050	5007080	507080	508080
5011050	511050	512050	5008080	508080	509080
5012050	512050	513050	5009080	509080	510080
5013050	513050	514050	5010080	510080	511080
5014050	514050	515050	5011080	511080	512080
5015050	515050	516050	5012080	512080	513080
5016050	516050	517050	5013080	513080	514080
5001060	501060	502060	5014080	514080	515080
5002060	502060	503060	5015080	515080	516080
5003060	503060	504060	5016080	516080	517080
5004060	504060	505060	5001090	501090	502090
5005060	505060	506060	5002090	502090	503090
5006060	506060	507060	5003090	503090	504090
5007060	507060	508060	5004090	504090	505090
5008060	508060	509060	5005090	505090	506090
5009060	509060	510060	5006090	506090	507090
5010060	510060	511060	5007090	507090	508090
5011060	511060	512060	5008090	508090	509090
5012060	512060	513060	5009090	509090	510090
5013060	513060	514060	5010090	510090	511090
5014060	514060	515060	5011090	511090	512090
5015060	515060	516060	5012090	512090	513090
5016060	516060	517060	5013090	513090	514090
5001070	501070	502070	5014090	514090	515090
5002070	502070	503070	5015090	515090	516090
5003070	503070	504070	5016090	516090	517090
5004070	504070	505070	5001100	501100	502100
5005070	505070	506070	5002100	502100	503100
5006070	506070	507070	5003100	503100	504100
5007070	507070	508070	5004100	504100	505100
5008070	508070	509070	5005100	505100	506100
5009070	509070	510070	5006100	506100	507100
5010070	510070	511070	5007100	507100	508100
5011070	511070	512070	5008100	508100	509100
5012070	512070	513070	5009100	509100	510100
5013070	513070	514070	5010100	510100	511100
5014070	514070	515070	5011100	511100	512100
5015070	515070	516070	5012100	512100	513100

Table I-3 (continued)

Element No	Connecting Nodes		Element No	Connecting Nodes	
	Node 1	Node 2		Node 1	Node 2
5013100	513100	514100	6006040	606040	607040
5014100	514100	515100	6007040	607040	608040
5015100	515100	516100	6008040	608040	609040
5016100	516100	517100	6009040	609040	610040
5001110	501110	502110	6010040	610040	611040
5002110	502110	503110	6011040	611040	612040
5003110	503110	504110	6012040	612040	613040
5004110	504110	505110	6005050	605050	606050
5005110	505110	506110	6006050	606050	607050
5006110	506110	507110	6007050	607050	608050
5007110	507110	508110	6008050	608050	609050
5008110	508110	509110	6009050	609050	610050
5009110	509110	510110	6010050	610050	611050
5010110	510110	511110	6011050	611050	612050
5011110	511110	512110	6012050	612050	613050
5012110	512110	513110	6005060	605060	606060
5013110	513110	514110	6006060	606060	607060
5014110	514110	515110	6007060	607060	608060
5015110	515110	516110	6008060	608060	609060
5016110	516110	517110	6009060	609060	610060
6005010	605010	606010	6010060	610060	611060
6006010	606010	607010	6011060	611060	612060
6007010	607010	608010	6012060	612060	613060
6008010	608010	609010	6005070	605070	606070
6009010	609010	610010	6006070	606070	607070
6010010	610010	611010	6007070	607070	608070
6011010	611010	612010	6008070	608070	609070
6012010	612010	613010	6009070	609070	610070
6005020	605020	606020	6010070	610070	611070
6006020	606020	607020	6011070	611070	612070
6007020	607020	608020	6012070	612070	613070
6008020	608020	609020	6005080	605080	606080
6009020	609020	610020	6006080	606080	607080
6010020	610020	611020	6007080	607080	608080
6011020	611020	612020	6008080	608080	609080
6012020	612020	613020	6009080	609080	610080
6005030	605030	606030	6010080	610080	611080
6006030	606030	607030	6011080	611080	612080
6007030	607030	608030	6012080	612080	613080
6008030	608030	609030	6005090	605090	606090
6009030	609030	610030	6006090	606090	607090
6010030	610030	611030	6007090	607090	608090
6011030	611030	612030	6008090	608090	609090
6012030	612030	613030	6009090	609090	610090
6005040	605040	606040	6010090	610090	611090

Table I-3 (continued)

Element No	Connecting Nodes		Element No	Connecting Nodes	
	Node 1	Node 2		Node 1	Node 2
6011090	611090	612090	7008040	708040	709040
6012090	612090	613090	7009040	709040	710040
6005100	605100	606100	7010040	710040	711040
6006100	606100	607100	7011040	711040	712040
6007100	607100	608100	7012040	712040	713040
6008100	608100	609100	7005050	705050	706050
6009100	609100	610100	7006050	706050	707050
6010100	610100	611100	7007050	707050	708050
6011100	611100	612100	7008050	708050	709050
6012100	612100	613100	7009050	709050	710050
6005110	605110	606110	7010050	710050	711050
6006110	606110	607110	7011050	711050	712050
6007110	607110	608110	7012050	712050	713050
6008110	608110	609110	7005060	705060	706060
6009110	609110	610110	7006060	706060	707060
6010110	610110	611110	7007060	707060	708060
6011110	611110	612110	7008060	708060	709060
6012110	612110	613110	7009060	709060	710060
7005010	705010	706010	7010060	710060	711060
7006010	706010	707010	7011060	711060	712060
7007010	707010	708010	7012060	712060	713060
7008010	708010	709010	7005070	705070	706070
7009010	709010	710010	7006070	706070	707070
7010010	710010	711010	7007070	707070	708070
7011010	711010	712010	7008070	708070	709070
7012010	712010	713010	7009070	709070	710070
7005020	705020	706020	7010070	710070	711070
7006020	706020	707020	7011070	711070	712070
7007020	707020	708020	7012070	712070	713070
7008020	708020	709020	7005080	705080	706080
7009020	709020	710020	7006080	706080	707080
7010020	710020	711020	7007080	707080	708080
7011020	711020	712020	7008080	708080	709080
7012020	712020	713020	7009080	709080	710080
7005030	705030	706030	7010080	710080	711080
7006030	706030	707030	7011080	711080	712080
7007030	707030	708030	7012080	712080	713080
7008030	708030	709030	7005090	705090	706090
7009030	709030	710030	7006090	706090	707090
7010030	710030	711030	7007090	707090	708090
7011030	711030	712030	7008090	708090	709090
7012030	712030	713030	7009090	709090	710090
7005040	705040	706040	7010090	710090	711090
7006040	706040	707040	7011090	711090	712090
7007040	707040	708040	7012090	712090	713090

Table I-3 (continued)

Element No	Connecting Nodes		Element No	Connecting Nodes	
	Node 1	Node 2		Node 1	Node 2
7005100	705100	706100	8010040	810040	811040
7006100	706100	707100	8011040	811040	812040
7007100	707100	708100	8012040	812040	813040
7008100	708100	709100	8005050	805050	806050
7009100	709100	710100	8006050	806050	807050
7010100	710100	711100	8007050	807050	808050
7011100	711100	712100	8008050	808050	809050
7012100	712100	713100	8009050	809050	810050
7005110	705110	706110	8010050	810050	811050
7006110	706110	707110	8011050	811050	812050
7007110	707110	708110	8012050	812050	813050
7008110	708110	709110	8005060	805060	806060
7009110	709110	710110	8006060	806060	807060
7010110	710110	711110	8007060	807060	808060
7011110	711110	712110	8008060	808060	809060
7012110	712110	713110	8009060	809060	810060
8005010	805010	806010	8010060	810060	811060
8006010	806010	807010	8011060	811060	812060
8007010	807010	808010	8012060	812060	813060
8008010	808010	809010	8005070	805070	806070
8009010	809010	810010	8006070	806070	807070
8010010	810010	811010	8007070	807070	808070
8011010	811010	812010	8008070	808070	809070
8012010	812010	813010	8009070	809070	810070
8005020	805020	806020	8010070	810070	811070
8006020	806020	807020	8011070	811070	812070
8007020	807020	808020	8012070	812070	813070
8008020	808020	809020	8005080	805080	806080
8009020	809020	810020	8006080	806080	807080
8010020	810020	811020	8007080	807080	808080
8011020	811020	812020	8008080	808080	809080
8012020	812020	813020	8009080	809080	810080
8005030	805030	806030	8010080	810080	811080
8006030	806030	807030	8011080	811080	812080
8007030	807030	808030	8012080	812080	813080
8008030	808030	809030	8005090	805090	806090
8009030	809030	810030	8006090	806090	807090
8010030	810030	811030	8007090	807090	808090
8011030	811030	812030	8008090	808090	809090
8012030	812030	813030	8009090	809090	810090
8005040	805040	806040	8010090	810090	811090
8006040	806040	807040	8011090	811090	812090
8007040	807040	808040	8012090	812090	813090
8008040	808040	809040	8005100	805100	806100
8009040	809040	810040	8006100	806100	807100

Table I-3 (continued)

Element No	Connecting Nodes		Element No	Connecting Nodes	
	Node 1	Node 2		Node 1	Node 2
8007100	807100	808100	9012040	912040	913040
8008100	808100	809100	9005050	905050	906050
8009100	809100	810100	9006050	906050	907050
8010100	810100	811100	9007050	907050	908050
8011100	811100	812100	9008050	908050	909050
8012100	812100	813100	9009050	909050	910050
8005110	805110	806110	9010050	910050	911050
8006110	806110	807110	9011050	911050	912050
8007110	807110	808110	9012050	912050	913050
8008110	808110	809110	9005060	905060	906060
8009110	809110	810110	9006060	906060	907060
8010110	810110	811110	9007060	907060	908060
8011110	811110	812110	9008060	908060	909060
8012110	812110	813110	9009060	909060	910060
9005010	905010	906010	9010060	910060	911060
9006010	906010	907010	9011060	911060	912060
9007010	907010	908010	9012060	912060	913060
9008010	908010	909010	9005070	905070	906070
9009010	909010	910010	9006070	906070	907070
9010010	910010	911010	9007070	907070	908070
9011010	911010	912010	9008070	908070	909070
9012010	912010	913010	9009070	909070	910070
9005020	905020	906020	9010070	910070	911070
9006020	906020	907020	9011070	911070	912070
9007020	907020	908020	9012070	912070	913070
9008020	908020	909020	9005080	905080	906080
9009020	909020	910020	9006080	906080	907080
9010020	910020	911020	9007080	907080	908080
9011020	911020	912020	9008080	908080	909080
9012020	912020	913020	9009080	909080	910080
9005030	905030	906030	9010080	910080	911080
9006030	906030	907030	9011080	911080	912080
9007030	907030	908030	9012080	912080	913080
9008030	908030	909030	9005090	905090	906090
9009030	909030	910030	9006090	906090	907090
9010030	910030	911030	9007090	907090	908090
9011030	911030	912030	9008090	908090	909090
9012030	912030	913030	9009090	909090	910090
9005040	905040	906040	9010090	910090	911090
9006040	906040	907040	9011090	911090	912090
9007040	907040	908040	9012090	912090	913090
9008040	908040	909040	9005100	905100	906100
9009040	909040	910040	9006100	906100	907100
9010040	910040	911040	9007100	907100	908100
9011040	911040	912040	9008100	908100	909100

Table I-3 (continued)

Element No	Connecting Nodes	
	Node 1	Node 2
9009100	909100	910100
9010100	910100	911100
9011100	911100	912100
9012100	912100	913100
9005110	905110	906110
9006110	906110	907110
9007110	907110	908110
9008110	908110	909110
9009110	909110	910110
9010110	910110	911110
9011110	911110	912110
9012110	912110	913110

Table I-4: Area moments of inertia of the vertical elements of the ASB

Element No	Connecting Nodes		Area moment of inertia about axis (m^4)	
	Node 1	Node 2	Y	X
10001010	101010	201010	7.27	5.44
20001010	201010	301010	4.40	3.29
30001010	301010	401010	4.40	3.29
40001010	401010	501010	4.40	3.29
10001020	101020	201020	7.27	5.44
20001020	201020	301020	4.40	3.29
30001020	301020	401020	4.40	3.29
40001020	401020	501020	4.40	3.29
10001030	101030	201030	7.27	5.44
20001030	201030	301030	4.40	3.29
30001030	301030	401030	4.40	3.29
40001030	401030	501030	4.40	3.29
10001040	101040	201040	7.27	5.44
20001040	201040	301040	4.40	3.29
30001040	301040	401040	4.40	3.29
40001040	401040	501040	4.40	3.29
10001050	101050	201050	7.27	5.44
20001050	201050	301050	4.40	3.29
30001050	301050	401050	4.40	3.29
40001050	401050	501050	4.40	3.29
10001060	101060	201060	7.27	5.44
20001060	201060	301060	4.40	3.29
30001060	301060	401060	4.40	3.29
40001060	401060	501060	4.40	3.29
10001070	101070	201070	7.27	5.44
20001070	201070	301070	4.40	3.29
30001070	301070	401070	4.40	3.29
40001070	401070	501070	4.40	3.29
10001080	101080	201080	7.27	5.44
20001080	201080	301080	4.40	3.29
30001080	301080	401080	4.40	3.29
40001080	401080	501080	4.40	3.29
10001090	101090	201090	7.27	5.44
20001090	201090	301090	4.40	3.29
30001090	301090	401090	4.40	3.29
40001090	401090	501090	4.40	3.29
10001100	101100	201100	7.27	5.44
20001100	201100	301100	4.40	3.29
30001100	301100	401100	4.40	3.29
40001100	401100	501100	4.40	3.29
10001110	101110	201110	7.27	5.44
20001110	201110	301110	4.40	3.29
30001110	301110	401110	4.40	3.29
40001110	401110	501110	4.40	3.29
10002010	102010	202010	7.27	5.44

Table I-4 (continued)

Element No	Connecting Nodes		Area moment of inertia about axis (m^4)	
	Node 1	Node 2	Y	X
20002010	202010	302010	4.40	3.29
30002010	302010	402010	4.40	3.29
40002010	402010	502010	4.40	3.29
10002020	102020	202020	7.27	5.44
20002020	202020	302020	4.40	3.29
30002020	302020	402020	4.40	3.29
40002020	402020	502020	4.40	3.29
10002030	102030	202030	7.27	5.44
20002030	202030	302030	4.40	3.29
30002030	302030	402030	4.40	3.29
40002030	402030	502030	4.40	3.29
10002040	102040	202040	7.27	5.44
20002040	202040	302040	4.40	3.29
30002040	302040	402040	4.40	3.29
40002040	402040	502040	4.40	3.29
10002050	102050	202050	7.27	5.44
20002050	202050	302050	4.40	3.29
30002050	302050	402050	4.40	3.29
40002050	402050	502050	4.40	3.29
10002060	102060	202060	7.27	5.44
20002060	202060	302060	4.40	3.29
30002060	302060	402060	4.40	3.29
40002060	402060	502060	4.40	3.29
10002070	102070	202070	7.27	5.44
20002070	202070	302070	4.40	3.29
30002070	302070	402070	4.40	3.29
40002070	402070	502070	4.40	3.29
10002080	102080	202080	7.27	5.44
20002080	202080	302080	4.40	3.29
30002080	302080	402080	4.40	3.29
40002080	402080	502080	4.40	3.29
10002090	102090	202090	7.27	5.44
20002090	202090	302090	4.40	3.29
30002090	302090	402090	4.40	3.29
40002090	402090	502090	4.40	3.29
10002100	102100	202100	7.27	5.44
20002100	202100	302100	4.40	3.29
30002100	302100	402100	4.40	3.29
40002100	402100	502100	4.40	3.29
10002110	102110	202110	7.27	5.44
20002110	202110	302110	4.40	3.29
30002110	302110	402110	4.40	3.29
40002110	402110	502110	4.40	3.29
10003010	103010	203010	7.27	5.44
20003010	203010	303010	4.40	3.29

Table I-4 (continued)

Element No	Connecting Nodes		Area moment of inertia about axis (m^4)	
	Node 1	Node 2	Y	X
30003010	303010	403010	4.40	3.29
40003010	403010	503010	4.40	3.29
10003020	103020	203020	7.27	5.44
20003020	203020	303020	4.40	3.29
30003020	303020	403020	4.40	3.29
40003020	403020	503020	4.40	3.29
10003030	103030	203030	7.27	5.44
20003030	203030	303030	4.40	3.29
30003030	303030	403030	4.40	3.29
40003030	403030	503030	4.40	3.29
10003040	103040	203040	7.27	5.44
20003040	203040	303040	4.40	3.29
30003040	303040	403040	4.40	3.29
40003040	403040	503040	4.40	3.29
10003050	103050	203050	7.27	5.44
20003050	203050	303050	4.40	3.29
30003050	303050	403050	4.40	3.29
40003050	403050	503050	4.40	3.29
10003060	103060	203060	7.27	5.44
20003060	203060	303060	4.40	3.29
30003060	303060	403060	4.40	3.29
40003060	403060	503060	4.40	3.29
10003070	103070	203070	7.27	5.44
20003070	203070	303070	4.40	3.29
30003070	303070	403070	4.40	3.29
40003070	403070	503070	4.40	3.29
10003080	103080	203080	7.27	5.44
20003080	203080	303080	4.40	3.29
30003080	303080	403080	4.40	3.29
40003080	403080	503080	4.40	3.29
10003090	103090	203090	7.27	5.44
20003090	203090	303090	4.40	3.29
30003090	303090	403090	4.40	3.29
40003090	403090	503090	4.40	3.29
10003100	103100	203100	7.27	5.44
20003100	203100	303100	4.40	3.29
30003100	303100	403100	4.40	3.29
40003100	403100	503100	4.40	3.29
10003110	103110	203110	7.27	5.44
20003110	203110	303110	4.40	3.29
30003110	303110	403110	4.40	3.29
40003110	403110	503110	4.40	3.29
10004010	104010	204010	7.27	5.44
20004010	204010	304010	4.40	3.29
30004010	304010	404010	4.40	3.29

Table I-4 (continued)

Element No	Connecting Nodes		Area moment of inertia about axis (m^4)	
	Node 1	Node 2	Y	X
40004010	404010	504010	4.40	3.29
10004020	104020	204020	7.27	5.44
20004020	204020	304020	4.40	3.29
30004020	304020	404020	4.40	3.29
40004020	404020	504020	4.40	3.29
10004030	104030	204030	7.27	5.44
20004030	204030	304030	4.40	3.29
30004030	304030	404030	4.40	3.29
40004030	404030	504030	4.40	3.29
10004040	104040	204040	7.27	5.44
20004040	204040	304040	4.40	3.29
30004040	304040	404040	4.40	3.29
40004040	404040	504040	4.40	3.29
10004050	104050	204050	7.27	5.44
20004050	204050	304050	4.40	3.29
30004050	304050	404050	4.40	3.29
40004050	404050	504050	4.40	3.29
10004060	104060	204060	7.27	5.44
20004060	204060	304060	4.40	3.29
30004060	304060	404060	4.40	3.29
40004060	404060	504060	4.40	3.29
10004070	104070	204070	7.27	5.44
20004070	204070	304070	4.40	3.29
30004070	304070	404070	4.40	3.29
40004070	404070	504070	4.40	3.29
10004080	104080	204080	7.27	5.44
20004080	204080	304080	4.40	3.29
30004080	304080	404080	4.40	3.29
40004080	404080	504080	4.40	3.29
10004090	104090	204090	7.27	5.44
20004090	204090	304090	4.40	3.29
30004090	304090	404090	4.40	3.29
40004090	404090	504090	4.40	3.29
10004100	104100	204100	7.27	5.44
20004100	204100	304100	4.40	3.29
30004100	304100	404100	4.40	3.29
40004100	404100	504100	4.40	3.29
10004110	104110	204110	7.27	5.44
20004110	204110	304110	4.40	3.29
30004110	304110	404110	4.40	3.29
40004110	404110	504110	4.40	3.29
10005010	105010	205010	8.65	7.63
20005010	205010	305010	4.55	3.93
30005010	305010	405010	4.55	3.93
40005010	405010	505010	4.55	3.93

Table I-4 (continued)

Element No	Connecting Nodes		Area moment of inertia about axis (m^4)	
	Node 1	Node 2	Y	X
50005010	505010	605010	4.84	4.84
60005010	605010	705010	4.84	4.84
70005010	705010	805010	4.84	4.84
80005010	805010	905010	0.98	0.98
10005020	105020	205020	8.65	7.63
20005020	205020	305020	4.55	3.93
30005020	305020	405020	4.55	3.93
40005020	405020	505020	4.55	3.93
50005020	505020	605020	4.84	4.84
60005020	605020	705020	4.84	4.84
70005020	705020	805020	4.84	4.84
80005020	805020	905020	0.98	0.98
10005030	105030	205030	8.65	7.63
20005030	205030	305030	4.55	3.93
30005030	305030	405030	4.55	3.93
40005030	405030	505030	4.55	3.93
50005030	505030	605030	4.84	4.84
60005030	605030	705030	4.84	4.84
70005030	705030	805030	4.84	4.84
80005030	805030	905030	0.98	0.98
10005040	105040	205040	8.65	7.63
20005040	205040	305040	4.55	3.93
30005040	305040	405040	4.55	3.93
40005040	405040	505040	4.55	3.93
50005040	505040	605040	4.84	4.84
60005040	605040	705040	4.84	4.84
70005040	705040	805040	4.84	4.84
80005040	805040	905040	0.98	0.98
10005050	105050	205050	8.65	7.63
20005050	205050	305050	4.55	3.93
30005050	305050	405050	4.55	3.93
40005050	405050	505050	4.55	3.93
50005050	505050	605050	4.84	4.84
60005050	605050	705050	4.84	4.84
70005050	705050	805050	4.84	4.84
80005050	805050	905050	0.98	0.98
10005060	105060	205060	8.65	7.63
20005060	205060	305060	4.55	3.93
30005060	305060	405060	4.55	3.93
40005060	405060	505060	4.55	3.93
50005060	505060	605060	4.84	4.84
60005060	605060	705060	4.84	4.84
70005060	705060	805060	4.84	4.84
80005060	805060	905060	0.98	0.98
10005070	105070	205070	8.65	7.63

Table I-4 (continued)

Element No	Connecting Nodes		Area moment of inertia about axis (m^4)	
	Node 1	Node 2	Y	X
20005070	205070	305070	4.55	3.93
30005070	305070	405070	4.55	3.93
40005070	405070	505070	4.55	3.93
50005070	505070	605070	4.84	4.84
60005070	605070	705070	4.84	4.84
70005070	705070	805070	4.84	4.84
80005070	805070	905070	0.98	0.98
10005080	105080	205080	8.65	7.63
20005080	205080	305080	4.55	3.93
30005080	305080	405080	4.55	3.93
40005080	405080	505080	4.55	3.93
50005080	505080	605080	4.84	4.84
60005080	605080	705080	4.84	4.84
70005080	705080	805080	4.84	4.84
80005080	805080	905080	0.98	0.98
10005090	105090	205090	8.65	7.63
20005090	205090	305090	4.55	3.93
30005090	305090	405090	4.55	3.93
40005090	405090	505090	4.55	3.93
50005090	505090	605090	4.84	4.84
60005090	605090	705090	4.84	4.84
70005090	705090	805090	4.84	4.84
80005090	805090	905090	0.98	0.98
10005100	105100	205100	8.65	7.63
20005100	205100	305100	4.55	3.93
30005100	305100	405100	4.55	3.93
40005100	405100	505100	4.55	3.93
50005100	505100	605100	4.84	4.84
60005100	605100	705100	4.84	4.84
70005100	705100	805100	4.84	4.84
80005100	805100	905100	0.98	0.98
10005110	105110	205110	8.65	7.63
20005110	205110	305110	4.55	3.93
30005110	305110	405110	4.55	3.93
40005110	405110	505110	4.55	3.93
50005110	505110	605110	4.84	4.84
60005110	605110	705110	4.84	4.84
70005110	705110	805110	4.84	4.84
80005110	805110	905110	0.98	0.98
10006010	106010	206010	8.65	7.63
20006010	206010	306010	4.55	3.93
30006010	306010	406010	4.55	3.93
40006010	406010	506010	4.55	3.93
50006010	506010	606010	4.84	4.84
60006010	606010	706010	4.84	4.84

Table I-4 (continued)

Element No	Connecting Nodes		Area moment of inertia about axis (m^4)	
	Node 1	Node 2	Y	X
70006010	706010	806010	4.84	4.84
80006010	806010	906010	0.98	0.98
10006020	106020	206020	8.65	7.63
20006020	206020	306020	4.55	3.93
30006020	306020	406020	4.55	3.93
40006020	406020	506020	4.55	3.93
50006020	506020	606020	4.84	4.84
60006020	606020	706020	4.84	4.84
70006020	706020	806020	4.84	4.84
80006020	806020	906020	0.98	0.98
10006030	106030	206030	8.65	7.63
20006030	206030	306030	4.55	3.93
30006030	306030	406030	4.55	3.93
40006030	406030	506030	4.55	3.93
50006030	506030	606030	4.84	4.84
60006030	606030	706030	4.84	4.84
70006030	706030	806030	4.84	4.84
80006030	806030	906030	0.98	0.98
10006040	106040	206040	8.65	7.63
20006040	206040	306040	4.55	3.93
30006040	306040	406040	4.55	3.93
40006040	406040	506040	4.55	3.93
50006040	506040	606040	4.84	4.84
60006040	606040	706040	4.84	4.84
70006040	706040	806040	4.84	4.84
80006040	806040	906040	0.98	0.98
10006050	106050	206050	8.65	7.63
20006050	206050	306050	4.55	3.93
30006050	306050	406050	4.55	3.93
40006050	406050	506050	4.55	3.93
50006050	506050	606050	4.84	4.84
60006050	606050	706050	4.84	4.84
70006050	706050	806050	4.84	4.84
80006050	806050	906050	0.98	0.98
10006060	106060	206060	8.65	7.63
20006060	206060	306060	4.55	3.93
30006060	306060	406060	4.55	3.93
40006060	406060	506060	4.55	3.93
50006060	506060	606060	4.84	4.84
60006060	606060	706060	4.84	4.84
70006060	706060	806060	4.84	4.84
80006060	806060	906060	0.98	0.98
10006070	106070	206070	8.65	7.63
20006070	206070	306070	4.55	3.93
30006070	306070	406070	4.55	3.93

Table I-4 (continued)

Element No	Connecting Nodes		Area moment of inertia about axis (m^4)	
	Node 1	Node 2	Y	X
40006070	406070	506070	4.55	3.93
50006070	506070	606070	4.84	4.84
60006070	606070	706070	4.84	4.84
70006070	706070	806070	4.84	4.84
80006070	806070	906070	0.98	0.98
10006080	106080	206080	8.65	7.63
20006080	206080	306080	4.55	3.93
30006080	306080	406080	4.55	3.93
40006080	406080	506080	4.55	3.93
50006080	506080	606080	4.84	4.84
60006080	606080	706080	4.84	4.84
70006080	706080	806080	4.84	4.84
80006080	806080	906080	0.98	0.98
10006090	106090	206090	8.65	7.63
20006090	206090	306090	4.55	3.93
30006090	306090	406090	4.55	3.93
40006090	406090	506090	4.55	3.93
50006090	506090	606090	4.84	4.84
60006090	606090	706090	4.84	4.84
70006090	706090	806090	4.84	4.84
80006090	806090	906090	0.98	0.98
10006100	106100	206100	8.65	7.63
20006100	206100	306100	4.55	3.93
30006100	306100	406100	4.55	3.93
40006100	406100	506100	4.55	3.93
50006100	506100	606100	4.84	4.84
60006100	606100	706100	4.84	4.84
70006100	706100	806100	4.84	4.84
80006100	806100	906100	0.98	0.98
10006110	106110	206110	8.65	7.63
20006110	206110	306110	4.55	3.93
30006110	306110	406110	4.55	3.93
40006110	406110	506110	4.55	3.93
50006110	506110	606110	4.84	4.84
60006110	606110	706110	4.84	4.84
70006110	706110	806110	4.84	4.84
80006110	806110	906110	0.98	0.98
10007010	107010	207010	8.65	7.63
20007010	207010	307010	4.55	3.93
30007010	307010	407010	4.55	3.93
40007010	407010	507010	4.55	3.93
50007010	507010	607010	4.84	4.84
60007010	607010	707010	4.84	4.84
70007010	707010	807010	4.84	4.84
80007010	807010	907010	0.98	0.98

Table I-4 (continued)

Element No	Connecting Nodes		Area moment of inertia about axis (m^4)	
	Node 1	Node 2	Y	X
10007020	107020	207020	8.65	7.63
20007020	207020	307020	4.55	3.93
30007020	307020	407020	4.55	3.93
40007020	407020	507020	4.55	3.93
50007020	507020	607020	4.84	4.84
60007020	607020	707020	4.84	4.84
70007020	707020	807020	4.84	4.84
80007020	807020	907020	0.98	0.98
10007030	107030	207030	8.65	7.63
20007030	207030	307030	4.55	3.93
30007030	307030	407030	4.55	3.93
40007030	407030	507030	4.55	3.93
50007030	507030	607030	4.84	4.84
60007030	607030	707030	4.84	4.84
70007030	707030	807030	4.84	4.84
80007030	807030	907030	0.98	0.98
10007040	107040	207040	8.65	7.63
20007040	207040	307040	4.55	3.93
30007040	307040	407040	4.55	3.93
40007040	407040	507040	4.55	3.93
50007040	507040	607040	4.84	4.84
60007040	607040	707040	4.84	4.84
70007040	707040	807040	4.84	4.84
80007040	807040	907040	0.98	0.98
10007050	107050	207050	8.65	7.63
20007050	207050	307050	4.55	3.93
30007050	307050	407050	4.55	3.93
40007050	407050	507050	4.55	3.93
50007050	507050	607050	4.84	4.84
60007050	607050	707050	4.84	4.84
70007050	707050	807050	4.84	4.84
80007050	807050	907050	0.98	0.98
10007060	107060	207060	8.65	7.63
20007060	207060	307060	4.55	3.93
30007060	307060	407060	4.55	3.93
40007060	407060	507060	4.55	3.93
50007060	507060	607060	4.84	4.84
60007060	607060	707060	4.84	4.84
70007060	707060	807060	4.84	4.84
80007060	807060	907060	0.98	0.98
10007070	107070	207070	8.65	7.63
20007070	207070	307070	4.55	3.93
30007070	307070	407070	4.55	3.93
40007070	407070	507070	4.55	3.93
50007070	507070	607070	4.84	4.84

Table I-4 (continued)

Element No	Connecting Nodes		Area moment of inertia about axis (m^4)	
	Node 1	Node 2	Y	X
60007070	607070	707070	4.84	4.84
70007070	707070	807070	4.84	4.84
80007070	807070	907070	0.98	0.98
10007080	107080	207080	8.65	7.63
20007080	207080	307080	4.55	3.93
30007080	307080	407080	4.55	3.93
40007080	407080	507080	4.55	3.93
50007080	507080	607080	4.84	4.84
60007080	607080	707080	4.84	4.84
70007080	707080	807080	4.84	4.84
80007080	807080	907080	0.98	0.98
10007090	107090	207090	8.65	7.63
20007090	207090	307090	4.55	3.93
30007090	307090	407090	4.55	3.93
40007090	407090	507090	4.55	3.93
50007090	507090	607090	4.84	4.84
60007090	607090	707090	4.84	4.84
70007090	707090	807090	4.84	4.84
80007090	807090	907090	0.98	0.98
10007100	107100	207100	8.65	7.63
20007100	207100	307100	4.55	3.93
30007100	307100	407100	4.55	3.93
40007100	407100	507100	4.55	3.93
50007100	507100	607100	4.84	4.84
60007100	607100	707100	4.84	4.84
70007100	707100	807100	4.84	4.84
80007100	807100	907100	0.98	0.98
10007110	107110	207110	8.65	7.63
20007110	207110	307110	4.55	3.93
30007110	307110	407110	4.55	3.93
40007110	407110	507110	4.55	3.93
50007110	507110	607110	4.84	4.84
60007110	607110	707110	4.84	4.84
70007110	707110	807110	4.84	4.84
80007110	807110	907110	0.98	0.98
10008010	108010	208010	8.65	7.63
20008010	208010	308010	4.55	3.93
30008010	308010	408010	4.55	3.93
40008010	408010	508010	4.55	3.93
50008010	508010	608010	4.84	4.84
60008010	608010	708010	4.84	4.84
70008010	708010	808010	4.84	4.84
80008010	808010	908010	0.98	0.98
10008020	108020	208020	8.65	7.63
20008020	208020	308020	4.55	3.93

Table I-4 (continued)

Element No	Connecting Nodes		Area moment of inertia about axis (m^4)	
	Node 1	Node 2	Y	X
30008020	308020	408020	4.55	3.93
40008020	408020	508020	4.55	3.93
50008020	508020	608020	4.84	4.84
60008020	608020	708020	4.84	4.84
70008020	708020	808020	4.84	4.84
80008020	808020	908020	0.98	0.98
10008030	108030	208030	8.65	7.63
20008030	208030	308030	4.55	3.93
30008030	308030	408030	4.55	3.93
40008030	408030	508030	4.55	3.93
50008030	508030	608030	4.84	4.84
60008030	608030	708030	4.84	4.84
70008030	708030	808030	4.84	4.84
80008030	808030	908030	0.98	0.98
10008040	108040	208040	8.65	7.63
20008040	208040	308040	4.55	3.93
30008040	308040	408040	4.55	3.93
40008040	408040	508040	4.55	3.93
50008040	508040	608040	4.84	4.84
60008040	608040	708040	4.84	4.84
70008040	708040	808040	4.84	4.84
80008040	808040	908040	0.98	0.98
10008050	108050	208050	8.65	7.63
20008050	208050	308050	4.55	3.93
30008050	308050	408050	4.55	3.93
40008050	408050	508050	4.55	3.93
50008050	508050	608050	4.84	4.84
60008050	608050	708050	4.84	4.84
70008050	708050	808050	4.84	4.84
80008050	808050	908050	0.98	0.98
10008060	108060	208060	8.65	7.63
20008060	208060	308060	4.55	3.93
30008060	308060	408060	4.55	3.93
40008060	408060	508060	4.55	3.93
50008060	508060	608060	4.84	4.84
60008060	608060	708060	4.84	4.84
70008060	708060	808060	4.84	4.84
80008060	808060	908060	0.98	0.98
10008070	108070	208070	8.65	7.63
20008070	208070	308070	4.55	3.93
30008070	308070	408070	4.55	3.93
40008070	408070	508070	4.55	3.93
50008070	508070	608070	4.84	4.84
60008070	608070	708070	4.84	4.84
70008070	708070	808070	4.84	4.84

Table I-4 (continued)

Element No	Connecting Nodes		Area moment of inertia about axis (m^4)	
	Node 1	Node 2	Y	X
80008070	808070	908070	0.98	0.98
10008080	108080	208080	8.65	7.63
20008080	208080	308080	4.55	3.93
30008080	308080	408080	4.55	3.93
40008080	408080	508080	4.55	3.93
50008080	508080	608080	4.84	4.84
60008080	608080	708080	4.84	4.84
70008080	708080	808080	4.84	4.84
80008080	808080	908080	0.98	0.98
10008090	108090	208090	8.65	7.63
20008090	208090	308090	4.55	3.93
30008090	308090	408090	4.55	3.93
40008090	408090	508090	4.55	3.93
50008090	508090	608090	4.84	4.84
60008090	608090	708090	4.84	4.84
70008090	708090	808090	4.84	4.84
80008090	808090	908090	0.98	0.98
10008100	108100	208100	8.65	7.63
20008100	208100	308100	4.55	3.93
30008100	308100	408100	4.55	3.93
40008100	408100	508100	4.55	3.93
50008100	508100	608100	4.84	4.84
60008100	608100	708100	4.84	4.84
70008100	708100	808100	4.84	4.84
80008100	808100	908100	0.98	0.98
10008110	108110	208110	8.65	7.63
20008110	208110	308110	4.55	3.93
30008110	308110	408110	4.55	3.93
40008110	408110	508110	4.55	3.93
50008110	508110	608110	4.84	4.84
60008110	608110	708110	4.84	4.84
70008110	708110	808110	4.84	4.84
80008110	808110	908110	0.98	0.98
10009010	109010	209010	8.65	7.63
20009010	209010	309010	4.55	3.93
30009010	309010	409010	4.55	3.93
40009010	409010	509010	4.55	3.93
50009010	509010	609010	4.84	4.84
60009010	609010	709010	4.84	4.84
70009010	709010	809010	4.84	4.84
80009010	809010	909010	0.98	0.98
10009020	109020	209020	8.65	7.63
20009020	209020	309020	4.55	3.93
30009020	309020	409020	4.55	3.93
40009020	409020	509020	4.55	3.93

Table I-4 (continued)

Element No	Connecting Nodes		Area moment of inertia about axis (m^4)	
	Node 1	Node 2	Y	X
50009020	509020	609020	4.84	4.84
60009020	609020	709020	4.84	4.84
70009020	709020	809020	4.84	4.84
80009020	809020	909020	0.98	0.98
10009030	109030	209030	8.65	7.63
20009030	209030	309030	4.55	3.93
30009030	309030	409030	4.55	3.93
40009030	409030	509030	4.55	3.93
50009030	509030	609030	4.84	4.84
60009030	609030	709030	4.84	4.84
70009030	709030	809030	4.84	4.84
80009030	809030	909030	0.98	0.98
10009040	109040	209040	8.65	7.63
20009040	209040	309040	4.55	3.93
30009040	309040	409040	4.55	3.93
40009040	409040	509040	4.55	3.93
50009040	509040	609040	4.84	4.84
60009040	609040	709040	4.84	4.84
70009040	709040	809040	4.84	4.84
80009040	809040	909040	0.98	0.98
10009050	109050	209050	8.65	7.63
20009050	209050	309050	4.55	3.93
30009050	309050	409050	4.55	3.93
40009050	409050	509050	4.55	3.93
50009050	509050	609050	4.84	4.84
60009050	609050	709050	4.84	4.84
70009050	709050	809050	4.84	4.84
80009050	809050	909050	0.98	0.98
10009060	109060	209060	8.65	7.63
20009060	209060	309060	4.55	3.93
30009060	309060	409060	4.55	3.93
40009060	409060	509060	4.55	3.93
50009060	509060	609060	4.84	4.84
60009060	609060	709060	4.84	4.84
70009060	709060	809060	4.84	4.84
80009060	809060	909060	0.98	0.98
10009070	109070	209070	8.65	7.63
20009070	209070	309070	4.55	3.93
30009070	309070	409070	4.55	3.93
40009070	409070	509070	4.55	3.93
50009070	509070	609070	4.84	4.84
60009070	609070	709070	4.84	4.84
70009070	709070	809070	4.84	4.84
80009070	809070	909070	0.98	0.98
10009080	109080	209080	8.65	7.63

Table I-4 (continued)

Element No	Connecting Nodes		Area moment of inertia about axis (m^4)	
	Node 1	Node 2	Y	X
20009080	209080	309080	4.55	3.93
30009080	309080	409080	4.55	3.93
40009080	409080	509080	4.55	3.93
50009080	509080	609080	4.84	4.84
60009080	609080	709080	4.84	4.84
70009080	709080	809080	4.84	4.84
80009080	809080	909080	0.98	0.98
10009090	109090	209090	8.65	7.63
20009090	209090	309090	4.55	3.93
30009090	309090	409090	4.55	3.93
40009090	409090	509090	4.55	3.93
50009090	509090	609090	4.84	4.84
60009090	609090	709090	4.84	4.84
70009090	709090	809090	4.84	4.84
80009090	809090	909090	0.98	0.98
10009100	109100	209100	8.65	7.63
20009100	209100	309100	4.55	3.93
30009100	309100	409100	4.55	3.93
40009100	409100	509100	4.55	3.93
50009100	509100	609100	4.84	4.84
60009100	609100	709100	4.84	4.84
70009100	709100	809100	4.84	4.84
80009100	809100	909100	0.98	0.98
10009110	109110	209110	8.65	7.63
20009110	209110	309110	4.55	3.93
30009110	309110	409110	4.55	3.93
40009110	409110	509110	4.55	3.93
50009110	509110	609110	4.84	4.84
60009110	609110	709110	4.84	4.84
70009110	709110	809110	4.84	4.84
80009110	809110	909110	0.98	0.98
10010010	110010	210010	8.65	7.63
20010010	210010	310010	4.55	3.93
30010010	310010	410010	4.55	3.93
40010010	410010	510010	4.55	3.93
50010010	510010	610010	4.84	4.84
60010010	610010	710010	4.84	4.84
70010010	710010	810010	4.84	4.84
80010010	810010	910010	0.98	0.98
10010020	110020	210020	8.65	7.63
20010020	210020	310020	4.55	3.93
30010020	310020	410020	4.55	3.93
40010020	410020	510020	4.55	3.93
50010020	510020	610020	4.84	4.84
60010020	610020	710020	4.84	4.84

Table I-4 (continued)

Element No	Connecting Nodes		Area moment of inertia about axis (m^4)	
	Node 1	Node 2	Y	X
70010020	710020	810020	4.84	4.84
80010020	810020	910020	0.98	0.98
10010030	110030	210030	8.65	7.63
20010030	210030	310030	4.55	3.93
30010030	310030	410030	4.55	3.93
40010030	410030	510030	4.55	3.93
50010030	510030	610030	4.84	4.84
60010030	610030	710030	4.84	4.84
70010030	710030	810030	4.84	4.84
80010030	810030	910030	0.98	0.98
10010040	110040	210040	8.65	7.63
20010040	210040	310040	4.55	3.93
30010040	310040	410040	4.55	3.93
40010040	410040	510040	4.55	3.93
50010040	510040	610040	4.84	4.84
60010040	610040	710040	4.84	4.84
70010040	710040	810040	4.84	4.84
80010040	810040	910040	0.98	0.98
10010050	110050	210050	8.65	7.63
20010050	210050	310050	4.55	3.93
30010050	310050	410050	4.55	3.93
40010050	410050	510050	4.55	3.93
50010050	510050	610050	4.84	4.84
60010050	610050	710050	4.84	4.84
70010050	710050	810050	4.84	4.84
80010050	810050	910050	0.98	0.98
10010060	110060	210060	8.65	7.63
20010060	210060	310060	4.55	3.93
30010060	310060	410060	4.55	3.93
40010060	410060	510060	4.55	3.93
50010060	510060	610060	4.84	4.84
60010060	610060	710060	4.84	4.84
70010060	710060	810060	4.84	4.84
80010060	810060	910060	0.98	0.98
10010070	110070	210070	8.65	7.63
20010070	210070	310070	4.55	3.93
30010070	310070	410070	4.55	3.93
40010070	410070	510070	4.55	3.93
50010070	510070	610070	4.84	4.84
60010070	610070	710070	4.84	4.84
70010070	710070	810070	4.84	4.84
80010070	810070	910070	0.98	0.98
10010080	110080	210080	8.65	7.63
20010080	210080	310080	4.55	3.93
30010080	310080	410080	4.55	3.93

Table I-4 (continued)

Element No	Connecting Nodes		Area moment of inertia about axis (m^4)	
	Node 1	Node 2	Y	X
40010080	410080	510080	4.55	3.93
50010080	510080	610080	4.84	4.84
60010080	610080	710080	4.84	4.84
70010080	710080	810080	4.84	4.84
80010080	810080	910080	0.98	0.98
10010090	110090	210090	8.65	7.63
20010090	210090	310090	4.55	3.93
30010090	310090	410090	4.55	3.93
40010090	410090	510090	4.55	3.93
50010090	510090	610090	4.84	4.84
60010090	610090	710090	4.84	4.84
70010090	710090	810090	4.84	4.84
80010090	810090	910090	0.98	0.98
10010100	110100	210100	8.65	7.63
20010100	210100	310100	4.55	3.93
30010100	310100	410100	4.55	3.93
40010100	410100	510100	4.55	3.93
50010100	510100	610100	4.84	4.84
60010100	610100	710100	4.84	4.84
70010100	710100	810100	4.84	4.84
80010100	810100	910100	0.98	0.98
10010110	110110	210110	8.65	7.63
20010110	210110	310110	4.55	3.93
30010110	310110	410110	4.55	3.93
40010110	410110	510110	4.55	3.93
50010110	510110	610110	4.84	4.84
60010110	610110	710110	4.84	4.84
70010110	710110	810110	4.84	4.84
80010110	810110	910110	0.98	0.98
10011010	111010	211010	8.65	7.63
20011010	211010	311010	4.55	3.93
30011010	311010	411010	4.55	3.93
40011010	411010	511010	4.55	3.93
50011010	511010	611010	4.84	4.84
60011010	611010	711010	4.84	4.84
70011010	711010	811010	4.84	4.84
80011010	811010	911010	0.98	0.98
10011020	111020	211020	8.65	7.63
20011020	211020	311020	4.55	3.93
30011020	311020	411020	4.55	3.93
40011020	411020	511020	4.55	3.93
50011020	511020	611020	4.84	4.84
60011020	611020	711020	4.84	4.84
70011020	711020	811020	4.84	4.84
80011020	811020	911020	0.98	0.98

Table I-4 (continued)

Element No	Connecting Nodes		Area moment of inertia about axis (m^4)	
	Node 1	Node 2	Y	X
10011030	111030	211030	8.65	7.63
20011030	211030	311030	4.55	3.93
30011030	311030	411030	4.55	3.93
40011030	411030	511030	4.55	3.93
50011030	511030	611030	4.84	4.84
60011030	611030	711030	4.84	4.84
70011030	711030	811030	4.84	4.84
80011030	811030	911030	0.98	0.98
10011040	111040	211040	8.65	7.63
20011040	211040	311040	4.55	3.93
30011040	311040	411040	4.55	3.93
40011040	411040	511040	4.55	3.93
50011040	511040	611040	4.84	4.84
60011040	611040	711040	4.84	4.84
70011040	711040	811040	4.84	4.84
80011040	811040	911040	0.98	0.98
10011050	111050	211050	8.65	7.63
20011050	211050	311050	4.55	3.93
30011050	311050	411050	4.55	3.93
40011050	411050	511050	4.55	3.93
50011050	511050	611050	4.84	4.84
60011050	611050	711050	4.84	4.84
70011050	711050	811050	4.84	4.84
80011050	811050	911050	0.98	0.98
10011060	111060	211060	8.65	7.63
20011060	211060	311060	4.55	3.93
30011060	311060	411060	4.55	3.93
40011060	411060	511060	4.55	3.93
50011060	511060	611060	4.84	4.84
60011060	611060	711060	4.84	4.84
70011060	711060	811060	4.84	4.84
80011060	811060	911060	0.98	0.98
10011070	111070	211070	8.65	7.63
20011070	211070	311070	4.55	3.93
30011070	311070	411070	4.55	3.93
40011070	411070	511070	4.55	3.93
50011070	511070	611070	4.84	4.84
60011070	611070	711070	4.84	4.84
70011070	711070	811070	4.84	4.84
80011070	811070	911070	0.98	0.98
10011080	111080	211080	8.65	7.63
20011080	211080	311080	4.55	3.93
30011080	311080	411080	4.55	3.93
40011080	411080	511080	4.55	3.93
50011080	511080	611080	4.84	4.84

Table I-4 (continued)

Element No	Connecting Nodes		Area moment of inertia about axis (m^4)	
	Node 1	Node 2	Y	X
60011080	611080	711080	4.84	4.84
70011080	711080	811080	4.84	4.84
80011080	811080	911080	0.98	0.98
10011090	111090	211090	8.65	7.63
20011090	211090	311090	4.55	3.93
30011090	311090	411090	4.55	3.93
40011090	411090	511090	4.55	3.93
50011090	511090	611090	4.84	4.84
60011090	611090	711090	4.84	4.84
70011090	711090	811090	4.84	4.84
80011090	811090	911090	0.98	0.98
10011100	111100	211100	8.65	7.63
20011100	211100	311100	4.55	3.93
30011100	311100	411100	4.55	3.93
40011100	411100	511100	4.55	3.93
50011100	511100	611100	4.84	4.84
60011100	611100	711100	4.84	4.84
70011100	711100	811100	4.84	4.84
80011100	811100	911100	0.98	0.98
10011110	111110	211110	8.65	7.63
20011110	211110	311110	4.55	3.93
30011110	311110	411110	4.55	3.93
40011110	411110	511110	4.55	3.93
50011110	511110	611110	4.84	4.84
60011110	611110	711110	4.84	4.84
70011110	711110	811110	4.84	4.84
80011110	811110	911110	0.98	0.98
10012010	112010	212010	8.65	7.63
20012010	212010	312010	4.55	3.93
30012010	312010	412010	4.55	3.93
40012010	412010	512010	4.55	3.93
50012010	512010	612010	4.84	4.84
60012010	612010	712010	4.84	4.84
70012010	712010	812010	4.84	4.84
80012010	812010	912010	0.98	0.98
10012020	112020	212020	8.65	7.63
20012020	212020	312020	4.55	3.93
30012020	312020	412020	4.55	3.93
40012020	412020	512020	4.55	3.93
50012020	512020	612020	4.84	4.84
60012020	612020	712020	4.84	4.84
70012020	712020	812020	4.84	4.84
80012020	812020	912020	0.98	0.98
10012030	112030	212030	8.65	7.63
20012030	212030	312030	4.55	3.93

Table I-4 (continued)

Element No	Connecting Nodes		Area moment of inertia about axis (m^4)	
	Node 1	Node 2	Y	X
30012030	312030	412030	4.55	3.93
40012030	412030	512030	4.55	3.93
50012030	512030	612030	4.84	4.84
60012030	612030	712030	4.84	4.84
70012030	712030	812030	4.84	4.84
80012030	812030	912030	0.98	0.98
10012040	112040	212040	8.65	7.63
20012040	212040	312040	4.55	3.93
30012040	312040	412040	4.55	3.93
40012040	412040	512040	4.55	3.93
50012040	512040	612040	4.84	4.84
60012040	612040	712040	4.84	4.84
70012040	712040	812040	4.84	4.84
80012040	812040	912040	0.98	0.98
10012050	112050	212050	8.65	7.63
20012050	212050	312050	4.55	3.93
30012050	312050	412050	4.55	3.93
40012050	412050	512050	4.55	3.93
50012050	512050	612050	4.84	4.84
60012050	612050	712050	4.84	4.84
70012050	712050	812050	4.84	4.84
80012050	812050	912050	0.98	0.98
10012060	112060	212060	8.65	7.63
20012060	212060	312060	4.55	3.93
30012060	312060	412060	4.55	3.93
40012060	412060	512060	4.55	3.93
50012060	512060	612060	4.84	4.84
60012060	612060	712060	4.84	4.84
70012060	712060	812060	4.84	4.84
80012060	812060	912060	0.98	0.98
10012070	112070	212070	8.65	7.63
20012070	212070	312070	4.55	3.93
30012070	312070	412070	4.55	3.93
40012070	412070	512070	4.55	3.93
50012070	512070	612070	4.84	4.84
60012070	612070	712070	4.84	4.84
70012070	712070	812070	4.84	4.84
80012070	812070	912070	0.98	0.98
10012080	112080	212080	8.65	7.63
20012080	212080	312080	4.55	3.93
30012080	312080	412080	4.55	3.93
40012080	412080	512080	4.55	3.93
50012080	512080	612080	4.84	4.84
60012080	612080	712080	4.84	4.84
70012080	712080	812080	4.84	4.84

Table I-4 (continued)

Element No	Connecting Nodes		Area moment of inertia about axis (m^4)	
	Node 1	Node 2	Y	X
80012080	812080	912080	0.98	0.98
10012090	112090	212090	8.65	7.63
20012090	212090	312090	4.55	3.93
30012090	312090	412090	4.55	3.93
40012090	412090	512090	4.55	3.93
50012090	512090	612090	4.84	4.84
60012090	612090	712090	4.84	4.84
70012090	712090	812090	4.84	4.84
80012090	812090	912090	0.98	0.98
10012100	112100	212100	8.65	7.63
20012100	212100	312100	4.55	3.93
30012100	312100	412100	4.55	3.93
40012100	412100	512100	4.55	3.93
50012100	512100	612100	4.84	4.84
60012100	612100	712100	4.84	4.84
70012100	712100	812100	4.84	4.84
80012100	812100	912100	0.98	0.98
10012110	112110	212110	8.65	7.63
20012110	212110	312110	4.55	3.93
30012110	312110	412110	4.55	3.93
40012110	412110	512110	4.55	3.93
50012110	512110	612110	4.84	4.84
60012110	612110	712110	4.84	4.84
70012110	712110	812110	4.84	4.84
80012110	812110	912110	0.98	0.98
10013010	113010	213010	8.65	7.63
20013010	213010	313010	4.55	3.93
30013010	313010	413010	4.55	3.93
40013010	413010	513010	4.55	3.93
50013010	513010	613010	4.84	4.84
60013010	613010	713010	4.84	4.84
70013010	713010	813010	4.84	4.84
80013010	813010	913010	0.98	0.98
10013020	113020	213020	8.65	7.63
20013020	213020	313020	4.55	3.93
30013020	313020	413020	4.55	3.93
40013020	413020	513020	4.55	3.93
50013020	513020	613020	4.84	4.84
60013020	613020	713020	4.84	4.84
70013020	713020	813020	4.84	4.84
80013020	813020	913020	0.98	0.98
10013030	113030	213030	8.65	7.63
20013030	213030	313030	4.55	3.93
30013030	313030	413030	4.55	3.93
40013030	413030	513030	4.55	3.93

Table I-4 (continued)

Element No	Connecting Nodes		Area moment of inertia about axis (m^4)	
	Node 1	Node 2	Y	X
50013030	513030	613030	4.84	4.84
60013030	613030	713030	4.84	4.84
70013030	713030	813030	4.84	4.84
80013030	813030	913030	0.98	0.98
10013040	113040	213040	8.65	7.63
20013040	213040	313040	4.55	3.93
30013040	313040	413040	4.55	3.93
40013040	413040	513040	4.55	3.93
50013040	513040	613040	4.84	4.84
60013040	613040	713040	4.84	4.84
70013040	713040	813040	4.84	4.84
80013040	813040	913040	0.98	0.98
10013050	113050	213050	8.65	7.63
20013050	213050	313050	4.55	3.93
30013050	313050	413050	4.55	3.93
40013050	413050	513050	4.55	3.93
50013050	513050	613050	4.84	4.84
60013050	613050	713050	4.84	4.84
70013050	713050	813050	4.84	4.84
80013050	813050	913050	0.98	0.98
10013060	113060	213060	8.65	7.63
20013060	213060	313060	4.55	3.93
30013060	313060	413060	4.55	3.93
40013060	413060	513060	4.55	3.93
50013060	513060	613060	4.84	4.84
60013060	613060	713060	4.84	4.84
70013060	713060	813060	4.84	4.84
80013060	813060	913060	0.98	0.98
10013070	113070	213070	8.65	7.63
20013070	213070	313070	4.55	3.93
30013070	313070	413070	4.55	3.93
40013070	413070	513070	4.55	3.93
50013070	513070	613070	4.84	4.84
60013070	613070	713070	4.84	4.84
70013070	713070	813070	4.84	4.84
80013070	813070	913070	0.98	0.98
10013080	113080	213080	8.65	7.63
20013080	213080	313080	4.55	3.93
30013080	313080	413080	4.55	3.93
40013080	413080	513080	4.55	3.93
50013080	513080	613080	4.84	4.84
60013080	613080	713080	4.84	4.84
70013080	713080	813080	4.84	4.84
80013080	813080	913080	0.98	0.98
10013090	113090	213090	8.65	7.63

Table I-4 (continued)

Element No	Connecting Nodes		Area moment of inertia about axis (m^4)	
	Node 1	Node 2	Y	X
20013090	213090	313090	4.55	3.93
30013090	313090	413090	4.55	3.93
40013090	413090	513090	4.55	3.93
50013090	513090	613090	4.84	4.84
60013090	613090	713090	4.84	4.84
70013090	713090	813090	4.84	4.84
80013090	813090	913090	0.98	0.98
10013100	113100	213100	8.65	7.63
20013100	213100	313100	4.55	3.93
30013100	313100	413100	4.55	3.93
40013100	413100	513100	4.55	3.93
50013100	513100	613100	4.84	4.84
60013100	613100	713100	4.84	4.84
70013100	713100	813100	4.84	4.84
80013100	813100	913100	0.98	0.98
10013110	113110	213110	8.65	7.63
20013110	213110	313110	4.55	3.93
30013110	313110	413110	4.55	3.93
40013110	413110	513110	4.55	3.93
50013110	513110	613110	4.84	4.84
60013110	613110	713110	4.84	4.84
70013110	713110	813110	4.84	4.84
80013110	813110	913110	0.98	0.98
10014010	114010	214010	7.27	5.44
20014010	214010	314010	4.40	3.29
30014010	314010	414010	4.40	3.29
40014010	414010	514010	4.40	3.29
10014020	114020	214020	7.27	5.44
20014020	214020	314020	4.40	3.29
30014020	314020	414020	4.40	3.29
40014020	414020	514020	4.40	3.29
10014030	114030	214030	7.27	5.44
20014030	214030	314030	4.40	3.29
30014030	314030	414030	4.40	3.29
40014030	414030	514030	4.40	3.29
10014040	114040	214040	7.27	5.44
20014040	214040	314040	4.40	3.29
30014040	314040	414040	4.40	3.29
40014040	414040	514040	4.40	3.29
10014050	114050	214050	7.27	5.44
20014050	214050	314050	4.40	3.29
30014050	314050	414050	4.40	3.29
40014050	414050	514050	4.40	3.29
10014060	114060	214060	7.27	5.44
20014060	214060	314060	4.40	3.29

Table I-4 (continued)

Element No	Connecting Nodes		Area moment of inertia about axis (m^4)	
	Node 1	Node 2	Y	X
30014060	314060	414060	4.40	3.29
40014060	414060	514060	4.40	3.29
10014070	114070	214070	7.27	5.44
20014070	214070	314070	4.40	3.29
30014070	314070	414070	4.40	3.29
40014070	414070	514070	4.40	3.29
10014080	114080	214080	7.27	5.44
20014080	214080	314080	4.40	3.29
30014080	314080	414080	4.40	3.29
40014080	414080	514080	4.40	3.29
10014090	114090	214090	7.27	5.44
20014090	214090	314090	4.40	3.29
30014090	314090	414090	4.40	3.29
40014090	414090	514090	4.40	3.29
10014100	114100	214100	7.27	5.44
20014100	214100	314100	4.40	3.29
30014100	314100	414100	4.40	3.29
40014100	414100	514100	4.40	3.29
10014110	114110	214110	7.27	5.44
20014110	214110	314110	4.40	3.29
30014110	314110	414110	4.40	3.29
40014110	414110	514110	4.40	3.29
10015010	115010	215010	7.27	5.44
20015010	215010	315010	4.40	3.29
30015010	315010	415010	4.40	3.29
40015010	415010	515010	4.40	3.29
10015020	115020	215020	7.27	5.44
20015020	215020	315020	4.40	3.29
30015020	315020	415020	4.40	3.29
40015020	415020	515020	4.40	3.29
10015030	115030	215030	7.27	5.44
20015030	215030	315030	4.40	3.29
30015030	315030	415030	4.40	3.29
40015030	415030	515030	4.40	3.29
10015040	115040	215040	7.27	5.44
20015040	215040	315040	4.40	3.29
30015040	315040	415040	4.40	3.29
40015040	415040	515040	4.40	3.29
10015050	115050	215050	7.27	5.44
20015050	215050	315050	4.40	3.29
30015050	315050	415050	4.40	3.29
40015050	415050	515050	4.40	3.29
10015060	115060	215060	7.27	5.44
20015060	215060	315060	4.40	3.29
30015060	315060	415060	4.40	3.29

Table I-4 (continued)

Element No	Connecting Nodes		Area moment of inertia about axis (m^4)	
	Node 1	Node 2	Y	X
40015060	415060	515060	4.40	3.29
10015070	115070	215070	7.27	5.44
20015070	215070	315070	4.40	3.29
30015070	315070	415070	4.40	3.29
40015070	415070	515070	4.40	3.29
10015080	115080	215080	7.27	5.44
20015080	215080	315080	4.40	3.29
30015080	315080	415080	4.40	3.29
40015080	415080	515080	4.40	3.29
10015090	115090	215090	7.27	5.44
20015090	215090	315090	4.40	3.29
30015090	315090	415090	4.40	3.29
40015090	415090	515090	4.40	3.29
10015100	115100	215100	7.27	5.44
20015100	215100	315100	4.40	3.29
30015100	315100	415100	4.40	3.29
40015100	415100	515100	4.40	3.29
10015110	115110	215110	7.27	5.44
20015110	215110	315110	4.40	3.29
30015110	315110	415110	4.40	3.29
40015110	415110	515110	4.40	3.29
10016010	116010	216010	7.27	5.44
20016010	216010	316010	4.40	3.29
30016010	316010	416010	4.40	3.29
40016010	416010	516010	4.40	3.29
10016020	116020	216020	7.27	5.44
20016020	216020	316020	4.40	3.29
30016020	316020	416020	4.40	3.29
40016020	416020	516020	4.40	3.29
10016030	116030	216030	7.27	5.44
20016030	216030	316030	4.40	3.29
30016030	316030	416030	4.40	3.29
40016030	416030	516030	4.40	3.29
10016040	116040	216040	7.27	5.44
20016040	216040	316040	4.40	3.29
30016040	316040	416040	4.40	3.29
40016040	416040	516040	4.40	3.29
10016050	116050	216050	7.27	5.44
20016050	216050	316050	4.40	3.29
30016050	316050	416050	4.40	3.29
40016050	416050	516050	4.40	3.29
10016060	116060	216060	7.27	5.44
20016060	216060	316060	4.40	3.29
30016060	316060	416060	4.40	3.29
40016060	416060	516060	4.40	3.29

Table I-4 (continued)

Element No	Connecting Nodes		Area moment of inertia about axis (m^4)	
	Node 1	Node 2	Y	X
10016070	116070	216070	7.27	5.44
20016070	216070	316070	4.40	3.29
30016070	316070	416070	4.40	3.29
40016070	416070	516070	4.40	3.29
10016080	116080	216080	7.27	5.44
20016080	216080	316080	4.40	3.29
30016080	316080	416080	4.40	3.29
40016080	416080	516080	4.40	3.29
10016090	116090	216090	7.27	5.44
20016090	216090	316090	4.40	3.29
30016090	316090	416090	4.40	3.29
40016090	416090	516090	4.40	3.29
10016100	116100	216100	7.27	5.44
20016100	216100	316100	4.40	3.29
30016100	316100	416100	4.40	3.29
40016100	416100	516100	4.40	3.29
10016110	116110	216110	7.27	5.44
20016110	216110	316110	4.40	3.29
30016110	316110	416110	4.40	3.29
40016110	416110	516110	4.40	3.29
10017010	117010	217010	7.27	5.44
20017010	217010	317010	4.40	3.29
30017010	317010	417010	4.40	3.29
40017010	417010	517010	4.40	3.29
10017020	117020	217020	7.27	5.44
20017020	217020	317020	4.40	3.29
30017020	317020	417020	4.40	3.29
40017020	417020	517020	4.40	3.29
10017030	117030	217030	7.27	5.44
20017030	217030	317030	4.40	3.29
30017030	317030	417030	4.40	3.29
40017030	417030	517030	4.40	3.29
10017040	117040	217040	7.27	5.44
20017040	217040	317040	4.40	3.29
30017040	317040	417040	4.40	3.29
40017040	417040	517040	4.40	3.29
10017050	117050	217050	7.27	5.44
20017050	217050	317050	4.40	3.29
30017050	317050	417050	4.40	3.29
40017050	417050	517050	4.40	3.29
10017060	117060	217060	7.27	5.44
20017060	217060	317060	4.40	3.29
30017060	317060	417060	4.40	3.29
40017060	417060	517060	4.40	3.29
10017070	117070	217070	7.27	5.44

Table I-4 (continued)

Element No	Connecting Nodes		Area moment of inertia about axis (m^4)	
	Node 1	Node 2	Y	X
20017070	217070	317070	4.40	3.29
30017070	317070	417070	4.40	3.29
40017070	417070	517070	4.40	3.29
10017080	117080	217080	7.27	5.44
20017080	217080	317080	4.40	3.29
30017080	317080	417080	4.40	3.29
40017080	417080	517080	4.40	3.29
10017090	117090	217090	7.27	5.44
20017090	217090	317090	4.40	3.29
30017090	317090	417090	4.40	3.29
40017090	417090	517090	4.40	3.29
10017100	117100	217100	7.27	5.44
20017100	217100	317100	4.40	3.29
30017100	317100	417100	4.40	3.29
40017100	417100	517100	4.40	3.29
10017110	117110	217110	7.27	5.44
20017110	217110	317110	4.40	3.29
30017110	317110	417110	4.40	3.29
40017110	417110	517110	4.40	3.29

MCEER Technical Reports

MCEER publishes technical reports on a variety of subjects written by authors funded through MCEER. These reports are available from both MCEER Publications and the National Technical Information Service (NTIS). Requests for reports should be directed to MCEER Publications, MCEER, University at Buffalo, State University of New York, 212 Ketter Hall, Buffalo, New York 14260. Reports can also be requested through NTIS, P.O. Box 1425, Springfield, Virginia 22151. NTIS accession numbers are shown in parenthesis, if available.

NCEER-87-0001 "First-Year Program in Research, Education and Technology Transfer," 3/5/87, (PB88-134275, A04, MF-A01).

NCEER-87-0002 "Experimental Evaluation of Instantaneous Optimal Algorithms for Structural Control," by R.C. Lin, T.T. Soong and A.M. Reinhorn, 4/20/87, (PB88-134341, A04, MF-A01).

NCEER-87-0003 "Experimentation Using the Earthquake Simulation Facilities at University at Buffalo," by A.M. Reinhorn and R.L. Ketter, not available.

NCEER-87-0004 "The System Characteristics and Performance of a Shaking Table," by J.S. Hwang, K.C. Chang and G.C. Lee, 6/1/87, (PB88-134259, A03, MF-A01). This report is available only through NTIS (see address given above).

NCEER-87-0005 "A Finite Element Formulation for Nonlinear Viscoplastic Material Using a Q Model," by O. Gyebi and G. Dasgupta, 11/2/87, (PB88-213764, A08, MF-A01).

NCEER-87-0006 "Symbolic Manipulation Program (SMP) - Algebraic Codes for Two and Three Dimensional Finite Element Formulations," by X. Lee and G. Dasgupta, 11/9/87, (PB88-218522, A05, MF-A01).

NCEER-87-0007 "Instantaneous Optimal Control Laws for Tall Buildings Under Seismic Excitations," by J.N. Yang, A. Akbarpour and P. Ghaemmaghami, 6/10/87, (PB88-134333, A06, MF-A01). This report is only available through NTIS (see address given above).

NCEER-87-0008 "IDARC: Inelastic Damage Analysis of Reinforced Concrete Frame - Shear-Wall Structures," by Y.J. Park, A.M. Reinhorn and S.K. Kunnath, 7/20/87, (PB88-134325, A09, MF-A01). This report is only available through NTIS (see address given above).

NCEER-87-0009 "Liquefaction Potential for New York State: A Preliminary Report on Sites in Manhattan and Buffalo," by M. Budhu, V. Vijayakumar, R.F. Giese and L. Baumgras, 8/31/87, (PB88-163704, A03, MF-A01). This report is available only through NTIS (see address given above).

NCEER-87-0010 "Vertical and Torsional Vibration of Foundations in Inhomogeneous Media," by A.S. Veletsos and K.W. Dotson, 6/1/87, (PB88-134291, A03, MF-A01). This report is only available through NTIS (see address given above).

NCEER-87-0011 "Seismic Probabilistic Risk Assessment and Seismic Margins Studies for Nuclear Power Plants," by Howard H.M. Hwang, 6/15/87, (PB88-134267, A03, MF-A01). This report is only available through NTIS (see address given above).

NCEER-87-0012 "Parametric Studies of Frequency Response of Secondary Systems Under Ground-Acceleration Excitations," by Y. Yong and Y.K. Lin, 6/10/87, (PB88-134309, A03, MF-A01). This report is only available through NTIS (see address given above).

NCEER-87-0013 "Frequency Response of Secondary Systems Under Seismic Excitation," by J.A. HoLung, J. Cai and Y.K. Lin, 7/31/87, (PB88-134317, A05, MF-A01). This report is only available through NTIS (see address given above).

NCEER-87-0014 "Modelling Earthquake Ground Motions in Seismically Active Regions Using Parametric Time Series Methods," by G.W. Ellis and A.S. Cakmak, 8/25/87, (PB88-134283, A08, MF-A01). This report is only available through NTIS (see address given above).

NCEER-87-0015 "Detection and Assessment of Seismic Structural Damage," by E. DiPasquale and A.S. Cakmak, 8/25/87, (PB88-163712, A05, MF-A01). This report is only available through NTIS (see address given above).

NCEER-87-0016 "Pipeline Experiment at Parkfield, California," by J. Isenberg and E. Richardson, 9/15/87, (PB88-163720, A03, MF-A01). This report is available only through NTIS (see address given above).

NCEER-87-0017 "Digital Simulation of Seismic Ground Motion," by M. Shinozuka, G. Deodatis and T. Harada, 8/31/87, (PB88-155197, A04, MF-A01). This report is available only through NTIS (see address given above).

NCEER-87-0018 "Practical Considerations for Structural Control: System Uncertainty, System Time Delay and Truncation of Small Control Forces," J.N. Yang and A. Akbarpour, 8/10/87, (PB88-163738, A08, MF-A01). This report is only available through NTIS (see address given above).

NCEER-87-0019 "Modal Analysis of Nonclassically Damped Structural Systems Using Canonical Transformation," by J.N. Yang, S. Sarkani and F.X. Long, 9/27/87, (PB88-187851, A04, MF-A01).

NCEER-87-0020 "A Nonstationary Solution in Random Vibration Theory," by J.R. Red-Horse and P.D. Spanos, 11/3/87, (PB88-163746, A03, MF-A01).

NCEER-87-0021 "Horizontal Impedances for Radially Inhomogeneous Viscoelastic Soil Layers," by A.S. Veletsos and K.W. Dotson, 10/15/87, (PB88-150859, A04, MF-A01).

NCEER-87-0022 "Seismic Damage Assessment of Reinforced Concrete Members," by Y.S. Chung, C. Meyer and M. Shinozuka, 10/9/87, (PB88-150867, A05, MF-A01). This report is available only through NTIS (see address given above).

NCEER-87-0023 "Active Structural Control in Civil Engineering," by T.T. Soong, 11/11/87, (PB88-187778, A03, MF-A01).

NCEER-87-0024 "Vertical and Torsional Impedances for Radially Inhomogeneous Viscoelastic Soil Layers," by K.W. Dotson and A.S. Veletsos, 12/87, (PB88-187786, A03, MF-A01).

NCEER-87-0025 "Proceedings from the Symposium on Seismic Hazards, Ground Motions, Soil-Liquefaction and Engineering Practice in Eastern North America," October 20-22, 1987, edited by K.H. Jacob, 12/87, (PB88-188115, A23, MF-A01). This report is available only through NTIS (see address given above).

NCEER-87-0026 "Report on the Whittier-Narrows, California, Earthquake of October 1, 1987," by J. Pantelic and A. Reinhorn, 11/87, (PB88-187752, A03, MF-A01). This report is available only through NTIS (see address given above).

NCEER-87-0027 "Design of a Modular Program for Transient Nonlinear Analysis of Large 3-D Building Structures," by S. Srivastav and J.F. Abel, 12/30/87, (PB88-187950, A05, MF-A01). This report is only available through NTIS (see address given above).

NCEER-87-0028 "Second-Year Program in Research, Education and Technology Transfer," 3/8/88, (PB88-219480, A04, MF-A01).

NCEER-88-0001 "Workshop on Seismic Computer Analysis and Design of Buildings With Interactive Graphics," by W. McGuire, J.F. Abel and C.H. Conley, 1/18/88, (PB88-187760, A03, MF-A01). This report is only available through NTIS (see address given above).

NCEER-88-0002 "Optimal Control of Nonlinear Flexible Structures," by J.N. Yang, F.X. Long and D. Wong, 1/22/88, (PB88-213772, A06, MF-A01).

NCEER-88-0003 "Substructuring Techniques in the Time Domain for Primary-Secondary Structural Systems," by G.D. Manolis and G. Juhn, 2/10/88, (PB88-213780, A04, MF-A01).

NCEER-88-0004 "Iterative Seismic Analysis of Primary-Secondary Systems," by A. Singhal, L.D. Lutes and P.D. Spanos, 2/23/88, (PB88-213798, A04, MF-A01).

NCEER-88-0005 "Stochastic Finite Element Expansion for Random Media," by P.D. Spanos and R. Ghanem, 3/14/88, (PB88-213806, A03, MF-A01).

NCEER-88-0006 "Combining Structural Optimization and Structural Control," by F.Y. Cheng and C.P. Pantelides, 1/10/88, (PB88-213814, A05, MF-A01).

NCEER-88-0007 "Seismic Performance Assessment of Code-Designed Structures," by H.H-M. Hwang, J-W. Jaw and H-J. Shau, 3/20/88, (PB88-219423, A04, MF-A01). This report is only available through NTIS (see address given above).

NCEER-88-0008 "Reliability Analysis of Code-Designed Structures Under Natural Hazards," by H.H-M. Hwang, H. Ushiba and M. Shinozuka, 2/29/88, (PB88-229471, A07, MF-A01). This report is only available through NTIS (see address given above).

NCEER-88-0009 "Seismic Fragility Analysis of Shear Wall Structures," by J-W Jaw and H.H-M. Hwang, 4/30/88, (PB89-102867, A04, MF-A01).

NCEER-88-0010 "Base Isolation of a Multi-Story Building Under a Harmonic Ground Motion - A Comparison of Performances of Various Systems," by F-G Fan, G. Ahmadi and I.G. Tadjbakhsh, 5/18/88, (PB89-122238, A06, MF-A01). This report is only available through NTIS (see address given above).

NCEER-88-0011 "Seismic Floor Response Spectra for a Combined System by Green's Functions," by F.M. Lavelle, L.A. Bergman and P.D. Spanos, 5/1/88, (PB89-102875, A03, MF-A01).

NCEER-88-0012 "A New Solution Technique for Randomly Excited Hysteretic Structures," by G.Q. Cai and Y.K. Lin, 5/16/88, (PB89-102883, A03, MF-A01).

NCEER-88-0013 "A Study of Radiation Damping and Soil-Structure Interaction Effects in the Centrifuge," by K. Weissman, supervised by J.H. Prevost, 5/24/88, (PB89-144703, A06, MF-A01).

NCEER-88-0014 "Parameter Identification and Implementation of a Kinematic Plasticity Model for Frictional Soils," by J.H. Prevost and D.V. Griffiths, not available.

NCEER-88-0015 "Two- and Three- Dimensional Dynamic Finite Element Analyses of the Long Valley Dam," by D.V. Griffiths and J.H. Prevost, 6/17/88, (PB89-144711, A04, MF-A01).

NCEER-88-0016 "Damage Assessment of Reinforced Concrete Structures in Eastern United States," by A.M. Reinhorn, M.J. Seidel, S.K. Kunnath and Y.J. Park, 6/15/88, (PB89-122220, A04, MF-A01). This report is only available through NTIS (see address given above).

NCEER-88-0017 "Dynamic Compliance of Vertically Loaded Strip Foundations in Multilayered Viscoelastic Soils," by S. Ahmad and A.S.M. Israil, 6/17/88, (PB89-102891, A04, MF-A01).

NCEER-88-0018 "An Experimental Study of Seismic Structural Response With Added Viscoelastic Dampers," by R.C. Lin, Z. Liang, T.T. Soong and R.H. Zhang, 6/30/88, (PB89-122212, A05, MF-A01). This report is available only through NTIS (see address given above).

NCEER-88-0019 "Experimental Investigation of Primary - Secondary System Interaction," by G.D. Manolis, G. Juhn and A.M. Reinhorn, 5/27/88, (PB89-122204, A04, MF-A01).

NCEER-88-0020 "A Response Spectrum Approach For Analysis of Nonclassically Damped Structures," by J.N. Yang, S. Sarkani and F.X. Long, 4/22/88, (PB89-102909, A04, MF-A01).

NCEER-88-0021 "Seismic Interaction of Structures and Soils: Stochastic Approach," by A.S. Veletsos and A.M. Prasad, 7/21/88, (PB89-122196, A04, MF-A01). This report is only available through NTIS (see address given above).

NCEER-88-0022 "Identification of the Serviceability Limit State and Detection of Seismic Structural Damage," by E. DiPasquale and A.S. Cakmak, 6/15/88, (PB89-122188, A05, MF-A01). This report is available only through NTIS (see address given above).

NCEER-88-0023 "Multi-Hazard Risk Analysis: Case of a Simple Offshore Structure," by B.K. Bhartia and E.H. Vanmarcke, 7/21/88, (PB89-145213, A05, MF-A01).

NCEER-88-0024 "Automated Seismic Design of Reinforced Concrete Buildings," by Y.S. Chung, C. Meyer and M. Shinozuka, 7/5/88, (PB89-122170, A06, MF-A01). This report is available only through NTIS (see address given above).

NCEER-88-0025 "Experimental Study of Active Control of MDOF Structures Under Seismic Excitations," by L.L. Chung, R.C. Lin, T.T. Soong and A.M. Reinhorn, 7/10/88, (PB89-122600, A04, MF-A01).

NCEER-88-0026 "Earthquake Simulation Tests of a Low-Rise Metal Structure," by J.S. Hwang, K.C. Chang, G.C. Lee and R.L. Ketter, 8/1/88, (PB89-102917, A04, MF-A01).

NCEER-88-0027 "Systems Study of Urban Response and Reconstruction Due to Catastrophic Earthquakes," by F. Kozin and H.K. Zhou, 9/22/88, (PB90-162348, A04, MF-A01).

NCEER-88-0028 "Seismic Fragility Analysis of Plane Frame Structures," by H.H-M. Hwang and Y.K. Low, 7/31/88, (PB89-131445, A06, MF-A01).

NCEER-88-0029 "Response Analysis of Stochastic Structures," by A. Kardara, C. Bucher and M. Shinozuka, 9/22/88, (PB89-174429, A04, MF-A01).

NCEER-88-0030 "Nonnormal Accelerations Due to Yielding in a Primary Structure," by D.C.K. Chen and L.D. Lutes, 9/19/88, (PB89-131437, A04, MF-A01).

NCEER-88-0031 "Design Approaches for Soil-Structure Interaction," by A.S. Veletsos, A.M. Prasad and Y. Tang, 12/30/88, (PB89-174437, A03, MF-A01). This report is available only through NTIS (see address given above).

NCEER-88-0032 "A Re-evaluation of Design Spectra for Seismic Damage Control," by C.J. Turkstra and A.G. Tallin, 11/7/88, (PB89-145221, A05, MF-A01).

NCEER-88-0033 "The Behavior and Design of Noncontact Lap Splices Subjected to Repeated Inelastic Tensile Loading," by V.E. Sagan, P. Gergely and R.N. White, 12/8/88, (PB89-163737, A08, MF-A01).

NCEER-88-0034 "Seismic Response of Pile Foundations," by S.M. Mamoon, P.K. Banerjee and S. Ahmad, 11/1/88, (PB89-145239, A04, MF-A01).

NCEER-88-0035 "Modeling of R/C Building Structures With Flexible Floor Diaphragms (IDARC2)," by A.M. Reinhorn, S.K. Kunnath and N. Panahshahi, 9/7/88, (PB89-207153, A07, MF-A01).

NCEER-88-0036 "Solution of the Dam-Reservoir Interaction Problem Using a Combination of FEM, BEM with Particular Integrals, Modal Analysis, and Substructuring," by C-S. Tsai, G.C. Lee and R.L. Ketter, 12/31/88, (PB89-207146, A04, MF-A01).

NCEER-88-0037 "Optimal Placement of Actuators for Structural Control," by F.Y. Cheng and C.P. Pantelides, 8/15/88, (PB89-162846, A05, MF-A01).

NCEER-88-0038 "Teflon Bearings in Aseismic Base Isolation: Experimental Studies and Mathematical Modeling," by A. Mokha, M.C. Constantinou and A.M. Reinhorn, 12/5/88, (PB89-218457, A10, MF-A01). This report is available only through NTIS (see address given above).

NCEER-88-0039 "Seismic Behavior of Flat Slab High-Rise Buildings in the New York City Area," by P. Weidlinger and M. Ettouney, 10/15/88, (PB90-145681, A04, MF-A01).

NCEER-88-0040 "Evaluation of the Earthquake Resistance of Existing Buildings in New York City," by P. Weidlinger and M. Ettouney, 10/15/88, not available.

NCEER-88-0041 "Small-Scale Modeling Techniques for Reinforced Concrete Structures Subjected to Seismic Loads," by W. Kim, A. El-Attar and R.N. White, 11/22/88, (PB89-189625, A05, MF-A01).

NCEER-88-0042 "Modeling Strong Ground Motion from Multiple Event Earthquakes," by G.W. Ellis and A.S. Cakmak, 10/15/88, (PB89-174445, A03, MF-A01).

NCEER-88-0043 "Nonstationary Models of Seismic Ground Acceleration," by M. Grigoriu, S.E. Ruiz and E. Rosenblueth, 7/15/88, (PB89-189617, A04, MF-A01).

NCEER-88-0044 "SARCF User's Guide: Seismic Analysis of Reinforced Concrete Frames," by Y.S. Chung, C. Meyer and M. Shinozuka, 11/9/88, (PB89-174452, A08, MF-A01).

NCEER-88-0045 "First Expert Panel Meeting on Disaster Research and Planning," edited by J. Pantelic and J. Stoyle, 9/15/88, (PB89-174460, A05, MF-A01).

NCEER-88-0046 "Preliminary Studies of the Effect of Degrading Infill Walls on the Nonlinear Seismic Response of Steel Frames," by C.Z. Chrysostomou, P. Gergely and J.F. Abel, 12/19/88, (PB89-208383, A05, MF-A01).

NCEER-88-0047 "Reinforced Concrete Frame Component Testing Facility - Design, Construction, Instrumentation and Operation," by S.P. Pessiki, C. Conley, T. Bond, P. Gergely and R.N. White, 12/16/88, (PB89-174478, A04, MF-A01).

NCEER-89-0001 "Effects of Protective Cushion and Soil Compliancy on the Response of Equipment Within a Seismically Excited Building," by J.A. HoLung, 2/16/89, (PB89-207179, A04, MF-A01).

NCEER-89-0002 "Statistical Evaluation of Response Modification Factors for Reinforced Concrete Structures," by H.H-M. Hwang and J-W. Jaw, 2/17/89, (PB89-207187, A05, MF-A01).

NCEER-89-0003 "Hysteretic Columns Under Random Excitation," by G-Q. Cai and Y.K. Lin, 1/9/89, (PB89-196513, A03, MF-A01).

NCEER-89-0004 "Experimental Study of `Elephant Foot Bulge' Instability of Thin-Walled Metal Tanks," by Z-H. Jia and R.L. Ketter, 2/22/89, (PB89-207195, A03, MF-A01).

NCEER-89-0005 "Experiment on Performance of Buried Pipelines Across San Andreas Fault," by J. Isenberg, E. Richardson and T.D. O'Rourke, 3/10/89, (PB89-218440, A04, MF-A01). This report is available only through NTIS (see address given above).

NCEER-89-0006 "A Knowledge-Based Approach to Structural Design of Earthquake-Resistant Buildings," by M. Subramani, P. Gergely, C.H. Conley, J.F. Abel and A.H. Zaghw, 1/15/89, (PB89-218465, A06, MF-A01).

NCEER-89-0007 "Liquefaction Hazards and Their Effects on Buried Pipelines," by T.D. O'Rourke and P.A. Lane, 2/1/89, (PB89-218481, A09, MF-A01).

NCEER-89-0008 "Fundamentals of System Identification in Structural Dynamics," by H. Imai, C-B. Yun, O. Maruyama and M. Shinozuka, 1/26/89, (PB89-207211, A04, MF-A01).

NCEER-89-0009 "Effects of the 1985 Michoacan Earthquake on Water Systems and Other Buried Lifelines in Mexico," by A.G. Ayala and M.J. O'Rourke, 3/8/89, (PB89-207229, A06, MF-A01).

NCEER-89-R010 "NCEER Bibliography of Earthquake Education Materials," by K.E.K. Ross, Second Revision, 9/1/89, (PB90-125352, A05, MF-A01). This report is replaced by NCEER-92-0018.

NCEER-89-0011 "Inelastic Three-Dimensional Response Analysis of Reinforced Concrete Building Structures (IDARC-3D), Part I - Modeling," by S.K. Kunnath and A.M. Reinhorn, 4/17/89, (PB90-114612, A07, MF-A01). This report is available only through NTIS (see address given above).

NCEER-89-0012 "Recommended Modifications to ATC-14," by C.D. Poland and J.O. Malley, 4/12/89, (PB90-108648, A15, MF-A01).

NCEER-89-0013 "Repair and Strengthening of Beam-to-Column Connections Subjected to Earthquake Loading," by M. Corazao and A.J. Durrani, 2/28/89, (PB90-109885, A06, MF-A01).

NCEER-89-0014 "Program EXKAL2 for Identification of Structural Dynamic Systems," by O. Maruyama, C-B. Yun, M. Hoshiya and M. Shinozuka, 5/19/89, (PB90-109877, A09, MF-A01).

NCEER-89-0015 "Response of Frames With Bolted Semi-Rigid Connections, Part I - Experimental Study and Analytical Predictions," by P.J. DiCorso, A.M. Reinhorn, J.R. Dickerson, J.B. Radziminski and W.L. Harper, 6/1/89, not available.

NCEER-89-0016 "ARMA Monte Carlo Simulation in Probabilistic Structural Analysis," by P.D. Spanos and M.P. Mignolet, 7/10/89, (PB90-109893, A03, MF-A01).

NCEER-89-P017 "Preliminary Proceedings from the Conference on Disaster Preparedness - The Place of Earthquake Education in Our Schools," Edited by K.E.K. Ross, 6/23/89, (PB90-108606, A03, MF-A01).

NCEER-89-0017 "Proceedings from the Conference on Disaster Preparedness - The Place of Earthquake Education in Our Schools," Edited by K.E.K. Ross, 12/31/89, (PB90-207895, A012, MF-A02). This report is available only through NTIS (see address given above).

NCEER-89-0018 "Multidimensional Models of Hysteretic Material Behavior for Vibration Analysis of Shape Memory Energy Absorbing Devices, by E.J. Graesser and F.A. Cozzarelli, 6/7/89, (PB90-164146, A04, MF-A01).

NCEER-89-0019 "Nonlinear Dynamic Analysis of Three-Dimensional Base Isolated Structures (3D-BASIS)," by S. Nagarajaiah, A.M. Reinhorn and M.C. Constantinou, 8/3/89, (PB90-161936, A06, MF-A01). This report has been replaced by NCEER-93-0011.

NCEER-89-0020 "Structural Control Considering Time-Rate of Control Forces and Control Rate Constraints," by F.Y. Cheng and C.P. Pantelides, 8/3/89, (PB90-120445, A04, MF-A01).

NCEER-89-0021 "Subsurface Conditions of Memphis and Shelby County," by K.W. Ng, T-S. Chang and H-H.M. Hwang, 7/26/89, (PB90-120437, A03, MF-A01).

NCEER-89-0022 "Seismic Wave Propagation Effects on Straight Jointed Buried Pipelines," by K. Elhmadi and M.J. O'Rourke, 8/24/89, (PB90-162322, A10, MF-A02).

NCEER-89-0023 "Workshop on Serviceability Analysis of Water Delivery Systems," edited by M. Grigoriu, 3/6/89, (PB90-127424, A03, MF-A01).

NCEER-89-0024 "Shaking Table Study of a 1/5 Scale Steel Frame Composed of Tapered Members," by K.C. Chang, J.S. Hwang and G.C. Lee, 9/18/89, (PB90-160169, A04, MF-A01).

NCEER-89-0025 "DYNA1D: A Computer Program for Nonlinear Seismic Site Response Analysis - Technical Documentation," by Jean H. Prevost, 9/14/89, (PB90-161944, A07, MF-A01). This report is available only through NTIS (see address given above).

NCEER-89-0026 "1:4 Scale Model Studies of Active Tendon Systems and Active Mass Dampers for Aseismic Protection," by A.M. Reinhorn, T.T. Soong, R.C. Lin, Y.P. Yang, Y. Fukao, H. Abe and M. Nakai, 9/15/89, (PB90-173246, A10, MF-A02). This report is available only through NTIS (see address given above).

NCEER-89-0027 "Scattering of Waves by Inclusions in a Nonhomogeneous Elastic Half Space Solved by Boundary Element Methods," by P.K. Hadley, A. Askar and A.S. Cakmak, 6/15/89, (PB90-145699, A07, MF-A01).

NCEER-89-0028 "Statistical Evaluation of Deflection Amplification Factors for Reinforced Concrete Structures," by H.H.M. Hwang, J-W. Jaw and A.L. Ch'ng, 8/31/89, (PB90-164633, A05, MF-A01).

NCEER-89-0029 "Bedrock Accelerations in Memphis Area Due to Large New Madrid Earthquakes," by H.H.M. Hwang, C.H.S. Chen and G. Yu, 11/7/89, (PB90-162330, A04, MF-A01).

NCEER-89-0030 "Seismic Behavior and Response Sensitivity of Secondary Structural Systems," by Y.Q. Chen and T.T. Soong, 10/23/89, (PB90-164658, A08, MF-A01).

NCEER-89-0031 "Random Vibration and Reliability Analysis of Primary-Secondary Structural Systems," by Y. Ibrahim, M. Grigoriu and T.T. Soong, 11/10/89, (PB90-161951, A04, MF-A01).

NCEER-89-0032 "Proceedings from the Second U.S. - Japan Workshop on Liquefaction, Large Ground Deformation and Their Effects on Lifelines, September 26-29, 1989," Edited by T.D. O'Rourke and M. Hamada, 12/1/89, (PB90-209388, A22, MF-A03).

NCEER-89-0033 "Deterministic Model for Seismic Damage Evaluation of Reinforced Concrete Structures," by J.M. Bracci, A.M. Reinhorn, J.B. Mander and S.K. Kunnath, 9/27/89, (PB91-108803, A06, MF-A01).

NCEER-89-0034 "On the Relation Between Local and Global Damage Indices," by E. DiPasquale and A.S. Cakmak, 8/15/89, (PB90-173865, A05, MF-A01).

NCEER-89-0035 "Cyclic Undrained Behavior of Nonplastic and Low Plasticity Silts," by A.J. Walker and H.E. Stewart, 7/26/89, (PB90-183518, A10, MF-A01).

NCEER-89-0036 "Liquefaction Potential of Surficial Deposits in the City of Buffalo, New York," by M. Budhu, R. Giese and L. Baumgrass, 1/17/89, (PB90-208455, A04, MF-A01).

NCEER-89-0037 "A Deterministic Assessment of Effects of Ground Motion Incoherence," by A.S. Veletsos and Y. Tang, 7/15/89, (PB90-164294, A03, MF-A01).

NCEER-89-0038 "Workshop on Ground Motion Parameters for Seismic Hazard Mapping," July 17-18, 1989, edited by R.V. Whitman, 12/1/89, (PB90-173923, A04, MF-A01).

NCEER-89-0039 "Seismic Effects on Elevated Transit Lines of the New York City Transit Authority," by C.J. Costantino, C.A. Miller and E. Heymsfield, 12/26/89, (PB90-207887, A06, MF-A01).

NCEER-89-0040 "Centrifugal Modeling of Dynamic Soil-Structure Interaction," by K. Weissman, Supervised by J.H. Prevost, 5/10/89, (PB90-207879, A07, MF-A01).

NCEER-89-0041 "Linearized Identification of Buildings With Cores for Seismic Vulnerability Assessment," by I-K. Ho and A.E. Aktan, 11/1/89, (PB90-251943, A07, MF-A01).

NCEER-90-0001 "Geotechnical and Lifeline Aspects of the October 17, 1989 Loma Prieta Earthquake in San Francisco," by T.D. O'Rourke, H.E. Stewart, F.T. Blackburn and T.S. Dickerman, 1/90, (PB90-208596, A05, MF-A01).

NCEER-90-0002 "Nonnormal Secondary Response Due to Yielding in a Primary Structure," by D.C.K. Chen and L.D. Lutes, 2/28/90, (PB90-251976, A07, MF-A01).

NCEER-90-0003 "Earthquake Education Materials for Grades K-12," by K.E.K. Ross, 4/16/90, (PB91-251984, A05, MF-A05). This report has been replaced by NCEER-92-0018.

NCEER-90-0004 "Catalog of Strong Motion Stations in Eastern North America," by R.W. Busby, 4/3/90, (PB90-251984, A05, MF-A01).

NCEER-90-0005 "NCEER Strong-Motion Data Base: A User Manual for the GeoBase Release (Version 1.0 for the Sun3)," by P. Friberg and K. Jacob, 3/31/90 (PB90-258062, A04, MF-A01).

NCEER-90-0006 "Seismic Hazard Along a Crude Oil Pipeline in the Event of an 1811-1812 Type New Madrid Earthquake," by H.H.M. Hwang and C-H.S. Chen, 4/16/90, (PB90-258054, A04, MF-A01).

NCEER-90-0007 "Site-Specific Response Spectra for Memphis Sheahan Pumping Station," by H.H.M. Hwang and C.S. Lee, 5/15/90, (PB91-108811, A05, MF-A01).

NCEER-90-0008 "Pilot Study on Seismic Vulnerability of Crude Oil Transmission Systems," by T. Ariman, R. Dobry, M. Grigoriu, F. Kozin, M. O'Rourke, T. O'Rourke and M. Shinozuka, 5/25/90, (PB91-108837, A06, MF-A01).

NCEER-90-0009 "A Program to Generate Site Dependent Time Histories: EQGEN," by G.W. Ellis, M. Srinivasan and A.S. Cakmak, 1/30/90, (PB91-108829, A04, MF-A01).

NCEER-90-0010 "Active Isolation for Seismic Protection of Operating Rooms," by M.E. Talbott, Supervised by M. Shinozuka, 6/8/9, (PB91-110205, A05, MF-A01).

NCEER-90-0011 "Program LINEARID for Identification of Linear Structural Dynamic Systems," by C-B. Yun and M. Shinozuka, 6/25/90, (PB91-110312, A08, MF-A01).

NCEER-90-0012 "Two-Dimensional Two-Phase Elasto-Plastic Seismic Response of Earth Dams," by A.N. Yiagos, Supervised by J.H. Prevost, 6/20/90, (PB91-110197, A13, MF-A02).

NCEER-90-0013 "Secondary Systems in Base-Isolated Structures: Experimental Investigation, Stochastic Response and Stochastic Sensitivity," by G.D. Manolis, G. Juhn, M.C. Constantinou and A.M. Reinhorn, 7/1/90, (PB91-110320, A08, MF-A01).

NCEER-90-0014 "Seismic Behavior of Lightly-Reinforced Concrete Column and Beam-Column Joint Details," by S.P. Pessiki, C.H. Conley, P. Gergely and R.N. White, 8/22/90, (PB91-108795, A11, MF-A02).

NCEER-90-0015 "Two Hybrid Control Systems for Building Structures Under Strong Earthquakes," by J.N. Yang and A. Danielians, 6/29/90, (PB91-125393, A04, MF-A01).

NCEER-90-0016 "Instantaneous Optimal Control with Acceleration and Velocity Feedback," by J.N. Yang and Z. Li, 6/29/90, (PB91-125401, A03, MF-A01).

NCEER-90-0017 "Reconnaissance Report on the Northern Iran Earthquake of June 21, 1990," by M. Mehrain, 10/4/90, (PB91-125377, A03, MF-A01).

NCEER-90-0018 "Evaluation of Liquefaction Potential in Memphis and Shelby County," by T.S. Chang, P.S. Tang, C.S. Lee and H. Hwang, 8/10/90, (PB91-125427, A09, MF-A01).

NCEER-90-0019 "Experimental and Analytical Study of a Combined Sliding Disc Bearing and Helical Steel Spring Isolation System," by M.C. Constantinou, A.S. Mokha and A.M. Reinhorn, 10/4/90, (PB91-125385, A06, MF-A01). This report is available only through NTIS (see address given above).

NCEER-90-0020 "Experimental Study and Analytical Prediction of Earthquake Response of a Sliding Isolation System with a Spherical Surface," by A.S. Mokha, M.C. Constantinou and A.M. Reinhorn, 10/11/90, (PB91-125419, A05, MF-A01).

NCEER-90-0021 "Dynamic Interaction Factors for Floating Pile Groups," by G. Gazetas, K. Fan, A. Kaynia and E. Kausel, 9/10/90, (PB91-170381, A05, MF-A01).

NCEER-90-0022 "Evaluation of Seismic Damage Indices for Reinforced Concrete Structures," by S. Rodriguez-Gomez and A.S. Cakmak, 9/30/90, PB91-171322, A06, MF-A01).

NCEER-90-0023 "Study of Site Response at a Selected Memphis Site," by H. Desai, S. Ahmad, E.S. Gazetas and M.R. Oh, 10/11/90, (PB91-196857, A03, MF-A01).

NCEER-90-0024 "A User's Guide to Strongmo: Version 1.0 of NCEER's Strong-Motion Data Access Tool for PCs and Terminals," by P.A. Friberg and C.A.T. Susch, 11/15/90, (PB91-171272, A03, MF-A01).

NCEER-90-0025 "A Three-Dimensional Analytical Study of Spatial Variability of Seismic Ground Motions," by L-L. Hong and A.H.-S. Ang, 10/30/90, (PB91-170399, A09, MF-A01).

NCEER-90-0026 "MUMOID User's Guide - A Program for the Identification of Modal Parameters," by S. Rodriguez-Gomez and E. DiPasquale, 9/30/90, (PB91-171298, A04, MF-A01).

NCEER-90-0027 "SARCF-II User's Guide - Seismic Analysis of Reinforced Concrete Frames," by S. Rodriguez-Gomez, Y.S. Chung and C. Meyer, 9/30/90, (PB91-171280, A05, MF-A01).

NCEER-90-0028 "Viscous Dampers: Testing, Modeling and Application in Vibration and Seismic Isolation," by N. Makris and M.C. Constantinou, 12/20/90 (PB91-190561, A06, MF-A01).

NCEER-90-0029 "Soil Effects on Earthquake Ground Motions in the Memphis Area," by H. Hwang, C.S. Lee, K.W. Ng and T.S. Chang, 8/2/90, (PB91-190751, A05, MF-A01).

NCEER-91-0001 "Proceedings from the Third Japan-U.S. Workshop on Earthquake Resistant Design of Lifeline Facilities and Countermeasures for Soil Liquefaction, December 17-19, 1990," edited by T.D. O'Rourke and M. Hamada, 2/1/91, (PB91-179259, A99, MF-A04).

NCEER-91-0002 "Physical Space Solutions of Non-Proportionally Damped Systems," by M. Tong, Z. Liang and G.C. Lee, 1/15/91, (PB91-179242, A04, MF-A01).

NCEER-91-0003 "Seismic Response of Single Piles and Pile Groups," by K. Fan and G. Gazetas, 1/10/91, (PB92-174994, A04, MF-A01).

NCEER-91-0004 "Damping of Structures: Part 1 - Theory of Complex Damping," by Z. Liang and G. Lee, 10/10/91, (PB92-197235, A12, MF-A03).

NCEER-91-0005 "3D-BASIS - Nonlinear Dynamic Analysis of Three Dimensional Base Isolated Structures: Part II," by S. Nagarajaiah, A.M. Reinhorn and M.C. Constantinou, 2/28/91, (PB91-190553, A07, MF-A01). This report has been replaced by NCEER-93-0011.

NCEER-91-0006 "A Multidimensional Hysteretic Model for Plasticity Deforming Metals in Energy Absorbing Devices," by E.J. Graesser and F.A. Cozzarelli, 4/9/91, (PB92-108364, A04, MF-A01).

NCEER-91-0007 "A Framework for Customizable Knowledge-Based Expert Systems with an Application to a KBES for Evaluating the Seismic Resistance of Existing Buildings," by E.G. Ibarra-Anaya and S.J. Fenves, 4/9/91, (PB91-210930, A08, MF-A01).

NCEER-91-0008 "Nonlinear Analysis of Steel Frames with Semi-Rigid Connections Using the Capacity Spectrum Method," by G.G. Deierlein, S-H. Hsieh, Y-J. Shen and J.F. Abel, 7/2/91, (PB92-113828, A05, MF-A01).

NCEER-91-0009 "Earthquake Education Materials for Grades K-12," by K.E.K. Ross, 4/30/91, (PB91-212142, A06, MF-A01). This report has been replaced by NCEER-92-0018.

NCEER-91-0010 "Phase Wave Velocities and Displacement Phase Differences in a Harmonically Oscillating Pile," by N. Makris and G. Gazetas, 7/8/91, (PB92-108356, A04, MF-A01).

NCEER-91-0011 "Dynamic Characteristics of a Full-Size Five-Story Steel Structure and a 2/5 Scale Model," by K.C. Chang, G.C. Yao, G.C. Lee, D.S. Hao and Y.C. Yeh," 7/2/91, (PB93-116648, A06, MF-A02).

NCEER-91-0012 "Seismic Response of a 2/5 Scale Steel Structure with Added Viscoelastic Dampers," by K.C. Chang, T.T. Soong, S-T. Oh and M.L. Lai, 5/17/91, (PB92-110816, A05, MF-A01).

NCEER-91-0013 "Earthquake Response of Retaining Walls; Full-Scale Testing and Computational Modeling," by S. Alampalli and A-W.M. Elgamal, 6/20/91, not available.

NCEER-91-0014 "3D-BASIS-M: Nonlinear Dynamic Analysis of Multiple Building Base Isolated Structures," by P.C. Tsopelas, S. Nagarajaiah, M.C. Constantinou and A.M. Reinhorn, 5/28/91, (PB92-113885, A09, MF-A02).

NCEER-91-0015 "Evaluation of SEAOC Design Requirements for Sliding Isolated Structures," by D. Theodossiou and M.C. Constantinou, 6/10/91, (PB92-114602, A11, MF-A03).

NCEER-91-0016 "Closed-Loop Modal Testing of a 27-Story Reinforced Concrete Flat Plate-Core Building," by H.R. Somaprasad, T. Toksoy, H. Yoshiyuki and A.E. Aktan, 7/15/91, (PB92-129980, A07, MF-A02).

NCEER-91-0017 "Shake Table Test of a 1/6 Scale Two-Story Lightly Reinforced Concrete Building," by A.G. El-Attar, R.N. White and P. Gergely, 2/28/91, (PB92-222447, A06, MF-A02).

NCEER-91-0018 "Shake Table Test of a 1/8 Scale Three-Story Lightly Reinforced Concrete Building," by A.G. El-Attar, R.N. White and P. Gergely, 2/28/91, (PB93-116630, A08, MF-A02).

NCEER-91-0019 "Transfer Functions for Rigid Rectangular Foundations," by A.S. Veletsos, A.M. Prasad and W.H. Wu, 7/31/91, not available.

NCEER-91-0020 "Hybrid Control of Seismic-Excited Nonlinear and Inelastic Structural Systems," by J.N. Yang, Z. Li and A. Danielians, 8/1/91, (PB92-143171, A06, MF-A02).

NCEER-91-0021 "The NCEER-91 Earthquake Catalog: Improved Intensity-Based Magnitudes and Recurrence Relations for U.S. Earthquakes East of New Madrid," by L. Seeber and J.G. Armbruster, 8/28/91, (PB92-176742, A06, MF-A02).

NCEER-91-0022 "Proceedings from the Implementation of Earthquake Planning and Education in Schools: The Need for Change - The Roles of the Changemakers," by K.E.K. Ross and F. Winslow, 7/23/91, (PB92-129998, A12, MF-A03).

NCEER-91-0023 "A Study of Reliability-Based Criteria for Seismic Design of Reinforced Concrete Frame Buildings," by H.H.M. Hwang and H-M. Hsu, 8/10/91, (PB92-140235, A09, MF-A02).

NCEER-91-0024 "Experimental Verification of a Number of Structural System Identification Algorithms," by R.G. Ghanem, H. Gavin and M. Shinozuka, 9/18/91, (PB92-176577, A18, MF-A04).

NCEER-91-0025 "Probabilistic Evaluation of Liquefaction Potential," by H.H.M. Hwang and C.S. Lee," 11/25/91, (PB92-143429, A05, MF-A01).

NCEER-91-0026 "Instantaneous Optimal Control for Linear, Nonlinear and Hysteretic Structures - Stable Controllers," by J.N. Yang and Z. Li, 11/15/91, (PB92-163807, A04, MF-A01).

NCEER-91-0027 "Experimental and Theoretical Study of a Sliding Isolation System for Bridges," by M.C. Constantinou, A. Kartoum, A.M. Reinhorn and P. Bradford, 11/15/91, (PB92-176973, A10, MF-A03).

NCEER-92-0001 "Case Studies of Liquefaction and Lifeline Performance During Past Earthquakes, Volume 1: Japanese Case Studies," Edited by M. Hamada and T. O'Rourke, 2/17/92, (PB92-197243, A18, MF-A04).

NCEER-92-0002 "Case Studies of Liquefaction and Lifeline Performance During Past Earthquakes, Volume 2: United States Case Studies," Edited by T. O'Rourke and M. Hamada, 2/17/92, (PB92-197250, A20, MF-A04).

NCEER-92-0003 "Issues in Earthquake Education," Edited by K. Ross, 2/3/92, (PB92-222389, A07, MF-A02).

NCEER-92-0004 "Proceedings from the First U.S. - Japan Workshop on Earthquake Protective Systems for Bridges," Edited by I.G. Buckle, 2/4/92, (PB94-142239, A99, MF-A06).

NCEER-92-0005 "Seismic Ground Motion from a Haskell-Type Source in a Multiple-Layered Half-Space," A.P. Theoharis, G. Deodatis and M. Shinozuka, 1/2/92, not available.

NCEER-92-0006 "Proceedings from the Site Effects Workshop," Edited by R. Whitman, 2/29/92, (PB92-197201, A04, MF-A01).

NCEER-92-0007 "Engineering Evaluation of Permanent Ground Deformations Due to Seismically-Induced Liquefaction," by M.H. Baziar, R. Dobry and A-W.M. Elgamal, 3/24/92, (PB92-222421, A13, MF-A03).

NCEER-92-0008 "A Procedure for the Seismic Evaluation of Buildings in the Central and Eastern United States," by C.D. Poland and J.O. Malley, 4/2/92, (PB92-222439, A20, MF-A04).

NCEER-92-0009 "Experimental and Analytical Study of a Hybrid Isolation System Using Friction Controllable Sliding Bearings," by M.Q. Feng, S. Fujii and M. Shinozuka, 5/15/92, (PB93-150282, A06, MF-A02).

NCEER-92-0010 "Seismic Resistance of Slab-Column Connections in Existing Non-Ductile Flat-Plate Buildings," by A.J. Durrani and Y. Du, 5/18/92, (PB93-116812, A06, MF-A02).

NCEER-92-0011 "The Hysteretic and Dynamic Behavior of Brick Masonry Walls Upgraded by Ferrocement Coatings Under Cyclic Loading and Strong Simulated Ground Motion," by H. Lee and S.P. Prawel, 5/11/92, not available.

NCEER-92-0012 "Study of Wire Rope Systems for Seismic Protection of Equipment in Buildings," by G.F. Demetriades, M.C. Constantinou and A.M. Reinhorn, 5/20/92, (PB93-116655, A08, MF-A02).

NCEER-92-0013 "Shape Memory Structural Dampers: Material Properties, Design and Seismic Testing," by P.R. Witting and F.A. Cozzarelli, 5/26/92, (PB93-116663, A05, MF-A01).

NCEER-92-0014 "Longitudinal Permanent Ground Deformation Effects on Buried Continuous Pipelines," by M.J. O'Rourke, and C. Nordberg, 6/15/92, (PB93-116671, A08, MF-A02).

NCEER-92-0015 "A Simulation Method for Stationary Gaussian Random Functions Based on the Sampling Theorem," by M. Grigoriu and S. Balopoulou, 6/11/92, (PB93-127496, A05, MF-A01).

NCEER-92-0016 "Gravity-Load-Designed Reinforced Concrete Buildings: Seismic Evaluation of Existing Construction and Detailing Strategies for Improved Seismic Resistance," by G.W. Hoffmann, S.K. Kunnath, A.M. Reinhorn and J.B. Mander, 7/15/92, (PB94-142007, A08, MF-A02).

NCEER-92-0017 "Observations on Water System and Pipeline Performance in the Limón Area of Costa Rica Due to the April 22, 1991 Earthquake," by M. O'Rourke and D. Ballantyne, 6/30/92, (PB93-126811, A06, MF-A02).

NCEER-92-0018 "Fourth Edition of Earthquake Education Materials for Grades K-12," Edited by K.E.K. Ross, 8/10/92, (PB93-114023, A07, MF-A02).

NCEER-92-0019 "Proceedings from the Fourth Japan-U.S. Workshop on Earthquake Resistant Design of Lifeline Facilities and Countermeasures for Soil Liquefaction," Edited by M. Hamada and T.D. O'Rourke, 8/12/92, (PB93-163939, A99, MF-E11).

NCEER-92-0020 "Active Bracing System: A Full Scale Implementation of Active Control," by A.M. Reinhorn, T.T. Soong, R.C. Lin, M.A. Riley, Y.P. Wang, S. Aizawa and M. Higashino, 8/14/92, (PB93-127512, A06, MF-A02).

NCEER-92-0021 "Empirical Analysis of Horizontal Ground Displacement Generated by Liquefaction-Induced Lateral Spreads," by S.F. Bartlett and T.L. Youd, 8/17/92, (PB93-188241, A06, MF-A02).

NCEER-92-0022 "IDARC Version 3.0: Inelastic Damage Analysis of Reinforced Concrete Structures," by S.K. Kunnath, A.M. Reinhorn and R.F. Lobo, 8/31/92, (PB93-227502, A07, MF-A02).

NCEER-92-0023 "A Semi-Empirical Analysis of Strong-Motion Peaks in Terms of Seismic Source, Propagation Path and Local Site Conditions, by M. Kamiyama, M.J. O'Rourke and R. Flores-Berrones, 9/9/92, (PB93-150266, A08, MF-A02).

NCEER-92-0024 "Seismic Behavior of Reinforced Concrete Frame Structures with Nonductile Details, Part I: Summary of Experimental Findings of Full Scale Beam-Column Joint Tests," by A. Beres, R.N. White and P. Gergely, 9/30/92, (PB93-227783, A05, MF-A01).

NCEER-92-0025 "Experimental Results of Repaired and Retrofitted Beam-Column Joint Tests in Lightly Reinforced Concrete Frame Buildings," by A. Beres, S. El-Borgi, R.N. White and P. Gergely, 10/29/92, (PB93-227791, A05, MF-A01).

NCEER-92-0026 "A Generalization of Optimal Control Theory: Linear and Nonlinear Structures," by J.N. Yang, Z. Li and S. Vongchavalitkul, 11/2/92, (PB93-188621, A05, MF-A01).

NCEER-92-0027 "Seismic Resistance of Reinforced Concrete Frame Structures Designed Only for Gravity Loads: Part I - Design and Properties of a One-Third Scale Model Structure," by J.M. Bracci, A.M. Reinhorn and J.B. Mander, 12/1/92, (PB94-104502, A08, MF-A02).

NCEER-92-0028 "Seismic Resistance of Reinforced Concrete Frame Structures Designed Only for Gravity Loads: Part II - Experimental Performance of Subassemblages," by L.E. Aycardi, J.B. Mander and A.M. Reinhorn, 12/1/92, (PB94-104510, A08, MF-A02).

NCEER-92-0029 "Seismic Resistance of Reinforced Concrete Frame Structures Designed Only for Gravity Loads: Part III - Experimental Performance and Analytical Study of a Structural Model," by J.M. Bracci, A.M. Reinhorn and J.B. Mander, 12/1/92, (PB93-227528, A09, MF-A01).

NCEER-92-0030 "Evaluation of Seismic Retrofit of Reinforced Concrete Frame Structures: Part I - Experimental Performance of Retrofitted Subassemblages," by D. Choudhuri, J.B. Mander and A.M. Reinhorn, 12/8/92, (PB93-198307, A07, MF-A02).

NCEER-92-0031 "Evaluation of Seismic Retrofit of Reinforced Concrete Frame Structures: Part II - Experimental Performance and Analytical Study of a Retrofitted Structural Model," by J.M. Bracci, A.M. Reinhorn and J.B. Mander, 12/8/92, (PB93-198315, A09, MF-A03).

NCEER-92-0032 "Experimental and Analytical Investigation of Seismic Response of Structures with Supplemental Fluid Viscous Dampers," by M.C. Constantinou and M.D. Symans, 12/21/92, (PB93-191435, A10, MF-A03). This report is available only through NTIS (see address given above).

NCEER-92-0033 "Reconnaissance Report on the Cairo, Egypt Earthquake of October 12, 1992," by M. Khater, 12/23/92, (PB93-188621, A03, MF-A01).

NCEER-92-0034 "Low-Level Dynamic Characteristics of Four Tall Flat-Plate Buildings in New York City," by H. Gavin, S. Yuan, J. Grossman, E. Pekelis and K. Jacob, 12/28/92, (PB93-188217, A07, MF-A02).

NCEER-93-0001 "An Experimental Study on the Seismic Performance of Brick-Infilled Steel Frames With and Without Retrofit," by J.B. Mander, B. Nair, K. Wojtkowski and J. Ma, 1/29/93, (PB93-227510, A07, MF-A02).

NCEER-93-0002 "Social Accounting for Disaster Preparedness and Recovery Planning," by S. Cole, E. Pantoja and V. Razak, 2/22/93, (PB94-142114, A12, MF-A03).

NCEER-93-0003 "Assessment of 1991 NEHRP Provisions for Nonstructural Components and Recommended Revisions," by T.T. Soong, G. Chen, Z. Wu, R-H. Zhang and M. Grigoriu, 3/1/93, (PB93-188639, A06, MF-A02).

NCEER-93-0004 "Evaluation of Static and Response Spectrum Analysis Procedures of SEAOC/UBC for Seismic Isolated Structures," by C.W. Winters and M.C. Constantinou, 3/23/93, (PB93-198299, A10, MF-A03).

NCEER-93-0005 "Earthquakes in the Northeast - Are We Ignoring the Hazard? A Workshop on Earthquake Science and Safety for Educators," edited by K.E.K. Ross, 4/2/93, (PB94-103066, A09, MF-A02).

NCEER-93-0006 "Inelastic Response of Reinforced Concrete Structures with Viscoelastic Braces," by R.F. Lobo, J.M. Bracci, K.L. Shen, A.M. Reinhorn and T.T. Soong, 4/5/93, (PB93-227486, A05, MF-A02).

NCEER-93-0007 "Seismic Testing of Installation Methods for Computers and Data Processing Equipment," by K. Kosar, T.T. Soong, K.L. Shen, J.A. HoLung and Y.K. Lin, 4/12/93, (PB93-198299, A07, MF-A02).

NCEER-93-0008 "Retrofit of Reinforced Concrete Frames Using Added Dampers," by A. Reinhorn, M. Constantinou and C. Li, not available.

NCEER-93-0009 "Seismic Behavior and Design Guidelines for Steel Frame Structures with Added Viscoelastic Dampers," by K.C. Chang, M.L. Lai, T.T. Soong, D.S. Hao and Y.C. Yeh, 5/1/93, (PB94-141959, A07, MF-A02).

NCEER-93-0010 "Seismic Performance of Shear-Critical Reinforced Concrete Bridge Piers," by J.B. Mander, S.M. Waheed, M.T.A. Chaudhary and S.S. Chen, 5/12/93, (PB93-227494, A08, MF-A02).

NCEER-93-0011 "3D-BASIS-TABS: Computer Program for Nonlinear Dynamic Analysis of Three Dimensional Base Isolated Structures," by S. Nagarajaiah, C. Li, A.M. Reinhorn and M.C. Constantinou, 8/2/93, (PB94-141819, A09, MF-A02).

NCEER-93-0012 "Effects of Hydrocarbon Spills from an Oil Pipeline Break on Ground Water," by O.J. Helweg and H.H.M. Hwang, 8/3/93, (PB94-141942, A06, MF-A02).

NCEER-93-0013 "Simplified Procedures for Seismic Design of Nonstructural Components and Assessment of Current Code Provisions," by M.P. Singh, L.E. Suarez, E.E. Matheu and G.O. Maldonado, 8/4/93, (PB94-141827, A09, MF-A02).

NCEER-93-0014 "An Energy Approach to Seismic Analysis and Design of Secondary Systems," by G. Chen and T.T. Soong, 8/6/93, (PB94-142767, A11, MF-A03).

NCEER-93-0015 "Proceedings from School Sites: Becoming Prepared for Earthquakes - Commemorating the Third Anniversary of the Loma Prieta Earthquake," Edited by F.E. Winslow and K.E.K. Ross, 8/16/93, (PB94-154275, A16, MF-A02).

NCEER-93-0016 "Reconnaissance Report of Damage to Historic Monuments in Cairo, Egypt Following the October 12, 1992 Dahshur Earthquake," by D. Sykora, D. Look, G. Croci, E. Karaesmen and E. Karaesmen, 8/19/93, (PB94-142221, A08, MF-A02).

NCEER-93-0017 "The Island of Guam Earthquake of August 8, 1993," by S.W. Swan and S.K. Harris, 9/30/93, (PB94-141843, A04, MF-A01).

NCEER-93-0018 "Engineering Aspects of the October 12, 1992 Egyptian Earthquake," by A.W. Elgamal, M. Amer, K. Adalier and A. Abul-Fadl, 10/7/93, (PB94-141983, A05, MF-A01).

NCEER-93-0019 "Development of an Earthquake Motion Simulator and its Application in Dynamic Centrifuge Testing," by I. Krstelj, Supervised by J.H. Prevost, 10/23/93, (PB94-181773, A-10, MF-A03).

NCEER-93-0020 "NCEER-Taisei Corporation Research Program on Sliding Seismic Isolation Systems for Bridges: Experimental and Analytical Study of a Friction Pendulum System (FPS)," by M.C. Constantinou, P. Tsopelas, Y-S. Kim and S. Okamoto, 11/1/93, (PB94-142775, A08, MF-A02).

NCEER-93-0021 "Finite Element Modeling of Elastomeric Seismic Isolation Bearings," by L.J. Billings, Supervised by R. Shepherd, 11/8/93, not available.

NCEER-93-0022 "Seismic Vulnerability of Equipment in Critical Facilities: Life-Safety and Operational Consequences," by K. Porter, G.S. Johnson, M.M. Zadeh, C. Scawthorn and S. Eder, 11/24/93, (PB94-181765, A16, MF-A03).

NCEER-93-0023 "Hokkaido Nansei-oki, Japan Earthquake of July 12, 1993, by P.I. Yanev and C.R. Scawthorn, 12/23/93, (PB94-181500, A07, MF-A01).

NCEER-94-0001 "An Evaluation of Seismic Serviceability of Water Supply Networks with Application to the San Francisco Auxiliary Water Supply System," by I. Markov, Supervised by M. Grigoriu and T. O'Rourke, 1/21/94, (PB94-204013, A07, MF-A02).

NCEER-94-0002 "NCEER-Taisei Corporation Research Program on Sliding Seismic Isolation Systems for Bridges: Experimental and Analytical Study of Systems Consisting of Sliding Bearings, Rubber Restoring Force Devices and Fluid Dampers," Volumes I and II, by P. Tsopelas, S. Okamoto, M.C. Constantinou, D. Ozaki and S. Fujii, 2/4/94, (PB94-181740, A09, MF-A02 and PB94-181757, A12, MF-A03).

NCEER-94-0003 "A Markov Model for Local and Global Damage Indices in Seismic Analysis," by S. Rahman and M. Grigoriu, 2/18/94, (PB94-206000, A12, MF-A03).

NCEER-94-0004 "Proceedings from the NCEER Workshop on Seismic Response of Masonry Infills," edited by D.P. Abrams, 3/1/94, (PB94-180783, A07, MF-A02).

NCEER-94-0005 "The Northridge, California Earthquake of January 17, 1994: General Reconnaissance Report," edited by J.D. Goltz, 3/11/94, (PB94-193943, A10, MF-A03).

NCEER-94-0006 "Seismic Energy Based Fatigue Damage Analysis of Bridge Columns: Part I - Evaluation of Seismic Capacity," by G.A. Chang and J.B. Mander, 3/14/94, (PB94-219185, A11, MF-A03).

NCEER-94-0007 "Seismic Isolation of Multi-Story Frame Structures Using Spherical Sliding Isolation Systems," by T.M. Al-Hussaini, V.A. Zayas and M.C. Constantinou, 3/17/94, (PB94-193745, A09, MF-A02).

NCEER-94-0008 "The Northridge, California Earthquake of January 17, 1994: Performance of Highway Bridges," edited by I.G. Buckle, 3/24/94, (PB94-193851, A06, MF-A02).

NCEER-94-0009 "Proceedings of the Third U.S.-Japan Workshop on Earthquake Protective Systems for Bridges," edited by I.G. Buckle and I. Friedland, 3/31/94, (PB94-195815, A99, MF-A06).

NCEER-94-0010 "3D-BASIS-ME: Computer Program for Nonlinear Dynamic Analysis of Seismically Isolated Single and Multiple Structures and Liquid Storage Tanks," by P.C. Tsopelas, M.C. Constantinou and A.M. Reinhorn, 4/12/94, (PB94-204922, A09, MF-A02).

NCEER-94-0011 "The Northridge, California Earthquake of January 17, 1994: Performance of Gas Transmission Pipelines," by T.D. O'Rourke and M.C. Palmer, 5/16/94, (PB94-204989, A05, MF-A01).

NCEER-94-0012 "Feasibility Study of Replacement Procedures and Earthquake Performance Related to Gas Transmission Pipelines," by T.D. O'Rourke and M.C. Palmer, 5/25/94, (PB94-206638, A09, MF-A02).

NCEER-94-0013 "Seismic Energy Based Fatigue Damage Analysis of Bridge Columns: Part II - Evaluation of Seismic Demand," by G.A. Chang and J.B. Mander, 6/1/94, (PB95-18106, A08, MF-A02).

NCEER-94-0014 "NCEER-Taisei Corporation Research Program on Sliding Seismic Isolation Systems for Bridges: Experimental and Analytical Study of a System Consisting of Sliding Bearings and Fluid Restoring Force/Damping Devices," by P. Tsopelas and M.C. Constantinou, 6/13/94, (PB94-219144, A10, MF-A03).

NCEER-94-0015 "Generation of Hazard-Consistent Fragility Curves for Seismic Loss Estimation Studies," by H. Hwang and J-R. Huo, 6/14/94, (PB95-181996, A09, MF-A02).

NCEER-94-0016 "Seismic Study of Building Frames with Added Energy-Absorbing Devices," by W.S. Pong, C.S. Tsai and G.C. Lee, 6/20/94, (PB94-219136, A10, A03).

NCEER-94-0017 "Sliding Mode Control for Seismic-Excited Linear and Nonlinear Civil Engineering Structures," by J. Yang, J. Wu, A. Agrawal and Z. Li, 6/21/94, (PB95-138483, A06, MF-A02).

NCEER-94-0018 "3D-BASIS-TABS Version 2.0: Computer Program for Nonlinear Dynamic Analysis of Three Dimensional Base Isolated Structures," by A.M. Reinhorn, S. Nagarajaiah, M.C. Constantinou, P. Tsopelas and R. Li, 6/22/94, (PB95-182176, A08, MF-A02).

NCEER-94-0019 "Proceedings of the International Workshop on Civil Infrastructure Systems: Application of Intelligent Systems and Advanced Materials on Bridge Systems," Edited by G.C. Lee and K.C. Chang, 7/18/94, (PB95-252474, A20, MF-A04).

NCEER-94-0020 "Study of Seismic Isolation Systems for Computer Floors," by V. Lambrou and M.C. Constantinou, 7/19/94, (PB95-138533, A10, MF-A03).

NCEER-94-0021 "Proceedings of the U.S.-Italian Workshop on Guidelines for Seismic Evaluation and Rehabilitation of Unreinforced Masonry Buildings," Edited by D.P. Abrams and G.M. Calvi, 7/20/94, (PB95-138749, A13, MF-A03).

NCEER-94-0022 "NCEER-Taisei Corporation Research Program on Sliding Seismic Isolation Systems for Bridges: Experimental and Analytical Study of a System Consisting of Lubricated PTFE Sliding Bearings and Mild Steel Dampers," by P. Tsopelas and M.C. Constantinou, 7/22/94, (PB95-182184, A08, MF-A02).

NCEER-94-0023 "Development of Reliability-Based Design Criteria for Buildings Under Seismic Load," by Y.K. Wen, H. Hwang and M. Shinozuka, 8/1/94, (PB95-211934, A08, MF-A02).

NCEER-94-0024 "Experimental Verification of Acceleration Feedback Control Strategies for an Active Tendon System," by S.J. Dyke, B.F. Spencer, Jr., P. Quast, M.K. Sain, D.C. Kaspari, Jr. and T.T. Soong, 8/29/94, (PB95-212320, A05, MF-A01).

NCEER-94-0025 "Seismic Retrofitting Manual for Highway Bridges," Edited by I.G. Buckle and I.F. Friedland, published by the Federal Highway Administration (PB95-212676, A15, MF-A03).

NCEER-94-0026 "Proceedings from the Fifth U.S.-Japan Workshop on Earthquake Resistant Design of Lifeline Facilities and Countermeasures Against Soil Liquefaction," Edited by T.D. O'Rourke and M. Hamada, 11/7/94, (PB95-220802, A99, MF-E08).

NCEER-95-0001 "Experimental and Analytical Investigation of Seismic Retrofit of Structures with Supplemental Damping: Part 1 - Fluid Viscous Damping Devices," by A.M. Reinhorn, C. Li and M.C. Constantinou, 1/3/95, (PB95-266599, A09, MF-A02).

NCEER-95-0002 "Experimental and Analytical Study of Low-Cycle Fatigue Behavior of Semi-Rigid Top-And-Seat Angle Connections," by G. Pekcan, J.B. Mander and S.S. Chen, 1/5/95, (PB95-220042, A07, MF-A02).

NCEER-95-0003 "NCEER-ATC Joint Study on Fragility of Buildings," by T. Anagnos, C. Rojahn and A.S. Kiremidjian, 1/20/95, (PB95-220026, A06, MF-A02).

NCEER-95-0004 "Nonlinear Control Algorithms for Peak Response Reduction," by Z. Wu, T.T. Soong, V. Gattulli and R.C. Lin, 2/16/95, (PB95-220349, A05, MF-A01).

NCEER-95-0005 "Pipeline Replacement Feasibility Study: A Methodology for Minimizing Seismic and Corrosion Risks to Underground Natural Gas Pipelines," by R.T. Eguchi, H.A. Seligson and D.G. Honegger, 3/2/95, (PB95-252326, A06, MF-A02).

NCEER-95-0006 "Evaluation of Seismic Performance of an 11-Story Frame Building During the 1994 Northridge Earthquake," by F. Naeim, R. DiSulio, K. Benuska, A. Reinhorn and C. Li, not available.

NCEER-95-0007 "Prioritization of Bridges for Seismic Retrofitting," by N. Basöz and A.S. Kiremidjian, 4/24/95, (PB95-252300, A08, MF-A02).

NCEER-95-0008 "Method for Developing Motion Damage Relationships for Reinforced Concrete Frames," by A. Singhal and A.S. Kiremidjian, 5/11/95, (PB95-266607, A06, MF-A02).

NCEER-95-0009 "Experimental and Analytical Investigation of Seismic Retrofit of Structures with Supplemental Damping: Part II - Friction Devices," by C. Li and A.M. Reinhorn, 7/6/95, (PB96-128087, A11, MF-A03).

NCEER-95-0010 "Experimental Performance and Analytical Study of a Non-Ductile Reinforced Concrete Frame Structure Retrofitted with Elastomeric Spring Dampers," by G. Pekcan, J.B. Mander and S.S. Chen, 7/14/95, (PB96-137161, A08, MF-A02).

NCEER-95-0011 "Development and Experimental Study of Semi-Active Fluid Damping Devices for Seismic Protection of Structures," by M.D. Symans and M.C. Constantinou, 8/3/95, (PB96-136940, A23, MF-A04).

NCEER-95-0012 "Real-Time Structural Parameter Modification (RSPM): Development of Innervated Structures," by Z. Liang, M. Tong and G.C. Lee, 4/11/95, (PB96-137153, A06, MF-A01).

NCEER-95-0013 "Experimental and Analytical Investigation of Seismic Retrofit of Structures with Supplemental Damping: Part III - Viscous Damping Walls," by A.M. Reinhorn and C. Li, 10/1/95, (PB96-176409, A11, MF-A03).

NCEER-95-0014 "Seismic Fragility Analysis of Equipment and Structures in a Memphis Electric Substation," by J-R. Huo and H.H.M. Hwang, 8/10/95, (PB96-128087, A09, MF-A02).

NCEER-95-0015 "The Hanshin-Awaji Earthquake of January 17, 1995: Performance of Lifelines," Edited by M. Shinozuka, 11/3/95, (PB96-176383, A15, MF-A03).

NCEER-95-0016 "Highway Culvert Performance During Earthquakes," by T.L. Youd and C.J. Beckman, available as NCEER-96-0015.

NCEER-95-0017 "The Hanshin-Awaji Earthquake of January 17, 1995: Performance of Highway Bridges," Edited by I.G. Buckle, 12/1/95, not available.

NCEER-95-0018 "Modeling of Masonry Infill Panels for Structural Analysis," by A.M. Reinhorn, A. Madan, R.E. Valles, Y. Reichmann and J.B. Mander, 12/8/95, (PB97-110886, MF-A01, A06).

NCEER-95-0019 "Optimal Polynomial Control for Linear and Nonlinear Structures," by A.K. Agrawal and J.N. Yang, 12/11/95, (PB96-168737, A07, MF-A02).

NCEER-95-0020 "Retrofit of Non-Ductile Reinforced Concrete Frames Using Friction Dampers," by R.S. Rao, P. Gergely and R.N. White, 12/22/95, (PB97-133508, A10, MF-A02).

NCEER-95-0021 "Parametric Results for Seismic Response of Pile-Supported Bridge Bents," by G. Mylonakis, A. Nikolaou and G. Gazetas, 12/22/95, (PB97-100242, A12, MF-A03).

NCEER-95-0022 "Kinematic Bending Moments in Seismically Stressed Piles," by A. Nikolaou, G. Mylonakis and G. Gazetas, 12/23/95, (PB97-113914, MF-A03, A13).

NCEER-96-0001 "Dynamic Response of Unreinforced Masonry Buildings with Flexible Diaphragms," by A.C. Costley and D.P. Abrams," 10/10/96, (PB97-133573, MF-A03, A15).

NCEER-96-0002 "State of the Art Review: Foundations and Retaining Structures," by I. Po Lam, not available.

NCEER-96-0003 "Ductility of Rectangular Reinforced Concrete Bridge Columns with Moderate Confinement," by N. Wehbe, M. Saiidi, D. Sanders and B. Douglas, 11/7/96, (PB97-133557, A06, MF-A02).

NCEER-96-0004 "Proceedings of the Long-Span Bridge Seismic Research Workshop," edited by I.G. Buckle and I.M. Friedland, not available.

NCEER-96-0005 "Establish Representative Pier Types for Comprehensive Study: Eastern United States," by J. Kulicki and Z. Prucz, 5/28/96, (PB98-119217, A07, MF-A02).

NCEER-96-0006 "Establish Representative Pier Types for Comprehensive Study: Western United States," by R. Imbsen, R.A. Schamber and T.A. Osterkamp, 5/28/96, (PB98-118607, A07, MF-A02).

NCEER-96-0007 "Nonlinear Control Techniques for Dynamical Systems with Uncertain Parameters," by R.G. Ghanem and M.I. Bujakov, 5/27/96, (PB97-100259, A17, MF-A03).

NCEER-96-0008 "Seismic Evaluation of a 30-Year Old Non-Ductile Highway Bridge Pier and Its Retrofit," by J.B. Mander, B. Mahmoodzadegan, S. Bhadra and S.S. Chen, 5/31/96, (PB97-110902, MF-A03, A10).

NCEER-96-0009 "Seismic Performance of a Model Reinforced Concrete Bridge Pier Before and After Retrofit," by J.B. Mander, J.H. Kim and C.A. Ligozio, 5/31/96, (PB97-110910, MF-A02, A10).

NCEER-96-0010 "IDARC2D Version 4.0: A Computer Program for the Inelastic Damage Analysis of Buildings," by R.E. Valles, A.M. Reinhorn, S.K. Kunnath, C. Li and A. Madan, 6/3/96, (PB97-100234, A17, MF-A03).

NCEER-96-0011 "Estimation of the Economic Impact of Multiple Lifeline Disruption: Memphis Light, Gas and Water Division Case Study," by S.E. Chang, H.A. Seligson and R.T. Eguchi, 8/16/96, (PB97-133490, A11, MF-A03).

NCEER-96-0012 "Proceedings from the Sixth Japan-U.S. Workshop on Earthquake Resistant Design of Lifeline Facilities and Countermeasures Against Soil Liquefaction, Edited by M. Hamada and T. O'Rourke, 9/11/96, (PB97-133581, A99, MF-A06).

NCEER-96-0013 "Chemical Hazards, Mitigation and Preparedness in Areas of High Seismic Risk: A Methodology for Estimating the Risk of Post-Earthquake Hazardous Materials Release," by H.A. Seligson, R.T. Eguchi, K.J. Tierney and K. Richmond, 11/7/96, (PB97-133565, MF-A02, A08).

NCEER-96-0014 "Response of Steel Bridge Bearings to Reversed Cyclic Loading," by J.B. Mander, D-K. Kim, S.S. Chen and G.J. Premus, 11/13/96, (PB97-140735, A12, MF-A03).

NCEER-96-0015 "Highway Culvert Performance During Past Earthquakes," by T.L. Youd and C.J. Beckman, 11/25/96, (PB97-133532, A06, MF-A01).

NCEER-97-0001 "Evaluation, Prevention and Mitigation of Pounding Effects in Building Structures," by R.E. Valles and A.M. Reinhorn, 2/20/97, (PB97-159552, A14, MF-A03).

NCEER-97-0002 "Seismic Design Criteria for Bridges and Other Highway Structures," by C. Rojahn, R. Mayes, D.G. Anderson, J. Clark, J.H. Hom, R.V. Nutt and M.J. O'Rourke, 4/30/97, (PB97-194658, A06, MF-A03).

NCEER-97-0003 “Proceedings of the U.S.-Italian Workshop on Seismic Evaluation and Retrofit,” Edited by D.P. Abrams and G.M. Calvi, 3/19/97, (PB97-194666, A13, MF-A03).

NCEER-97-0004 "Investigation of Seismic Response of Buildings with Linear and Nonlinear Fluid Viscous Dampers," by A.A. Seleemah and M.C. Constantinou, 5/21/97, (PB98-109002, A15, MF-A03).

NCEER-97-0005 "Proceedings of the Workshop on Earthquake Engineering Frontiers in Transportation Facilities," edited by G.C. Lee and I.M. Friedland, 8/29/97, (PB98-128911, A25, MR-A04).

NCEER-97-0006 "Cumulative Seismic Damage of Reinforced Concrete Bridge Piers," by S.K. Kunnath, A. El-Bahy, A. Taylor and W. Stone, 9/2/97, (PB98-108814, A11, MF-A03).

NCEER-97-0007 "Structural Details to Accommodate Seismic Movements of Highway Bridges and Retaining Walls," by R.A. Imbsen, R.A. Schamber, E. Thorkildsen, A. Kartoum, B.T. Martin, T.N. Rosser and J.M. Kulicki, 9/3/97, (PB98-108996, A09, MF-A02).

NCEER-97-0008 "A Method for Earthquake Motion-Damage Relationships with Application to Reinforced Concrete Frames," by A. Singhal and A.S. Kiremidjian, 9/10/97, (PB98-108988, A13, MF-A03).

NCEER-97-0009 "Seismic Analysis and Design of Bridge Abutments Considering Sliding and Rotation," by K. Fishman and R. Richards, Jr., 9/15/97, (PB98-108897, A06, MF-A02).

NCEER-97-0010 "Proceedings of the FHWA/NCEER Workshop on the National Representation of Seismic Ground Motion for New and Existing Highway Facilities," edited by I.M. Friedland, M.S. Power and R.L. Mayes, 9/22/97, (PB98-128903, A21, MF-A04).

NCEER-97-0011 "Seismic Analysis for Design or Retrofit of Gravity Bridge Abutments," by K.L. Fishman, R. Richards, Jr. and R.C. Divito, 10/2/97, (PB98-128937, A08, MF-A02).

NCEER-97-0012 "Evaluation of Simplified Methods of Analysis for Yielding Structures," by P. Tsopelas, M.C. Constantinou, C.A. Kircher and A.S. Whittaker, 10/31/97, (PB98-128929, A10, MF-A03).

NCEER-97-0013 "Seismic Design of Bridge Columns Based on Control and Repairability of Damage," by C-T. Cheng and J.B. Mander, 12/8/97, (PB98-144249, A11, MF-A03).

NCEER-97-0014 "Seismic Resistance of Bridge Piers Based on Damage Avoidance Design," by J.B. Mander and C-T. Cheng, 12/10/97, (PB98-144223, A09, MF-A02).

NCEER-97-0015 “Seismic Response of Nominally Symmetric Systems with Strength Uncertainty,” by S. Balopoulou and M. Grigoriu, 12/23/97, (PB98-153422, A11, MF-A03).

NCEER-97-0016 “Evaluation of Seismic Retrofit Methods for Reinforced Concrete Bridge Columns,” by T.J. Wipf, F.W. Klaiber and F.M. Russo, 12/28/97, (PB98-144215, A12, MF-A03).

NCEER-97-0017 “Seismic Fragility of Existing Conventional Reinforced Concrete Highway Bridges,” by C.L. Mullen and A.S. Cakmak, 12/30/97, (PB98-153406, A08, MF-A02).

NCEER-97-0018 “Loss Asssessment of Memphis Buildings,” edited by D.P. Abrams and M. Shinozuka, 12/31/97, (PB98-144231, A13, MF-A03).

NCEER-97-0019 “Seismic Evaluation of Frames with Infill Walls Using Quasi-static Experiments,” by K.M. Mosalam, R.N. White and P. Gergely, 12/31/97, (PB98-153455, A07, MF-A02).

NCEER-97-0020 “Seismic Evaluation of Frames with Infill Walls Using Pseudo-dynamic Experiments,” by K.M. Mosalam, R.N. White and P. Gergely, 12/31/97, (PB98-153430, A07, MF-A02).

NCEER-97-0021 “Computational Strategies for Frames with Infill Walls: Discrete and Smeared Crack Analyses and Seismic Fragility,” by K.M. Mosalam, R.N. White and P. Gergely, 12/31/97, (PB98-153414, A10, MF-A02).

NCEER-97-0022 "Proceedings of the NCEER Workshop on Evaluation of Liquefaction Resistance of Soils," edited by T.L. Youd and I.M. Idriss, 12/31/97, (PB98-155617, A15, MF-A03).

MCEER-98-0001 "Extraction of Nonlinear Hysteretic Properties of Seismically Isolated Bridges from Quick-Release Field Tests," by Q. Chen, B.M. Douglas, E.M. Maragakis and I.G. Buckle, 5/26/98, (PB99-118838, A06, MF-A01).

MCEER-98-0002 "Methodologies for Evaluating the Importance of Highway Bridges," by A. Thomas, S. Eshenaur and J. Kulicki, 5/29/98, (PB99-118846, A10, MF-A02).

MCEER-98-0003 "Capacity Design of Bridge Piers and the Analysis of Overstrength," by J.B. Mander, A. Dutta and P. Goel, 6/1/98, (PB99-118853, A09, MF-A02).

MCEER-98-0004 "Evaluation of Bridge Damage Data from the Loma Prieta and Northridge, California Earthquakes," by N. Basoz and A. Kiremidjian, 6/2/98, (PB99-118861, A15, MF-A03).

MCEER-98-0005 "Screening Guide for Rapid Assessment of Liquefaction Hazard at Highway Bridge Sites," by T. L. Youd, 6/16/98, (PB99-118879, A06, not available on microfiche).

MCEER-98-0006 "Structural Steel and Steel/Concrete Interface Details for Bridges," by P. Ritchie, N. Kauhl and J. Kulicki, 7/13/98, (PB99-118945, A06, MF-A01).

MCEER-98-0007 "Capacity Design and Fatigue Analysis of Confined Concrete Columns," by A. Dutta and J.B. Mander, 7/14/98, (PB99-118960, A14, MF-A03).

MCEER-98-0008 "Proceedings of the Workshop on Performance Criteria for Telecommunication Services Under Earthquake Conditions," edited by A.J. Schiff, 7/15/98, (PB99-118952, A08, MF-A02).

MCEER-98-0009 "Fatigue Analysis of Unconfined Concrete Columns," by J.B. Mander, A. Dutta and J.H. Kim, 9/12/98, (PB99-123655, A10, MF-A02).

MCEER-98-0010 "Centrifuge Modeling of Cyclic Lateral Response of Pile-Cap Systems and Seat-Type Abutments in Dry Sands," by A.D. Gadre and R. Dobry, 10/2/98, (PB99-123606, A13, MF-A03).

MCEER-98-0011 "IDARC-BRIDGE: A Computational Platform for Seismic Damage Assessment of Bridge Structures," by A.M. Reinhorn, V. Simeonov, G. Mylonakis and Y. Reichman, 10/2/98, (PB99-162919, A15, MF-A03).

MCEER-98-0012 "Experimental Investigation of the Dynamic Response of Two Bridges Before and After Retrofitting with Elastomeric Bearings," by D.A. Wendichansky, S.S. Chen and J.B. Mander, 10/2/98, (PB99-162927, A15, MF-A03).

MCEER-98-0013 "Design Procedures for Hinge Restrainers and Hinge Sear Width for Multiple-Frame Bridges," by R. Des Roches and G.L. Fenves, 11/3/98, (PB99-140477, A13, MF-A03).

MCEER-98-0014 "Response Modification Factors for Seismically Isolated Bridges," by M.C. Constantinou and J.K. Quarshie, 11/3/98, (PB99-140485, A14, MF-A03).

MCEER-98-0015 "Proceedings of the U.S.-Italy Workshop on Seismic Protective Systems for Bridges," edited by I.M. Friedland and M.C. Constantinou, 11/3/98, (PB2000-101711, A22, MF-A04).

MCEER-98-0016 "Appropriate Seismic Reliability for Critical Equipment Systems: Recommendations Based on Regional Analysis of Financial and Life Loss," by K. Porter, C. Scawthorn, C. Taylor and N. Blais, 11/10/98, (PB99-157265, A08, MF-A02).

MCEER-98-0017 "Proceedings of the U.S. Japan Joint Seminar on Civil Infrastructure Systems Research," edited by M. Shinozuka and A. Rose, 11/12/98, (PB99-156713, A16, MF-A03).

MCEER-98-0018 "Modeling of Pile Footings and Drilled Shafts for Seismic Design," by I. PoLam, M. Kapuskar and D. Chaudhuri, 12/21/98, (PB99-157257, A09, MF-A02).

MCEER-99-0001 "Seismic Evaluation of a Masonry Infilled Reinforced Concrete Frame by Pseudodynamic Testing," by S.G. Buonopane and R.N. White, 2/16/99, (PB99-162851, A09, MF-A02).

MCEER-99-0002 "Response History Analysis of Structures with Seismic Isolation and Energy Dissipation Systems: Verification Examples for Program SAP2000," by J. Scheller and M.C. Constantinou, 2/22/99, (PB99-162869, A08, MF-A02).

MCEER-99-0003 "Experimental Study on the Seismic Design and Retrofit of Bridge Columns Including Axial Load Effects," by A. Dutta, T. Kokorina and J.B. Mander, 2/22/99, (PB99-162877, A09, MF-A02).

MCEER-99-0004 "Experimental Study of Bridge Elastomeric and Other Isolation and Energy Dissipation Systems with Emphasis on Uplift Prevention and High Velocity Near-source Seismic Excitation," by A. Kasalanati and M. C. Constantinou, 2/26/99, (PB99-162885, A12, MF-A03).

MCEER-99-0005 "Truss Modeling of Reinforced Concrete Shear-flexure Behavior," by J.H. Kim and J.B. Mander, 3/8/99, (PB99-163693, A12, MF-A03).

MCEER-99-0006 "Experimental Investigation and Computational Modeling of Seismic Response of a 1:4 Scale Model Steel Structure with a Load Balancing Supplemental Damping System," by G. Pekcan, J.B. Mander and S.S. Chen, 4/2/99, (PB99-162893, A11, MF-A03).

MCEER-99-0007 "Effect of Vertical Ground Motions on the Structural Response of Highway Bridges," by M.R. Button, C.J. Cronin and R.L. Mayes, 4/10/99, (PB2000-101411, A10, MF-A03).

MCEER-99-0008 "Seismic Reliability Assessment of Critical Facilities: A Handbook, Supporting Documentation, and Model Code Provisions," by G.S. Johnson, R.E. Sheppard, M.D. Quilici, S.J. Eder and C.R. Scawthorn, 4/12/99, (PB2000-101701, A18, MF-A04).

MCEER-99-0009 "Impact Assessment of Selected MCEER Highway Project Research on the Seismic Design of Highway Structures," by C. Rojahn, R. Mayes, D.G. Anderson, J.H. Clark, D'Appolonia Engineering, S. Gloyd and R.V. Nutt, 4/14/99, (PB99-162901, A10, MF-A02).

MCEER-99-0010 "Site Factors and Site Categories in Seismic Codes," by R. Dobry, R. Ramos and M.S. Power, 7/19/99, (PB2000-101705, A08, MF-A02).

MCEER-99-0011 "Restrainer Design Procedures for Multi-Span Simply-Supported Bridges," by M.J. Randall, M. Saiidi, E. Maragakis and T. Isakovic, 7/20/99, (PB2000-101702, A10, MF-A02).

MCEER-99-0012 "Property Modification Factors for Seismic Isolation Bearings," by M.C. Constantinou, P. Tsopelas, A. Kasalanati and E. Wolff, 7/20/99, (PB2000-103387, A11, MF-A03).

MCEER-99-0013 "Critical Seismic Issues for Existing Steel Bridges," by P. Ritchie, N. Kauhl and J. Kulicki, 7/20/99, (PB2000-101697, A09, MF-A02).

MCEER-99-0014 "Nonstructural Damage Database," by A. Kao, T.T. Soong and A. Vender, 7/24/99, (PB2000-101407, A06, MF-A01).

MCEER-99-0015 "Guide to Remedial Measures for Liquefaction Mitigation at Existing Highway Bridge Sites," by H.G. Cooke and J. K. Mitchell, 7/26/99, (PB2000-101703, A11, MF-A03).

MCEER-99-0016 "Proceedings of the MCEER Workshop on Ground Motion Methodologies for the Eastern United States," edited by N. Abrahamson and A. Becker, 8/11/99, (PB2000-103385, A07, MF-A02).

MCEER-99-0017 "Quindío, Colombia Earthquake of January 25, 1999: Reconnaissance Report," by A.P. Asfura and P.J. Flores, 10/4/99, (PB2000-106893, A06, MF-A01).

MCEER-99-0018 "Hysteretic Models for Cyclic Behavior of Deteriorating Inelastic Structures," by M.V. Sivaselvan and A.M. Reinhorn, 11/5/99, (PB2000-103386, A08, MF-A02).

MCEER-99-0019 "Proceedings of the 7th U.S.- Japan Workshop on Earthquake Resistant Design of Lifeline Facilities and Countermeasures Against Soil Liquefaction," edited by T.D. O'Rourke, J.P. Bardet and M. Hamada, 11/19/99, (PB2000-103354, A99, MF-A06).

MCEER-99-0020 "Development of Measurement Capability for Micro-Vibration Evaluations with Application to Chip Fabrication Facilities," by G.C. Lee, Z. Liang, J.W. Song, J.D. Shen and W.C. Liu, 12/1/99, (PB2000-105993, A08, MF-A02).

MCEER-99-0021 "Design and Retrofit Methodology for Building Structures with Supplemental Energy Dissipating Systems," by G. Pekcan, J.B. Mander and S.S. Chen, 12/31/99, (PB2000-105994, A11, MF-A03).

MCEER-00-0001 "The Marmara, Turkey Earthquake of August 17, 1999: Reconnaissance Report," edited by C. Scawthorn; with major contributions by M. Bruneau, R. Eguchi, T. Holzer, G. Johnson, J. Mander, J. Mitchell, W. Mitchell, A. Papageorgiou, C. Scaethorn, and G. Webb, 3/23/00, (PB2000-106200, A11, MF-A03).

MCEER-00-0002 "Proceedings of the MCEER Workshop for Seismic Hazard Mitigation of Health Care Facilities," edited by G.C. Lee, M. Ettouney, M. Grigoriu, J. Hauer and J. Nigg, 3/29/00, (PB2000-106892, A08, MF-A02).

MCEER-00-0003 "The Chi-Chi, Taiwan Earthquake of September 21, 1999: Reconnaissance Report," edited by G.C. Lee and C.H. Loh, with major contributions by G.C. Lee, M. Bruneau, I.G. Buckle, S.E. Chang, P.J. Flores, T.D. O'Rourke, M. Shinozuka, T.T. Soong, C-H. Loh, K-C. Chang, Z-J. Chen, J-S. Hwang, M-L. Lin, G-Y. Liu, K-C. Tsai, G.C. Yao and C-L. Yen, 4/30/00, (PB2001-100980, A10, MF-A02).

MCEER-00-0004 "Seismic Retrofit of End-Sway Frames of Steel Deck-Truss Bridges with a Supplemental Tendon System: Experimental and Analytical Investigation," by G. Pekcan, J.B. Mander and S.S. Chen, 7/1/00, (PB2001-100982, A10, MF-A02).

MCEER-00-0005 "Sliding Fragility of Unrestrained Equipment in Critical Facilities," by W.H. Chong and T.T. Soong, 7/5/00, (PB2001-100983, A08, MF-A02).

MCEER-00-0006 "Seismic Response of Reinforced Concrete Bridge Pier Walls in the Weak Direction," by N. Abo-Shadi, M. Saiidi and D. Sanders, 7/17/00, (PB2001-100981, A17, MF-A03).

MCEER-00-0007 "Low-Cycle Fatigue Behavior of Longitudinal Reinforcement in Reinforced Concrete Bridge Columns," by J. Brown and S.K. Kunnath, 7/23/00, (PB2001-104392, A08, MF-A02).

MCEER-00-0008 "Soil Structure Interaction of Bridges for Seismic Analysis," I. PoLam and H. Law, 9/25/00, (PB2001-105397, A08, MF-A02).

MCEER-00-0009 "Proceedings of the First MCEER Workshop on Mitigation of Earthquake Disaster by Advanced Technologies (MEDAT-1), edited by M. Shinozuka, D.J. Inman and T.D. O'Rourke, 11/10/00, (PB2001-105399, A14, MF-A03).

MCEER-00-0010 "Development and Evaluation of Simplified Procedures for Analysis and Design of Buildings with Passive Energy Dissipation Systems, Revision 01," by O.M. Ramirez, M.C. Constantinou, C.A. Kircher, A.S. Whittaker, M.W. Johnson, J.D. Gomez and C. Chrysostomou, 11/16/01, (PB2001-105523, A23, MF-A04).

MCEER-00-0011 "Dynamic Soil-Foundation-Structure Interaction Analyses of Large Caissons," by C-Y. Chang, C-M. Mok, Z-L. Wang, R. Settgast, F. Waggoner, M.A. Ketchum, H.M. Gonnermann and C-C. Chin, 12/30/00, (PB2001-104373, A07, MF-A02).

MCEER-00-0012 "Experimental Evaluation of Seismic Performance of Bridge Restrainers," by A.G. Vlassis, E.M. Maragakis and M. Saiid Saiidi, 12/30/00, (PB2001-104354, A09, MF-A02).

MCEER-00-0013 "Effect of Spatial Variation of Ground Motion on Highway Structures," by M. Shinozuka, V. Saxena and G. Deodatis, 12/31/00, (PB2001-108755, A13, MF-A03).

MCEER-00-0014 "A Risk-Based Methodology for Assessing the Seismic Performance of Highway Systems," by S.D. Werner, C.E. Taylor, J.E. Moore, II, J.S. Walton and S. Cho, 12/31/00, (PB2001-108756, A14, MF-A03).

MCEER-01-0001 "Experimental Investigation of P-Delta Effects to Collapse During Earthquakes," by D. Vian and M. Bruneau, 6/25/01, (PB2002-100534, A17, MF-A03).

MCEER-01-0002 "Proceedings of the Second MCEER Workshop on Mitigation of Earthquake Disaster by Advanced Technologies (MEDAT-2)," edited by M. Bruneau and D.J. Inman, 7/23/01, (PB2002-100434, A16, MF-A03).

MCEER-01-0003 "Sensitivity Analysis of Dynamic Systems Subjected to Seismic Loads," by C. Roth and M. Grigoriu, 9/18/01, (PB2003-100884, A12, MF-A03).

MCEER-01-0004 "Overcoming Obstacles to Implementing Earthquake Hazard Mitigation Policies: Stage 1 Report," by D.J. Alesch and W.J. Petak, 12/17/01, (PB2002-107949, A07, MF-A02).

MCEER-01-0005 "Updating Real-Time Earthquake Loss Estimates: Methods, Problems and Insights," by C.E. Taylor, S.E. Chang and R.T. Eguchi, 12/17/01, (PB2002-107948, A05, MF-A01).

MCEER-01-0006 "Experimental Investigation and Retrofit of Steel Pile Foundations and Pile Bents Under Cyclic Lateral Loadings," by A. Shama, J. Mander, B. Blabac and S. Chen, 12/31/01, (PB2002-107950, A13, MF-A03).

MCEER-02-0001 "Assessment of Performance of Bolu Viaduct in the 1999 Duzce Earthquake in Turkey" by P.C. Roussis, M.C. Constantinou, M. Erdik, E. Durukal and M. Dicleli, 5/8/02, (PB2003-100883, A08, MF-A02).

MCEER-02-0002 "Seismic Behavior of Rail Counterweight Systems of Elevators in Buildings," by M.P. Singh, Rildova and L.E. Suarez, 5/27/02. (PB2003-100882, A11, MF-A03).

MCEER-02-0003 "Development of Analysis and Design Procedures for Spread Footings," by G. Mylonakis, G. Gazetas, S. Nikolaou and A. Chauncey, 10/02/02, (PB2004-101636, A13, MF-A03, CD-A13).

MCEER-02-0004 "Bare-Earth Algorithms for Use with SAR and LIDAR Digital Elevation Models," by C.K. Huyck, R.T. Eguchi and B. Houshmand, 10/16/02, (PB2004-101637, A07, CD-A07).

MCEER-02-0005 "Review of Energy Dissipation of Compression Members in Concentrically Braced Frames," by K.Lee and M. Bruneau, 10/18/02, (PB2004-101638, A10, CD-A10).

MCEER-03-0001 "Experimental Investigation of Light-Gauge Steel Plate Shear Walls for the Seismic Retrofit of Buildings" by J. Berman and M. Bruneau, 5/2/03, (PB2004-101622, A10, MF-A03, CD-A10).

MCEER-03-0002 "Statistical Analysis of Fragility Curves," by M. Shinozuka, M.Q. Feng, H. Kim, T. Uzawa and T. Ueda, 6/16/03, (PB2004-101849, A09, CD-A09).

MCEER-03-0003 "Proceedings of the Eighth U.S.-Japan Workshop on Earthquake Resistant Design f Lifeline Facilities and Countermeasures Against Liquefaction," edited by M. Hamada, J.P. Bardet and T.D. O'Rourke, 6/30/03, (PB2004-104386, A99, CD-A99).

MCEER-03-0004 "Proceedings of the PRC-US Workshop on Seismic Analysis and Design of Special Bridges," edited by L.C. Fan and G.C. Lee, 7/15/03, (PB2004-104387, A14, CD-A14).

MCEER-03-0005 "Urban Disaster Recovery: A Framework and Simulation Model," by S.B. Miles and S.E. Chang, 7/25/03, (PB2004-104388, A07, CD-A07).

MCEER-03-0006 "Behavior of Underground Piping Joints Due to Static and Dynamic Loading," by R.D. Meis, M. Maragakis and R. Siddharthan, 11/17/03, (PB2005-102194, A13, MF-A03, CD-A00).

MCEER-04-0001 "Experimental Study of Seismic Isolation Systems with Emphasis on Secondary System Response and Verification of Accuracy of Dynamic Response History Analysis Methods," by E. Wolff and M. Constantinou, 1/16/04 (PB2005-102195, A99, MF-E08, CD-A00).

MCEER-04-0002 "Tension, Compression and Cyclic Testing of Engineered Cementitious Composite Materials," by K. Kesner and S.L. Billington, 3/1/04, (PB2005-102196, A08, CD-A08).

MCEER-04-0003 “Cyclic Testing of Braces Laterally Restrained by Steel Studs to Enhance Performance During Earthquakes,” by O.C. Celik, J.W. Berman and M. Bruneau, 3/16/04, (PB2005-102197, A13, MF-A03, CD-A00).

MCEER-04-0004 “Methodologies for Post Earthquake Building Damage Detection Using SAR and Optical Remote Sensing: Application to the August 17, 1999 Marmara, Turkey Earthquake,” by C.K. Huyck, B.J. Adams, S. Cho, R.T. Eguchi, B. Mansouri and B. Houshmand, 6/15/04, (PB2005-104888, A10, CD-A00).

MCEER-04-0005 “Nonlinear Structural Analysis Towards Collapse Simulation: A Dynamical Systems Approach,” by M.V. Sivaselvan and A.M. Reinhorn, 6/16/04, (PB2005-104889, A11, MF-A03, CD-A00).

MCEER-04-0006 “Proceedings of the Second PRC-US Workshop on Seismic Analysis and Design of Special Bridges,” edited by G.C. Lee and L.C. Fan, 6/25/04, (PB2005-104890, A16, CD-A00).

MCEER-04-0007 “Seismic Vulnerability Evaluation of Axially Loaded Steel Built-up Laced Members,” by K. Lee and M. Bruneau, 6/30/04, (PB2005-104891, A16, CD-A00).

MCEER-04-0008 “Evaluation of Accuracy of Simplified Methods of Analysis and Design of Buildings with Damping Systems for Near-Fault and for Soft-Soil Seismic Motions,” by E.A. Pavlou and M.C. Constantinou, 8/16/04, (PB2005-104892, A08, MF-A02, CD-A00).

MCEER-04-0009 “Assessment of Geotechnical Issues in Acute Care Facilities in California,” by M. Lew, T.D. O’Rourke, R. Dobry and M. Koch, 9/15/04, (PB2005-104893, A08, CD-A00).

MCEER-04-0010 “Scissor-Jack-Damper Energy Dissipation System,” by A.N. Sigaher-Boyle and M.C. Constantinou, 12/1/04 (PB2005-108221).

MCEER-04-0011 “Seismic Retrofit of Bridge Steel Truss Piers Using a Controlled Rocking Approach,” by M. Pollino and M. Bruneau, 12/20/04 (PB2006-105795).

MCEER-05-0001 “Experimental and Analytical Studies of Structures Seismically Isolated with an Uplift-Restraint Isolation System,” by P.C. Roussis and M.C. Constantinou, 1/10/05 (PB2005-108222).

MCEER-05-0002 “A Versatile Experimentation Model for Study of Structures Near Collapse Applied to Seismic Evaluation of Irregular Structures,” by D. Kusumastuti, A.M. Reinhorn and A. Rutenberg, 3/31/05 (PB2006-101523).

MCEER-05-0003 “Proceedings of the Third PRC-US Workshop on Seismic Analysis and Design of Special Bridges,” edited by L.C. Fan and G.C. Lee, 4/20/05, (PB2006-105796).

MCEER-05-0004 “Approaches for the Seismic Retrofit of Braced Steel Bridge Piers and Proof-of-Concept Testing of an Eccentrically Braced Frame with Tubular Link,” by J.W. Berman and M. Bruneau, 4/21/05 (PB2006-101524).

MCEER-05-0005 “Simulation of Strong Ground Motions for Seismic Fragility Evaluation of Nonstructural Components in Hospitals,” by A. Wanitkorkul and A. Filiatrault, 5/26/05 (PB2006-500027).

MCEER-05-0006 “Seismic Safety in California Hospitals: Assessing an Attempt to Accelerate the Replacement or Seismic Retrofit of Older Hospital Facilities,” by D.J. Alesch, L.A. Arendt and W.J. Petak, 6/6/05 (PB2006-105794).

MCEER-05-0007 “Development of Seismic Strengthening and Retrofit Strategies for Critical Facilities Using Engineered Cementitious Composite Materials,” by K. Kesner and S.L. Billington, 8/29/05 (PB2006-111701).

MCEER-05-0008 “Experimental and Analytical Studies of Base Isolation Systems for Seismic Protection of Power Transformers,” by N. Murota, M.Q. Feng and G-Y. Liu, 9/30/05 (PB2006-111702).

MCEER-05-0009 “3D-BASIS-ME-MB: Computer Program for Nonlinear Dynamic Analysis of Seismically Isolated Structures,” by P.C. Tsopelas, P.C. Roussis, M.C. Constantinou, R. Buchanan and A.M. Reinhorn, 10/3/05 (PB2006-111703).

MCEER-05-0010 “Steel Plate Shear Walls for Seismic Design and Retrofit of Building Structures,” by D. Vian and M. Bruneau, 12/15/05 (PB2006-111704).

MCEER-05-0011 "The Performance-Based Design Paradigm," by M.J. Astrella and A. Whittaker, 12/15/05 (PB2006-111705).

MCEER-06-0001 "Seismic Fragility of Suspended Ceiling Systems," H. Badillo-Almaraz, A.S. Whittaker, A.M. Reinhorn and G.P. Cimellaro, 2/4/06 (PB2006-111706).

MCEER-06-0002 "Multi-Dimensional Fragility of Structures," by G.P. Cimellaro, A.M. Reinhorn and M. Bruneau, 3/1/06 (PB2007-106974, A09, MF-A02, CD A00).

MCEER-06-0003 "Built-Up Shear Links as Energy Dissipators for Seismic Protection of Bridges," by P. Dusicka, A.M. Itani and I.G. Buckle, 3/15/06 (PB2006-111708).

MCEER-06-0004 "Analytical Investigation of the Structural Fuse Concept," by R.E. Vargas and M. Bruneau, 3/16/06 (PB2006-111709).

MCEER-06-0005 "Experimental Investigation of the Structural Fuse Concept," by R.E. Vargas and M. Bruneau, 3/17/06 (PB2006-111710).

MCEER-06-0006 "Further Development of Tubular Eccentrically Braced Frame Links for the Seismic Retrofit of Braced Steel Truss Bridge Piers," by J.W. Berman and M. Bruneau, 3/27/06 (PB2007-105147).

MCEER-06-0007 "REDARS Validation Report," by S. Cho, C.K. Huyck, S. Ghosh and R.T. Eguchi, 8/8/06 (PB2007-106983).

MCEER-06-0008 "Review of Current NDE Technologies for Post-Earthquake Assessment of Retrofitted Bridge Columns," by J.W. Song, Z. Liang and G.C. Lee, 8/21/06 (PB2007-106984).

MCEER-06-0009 "Liquefaction Remediation in Silty Soils Using Dynamic Compaction and Stone Columns," by S. Thevanayagam, G.R. Martin, R. Nashed, T. Shenthan, T. Kanagalingam and N. Ecemis, 8/28/06 (PB2007-106985).

MCEER-06-0010 "Conceptual Design and Experimental Investigation of Polymer Matrix Composite Infill Panels for Seismic Retrofitting," by W. Jung, M. Chiewanichakorn and A.J. Aref, 9/21/06 (PB2007-106986).

MCEER-06-0011 "A Study of the Coupled Horizontal-Vertical Behavior of Elastomeric and Lead-Rubber Seismic Isolation Bearings," by G.P. Warn and A.S. Whittaker, 9/22/06 (PB2007-108679).

MCEER-06-0012 "Proceedings of the Fourth PRC-US Workshop on Seismic Analysis and Design of Special Bridges: Advancing Bridge Technologies in Research, Design, Construction and Preservation," Edited by L.C. Fan, G.C. Lee and L. Ziang, 10/12/06 (PB2007-109042).

MCEER-06-0013 "Cyclic Response and Low Cycle Fatigue Characteristics of Plate Steels," by P. Dusicka, A.M. Itani and I.G. Buckle, 11/1/06 06 (PB2007-106987).

MCEER-06-0014 "Proceedings of the Second US-Taiwan Bridge Engineering Workshop," edited by W.P. Yen, J. Shen, J-Y. Chen and M. Wang, 11/15/06 (PB2008-500041).

MCEER-06-0015 "User Manual and Technical Documentation for the REDARS^{TM} Import Wizard," by S. Cho, S. Ghosh, C.K. Huyck and S.D. Werner, 11/30/06 (PB2007-114766).

MCEER-06-0016 "Hazard Mitigation Strategy and Monitoring Technologies for Urban and Infrastructure Public Buildings: Proceedings of the China-US Workshops," edited by X.Y. Zhou, A.L. Zhang, G.C. Lee and M. Tong, 12/12/06 (PB2008-500018).

MCEER-07-0001 "Static and Kinetic Coefficients of Friction for Rigid Blocks," by C. Kafali, S. Fathali, M. Grigoriu and A.S. Whittaker, 3/20/07 (PB2007-114767).

MCEER-07-0002 "Hazard Mitigation Investment Decision Making: Organizational Response to Legislative Mandate," by L.A. Arendt, D.J. Alesch and W.J. Petak, 4/9/07 (PB2007-114768).

MCEER-07-0003 "Seismic Behavior of Bidirectional-Resistant Ductile End Diaphragms with Unbonded Braces in Straight or Skewed Steel Bridges," by O. Celik and M. Bruneau, 4/11/07 (PB2008-105141).

MCEER-07-0004 "Modeling Pile Behavior in Large Pile Groups Under Lateral Loading," by A.M. Dodds and G.R. Martin, 4/16/07(PB2008-105142).

MCEER-07-0005 "Experimental Investigation of Blast Performance of Seismically Resistant Concrete-Filled Steel Tube Bridge Piers," by S. Fujikura, M. Bruneau and D. Lopez-Garcia, 4/20/07 (PB2008-105143).

MCEER-07-0006 "Seismic Analysis of Conventional and Isolated Liquefied Natural Gas Tanks Using Mechanical Analogs," by I.P. Christovasilis and A.S. Whittaker, 5/1/07, not available.

MCEER-07-0007 "Experimental Seismic Performance Evaluation of Isolation/Restraint Systems for Mechanical Equipment – Part 1: Heavy Equipment Study," by S. Fathali and A. Filiatrault, 6/6/07 (PB2008-105144).

MCEER-07-0008 "Seismic Vulnerability of Timber Bridges and Timber Substructures," by A.A. Sharma, J.B. Mander, I.M. Friedland and D.R. Allicock, 6/7/07 (PB2008-105145).

MCEER-07-0009 "Experimental and Analytical Study of the XY-Friction Pendulum (XY-FP) Bearing for Bridge Applications," by C.C. Marin-Artieda, A.S. Whittaker and M.C. Constantinou, 6/7/07 (PB2008-105191).

MCEER-07-0010 "Proceedings of the PRC-US Earthquake Engineering Forum for Young Researchers," Edited by G.C. Lee and X.Z. Qi, 6/8/07 (PB2008-500058).

MCEER-07-0011 "Design Recommendations for Perforated Steel Plate Shear Walls," by R. Purba and M. Bruneau, 6/18/07, (PB2008-105192).

MCEER-07-0012 "Performance of Seismic Isolation Hardware Under Service and Seismic Loading," by M.C. Constantinou, A.S. Whittaker, Y. Kalpakidis, D.M. Fenz and G.P. Warn, 8/27/07, (PB2008-105193).

MCEER-07-0013 "Experimental Evaluation of the Seismic Performance of Hospital Piping Subassemblies," by E.R. Goodwin, E. Maragakis and A.M. Itani, 9/4/07, (PB2008-105194).

MCEER-07-0014 "A Simulation Model of Urban Disaster Recovery and Resilience: Implementation for the 1994 Northridge Earthquake," by S. Miles and S.E. Chang, 9/7/07, (PB2008-106426).

MCEER-07-0015 "Statistical and Mechanistic Fragility Analysis of Concrete Bridges," by M. Shinozuka, S. Banerjee and S-H. Kim, 9/10/07, (PB2008-106427).

MCEER-07-0016 "Three-Dimensional Modeling of Inelastic Buckling in Frame Structures," by M. Schachter and AM. Reinhorn, 9/13/07, (PB2008-108125).

MCEER-07-0017 "Modeling of Seismic Wave Scattering on Pile Groups and Caissons," by I. Po Lam, H. Law and C.T. Yang, 9/17/07 (PB2008-108150).

MCEER-07-0018 "Bridge Foundations: Modeling Large Pile Groups and Caissons for Seismic Design," by I. Po Lam, H. Law and G.R. Martin (Coordinating Author), 12/1/07 (PB2008-111190).

MCEER-07-0019 "Principles and Performance of Roller Seismic Isolation Bearings for Highway Bridges," by G.C. Lee, Y.C. Ou, Z. Liang, T.C. Niu and J. Song, 12/10/07 (PB2009-110466).

MCEER-07-0020 "Centrifuge Modeling of Permeability and Pinning Reinforcement Effects on Pile Response to Lateral Spreading," by L.L Gonzalez-Lagos, T. Abdoun and R. Dobry, 12/10/07 (PB2008-111191).

MCEER-07-0021 "Damage to the Highway System from the Pisco, Perú Earthquake of August 15, 2007," by J.S. O'Connor, L. Mesa and M. Nykamp, 12/10/07, (PB2008-108126).

MCEER-07-0022 "Experimental Seismic Performance Evaluation of Isolation/Restraint Systems for Mechanical Equipment – Part 2: Light Equipment Study," by S. Fathali and A. Filiatrault, 12/13/07 (PB2008-111192).

MCEER-07-0023 "Fragility Considerations in Highway Bridge Design," by M. Shinozuka, S. Banerjee and S.H. Kim, 12/14/07 (PB2008-111193).

MCEER-07-0024 "Performance Estimates for Seismically Isolated Bridges," by G.P. Warn and A.S. Whittaker, 12/30/07 (PB2008-112230).

MCEER-08-0001 "Seismic Performance of Steel Girder Bridge Superstructures with Conventional Cross Frames," by L.P. Carden, A.M. Itani and I.G. Buckle, 1/7/08, (PB2008-112231).

MCEER-08-0002 "Seismic Performance of Steel Girder Bridge Superstructures with Ductile End Cross Frames with Seismic Isolators," by L.P. Carden, A.M. Itani and I.G. Buckle, 1/7/08 (PB2008-112232).

MCEER-08-0003 "Analytical and Experimental Investigation of a Controlled Rocking Approach for Seismic Protection of Bridge Steel Truss Piers," by M. Pollino and M. Bruneau, 1/21/08 (PB2008-112233).

MCEER-08-0004 "Linking Lifeline Infrastructure Performance and Community Disaster Resilience: Models and Multi-Stakeholder Processes," by S.E. Chang, C. Pasion, K. Tatebe and R. Ahmad, 3/3/08 (PB2008-112234).

MCEER-08-0005 "Modal Analysis of Generally Damped Linear Structures Subjected to Seismic Excitations," by J. Song, Y-L. Chu, Z. Liang and G.C. Lee, 3/4/08 (PB2009-102311).

MCEER-08-0006 "System Performance Under Multi-Hazard Environments," by C. Kafali and M. Grigoriu, 3/4/08 (PB2008-112235).

MCEER-08-0007 "Mechanical Behavior of Multi-Spherical Sliding Bearings," by D.M. Fenz and M.C. Constantinou, 3/6/08 (PB2008-112236).

MCEER-08-0008 "Post-Earthquake Restoration of the Los Angeles Water Supply System," by T.H.P. Tabucchi and R.A. Davidson, 3/7/08 (PB2008-112237).

MCEER-08-0009 "Fragility Analysis of Water Supply Systems," by A. Jacobson and M. Grigoriu, 3/10/08 (PB2009-105545).

MCEER-08-0010 "Experimental Investigation of Full-Scale Two-Story Steel Plate Shear Walls with Reduced Beam Section Connections," by B. Qu, M. Bruneau, C-H. Lin and K-C. Tsai, 3/17/08 (PB2009-106368).

MCEER-08-0011 "Seismic Evaluation and Rehabilitation of Critical Components of Electrical Power Systems," S. Ersoy, B. Feizi, A. Ashrafi and M. Ala Saadeghvaziri, 3/17/08 (PB2009-105546).

MCEER-08-0012 "Seismic Behavior and Design of Boundary Frame Members of Steel Plate Shear Walls," by B. Qu and M. Bruneau, 4/26/08 . (PB2009-106744).

MCEER-08-0013 "Development and Appraisal of a Numerical Cyclic Loading Protocol for Quantifying Building System Performance," by A. Filiatrault, A. Wanitkorkul and M. Constantinou, 4/27/08 (PB2009-107906).

MCEER-08-0014 "Structural and Nonstructural Earthquake Design: The Challenge of Integrating Specialty Areas in Designing Complex, Critical Facilities," by W.J. Petak and D.J. Alesch, 4/30/08 (PB2009-107907).

MCEER-08-0015 "Seismic Performance Evaluation of Water Systems," by Y. Wang and T.D. O'Rourke, 5/5/08 (PB2009-107908).

MCEER-08-0016 "Seismic Response Modeling of Water Supply Systems," by P. Shi and T.D. O'Rourke, 5/5/08 (PB2009-107910).

MCEER-08-0017 "Numerical and Experimental Studies of Self-Centering Post-Tensioned Steel Frames," by D. Wang and A. Filiatrault, 5/12/08 (PB2009-110479).

MCEER-08-0018 "Development, Implementation and Verification of Dynamic Analysis Models for Multi-Spherical Sliding Bearings," by D.M. Fenz and M.C. Constantinou, 8/15/08 (PB2009-107911).

MCEER-08-0019 "Performance Assessment of Conventional and Base Isolated Nuclear Power Plants for Earthquake Blast Loadings," by Y.N. Huang, A.S. Whittaker and N. Luco, 10/28/08 (PB2009-107912).

MCEER-08-0020 “Remote Sensing for Resilient Multi-Hazard Disaster Response – Volume I: Introduction to Damage Assessment Methodologies,” by B.J. Adams and R.T. Eguchi, 11/17/08 (PB2010-102695).

MCEER-08-0021 “Remote Sensing for Resilient Multi-Hazard Disaster Response – Volume II: Counting the Number of Collapsed Buildings Using an Object-Oriented Analysis: Case Study of the 2003 Bam Earthquake,” by L. Gusella, C.K. Huyck and B.J. Adams, 11/17/08 (PB2010-100925).

MCEER-08-0022 “Remote Sensing for Resilient Multi-Hazard Disaster Response – Volume III: Multi-Sensor Image Fusion Techniques for Robust Neighborhood-Scale Urban Damage Assessment,” by B.J. Adams and A. McMillan, 11/17/08 (PB2010-100926).

MCEER-08-0023 “Remote Sensing for Resilient Multi-Hazard Disaster Response – Volume IV: A Study of Multi-Temporal and Multi-Resolution SAR Imagery for Post-Katrina Flood Monitoring in New Orleans,” by A. McMillan, J.G. Morley, B.J. Adams and S. Chesworth, 11/17/08 (PB2010-100927).

MCEER-08-0024 “Remote Sensing for Resilient Multi-Hazard Disaster Response – Volume V: Integration of Remote Sensing Imagery and VIEWS^{TM} Field Data for Post-Hurricane Charley Building Damage Assessment,” by J.A. Womble, K. Mehta and B.J. Adams, 11/17/08 (PB2009-115532).

MCEER-08-0025 “Building Inventory Compilation for Disaster Management: Application of Remote Sensing and Statistical Modeling,” by P. Sarabandi, A.S. Kiremidjian, R.T. Eguchi and B. J. Adams, 11/20/08 (PB2009-110484).

MCEER-08-0026 “New Experimental Capabilities and Loading Protocols for Seismic Qualification and Fragility Assessment of Nonstructural Systems,” by R. Retamales, G. Mosqueda, A. Filiatrault and A. Reinhorn, 11/24/08 (PB2009-110485).

MCEER-08-0027 “Effects of Heating and Load History on the Behavior of Lead-Rubber Bearings,” by I.V. Kalpakidis and M.C. Constantinou, 12/1/08 (PB2009-115533).

MCEER-08-0028 “Experimental and Analytical Investigation of Blast Performance of Seismically Resistant Bridge Piers,” by S.Fujikura and M. Bruneau, 12/8/08 (PB2009-115534).

MCEER-08-0029 “Evolutionary Methodology for Aseismic Decision Support,” by Y. Hu and G. Dargush, 12/15/08.

MCEER-08-0030 “Development of a Steel Plate Shear Wall Bridge Pier System Conceived from a Multi-Hazard Perspective,” by D. Keller and M. Bruneau, 12/19/08 (PB2010-102696).

MCEER-09-0001 “Modal Analysis of Arbitrarily Damped Three-Dimensional Linear Structures Subjected to Seismic Excitations,” by Y.L. Chu, J. Song and G.C. Lee, 1/31/09 (PB2010-100922).

MCEER-09-0002 “Air-Blast Effects on Structural Shapes,” by G. Ballantyne, A.S. Whittaker, A.J. Aref and G.F. Dargush, 2/2/09 (PB2010-102697).

MCEER-09-0003 “Water Supply Performance During Earthquakes and Extreme Events,” by A.L. Bonneau and T.D. O’Rourke, 2/16/09 (PB2010-100923).

MCEER-09-0004 “Generalized Linear (Mixed) Models of Post-Earthquake Ignitions,” by R.A. Davidson, 7/20/09 (PB2010-102698).

MCEER-09-0005 “Seismic Testing of a Full-Scale Two-Story Light-Frame Wood Building: NEESWood Benchmark Test,” by I.P. Christovasilis, A. Filiatrault and A. Wanitkorkul, 7/22/09 (PB2012-102401).

MCEER-09-0006 “IDARC2D Version 7.0: A Program for the Inelastic Damage Analysis of Structures,” by A.M. Reinhorn, H. Roh, M. Sivaselvan, S.K. Kunnath, R.E. Valles, A. Madan, C. Li, R. Lobo and Y.J. Park, 7/28/09 (PB2010-103199).

MCEER-09-0007 “Enhancements to Hospital Resiliency: Improving Emergency Planning for and Response to Hurricanes,” by D.B. Hess and L.A. Arendt, 7/30/09 (PB2010-100924).

MCEER-09-0008 "Assessment of Base-Isolated Nuclear Structures for Design and Beyond-Design Basis Earthquake Shaking," by Y.N. Huang, A.S. Whittaker, R.P. Kennedy and R.L. Mayes, 8/20/09 (PB2010-102699).

MCEER-09-0009 "Quantification of Disaster Resilience of Health Care Facilities," by G.P. Cimellaro, C. Fumo, A.M Reinhorn and M. Bruneau, 9/14/09 (PB2010-105384).

MCEER-09-0010 "Performance-Based Assessment and Design of Squat Reinforced Concrete Shear Walls," by C.K. Gulec and A.S. Whittaker, 9/15/09 (PB2010-102700).

MCEER-09-0011 "Proceedings of the Fourth US-Taiwan Bridge Engineering Workshop," edited by W.P. Yen, J.J. Shen, T.M. Lee and R.B. Zheng, 10/27/09 (PB2010-500009).

MCEER-09-0012 "Proceedings of the Special International Workshop on Seismic Connection Details for Segmental Bridge Construction," edited by W. Phillip Yen and George C. Lee, 12/21/09 (PB2012-102402).

MCEER-10-0001 "Direct Displacement Procedure for Performance-Based Seismic Design of Multistory Woodframe Structures," by W. Pang and D. Rosowsky, 4/26/10 (PB2012-102403).

MCEER-10-0002 "Simplified Direct Displacement Design of Six-Story NEESWood Capstone Building and Pre-Test Seismic Performance Assessment," by W. Pang, D. Rosowsky, J. van de Lindt and S. Pei, 5/28/10 (PB2012-102404).

MCEER-10-0003 "Integration of Seismic Protection Systems in Performance-Based Seismic Design of Woodframed Structures," by J.K. Shinde and M.D. Symans, 6/18/10 (PB2012-102405).

MCEER-10-0004 "Modeling and Seismic Evaluation of Nonstructural Components: Testing Frame for Experimental Evaluation of Suspended Ceiling Systems," by A.M. Reinhorn, K.P. Ryu and G. Maddaloni, 6/30/10 (PB2012-102406).

MCEER-10-0005 "Analytical Development and Experimental Validation of a Structural-Fuse Bridge Pier Concept," by S. El-Bahey and M. Bruneau, 10/1/10 (PB2012-102407).

MCEER-10-0006 "A Framework for Defining and Measuring Resilience at the Community Scale: The PEOPLES Resilience Framework," by C.S. Renschler, A.E. Frazier, L.A. Arendt, G.P. Cimellaro, A.M. Reinhorn and M. Bruneau, 10/8/10 (PB2012-102408).

MCEER-10-0007 "Impact of Horizontal Boundary Elements Design on Seismic Behavior of Steel Plate Shear Walls," by R. Purba and M. Bruneau, 11/14/10 (PB2012-102409).

MCEER-10-0008 "Seismic Testing of a Full-Scale Mid-Rise Building: The NEESWood Capstone Test," by S. Pei, J.W. van de Lindt, S.E. Pryor, H. Shimizu, H. Isoda and D.R. Rammer, 12/1/10 (PB2012-102410).

MCEER-10-0009 "Modeling the Effects of Detonations of High Explosives to Inform Blast-Resistant Design," by P. Sherkar, A.S. Whittaker and A.J. Aref, 12/1/10 (PB2012-102411).

MCEER-10-0010 "L'Aquila Earthquake of April 6, 2009 in Italy: Rebuilding a Resilient City to Withstand Multiple Hazards," by G.P. Cimellaro, I.P. Christovasilis, A.M. Reinhorn, A. De Stefano and T. Kirova, 12/29/10.

MCEER-11-0001 "Numerical and Experimental Investigation of the Seismic Response of Light-Frame Wood Structures," by I.P. Christovasilis and A. Filiatrault, 8/8/11 (PB2012-102412).

MCEER-11-0002 "Seismic Design and Analysis of a Precast Segmental Concrete Bridge Model," by M. Anagnostopoulou, A. Filiatrault and A. Aref, 9/15/11.

MCEER-11-0003 'Proceedings of the Workshop on Improving Earthquake Response of Substation Equipment," Edited by A.M. Reinhorn, 9/19/11 (PB2012-102413).

MCEER-11-0004 "LRFD-Based Analysis and Design Procedures for Bridge Bearings and Seismic Isolators," by M.C. Constantinou, I. Kalpakidis, A. Filiatrault and R.A. Ecker Lay, 9/26/11.

MCEER-11-0005 "Experimental Seismic Evaluation, Model Parameterization, and Effects of Cold-Formed Steel-Framed Gypsum Partition Walls on the Seismic Performance of an Essential Facility," by R. Davies, R. Retamales, G. Mosqueda and A. Filiatrault, 10/12/11.

MCEER-11-0006 "Modeling and Seismic Performance Evaluation of High Voltage Transformers and Bushings," by A.M. Reinhorn, K. Oikonomou, H. Roh, A. Schiff and L. Kempner, Jr., 10/3/11.

MCEER-11-0007 "Extreme Load Combinations: A Survey of State Bridge Engineers," by G.C. Lee, Z. Liang, J.J. Shen and J.S. O'Connor, 10/14/11.

MCEER-12-0001 "Simplified Analysis Procedures in Support of Performance Based Seismic Design," by Y.N. Huang and A.S. Whittaker.

MCEER-12-0002 "Seismic Protection of Electrical Transformer Bushing Systems by Stiffening Techniques," by M. Koliou, A. Filiatrault, A.M. Reinhorn and N. Oliveto, 6/1/12.

MCEER-12-0003 "Post-Earthquake Bridge Inspection Guidelines," by J.S. O'Connor and S. Alampalli, 6/8/12.

MCEER-12-0004 "Integrated Design Methodology for Isolated Floor Systems in Single-Degree-of-Freedom Structural Fuse Systems," by S. Cui, M. Bruneau and M.C. Constantinou, 6/13/12.

MCEER-12-0005 "Characterizing the Rotational Components of Earthquake Ground Motion," by D. Basu, A.S. Whittaker and M.C. Constantinou, 6/15/12.

MCEER-12-0006 "Bayesian Fragility for Nonstructural Systems," by C.H. Lee and M.D. Grigoriu, 9/12/12.

MCEER-12-0007 "A Numerical Model for Capturing the In-Plane Seismic Response of Interior Metal Stud Partition Walls," by R.L. Wood and T.C. Hutchinson, 9/12/12.

MCEER-12-0008 "Assessment of Floor Accelerations in Yielding Buildings," by J.D. Wieser, G. Pekcan, A.E. Zaghi, A.M. Itani and E. Maragakis, 10/5/12.

MCEER-13-0001 "Experimental Seismic Study of Pressurized Fire Sprinkler Piping Systems," by Y. Tian, A. Filiatrault and G. Mosqueda, 4/8/13.

MCEER-13-0002 "Enhancing Resource Coordination for Multi-Modal Evacuation Planning," by D.B. Hess, B.W. Conley and C.M. Farrell, 2/8/13.

MCEER-13-0003 "Seismic Response of Base Isolated Buildings Considering Pounding to Moat Walls," by A. Masroor and G. Mosqueda, 2/26/13.

MCEER-13-0004 "Seismic Response Control of Structures Using a Novel Adaptive Passive Negative Stiffness Device," by D.T.R. Pasala, A.A. Sarlis, S. Nagarajaiah, A.M. Reinhorn, M.C. Constantinou and D.P. Taylor, 6/10/13.

MCEER-13-0005 "Negative Stiffness Device for Seismic Protection of Structures," by A.A. Sarlis, D.T.R. Pasala, M.C. Constantinou, A.M. Reinhorn, S. Nagarajaiah and D.P. Taylor, 6/12/13.

MCEER-13-0006 "Emilia Earthquake of May 20, 2012 in Northern Italy: Rebuilding a Resilient Community to Withstand Multiple Hazards," by G.P. Cimellaro, M. Chiriatti, A.M. Reinhorn and L. Tirca, June 30, 2013.

MCEER-13-0007 "Precast Concrete Segmental Components and Systems for Accelerated Bridge Construction in Seismic Regions," by A.J. Aref, G.C. Lee, Y.C. Ou and P. Sideris, with contributions from K.C. Chang, S. Chen, A. Filiatrault and Y. Zhou, June 13, 2013.

MCEER-13-0008 "A Study of U.S. Bridge Failures (1980-2012)," by G.C. Lee, S.B. Mohan, C. Huang and B.N. Fard, June 15, 2013.

MCEER-13-0009 "Development of a Database Framework for Modeling Damaged Bridges," by G.C. Lee, J.C. Qi and C. Huang, June 16, 2013.

MCEER-13-0010 "Model of Triple Friction Pendulum Bearing for General Geometric and Frictional Parameters and for Uplift Conditions," by A.A. Sarlis and M.C. Constantinou, July 1, 2013.

MCEER-13-0011 "Shake Table Testing of Triple Friction Pendulum Isolators under Extreme Conditions," by A.A. Sarlis, M.C. Constantinou and A.M. Reinhorn, July 2, 2013.

MCEER-13-0012 "Theoretical Framework for the Development of MH-LRFD," by G.C. Lee (coordinating author), H.A Capers, Jr., C. Huang, J.M. Kulicki, Z. Liang, T. Murphy, J.J.D. Shen, M. Shinozuka and P.W.H. Yen, July 31, 2013.

MCEER-13-0013 "Seismic Protection of Highway Bridges with Negative Stiffness Devices," by N.K.A. Attary, M.D. Symans, S. Nagarajaiah, A.M. Reinhorn, M.C. Constantinou, A.A. Sarlis, D.T.R. Pasala, and D.P. Taylor, September 3, 2014.

MCEER-14-0001 "Simplified Seismic Collapse Capacity-Based Evaluation and Design of Frame Buildings with and without Supplemental Damping Systems," by M. Hamidia, A. Filiatrault, and A. Aref, May 19, 2014.

MCEER-14-0002 "Comprehensive Analytical Seismic Fragility of Fire Sprinkler Piping Systems," by Siavash Soroushian, Emmanuel "Manos" Maragakis, Arash E. Zaghi, Alicia Echevarria, Yuan Tian and Andre Filiatrault, August 26, 2014.

MCEER-14-0003 "Hybrid Simulation of the Seismic Response of a Steel Moment Frame Building Structure through Collapse," by M. Del Carpio Ramos, G. Mosqueda and D.G. Lignos, October 30, 2014.

MCEER-14-0004 "Blast and Seismic Resistant Concrete-Filled Double Skin Tubes and Modified Steel Jacketed Bridge Columns," by P.P. Fouche and M. Bruneau, June 30, 2015.

MCEER-14-0005 "Seismic Performance of Steel Plate Shear Walls Considering Various Design Approaches," by R. Purba and M. Bruneau, October 31, 2014.

MCEER-14-0006 "Air-Blast Effects on Civil Structures," by Jinwon Shin, Andrew S. Whittaker, Amjad J. Aref and David Cormie, October 30, 2014.

MCEER-14-0007 "Seismic Performance Evaluation of Precast Girders with Field-Cast Ultra High Performance Concrete (UHPC) Connections," by G.C. Lee, C. Huang, J. Song, and J. S. O'Connor, July 31, 2014.

MCEER-14-0008 "Post-Earthquake Fire Resistance of Ductile Concrete-Filled Double-Skin Tube Columns," by Reza Imani, Gilberto Mosqueda and Michel Bruneau, December 1, 2014.

MCEER-14-0009 "Cyclic Inelastic Behavior of Concrete Filled Sandwich Panel Walls Subjected to In-Plane Flexure," by Y. Alzeni and M. Bruneau, December 19, 2014.

MCEER-14-0010 "Analytical and Experimental Investigation of Self-Centering Steel Plate Shear Walls," by D.M. Dowden and M. Bruneau, December 19, 2014.

MCEER-15-0001 "Seismic Analysis of Multi-story Unreinforced Masonry Buildings with Flexible Diaphragms," by J. Aleman, G. Mosqueda and A.S. Whittaker, June 12, 2015.

MCEER-15-0002 "Site Response, Soil-Structure Interaction and Structure-Soil-Structure Interaction for Performance Assessment of Buildings and Nuclear Structures," by C. Bolisetti and A.S. Whittaker, June 15, 2015.

MCEER-15-0003 "Stress Wave Attenuation in Solids for Mitigating Impulsive Loadings," by R. Rafiee-Dehkharghani, A.J. Aref and G. Dargush, August 15, 2015.

MCEER-15-0004 "Computational, Analytical, and Experimental Modeling of Masonry Structures," by K.M. Dolatshahi and A.J. Aref, November 16, 2015.

MCEER-15-0005 "Property Modification Factors for Seismic Isolators: Design Guidance for Buildings," by W.J. McVitty and M.C. Constantinou, June 30, 2015.

MCEER-15-0006 "Seismic Isolation of Nuclear Power Plants using Sliding Isolation Bearings," by Manish Kumar, Andrew S. Whittaker and Michael C. Constantinou, December 27, 2015.

MCEER
EARTHQUAKE ENGINEERING TO EXTREME EVENTS
University at Buffalo, The State University of New York
133A Ketter Hall ▪ Buffalo, New York 14260-4300
Phone: (716) 645-3391 ▪ Fax: (716) 645-3399
Email: *mceer@buffalo.edu* ▪ Web: *http://mceer.buffalo.edu*
University at Buffalo *The State University of New York*

ISSN 1520-295X